Methods in Molecular Biology™

VOLUME 242

Atomic Force Microscopy

Biomedical Methods and Applications

Edited by

Pier Carlo Braga
Davide Ricci

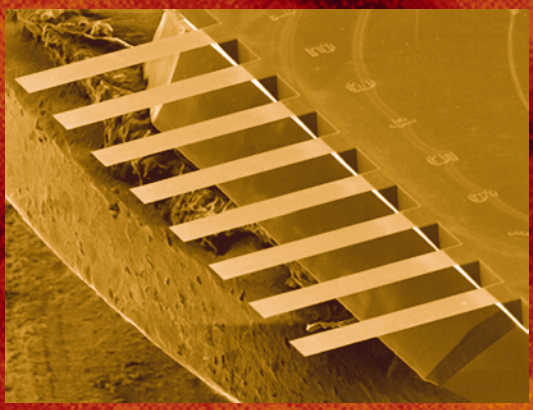

HUMANA PRESS

1

How the Atomic Force Microscope Works

Davide Ricci and Pier Carlo Braga

1. Introduction

Microscopes have always been one of the essential instruments for research in the biomedical field. Radiation-based microscopes (such as the light microscope and the electron microscope) have become trustworthy companions in the laboratory and have contributed greatly to our scientific knowledge. However, although digital techniques in recent years have still enhanced their performance, the limits of their inherent capabilities have been progressively reached.

The advent of scanning probe microscopes and especially of the atomic force microscope (AFM; **ref. *1***) has opened new perspectives in the investigation of biomedical specimens and induces to look again with rejuvenated excitement at what we can learn by "looking" at our samples. Novices are at first mesmerized by two features: the name of the instrument and the colorful 3D computer visualization of surfaces. One later learns that quite often it is not possible to obtain the "atomic" resolution that one hoped to achieve ***(2–4)*** but that nevertheless images do contain details not observable with any other instrument. The tri-dimensional mapping of the surface gains scientific relevance when one realizes that it is not just fancy surface reconstruction but that true topographic data with vertical resolution down to the subnanometer range is readily available. Moreover, when simplified sample preparation and the possibility of investigating specimens in liquid environment become apparent, one becomes convinced that he or she must find a way to apply AFM to his or her own research.

2. Performance Range of AFM

AFM images show significant information about surface features with unprecedented clarity. The AFM can examine any sufficiently rigid surface

From: *Methods in Molecular Biology, vol. 242: Atomic Force Microscopy: Biomedical Methods and Applications*
Edited by: P. C. Braga and D. Ricci © Humana Press Inc., Totowa, NJ

either in air or with the specimen immersed in a liquid. Recently developed instruments can allow temperature control of the sample, can be equipped with a closed chamber for environmental control, and can be mounted on an inverted microscope for simultaneous imaging through advanced optical techniques.

The field of view can vary from the atomic and molecular scale up to sizes larger than 125 μm so that data can be compared with other information obtained with lower resolution techniques. The AFM can also examine rough surfaces because its vertical range can be up to 8–10 μm. Large samples can be fitted directly in the microscope without cutting. With stand-alone instruments, any area on flat or nearly flat specimens can be investigated. In addition to its superior resolution with respect to optical microscopes, the AFM has these key advantages with respect to electron microscopes. Compared with the scanning electron microscope (SEM), the AFM provides superior topographic contrast, in addition to direct measurements of surface features providing quantitative height information.

Because the sample need not be electrically conductive, no metallic coating of the sample is required. Hence, no dehydration of the sample is necessary as with SEM, and samples may be imaged in their hydrated state. This eliminates the shrinkage of biofilm associated with imaging using SEM, yielding a non-destructive technique. The resolution of AFM is higher than that of environmental SEM, where hydrated images can also be obtained and extracellular polymeric substances may not be imaged.

Compared with transmission electron microscopes, 3D AFM images are obtained without expensive sample preparation and yield far more complete information than the 2D profiles available from cross-sectioned samples.

In the following subheadings we will give a brief outline of how the AFM works followed by a description of the parts that can be added to the basic instrument. Our overview makes no pretense to completeness but aims at simplicity. For a more thorough description of the physical principles involved in the operation of these instruments, we refer you to the specialized literature.

3. The Microscope

In **Fig. 1**, a schematic diagram of an AFM is shown ***(1,5)***. In principle, AFM can bring to mind the record player, but it incorporates a number of refinements that enable it to achieve atomic-scale resolution, such as very sharp tips, flexible cantilevers, a sensitive deflection sensor, and high-resolution tip–sample positioning.

3.1. The Tip and Cantilever

The tip, which is mounted at the end of a small cantilever, is the heart of the instrument because it is brought in closest contact with the sample and gives

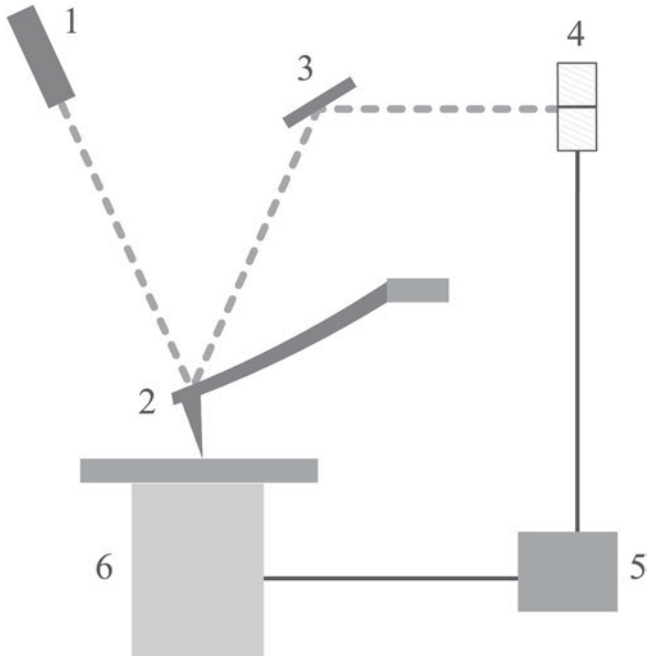

Fig. 1. Schematic diagram of a scanned-sample AFM. In the case of scanned probe, it is the tip that is scanned instead of the sample. *1*, Laser diode; *2,* cantilever; *3,* mirror; *4,* position-sensitive photodetector; *5,* electronics; and *6,* scanner with sample.

rise to the image though its force interactions with the surface. When the first AFM was made, a very small diamond fragment was carefully glued to one end of a tiny piece of gold foil. Today, the tip–cantilever assembly typically is fabricated from silicon or silicon nitride and, using technology similar to that applied to integrated circuit fabrication, allows a good uniformity of characteristics and reproducibility of results ***(6,7)***. The essential parameters are the sharpness of the apex, measured by the radius of curvature, and the aspect ratio of the whole tip (**Fig. 2**).

Although it would seem that sharper tips should yield more detailed images, this may not occur with all samples: in fact, quite often, so-called "atomic resolution" on crystals is obtained best with standard silicon nitride tips. In general, one can choose among one of three types of tip. The standard tip is usually a 3-μm tall pyramid with approx 30-nm end radius. The electron-beam-deposited tip or "super tip" improves on this with an electron-beam–induced deposit of material at the apex of the tip, offering a higher aspect ratio and end radius than the normal tip, albeit with the drawback of fragility. Finally, tips made from silicon (either polysilicon or single crystal) through improved

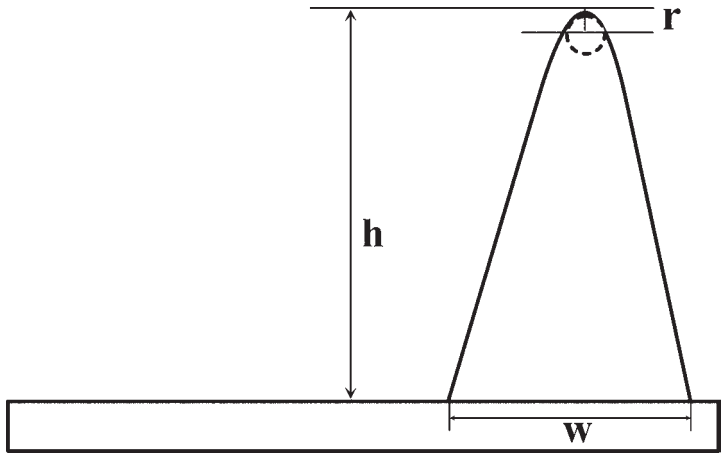

Fig. 2. The essential parameters in a tip are the radius of curvature (*r*) and the aspect ratio (ratio of *h* to *w*).

microlithographic techniques have a higher aspect ratio and small apex radius of curvature, maintaining reproducibility and durability ***(8)***.

The cantilever carrying the tip is attached to a small glass "chip" that allows easy handling and positioning in the instrument. There are essentially two designs for cantilevers, the "V" shaped and the single-arm kind (**Fig. 3**), which have different torsional properties. The length, width, and thickness of the beam(s) determine the mechanical properties of the cantilever and have to be chosen depending on mode of operation needed and on the sample to be investigated. Cantilevers are essentially classified by their force (or spring) constant and resonance frequency: soft and low-resonance frequency cantilevers are more suitable for imaging in contact and resonance mode in liquid, whereas stiff and high-resonance frequency cantilevers are more appropriate for resonance mode in air ***(9)***.

3.2. Deflection Sensor

AFMs can generally measure the vertical deflection of the cantilever with picometer resolution. To achieve this, most AFMs today use the optical lever or beam-bounce method, a device that achieves resolution comparable to an interferometer while remaining inexpensive and easy to use.

In this system, a laser beam is reflected from the backside of the cantilever (often coated by a thin metal layer to make a mirror) onto a position-sensitive

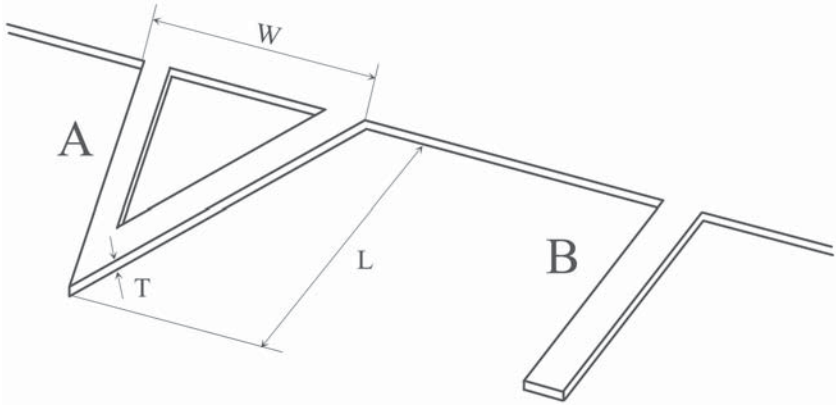

Fig. 3. Triangular **(A)** and single-beam **(B)** cantilevers. The mechanical properties, such as the force constant and resonant frequency, depend on the values of width (*W*), length (*L*), and thickness (*T*).

photodetector consisting of two side-by-side photodiodes. In this arrangement, a small deflection of the cantilever will tilt the reflected beam and change the position of beam on the photodetector. The difference between the two photodiode signals indicates the position of the laser spot on the detector and thus the angular deflection of the cantilever.

Because the distance between cantilever and detector is generally three orders of magnitude greater than the length of the cantilever (millimeters compared to micrometers), the optical lever greatly magnifies motions of the tip giving rise to an extremely high sensitivity.

3.3. Image Formation

Images are formed by recording the effects of the interaction forces between tip and surface as the cantilever is scanned over the sample. The scanner and the electronic feedback circuit, together with sample, cantilever, and optical lever form a feedback loop set up for the purpose. The presence of a feedback loop is a key difference between AFM and older stylus-based instruments so that AFM not only measures the force on the sample but also controls it, allowing acquisition of images at very low tip-to-sample forces ***(5,10)***.

The scanner is an extremely accurate positioning stage used to move the tip over the sample (or the sample under the tip) to form an image, and generally in modern instruments is made from a piezoelectric tube. The AFM electronics drives the scanner across the first line of the scan and back. It then steps in the

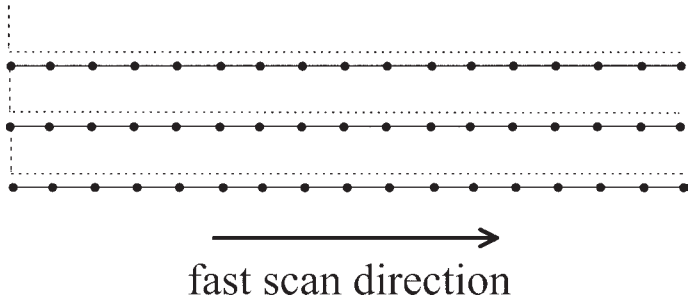

Fig. 4. Raster scan for image acquisition. The AFM electronics drive the scanner across the first line of the scan and back. The scanner then steps in the perpendicular direction to the second scan line, moves across it and back, then to the third line, and so forth.

perpendicular direction to the second scan line, moves across it and back, then to the third line, and so forth (**Fig. 4**).

As the probe is scanned over the surface, a topographic image is obtained storing the vertical control signals sent by the feedback circuit to the scanner moving it up and down to follow the surface morphology while keeping the interaction forces constant. The image data are sampled digitally at equally spaced intervals, generally from 64 up to 2048 points per line. The number of lines is usually chosen to be equal to the number of data points per line, obtaining at the end a square grid of data points each corresponding to the relative x, y, and z coordinates in space of the sample surface ***(11)***.

Usually during scanning data are represented by gray scale images, in which the brightness of points can range from black to white across 256 levels corresponding to the information acquired by the microscope (that can be height, force, phase, and so on).

4. A Variety of Instruments and Options

The first instruments introduced on the market had all very similar features and range of applications: they had scanners with small range, limited optical access, and could accommodate only small samples. Essentially they where built to make very high-resolution imaging on flat samples in a dry environment. As the possibilities of AFM were developed, a wider range of instruments, optimized for specific applications, have been developed. We can now find instruments that are specifically designed for large samples, such as silicon wafers, that have metrological capabilities, utilize scanner close loop operation, are optimized for liquid and electrochemistry operation, and can be

mounted on an inverted microscope for biological investigations. Usually, one single instrument can have different options to extend its capabilities, but to date it is not possible to have an instrument that covers all possible applications with maximum performance. For this reason, it is necessary to have clearly in mind what will be the main features that are desired in an instrument before its purchase, understanding at the same time that a loss of performance in other aspects may be possible.

One can distinguish between two main classes: scanned-sample and scanned-tip microscopes. We give a brief description of the advantages of one system with respect to the other.

4.1. Scanned Sample

This scanned-sample AFM is the first design in which the sample is attached to the scanner and moved under the tip. Depending on how the cantilever holder, laser, and photodetector are assembled, it can easily accommodate an overhead microscope provided that long focal length objectives are used. A clear view of where the tip is landing is usually possible, speeding up the time it takes to get a meaningful image of the sample.

Scanners with wide x,y, and z range are usually available and closed loop control feedback is more easily implemented in this scheme and often a lower mechanical noise level can be obtained allowing higher ultimate resolution.

There are quite a few drawbacks. First of all, the size and weight of the sample has to be limited because it is sitting on the scanner and may change its behavior. For the same reason, operation in liquid is impaired because liquid cells tend to be small and difficult to seal, and liquid flow or temperature control are more complicated to implement. Notwithstanding these difficulties, excellent results can be obtained on typical biomedical science specimens by ingeniously adapting them to the instruments characteristics.

4.2. Scanned Tip

In the scanned-tip method of operation, the sample stays still and it is the cantilever, attached to the scanner, which is moved across the surface. Although for scanning tunneling microscopes this was one of the first solutions applied, to build a scanned tip AFM requires overcoming some difficulties, essentially related to adapting the beam bounce detection scheme to a moving cantilever. For this reason, it has been only recently that models made according to this design have been marketed, after appropriate technology was developed. The first examples were the so-called “stand-alone” systems, usually an AFM resting on three legs and able to scan the surface of any object under its probe. Later, specialized instruments were developed, capable of being coupled or even integrated into inverted optical microscopes for biological applications.

With respect to the scanned-sample models, scanned-tip instruments can be more easily equipped with temperature-controlled stages, open or closed liquid cells, liquid flow systems, electrochemistry cells, and controlled atmosphere chambers. Concerning limitations, one could say that what is gained on one side is lost on the other. For example, often the overall noise level is higher, limiting ultimate resolution. Large scan areas are more difficult to scan because tracking systems have to be used to keep the laser spot on the back of the cantilever. A top view of samples is obstructed by the scanner assembly: special hollow tubes have been developed recently, but even so on-axis microscopes, which are useful on nontransparent samples, will still have limited resolution and lateral field of view.

5. Loading a Sample in the Microscope

5.1. Imaging Dry Samples

Samples to be imaged in atmospheric environment are often simply glued to a sample holder, usually a metal disk. The disk is then inserted in the AFM, where it is held firmly by a small magnet. An essential point is that the sample has to be firmly adherent to the sample holder; otherwise, very poor imaging will be achieved. For this reason, one has to be careful in the choice of the glue or sticky tape: slow drying glue or thick sticky tape should be avoided. A drawback is that after use in the AFM, the sample is difficult to take off without damage.

Some systems, usually scanned-tip, can accept samples directly, securing them with a metal clip or springs. This method allows sample recovery without damage for further use in other experiments, but it can be less stable and needs special care for high-resolution work.

Sometimes, because of the ease of use of the AFM, one forgets to be careful while handling the sample and either fingerprints or dust from a dirty environment contaminates the sample. It is best to keep a reserved area of the laboratory free from contaminants for the operations of sample and cantilever mounting.

5.2. Imaging in Liquid

One of the main reasons for the success of AFM in biomedical investigations is its ability to scan samples in physiological condition, that is, immersed in liquid solutions ***(12,13)***. Just to make an example, scanned-tip systems can often be directly used to image cells into a standard Petri dish. Each manufacturer has its own design of liquid cells, sometimes different ones depending on the application, and users may decide to make their own to fit specific needs. A few additional things that have to be taken care of when imaging in liquid are

the temperature of the solution (eventually added during imaging; **ref. *14***) and maintenance of the liquid cell and cantilever holder assembly. Because the cantilever is extremely sensitive to temperature changes, it is important to let the system equilibrate before taking images. For example, in the case of contact mode imaging with silicon nitride cantilevers and tips, a large change in time of the signal on the photodetector corresponding to cantilever deflection can be observed in the presence of a temperature change ***(15)***. If temperature is not stable prior to approach of the tip to the sample and one starts taking images, after some time the applied force could be quite different than at the beginning of the imaging session.

Once finished using the microscope for imaging in liquid, it is essential to immediately clean thoroughly all parts that have been in contact with the solution to avoid contamination of future experiments. Usually, it should be possible to disassemble and sonicate all vital parts of the liquid cell and the cantilever holder.

6. Future Developments

The AFM is part of a family of scanning probe microscopes that has a great growth potential. It is a fact that the majority of novel applications and techniques developed in scanning probe microscopes in the last years are related to the life sciences. There is still much room for technical improvement: electronics, scanners, and tips are constantly improving. Scan speed limitations, sample accessibility, and ease of use have been addressed and can be still improved. As more and more biomedical researchers will be involved in the use of AFM, with their experience they will be able contribute in developing an instrument less related to the physical science (its origin) and more tailored to our specific needs.

References

1. Binnig, G., Quate, C. F., and Gerber, Ch. (1986) Atomic force microscope. *Phys. Rev. Lett.* **56,** 930–933.
2. Binnig, G., Gerber, C., Stoll, E., Albrecht, T. R., and Quate, C. F. (1987) Atomic resolution with the atomic force microscope. *Europhys. Lett.* **3,** 1281–1286.
3. Hug, H. J., Lantz, M. A., Abdurixit, A., et al. (2001) Subatomic features in atomic force microscopy images. *Science* **291,** 2509.
4. Jarvis, M. R., Perez, R., and Payne, M. C. (2001) Can atomic force microscopy achieve atomic resolution in contact mode? *Phys. Rev. Lett.* **86,** 1287–1290.
5. Alexander, S., Hellemans, L., Marti, O., et al. (1989) An atomic-resolution atomic-force microscope implemented using an optical lever. *J. Appl. Phys.* **65,** 164–167.
6. Albrecht, T. R., Akamine, S., Carver, T.E., and Quate, C. F. (1990) Microfabrication of cantilever styli for the atomic force microscope. *J. Vac. Sci. Technol. A* **8,** 3386–3396.
7. Tortonese, M. (1997). Cantilevers and tips for atomic force microscopy. *IEEE Engl. Med. Biol. Mag.* **16,** 28–33.

8. Sheng, S., Czajkowsky, D. M., and Shao, Z. (1999) AFM tips: How sharp are they? *J. Microsc.* **196,** 1–5.
9. Cleveland, J. P., Manne, S., Bocek, D., and Hansma, P. K. (1993) A non-destructive method for determining the spring constant of cantilevers for scanning force microscopy. *Rev. Sci. Instrum.* **64,** 403–405.
10. Meyer, G. and Amer, N. M. (1988) Novel approach to atomic force microscopy. *Appl. Plrys. Lett.* **53,** 1045–1047.
11. Baselt, D. R., Clark, S. M., Youngquist, M. G., Spence, C. F., and Baldeschwieler, J. D. (1993) Digital signal control of scanned probe microscopes. *Rev. Sci. Instrum.* **64,** 1874–1882.
12. Wade, T., Garst, J. F., and Stickney, J. L. (1999). A simple modification of a commercial atomic force microscopy liquid cell for in situ imaging in organic, reactive or air sensitive environments. *Rev. Sci. Instr.* **70,** 121–124.
13. Lehenkari, P. P., Charras, G. T., Nykanen, A., and Horton, M. A. (2000) Adapting atomic force microscopy for cell biology. *Ultramicroscopy* **82,** 289–295.
14. Workman, R. K. and Manne, S. (2000) Variable temperature fluid stage for atomic force microscopy. *Rev. Sci. Instrum.* **71,** 431–436.
15. Radmacher, M., Cleveland, J. P., and Hansma, P. K. (1995) Improvement of thermally induced bending of cantilevers used for atomic force microscopy. *Scanning* **17,** 117–121.

2

Imaging Methods in Atomic Force Microscopy

Davide Ricci and Pier Carlo Braga

1. Introduction

One can easily distinguish between two general modes of operation of the atomic force microscope (AFM) depending on absence or presence in the instrumentation of an additional device that forces the cantilever to oscillate in the proximity of its resonant frequency. The first case is usually called static mode, or DC mode, because it records the static deflection of the cantilever, whereas the second takes a variety of names (some patented) among which we may point out the resonant or AC mode. In this case, the feedback loop will try to keep at a set value not the deflection but the amplitude of the oscillation of the cantilever while scanning the surface. To do this, additional electronics are necessary in the detection circuit, such as a lock-in or a phase-locked loop amplifier, and also in the cantilever holder to induce the oscillatory excitation.

From a physical point of view, one can make a distinction between the two modes depending on the sign of the forces involved in the interaction between tip and sample, that is, by whether the forces there are attractive or repulsive ***(1)***. In **Fig. 1**, an idealized plot of the forces between tip and sample is shown, highlighting where typical imaging modes operate. In the following we briefly describe the DC and AC modes of operation relevant to the kind of samples that usually are investigated in the biomedical field.

2. DC Modes

2.1. Contact Mode

Also called constant force mode, the contact mode is the most direct AFM mode, where the tip is brought in contact with the surface and the cantilever deflection is kept constant during scanning by the feedback loop. Image contrast depends on the applied force, which again depends on the cantilever spring

From: *Methods in Molecular Biology, vol. 242: Atomic Force Microscopy: Biomedical Methods and Applications*
Edited by: P. C. Braga and D. Ricci © Humana Press Inc., Totowa, NJ

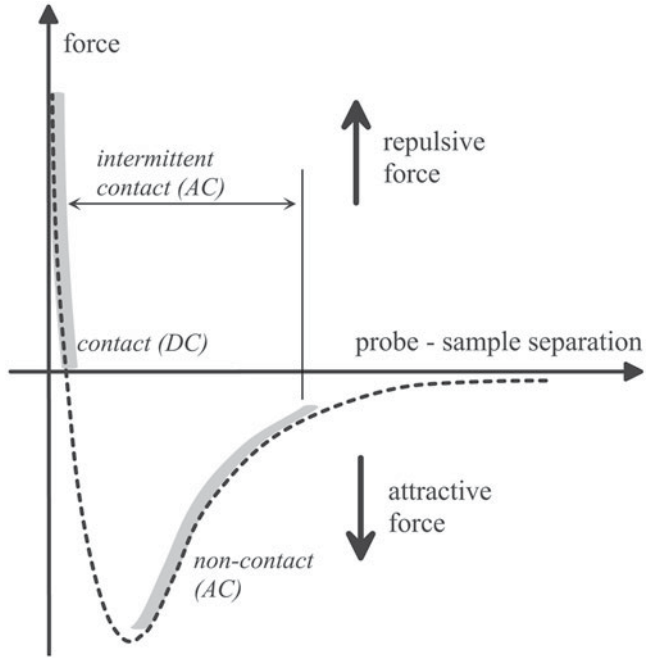

Fig. 1. Idealized plot of the forces between tip and sample, highlighting where typical imaging modes are operative.

Fig. 2. In contact mode, the tip follows directly the topography of the surface while it is scanned.

constant (**Fig. 2**). Softer cantilevers are used for softer samples. It can be used easily also in liquids, allowing a considerable reduction of capillary forces between tip and sample and, hence, damage to the surface (**Fig. 3;** refs. ***2,3***). Because the tip is permanently in contact with the surface while scanning, a considerable shear force can be generated, causing damage to the sample, especially on very soft specimens like biomolecules or living cells ***(4)***.

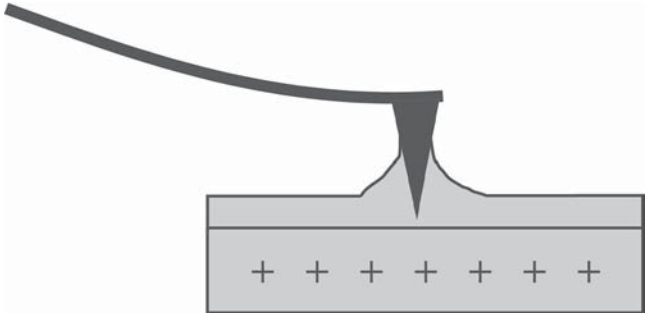

Fig. 3. In contact mode, capillary forces caused by a thin water layer and electrostatic forces can considerably increase the total force between sample and tip.

2.2. Deflection or Error Mode

In same cases, especially on rough and relatively rigid samples, the error signal (i.e., the difference between the set point and the effective deflection of the cantilever that occurs during scanning as a result of the finite time response of the feedback loop) is used to record images. By turning down on purpose the feedback gain, the cantilever will press harder on asperities and less on depressions, giving rise to images that contain high-frequency information otherwise not visible ***(5)***. This method has been extensively used to image submembrane features in living cells. The same method is also often used to record high-resolution images on crystals.

2.3. Lateral Force Microscopy

In this case (a variation of standard contact mode), while scanning the sample not only the vertical deflection of the cantilever but also the lateral deflection (torsion) is measured by the photodetector assembly, which in this case will have four photodiodes instead of two (**Fig. 4**). The degree of torsion of the cantilever supporting the probe is a relative measure of surface friction caused by the lateral force exerted on the scanning probe ***(6)***. This method has been used to discriminate between areas of the sample that have the same height (i.e., that are on a same plane) but that present different frictional properties because of absorbates.

3. AC Modes

All AC modes require setting the cantilever in oscillation using an additional driving signal. This can be accomplished by driving the cantilever with a piezoelectric motor (acoustic mode) or, as developed more recently, by directly driving by external coils a probe coated with a magnetic layer (magnetic mode).

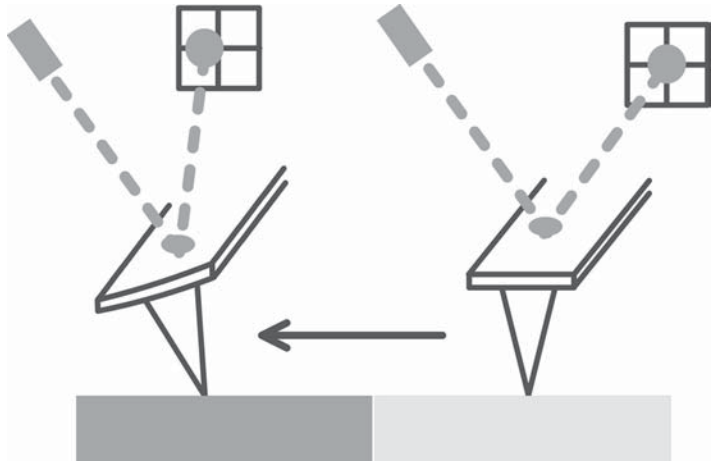

Fig. 4. Using a four-section photodetector, it is possible to measure also the torsion of the cantilever during contact mode AFM scanning. The torsion of the cantilever reflects changes in the surface chemical composition.

This second method is giving interesting results, especially in liquid, as it allows better control of the oscillation dynamics and has inherently less noise *(7,8)*.

3.1. Noncontact Mode

An oscillating probe is brought into proximity of (but without touching) the surface of the sample and senses the van der Waals attractive forces that induce a frequency shift in the resonant frequency of a stiff cantilever (**Fig. 5**; **ref. *9***). Images are taken by keeping a constant frequency shift during scanning, and usually this is performed by monitoring the amplitude of the cantilever oscillation at a fixed frequency and feeding the corresponding value to the feedback loop exactly as for the DC modes. The tip–sample interactions are very small in noncontact mode, and good vertical resolution can be achieved, whereas lateral resolution is lower than in other operating modes. The greatest drawback is that it cannot be used in liquid environment, only on dry samples. Also, even on dry samples, if a thick contamination or water layer is present the tip can sometimes be trapped, not having sufficient energy to detach from the sample because of the small amplitude of oscillation.

3.2. Intermittent Contact Mode

The general scheme is similar to that of noncontact mode, but in this case during oscillation the tip is brought into contact with the sample surface so that a dampening of the cantilever oscillation amplitude is induced by the same

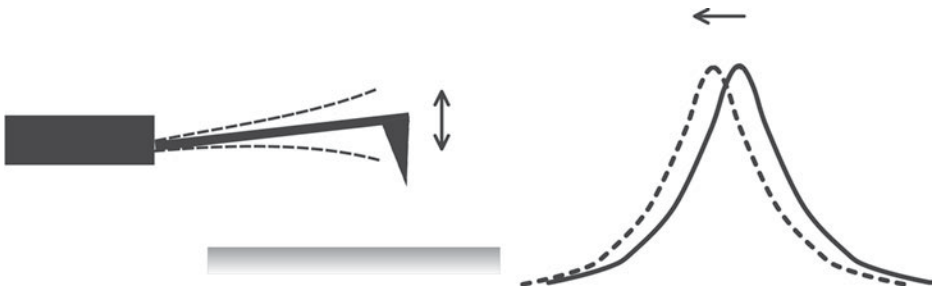

Fig. 5. In noncontact mode of operation, a vibrating tip is brought near the sample surface, sensing the attractive forces. This induces a frequency shift in the resonance peak of the cantilever that is used to operate the feedback.

repulsive forces that are present in contact mode (**Fig. 6**). Usually in intermittent contact the oscillation amplitude of the cantilever is larger than the one used for noncontact. There are several advantages that have made this mode of operation quite popular. The vertical resolution is very good together with lateral resolution, there is less interaction with the sample compared with contact mode (especially lateral forces are greatly reduced), and it can be used in liquid environment ***(10–14)***. This mode of operation is the most generally used for imaging biological samples and is still under constant improvement, thanks to additional features such as Q-control ***(15)*** or magnetically driven tips ***(7,8)***.

3.3. Phase Imaging Mode

If the phase lag of the cantilever oscillation relative to driving signal is recorded in a second acquisition channel during imaging in intermittent contact mode, noteworthy information on local properties, such as stiffness, viscosity, and adhesion, can be detected that are not revealed by other AFM techniques ***(16)***. In fact, it is good practice to always acquire simultaneously both the amplitude and phase signals during intermittent contact operation, as the physical information is entwined and all the data is necessary to interpret the images obtained ***(17–21)***.

3.4. Force Modulation

In this case, a low-frequency oscillation is induced (usually to the sample) and the corresponding cantilever deflection recorded while the tip is kept in contact with the sample (**Fig. 7**). The varying stiffness of surface features will induce a corresponding dampening of the cantilever oscillation, so that local relative visco-elastic properties can be imaged.

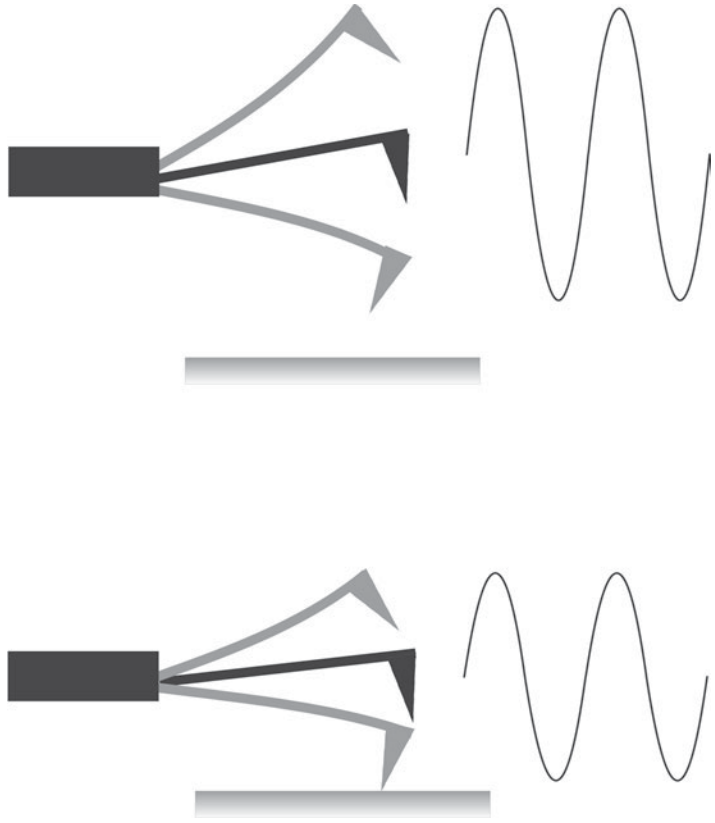

Fig. 6. In intermittent contact mode, the free oscillation of a vibrating cantilever is dampened when the tip touches the sample surface at each cycle. The image is performed keeping constant the oscillation amplitude decrease while scanning.

4. Beyond Topography Using Force Curves

The AFM can provide much more information than taking images of the surface of the sample. The instrument can be used to record the amount of force felt by the cantilever as the probe tip is brought close to a sample surface, eventually indent the surface and then pulled away. By doing this, the long-range attractive or repulsive forces between the probe tip and the sample surface can be studied, local chemical and mechanical properties like adhesion and elasticity may be investigated, and even the bonding forces between molecules may be directly measured ***(22–24)***. By acquiring a series of force curves, one at each point of a square grid, it is possible to acquire a so called force-vs-volume map that will allow the user to compute images representing local mechanical properties of the sample observed.

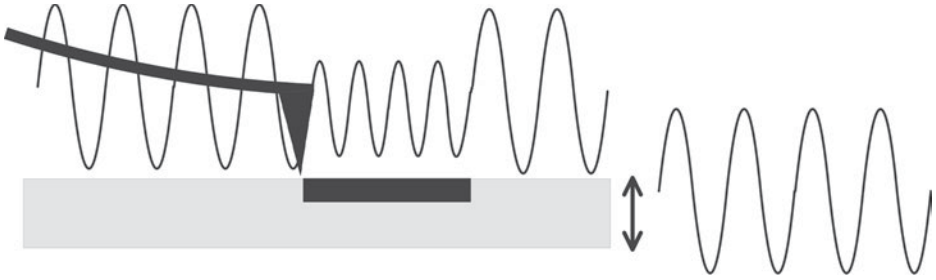

Fig. 7. During force modulation, the tip is kept in contact with the sample and the different local properties of the sample will be reflected in the amplitude of the oscillation induced in the cantilever.

Force curves typically show the deflection of the cantilever as the probe is brought vertically towards and then away from the sample surface using the vertical motion of the scanner driven by a triangular wave (**Fig. 8**). By controlling the amplitude and frequency of the vertical movement of the scanner it is possible to change the distance and speed that the AFM probe travels during the force measurement. Conceptually what happens during a force curve is not much different from what happens between tip and sample during intermittent contact imaging. The differences are in the frequency, much lower for force curves, and the distance of travel of the probe, much smaller in intermittent contact. In a force curve, many data points are acquired during the motion, so that very small forces can be detected and interpreted by fitting the force curve according to theoretical models.

Two details of technique are worth special care when obtaining quantitative data from force-vs-distance curves. The position-sensitive photodetector signal has to be calibrated so to measure accurately the deflection of the cantilever, and after calibration it is essential that the laser alignment is left unchanged. Usually the software of the AFM has a routine for such calibration, performed by taking a force curve on a hard sample and using the scanner's vertical movement as reference (which means that the scanner also has to be accurately calibrated). At this point, the curve we are plotting is not yet a force curve but a calibrated deflection curve. The next step is to convert it to a force curve using the force constant of the cantilever we are using. Manufacturers usually specify this value, but for each cantilever there can be quite large variations, so that for accurate work direct determination becomes necessary. There are different ways to measure the force constant, some requiring external equipment for measuring resonant frequency (such as spectrum analyzers) and others making use of reference cantilevers ***(25,26)***.

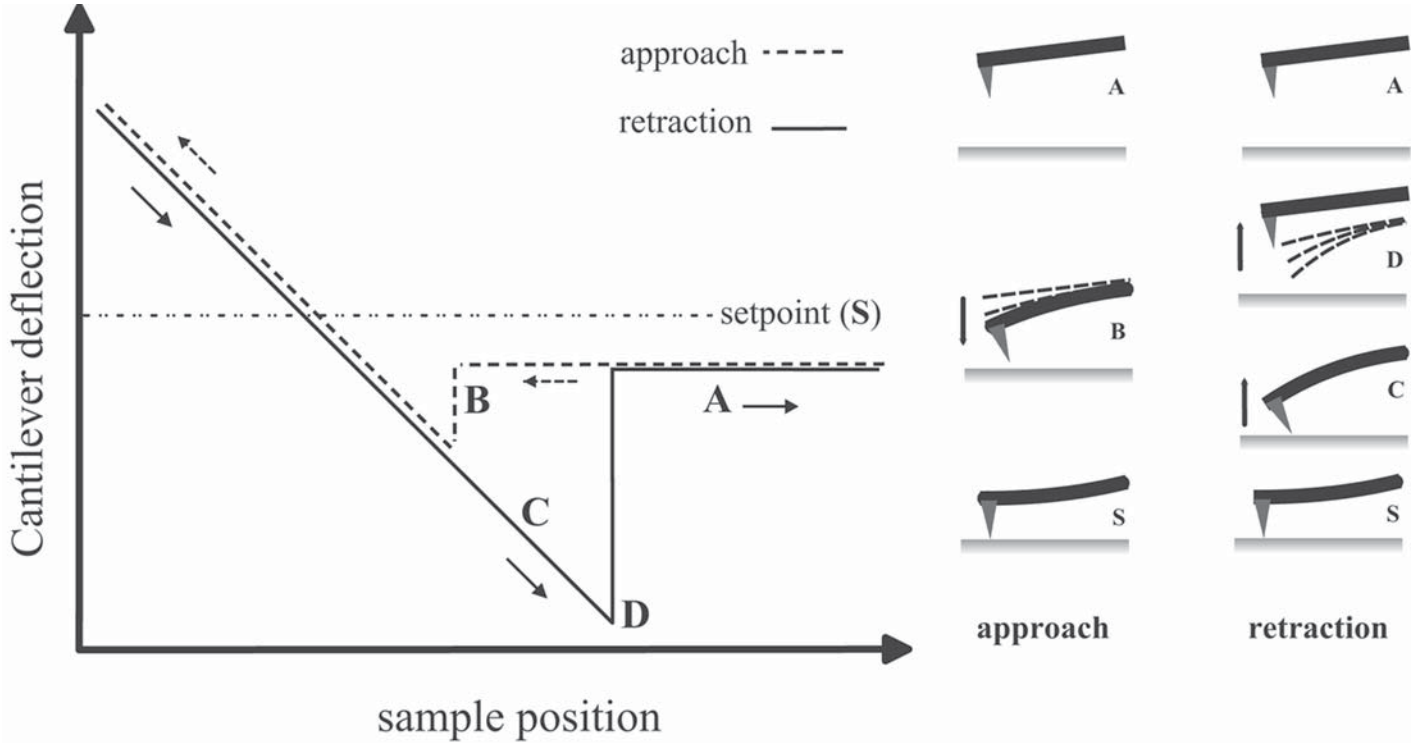

Fig. 8. Idealized force curve and cantilever behavior. From positions A to B, the tip is approaching the surface, and at position B contact is made (if an attractive or repulsive force is active before contact, the portion of the force curve will reflect it). After B, the cantilever bends until it reaches the specified force limit that is to be applied (S). Depending on the relative stiffness of the cantilever with respect to the sample, during this portion of the curve the tip can indent the surface. The tip is then withdrawn towards positions C and D. At position D, under application of the retraction force, the tip detaches from the sample (often referred to as 'snap off'). Between positions D and A, the cantilever returns to its resting position and is ready for another measurement.

Form the point of view of biomedical applications, interesting experiments can be performed by coating the tip with a ligand and approaching through a force curve a surface where receptor molecules can be found. In this case the portion of the curve before snap off will have a different shape, reflecting the elongation of the bond between ligand and receptor before dissociation: from the shape the curve, it is possible to derive quantitative information on the binding forces ***(27–29)***.

If a force curve is taken at each point of a $N \times N$ grid, it is possible to derive images that are directly correlated to a physical property of the surface of the sample. For example, if the approach portion of each curve after contact is fitted using indentation theory, a map of the sample stiffness can be calculated. This data can be represented by an image in which the level of gray of each pixel, instead of representing the height of the sample, will correspond to the elasticity modulus. Similar images can be calculated for adhesion, binding, electrostatic forces, and so on ***(30,31)***.

References

1. Israelachvili, J. N. (1992) *Intermolecular and Surface Forces*, 2nd ed. Academic Press, London.
2. Weisenhorn A. L., Maivald, P., Butt, H. J., and Hansma, P. K. (1992) Measuring adhesion, attraction, and repulsion between surfaces in liquids with an atomic-force microscope. *Phys. Rev. B.* **45,** 11,226–11,232.
3. Weisenhorn A.L., Hansma, P. K., Albrecht T. R., and Quate, C. F. (1989) Forces in atomic force microscopy in air and water. *Appl. Phys. Lett.* **54,** 2651–2653.
4. Butt, H.-J., Siedle, P., Seifert, K., et al. (1993) Scan speed limit in atomic force microscopy. *J. Microsc.* **169,** 75–84.
5. Putman, C. A., van der Werf, K. O., de Grooth, B. G., van Hulst, N. F., and Greve, J. (1992) New imaging mode in atomic-force microscopy based on the error signal. *SPIE Proceedings* **1639,** 198–204.
6. Gibson, C. T., Watson, G. S., and Myhra, S. (1997) Lateral force microscopy–a quantitative approach. *Wear* **213,** 72–79.
7. Han, W. and Lindsay, S. M. (1998) Precision interfacial molecular force measurements with a MAC mode atomic force microscope. *Appl. Phys. Lett.* **72,** 1656–1658.
8. Han, W., Lindsay, S. M., and Jing, T. (1996) A magnetically-driven oscillating probe microscope for operation in liquids. *Appl. Phys. Lett.* **69,** 4111–4113.
9. Garcia, R. and San Paulo, A. (2000) Amplitude curves and operating regimes in dynamic atomic force microscopy. *Ultramicroscopy* **82,** 79–83.
10. Hansma, P. K., Cleveland, J. P., Radmacher, M., et al. (1994) Tapping mode atomic force microscopy in liquids. *Appl. Phys. Lett.* **64,** 1738–1740.
11. Lantz, M., Liu, Y. Z., Cui, X. D., Tokumoto, H., and Lindsay, S. M. (1999) Dynamic force microscopy in fluid. *Surface Interface Anal.* **27,** 354–360.

12. Tamayo, J., Humphris, A. D., Owen, R. J., and Miles, M. J. (2001) High-Q dynamic force microscopy in liquid and its application to living cells. *Biophys. J.* **81,** 526–537.
13. Burnham, N. A., Behrend, O. P., Oulevey, F., et al. (1997) How does a tip tap? *Nanotechnology* **8,** 67–75.
14. Behrend, O. P., Oulevey, F., Gourdon, D., et al. (1998) Intermittent contact: Tapping or hammering? *Appl. Phys.* **A66,** S219–S221.
15. Tamayo, J., Humphris, A. D., Owen, R. J., and Miles, M. J. (2001) High-Q dynamic force microscopy in liquid and its application to living cells. *Biophys. J.* **81,** 526–537.
16. Magonov, S. N., Elings, V., and Whangbo, M.-H. (1997) Phase imaging and stiffness in tapping mode AFM. *Surface Sci.* **375,** L385–L391.
17. Bar, G., Delineau, L., Brandsch, R., Bruch, M., and Whangbo, M.-H. (1999) Importance of the indentation depth in tapping-mode atomic force microscopy study of compliant materials. *Appl. Phys. Lett.* **75,** 4198–4200.
18. Bar, G. and Brandsch, R. (1998) Effect of viscoelastic properties of polymers on the phase shift in tapping mode atomic force microscopy. *Langmuir.* **14,** 7343–7347.
19. Cleveland, J. P., Anczykowski, B., Schmid, A. E., and Elings, V. B. (1998) nergy dissipation in tappingmode atomic force microscopy. *Appl. Phys. Lett.* **72,** 2613–2615.
20. Chen, X., Davies, M. C., Roberts, C. J., Tendler, S. J. B., and Williams, P. M. (2000) Optimizing phase imaging via dynamic force curves. *Surface Sci* **460,** 292–300.
21. Pang, G. K., Baba-Kishi, K. Z., and Patel, A. (2000) Topographic and phase-contrast imaging in atomic force microscopy. *Ultramicroscopy* **81(2)**, 35–40.
22. Butt, H-J. (1991) Measuring electrostatic, van der Waals, and hydration forces in electrolyte solutions with an atomic force microscope. *Biophys. J.* **60,** 1438–1444.
23. Vinckier, A. and Semenza, G. (1998) Measuring elasticity of biological materials by atomic force microscopy. *FEBS Lett.* **430,** 12–16.
24. Hutter Jeffrey L. and John Bechhoefer (1994) Measurement and manipulation of Van der Waals forces in atomic force microscopy. *J. Vacuum Sci. Technol. B,* **12,** 2251–2253.
25. Cleveland, J. P., Manne, S., Bocek, D., and Hansma, P. K. (1993) A non-destructive method for determining the spring constant of cantilevers for scanning force microscopy. *Rev. Sci. Instrum.* **64,** 403–405.
26. D'Costa, N. P. and Hoh, J. H. (1995) Calibration of optical lever sensitivity for atomic force microscopy. *Rev. Sci. Instrum.* **66,**5096–5097.
27. Hoh, I., Cleveland, J. P., Prater, C. B., Revel, J.-P., and Hansma, P. K. (1992) Quantized adhesion detected with the atomic force microscope. *J. Am. Chem. Soc.* 4917–4918.
28. Mckendry, R. A., Theoclitou, M., Rayment, T., and Abell, C. (1998) Chiral discrimination by chemical force microscopy. *Nature* **14,** 2846–2849.
29. Okabe, Y., Furugori, M., Tani, Y., Akiba, U., and Fujihira, M. (2000) Chemical force microscopy of microcontact-printed self-assembled monolayers by pulsed-force-mode atomic force microscopy. *Ultramicroscopy* **82,** 203–212.

30. Willemsen, O. H., Snel, M. M., van Noort, S. J., et al. (1999) Optimization of adhesion mode atomic force microscopy resolves individual molecules in topography and adhesion. *Ultramicroscopy* **80,** 133–144.
31. Thundat, T., Oden, P. I., and Warmack, R. J. (1997) Chemical, physical, and biological detection using microcantilevers. *Electrochem. Society Proc.* **97,** 179–187.

3

Recognizing and Avoiding Artifacts in AFM Imaging

Davide Ricci and Pier Carlo Braga

1. Introduction

Images taken with the atomic force microscope (AFM) originate in physical interactions that are totally different from those used for image formation in conventional light and electron microscopy. One of the effects is that a new series of artifacts can appear in images that may not be readily recognized by users accustomed to conventional microscopy. Because we are addressing ourselves to novices in this field, we would like to give an idea of what can happen while taking images with the AFM, how one can recognize the source of the artifact, and then try to avoid it or minimize it. Essentially, one can identify the following sources of artifacts in AFM images: the tip, the scanner, vibrations, the feedback circuit, and image-processing software.

2. Tip Artifacts

The geometrical shape of the tip being used will always affect the AFM images taken with it. Quite intuitively, as long as the tip is much sharper than the feature under observation, the profile will resemble closely its true shape. Depending on the lateral size and height of the feature to be imaged, both the sharpness of the apex and the sidewall angle of the tip will become important. In general, the height of the features is not affected by the tip shape and is reproduced accurately, whereas the greatest artifacts are evident on the lateral geometry of objects, especially if they have steep sides.

Avoiding artifacts from tips is achieved by using the optimal probe for the application: the smaller the size of the object, the sharper the tip. A notable exception arises in the case of high-resolution imaging on ordered crystals, where often better images are obtained with standard tips. This can be explained by realizing that at this dimensional scale the measurable radius of curvature of the tip is not in fact involved in the imaging process, but instead smaller local

From: *Methods in Molecular Biology, vol. 242: Atomic Force Microscopy: Biomedical Methods and Applications*
Edited by: P. C. Braga and D. Ricci © Humana Press Inc., Totowa, NJ

protrusions on the apex of the probe will be the real tip (or tips) effectively taking the image.

Further understanding of AFM tip properties and related artifacts can be gathered from the vast literature on the subject, together with a variety of methods for their correction ***(1–9)***. Specific artifacts, depending on the mode of operation, have been investigated and explanations have been proposed ***(10–14)***.

Because we are now interested in showing a general overview of the subject for beginners in the field, we shall have a look at the main tip artifacts in a very simple way.

2.1. Features Protruding on the Surface Appear Larger Than Expected

In **Fig. 1**, the different profiles were obtained using a dull or a sharp tip when scanning a surface feature. In addition to sharpness, the geometrical shape also is important: a conical tip will affect the lateral shape of the feature less than a pyramidal one. Very small features, such as nanoparticles, nanotubes, globular proteins, and DNA strands, will always be subject to image broadening, so that the measured lateral size should be taken as an upper limit for the true size. Note that in all these cases the height of the sample will be reported accurately.

2.2. Repetitive Abnormal Patterns in an Image

When the size of the features on a flat surface is significantly smaller than the tip, repetitive patterns may appear in an image. Spherical nanoparticles or small proteins may assume an elongated or triangular shape reflecting the geometry of the apex of the tip. Sometimes a so-called "double image" will appear along the fast scanning direction as a result of the presence on the tip of more than one protrusion slightly separated from one another and making contact with the sample (**Fig. 2**).

2.3. Pits and Holes in the Image Appear Smaller and Shallower

When the tip has to go into a feature that is below the surface, such as a hole, the lateral size and depth can appear too small and the tip may not reach the bottom. The geometry of the probe will dominate the geometry of the sample as is apparent from the line profile shown in **Fig. 3**. However, it is still possible to measure the opening of the hole from this type of image. Also, the pitch of repeating patterns can be accurately measured with probes that do not reach the bottom of the features being imaged.

2.4. Damaged or Contaminated Tips

If the probe is badly damaged or has been contaminated by debris from a less-than-clean sample surface, strangely shaped objects may be observed in

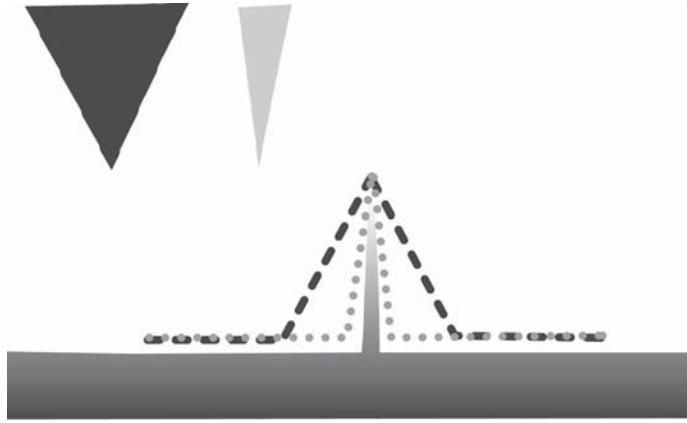

Fig. 1. Traces followed by a dull and a sharp probe as they go over a protruding feature. In such a measurement, the side of the tip will cause a broadening of objects in the image.

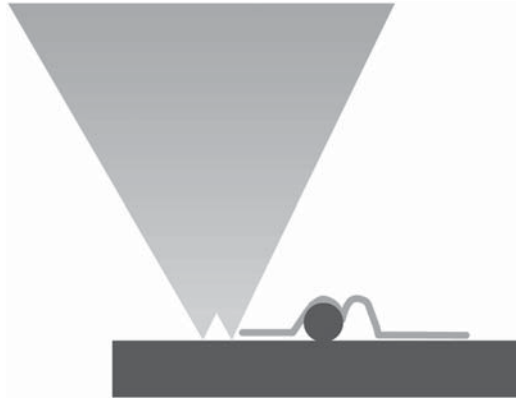

Fig. 2. A double tip will cause a shadow or double image along the scanning direction

the image and difficult to explain. For example, a damaged tip following the geometry of a regular test pattern (as in **Fig. 4**) will produce an asymmetric profile. In the case of contaminants, one often notices an abrupt change of detail contrast during scanning and a blurring of the image. Sometimes the debris particle may partially detach and is dragged along during scanning, leaving a diagonal track on the image that could be erroneously interpreted as a

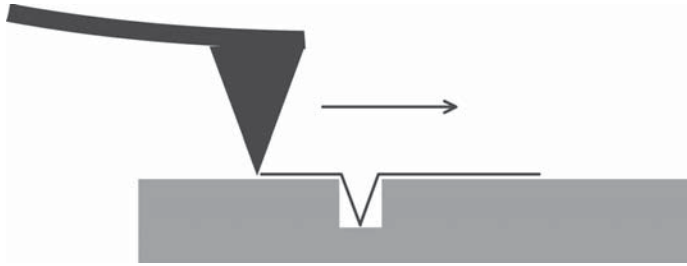

Fig. 3. Because of the width of the tip, the hole will not be faithfully reproduced.

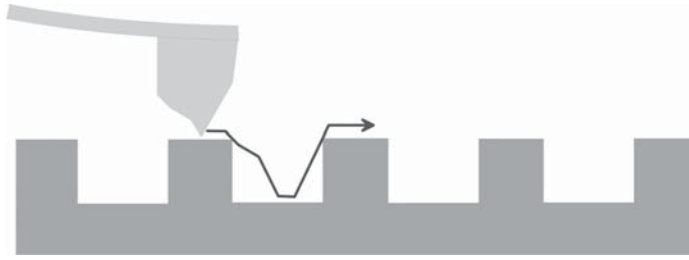

Fig. 4. A badly damaged tip creates artifacts while scanning a regular test pattern.

surface feature. Telltale signs in this case are the instabilities and glitches in the feedback signal that occur each time the particle is dragged along.

3. Scanner Artifacts

Piezoelectric ceramic scanners were one of the breakthroughs that made AFM possible. Their design has been constantly improved, but a number of artifacts still arise from their physical and mechanical properties. One point that must not be neglected is that scanner properties change with time and use. In fact, the piezoelectric material will change its sensitivity to driving signals if it is often used (it will become slightly more sensitive) or if it is left idle (it will depolarize and become less sensitive). The best thing to do is to periodically calibrate the scanner following the manufacturer's instructions.

3.1. Effects of Intrinsic Nonlinearity

If the extension of the scanner in any one direction is plotted as a function of the driving signal, the plot will not be a straight line but a curve similar to the one shown in **Fig. 5**. The nonlinearity may be expressed as a percentage (describing the deviation from linear behavior), and it typically ranges from 2–

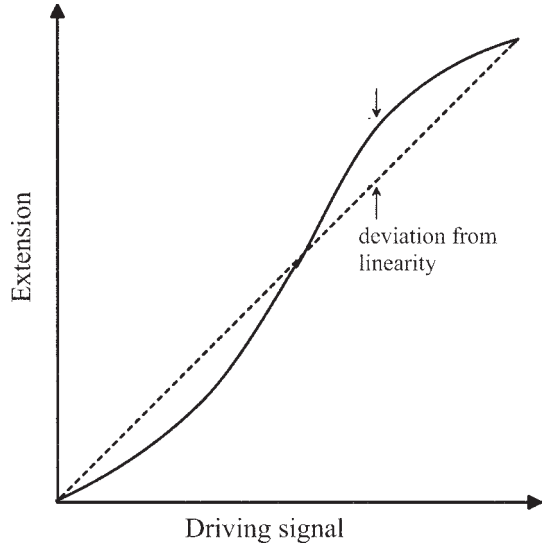

Fig. 5. Plot of the scanner extension vs driving signal. Notice the large deviation from linearity.

25%, depending on the driving signal applied and scanner construction. The effects will be present both in the plane and in the vertical direction.

3.1.1. In the Plane

An AFM image of a calibration grid with periodic structures such as squares will appear severely distorted, with nonuniform spacing and curvature of features, typically appearing smaller on one side of the image than on the other (**Fig. 6**). On a generic sample with no regular pattern the distortion may not be recognizable, but it will be certainly present. Once the scanner is properly linearized, it is also critical that the scanner be calibrated. For example, it is possible for the scanner to be linear but not calibrated. If the calibration is incorrect, then the *x* and *y* values measured from line profiles will be incorrect.

3.1.1.1. In Plane Linearization

There are essentially two methods to linearize a scanner in the *x* and *y* directions: by software or hardware. Software correction is performed by mathematically modeling the nonlinear behavior of the scanner, finding the parameters for a correction algorithm imaging a known grid, and then applying the algorithm during scanning using the parameters stored in a look-up table. The limits of this method lie in the fact that unfortunately the corrections strongly

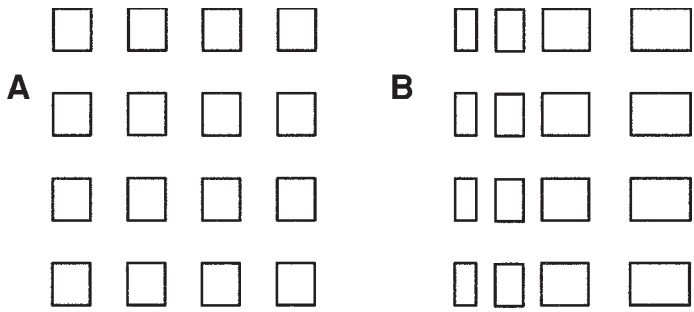

Fig. 6. Distortion of a test pattern caused by scanner nonlinearity.

depend upon the scan speed, scan direction, and offset that have been used during the calibration procedure. When images in normal use are taken under conditions similar to the calibration, the correction will be accurate; otherwise, nonlinearities will be again present. More recently hardware correction for large scanners has become popular ***(15)*** because it gives better results. In this case, the true position of the scanner in the *x* and *y* directions is measured by a sensor during scanning and compared with the intended scanner position. A feedback circuit applies an appropriate driving signal to the scanner in order to attain the desired position.

3.1.2. In Height Measurements

Because the height range of scanners is usually an order of magnitude smaller than the range in the scanning plane, effects of nonlinearity are less severe but still present. To make accurate height measurements with an AFM, it is necessary to calibrate the scanner in the *z*-axis. Often the microscope is calibrated at only one height. This means that if the relationship between the measured *z* height and the actual *z* height is not linear, then the height measurements will not be correct unless the feature being observed has a height close to the calibration measurement (**Fig. 7**). It is also to be noted that although calibration gratings are reasonably easy to make by lithographic techniques, step–height calibration standards are more difficult to obtain, especially for very high-resolution work. Often researchers make their one reproducible height standards for accurate measurements in this range from crystals that have known height steps.

3.2. Effects of Hysteresis

All piezoelectric ceramics display hysteretic behavior, that is, if slowly scanned back and forth cyclically, to the same driving signal does not correspond the same position in the two scanning directions. This can be easily

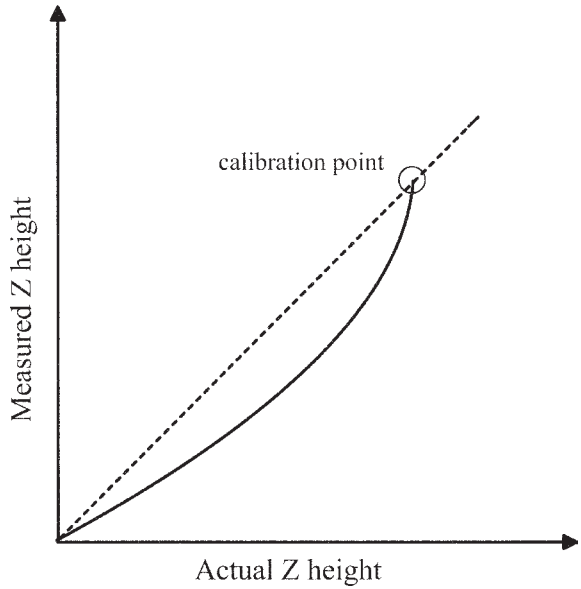

Fig. 7. Quite often, the z height response of the scanner is calibrated in only one point. The plot represents the deviation from the true value for measurement of heights that differ from the one at which the scanner has been calibrated.

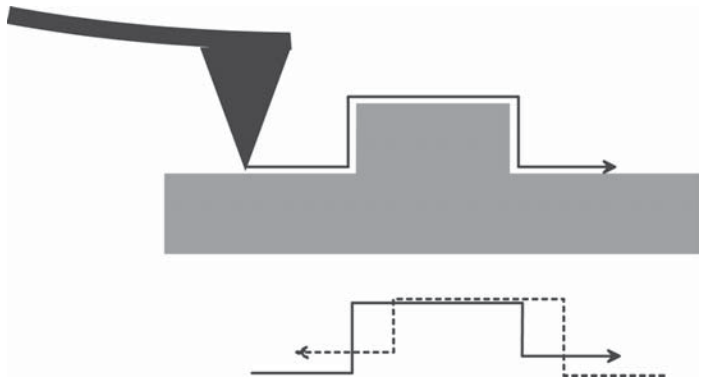

Fig. 8. Effect of scanner hysteresis on a scan (trace and retrace) of a step.

observed by comparing the profiles taken from left to right and in the opposite direction on a feature on the surface of a sample. The result would be like **Fig. 8**, where there is a lateral shift between the two profiles. Notice that an effect is also present in the vertical direction because the contraction and extension

response of the scanner to the driving signal will be different, giving rise to an asymmetric step height.

3.3. Effects of Creep

When the scanner is subjected to a very fast variation in the driving voltage, it does not change its position all at once. The dimensional change occurs in two steps: the first step takes place in less than a millisecond, the second on a much longer time scale. The second slower movement is called creep. This causes several effects. Scans taken at different scan rates will have slightly different magnification. If one tries to zoom-up onto a feature, making a smaller scan just after a larger scan, the feature will not be centered and may be distorted in the second image because of creep. On a structure made of parallel lines the effect will be a bending of the lines in the first portion of the scanned image (**Fig. 9**). This is often also called drift, but must not be confused with thermal drift, which is different.

In the vertical direction, creep becomes apparent as an overshoot of the scanner position at the leading and trailing edge of features that have steep sides (**Fig. 10**). This can be often found as a lateral "shading" of protruding features on flat substrates in top view topographical images.

3.4. Effects of Cross Coupling and Sample Tilting

Usually scanners are assembled in the AFM having a free end that is scanned (to which either the cantilever or the sample is attached) and the other end is attached to the microscope body. For this reason the motion of the scanner will follow an arc (spherical or parabolic depending on the type of scanner) and not a plane (**Fig. 11**). The affected images will show a bow, which is especially evident in large scans. This artifact can easily be subtracted by image processing. When very small features have to be detected on flat surfaces, the bow will not allow them to be seen during scanning as the vertical scale of the image would have to adjust to accommodate it: for this reason, the AFM often has the option to subtract the appropriate curve from each line during acquisition, allowing small features to become immediately evident. When there is mechanical or electronic cross coupling between the x and y direction elements of the scanner, this will become apparent in the image of test structures, where the angles between features in the x and y plane will be modified. Mechanical coupling between the piezoelectric ceramics that move the probe in the x or y directions and in the z direction can cause substantial errors when measuring sidewall angles.

Another source of cross coupling arises when the scan direction is not parallel to one of the piezoelectric elements that constitute the scanner. Rotated scans are obtained by sending appropriately mixed driving signals to both the x

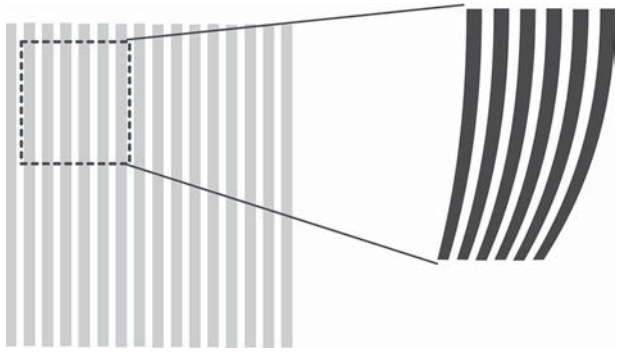

Fig. 9. Effect of creep on a scan performed zooming up onto a detail in a larger image.

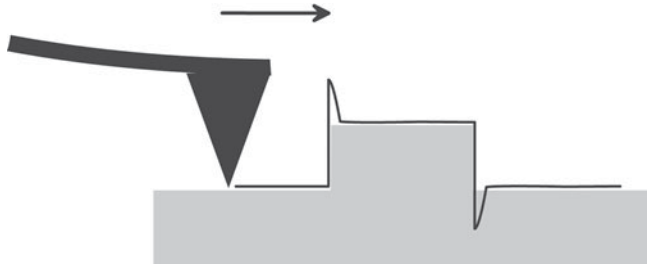

Fig. 10. Effect of creep in the vertical direction: overshooting at the edges of the step.

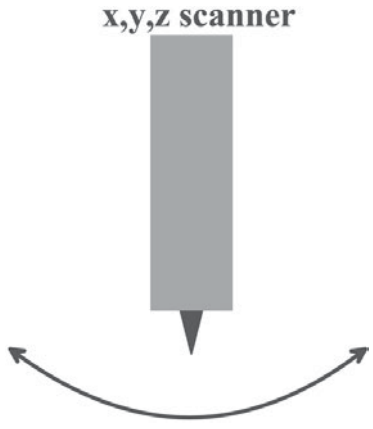

Fig. 11. The free end of the scanner will follow an arc during scanning, creating a bowl-like image. This effect is especially evident on large scans of flat surfaces.

and *y* piezoelectric elements: if they are not both accurately calibrated the image will be affected by a geometrical distortion.

It is useful to add that quite often (in fact, always) the sample will have a plane tilt relative to the motion of the scanner. Although all acquisition software allows for subtracting the tilt during scanning, it is good practice to try and mount the sample as planar as possible so that the piezoelectric element responsible for the vertical movement will operate across a smaller range and hence behaving linearly.

3.5. Thermal Drift

External temperature changes or gradients will affect the AFM and its scanner depending on their mechanical properties. AFMs are built in such a way as to minimize this phenomenon by using special materials and appropriate design, but nevertheless thermal drift can be present. In the case of very high-resolution imaging of atomic structures, it is often necessary to wait some time during scanning before the system will stabilize and stop drifting. Also, electronics and the laser spot on the cantilever can induce drift in measurement settings that need to stabilize in time. In the case of AFMs mounted onto inverted microscopes and eventually equipped with a heated stage, special care has to be taken. When a liquid cell is used and reagents are flowed in during an experiment, the problem becomes acute as temperature changes of even a fraction of a degree can cause large bending of the cantilever. Often, a good ambient air conditioning system can be useful in reducing thermal effects.

4. Vibrations

Because the AFM operates thanks to its very high sensitivity to the small deflections of the cantilever assembly, it is evident that if external vibrations affect the cantilever these will create artifacts in the images. Typically, the artifacts will appear as oscillations. Both acoustic and floor vibrations can excite vibrational modes in an AFM and cause artifacts.

The floor in a building can vibrate vertically several micrometers at frequencies below 5 Hz. The floor vibrations, if not properly filtered, can cause periodic structure in an image. This type of artifact is most often noticed when imaging very flat samples. Sometimes the vibrations can be started by an external event such as an elevator in motion, a train going by, or even people walking in a hallway. A special air table or bungee cords must be used to isolate the AFM from these vibrations. A good idea is also to install the instrument near a corner of the laboratory instead of at the center of a room, choosing if possible the lowest floor in the building.

A person speaking in the same room as the microscope, music, a door that shuts, an airplane going over the building can generate sound waves that will

generate artifacts in the AFM images. Some instruments have as an option an acoustic hood or enclosure to isolate the AFM from external noise.

5. Effects of Feedback and Other Parameter Settings

Depending on the mode of operation, several parameters have to be set by the user to obtain the best images. Among these, one can find deflection set point (in contact mode), oscillation amplitude and dampening (in AC modes), feedback gain (sometimes separated into a proportional gain setting and integral-derivative setting), low pass filters, scan speed, and so on.

The setting of these parameters is a trial-and-error process. Each time a new sample is put into the microscope, the best values must be searched and during the process many artifacts can be produced in images. Soft samples generally must be imaged at low scan speeds and low interaction forces, otherwise glitches in the scan direction or even sample deformation may occur. Rough samples again need to be imaged slowly, but larger amplitude or deflection might be needed to keep track of the surface. Especially in AC imaging modes (but also in DC mode) special care must be taken in tuning the gain parameters of the feedback. If the feedback loop of a scanning probe microscope is not optimized, the image can be affected. When feedback gains are too high, the system can oscillate, generating high-frequency periodic noise in the image. This may occur throughout the image or be localized to features with steep slopes. However, when feedback gains are too low, the tip cannot track the surface, and features will be distorted and smeared out. On large objects with sharp slopes, an overshoot can appear in the image as the tip travels up the slope, and an undershoot can appear as the tip travels down the slope. Taking a force-vs-distance curve to ascertain the presence of adhesion forces or other effects can help to guide the choice of imaging parameters.

6. Image Processing

Image processing is readily available in AFM as the data is stored digitally on a computer disk. One can easily access routines for flattening, polynomial-line or surface subtraction, removal of bad data, matrix filtering, and three-dimensional representation with sophisticated rendering. Often some kind of processing will be necessary to analyze data and compare it with other results, but care must be taken to avoid introducing artifacts. The most common ones stem from careless use of the powerful image processing tools available. For example, as we have seen in **Subheading 3.4.**, nearly all images are affected by a tilt and by a bow introduced by the scanner geometry. If the wrong curve fit is applied or if large features are not excluded from the surface subtraction parameter computation (all image analysis software allow to include or exclude surface area portions from the computation), distortions will be introduced. This is particularly true with line-by-line curve fit and subtraction.

Low-pass filters, although capable of reducing noise in the data, will introduce smoothing of sharp features and, in the worst cases, delete smaller details. Fourier transform and power spectrum filtering if misused can create periodic features that may seem to be atomic structures, wheres in reality they are only noise.

7. Some Guidelines for Artifact Testing

If during a measurement you get suspicious that an image may contain artifacts, here are some things you can do to be sure whether or not they are present:

- Take more that one image of the same area or the same line to ensure that it looks the same. When looking at a single scan line profile during acquisition, look if the traces are identical and stable in time.
- Try changing the scan direction and take a new image. You can do this also on a single scan line looking at the profile and observing directly the difference between the trace and retrace plots.
- Change the scan size and take an image to ensure that the features scale properly.
- Rotate the sample and take an image to identify artifacts induced by the shape of the tip.
- Change the scan speed and take another image (especially when suspicious periodic or quasiperiodic features are present). If they scale, you are looking at periodical noise.

References

1. Keller, D., and Chih-Chung, C. (1991) Reconstruction of STM and AFM images distorted by finite-size tips. *Surface Sci.* **253,** 353–364.
2. Hellemans, L., Waeyaert, K., Hennau, F., Stockman, L., Heyvaert, I., and Van Haesendonck, C. (1991) Can atomic force microscopy tips be inspected by atomic force microscopy? *J. Vac. Sci. Technol. B.* **9,** 1309–1312.
3. Keller, D. and Chou, C. C. (1992) Imaging steep, high structures by scanning force microscopy with electron beam deposited tips. *Surface Sci.* **268,** 333–339.
4. Keller, D., Deputy, D., Alduino, A., and Luo, K. (1992) Sharp, vertical-walled tips for SFM imaging of steep or soft samples. *Ultramicroscopy* **42–44,** 1481–1489.
5. Wang, W. L. and Whitehouse, D. J. (1995) Application of neural networks to the reconstitution of scanning probe microscope images distorted by finite-size tips. *Nanotechnology* **6,** 45–51.
6. Markiewicz, P. and Goh, M. C. (1995). Atomic force microscope tip deconvolution using calibration arrays. *Rev. Sci. Instrum.* **66,** 1–4.
7. Villarrubia, J. S. (1996) Scanned probe microscope tip characterization without cantilever tip characterizers. *J. Vac. Sci. Technol. B.* **14,** 1518–1521.
8. Sheng, S., Czajkowsky, D. M., and Shao, Z. (1999) AFM tips: How sharp are they? *J. Microsc.* **196,** 1–5.

9. Taatjes, D. J., Quinn, A. S., Lewis, M. R., and Bovill, E. G. (1999) Quality assessment of atomic force microscopy probes by scanning electron microscopy: Correlation of tip structure with rendered images. *Microsc. Res. Tech.* **44,** 312–326.
10. Dinte, B. P., Watson, G. S., Dobson, J. F., and Myhra, S. (1996) Artefacts in non-contact mode force microscopy: The role of adsorbed moisture. *Ultramicroscopy* **63**, 115–124.
11. Yang, J., Mou, J., Yuan, J.-Y., and Shao, Z. (1996) The effect of deformation on the lateral resolution of the atomic force microscopy. *J. Microsc.* **182,** 106–113.
12. van Noort, S. J., van der Werf, K. O., de Grooth, B. G., van Hulst, N. F., and Greve, J. (1997) Height anomalies in tapping mode atomic force microscopy in air caused by adhesion. *Ultramicroscopy* **69,** 117–127.
13. Kühle, A., Sorenson, A. H., Zandbergen, J. B., and Bohr, J. (1998) Contrast artifacts in tapping tip atomic force microscopy. *Appl. Phys. A.* **66**, S329–S332.
14. Paredes, J. I., Martinez-Alonso, A., and Tascon, J. M. (2000) Adhesion artefacts in atomic force microscopy imaging. *J. Microsc.* **200,** 109–113.
15. Barrett, R. C. and Quate, C. F. (1991) Optical scan-correction system applied to atomic force microscopy. *Rev. Sci. Instrum.* **62,** 1393–1399.

4

Advanced Biosensing Using Micromechanical Cantilever Arrays

Martin Hegner and Youri Arntz

1. Introduction

During the last few years, a series of new detection methods in the field of biosensors have been developed. Biosensors are analytical devices that combine a biologically sensitive element with a physical or chemical transducer to selectively and quantitatively detect the presence of specific compounds in a given external environment.

These new biosensor devices allow sensitive, fast, and real-time measurements. The interaction of biomolecules with the biosensor interface can be investigated by transduction of the signal into a magnetic ***(1)***, an impedance ***(2)***, or a nanomechanical ***(3)*** signal. In the field of nanomechanical transduction, a promising area is the use of cantilever arrays for biomolecular recognition of nucleic acids and proteins. One of the advantages of the cantilever array detection is the possibility to detect interacting compounds without the need of introducing an optically detectable label on the binding partners. For biomolecule detection, the liquid phase is the preferred one but it has been shown that the cantilever array technique is also very appropriate foruse as a sensor for stress ***(4)***, heat ***(5)***, and mass ***(6)***. Recent experiments showed that this technique could also be applied as an artificial nose for analyte vapors (e.g., flavors) in the gas phase ***(7)***.

2. Nanomechanical Cantilever as Detectors

The principle of detection is based on the functionalization of the complete cantilever surface with a layer that is sensitive to the compound to be investigated. The detection is feasible in different media (e.g., liquids or gas phase). The interaction of the analyte with the sensitive layer is transducted into a

From: *Methods in Molecular Biology, vol. 242: Atomic Force Microscopy: Biomedical Methods and Applications*
Edited by: P. C. Braga and D. Ricci © Humana Press Inc., Totowa, NJ

static deflection by inducing stress on one surface of the cantilever as the result of denser packing of the molecules ***(8)*** or a frequency shift in case of dynamic detection mode ***(9)*** as a result of changes in mass.

3. Overview of the Two Detection Modes

3.1. Static Mode

In static mode detection, the deflection of the individual cantilever depends on the stress induced by the binding reaction of the specific compounds to the interface. The interface has to be activated in an asymmetrical manner, as shown in **Fig. 1**. Most often one of the cantilever surfaces is coated with a metallic layer (e.g., gold) by vacuum deposition techniques and subsequently activated by binding a receptor molecule directly via a thiol group to the interface (e.g., thiol-modified DNA oligonucleotides) or, as in case of protein recognition, by activating the fresh gold interface with a self-assembling bifunctional bioreactive alky-thiol molecule to which the protein moiety is covalently coupled ***(10)***.

The radius R of the curvature of the cantilever is given by Stoney's law ***(11)***:

$$\sigma = Et^2_{\text{cant}}[6R(1-\gamma)]^{-1} \quad (1)$$

where σ is the stress, γ is the Poisson ratio, E Young's modulus, and t_{cant} the thickness of cantilever. The thickness of the lever is an important parameter that can be varied to increase or decrease the sensitivity of the device. By reducing the thickness of the cantilever a larger deflection is achieved. Reducing the thickness by factor '2' increases the bending signal due to stress at the interface by factor '4'. The interaction of the ligand with the receptor molecule has to occur immediately on the interface. No flexible linking of the receptor molecule is allowed as a result of the fact that the induced stress will be diminished. The receptor molecules should be presented in a tightly packed manner on the interface to interact with the substances to be analyzed.

3.2. Dynamic Mode

In the case of dynamic mode detection, the resonance frequency of the individual cantilever, which has to be excited, depends on the mass. The binding reaction of the analyte to the interfaces increases the mass, and the resonance frequency is normally decreased. In **Fig. 2**, the scheme of dynamic cantilever detection is shown.

The cantilever is excited by a piezo element. The change in mass (Δm) during the experiment as the result of an uptake of interacting biomolecules induces a change in the resonance frequency of the cantilever, which can be described by the following formula:

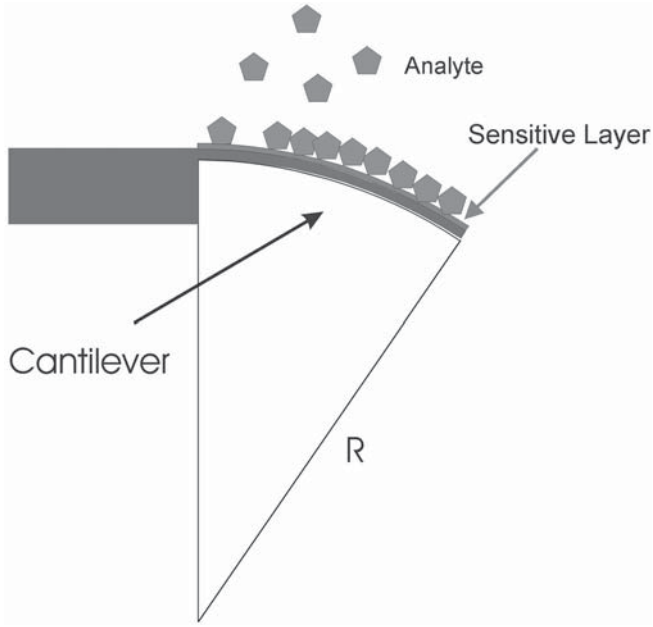

Fig. 1. Interaction of the analyte (light gray pentagons) with the sensitive layer induces a stress on the interface and bends the cantilever (note the asymmetric coating of the individual cantilever surface).

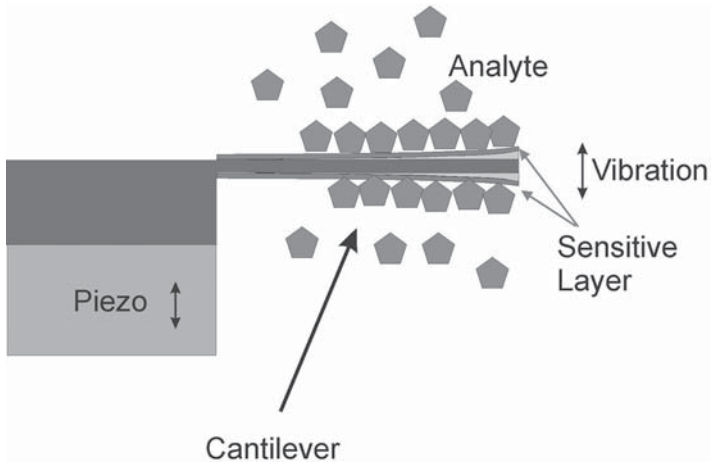

Fig. 2. Interaction of analyte (light gray pentagons) with sensitive layers induces a change in the resonance frequency of the cantilever.

$$\Delta m = k(4n\pi^2)^{-1}(f_1^{-2} - f_0^{-2}) \quad (2)$$

where the resonance frequency before and during the experiment are f_0 and f_1, k is the spring constant of cantilever, and n is a factor dependent of the geometry of the cantilever. The uptake of mass as a result of specifically interacting molecules is doubled in this manner, and the cantilever does not respond to temperature changes via a bimetallic effect. Additionally, the preparation involves fewer steps as in the case of the static detection mode ***(5)***.

4. Setups

At the Institute of Physics at the University of Basel, Basel, Switzlerland, in collaboration with the IBM Research Laboratory Zurich, we developed cantilever array setups both for static and dynamic mode operation in liquids and in the gas phase.

The principal part of the setup is an array of eight cantilevers produced by classic lithography technology with wet etching. A typical picture of such a cantilever array is shown in **Fig. 3**. The structure of an array is composed of eight cantilevers with a length of 500 µm, a width of 100 µm, and a pitch of 250 µm from lever to lever. The etching process provides cantilever thickness ranging from 250 nm to 7 µm adapted for the individual application (i.e., static or dynamic mode).

The cantilever deflection or motion detection is provided by a classic laser beam deflection optical detection for both the static and dynamic mode set up as shown in **Fig. 4**.

The laser source is an array of eight vertical-cavity surface-emitting lasers (VCESLs; 760 nm wavelength, 250 µm pitch), and position detection obtained through a linear position-sensitive detector). The array is mounted in a cell useable for gas or liquid phase measurement.

A scheme showing the setup is displayed in **Fig. 5**. The operation of the instrument is fully automatic and during the time course of a few hours up to eight different samples can be probed using the automatic fluid delivery. The instrumental noise of the static setup lies in the subnanometer range and the dynamic setup is able to detect mass changes in the order of picograms.

The key advantages of cantilever arrays are the possibility of *in situ* reference and the simultaneous detection of different substances. The *in situ* reference is needed to avoid the thermomechanical noise, especially in fluid-phase detection. Changes in refractive index when the buffer changes will also contribute to a so-called virtual motion of the cantilever. As visible in **Fig. 6**, only the real motion, which is the difference in between the cantilevers on the same chip, is originating from the specific biomolecular interaction.

In **Fig. 7A**, a raw signal of the cantilever array is displayed. Because there will always be instrumental or thermal drift, the differential signal detection is mandatory. **Figure 7** shows an experiment with a set of three cantilevers (thickness 500 nm).

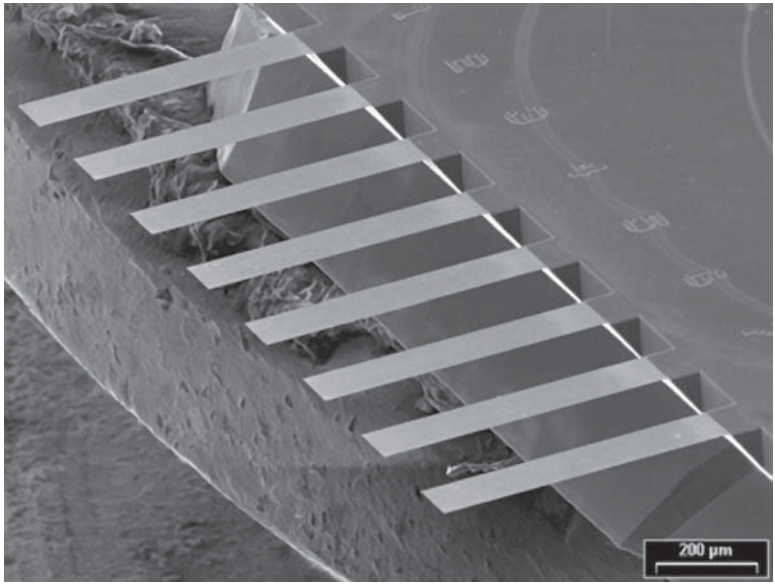

Fig. 3. Scanning electron micrograph of an array of eight cantilevers with individual thicknesses of 500 nm.

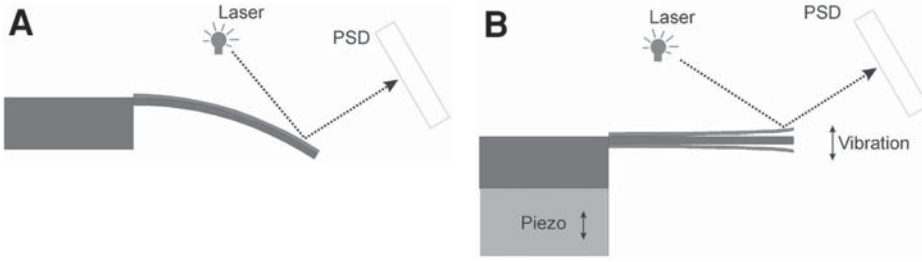

Fig. 4. Detection of average cantilever position using a multiple laser source vertical-cavity surface-emitting laser and a position-sensitive device. **(A)** Static mode; **(B)** dynamic mode.

In this experiment we used two reference cantilevers with different coatings and one specific biorecognition cantilever. By specifically binding biomolecules the cantilever is bending downwards due to stress generated on its surface. As visible in **Fig. 7B**, the differential signal lacks any external influences except for the specific biomolecular interaction, which induces a differential signal of approx 90 nm relative to the *in situ* reference. The experiment is reversible and can be repeated using different concentrations of analytes. In a recent work we presented data that allow the extraction of the

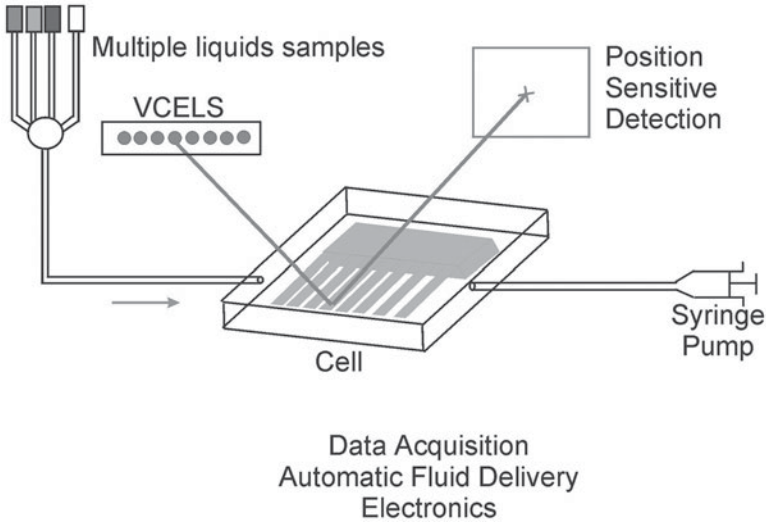

Fig. 5. General structure of cantilever array setups for gas/liquid samples.

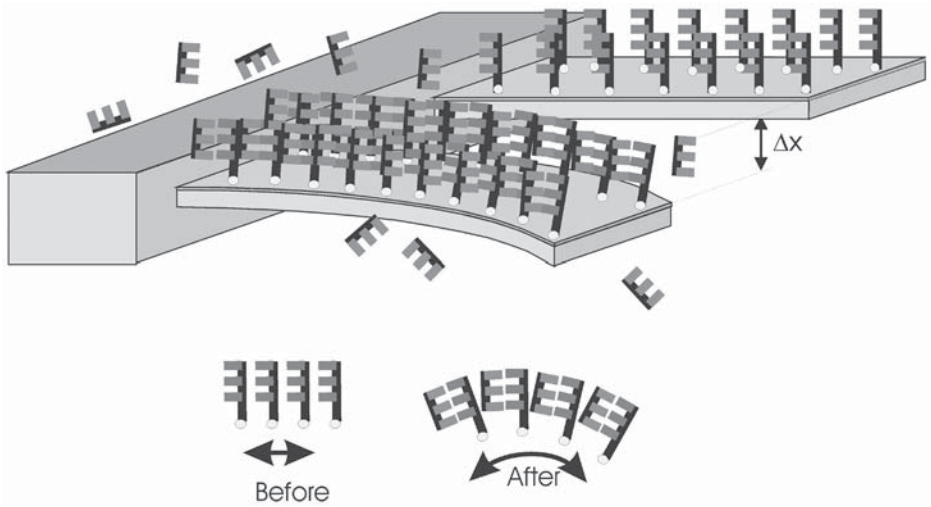

Fig. 6. Static detection of biomolecular interaction. The cantilevers have to be equilibrated before the biomolecule of interest is injected. Because of the specific interaction with the biomolecules (light gray) on the cantilever shown in front, stress builds up that deflects the individual cantilever specifically.

thermodynamics of the interacting biomolecules (i.e., DNA; **ref.** ***12***). Deflection signals as small as a few nanometers are easily detected. Currently, the detection limit in static experiments lies in the range of nanomolar concentra-

tions ***(12)*** but can be significantly lowered in the future by using cantilever arrays in the range of 250–500 nm of thickness.

Great care has to be taken in the selection of the internal reference lever. In the case of DNA detection, an oligonucleotide is chosen that displayed a sequence that does not induce crosstalk binding reactions with the sequences to be detected. Coating with thin layers of titanium and gold using vacuum deposition modifies one side of the cantilever array. Onto this metallic interface, a thiol-modified oligonucleotide self-assembles in a high-density layer. Complementary and unknown oligonucleotide sequences are then injected and the specific interaction is directly visible within minutes. Stress at the interface is built up because of a higher density of packing (*see* **Fig. 6**). In protein detection, a protection of the asymmetrically coated cantilever has to be considered ***(13)***. Preparation of protein-detecting cantilevers is a multistep procedure and requires surface chemistry knowledge. The side opposite to the biomolecular-modified side is generally protected by a polyethyleneglycol layer. The bioreference surface can be coated by using unspecifically interacting proteins (e.g., bovine serum albumin). In protein detection experiments, larger fluctuations of the cantilevers are observed (e.g., **Fig. 7**) than in the ssDNA–ssDNA experiments. A possible interpretation of this difference might be that it is caused by the proteins absorbing light within the visible spectrum and therefore inducing some local changes in the index of refraction. We always measure specific signals within minutes without problems. Normally, some drift of few tens of nanometers is observed in the complete set of cantilevers during the time course of the experiment, even though temperatures of the instruments are stabilized within ±0.05°C. However, these effects are completely eliminated by using a differential read out on the very same cantilever array.

Cantilever arrays are already employed as detectors in both static and dynamic modes ***(8,9)***. Recent articles show the potential for detection of DNA hybridization ***(3,12)***, cell capture, or toxin detection ***(1)***. Integrating cantilever arrays into microfluidic channels will significantly reduce the amount of sample required ***(14)***. Attempts have been made to get data from single-cantilever experiments for DNA ***(15)*** or antibody–antigen reactions ***(16)*** or from a two-cantilever setups using different stiffnesses for the individual cantilevers ***(17)***. We would like to point out that these approaches have serious drawbacks. Information extracted from these experiments, which often last multiple hours, cannot exclude unspecific drift of any kind ***(18)***.

The signal in these experiments is interpreted as specificity on the biomolecular level but no correlation from one lever to the next is applicable if only one lever is used at a time. In the second approach cantilevers with different stiffnesses are used to monitor the nanometer motions. Because the individual cantilever used shows a difference of factor four in terms of stiffness,

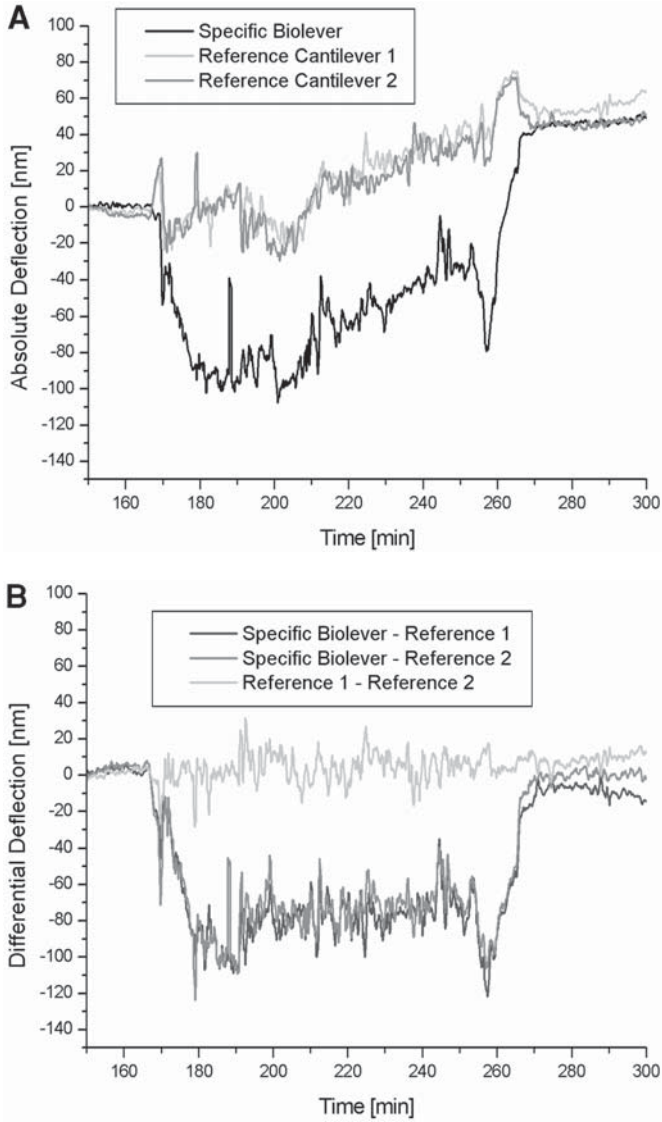

Fig. 7. **(A)** Raw data of a three-lever bioarray experiment. Two shades of gray indicate the motion of the reference cantilevers. In black color, the motion of the biologically specific cantilever is displayed. Upon injection of interacting biomolecules (approx 170 min) turbulences of the liquid cause all levers to undergo some motion, which is stabilized immediately when the flow is stopped (approx 180 min). The specific binding signal quickly builds up and remains stable. The interaction is fully reversible and can be broken by shifting the equilibrium of the binding reaction by injecting pure buffer solution (approx 260 min) into the fluid chamber. Over the course of 2–3 h, we

the response, which originates from a specific interaction, is difficult to extract. The sensitivity of this approach is hampered by the differences in stiffness, which are directly correlated to the thickness of the cantilever used (*see* Eq. 1). An interaction of the biomolecule with the stiffer reference cantilever might not be detectable if the stress signal lies within the thermal noise of that lever.

5. Conclusion

The cantilever array technology explores a wide area of applications; all biomolecular interactions are in principle able to be experimentally detected using cantilever array as long as mass change or surface stress is induced by the specific interaction. A few applications so far demonstrate promising results in the field of biological detection. The cantilever-based sensor platform might fill the gap between the sensitive but costly and relatively slow analytical instrumentation (e.g., mass-spectroscopy, high-performance liquid chromatography, surface plasmon resonance [SPR]) and the chip technologies (for example, gene-arrays) with their advantage of easy multiplexing capabilities, albeit with their need for fluorescence labeling and restriction to higher molecular-weight compounds like proteins and nucleic acids thus far.

In comparison with the methods just described, the cantilever technology is cheap, fast, sensitive, and applicable to a broad range of compounds. The lack of multiplexing could be overcome by the application of large cantilever arrays with >1000 cantilevers per chip. Projects are now underway to introduce commercial platforms providing arrays of eight cantilevers to applications in the liquid or gas phases. A critical point for future development in this field will be the access to the cantilevers arrays similar to that in the normal field biological applications using single-cantilever scanning force microscopy. At the moment there are no biological experiments published that use dynamic mode detection. We believe, however, that its ease of preparation (symmetrically as pointed out) and reduced sensitivity to environmental changes, makes this technology a strong candidate as the instrumental approach of choice for the future biological detection using cantilever arrays.

Fig. 7. *(continued)* regularly see a drift of the complete temperature-stabilized cantilever arrays on the order of tens of nanometers. **(B)** Differential data of the experimental set of Fig. **(A)**. In light grey color, the difference between the two reference cantilevers is shown. Except for some small motions, no differential bending is observed, whereas in the dark gray and black the difference of the specifically reacting cantilever with respect to the reference cantilevers is show. As shown after approx 260 min, pure buffer solution is injected and the differential signal collapses to values close to the starting point were no interacting biomolecules were present in the experiment.

Acknowledgments

Financial support of the NCCR "Nanoscale Science," the Swiss National Science Foundation, and the ELTEM Regio Project Nanotechnology is gratefully acknowledged. We would like to thank our colleagues from Basel and IBM Rüschlikon for the great collaborative effort and for their valuable contributions to progress in the field of cantilever arrays. We are grateful to Ernst Meyer, Christoph Gerber, Hans-Peter Lang, Peter Vettiger, Felice Battiston, Jiayun Zhang, and Hans-Joachim Güntherodt.

References

1. Baselt, D. R., Lee, G. U., and Colton, R. J. (1996) Biosensor based on force microscope technology. *Vacuum Sci. Technol. B* **14,** 789–793.
2. Masayuki, H., Yoshiaki, Y., Hideki, T., Hideo, O., Tsunenori, N., and Jun, M. (2002) A novel ISFET-type biosensor based on P450 monooxygenases *Biosensors Bioelectronics* **17,** 173–179.
3. Fritz, J., Baller, M. K., Lang, H. P., et al. (2000) Translating biomolecular recognition into nanomechanics. *Science* **288,** 316–318.
4. Berger, R., Delamarche, E., Lang, H. P., et al (1997) Surface stress in the self-assembly of alkanethiols on gold *Science* **276,** 2021–2024.
5. Berger, R., Gerber, C. H., Gimzewski, J. K., Meyer, E. and Güntherodt, H.-J. (1996) Thermal analysis using a micromechanical calorimeter *Appl. Phys. Lett.* **69,** 40–42.
6. Bachels, T., Schäfer, R., and Güntherodt, H.-J. (2000) Dependence of formation energies of tin nanoclusters on their size and shape *Phys. Rev. Lett.* **84,** 4890–4893.
7. Baller, M. K., Lang, H. P., Fritz, J., et al. (2000) A cantilever array-based artificial nose *Ultramicroscopy* **82,** 1–4.
8. Fritz J., Baller M. K., Lang H. P., et al. (2000) Stress at the solid-liquid interface of self-assembled monolayers on gold investigated with a nanomechanical sensor. *Langmuir* **16,** 9694–9696.
9. Battiston F. M., Ramseyer J. P., Lang H. P., et al. (2001) A chemical sensor based on a microfabricated cantilever array with simultaneous resonance-frequency and bending readout. *Sensors Actuators B* **77,** 122–131.
10. Wagner, P., Hegner, M., Kernen, P., Zaugg, F., and Semenza, G. (1996) N-hydroxysuccinimide ester functionalized self-assembled monolayers for covalent immobilization of biomolecules on gold. *Biophys. J.* **70,** 2052–2066.
11. Stoney, G. G. (1909) The tension of metallic films deposited by electrolysis. *Proc. R. Soc. London Soc. A* **82,** 172–175.
12. McKendry, R., Strunz, T., Arntz, Y., et al. (2002) Multiple label-free biodetection and quantitative DNA-binding assays on a nanomechanical cantilever array. *Proc. Natl. Acad. Sci. USA* **99,** 9783–9788.
13. Arntz, Y., Seelig, J.E., Zhang, J., et al. (2003) A label-free protein assay based on a nanomechanical cantilever array. *Nanotechnology* **14,** 86–90.

14. Thaysen J., Marie R., and Boisen A. (2001) Cantilever-based bio-chemical sensor integrated in a microfluidic handling system, in *IEEE Int. Conf. Micro. Electro. Mech. Syst., Tech. Dig*. Institute of Electrical and Electronic Engineers, New York, 14th, pp. 401–404.
15. Hansen, K. M., Ji, H. F., Wu, G. H., et al. (2001) Cantilever-based optical deflection assay for discrimination of DNA single-nucleotide mismatches. *Anal. Chem*. **73,** 1567–1571.
16. Wu, G. H., Datar, R. H., Hansen, K. M., Thundat, T., Cote, R. J., and Majumdar, A. (2001) Bioassay of prostate-specific antigen (PSA) using microcantilevers. *Nat. Biotech.* **19,** 856–860.
17. Grogan, C., Raiteri, R., O'Connor, G. M., et al. (2001) Characterisation of an antibody coated microcantilever as a potential immuno-based biosensor. *Biosens. Bioelectron.* **17,** 201–207.
18. Lang, H.P., Hegner, M., Meyer, E and Christoph Gerber (2002) Nanomechanics from atomic resolution to molecular recognition based on atomic force microscopy technology. *Nanotechnology* **13,** R29–R36.

5

Analysis of Human Fibroblasts by Atomic Force Microscopy

Gillian R. Bushell, Colm Cahill, Sverre Myhra, and Gregory S. Watson

1. Introduction

The force-sensing members of the large family of scanning probe microscopies have become important tools during the past decade for visualizing, characterizing, and manipulating objects and processes on the meso- and nanoscale level. The atomic force microscope (AFM), in particular, has had an impact in the life sciences. In cell science, the pioneering work with AFM was conducted in the early 1990s ***(1–3)***. The methodologies have now reached a stage of relative maturity ***(4)***. The principal merit of the AFM is as a nonintrusive local probe of live cells and their dynamics in the biofluid environment. As well as offering high spatial resolution imaging in one or more operational modes, the AFM can deliver characterization of mechanical properties and local chemistry through operation in the force-vs-distance (F-d) mode (e.g., **ref. *5***). The lateral resolution delivered by the AFM will in most cases, and especially for soft materials, be inferior to that obtained by electron-optical techniques, but the *z*-resolution is routinely in the nanometer range with a depth of focus equal to the dynamic range of the *z*-stage travel. The instrument may be operated in one of several modes, of which the most common ones are as follows: the contact mode, using a soft lever in which contours of constant strength of interaction are traced out; the intermittent-contact mode, in which a relatively stiff lever is vibrated at a frequency near that of a free-running resonance and in which contours of constant decrement of the free-running amplitude or a constant phase shift are mapped; and the F-d mode, in which the local stiffness of interaction between tip and specimen is determined over a range of applied force (lever deflection and *z*-stage travel being the two measurable variables).

From: *Methods in Molecular Biology, vol. 242: Atomic Force Microscopy: Biomedical Methods and Applications*
Edited by: P. C. Braga and D. Ricci © Humana Press Inc., Totowa, NJ

2. Materials

2.1. Cell Culture: Handling and Preparation for In Vitro Analysis by AFM

Primary human skin fibroblasts and 3T3 cells are generally maintained as monolayer cultures in Dulbecco's modified Eagles' medium/Ham F12 containing 15 m*M* $NaHCO_3$, 50 U/mL penicillin, 50 mg/mL streptomycin, and supplemented with 10% inactivated (by heat) fetal calf serum (FCS). The cultures are then grown in a humidified environment with a 5% CO_2 atmosphere at 37°C. There are two reliable methods for preparation of live cells for AFM analysis.

2.1.1. Live Cells—Method 1

The cells are harvested by trypsin treatment in preparation for AFM analysis and are then grown overnight on sterile untreated glass cover slips. The cover slips are washed five times with serum free media (Dulbecco's modified Eagles' medium/Ham F12) containing 20 m*M* HEPES at pH 7.3. The cover slips can then be attached to standard AFM mounting plates before being covered with a droplet of fluid, in anticipation of in vitro analysis.

2.1.2. Live Cells—Method 2

The cells are grown overnight in sterile tissue culture dishes 150- or 40-mm diameter (e.g., Corning, cat. no. 430599). The preferred dishes have been pretreated by the manufacturer so as to present a negatively charged and hydrophilic surface and thus ensure better cell adherence. The cells are then washed, as in the previous paragraph, and covered to a depth of 2–3 mm with serum-free media.

2.1.3. Fixed Cells

The preparation follows a modified procedure of Pietrasanta et al. ***(6)***.

The cells on cover slips are washed for 1 min in prewarmed (37°C) phosphate-buffered saline (PBS), and then for another 1 min in stabilizing S-buffer (0.1 *M* PIPES, pH 6.9, 0.5 m*M* $MgCl_2$, and 0.1 m*M* ethylenediamine tetraacetic acid). After stabilization the cover slips are washed again in PBS before fixing in 0.01% gluteraldehyde (in S buffer) for 10 min. This is followed by another wash in PBS before being thoroughly rinsed in deionized and distilled water. Finally, the specimens are dehydrated with ethanol (70, 80, 90, and 100% in sequence for 5 min per step). The specimens are then allowed to dry in air, whereupon they are ready for AFM analysis.

2.1.4. Dehydrated Cells

The preparatory sequence is identical to that described in the introductory paragraph. However, instead of placing the cultures in a biocompatible liquid for analysis, they are now rinsed to remove excess salts, allowed to dry in air for 30 min or more, and then investigated by AFM over periods up to 3 h. In some cases, it may be possible to continue analysis for periods up to 48 h.

2.2. AFM Instrumentation and Methodology

1. Instrumentation. The examples of AFM analyses described in **Subheading 3.** were performed with a ThermoMicroscope TMX-2000 multitechnique scanning probe microscopy system. Some of the results were obtained with a Discoverer Stage attachment using an open fluid cell defined by a droplet of water trapped between the glass window on the detector stage and the cover slip substrate (similar to that described in **ref. *3***. In this configuration, a $70 \times 70\ \mu m^2$ scanner with a z range of some 13 μm was used. Any one of the mainstream AFM instruments will offer a comparable facility. On other occasions, an Explorer Stage attachment provided increased flexibility and convenience. Again, an open cell could be defined by a trapped droplet as in the case of the Discoverer Stage. It is preferable to grow the cell culture directly in a culture dish that will then constitute the fluid cell for the Explorer Stage. Several of the AFM manufacturers now offer comparably equipped standalone instruments or equivalent optional attachments. The preferred scanner for the latter procedure should have a maximum field of view of some $130 \times 130\ \mu m^2$ and a z range of 10 μm. All combinations of instrumentation will accommodate the full range of relevant operational modes: contact, *in situ* intermittent-contact in fluid, and F-d analysis.
2. Probe. A range of probes, available from several suppliers, can be used for contact-mode imaging and F-d analysis. Live cells, especially the plasma membrane, are soft objects in the context of AFM analysis (with an effective Young's modulus of less than 1 MPa). Accordingly it is necessary to work with a lever with a spring constant, k_N, in the range 0.001–0.1 N/m to avoid excessive tip indentation. The lower end of that range is suitable for general imaging and F-d analysis of the unsupported plasma membrane, whereas the upper end may be used for imaging the harder elements of the intracellular and cytoskeletal structures. Typical choices include (1) a V-shaped Si_3N_4 lever, with integral square pyramidal tip (nominal radius of curvature, R_{tip} = 40 nm, and aspect ratio, A_r. = 0.7), and with nominal values for k_N of 0.03 and 0.06 N/m; (2) a V-shaped lever, with integral triangular pyramidal tips with smaller tip radii (R_{tip} = 10–20 nm), and greater aspect ratio (A_r = 3), and with k_N = 0.5 N/m. The actual spring constant for a particular lever can be calibrated in anticipation of F-d analysis in accord with a method described in the literature ***(7)***. Other methods will offer similar information ***(8)***.

3. Methods

3.1. Fluid Ambient Environment

3.1.1. Maintenance of Static Conditions

The principal variables requiring control are temperature and fluid volume. If the fluid cell is defined by a trapped droplet, then frequent replenishment of the reservoir is required. Thus, imaging conditions will need to be reestablished at regular intervals (typically 30 min), but there is then opportunity also to reestablish optimum temperature. A larger fluid cell, such as a culture dish, with a volume of some 5 mL or more, will have a longer life span with respect to evaporative losses, and the greater thermal inertia will promote temperature stability. However, long-term stability over some hours will require replenishment. The optimum temperature can then be reestablished by total replacement of the media. Although flow-through replacement from an external reservoir is another option, the imaging conditions are likely then to be affected when a soft lever is being used. Another alternative is that of continuous heating of the cell by a hot stage, the disadvantages then being associated with thermal contraction/expansion and with thermal convection currents in the fluid.

3.1.2. Injection of Reactants for Dynamic Studies

When slow dynamics are being investigated, reactants may be introduced when there is replenishment or replacement of media. A practiced operator can usually reestablish imaging/analysis conditions within a few minutes. More rapid injection and mixing is required if fast dynamics are being investigated. Access to the fluid cell is generally restricted by the compact design of most instruments. Accordingly, a flow-through cell arrangement may be the better choice when interruption of the imaging conditions cannot be tolerated or when a particular field of view needs to be tracked continuously.

3.2. AFM Imaging and F-d Analysis

3.2.1.Imaging of Cells

3.2.1.1. Fixed or Dehydrated Cells

When a cell is fixed, through cross-linking of the plasma membrane and/or dehydration, it becomes a hard object. Consequently, it can be imaged in air by routine AFM procedures; a typical contact mode image of a fixed cell is shown in **Fig. 1**. However, scanning electron microscopy (SEM)/tunnelling electron microscopy (TEM) are richer sources of information and are generally to be preferred for this type of investigation.

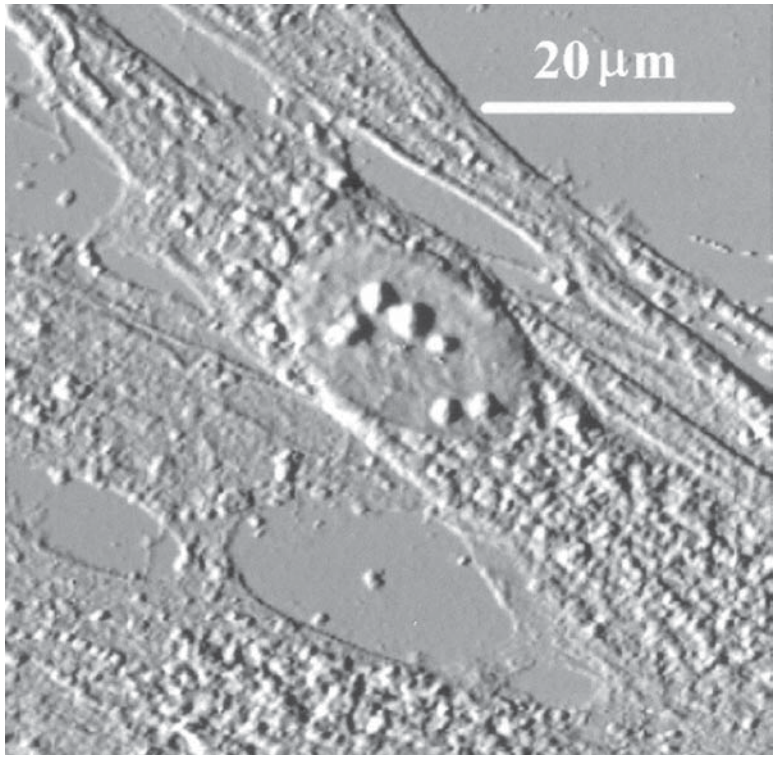

Fig. 1 Example of a fixed fibroblast imaged in air in the contact mode.

3.2.1.2. Live Cells In Vitro

Live cells on untreated cover slips rarely produce acceptable contact mode images because of poor adherence to the substrate, gross fouling of the tip, and destructive tip–membrane interactions (*see* **Notes 1–3**).

However, cells grown on surface-treated culture dishes offer greatly improved imaging conditions. Continuous scanning at linear scan speeds of 150 µm/s and at force loads in the low-nN range can now be conducted over several hours without any apparent damage to viable cells. A typical example of a contact mode image of a lamellipodial region of a fibroblast is shown in **Fig. 2**; the contour line reveals intracellular structure with a *z* resolution in the low-nm range.

3.2.2. Intermittent-Contact Resonance Mode Imaging

It is argued that the intermittent-contact resonance mode (also known as tapping mode) will result in better image quality for soft specimens. The mode

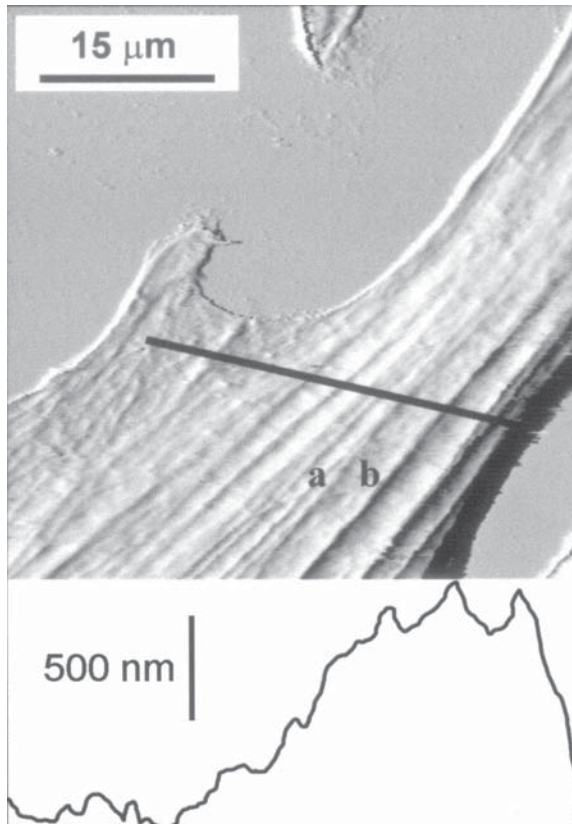

Fig. 2 Lamellipodial region of a live human fibroblast in its biocompatible fluid medium on a culture dish substrate. Contact mode imaging was performed with a standard probe having a pyramidal tip (radius of curvature of 40 nm) and a lever spring constant k_N = 0.03 N/m. The lever-imposed force loading was approx 3 nN and the fast-scan speed was 150 μm/s. The contour line reveals submembrane structure.

has two distinct advantages. The effect of lateral forces is effectively eliminated (important because cells have low resistance to shear stress). Because the interaction now arises from an impulse action at one extreme of the oscillatory motion of the tip, the inertia of the sample will resist deformation. However, the resolution of resonance mode imaging depends on the stiffness of the lever (i.e., the free-running frequency) and the width of the resonance envelope. The latter is severely degraded in water, and soft levers are preferred for analysis of live cells. Although resonance mode imaging has many advantages, the jury is probably still out in the case of in vitro analysis of cells ***(9–11)***.

3.2.3. Analysis of Cell Dynamics

As mentioned in **Subheading 1.**, the AFM is uniquely capable of tracking the temporal evolution of systems consisting of living cells in a biocompatible fluid. There are distinctly different methodologies for slow (>10 min) and fast (<10 min) dynamics.

3.2.3.1. Slow Dynamics

A skilled operator can establish good imaging conditions within a few minutes. The acquisition of an image takes typically 1–3 min. Thus, sequential imaging over a particular field of view can track cell dynamics in vitro on the time scale of some minutes. As in the cases described in **Subheading 3.1.2.**, a soft lever (k_N < 0.01 N/m) in combination with a low applied force (<1 nN) will enhance information arising from the softer elements of the cell, whereas a stiffer lever and greater applied force will deform the plasma membrane and enhance visualization of the less compressible cytoskeletal and intracellular structures. The more informative studies have exploited the latter strategy to gain insight into cytoskeletal dynamics (e.g., **refs. *5,12–14***). An example of investigations of slow intracellular dynamics is shown in a sequence of images in **Fig. 3,** where the intracellular nucleation and growth over a period of 3 h of formazan crystals is apparent. The crystals arise from enzymatic conversion of a tetrazolium salt during the MTT (3-[4,5-dimethyl thiazol-2-yl]-2,5-diphenyl tetrazolium bromide) assay of viable cells ***(5)***.

3.2.3.2. Fast Dynamics

Biological activity on the sub-second time scale can be observed and analyzed by AFM methodologies by monitoring the deflection of a lever stationary in the *x–y* plane and sensed effectively in the constant height mode (i.e., where the time-constant of the feedback loop is longer than that of the biological response mechanism). The tip is simply landed at an appropriate location predetermined from an image. The *x–y* scan function is deactivated, and the dynamic response is monitored through the *z* deflection of the lever. A soft lever is most appropriate because the probe is ideally a passive participant in the temporal evolution. The method has been deployed with considerable success in the case of cardiomyocytes ***(15,16)***. There is clearly considerable scope for applications of similar methodologies for investigations of other manifestations of cellular dynamics.

3.2.4. Analysis of Mechanical Properties

3.2.4.1. F-d Measurements

The interaction between a tip and a surface is a function of the force imposed by the lever and manifests itself as a force acting on the tip while being sensed

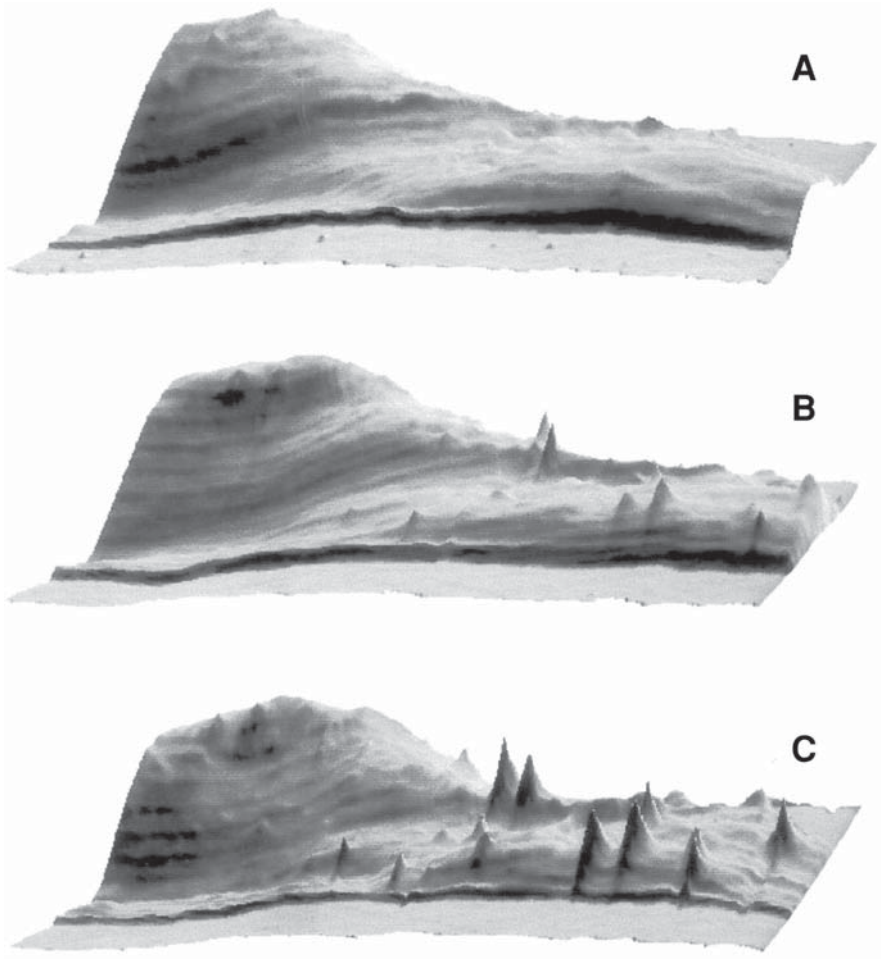

Fig. 3. Sequence of contact mode images from a lamellipodial region obtained in vitro showing nucleation and growth of formazan crystals within a viable cell. Images acquired after **(A)** 30 min; **(B)** 90 min; **(C)** 180 min.

by the lever. Such a system consists of two compliant elements–the lever and the surface–whereas all other components of the system are assumed to be rigid. Thus, compressional forces will cause bending of the lever and indentation of the surface by the tip. If the shape of the tip, the spring constant of the lever, the applied force, and the depth of indentation are known, then an effective Young's modulus for the surface can be calculated. Characteristic features of an F-d curve in combination with measurements of z stage travel and lever deflection allow such calculations to be conducted. The details of the proce-

dure have been described elsewhere (e.g., **refs. *5,17,18***). Adhesion between tip and surface manifests itself as an attractive force, causing deflection of the lever at the point of lift-off in the F-d curve. Because the strength of adhesion is a reflection of the local surface chemistry, then mapping of the surface adhesion of living cells may provide valuable additional information.

3.2.4.2. F-d Methodology for Fibroblasts

The effective Young's modulus of a supported section of the plasma membrane is in the range 1–10 kPa, whereas the corresponding value for a membrane more strongly supported by the cytoskeletal structure is in the range 15–50 kPa. The effective modulus of fixed cells is an order of magnitude higher ***(5,19)***. To obtain reliable information about mechanical properties, it is necessary that the spring constant of the lever be comparable with the effective force constant of interaction between tip and specimen. Thus, k_N in the range 0.01 N/m must be chosen. Given the extreme softness of the plasma membrane there is no incentive for working with sharp tips; even lever-imposed forces in the sub-nN range will give rise to tip indentations of 2–40 nm and contact areas of greater than 100 nm^2. Adhesive interactions add to the lever-imposed force and cause additional indentation and yet greater contact area.

3.3. Generic Outcomes of F-d Analysis of Live Fibroblasts

The results in **Fig. 4** illustrate typical outcomes of F-d analysis in vitro of fibroblasts. A standard probe with k_N = 0.03 N/m and a pyramidal tip shape, nominal radius of curvature of 40 nm, and an aspect ratio of 0.7 was used for the measurements. The data illustrate tip indentation, differences in stiffness measured at different locations, **a** and **b,** on the plasma membrane, the relative incompressibility of a fixed cell, and adhesive interactions between tip and membrane. The horizontal axis refers to *z*-stage travel, whereas the vertical axis shows lever deflection in the *z* direction.

3.4. Summary of AFM Studies Conducted on Fibroblasts

Table 1 summarizes critical methodological aspects of earlier AFM-based studies of flbroblasts and provides references for additional information.

4. Notes

1. Cell adhesion to substrate. Cell adhesion remains a significant methodological issue, although treated tissue culture substrates will generally offer acceptable performance. The extent of adhesion can readily be ascertained by running single line scans repetitively over a representative part of a cell. In extreme circumstances, a line scan will remove the entire cell from its substrate. The reproducibility of features in successive line scans is a useful monitor of stability of the

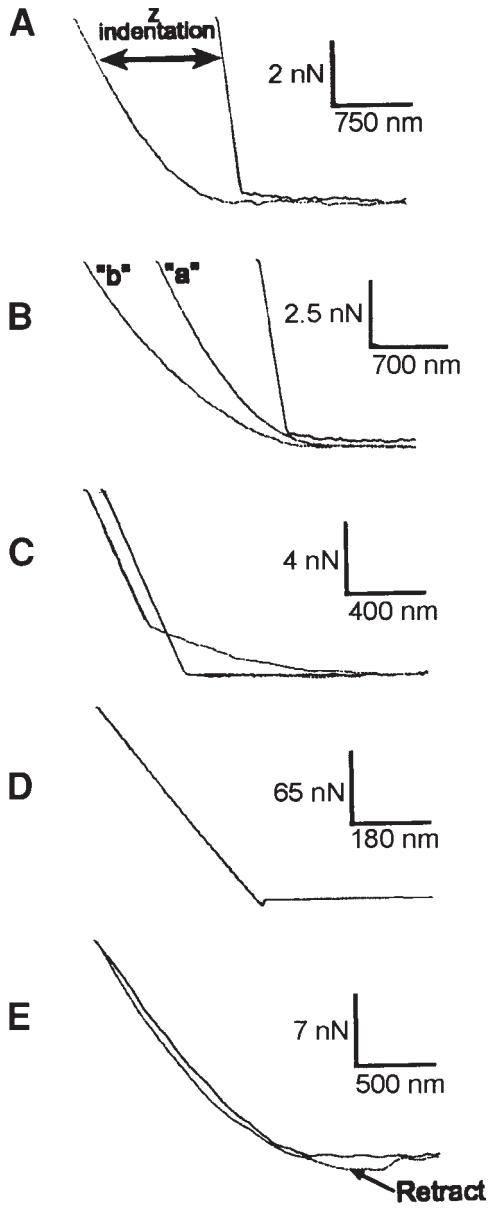

Fig. 4. **(A)** F-d curves obtained in vitro for a live flbroblast for different conditions. The steeper curve shows deflection of the lever by an incompressible surface and was used to calibrate the detector (relating nA difference current to lever deflection in nm). The less steep nonlinear curve reflects indentation by the tip in a compressible surface (i.e., the plasma membrane). In **(B)** are shown a calibration curve and the results of indenting a soft, **b**, and a stiffer, **a**, region of the plasma membrane. The data in **(C)**

Table 1
Methodological Aspects of Past Studies of Fibroblasts

Cell type	Substrate	Subst. coating	AFM mode	Probe(s)	Ref.
Fibroblasts, etc.	Glass cover slip	None	Contact	$Si_3N_4 k_N$ = 0.0 1,0.03	***20***
L929	Culture dish	None	Contact, F-d	$Si_3N_4 k_N$ = 0.03,0.06	***21***
Fibroblasts, etc.	Plastic dish	None	Contact	$Si_3N_4 k_N$ = 0.03	***13***
3T3	Plastic dish	None	Contact, F-d	$Si_3N_4 k_N$ = 0.08	***22***
3T6	Glass cover slip	None	Contact, F-d	$Si_3N_4 k_N$ = 0.01	***23***
3T3, NRK	Plastic dish	None	Contact, F-d	$Si_3N_4 k_N$ = 0.08	***14***
NIH3T3	Glass dish	Fibronectin	Contact, F-d	$Si_3N_4 k_N$ = 0.018	***24***
NIH3T3	Glass dish	Fibronectin	Contact, F-d(m)[a]	$Si_3N_4 k_N$ = 0.03	***25***

[a]A viscoelastic modulation method was adopted for the particular study.

cell during actual imaging conditions, as well as providing a measure of nondestructiveness of tip–cell interactions. Optimum quality of the image can also be obtained through adjustments of fast-scan speed and direction, force loading, parameters of the feedback loop, and field of view.

2. Tip contamination: effects and diagnostics. A cell cultured in a biofluid contains proteins, cell debris, and other contaminants in solution. The probe tip will inevitably become contaminated, at the very least, by nonspecific adsorption of proteins. Biofouling of the tip will alter the surface chemistry of the tip, and thus potentially its a destructive adherence to the cell, as well as its topography, with consequential degradation in resolution. The latter is not a serious problem, in the case of biomolecular adsorption, since extreme lateral resolution is not

---

Fig. 4. *(continued)* show that under compression the hard substrate will finally provide support for the cellular structures being compressed. The data in **(D)** demonstrate that fixing has the effect of making the cell more rigid; the cell is now effectively incompressible while the lever is the only compliant element. In **(E)** are shown both approach and retract half-cycles for a biofouled tip being used to analyze a cell. The adhesive interaction in the retract curve should be noted. Lever deflection for all curves can readily be converted to force applied, or sensed, by the lever by multiplying Z_L by k_N.

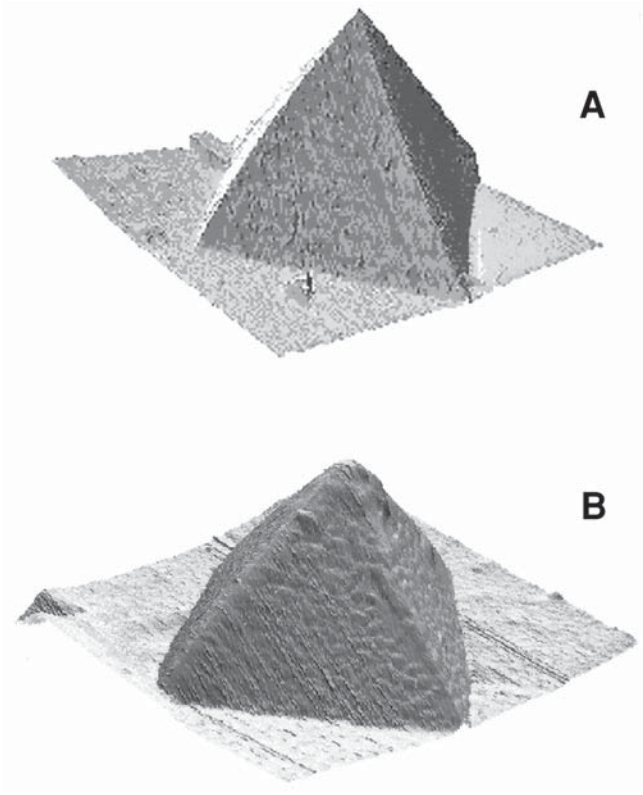

Fig. 5. Reverse images of a probe as-received **(A)** and after exposure to a biofluid **(B)**.

obtainable in any case because of the large contact area of the tip with the deformable plasma membrane. Cell debris attaching itself to the tip, however, has the effect of reducing image resolution, often to the point of complete obliteration. Here are several ways of diagnosing tip fouling, aside from its effect on the image quality. Because the general topography of the substrate can be determined at any time with a fresh tip, any subsequent deterioration in definition of topographical resolution must be caused by tip fouling. A more quantitative method is to conduct reverse imaging of the tip ***(8,26)***, whereby an image of the tip is generated from a scan over a spiky feature (e.g., an upturned tip attached to a substrate). **Figure 5** shows reverse images of an as-received tip, and of a tip after exposure to a biofluid. Finally, a contaminated tip may be analyzed in the F-d mode by indenting on a known hard substrate. If the tip is compliant, as a result of adherent biodebris, then it will be obvious from the F-d curves.

3. Common image artifacts. Several of the early studies have reported prominent effects because of precipitation of salts from the biofluid solution. If the analysis

is conducted in an open cell, and the cell is subject to evaporative losses, then the solution will become supersaturated in salts. Consequently, crystalline precipitates will form within the field of view. Moreover, the biofluid will no longer be compatible with cell viability. Frequent replacement of the biofluid will substantially eliminate that problem.

Tip-broadening and other tip-related artifacts will occur when the actual topography of the object being imaged is defined by radii of curvature less than or comparable to the radius of curvature of the tip, and/or when there are gradients exceeding that corresponding to the aspect ratio of the tip. For instance, images of tobacco mosaic virus (TMV) attached to a flat substrate obtained by AFM reveal the correct height of approx 18 nm, but the apparent lateral width will be in the range 60–100 nm as a result of the tip-shape convolution ***(27)***. Because the radius of the cylindrical TMV is known and is comparable to that of the apex of the tip, the apparent width of the object, *W*, in is given by the following:

$$W = 2[(R_{\mathrm{TMV}} + R_{\mathrm{Tip}})^2 - (R_{\mathrm{Tip}} - \mathrm{R}_{\mathrm{TMV}})^2]^{1/2}$$

When cytoskeletal structure is being imaged, the situation is somewhat more complicated by filamentary objects located some distance above the substrate. The aspect ratio then comes into play because the deformable membrane allows the tip to indent the cell on either side of the filamentary object. The apparent width will now depend on the height, *h*, of the object above the point of greatest indentation by the tip on either side of the object. The relevant expression is now as follows:

$$W \approx 2[hA_{\mathrm{r}}^{-1} + (r_{\mathrm{tip}} + r_{\mathrm{obj}})\cos\,\phi]$$

where the radii of the tip and object are r_{tip} and r_{obj}, respectively; A_{r}, is the aspect ratio of the tip, and the angle is defined by $\phi = \tan^{-1} A_{\mathrm{r}}^{-1}$.

Finally, other grosser artifacts will occur when the dynamic range of the *z* stage is exceeded; the image then becomes entirely featureless. A similar effect occurs when the *z*-height corrugations of the object exceed the height of the tip, and the surface of the lever defines the point of contact. The interaction is no longer localized, and the details of the image become washed out. Likewise, F-d analysis will now produce erroneous data since the spring constant will depend on an unknown and changing point of contact and the contact area will also be much greater leading to erroneous conclusions about indentation and adhesion.

Acknowledgments

Some of the work described above was funded in part by the Australian Research Council.

References

1. Gould, S. A. C., Drake, B., Prater, C. B., Weisenhorn, A. L., Manne, S., Hansma, H. G., et al. (1990) From atoms to integrated-circuit chips, blood-cells, and bacteria with the atomic force microscope. *J. Vac. Sci. Technol. A* **8,** 369–373.

2. Henderson, E., Haydon, P. G., and Sakaguchi, D. S. (1992) Actin filament dynamics in living glial cells imaged by atomic force microscopy. *Science* **257,** 1944–1946.
3. Hoh, J. H. and Hansma, P. K. (1992) Atomic force microscopy for high-resolution imaging in cell biology. *Trends Cell Biol.* **2,** 208–212.
4. Hong, X. and Lei, Y. (1999) Atomic force microscopy of living cells: progress, problems and prospects. *Methods Cell Sci.* **21,** 1–17.
5. Bushell, G. R., Cahill, C., Clarke, F. M, Gibson, C. T., Myhra, S., and Watson, G. S. (1999) Imaging and force-distance analysis of human fibroblasts in vitro by atomic force microscopy. *Cytometry* **36,** 254–264.
6. Pietrasanta, L. I., Schaper, A., and Jovin, T. M. (1994) Imaging subcellular structures of rat mammary carcinoma cells by scanning force microscopy. *J. Cell Sci.* **107,** 2427–2437.
7. Gibson, C. T., Watson, G. S., and Myhra, S. (1996) Determination of the spring constants of probes for force microscopy/spectroscopy. *Nanotechnology* **7,** 259–262.
8. Gibson, C. T., Watson, G. S., and Myhra, S. (1997) Scanning force microscopy - calibrative procedures for 'best practice'. *Scanning* **19,** 564–581.
9. Putman, C. A. J., van der Werf, K. O., de Grooth, B. G., van Hulst, N. F., and Greve, J. (1994) Viscoelsticity of living cells allows high resolution imaging by tapping mode atomic force microscopy. *Biophys. J.* **67,**1749–1753.
10. Le Grimellec, C., Lesniewska, E., Giocondi, M.-C., Finot, E., and Goudonnet, J.-P. (1997) Simultaneous imaging of the surface and submembraneous cytoskeleton hi living cells by tapping mode atomic force microscopy. *Acad. Sci. Biophys.* **320,** 637–643.
11. Vie, V., Giocondi, M.-C., Lesniewska, E., Finot, E., Goudonnet, J.-P., and Le Grimellec, C. (2000) Tapping-mode atomic force microscopy on intact cells: optimal adjustment of tapping conditions by using the dflection signal. *Ultramicroscopy* **82,** 279–288.
12. Schoenenberger, C.-A., and Hoh, J. H. (1994) Slow cellular dynamics in MDCK and R5 cells monitored by time-lapse atomic force microscopy. *Biophys. J.* **67,** 929–936.
13. Braet, F., Saynaeve, C., de Zanger, R., and Wisse, E. (1998) Imaging surface and submembraneous structures with the atomic force microscope: a study on living cancer cells, fibroblasts and macrophages. *J. Microsc.* **190,** 328–338.
14. Rotsch, C. and Radmacher, M. (2000) Drug-induced changes of cytoskeletal structure and mechanics in fibroblasts: an atomic force microscopy study. *Biophys. J.* **78,** 520–535.
15. Shroff, S. G., Saner, D. R., and Lai, R. (1995) Dynamic micromechanical properties of cultured rat atrial myocytes measured by atomic force microscopy. *Am. J. Physiol.* **269,** C286–C292.
16. Domke, J., Parak, W. J., George, M., Gaub, H. E., and Radmacher, M. (1999) Mapping the mechanical pulse of single cardiomyocytes with the atomic force microscope. *Eur. Biophys. J.* **28,**179–186.

17. Crossley, J. A. A., Gibson, C. T., Mapledoram, L. D., Huson, M. G., Myhra, S., Pham, D. K., et al. (2000) Atomic force microscopy analysis of wool fibre surfaces in air and under water. *Micron* **31,** 659–667.
18. Blach, J., Loughlin, W., Watson, G., and Myhra, S. (2001) Surface characterization of human hair by atomic force microscopy in the imaging and F-d modes. *Int. J. Cosm. Sci.* **23,**165–174.
19. Wu, H. W., Kuhn, T., and Moy, V. T. (1998) Mechanical properties of L929 cells measured by atomic force microscopy: effects of anticytoskeletal drugs and membrane crosslinking. *Scanning* **20,** 389–397.
20. Kuznetsov, Y. G., Malkin, A. J., and McPherson, A. (1997) Atomic force microscopy studies of living cells: Visualization of motility, division, aggregation, transformation and apoptosis. *J. Struct. Biol.* **120,**180–191.
21. Wu, H. W., Kuhn, T., and Moy, V. T. (1998) Mechanical properties of L929 cells measured by atomic force microscopy: effects of anticytoskeletal drugs and membrane crosslinking. *Scanning* **20,** 389–397.
22. Rotsch, C., Jacobson, K., and Radmacher, M. (1999) Dimensional and mechanical dynamics of active and stable edges in motile fibroblasts investigated by using atomic force microscopy. *Proc. Natl. Acad. Sci. USA* **96,** 921–926.
23. Ricci, D., Tedesco, M., and Grattarola, M. (1997) Mechanical and morphological properties of living 3T6 cells probed via scanning force microscopy. *Microsc. Res. Tech.* **36,** 165–171.
24. Haga, H., Sasaki, S., Kawabata, K., Ito, E., Ushiki, T., and Sambongi, T. (2000) Elasticity mapping of living fibroblasts by AFM and immunofluorescence observation of the cytoskeleton. *Ultramicroscopy* **82,** 253–258.
25. Haga, H., Nagayama., M., Kawabata, K., Ito, E., Ushiki, T., and Sambongi, T. (2000) Time-lapse viscoelastic imaging of living fibroblasts using force modulation in AFM. *J. Electron Microsc.* **49,** 473–481.
26. Hellemans, L., Waeyaert, K., and Hennau, F. (1991) Can atomic force microscopy tips be inspected by atomic force microscopy? *J. Vac. Sci. Technol.* **B9,** 1309–1312.
27. Bushell, G. R., Watson, G. S., Holt, S.A., and Myhra, S. (1995) Imaging and nano-dissection of tobacco mosaic virus by atomic force microscopy. *J. Microsc.* **180,**174–181.

6

Corneal Tissue Observed by Atomic Force Microscopy

Stylliani Lydataki, Miltiadis K. Tsilimbaris, Eric S. Lesniewska, Alain Bron, and Iannis G. Pallikaris

1. Introduction

The cornea is the transparent avascular part of the anterior segment of the eye and consists of a stratified nonkeratinizing squamous epithelium, a stromal dense connective tissue layer, and an endothelium facing the anterior chamber. The cornea contributes largely to the intraocular refraction of the light. Damage can impair its tissue transparency and lead to loss of vision. Significant diseases, such as corneal dystrophies, keratoconus, and refractive errors, are related to the structure and integrity of the cornea.

In conventional scanning electron microscopy studies, the corneal surface appears like a mosaic consisting of three types of cells, as it can be deduced from their electron reflex and size ***(1–4)***. The apical membrane of these cells is covered by the tear film. The inner corneal surface, facing the anterior chamber of the eye, is the apical membrane of the endothelium, which forms a monolayer of polygonal cells responsible for maintaining the state of relative deturgescence of the stroma through active transport ***(5–10)***. The stromal layer consists of regularly arranged dense connective tissue constituting 90% of the corneal thickness. It comprises sheets of lamellae of highly ordered collagen fibrils, embedded in a matrix of proteoglycans, and keratocytes. The former are interspersed between the lamellae, forming an interlinking network throughout the cornea ***(11–13)***.

AFM has been recently introduced with success in the research of corneal surfaces and components ***(11,14–16)***. Compared with other forms of microscopy used in corneal study, AFM offers several advantages: it can reach very high magnifications with high resolution, it requires minimal tissue preparation, and it is able to image samples in aqueous environments, thus permitting images to be obtained under conditions that resemble the tissue's native environment. Additional advantages include the possibility of dynamic in vivo

From: *Methods in Molecular Biology, vol. 242: Atomic Force Microscopy: Biomedical Methods and Applications*
Edited by: P. C. Braga and D. Ricci © Humana Press Inc., Totowa, NJ

study of biological processes and the capability of characterizing the nanomechanical properties of relatively smooth surfaces. Limitations of the method include the relatively small scan sizes and scan speeds and difficulties in imaging very soft biological samples. Because of such limitations, the AFM is currently used either as an investigational tool or as an adjuvant to other microscopic techniques. In long term, however, it has the potential to evolve in a unique multipotential instrument for the study of the morphology and mechanical properties of various biological tissues ***(17)***.

This chapter describes the methodology used to study the surface of the cornea in albino New Zealand rabbits and in humans. We describe the procedures necessary in rabbits to study the normal epithelial and endothelial surfaces as well as the corneal stroma after mechanical and excimer laser ablation. Samples were imaged in balanced salt solution (BSS) both fresh and after fixation in glutaraldehyde. We studied in humans the endothelial surface of two corneal buttons received after corneal transplantation for endothelial dystrophy. The tissue was imaged in BSS after fixation in glutaraldehyde.

2. Materials

2.1. Tissue Collection and Preparation

1. Rabbit corneas: New Zealand albino rabbits with 3–4 kg body weight.
2. Human corneas: Transplant recipient corneal button.
3. Anesthesia solution: 10 mg/kg xylazine hydrochloride + 10 mg/kg ketamine hydrochloride.
4. Proparacaine drops.
5. Operating microscope.
6. Surgical blades.
7. Excimer laser.
8. Surgical instruments for enucleation and corneal dissection.
9. Precision wipe paper.
10. Rinsing and observation solution (Alcon Laboratories, Fort Worth, TX).
11. Solutions for enzymatic preparation: 30 mU/mL neuraminidase in phosphate buffer solution (Sigma Chemical Co., St. Louis, MO); 30 mU/mL hyaluronidase in phosphate buffer solution (Sigma).
12. Fixative solution: glutaraldehyde, 2.5% buffered solution, pH 7.3, at 4°C.
13. Buffer solution for fixative preparation: 0.2 *M* stock solution of sodium cacodylate, pH 7.3, kept at 4°C.
14. Euthanasia solution: sodium pentobarbital.

2.2. Microscopy Equipment

1. AFM (Nanoscope IIIa, Digital Instruments, Veeco Inst., Santa Barbara, CA), including an optical viewing system and image analysis software.
2. Piezo-electric scanners, 12–150 μm.

3. V-shaped silicon nitride tips with a spring constant of 10 mN/m (Microlever; Park Scientific Instruments, Sunnyval, CA).
4. Magnetic stainless-steel punches.
5. Epoxy glue.
6. Fine forceps for tissue transfer and manipulation.

3. Methods

3.1. Tissue Collection (see *Notes 1–5)*

3.1.1. Rabbit Cornea

3.1.1.1. Anesthesia

The animals are anesthetized with a subcutaneous injection of xylazine and ketamine. Additional topical anesthesia with proparacaine drops is used to anesthetize the cornea.

3.1.1.2. Stromal Ablation

The anesthetized animal is placed under the operating microscope. Mechanical ablation is performed using a sharp surgical blade, and the anterior one third of the cornea is dissected taking care not to penetrate the cornea. Excimer laser ablation is performed following a standard protocol for myopia correction; a myopic correction of three diopters is aimed.

3.1.1.3. Euthanasia

Animals are euthanized by an injection of sodium pentobarbital overdose delivered via a peripheral ear vein.

3.1.1.4. Enucleation

The eye globes are carefully enucleated as soon as possible after death. Special care is taken not to contaminate the corneal surface with blood and not to touch or stress the tissue during manipulation. Eyes that will be imaged fresh are placed in BSS solution. For eyes that are going to be examined fixed, the fixation process described in the next paragraph is followed.

3.1.2. Human Corneas

The recipient corneal buttons from patients undergoing corneal transplantation are collected.

3.2. Fixation Process

3.2.1. Rabbit Eyes

Immediately after enucleation, the eye globes are placed into fixative solution. After 30 min and while the eye globe is still in the solution, a hole is

opened 6 mm behind the limbus to allow penetration of the fixative solution in the interior of the eye. The fixative solution is replaced with freshly prepared solution. The eyes are kept overnight in the solution at 4°C before AFM observation.

3.2.2. Human Corneal Buttons

Immediately after trephination, the recipient button is placed into fixative solution. The eyes are kept overnight in the solution at 4°C before AFM observation.

3.3. Preparation of Corneal Specimens

Handle all cornea specimens withfine instruments under microscopic observation, paying attention not to distort the tissue during manipulations such as cutting, transportation, and gluing

3.3.1. Rabbit Corneas

This step is performed immediately after enucleation in eyes that are going to be imaged fresh. Fixed eyes are processed after completion of the fixation. The anterior part of the eye is cut away and the cornea is freed from the underlying iris, cilliary body, and lens. The tissue is trimmed near the sclerocorneal limbus and it is dissected in two semicircular pieces.

Corneal specimens are transferred to magnetic stainless-steel punches and are fixed with epoxy glue. Specimens are maintained with the surface that is going to be examined upwards. Before transfer, the excess of solution is absorbed from the seating side by using a precision wipe paper. After transfer to the magnetic punches all specimens are covered with BSS solution and placed under the micoscope. For corneas that will be observed after enzymatic treatment the process described below is followed prior to transfer to the punches.

3.3.2. Human Corneas

The corneal button is dissected in two semicircular pieces. Corneal specimens are transferred to magnetic stainless-steel punches and are fixed with epoxy glue. Specimens are maintained with the surface that is going to be examined upwards. After transfer to the magnetic punches, all specimens are covered with BSS solution and placed under the microscope.

3.3.3. Enzymatic Preparation

The cornea freed from the underlying iris, cilliary body, and lens is immersed in neuraminidase or hyaluronidase enzymatic solution with the surface to be examined directed upwards. The dishes containing the enzymatic solutions are closed and kept at 37°C for 30 min. After the completion of this time, they are

removed from the solution and rinsed gently with BSS for 5 min to remove the excess of enzyme and the enzymatic digestion products. After that the specimens are transferred to magnetic punches.

3.4. AFM Imaging (see Notes 6–15)

3.4.1. Image Aquisition

1. The area of interest is chosen using the optical microscope attached to the viewing window of the AFM. The central area at a distance of some millimeters from the specimen's edges is considered the area most appropriate for observation.
2. Imaging starts using large scanning areas, when possible. Large scanning areas provide information about the general topography of the sample and allow for the selection of flat regions without defects for small-scale imaging. For imaging of areas from 20–100 µm (**Fig. 1**) a 100-µm scanner is used. For smaller areas ranging from 10–0.2 µm, high resolution can be achieved with a 12-mm scanner (**Fig. 2**).
3. To obtain good images, the force curve needs to be corrected repeatedly. In fresh tissue the adhesion of the surface glycocalyx sugars to the microscope tip, results in fuzzy images. In these sample it is often difficult to achieve a good forces-vs-distance curve and several tries are necessary until satisfactory images are acquired (**Fig. 3A**). Imaging of fixed tissue is considerably easier because the surface glycocalyx is removed during the fixation process (**Fig. 3B**).
4. The scan rate ranges between 0.5 and 10 Hz, depending on the scan size. Small frequencies are used to scan large areas (**Fig. 4**) and vice versa.
5. Imaging forces of not more than 100 pN are used. High forces are applied only as a means to mechanically remove the surface layer that adheres to the tip.
6. Images are obtained with a resolution 512 × 512 pixels of trace and retrace collecting data. Three types of images can be obtained during the contact mode imaging:
   a. In height images the color-coded contrast refers to the spatial variation of the Z-height of the tip (**Figs. 3** and **4**).
   b. In deflection images the contrast differences of the surface refer to the spatial variation of the strength of the probe–specimen interaction (**Fig. 5**).
   c. In lateral force microscopy or friction images, information concerning the friction on the surface f the specimen during the movement of the tip is displaced. However, interpretation and analysis of the later images of the cornea remains difficult.

3.4.2. Image Analysis

1. For a better presentation, height images are processed using a plane-fit adjustment, when the sample surface is not perpendicular to the scanner's z-axis.
2. To evaluate the surface structure, sections on the height images are used that present the profile of the surface. These sections are indispensable when features like protrusions, particles, holes, fibrils, and so on have to be measured. The sections are performed on raw data images. Zooming is necessary when small features of large-scanning images have to be measured.

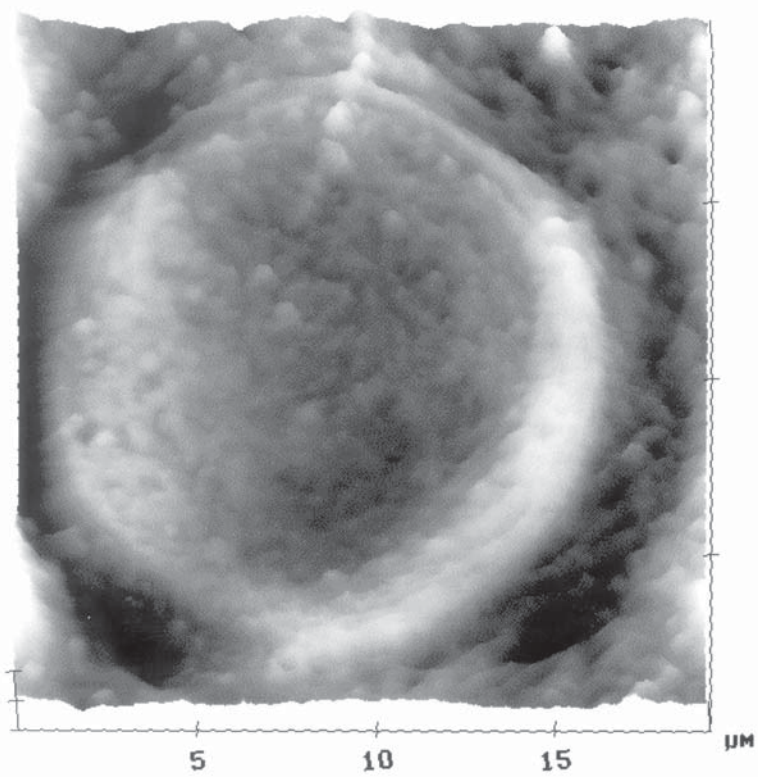

Fig. 1. Low-force contact-mode AFM image. Human corneal endothelium from a patient with corneal endothelial dystrophy who underwent corneal transplantation. The recipient corneal button was studied with AFM. 20-μm scan range; 1.5-Hz scan rate; scanning force <100 pN.

3. Quantitative data are acquired after the measurement of several morphological characteristics. The meta-analysis tools provided by the system's software facilitate for the calculation of statistical and topographic parameters. These include the ratio of the length along the longer axis over the height of measured structures as well as the measurement of surface roughness. Such quantitative analysis gives more precise information about the morphology of the surface.

Fig. 2. *(opposite)* Low-force contact-mode AFM images. **(A)** Height image of fixed rabbit corneal endothelium showing a detail of the intercellular contact of two epithelial cells and the micro-projections on their surface. 5-μm scan range; 2-Hz scan rate; scanning force <100 pN. **(B)** Height image of fixed rabbit corneal stroma after mechanical dissection. Collagen fibrils appear randomly arranged. In some of them the periodicity is apparent. 10-μm scan range; 2-Hz scan rate; scanning force <100 pN.

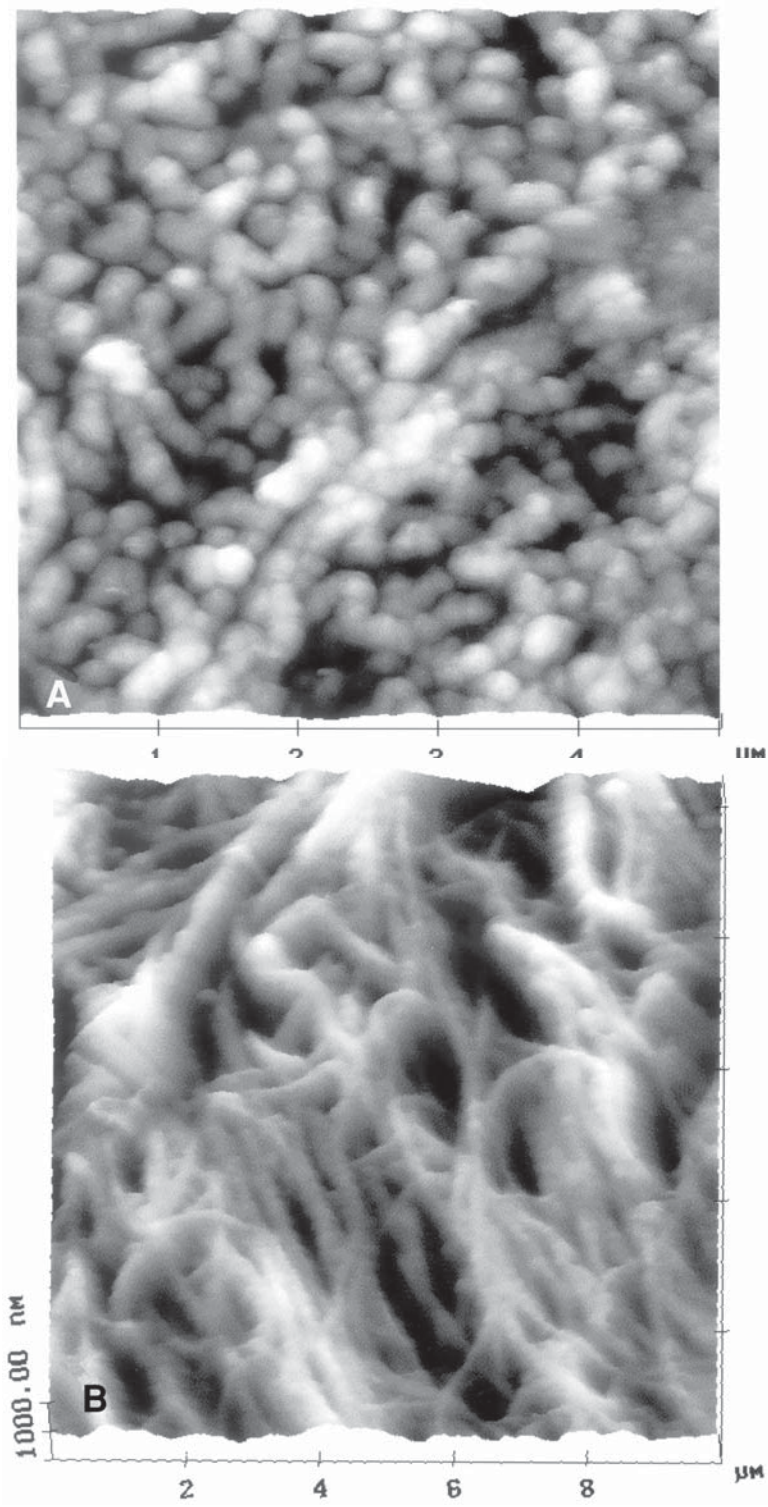
A
1
2
3
4
µm
B
1000.00 nm
2
4
6
8
µm

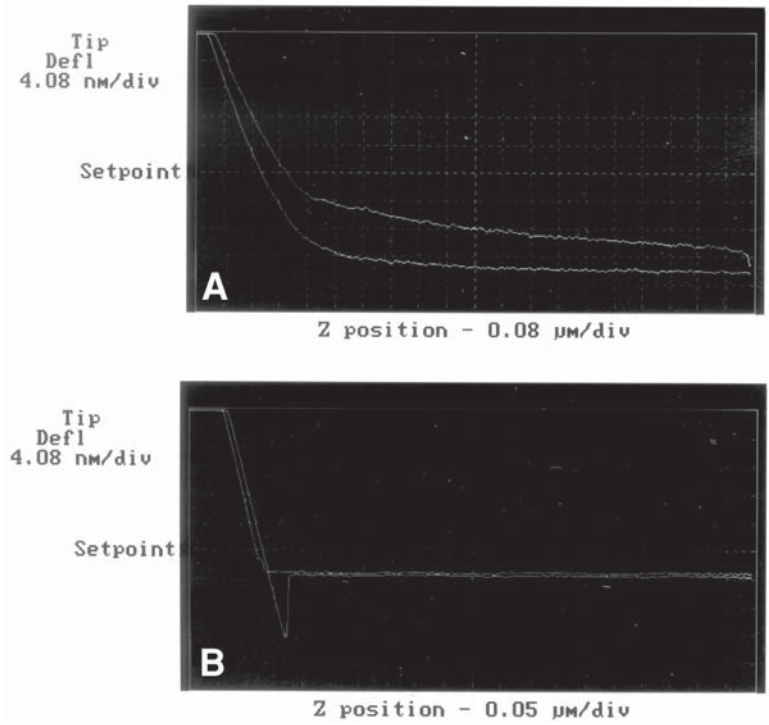

Fig. 3. **(A)** Force-vs-distance curve recorded on the fresh corneal surfaces. The cantilever's deflection in the vertical axis is converted into force using the relationship $F = k_{cl}$, where k_{cl} is the spring constant of the free cantilever. **(B)** Force-vs-distance curve recorded on the fixed corneal surfaces. Note the difference between fixed and fresh specimen curves.

4. Roughness statistics are performed on height images 5 × 5 µm. Mean roughness (*Ra*) and root mean square (RMS), or *R(q),* are calculated. *R(q)* is the standard deviation of the *Z* values in a given area whereas*Ra* is the mean roughness value of the surface relative to the center plane.

4. Notes

To be able to extract information from AFM imaging it is important to minimize the risk of artifacts before or during the imaging.

Fig. 4. *(opposite)* Low-force contact-mode AFM images. **(A)** Height image of fixed rabbit cornea showing one endothelial cell. 25-µm scan range; 1.5-Hz scan rate; scanning force <100 pN. **(B)** Height image of fixed corneal endothelium showing a very fine structure of a few nanometers on the surface. 200-nm scan range; 10 Hz-scan rate; scanning force <100 pN.

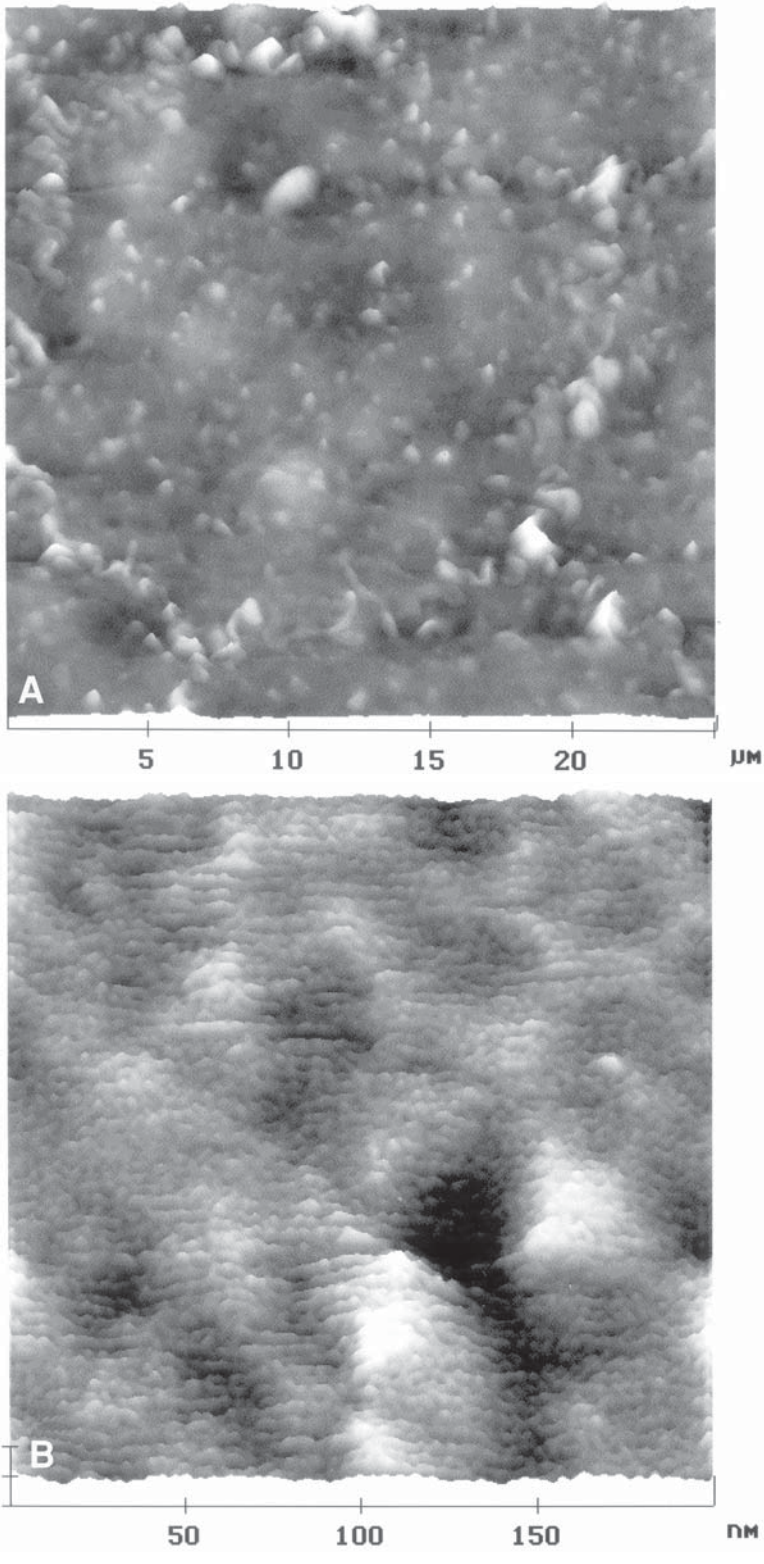
A
5
10
15
20
μm
B
50
100
150
nm

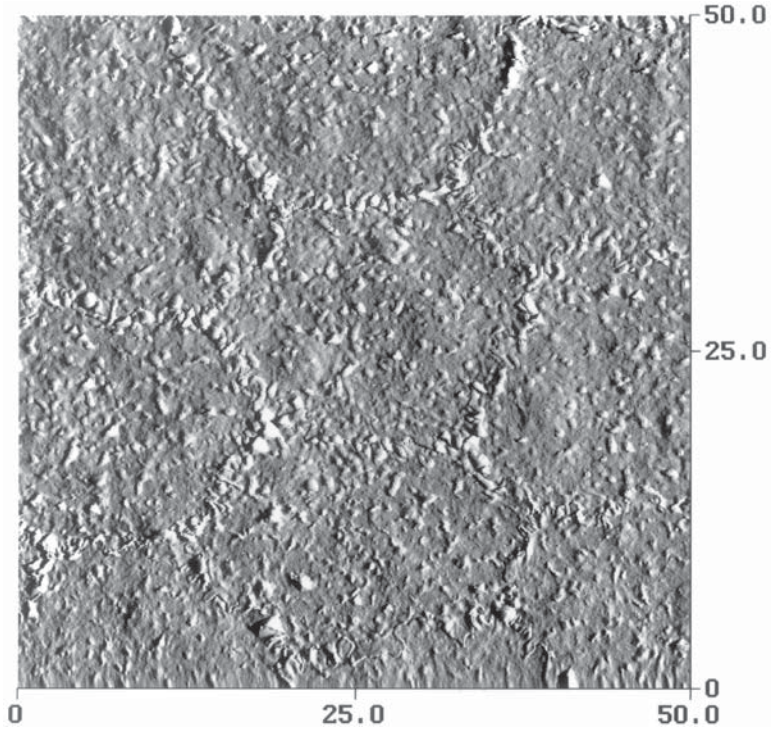

Fig. 5. Deflection AFM image. Fixed rabbit corneal endothelial surface. The contour of endothelial cells its easily detected. Because of their height contrast, these images are suitable for counting the features on the surface. 50-μm scan range; 0.5-Hz scan rate; scanning force <100 pN.

1. Before imaging, fresh tissue poses considerable imaging difficulties. The interaction of glycoaminoglycans chains of the glycocalyx layer with the microscope tip makes the imaging of the fresh tissue difficult (**Fig. 6**). When the imaging of a specimen is important not to fail, consider fixation. The removal of the glycocalyx that happens during fixation makes the imaging easier.
2. Enzymatic treatment represents another way to improve image acquisition from fresh tissue. The enzymatic process increases the unevenness of the sample surface thus increasing contrast. In addition, information concerning the sample's molecular composition can be revealed and help in the interpretation of the effect of the enzyme on the surface morphology (**Fig. 7**).
3. When imaging of the outer corneal surface is intended, it is important to handle the tissue very carefully during preparation. Contamination and distortion of the superficial corneal layers can happen very easily and will alter the surface morphology. When the tissue is going to be imaged fixed, the installation of a few fixative drops on the corneal surface while the animal is in deep anesthesia just

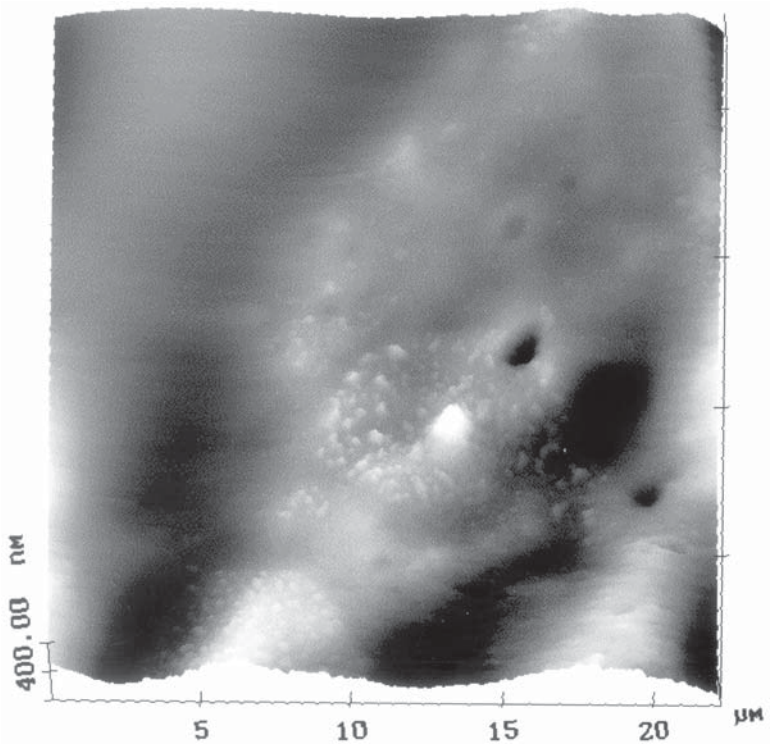

Fig. 6. Low-force contact-mode AFM image. Height image of fresh epithelium. 22-µm scan range; 1.5-Hz scan rate; scanning force <100 pN. A large part of the surface appears fuzzy.

prior to euthanasia ensures preservation of the superficial corneal layers in the best possible condition.

4. Gentle manipulation of the tissue in general is very important. Prepare all the instruments and materials in advance. It is essential to work under an operating microscope or a stereoscope especially when cutting the samples to be imaged. The working place, the instruments, and the solutions need to be very clean. Prior to imaging, inspect the sample's surface and ensure it is not defective or contaminated.
5. Time optimization: tissue preparation, cutting, and gluing on the pounches must be completed as quickly as possible to avoid tissue drying.
6. BSS represents our preferred medium for observation. This solution was selected because it contains all the essential ions necessary for maintenance of the rabbit and human corneal integrity ***(10,18,19)***.
7. Allow 15–30 min after the installation of the sample under the microscope for the system to reach a thermal equilibrium. This will elliminate thermal drifting.

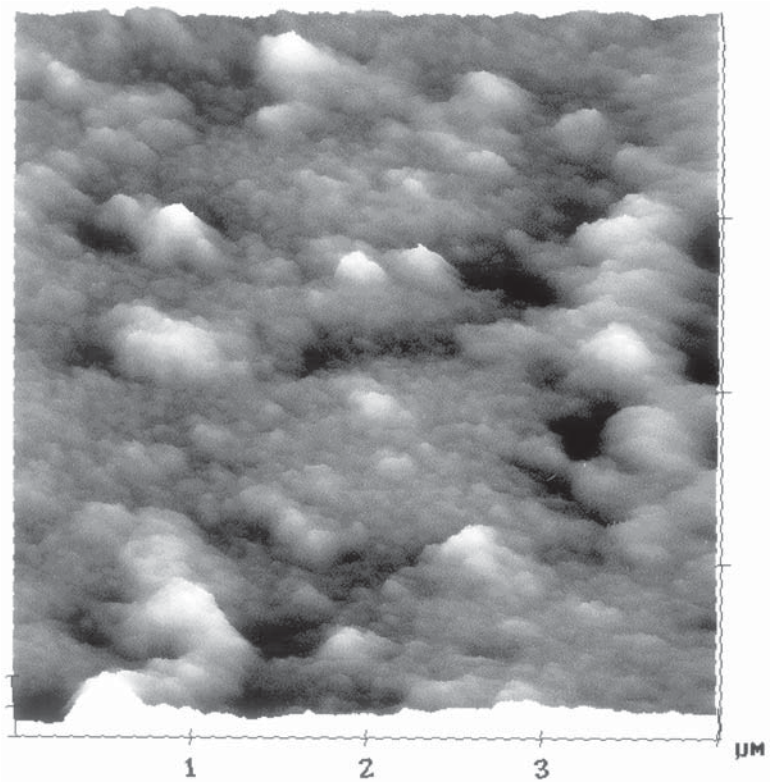

Fig. 7. Low-force contact-mode AFM image. Fresh rabbit corneal endothelium treated with neuraminidase. A microgranular structure can be seen on the surface together with elevated aggregates of different sizes. 4-μm scan range; 3-Hz scan rate; scanning force <100 pN.

8. Adjust the level of the set-point force by using the force-vs-distance curve (**Fig. 3**). This determines the force that the tip applies to the sample. A set–point level close to the jump-out point ensures an operation with minimal force.
9. When a soft cantilever is used, the applied force should be maintained in the sub-nano-newton level. Higher forces produce significant surface alterations. This effect is more pronounced in fresh tissue.
10. Duration of sample observation: in fixed tissue, the duration of observation of a specimen can be extended to 2.5 h without obvious morphological alterations. Observation of fresh tissue in BSS should not exceed 1–1.5 h. If the process is prolonged over this time the tissue hydration changes and edema occurs.
11. When there is any doubt concerning the tip's quality, check it and if necessary replace it.

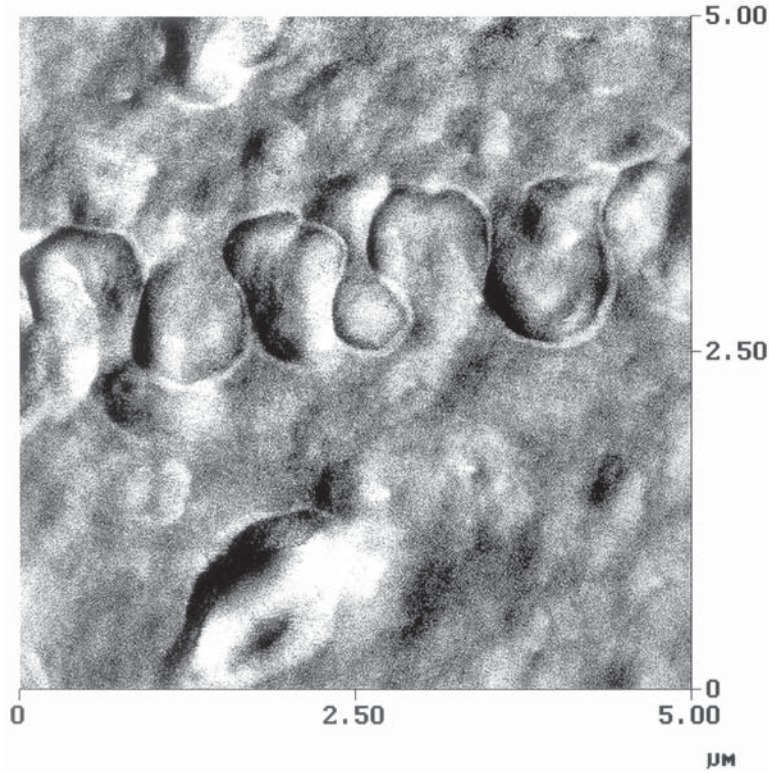

Fig. 8. Low-force tapping-mode AFM. Amplitude image of fixed rabbit cornea showing the corneal endothelial cell interdigitations. 5-µm scan range; scanning force <100 pN; 0.500-nm amplitude.

12. When the specimen's surface is rough, it may be necessary to alternate various imaging conditions (scan angle, scan frequency, etc.) to obtain an image of acceptable quality.
13. If the surface does not permit imaging using a large scanning area it is preferable to reduce the scanning area. This way you will save time and you will reduce the risk of damaging the sample and/or the tip.
14. Zooming to a smaller scanning area should be accompanied by an increase in the scanning speed.
15. Imaging is usually performed in contact mode. Taping mode gives height-images with a quality inferior to that of contact mode. The phase and amplitude images in tapping mode are usually of very good quality (**Fig. 8**). For the time being, however, the interpretation of these images is not easy.

References

1. Doughty, M. J. (1990) Morphometric analysis of the surface cells of rabbit corneal epithelium by scanning electron microscopy. *Am. J. Anat.* **189,** 316–328.
2. Doughty, M. J. (1990) On the evaluation of the corneal epithelial surface by scanning electron microscopy. *Optom. Vis. Sci.* **67,** 735–756.
3. Hazlett, L. D. (1993) Corneal and ocular surface histochemistry. *Prog. Histochem. Cytochem.* **25,** 1–60.
4. Hoffmann, F. (1972) The surface of epithelial cells of the cornea under the scanning electron microscope. *Ophthal. Res.* **3,** 207–214.
5. Hager, H., Hoffmann, F., and Dumitrescu, L. (1975) Scanning electron microscopy in ophthalmology. *Ann. Ophthalmol.* **7,** 1361–1371.
6. Doughty, M. J., Bergmanson, J. P., and Blocker, Y. (1997) Shrinkage and distortion of the rabbit corneal endothelial cell mosaic caused by a high osmolality glutaraldehyde-formaldehyde fixative compared to glutaraldehyde. *Tissue Cell* **29,** 533–547.
7. Doughty, M. J. (1994) The cornea and corneal endothelium in the aged rabbit. *Optom. Vis. Sci.* **71,** 809–818.
8. Hirsch, M., Renard, G., Faure, J.-P., and Pouliquen, Y. (1997) Study of the ultrastructure of the rabbit corneal endothelium by freeze-fracture technique: apical and lateral junctions. *Exp. Eye Res.* **25,** 277–288.
9. Lea, P. J., Hollenberg, M. J., Menon, I. A., Temkin, R. J., Persad, S. D., and Basu, P. K. (1989) High resolution scanning electron microscopy of rabbit corneal endothelium to show effects of UV-visible irradiation in the presence of chlorpromazine. *Lens Eye Toxic Res.* **6,** 119–133.
10. Edelhauser, H. F., Hanneken, A. M., Pederson, H. J., and Van Horn, D. L. (1981) Osmotic tolerance of rabbit and human corneal endothelium. *Arch. Ophthalmol.* **99,** 1281–1287.
11. Yamamoto, S., Hashiume, H., Hitomi, J., et al. (2000) The subfibrillar arrangement of corneal and scleral collagen fibrils as revealed by scanning electron and atomic force microscopy. *Arch. Histol. Cytol.* **63,** 127–135.
12. Bairaktaris, G., Lewis, D., Fullwood, N. J., et al. (1998) An ultrastructural investigation into proteoglycan distribution in human corneas. *Cornea* **17,** 396–402.
13. Borcherding, M. S., Blacik, L. J., Sittig, R. A., Bizzell, J. W., Breen, M., and Weinstein, H. G. (1975) Proteoglycans and collagen fibre organization in human corneoscleral tissue. *Exp. Eye Res.* **21,** 59–70.
14. Fullwood, N. J., Hammiche, A., Pollock, H. M., Hourston, D. J., and Song, A. M. (1995) Atomic force microscopy of the cornea and sclera. *Curr. Eye Res.* **14,** 529–535.
15. Tsilimbaris, M. K., Lesniewska, E., Lydataki, S., Le Grimellec, C., Goudonnet, J. P., and Pallikaris, I. G. (2000) The use of atomic force microscopy for the observation of corneal epithelium surface. *Invest. Ophthalmol. Vis. Sci.* **41,** 680–686.
16. Meller, D., Peters, K., and Meller, K. (1997) Human cornea and sclera studied by atomic force microscopy. *Cell Tissue Res.* **228,** 111–118.

17. Binning, G., Quate, C. F., and Gerber, C. (1986) Atomic force microscope. *Phys. Rev. Lett.* **56,** 930–933.
18. Doughty, M. J. (1992) Quantitative evaluation of the effects of a bicarbonate and glucose- free balanced salt solution on rabbit corneal endothelium in vitro. *Optom Vis. Sci.* **69,** 846–857.
19. Doughty, M. J., Newlander, K., and Olejnik, O. (1993) Effect of bicarbonate-free balanced salt solutions on fluid pump and endothelial morphology of rabbit corneas in-vitro. *J. Pharm. Pharmacol.* **45,** 102–109.

7

AFM Study of Surface Structure Changes in Mouse Spermatozoa Associated With Maturation

Hiroko Takano and Kazuhiro Abe

1. Introduction

If a sample has a comparatively even surface and is fixed on a sample stage, atomic force microscopy (AFM) will give a clear image of the surface structure at subnanometer level ***(1,2)***. Because a sperm head is flat and can be attached on the slide glass firmly after it is fixed, we consider that AFM is the competent tool for the study of the sperm surface structure.

Spermatozoa are produced in the testis and transferred into the epididymis. In the epididymis, they acquire a fertilization ability and mobility, which is called sperm maturation ***(3)***. It has been proved biochemically and immunocytochemically that glycoproteins on or in the sperm plasma membrane are altered, masked, or replaced by new glycoproteins of epididymal origin in the epididymal duct ***(4–6)***. These changes are considered to be necessary for fertilization ***(3,7)***. Thus, it is probable that the sperm surface structure changes progressively in the epididymal duct ***(8)***. We reported the changes in the surface structure of the spermatozoa in the hamster epididymis by AFM ***(9)***. Subsequently, we have studied the surface structure of the spermatozoa from mouse epididymis by AFM. In these studies we developed several tricks for improving AFM images. In this chapter, we will show our recent results and the materials and methods used , including the tricks we learned in these studies.

Histologically, the mouse epididymis is divided into five regions (segments I–V) in adult male mice **(Fig. 1;** refs. ***10,11***). These segments perform different roles in the process of sperm maturation ***(12)***. Spermatozoa are immature in segment I but mature in segment V ***(13)***. The epithelial cells in segment II appear to secrete glycoproteins for sperm maturation ***(10,14,15)***, so we examined the segments I, II, and V of the mouse spermatozoa by AFM.

From: *Methods in Molecular Biology, vol. 242: Atomic Force Microscopy: Biomedical Methods and Applications*
Edited by: P. C. Braga and D. Ricci © Humana Press Inc., Totowa, NJ

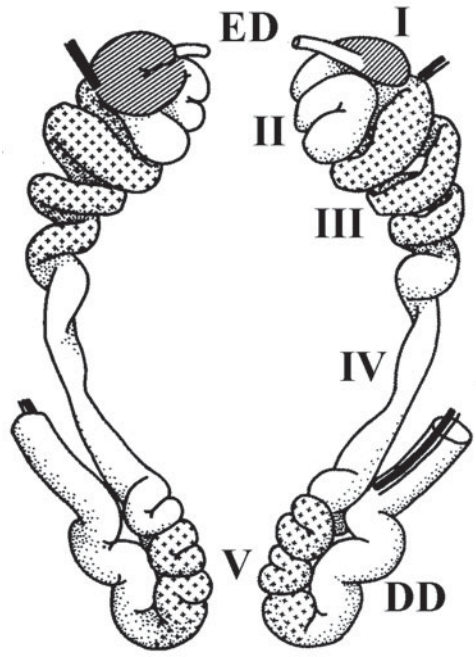

Fig. 1. Schematic diagram of the histological segmentation of the mouse epididymis. ED, efferent duct; I–V, epididymal segments; DD, deferent duct.

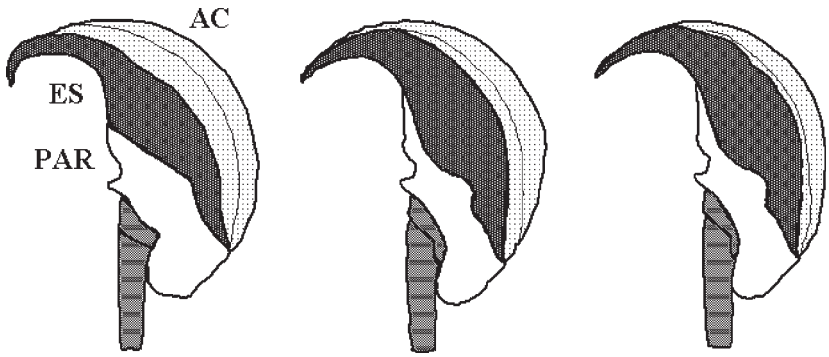

Fig. 2. Diagrams traced from the AFM images of the mouse spermatozoa from segments I *(left),* II *(middle),* and V *(right).* AC, acrosomal cap; ES, equatorial segment; PAR, post-acrosomal region.

The surface of the sperm head is classically divided into two domains, the acrosomal region and postacrosomal region (**Fig. 2**). The acrosomal region is subdivided into the acrosomal cap and equatorial segment (**Fig. 2**). These domains play the different roles at fertilization ***(16,17)***. The plasma membrane of the equatorial segment is maintained after acrosome reaction and fuses with

the plasma membrane of an oocyte at fertilization ***(3)***. Because of this, our study focused on the changes in the surface structure of the equatorial segment.

Dynamic force mode AFM, as used in our laboratory, provides images in constant height mode, amplitude mode, and phase mode. Images in constant height mode offer the topographical information of the sample height (**Fig. 3**). Those in amplitude mode and phase mode offer well-defined contours of the projections and hollows based on the changes in oscillation amplitude and phase, respectively (**Figs. 4–6**). Using a combination of these modes, the sperm head was shown to be covered with particles whose diameter was < 100 nm. The size of the surface particles differed between the acrosomal region and postacrosomal region in the same spermatozoon. Particularly, the particles covering the equatorial segment changed in size dramatically during the passage through the epididymal duct **(Figs. 4–6**). The surface of the equatorial segment was covered with the particles of 20–50 nm in diameter in segment I, 50–80 nm in segment II, and 20 nm in segment V. These size differences generated the different morphological surface features among the spermatozoa from segments I, II, and V (**Figs. 4–6**). Because the epithelial cells in segment II appear to secrete acid glycoproteins, which play a role as a sperm maturing factor ***(10,14,15)***, large particles covering the segment II sperm surface may be glycoproteins secreted from the epithelial cells in segment II.

AFM images also demonstrated the changes in shape of the acrosomal cap. The acrosome cap is flat and wider in the immature spermatozoa from segments I and II than in mature spermatozoa from segment V (**Figs. 2** and **3A** through **6A**). Thus, an application of AFM for the study of the surface structure of the mouse spermatozoa brought us noteworthy new findings.

2. Materials

1. A mature male dd-mouse at 90 days of age.
2. Modified tyrode solution (this medium is used for making sperm suspension and for washing spermatozoa by centrifugation): 500 mL distilled water, 2.05 g NaCl, 0.1 g KCl, 0.1 g $CaCl_2$(anhyd.), 0.05 g $MgCl_2/H_2O$, 0.025 g NaH_2PO_4/H_2O, 1.5 g $NaHCO_3$, approx pH 8.0. This stock solution can be used for one month if stored at 4°C.
3. Fixative: 2% glutaraldehyde in 0.1 *M* cacodylate buffer.
4. Ethyl alcohol (anhyd.).
5. 3-methylbutyl acetate.
6. Nitrogen gas.
7. A double-edged razor.
8. Small vials.
9. Test tubes.
10. Test-tube stand.
11. Disposable pipets.
12. Plastic dishes for ethyl alcohol.

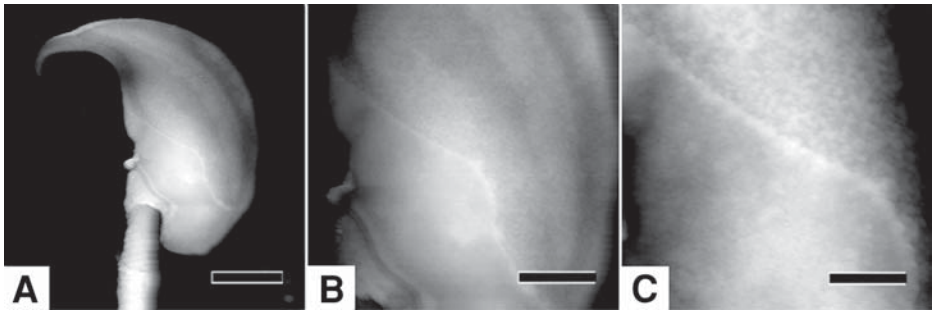

Fig. 3. AFM image in constant force mode of epididymal segment I.

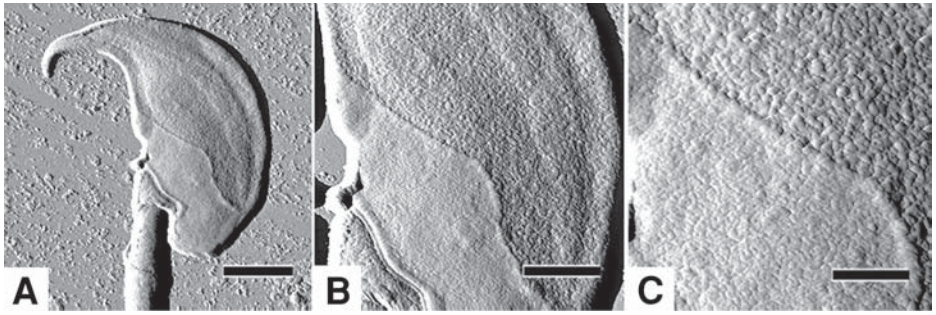

Fig. 4. AFM image in amplitude mode of the same spermatozoon as in **Fig. 3.**

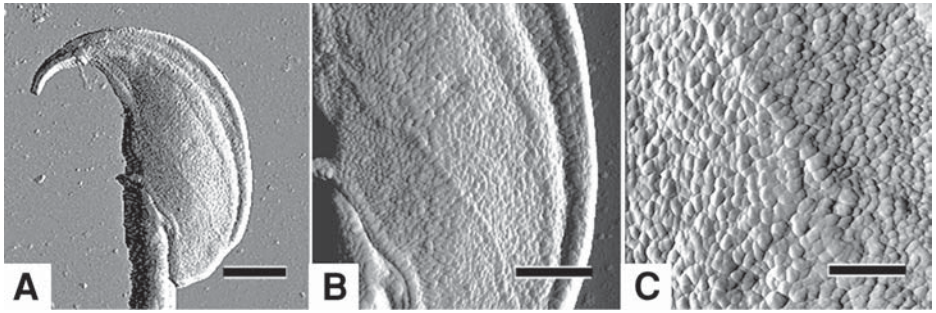

Fig. 5. AFM image in amplitude mode of the spermatozoon from segment II.

Fig. 6. AFM image in amplitude mode of the spermatozoon from segment V.

13 A glass dish for 3-butyl-ethyl acetate.
14. Micro slide glass coated with adhesive material (Superfrost, Matunami Glass IND., LTD, Japan).
    a. Cut the micro slide glass into 7-mm squares.
    b. Mark the surface of one side of of the slide glass squares with the glass cutter to distinguish the side of the sperm attachment.
15. Centrifugal separator.
16. Critical point drier.
17. AFM.
    a. Probe station/Unit SPI3800 /SPA300 (Seiko Instruments, Japan).
    b. Scanner table (a maximum scan range is 20 μm × 20 μm × 3 μm, (*x*, *y*, *z* direction).
    c. Lever table (20 N/m).
    d. Cantilever tips SI-DF20 (Seiko Instruments, Japan).
    e. Optical microscope.
    f. Antivibration platform and nitrogen gas bomb.

3. Methods

3.1. Preparation of Samples

1. Remove both sides of the epididymis from a mature dd-mouse. Separate the tissue of segments I–V of the epididymis (**Fig. 1**; **ref. *10***).Cut tissue blocks of segments I, II, and V into small pieces with razors and place in the bottom of small vials separately.
2. Pour 3 mL of medium into each small vial and make the small pieces of tissue separate in the medium with tweezers. Wait a few minutes for spermatozoa to submerge from the stumps of the epididymal duct.
3. Transfer 2 mL of sperm suspension to a centrifugal tube and centrifuge at 240*g* for 8 min.
4. Pour 3 mL of medium into each centrifugal tube to wash the spermatozoa, and centrifuge at 240*g* for 8 min twice more.
5. Fix the spermatozoa in 2% glutaraldehyde in 0.1 *M* cacodylate buffer solution for 1 h.
6. Adjust the total amount of the sperm suspension to be 0.3 mL with distilled water after centrifugation.
7. Place one drop of sperm suspension on the slide glass square. As the glass is coated with adhesive material, spermatozoa adhere to the surface of the glass in 5–10 min. Make 3 or 4 samples.
8. Move the slide glass in distilled water to allow the release of loosely-attached spermatozoa from the slide glass.
9. Check the density of the spermatozoa on the slide glass under a light microscope.
10. Transfer the slide glass with spermatozoa in turn to 80 (5 min), 90 (5 min), 95 (5 min), and 100% (10 min, twice) ethyl alcohol solutions for dehydration.

Figs. 3–6. *(facing page)* AFM images of mouse epididymal spermatozoa. **(B)** and **(C)** are enlarged images of **(A)**. Bar is 2 μm in **(A)**, 1 μm in **(B)**, and 0.5 μm in **(C)**.

11. Immerse the samples in 3-butyl-ethyl acetate solution for 15 min.
12. Put a sample in a cage and perform critical point drying.

3.2. Scanning Operation Method of Dynamic Force Mode (DFM)

1. Allow the nitrogen gas to flow into the antivibration platform.
2. Turn on the antivibration platform and CCD camera controller.
3. Turn on the light of the optical microscope.
4. Set the scanner table.
5. Turn on the power at the center of the front panel of SPI3800N probe station controller.
6. Turn on the computer and the display. Microsoft Windows startup menu will appear.
7. Double click the icon of *Spise132* on the desktop to open the application for AFM.
8. Select "DFM" in "SPA300/400" frame and click "OK"; the main program, *SPIWin,* will start.
9. Set the sample stage on the mount on top of the scanner.
10. Set the sample on the sample stage.
11. Select a spermatozoon and move it to the center of the eye field of the optical microscope by hand.
12. Install the DFM cantilever holder with a DFM cantilever into the unit.
13. Select "CCD Monitor" in the setup menu to display "CCD". Check the position of the cantilever and the specimen by CCD image. Use the Move-in command (Low or High) and set the distance between the sample and the cantilever at approx 0.1 mm (which corresponds to a 180°- rotation of the fine-focus dial of the optical microscope).
14. Set the laser unit on SPA 300.
15. Adjust the laser light spot to be in right position.
    a. Rotate adjustment knobs "Laser X" and "Laser Y" to put the laser light spot on the top of the cantilever under the optical microscope.
    b. Rotate adjustment knobs "Laser X" and "Laser Y" to maximize ADD output. The maximum value of ADD output is around 5 or 13 depending on the cantilever.
    c. Rotate adjustment knob "DIF" so that the output may be in the range from –1 to 1 V
    d. Rotate adjustment knobs "DIF" and "FFM" so that the output may be in the range from 0 to 1 V.
16. Measure the Q-curve.
    a. Select "Q-curve" in the Scan menu to display "Q-curve Console."
    b. Put the initial value of the parameter of the Q-curve Console. One example follows:

Freq. High	400 kHz
Low	1 kHz
Gain	1
Vib. Voltage	1 V
LPF	1 kHz

HPF 1 kHz
Time 5 s

c. Select "Left" in the Vib. Freq. frame.
d. Check "Phase," "Calibration," and "Auto Set."
e. Click "Configuration" button to display configuration dialog.
f. Set the value of the auto set. "Amplitude" is 1.000 V and "Frequency" is 3.000 kHz.
g. Click "Start" to measure the Q-curve and the phase curve. Computer calculates the optimal value for the vibration frequency (operation point) immediately and displays the values with the Q-curve. An example follows:

Freq. High	128.410 kHz
Low	125.410 kHz
Gain	1.000
Vib. Voltage	1.511 V
LPF	1.0 kHz
HPF	1.0 kHz
Time	5 s
Vib. Freq.	126.800
Amplitude	1.068 V
Peak Freq.	126.918 kHz
ΔF	0.335
Q	379.273
Phase	–56.520°

h. Click "Close" to close, on the Q-curve Console

18. Approach the force area.
    a. Select "Image" in the Scan menu to display "Approach" and "Scan Console."
    b. Preset the parameters in the Scan Console follows:
       Amplitude Reference -0.101
       I-gain 0.177, P-gain 0.0488, A-gain 0, S-gain 0
       when the maximum ADD value is around 5.
       I-gain 0.0592, P-gain 0.0122, A-gain 0, S-gain 0
       when the maximum ADD value is around 13.
    c. Open "Sub Console" to confirm the filter values for topography.
       Data Type Topo (servo)
       LPF 1.000 kHz, HPF 0.000 Hz, Range 1583.20 nm, Offset 0.715V
    d. Approach the sample to the cantilever by using the Approach button.
    e. Lower the value of the Amplitude Reference until the scanning voltage becomes stable.
    f. Make the Amplitude Reference 0.3–0.5 down from the value of getting stability of the scanning voltage.
19. Separate the sample from the cantilever until the scanning voltage displays –20.
20. Turn off the laser light.
21. Insert the head of the spermatozoa under the tip of the cantilever under the optic microscope.
22. Perform the test scan at 512 × 128 points in the area of 15,000 nm^2 at the scan speed of 1 Hz.

23. Approach the force area by using the "Approach" button and click "Start."
24. Execute **steps 21–23** again when the object is not displayed in the canvas.
25. Change the rotation angle, center of the image, and scan area to get the proper compositon. Use "Zoom" to change the center of the image.
26. Check the composition of the image by test scan.
27. Write the sample information in the column for comments.
28. Change the number of the scan points to 512 × 512.
29. The relation between "Scan Area" and "Scan Speed follows."

Scan area (nm)	*Scan speed (Hz)*
9,000	0.28
8,000	0.28
6,000	0.37
4,000	0.41
3,000	0.56
2,000	0.85
1,000	1.23

    It takes 40 min to get an image of 9,000 nm square.
30. Start to scan.
31. Set the S-gain value between 3 and 8 if the image is improved by this.
32. Separate the sample from the cantilever after completing the scan.
33. Save the measured data into HDD or MO as soon as possible.
34. When all measurements are finished, close the *SPIWin* software and *CCD* monitor.
35. Shut down the system.
36. Turn off the light of the optical microscope.
37. Turn off the power of CCD camera controller and antivibration platform.
38. Stop nitrogen gas to flow to the antivibration platform.
39. Turn off the power at the center of the front panel of SPI3800N Probe station controller.

4. Notes

1. When the ADD output does not move freely, readjust the position of the laser light on the cantilever or the distance between the specimen and the cantilever to be adequate (approx 0/1 mm).
2. The adequate value of the Amplitude Reference often moves in the minus direction during scanning. In this case the scanned image will become blurred and disappear at last. To avoid this, the value of the Amplitude Reference is better set 0.3–0.5 lower than the value necessary to stabilize the scanning voltage.
3. Caution the following items to prevent the cantilever tip from damages.
    a. Scanning should not be stopped on the way of image delineation, even if the image is not good.
    b. The rotation angle and the scan area of the image should not be changed when the sample is in the force area.
    c. When the computer freezes, the sample should be separated from the cantilever by using up-down lever equipped in SPA300 before application is stopped.
    d. FFM knob should not be rotated during scanning.

4. Pay attention to the appearance of double images or two or more triangle-shaped particles arranged in the same direction, which reflect damage to the cantilever tip. If these signs appear, replace the cantilever immediately.
5. When an image does not appear in the NC-force canvas, try again and you will get the image.
6. A test scan is recommended after the scan area is changed because the scan position often shifts after that.
7. When the scanning voltage shows 200, the following three reasons should be taken into consideration.
   a. The laser beam is now off.
   b. The proper value of the amplitude reference is changed spontaneously to minus direction. In this case remeasurement of Q-curve is effective.
   c. FFM value is out of ±1.0 V.
8. Check the FFM value just before scanning, because FFM value is easy to change.

References

1. Ushiki, T., Hitomi, J., Ogura S., Umemoto, T., and Shigeno M. (1996) Atomic force microscopy in histology and cytology. *Arch. Histol. Cytol.* **59,** 421–431.
2. Tojima, T., Hatakeyama, D., Kawabata, K., Abe, K., and Ito, E. (1999) Reexamination of fine surface topography of nerve cells revealed by atomic force microscopy. *Bioimages* **7,** 89–94.
3. Yanagimachi, R. (1994) Mammalian fertilization, in *The Physiology of Reproduction,* Vol. 1, 2nd ed . (Knobil, E. and Neill, J. D., eds.), Raven Press, New York, pp. 189–317.
4. Brooks, D. E. and Higgins, S. J. (1980) Characterization and androgen-dependence of proteins associated with luminal fluid and spermatozoa in the rat epididymis. *J. Reprod. Fertil.* **59,** 363–375.
5. Jones, R., Pholpramool, C., Setchell, B. P., and Brown, C. R. (1981) Labelling of membrane glycoproteins on rat spermatozoa collected from different regions of the epididymis. *Biochem J.* **200,** 457–460.
6. Echieverria, F. M. G., Cuasnicu, P. S., and Blaquier, J. A. (1982) Identification of androgen-dependent glycoproteins in the hamster epididymis and their association with spermatozoa. *J. Reprod. Fertil.* **64,** 1–7.
7. Moore, H. D. M. (1981) Glycoprotein secretions of the epididymis in the rabbit and hamster. Localization on epididymal spermatozoa and the effect of specific antibodies on fertilization in vivo. *J. Exp. Zool.* **215,** 77–85.
8. Bearer, E. L. and Friend, D. S. (1990) Morphology of mammalian sperm membranes during differentiation, maturation, and capacitation. *J. Electron Microsc. Tech.* **16,** 281–297.
9. Takano, H. and Abe, K. (2000) Changes in the surface structure of the hamster sperm head associated with maturation, in vitro capacitation and acrosome reaction: an atomic force microscopic study. *J. Electron Microsc.* **49,** 437–443.
10. Takano, H. (1980) Qualitative and quantitative histology and histogenesis of the mouse epididymis, with special emphasis on the regional difference. *Acta Anat. Nippon.* **55,** 573–587 (in Japanese).

11. Abe, K., Takano, H., and Ito, T. (1983) Ultrastructure of the mouse epididymal duct with special reference to the regional differences of the principal cells. *Arch. Histol. Jpn.* **46,** 51–68.
12. Abe, K., Takano, H., and Ito, T. (1982) Response of the epididymal duct in the corpus epididymidis to efferent or epididymal duct ligation in the mouse. *J. Reprod. Fertil.* **64,** 69–72.
13. Pavlok, A. (1974) Development of the penetration activity of mouse epididymal spermatozoa in vivo and in vitro. *J. Reprod. Fertil.* **36,** 203–205.
14. Lea, O. A., Petruz, P., and French, F. S. (1978) Purification and localization of acidic epididymal glycoprotein (AEG): a sperm coating protein secreted by the rat epididymis. *Int. J. Androl. Suppl.* **2,** 592–607.
15. Flickinger, C. J. (1983) Synthesis and secretion of glycoprotein by the epididymal epithelium. *J. Androl.* **4,** 157–161.
16. Koehler, J. K. (1982) The mammalian sperm surface: an overview of structure with particular reference to mouse spermatozoa, in *Prospects for Sexing Mammalian Sperm* (Amann, R. P. and Seidel, G. E Jr., eds.), Colorado Associated University Press, Boulder, pp. 23–42.
17. Peterson, R. N. and Russell, L. D. (1985) The mammalian spermatozoon: a model for the study of regional specificity in plasma membrane organization and function. *Tissue Cell* **17,** 769–791.

8

Calculation of Cuticle Step Heights from AFM Images of Outer Surfaces of Human Hair

James R. Smith

1. Introduction

Atomic force microscopy (AFM) is an ideal technique for noninvasive examination of hair surfaces ***(1–11)***, providing a wealth of structural information not always apparent from electron microscopy. The fine cuticular structure of human head hair is of interest to those engaged in the fields of dermatology ***(12–14)***, cosmetics ***(15–17)***, and forensic science ***(18–20***). In the former, the morphology of hair can be affected by an underlying inherited or congenital metabolic disorder, such as maple syrup urine disease ***(21)*** or monilethrix ***(22)***, respectively. The cosmetics industry is interested in the effects of haircare formulations, such as conditioning and bleaching agents, on hair cuticle surfaces ***(23)***. There is now increasing legislation on cosmetic manufacturers to be able to substantiate claims made concerning their products.

Cuticle step height, as shown in **Fig. 1**, is an important parameter for the quantitative assessment of human hair ***(5,24,25)***. Step heights typically range from 300–500 nm ***(5,15)*** but can vary further as a result of swelling or lifting caused by clinical, cosmetic, or environmental effects. This large variation in step height can be attributed to the heterogeneous character of hair cuticular structure.

The wide distribution of step height coupled with the need to obtain many step measurements clearly calls for a computational image processing technique. Such an approach is necessary to perform vast numbers of step height measurements for statistical comparisons. This becomes even more apparent when it is realized that there are a multitude of often-subtle differences in cuticle patterns between hairs from different parts of the head, between hairs from different body sites, and within each hair according to the distance from

From: *Methods in Molecular Biology, vol. 242: Atomic Force Microscopy: Biomedical Methods and Applications*
Edited by: P. C. Braga and D. Ricci © Humana Press Inc., Totowa, NJ

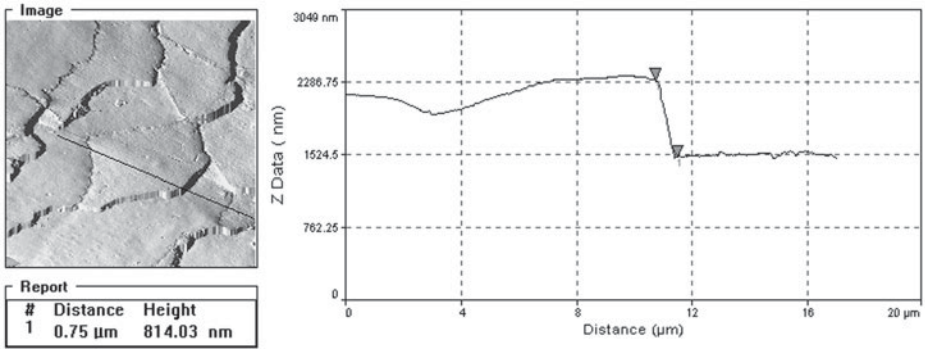

Fig. 1. A transect across an image of a hair cuticle showing a typical scale edge profile. In this case, the cuticle step height is shown to be 814 nm.

the skin surface. Except as a means for illustrating specific surface features, the single atomic force micrograph cannot be said to be representative of that hair and certainly not of a whole head of hair. This therefore focuses our attention on the need for quantitative extraction of surface architectural information, which by adequate sampling will enable systematic statistical comparisons to be made within and between hairs.

In this chapter, the method is demonstrated on a hair sample half of which has been bleached with a cosmetic formulation and the other left untreated. AFM topography imaging (**Fig. 2**) was conducted near the boarder region where the known length variation on surface architecture was considered to play a negligible role ***(8)***.

2. Materials

1. A tress of human hair. In this chapter, a tress of European brown hair, of length 20 cm, was used.
2. Sodium dodecyl sulfate solution (1%).
3. Cosmetic formulation for hair treatment. Here, a commercial bleaching product was used.
4. Double-sided, adhesive carbon tape (*see* **Note 1**).
5. Tweezers for manipulating hair fibers.
6. Atomic force microscope. Here, a TopoMetrix TMX2000 Discoverer Scanning Probe Microscope, operated in contact mode, in air, using 200-µm V-shaped silicon nitride cantilevers (spring constant 0.032 N/m) was used.

3. Methods

3.1. Sample Preparation

1. Place about 20 fibers in a 100-cm^3 beaker half filled with sodium dodecyl sulfate solution (1%), ensuring all the hairs are immersed.

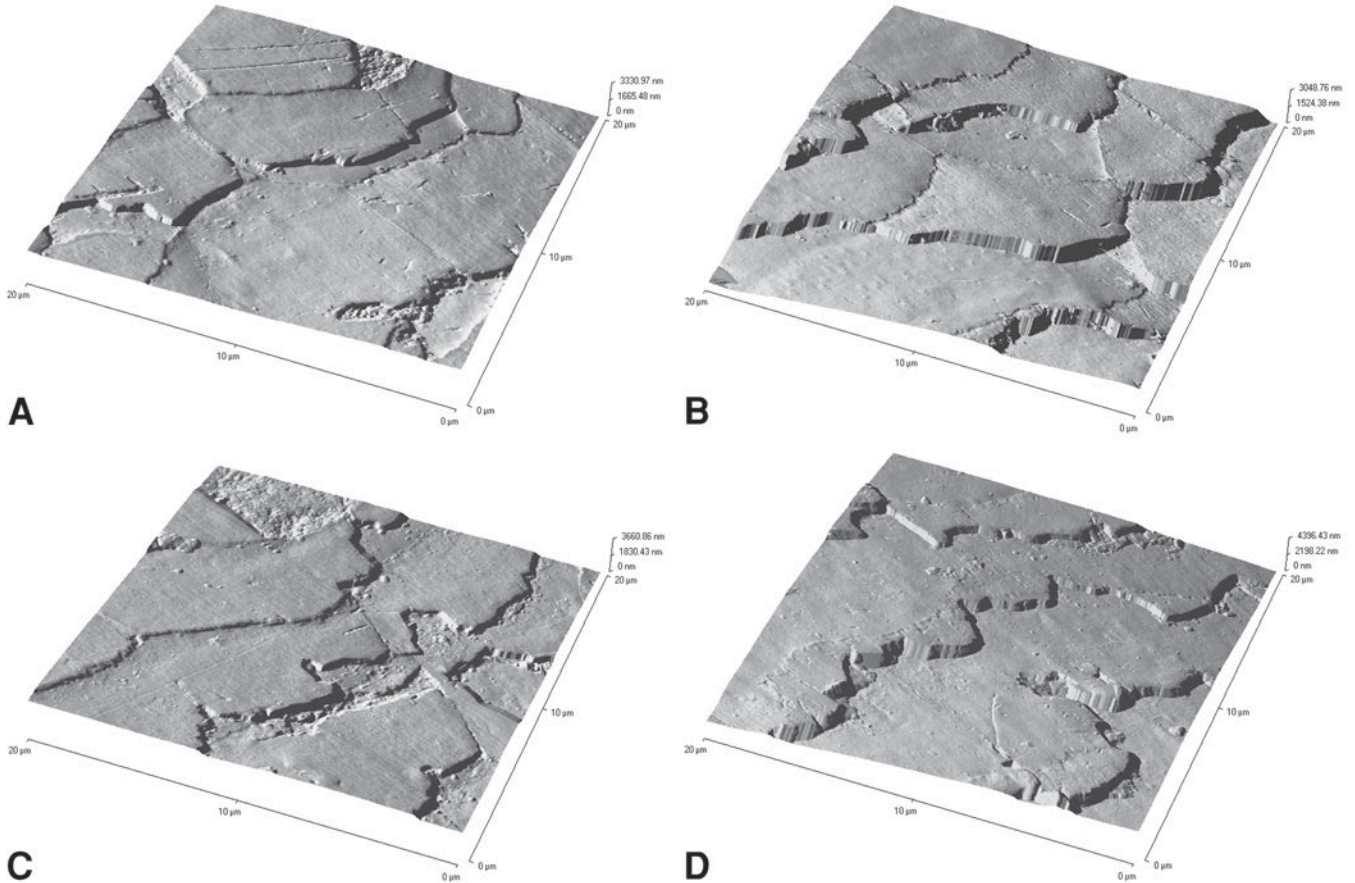

Fig. 2 . Typical AFM topography images of European brown human hairs: two untreated hairs: **(A)** hair 1, and **(B)** hair 2; and two bleached hairs: **(C)** hair 1, and **(D)** hair 2. Examination of 10 images of each hair for both conditions suggests that the bleached hairs appear to be more damaged than the untreated hairs.

2. Place the beaker in an ultrasonic bath and sonicate at room temperature for 30 s.
3. Pour away the detergent solution, rinse the hairs with copious amounts of double-distilled water, and allow to air dry. Fibers can be subsequently stored between filter papers.
4. Hair samples should be fixed to an AFM mounting assembly (nickel stub) using double-sided carbon tape before AFM imaging.

3.2. AFM Imaging

1. The end of the cantilever should be placed over the center of the short axis of the hair specimen.
2. The scan range should ideally be limited to an upper value of 20 µm. This obviates the scanner from exceeding its *z* range while tracking the curvature of hair surfaces. Such artifacts have been reported elsewhere ***(4)***.
3. The resolution should be set to 500, that is, the topography dataset will comprise 500 lines × 500 pixels. A greater resolution can be used if desired.
4. An optimal scan rate of 3 Hz is recommended.
5. Surface architecture information is best revealed using a hypothetical light source positioned to the left of the image.
6. Obtain an image of the hair surface and check the direction in which the cuticular sheets overlap one another.
7. Change the scan direction so that the cuticular sheets overlap from left (root end) to right (tip end; *see* **Note 2**).
8. Obtain 10 images each for treated and untreated regions for two hairs (4 × 10 images). Ideally, more hair fibers (approx 10) should be examined.

3.3. Image Analysis

1. Use the TopoMetrix Image analysis software (TopoMetrix SPM Lab. 1996, Version 3.06.06, TopoMetrix Corporation, Santa Clara, CA) to load the saved topography image and export the dataset as a text file. The images should not be levelled and/or shaded before exporting the data. The cuticle step height program requires the data to be delimited with comma separation and for the file header information (first 18 rows of data) to be retained. The 40 text files should be stored in a directory C:\subdirectory.
2. The text files should have three digit filenames. For example, "1b0.txt" refers to hair 1 (the prefix), bleached (b, or u for untreated), first image (0). Image numbers range from 0 to 9.
3. Use the cuticle step height program, coded in Microsoft MS-DOS QuickBasic, to calculate the cuticle step heights in all the images. A program listing is provided in **Subheading 3.4.** (*see* **Notes 3** and **4**).
4. Four output text files, consisting of one long column of cuticle step heights in nanometres (nm), are produced: hair 1, untreated; hair 1, treated (bleached); hair 2, untreated; and hair 2, treated.
5. The output text files can be read into a spreadsheet, such as Microsoft Excel, and imported into a software package such as Microcal Origin 4.2 to produce line

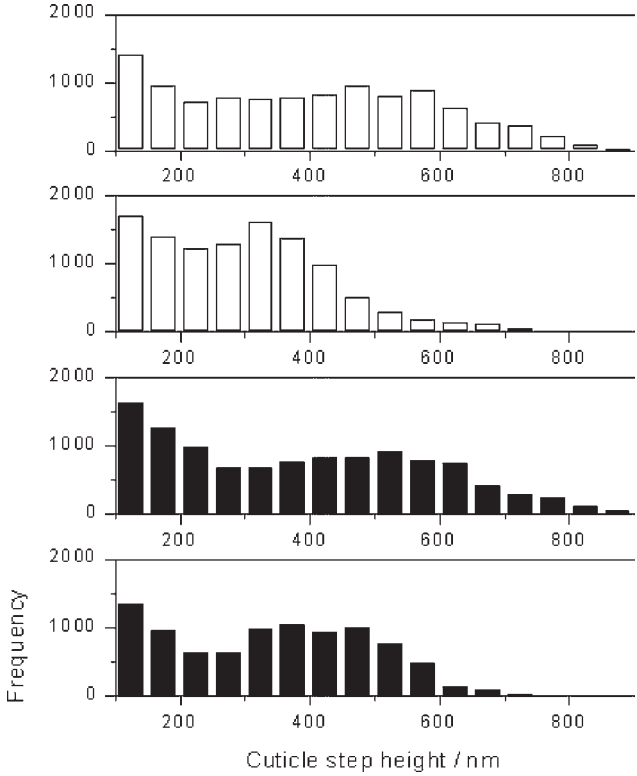

Fig. 3. Frequency histograms of cuticle step heights observed for bleach treated (unshaded) and untreated (shaded) hairs. One-way analysis of variance showed there to be no significant differences in the mean step heights for bleached and untreated hairs (p <0.05, N ≃ 10,000 steps per image).

graphs and histograms and to perform statistical analysis using, for example, one-way analysis of variance (**Fig. 3**).

3.4. Cuticle Step Height Program Listing

```
REM*************************************************************************
REM*** IMAGE ANALYSIS OF ATOMIC FORCE MICROSCOPY IMAGES     ***
REM*** OF HUMAN HAIR                                       ***
REM***                                                    ***
REM*** J.R. SMITH, SPM LABORATORY,                         ***
REM*** UNIVERSITY OF PORTSMOUTH                            ***
REM*************************************************************************

DIM height(1000): REM z-height at position 1 to 500
DIM deriv(1000): REM first derivative of height data
DIM maxgrad(1000): REM x-axis pixel position when deriv() >
              gradient threshold
```

```
DIM newstep(100): REM x-axis pixel position marking start of
                each cuticle step
DIM endstep(100): REM x-axis pixel position marking end of each
                cuticle step
DIM stepedge(100): REM calculated cuticle step height for output

sca = 20: REM scan range = 20 microns
res = 500: REM resolution = 500 pixels, image is 500 lines x 500
                pixels
minh = 100: REM minimum height accepted as cuticle step
maxh = 900: REM maximum height accepted as cuticle step
numhair = 2: REM number of hairs to be examined
numtrt = 2: REM number of treatments to be examined (untreated &
                bleached)
numimag = 10: REM number of AFM images per treatment, per hair

CLS
FOR hair = 1 TO numhair
  FOR treat = 1 TO numtrt
    IF treat = 1 THEN outname$ = RIGHT$(STR$(hair), 1) + "u"
                ELSE outname$ = RIGHT$(STR$(hair), 1) + "b"
     OPEN "C:\subdirectory\" + outname$ + ".txt" FOR OUTPUT AS
                #2

       FOR sample = 0 TO numimag-1
       file$ = outname$ + RIGHT$(STR$(sample), 1)
       OPEN "c:\subdirectory\" + file$ + ".txt" FOR INPUT AS #1

       FOR n = 1 TO 18:  REM reads superfluous header information
            INPUT #1, x$
         NEXT n

       FOR major = 1 TO res: REM for 'res' lines of data

         FOR n = 1 TO res: REM for 'res' columns of data
         INPUT #1, height(n)
         NEXT n

         deriv(1) = 0
         FOR n = 2 TO res
           deriv(n) = height(n) - height(n-1)
         NEXT n

         num = 0: REM number of pixels positions where deriv() >
                threshold, set to 10
         FOR n = 1 TO res
           check = ABS(deriv(n))
         IF check > 10 THEN num = num+1: maxgrad(num) = n
         NEXT n

         count = 1
         newstep(count) = maxgrad(count)
         FOR n = 2 TO num
```

```
            gap = maxgrad(n) - maxgrad(n-1)
              IF gap >= 10 AND n >= 5 THEN count = count+1:
                newstep(count) = maxgrad(n): endstep(count-1)
            maxgrad(n-1)
              NEXT n
            endstep(count) = maxgrad(num)

            FOR n = 1 TO count
              height1 = newstep(n)
              zheight1 = height(height1)
              height2 = endstep(n)
              zheight2 = height(zheight2)
              stepedge(n) = INT(ABS(zheight1-zheight2))
            NEXT n

            FOR n = 1 TO count: REM removes step heights equal to
                zero
                IF stepedge(n) = 0 THEN count = count-1
            NEXT n

            FOR n = 1 TO count
            IF stepedge(n) > minh AND stepedge(n) < maxh THEN
                PRINT #2, stepedge(n): PRINT hair; treat; sample;
                major; n; stepedge(n)
            NEXT n

        NEXT major

        CLOSE #1
      NEXT sample
      CLOSE #2
    NEXT treat
NEXT hair
END
```

4. Notes

1. Self-adhesive carbon discs (Agar Scientific, UK) tend to be more adhesive than carbon tape, and are especially suited for wet-cell work (although the experiments described here were performed in air).
2. The best way of viewing the surface architecture of cuticle scales is with the orientation such that scales overlap from top–left (root end, highest point) to bottom–right (tip end, lowest). With the TopoMetrix Discoverer TMX2000 instrument, this can be obtained by mounting the hair perpendicular to the long axis of the cantilever and performing the scan at a scan rotation of either 90 or 270°, depending on juxtapositions of the root and tip ends. However, the required orientation for the cuticle step height program is for the cuticle scales to overlap from left to right. This can either be achieved by rotating the scan direction before acquisition, or rotating the image, typically by about 20°, during the image-analysis routine (**Fig. 4**). The latter, less favorable method reduces the scan range of the image and so reduces the number of cuticle steps per image.

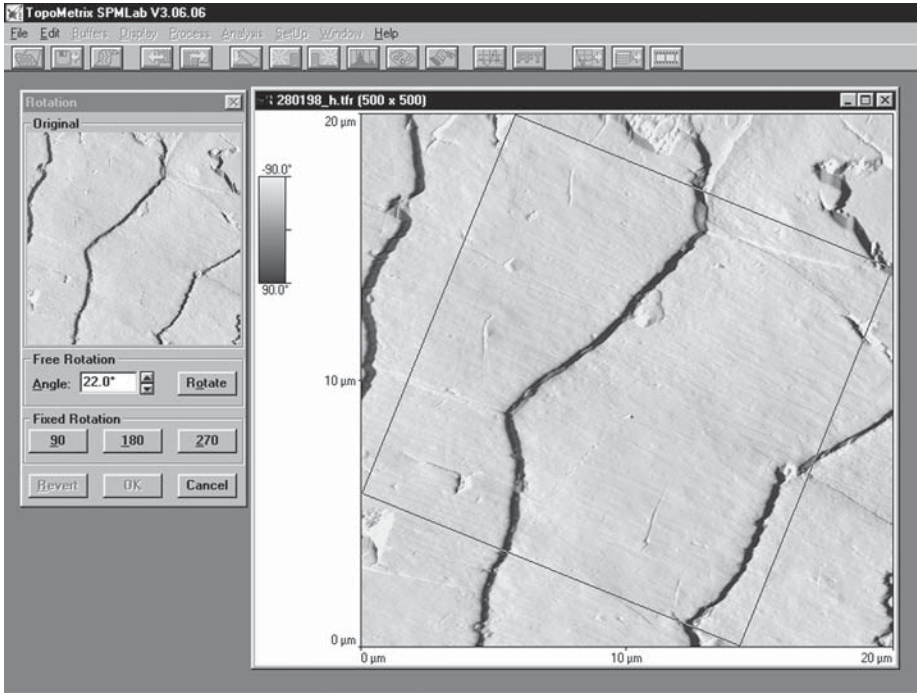

Fig. 4. The cuticle step height program requires the scales to overlap from left (root end) to right (tip end). This can be achieved either by rotating the sample (preferred method), or, as shown here, rotating the image (dataset) through 22°.

3. The program also assumes that the image is free from artefacts caused by the scanner going off-range as a result of the gross curvature of the hair sample (*see* **Subheading 3.2., step 4**). It is also necessary for the hair sample to be free from endocuticular debris, which is sometimes observed at the foot of cuticle steps, otherwise an erroneously low step height may be recorded.
4. The general program methodology is as follows: The program opens the input text file and examines the first line consisting of 500 data points of height values recorded in nanometres. The line of data is then derivatized using a first-order algorithm to locate the positions of the cuticle steps on the *x* axis. Markers are set that tag the start and end of each cuticle step on the line profile. This is achieved by defining a threshold gradient, currently set to –10 nm/pixel. The minus sign indicates that the cuticular sheets step down from left to right across the image; the units are simply a result of *z* data being recorded in nanometers and lateral information being recorded in pixels. The points where the derivative plot falls below the threshold and subsequently rise above it mark the start and end of the cuticle step, respectively. For this, the program considers all the points below the threshold gradient and measures the gap between the current pixel position and

its previous value. If the gap is greater than a given clearance, currently set to 10 pixels (0.4 μm for a resolution of 500 pixels), then a new cuticle has been identified. The routine continues until the end of the line. Cuticle step heights are then calculated by measuring the vertical distance between the start and end markers for each cuticle step. Steps heights less than 100 nm or greater than 900 nm are neglected. The process is repeated for the remaining 499 lines of the input text file. The program can easily be adapted to open further text files corresponding to more hair images to construct a more representative sample set.

Acknowledgments

Thanks are owed to the Royal Society of Chemistry and Royal Society for financial support.

References

1. Goddard, E. D. and Schmitt, R. L. (1994) Atomic force microscopy investigations into the absorption of cationic polymers. *Cosmet. Toiletr.* **109,** 55–61.
2. Schmitt, R. L. and Goddard, E. D. (1994) Atomic force microscopy. II. Investigation into the absorption of cationic polymers. *Cosmet. Toilet.* **109(12),** 83–93.
3. O'Connor, S. D., Komisarek, K. L. and Baldeschwielder, J. D. (1995) Atomic force microscopy of human hair cuticles: A microscopic study of environmental effects on hair morphology. *J. Invest. Dermatol.* **105,** 96–99.
4. Hössel, P., Sander, D. I. R., and Schrepp, W. (1996) Scanning force microscopy. *Cosmet. Toilet.***111,** 57–65.
5. You, H. and Yu, L. (1997) Atomic force microscopy as a tool for study of human hair. *Scanning* **19,** 431–437.
6. Smith, J. R. (1998) A quantitative method for analysing AFM images of the outer surfaces of human hair. *J. Microsc.* **191,** 223–228.
7. Smith, J. R., Connell, S. D., and Swift, J. A. (1999) Stereoscopic display of atomic force microscope images using anaglyph techniques. *J. Microsc.* **196,** 347–351.
8. Swift, J. A. and Smith, J. R. (2000) Atomic force microscopy of human hair. *Scanning* **22,** 310–318.
9. Swift, J. A. and Smith, J. R. (2000) Surface striations of human hair and other mammalian keratin fibres. *Proc. 10th Int. Wool Text. Res. Conf.*, Aachen, Germany, 26 Nov to 1 Dec 2000, HH-2, 1–9. ISBN 3–00–007905-X.
10. Swift, J. A. and Smith, J. R. (2001) Microscopic investigations on the epicuticle of mammalian keratin fibres. *J. Microsc.* **204,** 203–211.
11. Smith, J. R. and Swift, J. A. (2002) Lamellar sub-components of the cuticular cell membrane complex of mammalian keratin fibres show friction and hardness contrast by AFM. *J. Microsc.* **206,** 182–193.
12. Hashimoto and Shibazaki, 1976; Hashimoto, K. and Shibazaki, S. (1976) Ultrastructural study on differentiation and function of hair, in *Biology and Disease of the Hair* (Kobori, T. and Montagna, W. eds.), University Park Press Baltimore, pp. 23–57.

13. Baden, H. P. (1990) Hair keratin, in *Hair and Hair Diseases.,* Ch. 3, (Orfanos, C. E. and Happl, R., eds.), Springer-Verlag, Berlin, Heidelberg, pp. 45–71.
14. Nijeholt, J., Korertenm, H. K. and Wolff, F. (1994) Giant axonal degradation: Scanning electron microscopic and biochemical study of scalp hair. *Dermatology* **188,** 258–262.
15. Swift, J. A. (1979) Minimum depth electron probe X-ray microanalysis as a means for determining the sulphur content of the human hair surface. *Scanning* **2,** 83–88.
16. Swift, J. A. (1991) Fine details on the surface of human hair. *Int. J. Cosmet. Sci.* **13,** 143–159.
17. Smith, J. R. (1997) Use of atomic force microscopy for high-resolution non-invasive structural studies of human hair. *J. Soc. Cosmet. Chem.* **48,** 199–208.
18. Hoffmann, K. (1991) Statistical evaluation of the evidential value of human hairs possibly coming from multiple sources. *J. Forensic Sci.* **36,** 1053–1098.
19. Sachs, H. (1995) Theoretical limits of the evaluation of drug concentrations in hair due to irregular hair growth. *Forensic Sci. Intern.* **70,** 53–61.
20. Pötsch, L. (1996) A discourse on human hair fibres and reflections on the conservation of drug molecules. *Int. J. Legal Med.* **108,** 285–293.
21. Jones, L. N. and Steinert, P. M. (1996) Hair keratinization in health and disease. *Dermatol. Clin.* **14,** 633–650.
22. Gummer, C. L., Dawber, R. P. R., and Swift, J. A. (1981) Monilethrix: An electron microscopic and histochemical study. *Br. J. Dermatol.* **105,** 529–541.
23. Williams, D. F. and Schmitt, W. H. (1996) *Chemistry and Technology of the Cosmetics and Toiletries Industry*, 2nd ed. Blackie, London, ISBN 0-7514-0334-2.
24. Sauermann, G., Hoppe, U., Lunderstädt, R., and Schubert, B. (1988) Measurement of the surface profile of human hair by surface profilometry. *J. Soc. Cosmet. Chem.* **39,** 27–42.
25. Zielinski, M. (1989) A new approach to hair surface topography: Fourier transform and fractal analysis. *J. Soc. Cosmet. Chem.* **40,** 173–189.

9

Imaging Living Chondrocyte Surface Structures With AFM Contact Mode

Gerlinde Bischoff, Anke Bernstein, David Wohlrab, and Hans-Joachim Hein

1. Introduction

In its most established mode of operation, named constant force contact mode, atomic force microscopy (AFM) has been applied to image the 2D and 3D architecture of surfaces. Any deflection of the tip as a result of surface topography is recorded. The microscope reconstructs an image of the surface from the *x*, *y*, and *z* scan data to develop a 3D illustration of any surface at the micro- and nanometer level. The production of high-resolution images of a wide variety of biological samples at near-native conditions and the possibility to measure very low local forces is proving to be a powerful tool for cell analysis ***(1,2)***. In contrast with electron microscopy observations in particular, AFM improves biological studies involving imaging by also monitoring dynamic processes. However, the investigation of soft biomaterials with this special method is still challenging. This chapter reviews practical details of imaging two cell lines: human chondrocytes and human osteosarcoma. However, characteristics described are not unique to this type of cell. Principally, all types of adherently growing cells can be investigated with the techniques described here. Force curve analysis, as a backdrop for the understanding of the received images ***(1)***, will be introduced in detail in **Subheading 3.4.** Further sections explore how AFM can be used as a helpful tool in observations of the cell surface and the physical interactions that occur there, like adhesion or friction, and their influence on the active cell. In **Subheading 7.** common artifacts and troubles are described, along with the practical instructions.

From: *Methods in Molecular Biology, vol. 242: Atomic Force Microscopy: Biomedical Methods and Applications*
Edited by: P. C. Braga and D. Ricci © Humana Press Inc., Totowa, NJ

2. Cell Lines

2.1. Characteristics of Chondrocytes

Investigations were performed on human chondrocytes isolated from human osteoarthritic knee joint cartilage. The cartilage was isolated from cartilage bone fragments resected during the insertion of knee prostheses. All patients presented gonarthritis. No other relevant disease—particularly rheumatoid arthritis—was present. Immediately after the resection, the cartilage bone-fragments were potted in sterile L15 medium (Seromed, Berlin, Germany). Thereafter, the cartilage was handled as described elsewhere ***(3)***.

Cartilage is comprised of a large amount of functional extracellular matrix that is made and maintained by a small number of chondrocytes, the sole resident cell type. Chondroblasts and chondrocytes secrete cartilage matrix, and chondrocytes are also embedded therein. The bones of a developing or restoring limb form through the process of endochondral bone formation. In the beginning, mesenchymal cells condense and cells in the core differentiate into chondrocytes, and the cells at the periphery differentiate into the perichondrium. Articular cartilage has several features that impact on the fate of bioactive bodies. Chondrocytes are anchored in the extracellular matrix and are surrounded by a pericellular matrix. Of particular interest regarding dense connective tissues, recent experiments have shown that mechanotransduction is critically important in vivo in the cell-mediated feedback among physical stimuli, the molecular structure of matrix molecules (e.g., collagen), and the resulting macroscopic biomechanical properties of the tissue ***(4–7)***.

2.2. Characteristics of Human Osteosarcoma

Human osteosarcoma (HOS), a human osteogenic sarcoma cell line, was purchased from American Type Culture Collection (Rockville, MD). The cells were cultured in a medium volume equivalent to 1:1 mixture of Dulbecco's modified Eagle's medium (DMEM) and Ham's F-12 medium containing penicillin (100 U/mL) and streptomycin (100 µg/mL) and 10 vol% fetal bovine serum. The HOS cells exhibit a flat morphology, low saturation density, low plating efficiency in soft agar, and are sensitive to chemical and viral transformation ***(4)***.

The nontumorigenic, as well as the immortal tumorigenic, osteoblast-like human osteosarcoma cells are used in many laboratories along with their large number of derivatives. Because they are one type of potential hormone-related cancer, the number of studies is incredibly high ***(8,9)***. For these cells to reach their functional differentiated state the action of specific factors is required.

Mechanical stress is an important regulator of bone metabolism. Fluid shear stress caused by mechanical load in bone tissue has been shown to be impor-

tant to both the bone structure and function through its effects on osteocytes and osteoblasts. Many hypotheses about the mechanotransduction system in bone cells have been proposed. Recent findings suggest that the physiological level of fluid shear stress induces the production of crucial proteins in human osteosarcoma cells via the cation channel function and, as a result, may therefore promote bone formation ***(10)***.

3. AFM Contact Mode in Biology

In an AFM the tip is mounted on the end of a flexible cantilever. As the sample is scanned beneath the tip, small forces of interaction with the sample cause the cantilever to deflect, revealing the sample's topography. The most common approach—called an optical lever—is to reflect a laser beam off the backside (upper side) of the cantilever into a four-segment photodetector (quadrant). The difference in output between the detectors is then proportional to the deflection amplitude. Important to note is that the limiting factor in motion detectors is not the sensitivity of the photodetector itself (deflections as small as 0.01 nm can be detected), but the intrinsic vibration of the cantilever attributable to Brownian motion.

The cantilever is integrated with a sharp tip on the end and characterized by its material (usually silicon nitride for contact mode investigations), its spring constant, and its geometric properties (usually parabolic or pyramidal tip shape with a curvature radius of 20–40 nm). The spring constant, k_n (determined by thermal vibration in air) varies from 0.06–5 N/m. Low spring constants are sensitive to uncontrolled vibration of the tip released by tip–sample interactions.

3.1. Contact Mode Description

In the contact mode, the tip touches the surfaces at all times with constant force, sliding over the surface as the sample is scanned line by line. Thereby topographic information is received by monitoring the change in cantilever deflection. Force-distance curves are obtained by plotting the vertical displacement of the cantilever, as a function of the separation between the tip and the sample. The force curve is an approach-retract cycle, in which the sample first approaches the tip (*see* **Fig. 1**) and is subsequently retracted from the tip. The cantilever deflection Δz is then converted into force (F_n) according to the relationship ***(11)***:

$$F_n = k_N \Delta z$$

Since normal spring constants for cantilevers are 0.01–100 N/m and instrumental sensitivities for normal deflections are up to approx 0.01 nm, the corresponding limits in force detection are 10^{-13}–10^{-8} *N* ***(12)***.

Because of their softness, the biological membranes of viable cells become significantly indented upon contact by the AFM scanning tip, even at low

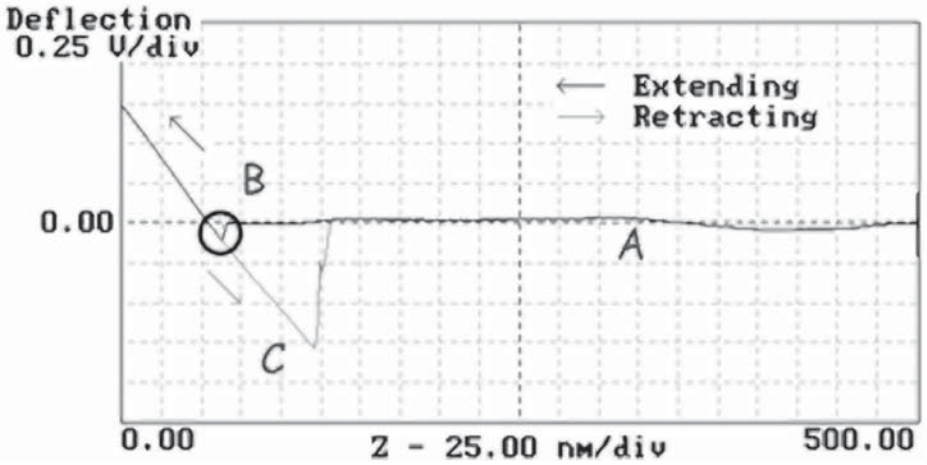

Fig. 1. Favorable force–distance curve of an adherent cell. **(A)** No interaction force detectable at large tip–sample distances. The distance of the scanner movement is represented by the horizontal axis, and the cantilever deflection is represented by the vertical axis. In the case shown, there are minimal long-range forces, so this "noncontact" part of the force curve shows no deflection. **(B)** As the probe tip is brought very close to the surface, it may jump into contact (see circled area), if it feels sufficient attractive force from the sample. Sometimes repulsion force induces elongation in other directions. As the tip moves further in the positive *z* direction, a positive linear cantilever deflection is observed as the tip and sample move together. If the cantilever is sufficiently stiff, the probe tip is able to indent into the surface at this point. If this takes place, the slope of the contact part of the force curve can provide information about the elasticity of the sample surface ***(12)***. After loading the cantilever to a desired force value, the process is reversed. As the sample moves in the opposite (negative) *z* direction, a similar cantilever deflection line is traced as the tip and sample remain in contact. **(C)** As the tip moves further in the negative *z* direction, the restoring force exerted by the bending of the cantilever overcomes the adhesive force of the tip–sample contact. At this point, the adhesion is broken and the cantilever comes free from the surface. This can be used to measure the rupture force required to break the bond or adhesion ***(12,13)***.

forces. Always exercise caution when interpreting the topographic features, however, because of the convolution of the tip shape ***(1,11–14)***.

To this point, we have focused on imaging mechanisms that rely on deflections of the tip with respect to the surface normal. The force generated when the tip is moved laterally over the sample surface can also be used as an imaging mechanism (phase or friction mode). The energy differences in trace-retrace plots are indicative of the energy dissipated in the scan. Attractive and repul-

sive forces lead to information about the hydrophobicity and hydrophilicity of the specimen ***(15)***. Changes in the "friction" images indicate quite well the tip–surface interactions. This is also true of a tip with a truncated apex ratio—the lateral force is rather insensitive to minor cantilever stiffness, different from the topography scan ***(16,17)***. In the case of round massive cells, high lateral forces, however, still hamper stable imaging (*see* Chapter 4).

4. AFM Instrumentations

AFM investigations were done at room temperature in air (samples covered with a droplet of water) or in buffer solution. We used the commercially available Digital Instruments Nanoscope III in constant force contact mode. Generally, the 512×512 pixel images were captured with a square scan-size between 0.6 and 100 µm at a scan rate of 0.2–5 scan lines/second (s) (0.2–5 Hz). Sharp Si_3N_4-cantilevers, each with a pyramidal tip, were used. Their spring constant was 0.1–5 N/m. Best results were obtained by using cantilevers with a spring constant about 0.5–1 N/m. To avoid cell damage, the feedback set point was adjusted frequently to 0.1–10 nN in order to optimize the contact force.

5. AFM Imaging Conditions

The data were acquired simultaneously with the height, the deflection, and the friction signals (*see* **Fig. 2** to distinguish between the modes). The height mode monitors the topography. The deflection mode, as the first derivation of the height mode, offers supplementary details of the cell structure. The friction signal was used to investigate the lateral force interaction between the tip and the sample.

AFM Si_3N_4 tips should in principle be oxidized and hydrophilic; however, in practice they will be hydrophobic owing to hydrocarbon contamination ***(11,12)***. Fluid imaging with AFM requires a special tip holder ("contact mode fluid cell" from VEECO Metrology Group [Mannheim, Germany] was used). For the microscopical studies, the chondrocytes and HOS cells were seeded onto round glass cover slips (4-mm diameter). These cover slips were attached to the bottom of the fluid cell with vacuum grease to standard magnetic AFM mounting plates, before being covered with some droplets of media. When the tip dives into the liquid medium, the laser reflections have to be carefully inspected to exclude "false" reflections, which occur when the tip comes in contact with the liquid surface. Usually our measurements were done at room temperature in aqueous phosphate buffer solution. Good imaging and detection of cell activity could be obtained in the constant force contact mode. The cantilever was carefully approached to the surface (*see* **Subheading 7.8.**), in order to collect the first images in the "low-contact" mode (**Fig. 1**, region B) and to avoid strong physical contact between the tip and the sample surface.

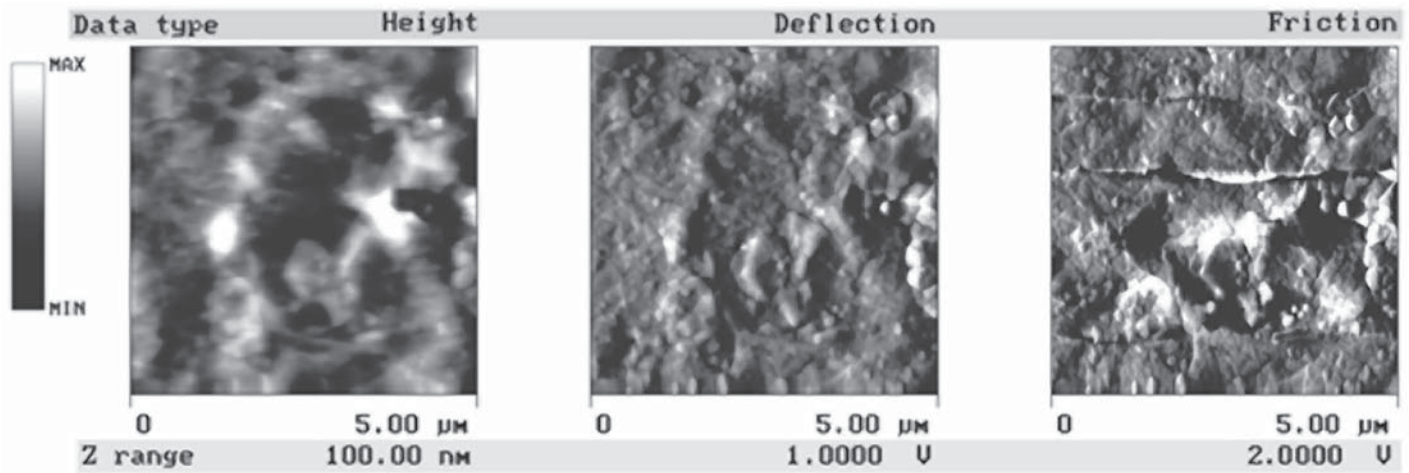

Fig. 2. Simultaneous AFM images of HOS cells in buffer observed with different modes: height (left), deflection (center), and friction (right). The topography is monitored by the height mode. The deflection mode, as the first derivation of the height mode, offers more details of the cell structure. The friction signal was used to investigate the lateral force interaction between the tip and the sample. Generally, large contrast in friction image often indicates active parts.

Later on, scans were done in contact mode with increased forces. Under favorable conditions, cells could be observed for up to 8 hours (h) depending on the cell viability ***(18)***. Frequently, undefinable cantilever vibrations induced by diffusion processes or cell motion are challenging problems. As a practical note, best observation conditions occur at night, when the neighborhood vibrations are minimized.

6. AFM Contact Mode Imaging of Living Cells

Cantilevers with a spring constant have a reduced sensitivity to vibrations and are used successfully to surmount undefinable cantilever deflection. It is of great importance to adjust and minimize the force carefully and to avoid cell damage (*see* **Subheading 7.**). In contact mode, true molecular resolutions could be achieved. The investigation of adherently growing cells with very low pressure on the tip resulted in diminished cell motion and improved the study. Well-resolved topographic information could be obtained. Zooming-in allows the recording of pictures with increasing detail. Especially in fluid medium, the investigation of active cells offers numerous facts. As an example of dynamic interactions, a series of images collected from chondrocytes and HOS cells in buffer is presented in **Figs. 3–6**).

High-resolution images of inner pore processes from the chondrocytes could be visualized (**Fig. 3** and **4**). During the pore diameter reduction, the surface potential in the immediate vicinity changes noticeably. The dynamic interaction is followed by secretion. Large differences (high contrast) in the friction images of several chondrocyte measurements (**Fig. 4**) point out an active part of the cell surface. The data was recorded during an interval of more than 2 h. The friction images remained a rather constant dynamic during this time ***(19)***. This is an indication of the viability of the material ***(18)***. This time interval of several hours seems long enough to study cell stimulations with mediators (e.g. cytokines, mitogens, enzyme substrates) and thus offers great promise for future experiments.

However, the round massive chondrocytes should not be as suitable for AFM observations as the flat HOS cells. In **(Fig. 5)**. the secretion on their cell surface is monitored (see in particular some cell excrements marked out in frames **A** and **B**). In this case, we were able to obtain good-quality images quite easily and visualize the cell structure. A collection of force-distance curves could be collected in order to control whether the tip indented the soft cell surface or not. Indentation increases with the applied force and reaches a maximum value, after which tip-soiling damage occurs. However, the surface penetration results in almost any case in more or less tip contamination. While the shape of the biofouled tip had broadened at the apex in comparison with that of the original

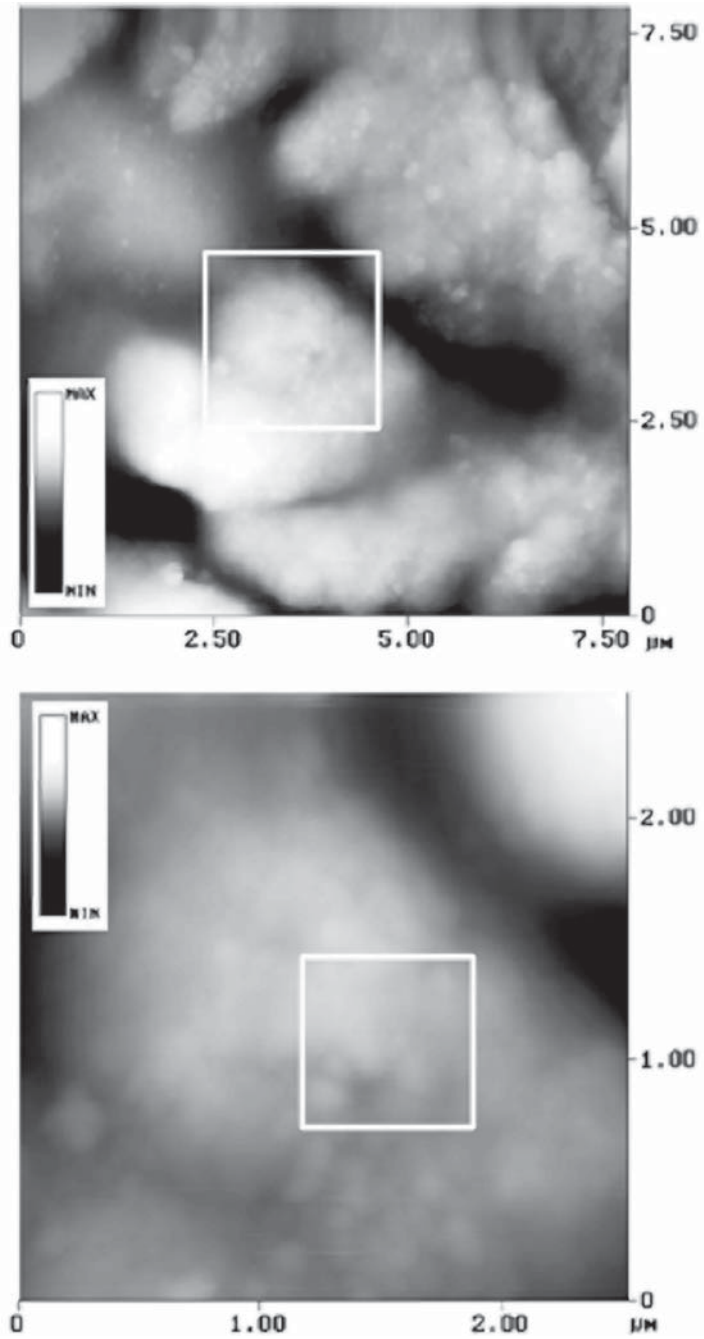

Fig. 3. Zooming in on chondrocyte topography. Frame marks zooming area of next image.

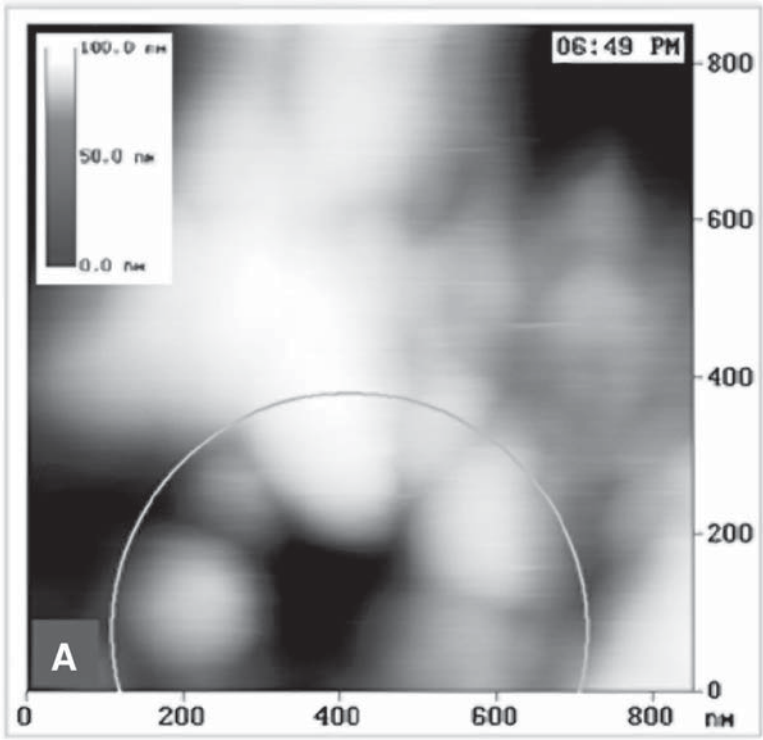

Fig. 4. Comparison between height and friction mode imaging. AFM observation of chondrocytes in buffer. The measurement time is shown in each picture. All images span an actual field of 850 × 850 nm. **(A)** Topography scan over 1 h simultaneous in height and friction mode. The approximate pore diameter is reduced from 382 ± 10 nm to 338 ± 10 nm.

tip, further investigation had to be done after replacing the tip. These effects and objections are described in more detail in **Subheading 5.**

7. Notes on Specific Details

7.1. Adherent Growing Cells Pose a Problem: Their Topography is Too Complexly Exhibited for Scanning

AFM was used to investigate different viable cells. Scanning whole cells under physiological conditions, in media or buffer solutions, poses some problems ***(12,16,18)***.

Since most cells are too large to observe them as a whole (**Fig. 5**), only portions of the cells can be investigated. **Figs. 7** and **8A** (pp. 117, 118) show rare examples of cancer cells that are small enough to scan whole. Numerous

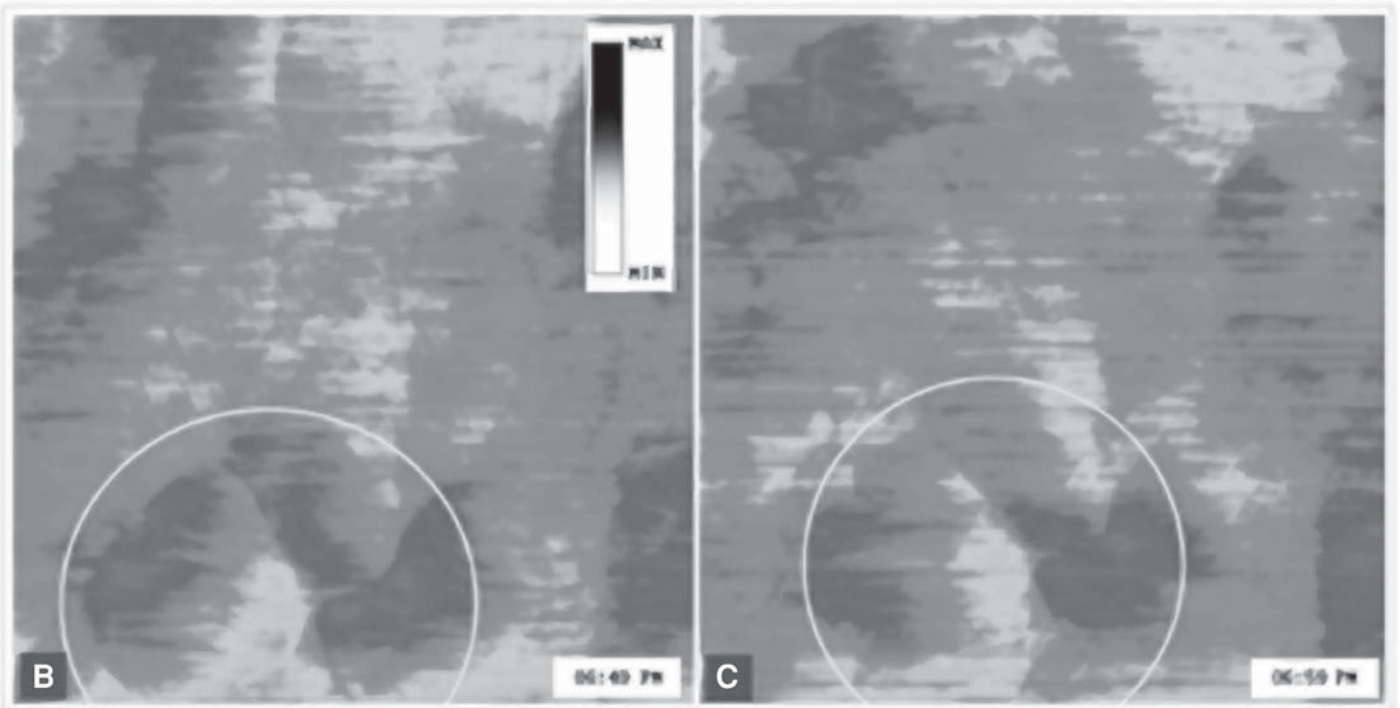

Fig. 4. **(B,C)** Large potential differences in the friction image of several measurements indicate an active part of the cell surface. During the pore diameter reduction, the surface potential in the immediate vicinity changes noticeably. A circle marks one active center on the cell surface. The timely changed contrast in friction mode between measurements indicates diminishing cell surface activity. This can be studied with much more detail by using different colors ***(15)***.

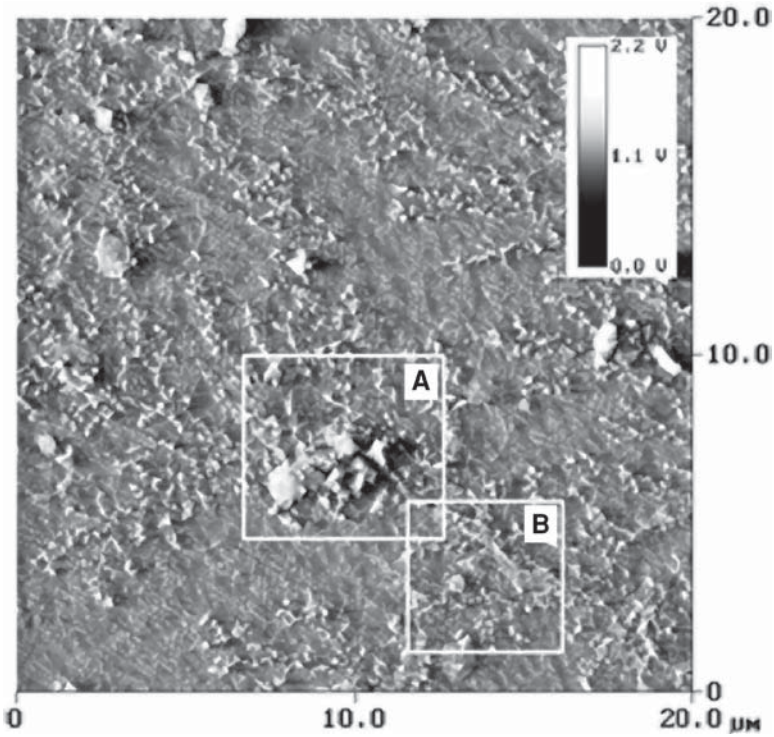

Fig. 5. Overview of the flat epithelial HOS cell in buffer observed in deflection mode. The secretion on the cell surface is monitored (some cell excrements in frame B are magnified in **Fig. 6**).

problems result in investigating the identical local position several times by AFM, after the material has left the Nanoscope instrument for other investigations. Molecular marker might help to solve this problem.

7.2. High Resolution Imaging of Cell Surfaces Requires Tight Attachment to Substrates

Imaging of loosely adhered cells enabled determination of the cell size and investigation of larger structures and pseudopodia but failed in resolving more detail.

7.3. Highly Dynamic Cell Surfaces Require Fast Scan Rates

Measurements in air only allow for limited examinations of the cells. Drying up processes strongly change the cell surface. As quickly as 10–30 min after beginning, dynamic interactions could no longer be monitored. Usually the cell structure collapses (example given in **Fig. 7**). When no dynamic

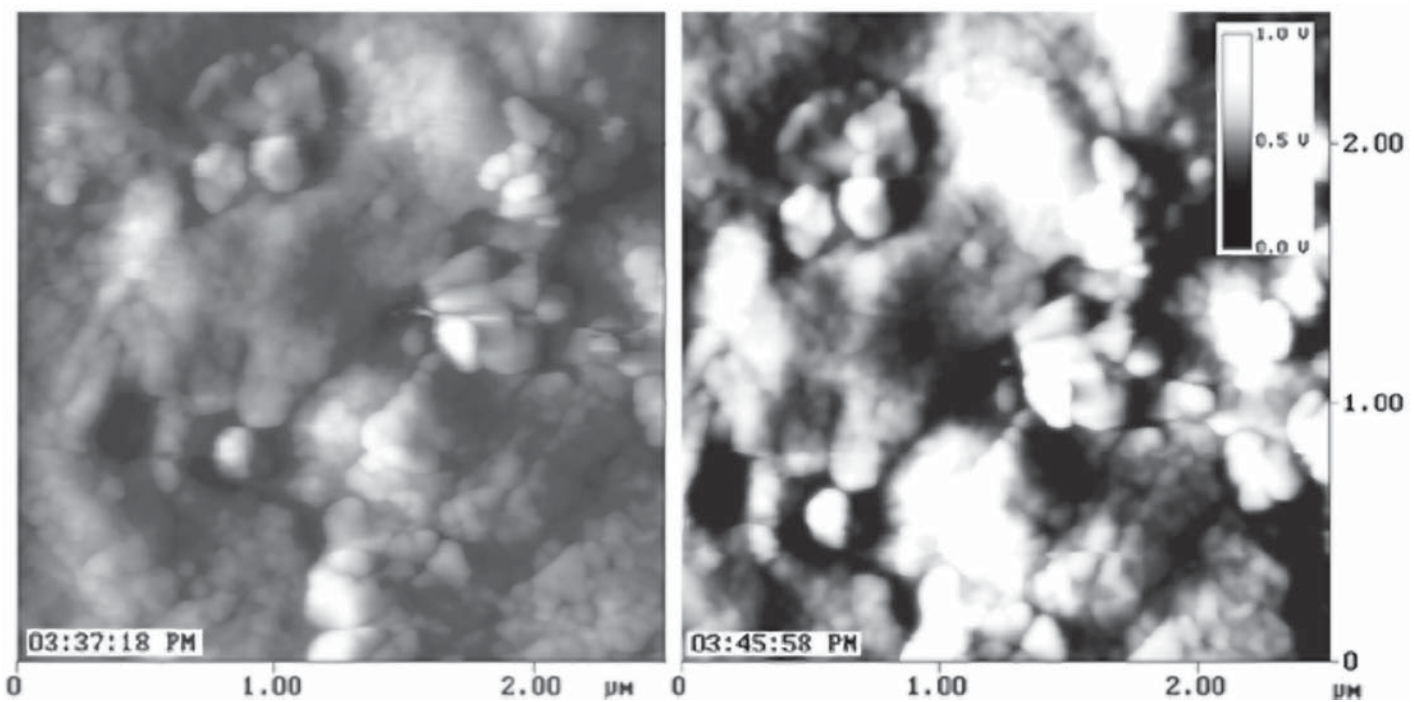

Fig. 6. Zooming in on frame B of **Fig. 5** (same z scale for both figures). Increasing contrast in the deflection mode indicates growing roughness of the surface.

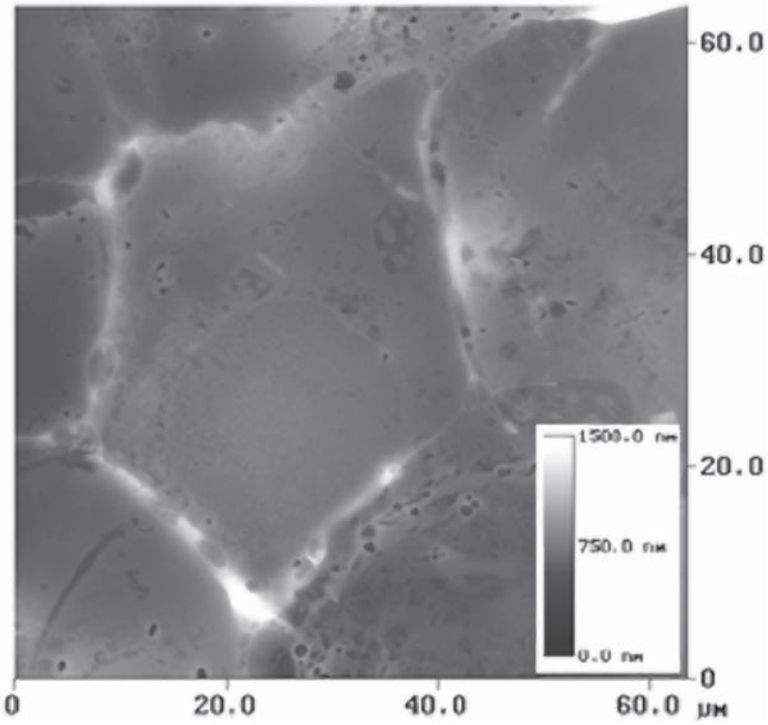

Fig. 7. Collapsed cell structure obtained in height mode AFM. The shape of the nucleus is visible. The cell margins (five white edges) are lifted on account of drying processes.

changes were detected (usually after 30 min), the scan rate can be reduced from 5–0.2 Hz to increase image quality and resolution.

Fast scan rates in buffer induce several troubles (such as buffer turbulences) and undefinable cell vibration. Therefore, the scan rate is critical and dynamic interactions can only be monitored with restriction.

7.4. The Buffer Sometimes Crystallizes During Liquid Evaporation

Under the required conditions, the buffer frequently crystallizes during liquid evaporation. These crystals can be identified easily by their symmetric structures (phosphate buffer crystals are marked out in **Fig. 8A**).

7.5. Protein Serum Covers the Cell Surface Like a Dense Carpet

The protein cover from a cell-culture procedure resembles to a high degree the protein surface of the washed cells, but it demonstrates a more homogeneous friction signal showing small changes with time. However, to distin-

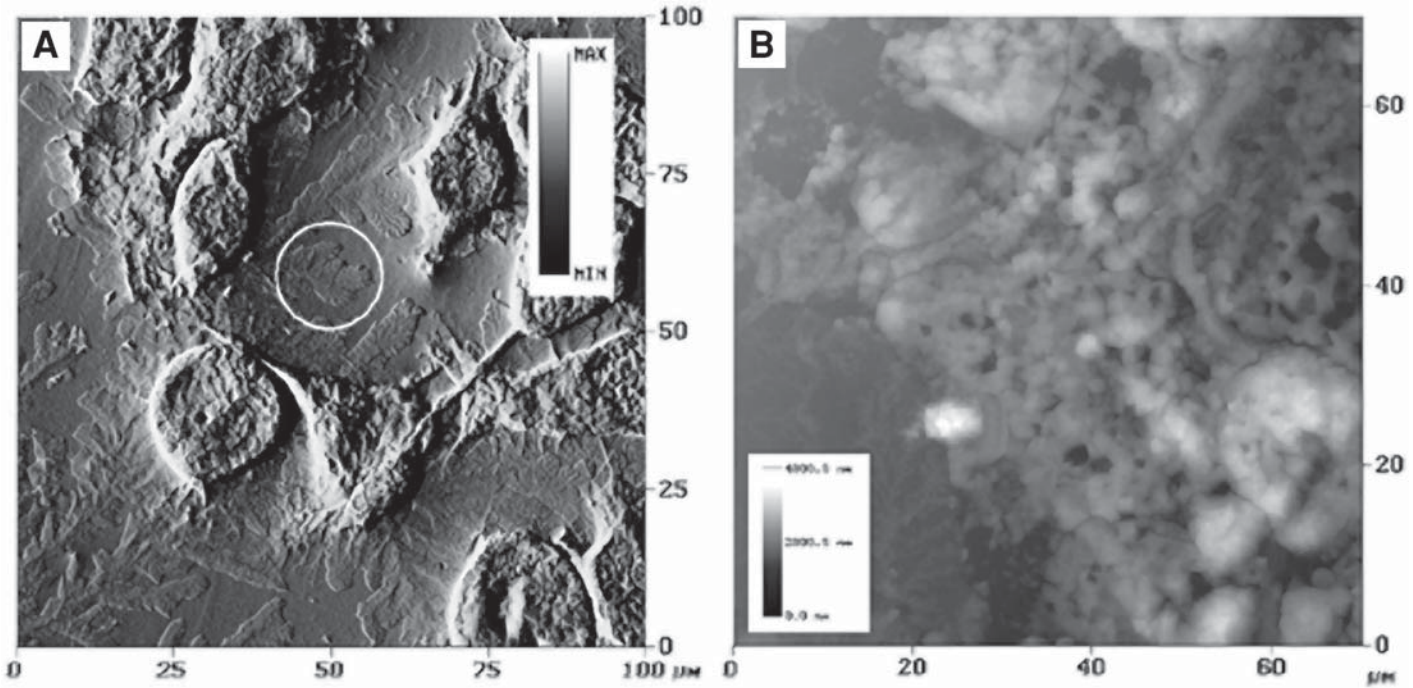

Fig. 8. Collection of frequent artifacts. **(A)** crystallization of phosphate buffer during liquid evaporation (*circle*); deflection mode data. **(B)** Serum protein layer from cell culture medium covers the cells (*see* **Subheading 7.5.**); height mode data.

guish between the serum cover and the actual cell surface is at times very difficult (*see* **Fig. 8B**). Rinsing the cover slips with PBS several times before AFM observation is always necessary to remove the coating.

7.6. Soft Collagen Material Differs Clearly from Viable Cell Material

As shown in the force calibration plots of pure collagen material (**Fig. 9**), the tip–surface interaction can be discriminated easily from active cell parts by the shape of the curve. Approaching the surface over a long range (around several micrometer) leads to a low-force indentation of the tip into the moist and soft collagen matrix (**Fig. 9A**). No change in the shape of the force curve can be observed by retracting the tip. Therefore, it can be concluded that the tip has no attraction or repulsion interaction with the collagen sample. This can be used as reference to identify local collagen collectives (*see* **Figs. 5** and **6**).

When collagen dries up, it becomes a stiffer material with less depth and consequently it would receive a shallower indentation. An example is shown in **Fig. 9B** and **C**. The sample structure collapses after water evaporation (*see* *x*-axis). As the sample is approached to the tip, a strong positive linear cantilever deflection is observed after contact when the tip and sample move toghether. When the motion of the sample is inverted (retracting portion of the curve), a similar cantilever deflection line is traced, but this time shifted several nanometers due to tip and sample remaining in contact.

7.7. The Shape of the AFM Tip Is Always Critical in Sample Measurements

The quality of the tip (e.g., radius of curvature, morphology, hardness, and surface composition) influences strongly the quality of AFM investigations. Most commercially available tips have a curvature radius of 30–50 nm with a pyramidal geometry. (Several others alter the tip morphology to enhance imaging capabilities.) Additionally, the tip may bind proteins or membrane debris that diminish the resolution. Special coatings exploit this situation and make molecular interaction force measurements possible ***(12)***.

7.8. Attraction and Repulsive Interactions of the Tip Cause Misinterpretations, Especially With Viable Cells

Typically, when the tip approaches the surface, the deflection value increases to the set point, indicating surface contact. As soon as the tip is in contact with the cell surface, the active cell induces electronic signals by disturbing the scan. Sometimes, it seems that the cells are tickled by the tip (or the applied potential) and shake themselves. This movement overestimates the determined cell-size (**Fig. 10**; **ref.** ***20***). Force-distance curves display uncontrolled vibrations of the tip. Undefinable surface tension forces could influence tip retraction (local attraction and repulsive forces could be detected).

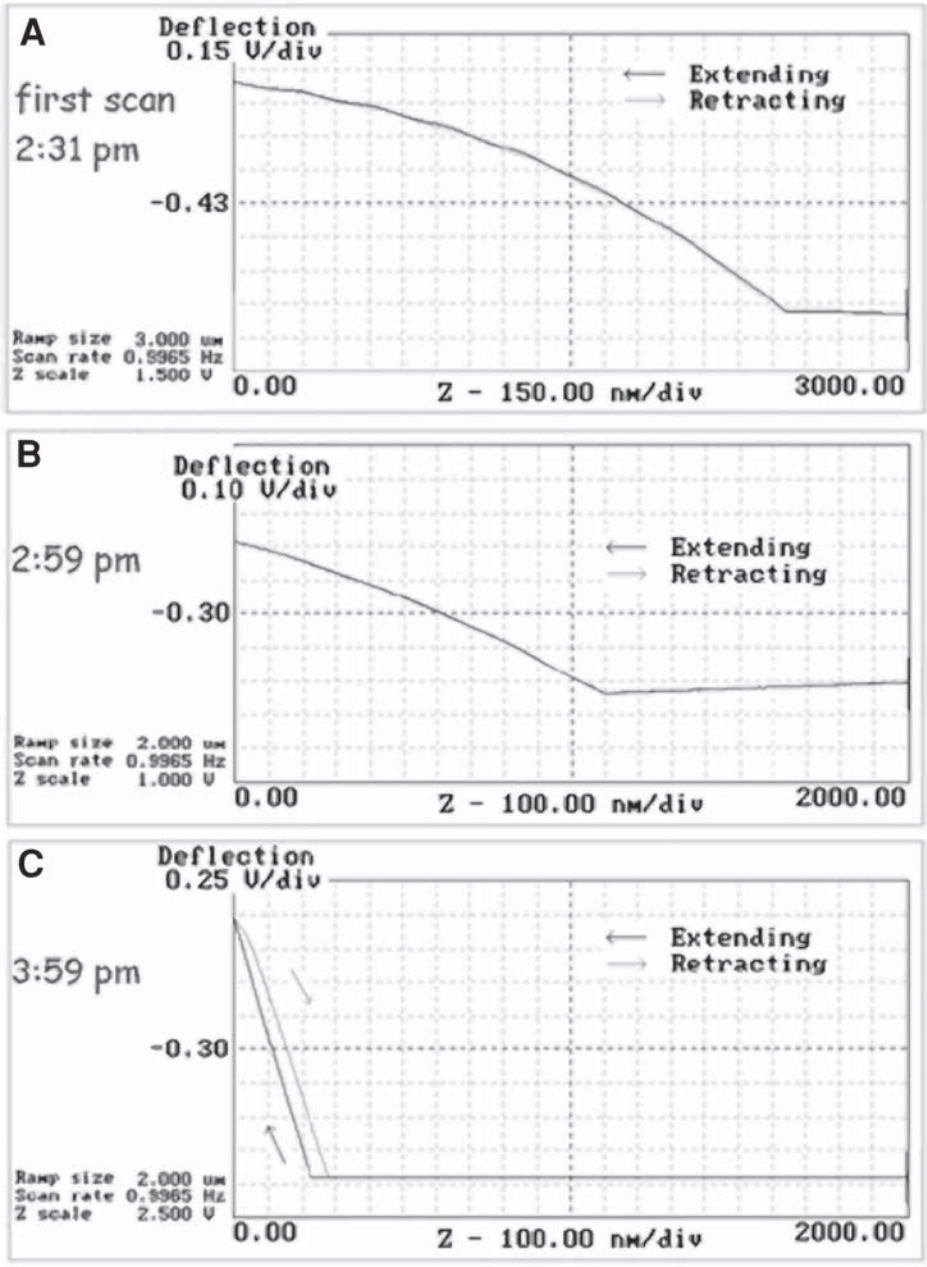

Fig. 9. Force calibration plots of dried up collagen material isolated from fibroblasts. The spring constant is 0.1 N/m. **(A)** Soft collagen sample with high amount of water. The average slope is about 0.4 mV/nm. **(B)** Partly dried up sample. The average slope is about 0.5 mV/nm. **(C)** Dry collagen sample. The average slope is about 6.0 mV/nm. Observation time is indicated.

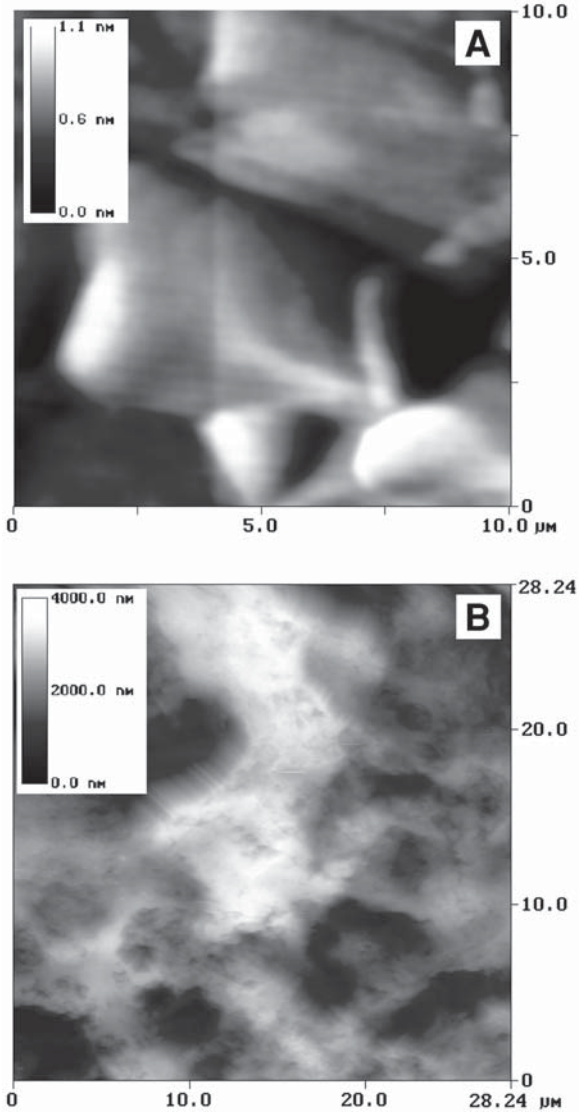

Fig. 10. AFM observation of adherently growing cells (hypopharynx carcinoma) ***(16)***. ***(A)*** Viable cells investigated in noncontact mode. The cells are displayed with an unreal softness. The *z* deflection changes by only a few nanometers. **(B)** Viable cells investigated in contact mode. Released from tip–surface contact the cells induce electronic signals and move. The *z* range changes are large. This movement overestimates the determined cell-size (same cell as **Fig. 10A**).

By repeating the approaching procedure to physical contact, nearby the set point (ΔU about –0.1 V) the tip–sample distance jumps to higher values and

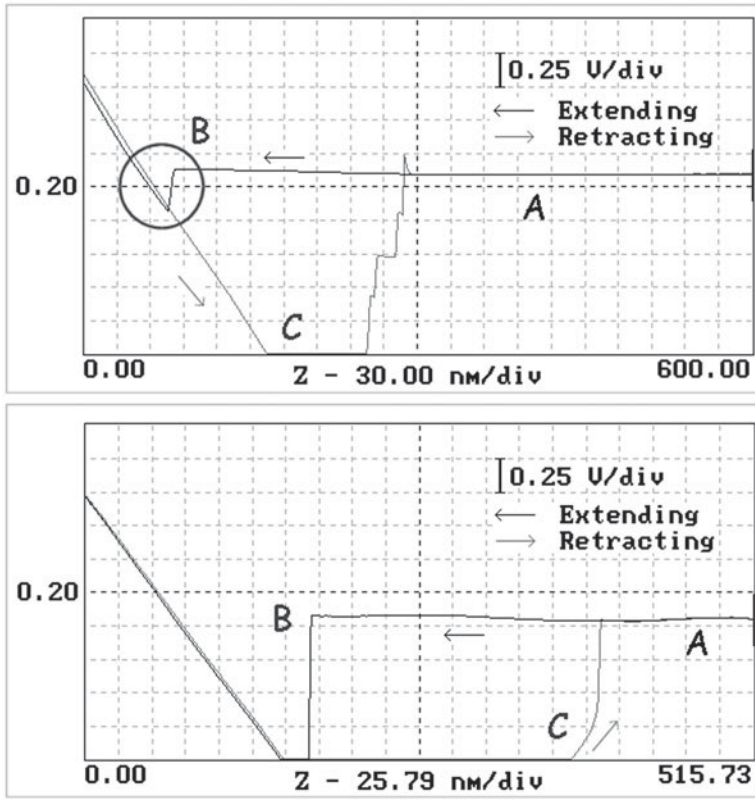

Fig. 11. Force–distance curve of a sample, which induce strong tip–sample interactions. Black line, approach curve; gray line, retraction curve. **(A)** At large tip–sample separations, there is no detectable interaction force. As the distance decreases, long- and short-range forces can be determined. **(B)** At some separation, the gradient of interaction energy exceeds the restoring force of the cantilever and the tip jumps to contact with the surface. If the interaction is too strong (bottom), no successful scan can be performed. **(C)** As the tip moves further in the negative z-direction (retracting), the restoring force exerted by the bending of the cantilever overcomes the adhesive force of the tip–sample contact and the tip breaks away from the sample. An idealized curve shows strong linear lines as shown in **Fig. 1**. The deflection curves presented here indicate tip contamination.

evades a successful approach. Strong tip vibrations are observed. An explanation could be that the cell dodges or repels the tip (data not shown). Even after a while, viable cells seem to remember the procedure, because they induce strong tip vibrations and make repeated scans impossible. Moving to another part of the sample (tested up to a few millimeters) cannot prevent the repul-

sion. If such a phenomenon occurs, another successful approach and further investigation are impracticable.

To avoid such troubles the force and the cantilever sensitivity have to be optimized. A higher spring constant prevents the uncontrolled vibration of the tip, but results more often in cell damage. When the interaction between the tip and the surface is very strong, it seems very much like a scan done in honey or highly viscous material. Tip contamination often occurs. This is explained in detail in **Fig. 11**.

7.9. Cells Can Contaminate or Stick to the Scanning Tip

Occasionally during the scanning procedure, the tip is covered with an indefinite cluster. Tip-biofouling caused by cellular damage and pick-up of loosely adhered particles generate artifacts that will compromise the experiment. Since the tip geometry is critical for force measurements and accurate topography determination, this has to be avoided in all cases.

Acknowledgments

The illustrations presented would not have been made without the encouragement and cooperation of Grit Helbing, Ottilie Pietz, and Angela Rosemeier of the Medical Faculty Halle. Their help is gratefully acknowledged. The authors thank Robert Bischoff and SENSOBI Sensoren GmbH. Their instrumental service is highly appreciated. The Ministry of Culture and Education of Saxony–Anhalt and the BMBF have supported our research.

References

1. Ricci, D. and Grattarola, M. (1994) Scanning force microscopy on live cultured cells: imaging and force-versus-distance investigations. *J. Microscopy* **176,** 254–261.
2. Oberleithner, H., Brinckmann, E., Giebisch, G., and Geibel, J. (1995) Visualizing life on biomembranes by atomic force microscopy. *Kidney Int.* **48,** 923–929.
3. Wohlrab, D., Wohlrab, J., Reichel, H., and Hein, W. (2001) Is the proliferation of human chondrocytes regulated by ionic channels? *J. Orthop. Sci.* **6,** 155–159.
4. Grodzinsky, A. J., Levenston, M. E., Jin, M., and Frank, E. H. (2000) Cartilage tissue remodeling in response to mechanical forces. *Annu. Rev. Biomed. Eng.* **2,** 691–713.
5. Hein, H.-J., Brandt, J., Bernstein, A., Engler, T., and Weisser, L. (1997) Zur Darstellung der Mikrostruktur des Knochens mit dem Raster-Sondenmikroskop. *Z. Med. Phys.* **7,** 21–26.
6. Henning, S., Adhikari, R., Michler, G. H., Seidel, P., Sandner, B., Bernstein, A., and Hein, H.-J. (2001) Analysis of the bone-implant interface of a partially resorbable bone cement by scanning electron and scanning force microscopy, in *Micro- and Nanostructures of Biological Systems*, (Bischoff, G. and Hein, H.-J., eds.), Shaker-Publ., Aachen, pp. 109–120.

7. Oda, Y., Matsumoto, Y., Harimaya, K., Iwamoto, Y., and Tsuneyoshi, M. (2000) Establishment of new multidrug-resistant human osteosarcoma cell lines. *Oncol-Rep.* **7,** 859–866.
8. Rodan, S. B., Imai, Y., Thiede, M. A., Wesolowski, G., Thompson, D., Bar-Shavit, Z., et al. (1987) Characterization of a human osteosarcoma cell line (Saos-2) with osteoblastic properties. *Cancer Res.* **47,** 4961–4966.
9. Rhim, J. S. (1993) Neoplastic transformation of human cells in vitro. *Crit. Rev. Oncogene* **4,** 313–335.
10. Sakai, K., Mohtai, M., and Iwamoto, Y. (1998) Fluid shear stress increases transforming growth factor beta 1 expression in human osteoblast-like cells: modulation by cation channel blockades. *Calcif. Tissue Int.* **63,** 515–520.
11. Grimsehl, E., (1989) *Lehrbuch der Physik Vol. 1: Mechanik, Akustik, Wärmelehre*, 25th ed. Teubners-Verlagsgesellschaft, Leipzig. pp. 43–56.
12. Takano, H., Kenseth, J. R., Wong, S.-S., O'Brien, J. C., and Porter, M. D. (1999) Chemical and biochemical analysis using scanning force microscopy. *Chem. Rev.* **99,** 2845–2890.
13. Hansma, H. G. (2001) Surface biology of DNA by atomic force microscopy. *Annu. Rev. Phys. Chem.* **52,** 71–92.
14. Linder, A., Weiland, U., and Apell, H. J. (1999)Novel polymer substrates for SFM investigations of living cells, biological membranes, and proteins. *J. Struct. Biol.* **126,** 16–26.
15. Bischoff, R., Berghaus, A., and Hein, H.-J. (1997) Inspection of silicone-biomaterials using SPM. *Biomed. Techn.* **42(Suppl. 2),** 482–483.
16. Bustamante, C. and Keller D (1995) Scanning force microscopy in biology. *Physics Today* 32–38.
17. Benoit, M., Holstein, T., and Gaub, H. E. (1997) Lateral forces in AFM imaging and immobilization of cells and organelles. *Eur. Biophys. J.* **26,** 283–290.
18. Bischoff, G. and Langner, J. (2001) SFM of living cells—a study of the method, in *Micro- and Nanostructures of Biological Systems*, (Bischoff, G. and Hein, H.-J., eds), Shaker Publ., Aachen, pp. 135–152.
19. Bischoff, R., Bischoff, G., and Hein, H.-J. (2002) Scanning force microscopy (SFM) visualization of adherently growing cells. *Am. Biotech. Lab.* **3,** 20–22.
20. Bischoff, R., Bischoff, G., and Hoffmann, S. (2001) Scanning force microscopy observation of tumor cells treated with hematoporphyrin IX derivatives. *Ann. Biomed. Eng.* **29,** 1092–1099.

10

Growth Cones of Living Neurons Probed by Atomic Force Microscopy

Davide Ricci, Massimo Grattarola, and Mariateresa Tedesco

1. Introduction

A large body of recent literature describes the use of atomic force microscopy (AFM; **ref.** ***1***) for the study of living cells. These experimental findings clearly indicate that AFM is a very valuable tool for the 3D imaging of flat biological samples strongly adhering to a substrate, with a lateral resolution in between the resolutions of optical and electron microscopy. Moreover, a very relevant feature of AFM is its capability of analyzing local mechanical properties of living cells.

The expression "flat biological samples" includes layers of cells, such as epithelia ***(2,3)***, and single cells, such as fibroblasts and glia cells ***(4,5***). AFM technique, in its present state, seems to be less appropriate for globular structures, such as neuron bodies ***(6)***, and for string-like structures, such as neuron arborizations ***(7,8***). However, neuron growth cones are subcellular structures that seem to be very appropriate for AFM analysis: they are flat, highly specialized regions, which make very strong adhesion to the substrate. Moreover, the mechanical properties of these structures (i.e., the cytoskeleton local organization) are of great relevance for understanding the development of neural architectures. The potential, therefore, of micromechanical information from AFM is of particular value.

On the basis of these premises, this chapter will be devoted to a detailed report of experimental findings concerning the use of AFM to probe growth cones of chick embryo spinal cord neurons under vital conditions.

From: *Methods in Molecular Biology, vol. 242: Atomic Force Microscopy: Biomedical Methods and Applications*
Edited by: P. C. Braga and D. Ricci © Humana Press Inc., Totowa, NJ

2. Materials

1. Chick embryos (7–8 days (d) old).
2. Chick embryo extract (Gibco 16460-016).
3. Hanks' balanced salt solution (HBSS; Gibco 24020-091).
4. Bovine serum albumin (BSA; Sigma A-7030).
5. Trypsin solution 0.25% (Gibco 25050-014).
6. Trypsin inhibitor (Sigma T-6522).
7. DNAse (Deoxyribonuclease, type I; Sigma D-5025).
8. DMEM-F12 (Gibco 31331-028).
9. Fetal bovine serum (FBS; heat inactivated; Gibco 10108-157).
10. Horse serum (heat inactivated; Gibco 26050-070).
11. Poly-D-Lysine (Sigma P-7280) or Poly-L-Lysine (Sigma P-9155).
12. Stock supplement solution N-2 (Gibco 17502-048).
13. 5-Fluoro-2'-deoxyuridine antimitotic agent (Sigma F-0503).
14. Phosphate buffered saline solution (PBS; Gibco 14287-080).
15. Glutaraldehyde solution (Sigma G-6257).
16. Atomic force microscope: Park Scientific Instrument Autoprobe CP (Thermomicroscopes, Sunnyvale, CA).
17. Silicon nitride pyramidal tips on cantilevers with 0.01 N/m nominal spring constant (Thermomicroscopes, Sunnyvale, CA).
18. Dissection microscope (WILD-LEITZ).
19. Microdissection forceps (Fine Science Tools [FST] Dumon #5 biologie).
20. Forceps, large, small (FST).
21. Scissors, fine (FST).
22. Disposable conical tubes (Falcon 2170, 2195, or equivalent).
23. Disposable cell culture dishes (100 mm Ø Falcon, 35 mm Ø Falcon).
24. Phase contrast microscope (Diavert-LEITZ).
25. Thermo-controlled waterbath (37.5°C).
26. Centrifuge.
27. Glass slides.

3. Methods

The methods described below outline: (1) the neuron cell culture and sample preparation, (2) the AFM setup for imaging, (3) the acquisition of force-vs-distance and indentation curves, (4) the results obtained and their interpretation, and (5) a comparison with other techniques.

3.1. Neuron Cell Culture and Sample Preparation

3.1.1. Chick Embryo Spinal Cord Neuron Extraction

Spinal cord neurons were obtained through dissection of spinal cords from 8-d chick embryos and plated on treated cover slips. Dissected cords were minced in HBSS and enzymatically dissociated in 0.05% trypsin at 37°C for

25 min, then washed in CMF-HBSS containing 0.3% BSA, 0.005% DNAse (deoxyribonuclease, type I), and 0.025% trypsin inhibitor. After mechanical dissociation, the resulting single cells were suspended in MEM-F12 (1:1) supplemented with 5% FBS, 5% inactivated horse serum, and 5% chick embryo extract for plating on culture substrata.

3.1.2. Neuron Cell Culture and Sample Preparation for AFM Investigations

To prepare the culture substrata, glass slides were first cut to 20- × 40-mm pieces and then cleaned and sterilized (*see* **Note 1**). They were then incubated overnight in a poly-D-lysin solution (5 mg in 50 mL of distilled water), rinsed three times in distilled water, and dried in a sterile hood (*see* **Note 2**). Plating was made on the glass slides, which were then placed into plastic Petri dishes. The cultures were incubated at 37°C, 5% CO_2 (*see* **Note 3**). Two days after plating, the medium was replaced with MEM-F12 96%, horse serum 3%, 1% stock supplement solution N2. To free cultures from non-neural cells, 72 hours (h) after plating an antimitotic agent (5-fluoro-2-deoxiuridine, 10^{-6} *M*) was added to the culture medium.

3.1.3. Cell Fixation

For the purpose of comparing results obtained on living cells, fixated cells were also prepared. In this case, after keeping cells for 4 or 5 d in culture, the medium was removed and cultures were briefly rinsed with PBS. Cells were fixed for 20–30 min using 0.8% glutaraldehyde in PBS. Finally, slides were rinsed twice with PBS and dried.

3.2. AFM Setup for Imaging

3.2.1. AFM Setup

A Park Scientific Instruments Autoprobe CP (Sunnyvale, CA) AFM was used, which was equipped with a scanner tube allowing 100 µm (x, y) maximum scan size and 6 µm (z) excursion (*see* **Note 4**). All experiments were performed using cantilevers with 0.01 N/m nominal spring constant (*see* **Note 5**) and silicon nitride pyramidal tips (*see* **Note 6**).

Special care was taken to avoid contact between liquids and scanner, as this would cause permanent damage to the piezoelectric element and eventually to the high-voltage electronics. For this purpose, the top half of the microscope containing the scanner was enclosed in a polyethylene film sheet. This allows the scanner to move freely and does not interfere with the magnetic coupling of the sample holder. The cantilever chip was mounted on a chip holder that has a glass window behind the cantilever chip. To avoid air bubble formation, before mounting the chip holder into the microscope we wet the glass and cantilever chip

with buffer solution from a syringe and allowed a droplet of water to be trapped (kept in place by surface tension) between the chip and the glass window.

The sample was then taken out of the Petri dish, with a film of buffer solution allowed to remain on the surface. To overcome the difficulties of gluing a wet glass slide to the sample holder metal disk and also to overcome the limitations of the *x*–*y* table that has only a 12- × 12-mm range, we used the following method. First, we fixed a whole glass slide with cyanoacrylate glue to the metal sample holder disk, which is then placed on the scanner as usual. Second, we placed Vaseline onto this glass slide and pressed the cell-covered glass slide firmly onto it. This allowed us to easily move the sample in search of a good area for imaging and also to quickly change it (*see* **Note 7**).

3.2.2. Tip to Sample Approach Procedure

The first step is to approach the tip to the sample as usual with the stepper motor until the drop hanging from the cantilever holder assembly meets the liquid covering the sample glass slide. A meniscus is then formed and from this moment the surface of the sample can be seen through the on-axis optical microscope (*see* **Note 8**).

Tip-to-sample approach was always performed on a glass area next to the cell to be imaged, and before scanning the force setpoint was lowered to a small value (0.5 nN) to avoid cell damage.

3.2.3. AFM Settings for Imaging

Force-vs-distance curves before and after imaging were recorded routinely for cantilever deflection calibration purposes and for sample stiffness estimation. These curves have been transformed into force-vs-indentation plots, using as reference a force-vs-distance curve taken on glass during the same session. Images were taken with two simultaneous acquisition channels in the AFM: the z-piezo driving voltage and the error signal from the feedback loop. The first signal is proportional to the z-piezo displacement necessary to maintain the cantilever deflection (force) at the setpoint during scanning, whereas the second one records deviations of the cantilever deflections (hence from the set force) from the setpoint value.

To obtain imaging with higher spatial frequency resolution, we tuned the feedback loop parameters so that only the average cantilever deflection was kept near the setpoint value, allowing the system to generate a meaningful image from the error-signal channel, which has a wider frequency band ***(9)***. Typical scanning speeds were between 13 and 41 μm/s (*see* **Note 9**).

3.3. Acquisition of Force-vs-Distance and Indentation Curves

3.3.1. Force-vs-Distance Curves

Force-vs-distance curves were obtained by using the standard PSI software, which records the cantilever deflection, while driving the piezo in the z direction after a triangular wave. The software allowed us to set the wave frequency and to average the force-vs-distance curves taken consecutively at the same point. The curves corresponding to a given image were stored in a digital file (1024 points for each force curve) for further processing. The force scale for these curves was calibrated by using, as a reference substrate, the glass the cells adhered to. Because the glass did not appreciably indent under the loads applied, from the slope of the linear portion (after tip contact) of the force-vs-distance curve we derived the conversion factor from the error signal (in mV) to the cantilever deflection (in nm) and hence to the applied force (in nN), through the spring constant K of the cantilever (Force = $K \times$ cantilever deflection, nominal $K = 0.01$ N/m). This conversion factor depended on the intensity of the laser beam reflected from the backside of the cantilever and on the area of the spot on the photodiode. Therefore, for each series of curves taken in the same session, we left the laser alignment unchanged and began and finished the experiment performing a calibration curve on the glass.

3.3.2. Force-vs-Indentation Curves

When pushed against a soft sample, the tip of the AFM will indent the surface and the shape of the indentation curve (i.e., the relationship between the load applied and the tip penetration) will give information on the stiffness of the sample. The force-vs-indentation curves were calculated by using the approach portion of the force-vs-distance curves. The first step was to take a force-vs-distance curve on a naked glass portion of the sample as reference. From this curve, the coefficient of linear relationship between the z-piezo displacement and cantilever deflection was derived. From each of the force-vs-distance curves taken on the cells the calibration line was subtracted, thus obtaining the force-vs-indentation curve (*see* **Note 10**).

3.4. Results and Interpretation

3.4.1. Imaging

Figure 1 is a collage of various images (acquired in error mode) taken on the same growth cone of a spinal cord neuron adhering to a treated slide just taken out of the incubator. **Figure 1A** shows a topview rendering of the growth cone. Filamentous cytoskeletal structures are evident in the thick region

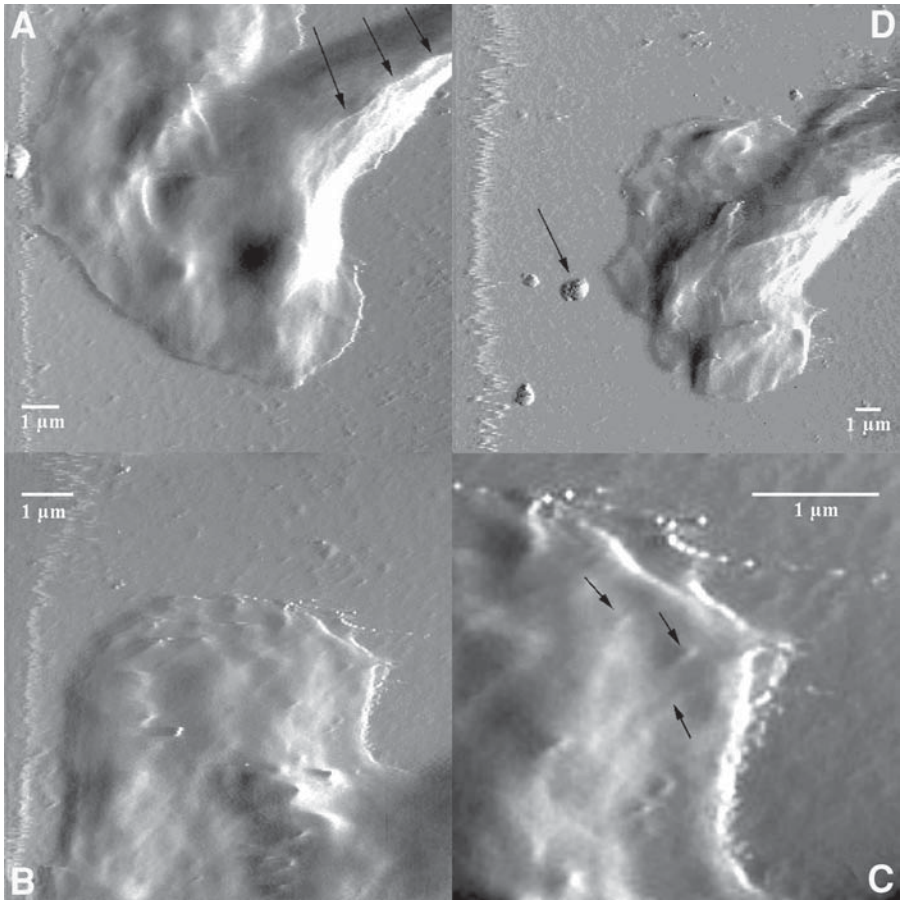

Fig. 1. Growth cone of a living spinal cord neuron adhering to a polylysine-coated glass slide. **(A)** Topview rendering of an error-mode image. Filamentous cytoskeletal structures are evident in the thick region (arrows). **(B)** Scan of the top region of the cone (partially missing in **A**). Small dot-like structures can be seen in the thick domain. **(C)** Zoom of the top right corner of the cone. A meshwork of cytoplasmic structures appears (arrows). **(D)** Image of the growth cone after about 10 min of continuous scanning. Most of the periphery of the growth cone has retracted.

(arrows). **Figure 1B** shows the top region of the cone (partially missing in **Fig. 1A**). Small dot-like structures are visible (arrows). A further zoom of the top right corner of the cone is shown in **Fig. 1C**. A meshwork of cytoplasmic structures appears (arrows). Finally, **Fig. 1D** shows the image of the growth cone after about 10 min of continuous scanning. The background globular structure on the left (arrow), present in both images, can be used to align the two images.

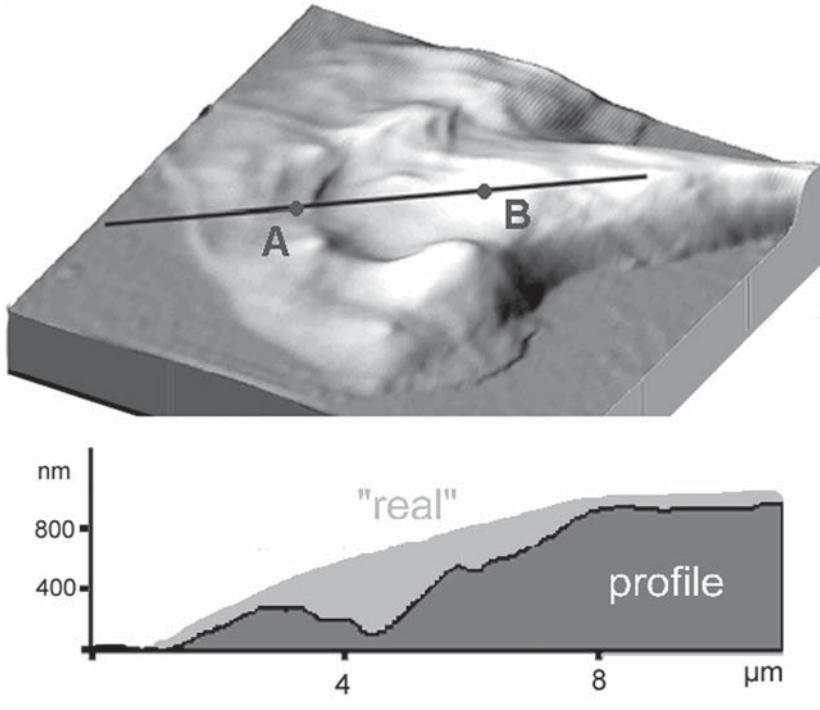

Fig. 2. 3D shaded rendering of the z-piezo signal image acquired simultaneously with the image in **Fig. 1A**, with a pictorial representation of the possible real-vs-measured profile on the growth cone.

Most of the periphery of the growth cone has clearly retracted. An increase in the relief of the filamentous structures projecting towards the neurite can be noticed. **Figure 2** shows a 3D rendering of the growth cone, as derived from the z-piezo (topographic) image (not shown), taken simultaneously with the image in **Fig. 1A**. It should be noted that the cone thickness shown in the figure is affected by the indentation of the tip on the neuron. Nevertheless, "true" thickness can be estimated and is described in **Subheading 3.4.2.** In the 3D image, a thick and a flat region can be tentatively identified, separated by a continuous relief.

Figures 3A and **B** show the growth cone of another neuron analyzed immediately after leaving the incubator. A thick tubular zone is again evident towards the neurite. Careful inspection allows one to detect a surrounding low-contrast region with flat protrusions (arrows). For comparison, **Fig. 3C** shows a similar growth cone after fixation. Similarly to **Fig. 3A**, **Fig. 3D** shows a growth cone from another living neuron, in which one can identify a thick tubular region surrounded by spiky structures (arrows).

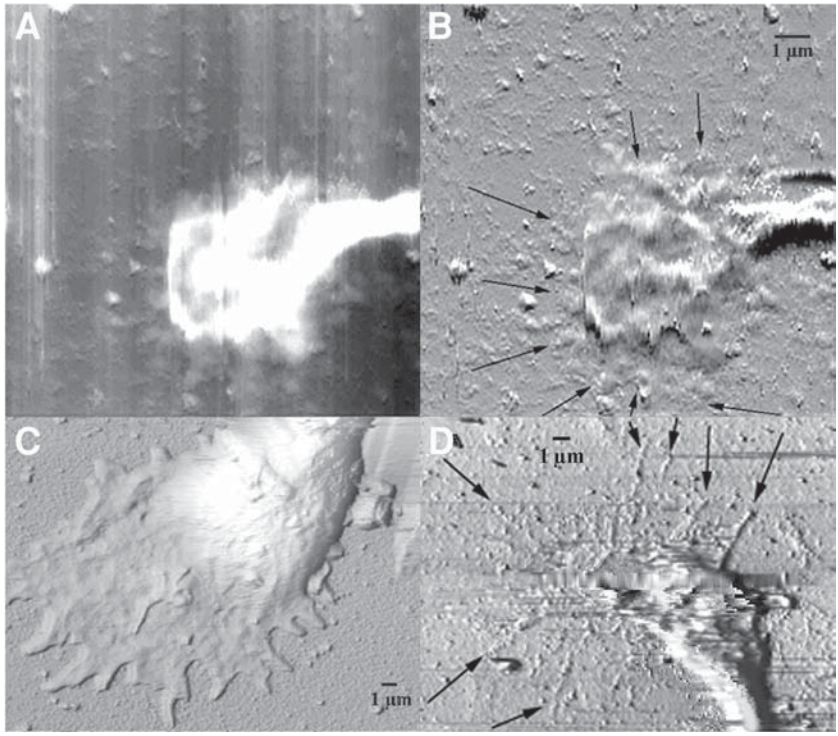

Fig. 3. Series of three images of different growth cones, in which the peripheral region has been detected by the AFM. **(A,B)** Growth cone of a living neuron analyzed immediately after leaving the incubator. A thick tubular zone is again evident. Careful inspection allows one to detect a surrounding low-contrast region with flat protrusions (arrowheads). Images obtained recording the z-piezo signal **(A)** and the error signal **(B)** simultaneously. **(C)** Image of a similar growth cone after fixation, shown for comparison. Z-piezo signal image. **(D)** Growth cone from another living neuron in which one can identify a thick tubular region surrounded by spiky structures (arrows). Image obtained recording the error signal.

Figure 4A shows a small whole neuron with several arborizations. Towards the apical end most of them seem to be disrupted. Interestingly enough, a "trace" of the borders of the arborizations is evident (**Fig. 4B** and **C**). The trace is made of small (150 nm in diameter) dot-like structures, which could be identified as clusters of adhesion molecules.

3.4.2. Indentation, Topography, and Mechanical Properties

Figure 5 shows a series of representative force-vs-indentation curves acquired upon a growth cone of a living neuron.

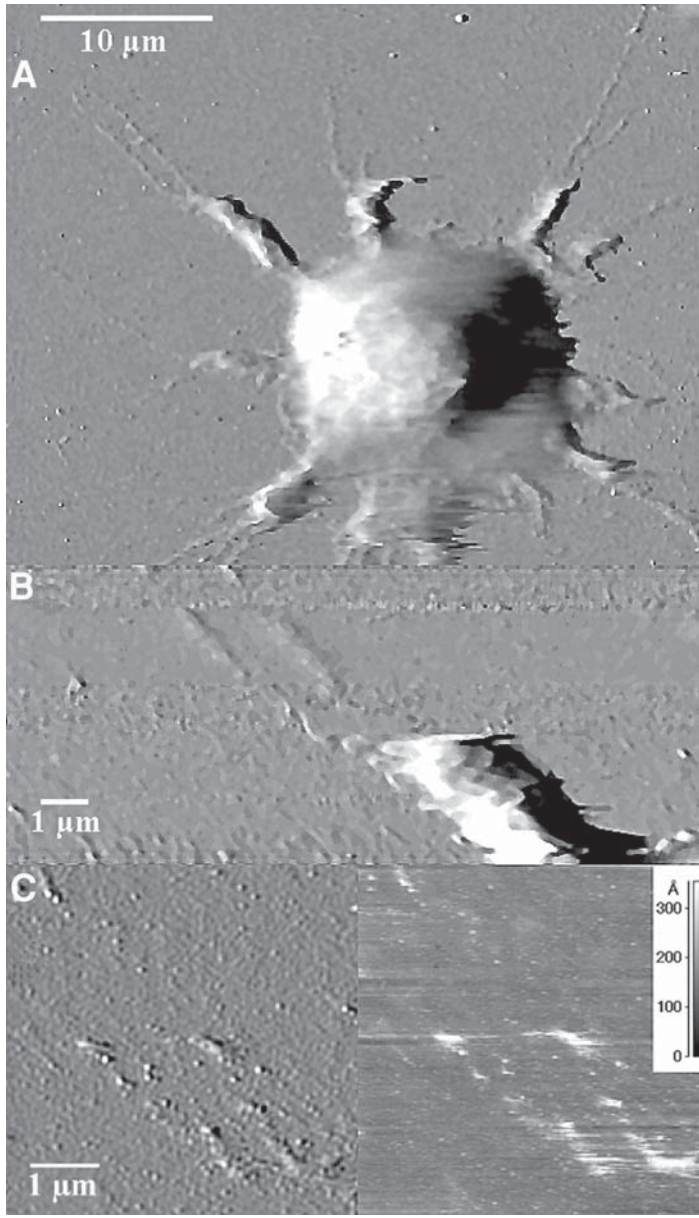

Fig. 4. **(A)** A small whole living neuron showing arborizations, imaged acquiring the error-channel signal. At the apical end most of the arborizations seem to be disrupted. **(B)** Higher magnification error-signal image of the apical end of an arborization. **(C)** Error signal and simultaneous z-piezo signal image of the same arborization apical end. The trace is made of small (approx 150 nm in diameter) dot-like structures that may be clusters of adhesion molecules.

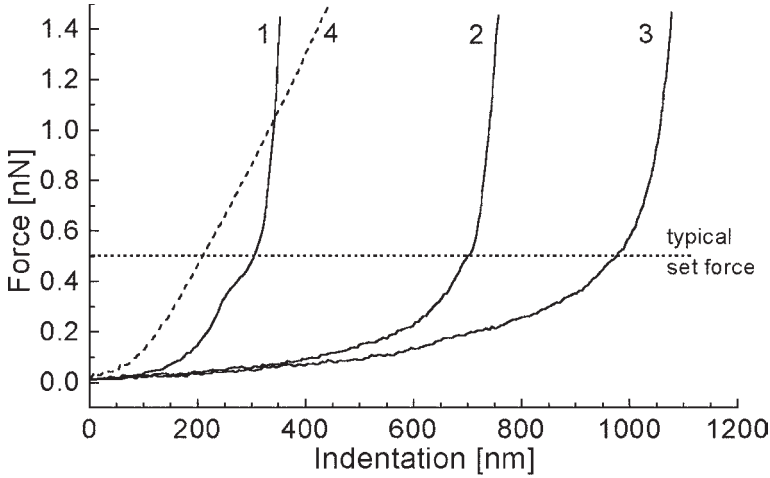

Fig. 5. Series of representative force-vs-indentation curves acquired upon a growth cone of a living neuron. Curves 1, 2, and 3 are taken moving away from the growth cone edge towards the neurite at steps of 3 μm. Each curve shows an increase in indentation with the applied force with a parabola-like behavior, until a quasivertical trend is reached. Curve 4 was taken next to the point were curve 3 was acquired but on a protrusion. A totally different trend can be observed: after an initial parabolic indentation a linear dependence on the force increase is established.

Curves 1, 2, and 3 in **Fig. 5** were taken moving away from the growth cone edge towards the neurite at steps of 3 μm and represent the typical behavior of a "soft" portion of a living cell ***(4,7)***. The indentation at first shows a parabolic-like trend followed, at higher applied forces, by a quasivertical slope. This can be explained for the first part with the classical indentation theory of a solid punch into a half space, progressively deviating from such behavior as the glass substrate contribution becomes dominant ***(10)***. The quasivertical trend with increasing force indicates that the maximum compression of the cell material has been reached and the indentation limit value attained will give an indication of the cell thickness ***(7)***. Let us now compare curves 3 and 4: curve 3 was taken onto an apparent depression of the surface, at a point like the one identified by A in **Fig. 2**, whereas curve 4 was recorded onto a stiff portion of the cell surface like the one identified by B. It is evident how in the case of curve 3 we are progressively indenting a thick portion of the cell until we reach the glass substrate, while in the second case, after a parabolic behavior for the first 100 nm of indentation, we reach a constant slope corresponding to an elastic spring constant of 0.0045 N/m. This means that, after indenting the most external "soft" cell surface, the tip interacts with submembrane structures that exhibit an elastic response ***(4)***. At the force value of 0.5 nN that corresponds to the

nominal setpoint used during imaging in the case of curve 3, we have an indentation of 950 nm, and for curve 4 we find 200 nm. We need to keep these features and figures in mind in order to understand the contrast mechanism of both the z-piezo signal and error-signal images on such specimens. This means that the deep shallows next to high peaks found in the z-piezo image cannot attributed solely to morphological features. In fact, because on thick and "soft" locations, indentations can reach the micrometer range and on stiffer ones it falls to the 100 nm range, the shallows and peaks in the "topographical" image must be essentially the result of differences in stiffness of the submembrane growth cone structure encountered by the cantilever during scanning. A pictorial representation of the possible "real"-vs-measured profile on the growth cone is shown in the second half of **Fig. 2**. Similar effects are found in the error images, where the gray scale levels represent the deviations from the feedback force (cantilever deflection) setpoint. Because the feedback loop has been tuned to give a high contrast in the error image, thus allowing temporary and relatively large deviations from the force setpoint, on the left hand side (scanning is from left to right) of an upwards slope or an increase in stiffness, the pixels will be darker, while on the right hand side they will be lighter. This can be clearly observed in **Fig. 1A**. Generally speaking, it is not possible to discriminate between a topographical change and a variation in stiffness, unless one has independent knowledge of the properties of the surface. By use of force-vs-indentation curves it is possible to discriminate the effects and estimate the thickness of the undeformed surface, at least in the point were the curve is taken. Extrapolation to similar areas can be made by an estimate of numerical values. A feature common to **Figs. 1** and **3** is a thick tubular region extending towards the neurite. The thickness of this region as read on the z-piezo image is in the order of 1 μm, to which at least 200 nm must be added to take into account indentation.

3.4.3. Identification of Growth Cone Regions

3.4.3.1. Lamellipodia

The filaments in evidence in **Fig. 1A** and **D** can be easily identified as microtubules. By comparison with images generated by the other techniques and described in the literature, the thick region can be easily identified as the so-called C domain. Note that submicrometer size structures are visible in this region. In **Figs. 1–3**, this domain is surrounded by a flat area, with thickness in the order of a few hundred nanometers. This could be identified as a lamellipodia-rich P domain.

The flat protrusions shown in **Figs. 3A** and **B** can be identified as lamellipodia structures. Their thickness is in the order of 30–60 nm. Irregulari-

ties, distortion along the scanning direction, and "islands" of biological material underline the extent of the tip–sample interaction. For comparison, **Fig. 3C** shows a similar growth cone after fixation. Lamellipodia structures with a smooth profile are now evident. The thickness is now in the 100–200-nm range: the fixation process has affected the membrane stiffness so that negligible indentation occurs during scanning.

3.4.3.2. Filopodia

The spiny protrusions surrounding the C domain in **Fig. 3D** can be identified as filopodia structures. Interestingly enough, these protrusions appear to be made of globular subunits, often arranged in a discontinuous way. These subunits have a diameter of 120–180 nm and a thickness ranging from 5 to 30 nm. They could be identified as clusters of proteins or patches of membrane adhering to the substrate, left after the tip–sample interaction. The distribution of proteins in the filopodia of growth cones is a subject of active research. Filopodia are known to be filled with bundles of actin filaments ***(11)***, and the presence of spots of tyrosine-phosphorylated proteins have been recently demonstrated at the tips of growth cones by immunofluorescence techniques ***(12)***. The formation of focal contacts by the tip of filopodia with the substrate is still an open question and further investigation of the described structures could contribute to answer it.

3.4.3.3. Arborizations

Finally, traces of discontinuous biological material are evident in the terminal regions of the arborizations of a whole neuron (**Fig. 4**). A fixed similar neuron is shown for comparison (**Fig. 6**). Here, the arborizations are smooth and continuous. The morphology of the biological details is better preserved, but no information about adhesion to the substrate can be inferred. On the contrary, we can conclude that the interaction of tip with living material does somehow affect the morphology but, at the same time, gives hints at the nanometer scale about the organization of the biological structure and about the way contact is made with the substrate.

3.5. Comparison With Other Techniques

Detailed AFM images of living flat cells, such as glia cells ***(5,6)***, fibroblasts ***(4,7)***, and epithelial cells ***(13)*** have already been analyzed in the literature. Low-resolution images of whole neurons have also been produced ***(6)***. The other available techniques for studying growth cones are as follows.

1. Whole-mount electron microscopy, which gives images with detailed information down to the nanometer ***(14)*** but on dead materials and without thickness quantification.

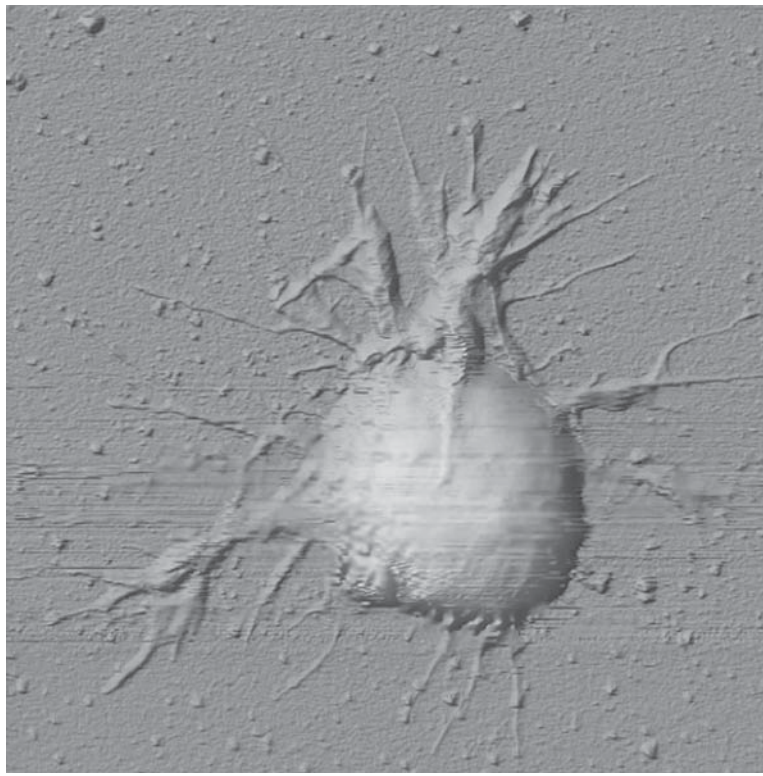

Fig. 6. A small whole fixated neuron showing arborization, to compare with the living one imaged in **Fig. 4**.

2. Fluorescence microscopy, which allows one to identify cytoskeleton components by immunofluorescence staining. Time-lapse analysis of stained (lipid probe Dioc6) living growth cones have also been described ***(15)***.
3. Video-enhanced differential interference contrast (DIC) imaging, which is widely used for generating detailed images of unstained living growth cones. This technique has allowed the identification of two distinct domains: a central, relatively thick, organelle-rich region (C domain) and a peripheral, thin, region devoid of organelles (P domain; **refs.** ***16*** and ***17***).

AFM shares with the last technique the capability of imaging unstained samples. Moreover, as compared with all the mentioned methods, it is the only one to have the potentiality of giving quantitative information on thickness. However, to put the last statement in the correct perspective, it should be underlined that any AFM-originated image of a soft sample is the result of a mechanical interaction between tip and sample. This implies indentation, and force-vs-distance curves must be used to correct the data and obtain actual

thickness. With indentation, a challenge to the adhesion of the living cone to the substrate is exerted. Finally, it is worth mentioning that, in principle, information about viscosity could also be obtained, similarly to the laser-tweezers technique ***(18)***, by carefully comparing the forward and retraction portions of the force-vs-distance curves.

4. Notes

1. Cut glass slides are used because the AFM employed for these investigations is a "scanned sample" model, able to accommodate only flat samples having maximum width of 25 mm and length of about 50 mm. When using "scanned tip" instruments, it is possible to apply the AFM directly onto the Petri dish. One advantage of using glass slides is their surface flatness with respect to Petri dishes.
2. Even if for some cell lines it is possible to grow cultures on bare substrates, for AFM investigation a good adhesion with the substrate is essential, allowing the cells to withstand the lateral forces induced by the tip during scanning
3. An advantage of using small glass slides is the possibility of preparing several samples in the Petri dish at one time that can be kept in the incubator until just before use. This allows one to increase the throughput of one single primary cell line culture both in time and number of observable cells, as usually it is not possible to maintain temperature and CO_2 control during AFM measurements. Recently, research groups have started developing systems that will allow one to control physiological environmental conditions during AFM imaging.
4. An important feature when using the AFM on living cells is the range available for the z direction in the scanner, as variations in height of several micrometers can be found during scanning. Also, x and y ranges should be several tens of micrometers.
5. Small spring constants avoid damage to the cell surface or even detachment of the cell from the substrate. We have also tried using 0.003 N/m spring constant cantilevers, but the adhesion forces between tip and sample did not result in good imaging.
6. Standard silicon nitride tips are quite sufficient for good imaging in contact mode on living cells as the visco-elasticity of the cell is the main limiting factor in resolution: in fact, a sharper tip does not improve resolution but can produce damage. Moreover, silicon nitride seems to behave better that silicon or polysilicon with respect to tip–sample adhesion.
7. A fresh supply of the buffer solution used for the culture, possibly held at 37°C, should be kept at hand, in order to be able to add it when missing.
8. An on-axis microscope is essential for positioning the tip on the sample in the required position. Either a scanned sample AFM equipped with a high magnification, long focal length microscope or a scanned tip AFM mounted onto an inverted microscope can be used. The latter obviously opens the possibility of using a wider range of optical microscopy techniques in conjunction with AFM.
9. One of the serious limitations of AFM is the low scanning speeds that have to be used on soft surfaces. A 10×10-µm image with 512 points per line is typically acquired in 8 min.

10. On the thinner portions of the cells, one observes at first the indentation process, and then a constant relationship between load and z-piezo travel is found. This means that all of the cell has been compressed and the glass surface has been "reached." One can use this last linear portion of the force-vs-distance curve to derive the coefficient and obtain the corresponding force-vs-indentation curve.

References

1. Binning, G., Quate, C. F., and Gerber, C. (1986) Atomic force microscope. *Phys. Rev. Lett.* **56,** 930–933.
2. Schoenenberger C.-A. and Hoh, J. H. (1994) Slow cellular dynamics in MDCK and R5 cells monitored by time-lapse atomic force microscopy. *Biophys. J.* **67,** 929–936.
3. Hoh, J. H. and Schoenenberger, C.-A. (1994) Surface morphology and mechanical properties of MDCK monolayers by atomic force microscopy. *J. Cell Sci.* **107,** 1105–1114.
4. Ricci, D., Tedesco, M., and Grattarola, M. (1997) Mechanical and morphological properties of living 3t6 cells probed via scanning force microscopy. *Microsc. Res. Tech.* **36,** 165–171.
5. Henderson, E., Haydon, P. G., and Sakaguchi, D. S. (1992) Actin filaments dynamics in living glial cells imaged by atomic force microscopy. *Science* **257,** 1944–1946.
6. Parpura, V., Haydon, P., and Henderson, E. (1993) Three-dimensional imaging of living neurons and glia with the atomic force microscope. *J. Cell Sci.* **104,** 427–432.
7. Ricci, D. and Grattarola M. (1994) Scanning force microscopy on live cultured cells: Imaging and force-versus-distance investigations. *J. Microsc.* **176,** 254–261.
8. Butt, H.-J., Siedle P., Seifert K., Fendler K., Seeger T., Bamberg E., et al. (1993) Scan speed limit in atomic force microscopy. *J. Microsc.* **169,** 75–84.
9. Putman, C. A. J., van der Werf. K.O., de Grooth B. G., van Hulst, N. F., Greve, J., and Hansma, P. K. (1992) A new imaging mode in atomic force microscopy based on the error signal. *Proc. SPIE.* **1639,** 198–204.
10. Sneddon, J. N. (1965) The relation between load and penetration in the axisymmetric Boussinesq problem for a punch of arbitrary profile. *Int. J. Eng. Sci.* **3,** 47–57.
11. Lewis, A. K. and Bridgam P. C. (1992) Nerve growth cone lamellipodia contain two populations of actin filaments that differ in organization and polarity. *J. Cell. Biol.* **119,** 1219–1243.
12. Da-Yu, W. and Golberg, D. J. (1993) Regulated tyrosine phosphorylation at the tips of growth cone filopodia. *J. Cell Biol.* **123,** 653–664.
13. Hoh, J. H., Sosinsky, G. E., Revel, J.-P., and Hansma, P. K. (1993) Structure of the extracellular surface of the gap junction by atomic force microscopy. *Biophys. J.* **65,** 149–163.
14. Bridgman, P. C. and Dailey M. E. (1989) The organization of myosin and actin in rapid frozen nerve growth cones. *J. Cell Biol.* **108,** 95–109.

15. Bridgman, P. C. (1991) Functional anatomy of the growth cone in relation to its role in locomotion and neurite assembly, in *The Nerve Growth Cone* (Letourneau, P. C., Kater, S. B., and Macagno E. R., eds.), Raven Press, New York, pp. 39–53.
16. Gordon-Weeks, P. R. and Mansfield G. S. (1991) Assembly of microtubules in growth cones: the role of microtubule-associated proteins, in *The Nerve Growth Cone* (Letourneau, P. C., Kater, S. B., and Macagno E. R., eds.), Raven Press, New York, pp. 55–64.
17. Goldberg, D. J., Burmeister, D. W., and Rivas, R. J. (1991) Video microscopic analysis of events in the growth cone underlying axon growth and the regulation of these events by substrate-bound proteins, in *The Nerve Growth Cone* (Letourneau, P. C., Kater, S. B., and Macagno E. R., eds.), Raven Press, New York, pp. 79–95.
18. Dai, J. and Sheetz, M. P. (1995) Mechanical properties of neuronal growth cone membranes studied by tether formation with laser optical tweezers. *Biophys. J.* **68,** 988–996.

11

Evaluating Demineralization and Mechanical Properties of Human Dentin With AFM

Grayson W. Marshall, Jr., Sally J. Marshall, Mehdi Balooch, and John H. Kinney

1. Introduction

Atomic force microscopy (AFM) is a valuable technique for the study of demineralization and the effects of other solutions and environments on the structure of human dentin because high-resolution studies of changes in structure and dimensions are possible in nearly any environment over time ***(1)***. Because dentin forms the bulk of the tooth and is subject to a variety of alterations as a result of disease, age, and treatment ***(1)***, such studies are useful for understanding the basic structure–property relations of dentin and for evaluation of various conservative and restorative dental treatments. Initial studies of demineralization and dehydration of dentin were reported in 1993 ***(2,3)*** in which relative changes in dimensions were used to evaluate these processes. It soon became apparent that a stable reference layer on the surface or embedded in the specimen would be most desirable for evaluation of time-dependent changes and to take advantage of the high-resolution capabilities of the AFM. In 1995, the use of paint-on varnish or photoresist ***(4)*** and evaporated gold layers ***(5)*** were developed that allowed evaluation of demineralization, either continuously or sequentially, for a variety of demineralizing agents. An additional technique of interest is the use of AFM-based nanoindention for measurements of site-specific hardness and elastic modulus of dentin. Such measurements can frequently be performed as a portion of the same study in which demineralization experiments are conducted. The development of indentation-based mechanical properties measurements stems from the work of Doerner and Nix ***(6)*** and can be performed with a variety of equipment types. We have been most interested in modified AFM methods because the AFM offers the possibility of both site-specific indentation and high-resolu-

From: *Methods in Molecular Biology, vol. 242: Atomic Force Microscopy: Biomedical Methods and Applications*
Edited by: P. C. Braga and D. Ricci © Humana Press Inc., Totowa, NJ

tion imaging in solution or on dry tissue, whereas many other methods allow only the study of dry tissue. Our initial work with AFM-based nanoindentation used a modified and stiffer cantilever and diamond tip that allowed hardness measurements to be made on either peritubular or intertubular dentin ***(7,8)***. However, modified transducer heads are now available that can measure load and displacement independently and provide site-specific load displacement curves and imaging in many environments. They offer substantial improvement and allow the determination of both hardness and indentation modulus (or reduced elastic modulus). Thus, we use this method in all current measurements of hardness and elastic modulus for dentin ***(9–13)***.

1.2. Continuous and Sequential Longitudinal Studies and Reference Layers

Continuous scanning is conducted by obtaining images continuously during demineralization in the wet cell of the AFM. Thus, each pixel of a line and each line of a scan represent different exposures and offer a continuous record of the demineralization process. In sequential scanning, a baseline image in water is obtained, and then the sample is removed, treated for an appropriate exposure time, washed, and reimaged in the AFM wet cell. This method has the advantage that start and stop times can be more easily controlled and each image represents a single exposure time so that changes can be measured on all the structures in an image.

Neither the varnish nor the evaporated gold procedures were ideal for establishing a stable reference area. For the varnish method, the thickness can be difficult to control, and if the thickness is too great, it makes a poor reference. In addition, the edge is usually rounded so that an abrupt step is not apparent and it is not always clear when the top surface is flat. Having a flat reference is useful when image processing, such as plane fitting, is used. Finally, the edge where varnish and dentin meet is the area that is used for measurement. This edge is often difficult to demineralize uniformly so that a typical image may have a rounded reference layer and a zone of uneven etching in the image field of interest, as shown in **Fig. 1**.

Thin evaporated gold layers (approx 10 nm) overcame many of these problems ***(5)*** and allowed measurement between the gold layer and intertubular and peritubular dentin structures. However, there were two remaining problems with this method. Firstly, the dentin had to be subjected to a high vacuum treatment during gold evaporation. This may be undesirable in a naturally hydrated tissue and introduces microstrains ***(3)***. Second, demineralization for long periods in dilute solution or with more concentrated acids resulted in etching under the edge of the gold layer. When this occurs, the gold area is no longer a stable reference and any measurements are subject to greatly increased error.

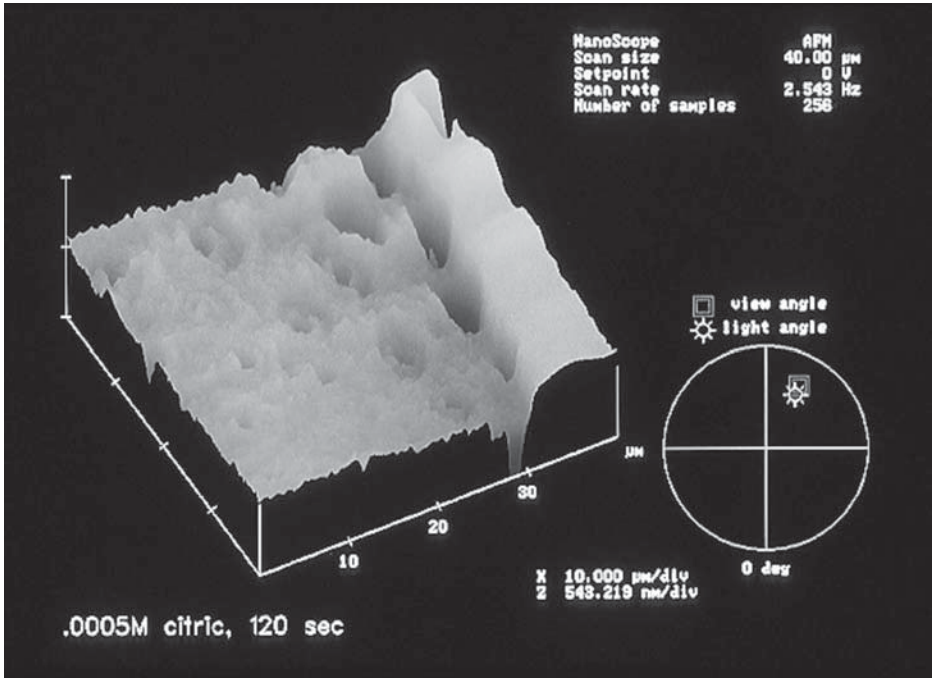

Fig. 1. Image of uneven etching that can be caused by a rounded edge of varnish, or the inability to apply the demineralizing agent uniformly at the edge of the reference layer. The etching time was 120 s with dilute citric acid. The reference area is in the upper right. A deep trough is adjacent to the layer and the uneven etching decreases with distance from the reference area, so that it is not possible to tell which areas of the dentin are representative of the etching exposure.

Three improved methods have been developed that can be used alone or in combination to overcome many of the preceding limitations. These include the use of an embedded cyanoacrylate reference layer that has been useful for demineralization studies in many dilute solutions as well as dehydration and rehydration studies ***(14)*** and an embedded glass reference layer that has been developed for studies in which the cyanoacrylate method is unstable ***(15)***. The third method is to use a tape mask to protect portions of the sample from the solution, allowing the protected portion to serve as the reference area. This has been useful for studies of single exposures to concentrated solutions and the effect of drying and rehydration ***(16,17)***. We recently have used the combination of a mask and embedded layer to evaluate the combined effects of demineralization and deproteinization of dentin ***(12)***.

1.3. Testing the Reference Layer Stability

When evaluating the effect of any new solution, the first step is to determine the stability of the reference layer. For example, cyanoacrylate is evaluated by bonding glass slides together with the cyanoacrylate, embedding in acrylic, followed by sequential metallographic polishing of the glass–cyanoacrylate–glass interface through a 0.05-μm alumina slurry. The sample is then imaged in the AFM, exposed to the solution of interest for appropriate periods, and then reimaged to determine any changes in height of the cyanoacrylate relative to the glass. For many solutions that we have studied, the cyanoacrylate has proven to be stable for exposure periods of at least 30 min. Preparing the cyanoacrylate embedded layer in dentin samples will be described in **Subheading 3.** We have found that for some solutions, such as ethanol and acetone, the cyanoacrylate is not stable, and this has led to the development of a glass reference layer method that requires additional steps for fabrication as described elsewhere ***(15)***. For dentin samples that have been etched extensively and then undergo dehydration, the interface between reference layer and dentin is damaged and often fails because of the drying stresses. To overcome this problem the extent of the etching must be limited ***(14)*** so that the interface withstands these stresses, or a masking technique can be used, in which part of the sample is protected from the acid and the unetched portion serves as a reference area. This method has been used in several studies ***(12,16–18)*** and only requires the identification of a tape that can be applied to the dentin and removed without leaving a residue. One such tape is Scotch Mounting Tape (3M, Minneapolis, MN). It also should be noted that the methods described here could be used for other calcified tissues. **Fig. 2** shows an example of enamel etched to reveal the enamel prism structure with an embedded cyanoacrylate reference layer.

2. Materials

1. Obtain teeth from human subjects following protocols approved by Institutional Review Boards and with informed consent.
2. Store whole teeth in filtered and purified water or Hanks' balanced salt solution (HBBS) at 4°C.
3. Teeth are potentially infectious and therefore should be disinfected or sterilized. Normally, we sterilize using low dose gamma-radiation ***(19)***.
4. Tooth sectioning is conducted using a low-speed water-cooled diamond saw (Isomet Low Speed Saw, Beuhler, Ltd., Lake Bluff, IL).
5. Store cut sections in HBBS at 4°C.
6. Sequential grinding is done using sand paper from 240, 320, 600, and 1200 grit (Buehler Ltd.).

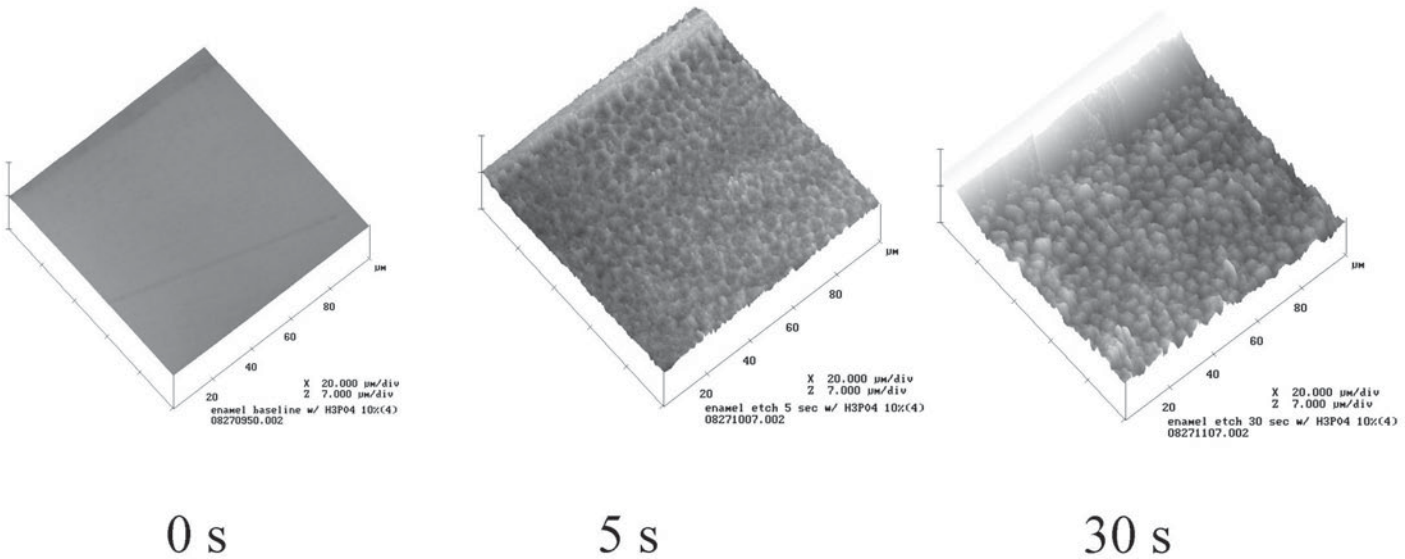

Fig. 2. Enamel etching sequence using the cyanoacrylate reference-layer method. Images for etching exposure to 10% phosphoric acid are shown at 0, 5, and 30 s. Also note that the etching pattern changed from one type to another during this treatment. The reference layer along the upper left of each image.

7. Final polishing is performed using aqueous suspensions of alumina powder or diamond (Buehler Ltd.). A fine polish will leave the structure with no detectable smear layer. Ultrasonic clean for 10–15 s between polishing steps.
8. Embedded reference layer is made from ethyl α-cyanoacrylate (MDS Adhesive QX-4, MDS Products, Anaheim, CA).
9. Solutions are usually prepared from reagent grade chemicals except for evaluations of commercial demineralization agents.
10. AFM imaging performed with a Nanoscope III (Digital Instruments, Santa Barbara, CA).
11. Nanomechanical properties (hardness and reduced elastic modulus) are ascertained with a Triboscope indentor system (Hysitron Inc., Minneapolis, MN).

3. Methods

3.1. Basic AFM Mode

AFM methods are well established. For studies of dentin recession and demineralization, we normally use the contact mode and standard S_3N_4 tips. Tapping mode also can be used and allows the tip force to be reduced. When coupled with high-aspect ratio Si tips with a very small tip diameter, it is most useful for high-resolution studies of particular features of the dentin. However, most steps of the demineralization studies do not require the high-resolution tips, which are expensive and fragile, and, therefore, the less-expensive standard tips and contact mode are used for most studies. Because dentin is a naturally moist hydrated biological composite, nearly all imaging is done in a wet cell filled with purified water at ambient temperature.

3.2. Dentin Disks With Embedded Reference Layer

1. An extracted human tooth is usually the sample of interest for studies of dentin. Because the tooth is a potential source of infection, after extraction we store the teeth in vials in distilled water or HBBS and sterilize with a low dose of gamma radiation ***(19)***. The tooth in its solution is then stored at 4°C until prepared.
2. The tooth is removed from its storage vial, cleaned of any soft tissue, and mounted on a wooden tongue depressor with hot glue. Portions of the tooth that are not of interest are usually cut off (e.g., pulp chamber and roots), and then the crown is sectioned longitudinally (sagittally) into two halves, as shown in **Fig. 3A**, using a water-cooled diamond cut-off saw (Buehler, Ltd Isomet Low Speed Saw, Lake Bluff, IL).
3. The cut surfaces (**Fig. 3B**) are then carefully polished through successive grits of sand paper (240–1200 grit) under flowing water, followed by aqueous suspensions of alumina in successive steps (1 and 0.3 μm) and ending with 0.05-μm alumina. Between steps, the sample is ultrasonically cleaned in distilled water for 10–15 s to remove remnants of the abrasives. Aqueous suspensions of diamond are another good alternative.

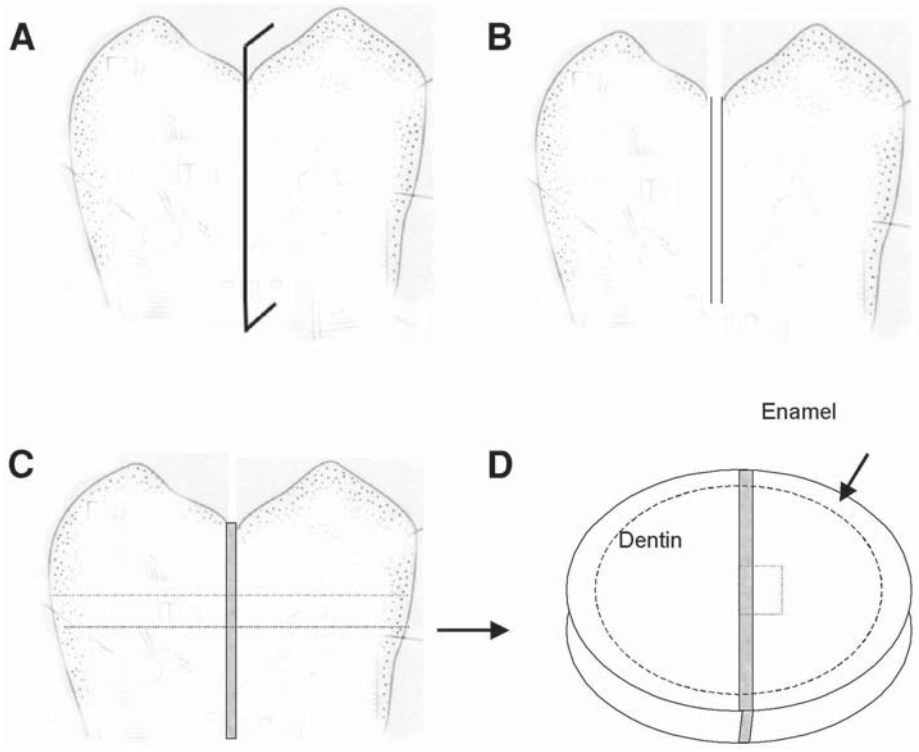

Fig. 3. Schematic diagram for construction of the cyanoacrylate reference-layer method. **(A)** Sample is sagittally sectioned; **(B)** two halves are polished; **(C)** two halves are bonded together and a disk is cut parallel to the occlusal surface; **(D)** the disk has an enamel periphery and inner dentin region with a thin layer (not drawn to scale) of cyanoacrylate that is used for the reference layer and area for study (small square).

4. The two polished halves are then blotted dry and bonded back together (**Fig. 3C**) with ethyl α-cyanoacrylate (MDS Adhesive QX-4, MDS Products, Anaheim, CA) using medium finger pressure (**Note 3**). The viscosity of the cyanoacrylate can be adjusted by air drying to increase viscosity or thinned by mixing with acetone.
5. Sections for AFM study then can be obtained by sectioning the reassembled tooth parallel to the occlusal surface using the same water-cooled diamond cut-off wheel (**Fig 3D**). Because the dentin structure varies with intratooth location ***(1)***, it is often of interest to prepare disks representative of either superficial dentin (close to the enamel) or deep dentin (close to the pulp chamber). Usually one or more disks of 1- to 1.5-mm thickness are obtained from a single tooth by repeated sectioning parallel to the occlusal surface (**Fig. 3D**).

6. After removal (**Fig. 3D**), the disk has a periphery of enamel surrounding the dentin and a thin cyanoacrylate bonded layer of about 10 μm in thickness through its center. This layer serves as the height reference layer in studies of demineralization and solution effects on the dentin.
7. The surface to be studied (either top or bottom) is then prepared using the same polishing steps, with ultrasonic cleaning between steps, which were described previously for the cut surfaces that were bonded together to reassemble the tooth. Various areas to one side or the other of the reference layer can be studied, first at baseline in water, and then after exposure to the selected treatment solution for various times. (*See* **Note 1**.)

3.3. Solutions

Typically, a dilute acid solution is prepared from reagent grade chemicals. Solutions with a pH of about 2 work well with this method and allow sequential measurements of the changes in height, relative to the reference layer, to be made at different locations in each field of view. However, nearly any solution of interest, including commercial etchants, can be used. Concentrated solutions etch the structure more rapidly and therefore the structural changes may be difficult to follow, which is the reason that dilute solutions are preferred. For example, in dilute solutions at pH 2–3, the changes in peritubular dentin can be sequentially measured after 5-s exposure steps for 20- to 60-s cumulative exposure time. After this, it is difficult to see the peritubular dentin because it etches more quickly and recedes below the level of the surrounding intertubular dentin. In contrast, a single 5-s exposure with a more concentrated acid, for example, 10% citric acid or 35% phosphoric acid, typical of those used for bonding procedures, will etch the peritubular dentin below the surface and will not allow contact with the AFM tip, so measurements cannot be made. Measurements of the changes in the intertubular dentin can be made with dilute or concentrated solutions.

3.4. Imaging and Demineralization Treatments

1. Usually initial images (baseline, *see* **Fig. 4A**) are taken by placing the polished dentin disk in the wet cell of the AFM and taking three to four images along the reference layer with dimensions of 20 μm × 20 μm to 50 μm × 50 μm (*see* **Note 2**).
2. Height differences between the reference layer and various locations in the dentin then can be determined, using the section analysis software program (**Fig. 4**). The image is processed using plane fit analysis procedures on the reference layer that was highly polished and is assumed to be flat. Site-to-site measurements are made of height differences between the reference layer and various locations on the peritubular dentin surrounding the dentin tubules and the intertubular dentin areas between the tubule units (**Fig. 4B**).

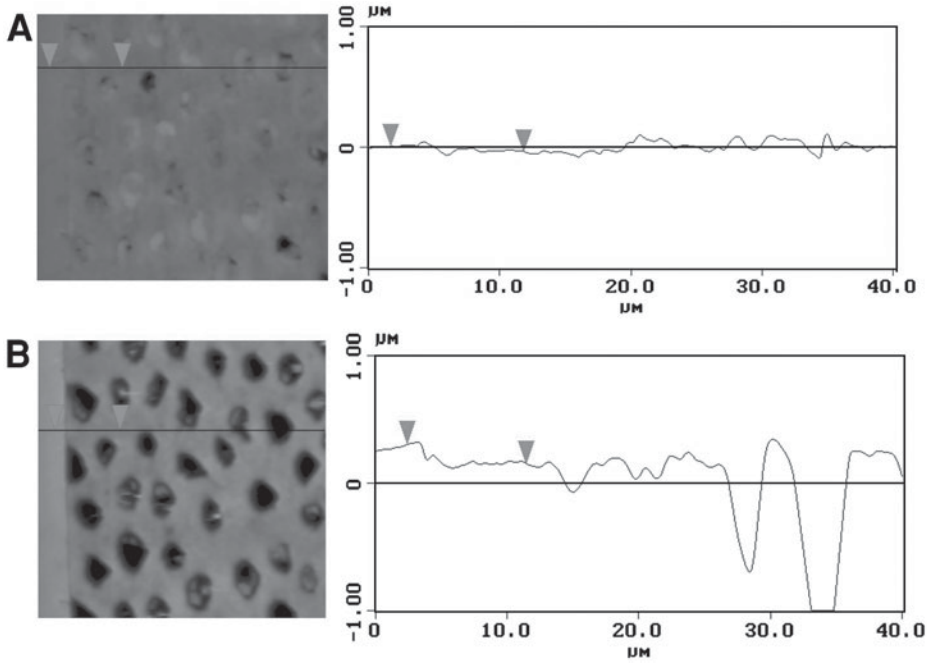

Fig. 4. Example of baseline and etched samples of dentin demineralized with citric acid These images are from the same area and the reference layer is at the left. **(A)** Baseline image in water of a 40 × 40 µm field of view. Many tubules are filled because this image was taken from transparent dentin that has mineral deposits inside tubule lumens. At the right side of the image is a section analysis showing height differences between selected points on the reference layer and the intertubular dentin (difference was 41 nm). **(B)** Same area after 30 s of etching showing enlarged tubule lumens and recession of the intertubular dentin as shown by the shading differences and the section analysis at the right. The height difference between selected points was 153 nm.

3. Normally, three to five measurements each for peritubular dentin and intertubular dentin are made per image. If there are other features of interest, such as intratubule mineral, these can be measured in the same way ***(20,21)***.
4. After baseline imaging, the disk is removed from the AFM and the desired solution is applied for a selected time. Application of the solution can be done in a number of ways, including immersion or application with a small sponge that is commonly provided in bonding kits (Sun Medical Co., Ltd, Moriyama, Japan).
5. After uniform application of the solution for the desired time the sample is thoroughly washed in purified water and placed back in the AFM wet cell and each of the previously imaged areas is reimaged.

6. Each image is plane fit, and measurements are made between the reference layer and the previously selected points (**Fig. 4B**). For dilute solutions, we usually use 5-s exposure increments for times up to 30- to 60-s cumulative exposure. The peritubular dentin is etched rapidly during this time period and gradually recedes below the surrounding intertubular dentin, leaving enlarged tubule lumens (**Fig. 4B**). Exposure increments are continued in steps of 10 s to a minute or more to follow continued changes in the dentin structure and the recession characteristics of the intertubular dentin. Normally we perform this procedure for cumulative periods of 1800 s, although shorter and much longer times have been used, depending on the aims of the study. The intertubular dentin also recedes initially at a high rate, but more slowly than the peritubular dentin. The intertubular recession generally slows, and after some time, appears to change very little with additional etching. Thus, when recession is plotted vs time for the intertubular dentin the surface recession appears to slow or reach a plateau. This is attributed to replacement of the mineral in the intertubular dentin with water that compensates for the differences in volume. However, if the dentin is dehydrated at any point during the procedure, the partially demineralized dentin will rapidly collapse ***(14,16,17)***. Thus, any dehydration will lead to errors in the measurements of surface recession and should be avoided. This is an additional motivation to make all measurements in a wet cell and under water.
   It should be noted that brief drying can be reversed rapidly, and therefore, inadvertent drying during handling will be overcome by re-immersion in the wet cell ***(14,16,17)***.

3.5. Sequential Surface Recession, Etching Rates, and Etching Characteristic Curves

For a selected field of view in a baseline image the point-to-point differences in height between the reference layer and each of the selected peritubular dentin locations and intertubular dentin areas give the initial surface height. Ideally, if all areas are perfectly polished, the differences would be zero, but in practice there is usually a small difference because the peritubular dentin, intertubular dentin, and reference layer; all have different hardness and different response to polishing. Our experience has been that peritubular dentin protrudes slightly above the intertubular dentin and the reference layer is usually at the same or a slightly higher level as well (**Fig. 4A**). The same locations are measured for each exposure interval using plane-fit processed images, based on the assumption that the reference layer is flat. Clearly, the more accurately the same points can be selected in sequential images, the more accurate will be the measurements of recession. **Figure 4B** illustrates a 30-s etch in dilute citric acid for the area shown in **Fig. 4A** and illustrates the measurements of height difference between the peritubular dentin and the reference layer, and between the intertubular dentin and the reference layer using the section analysis proce-

dure. After all the height differences from all the images are collected and corrected for any difference in height between the selected points and the reference layer at baseline, recession-vs-time curves can be constructed for peritubular dentin and intertubular dentin. As noted earlier, the recession curve for peritubular dentin can be measured only for a short time because of the rapid recession below the intertubular dentin that does not allow accurate contact with the pyramid-shape of the AFM tip. However, with data at exposure times between 0 and 20–30 s, the recession-vs-time curve can be used to estimate the etching rate of the peritubular dentin for the given solution. A similar procedure can be used for intertubular or other dentin structural components. However, the slowing of recession and the appearance of an apparent plateau in the recession for long periods makes it difficult to characterize the intertubular dentin behavior from a single short-term rate. We usually estimate the level and/or time at which the plateau occurs to characterize the intertubular dentin etching behavior (*see* **Fig. 5**). If this procedure is adopted, the features of the plateau are used rather than an estimated etching rate to describe the intertubular dentin. This seems appropriate because the AFM tip measures the intertubular dentin surface location, which is really a demineralized collagen network after an etching exposure, rather than the location of the demineralization front. The demineralization front increases with depth of continued etching although the surface recession appears to plateau, i.e., the recession rate approaches zero while the true etching rate does not. The difference between the location of the demineralization front and the apparent plateau can be determined with other techniques such as dehydration of the specimen ***(1)***, high-resolution computed tomography imaging ***(4)***, or scanning electron microscopy of fractured cross-sections.

The apparent plateau is probably not a real plateau and in fact depends on the overall depth of etching. When the location of an apparent plateau is compared with the extent of etching, samples with markedly deeper total demineralization demonstrate higher values for the level of the apparent plateau (greater recession). Thus, we speculate that the maximum value for the apparent plateau depends on total demineralization depth. This value could be determined by total demineralization of the sample and would, therefore, depend on the thickness of the original dentin disk. The experiment implied by this speculation has not as yet been conducted. If true, this means that the recession of the intertubular dentin would slowly increase with increased demineralization of the sample until a true plateau is reached, which is dependent on the thickness of the dentin disk. Despite these limitations, the apparent plateau and the time to reach this value has proven valuable in characterizing differences in demineralization response with different solutions and with different types of den-

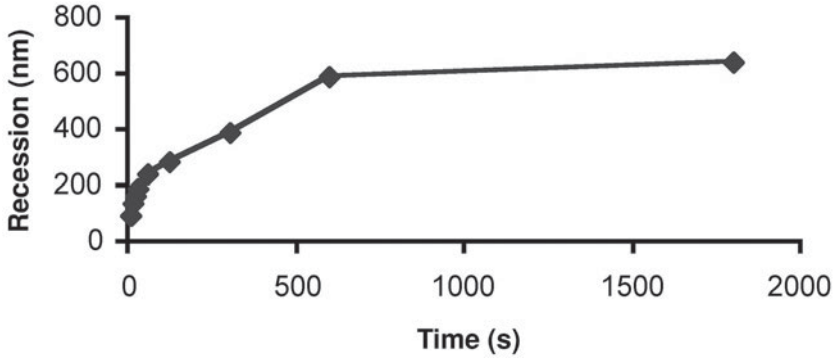

Fig. 5. Long-term decreases in height relative to the reference layer (recession) for demineralized intertubular dentin as a function of etching time in dilute citric acid for normal dentin. The recession level or time at which a plateau is observed is often useful in describing the characteristics of a particular form of intertubular dentin.

tin, such as caries-affected transparent dentin and sclerotic dentin ***(20,21)***. However, this also raises the question of how best to characterize the intertubular recession curve, define the plateau, and compare recession curves for intertubular dentin treated in different experiments. We have used different approaches to this problem. The apparent level of the plateau can be defined by a fixed criterion, for example, the point at which there is a change in dimension of less than some amount, from then until the conclusion of the experiment. With this level defined, statistical comparisons can be made to compare either the time or level of the plateau for different experimental conditions ***(20,21)***.

3.6. Other Dimensional Change Measurements

The effect of dehydration leading to the collapse of the demineralized dentin matrix (collagen) was previously mentioned and is of considerable interest from the standpoint of dentin bonding procedures, clinical treatments, and understanding the role of moisture in the dentin structure. In some experiments we have evaluated the effects of dehydration and rehydration using both the preceding reference layer method ***(14)*** and other masking methods ***(16,17)***. A difficulty arises in using the cyanoacrylate method because the etching procedure weakens the interface between the reference layer material and the dentin. On dehydration, the drying stresses often disrupt the layer and therefore do not allow measurements to be made. The weakening of the interface, as might be expected, increases with the extent of demineralization, so that for samples with shallow demineralization, the effect of dehydration and its reversal by rehydration can be followed. However, our experience has been that with

deeper (prolonged or higher concentration solutions) the interface is largely destroyed and other methods need to be used ***(16)***.

3.7. AFM-Based Nanoindentation for Hardness and Elasticity Measurements of Dentin

The same sample preparation methods can be used to prepare samples for mechanical properties measurements using the AFM. Although initial measurements were reported using a stiffer cantilever and diamond tip ***(7,8)***, improved equipment allowing recording of load-displacement curves now permits both hardness and elastic modulus determinations to be made. For these kinds of measurements the standard AFM head from the Nanoscope III is replaced with a Triboscope indenter system (**ref. *9***). In this configuration, the standard AFM head is replaced by a capacitive sensor. The sensor consists of two fixed outer drive plates that are driven by AC signals 180° out of phase relative to each other. Because of the small spacing between the two plates, the electric field changes linearly from one to the other. Therefore, the electric field potential is highest at the drive plates and zero at the center between the two plates. The center, or pickup, electrode is suspended in a manner so that it moves up and down in the region between the two drive plates. The pickup electrode assumes the electric potential of the space between the two drive plates. This results in a bipolar output signal that is equal in magnitude to the input signal at the maximum deflection, and zero at the center position. The synchronous detector converts the phase and amplitude information from the sensor output into a bipolar DC output signal. The output signal is actually a reading of the pickup electrode position. In the imaging mode, this signal is used as a feedback to the piezoceramic tube for constant force contact imaging. In the indentation mode, the feedback is cut off and a voltage ramp is applied to the lower drive plate. As a result, an electrostatic force is generated between the pickup electrode and the drive plate. The force can be described as follows:

$$F = k_e V^2 \tag{1}$$

where k_e is the electrostatic force constant and V is the applied voltage. The voltage ramps are formulated to produce triangular, trapezoidal, or square force loading profiles of the sample. For experiments in air, the force is applied to the sample through a diamond tip glued to a tapped polymer holder attached to the pickup electrode by a small screw. In liquid, the tip is glued to a tungsten rod with a large aspect ratio, which in turn is attached to the polymer holder. In this configuration, the diamond tip and portion of the tungsten rod are immersed in the solution and as a result the meniscus force remains constant as the height of liquid changes because of vaporization. This force can be easily accounted for before contacting the sample. In the imaging mode the minimum contact

force applied to the sample is about 1 μN. In the indentation mode, loads up to 30 mN can be applied. A variety of indenter shapes are available, including Berkovich and cube corner indenter. Because image quality depends on the tip radius-of-curvature, the image quality using this system may not be as good as that using the conventional AFM cantilever. However, imaging with the indenter tip allows precise selection of the area or region to be indented, and postindent imaging allows verification of the location and sharpness of each indent. The sharp cube corner indenter displaces more than three times the volume of the Berkovich indenter at the same load.

The cube tip is particularly useful when attempts are to be made to fracture a particular feature. The hardness, H, is calculated on the basis of maximum force, F_{max}, divided by the projected contact area at maximum load, a, whereas the indention or reduced elastic modulus, E^*, is calculated from the contact stiffness, S, defined as the slope of the linear portion of the force/displacement curve during unloading near the maximum load ***(6,9)***. The stiffness, S, can be determined from a polynomial expression for the unloading curve that is obtained from a least-squares fit of the data between 20 and 95% of the maximum force, and then the derivative of the unloading curve evaluated at the peak force is used as the contact stiffness, S (**Note 3; ref. *22***):

$$H = F_{max}/\boldsymbol{a} \tag{2}$$

$$E^* = \sqrt{\frac{\pi}{\boldsymbol{a}}} \cdot \frac{S}{2} \tag{3}$$

These equations appear to be straightforward, but several steps need to be taken to obtain correct values. The projected contact area, $\boldsymbol{a}$, is usually expressed in terms of contact depth, h. For an ideal pyramidal geometry tip (e.g., Berkovich), the relationship is simply as follows:

$$\boldsymbol{a} = C_0 h^2 \tag{4}$$

For a real tip the relationship can be conveniently expressed as follows:

$$\boldsymbol{a} = C_0 h^2 + C_1 h + C_2 h^{1/2} + C_3 h^{1/4} + C_4 h^{1/8} + C_5 h^{1/16} \tag{5}$$

where C_0 for a Berkovich tip is 24.5, whereas for a cube corner tip it is 2.598. To determine the relationship between h and $\boldsymbol{a}$ for a specific tip, a series of indents at various contact depths are performed on fused silica specimens and the contact area, $\boldsymbol{a}$, is calculated using Eq. 5. Finally, a plot of the computed area as a function of contact depth is plotted and fitted to Eq. 5 to obtain the coefficients in this equation.

The Young's modulus of the probed specimen, E_s, can then be obtained from E^* and the known modulus of the diamond indenter, E_i, and the known or assumed values for Poisson's ratios, ν:

$$1/E^* = (1 - \nu_s^2)/E_s + (1 - \nu_i^2)/E_i \quad (6)$$

Indentations can be made at intervals of 1–2 μm using indents of submicroscopic size (approx 300–500 nm). The spacing is needed to avoid influence of one indent on the adjacent indent (*see* discussion in **ref. *23***). Using this approach indents can be made on individual structural components of the dentin ***(10,13)*** or across junctions, such as the dentin–enamel junction ***(11)***, as shown in **Fig. 6**.

3.8. AFM-Based Nanoindentation of Demineralized Dentin

There is considerable interest in measuring dentin or other calcified tissues as modified by demineralization or hypomineralization. For example, etching procedures are used widely for bonding dentin; dentin caries (tooth decay) introduces modifications of structure that have various levels of mineralization; and genetic anomalies, such as dentinogenesis imperfecta, result in dentin of reduced mineral level. In other calcified tissues, hypomineralized or hypermineralized tissue states are of great interest. A detailed discussion of the methods for study of such calcified tissue alterations are beyond the scope of this work, but several factors need to be mentioned. Balooch et al. ***(9)*** used a modified indenter (flat-ended cylinder) to evaluate the viscoelastic properties and low elastic modulus of fully demineralized dentin when hydrated (approx 0.1 GPa) and dried (2 GPa), whereas normal hydrated intertubular mineralized dentin has an indentation modulus of about 20 GPa. Enamel modulus values are less than 100 GPa, so that AFM-based indentation methods can be used for measurement of calcified tissues over a range of at least three orders of magnitude. However, the measurements of demineralized tissue or partially demineralized tissue become extremely complex. Sharp indenter tips cannot be used reliably when the substrate consists of a demineralized feltwork of collagen fibrils ***(9)***. When a portion of the sample is demineralized and an underlying area remains mineralized, it becomes uncertain whether the underlying mineralized portion of the sample affects the measurement. We recently have studied several of these complex substrates ***(12,24)***. It is unlikely that indentations of areas with indentation modulus values below 2 GPa can be made with conventional tips. However, the limit is difficult to establish and we currently rely on careful examination of the indent shape. Furthermore, calibration of the indentation equipment and determination of the indentation tip properties are

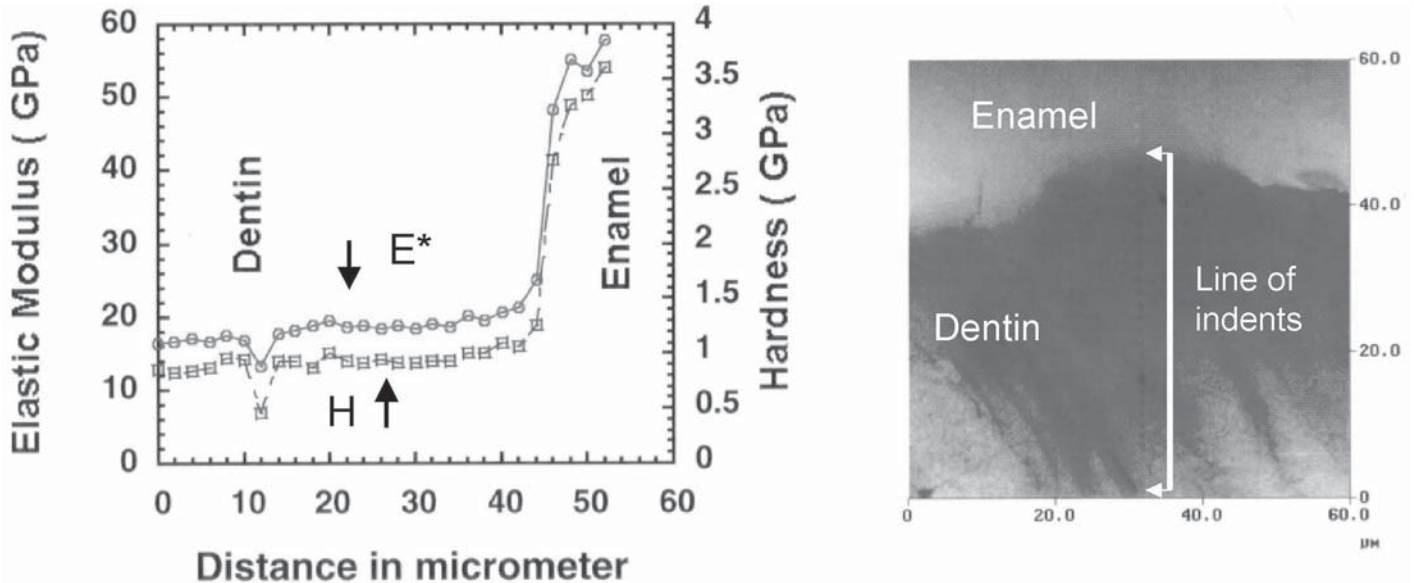

Fig. 6. Nanoindentation of enamel, dentin, and the junction between them (DEJ). The image at the right shows the line of indentations. The variations in hardness and indentation modulus as a function of position for each of the indentations are shown in the graph based on Eqs. 2 and 3.

currently carried out using quartz standards. This is an excellent procedure for mineralized tissues, but there is no adequate soft standard to insure that reliable indents can be made of the highly demineralized structures.

4. Notes

1. The cyanoacrylate viscosity is important. If the viscosity is too low, it will penetrate into the dentin and fill the tubules. This becomes evident during demineralization as the filled tubules become increasingly obvious as surrounding dentin recedes leaving them sticking up above the surface. Several cyanoacrylate gels have the desirable viscosity but were not found to be stable. Thus each product should be checked in the solution of interest. The MDS QX4 ethyl α-cyanoacrylate that we now use is too thin as dispensed and we therefore air dry a drop of the material for 2 h before bonding the polished halves of the teeth.
2. Placing fiduciary marks on the opposite side of the dentin that is to be studied can be used to facilitate identification of the same areas at each step of the demineralization experiment.
3. To obtain the real value of contact stiffness, S, we need to account for compliance (the inverse of stiffness) of the machine, C_m ***(8,10)***. The measured compliance is the sum of machine compliance C_m, and the contact compliance, C_c:

$$C_{measured} = C_m + C_c = C_m + \sqrt{\frac{\pi}{a}} / (2E^*)$$

Therefore, a linear plot of $C_{measured}$ and $1/\sqrt{a}$ for indentations made at various depths is used on a silica standard (for which C_m is well known) to determine machine compliance, which is simply the intercept of the linear plot on the compliance axis.

References

1. Marshall, G. W., Jr., Marshall, S. J., Kinney, J. H., and Balooch, M. (1997) The dentin substrate: Structure and properties related to bonding. *J. Dentistry* **25,** 441–458.
2. Marshall, G. W., Jr., Balooch, M., Tench, R. J., Kinney, J. H., and Marshall, S. J. (1993) Atomic force microscopy of acid effects on dentin. *Dental Mater.* **9,** 265–268.
3. Kinney, J. H., Balooch, M., Marshall, G. W., and Marshall, S. J. (1993) Atomic-force microscopic study of dimensional changes in human dentine during drying. *Arch. Oral Biol.* **38,** 1003–1007.
4. Kinney, J. H., Balooch, M., Haupt, D. L., Jr., Marshall, S. J., and Marshall, G. W., Jr. (1995) Mineral distribution and dimensional changes in human dentin during demineralization. *J. Dental Res.* **74,** 1179–1184.
5. Marshall, G. W., Jr., Balooch, M., Kinney, J. H., and Marshall, S. J. (1995) Atomic force microscopy of conditioning agents on dentin. *J. Biomed. Mater. Res.* **29,** 1381–1387.
6. Doerner, M. F. and Nix, W. D. (1986) A method for interpreting the data from depth-sensing indentation instruments. *J. Mater. Res.* **1,** 601–609.

7. Kinney, J. H., Balooch, M., Marshall, S. J., Marshall, G. W., Jr., and Weihs, T. P. (1996) Atomic force microscope measurements of the hardness and elasticity of peritubular and intertubular human dentin. *J. Biomech. Eng.* **118,** 133–135.
8. Kinney, J. H., Balooch, M., Marshall, S. J., Marshall, G. W., Jr., and Weihs, T. P. (1996) Hardness and Young's modulus of human peritubular and intertubular dentine. *Arch. Oral Biol.* **41,** 9–13.
9. Balooch, M., Wu-Magidi, I. C., Balazs, A., Lundkvist, A. S., Marshall, S. J., Marshall, G. W., et al. (1998) Viscoelastic properties of demineralized human dentin measured in water with atomic force microscope (AFM)-based indentation. *J. Mater. Res.* **40,** 539–544.
10. Kinney, J. H., Balooch, M., Marshall, G. W., and Marshall, S. J. (1999) A micromechanics model of the elastic properties of human dentine. *Arch. Oral Biol.* **44,** 813–822.
11. Marshall, G. W., Balooch, M., Gallagher, R. R., Gansky, S. A., and Marshall, S. J. (2001) Mechanical properties of the dentinoenamel junction. *J. Mater. Res.* **54,** 87–95.
12. Marshall, G. W., Yücel, N., Balooch, M., Kinney, J. H., Habelitz, S., and Marshall, S. J. (2001) Sodium hypochlorite alterations of dentin and dentin collagen. *Surface Sci.* **491,** 444–455.
13. Balooch, M., Demos, S. G., Kinney, J. H., Marshall, G. W., Balooch, G., and Marshall, S. J. (2001) Local mechanical and optical properties of normal and transparent root dentin. *J. Mater. Sci.*. **12,** 507–514.
14. Marshall, G. W., Jr., Wu-Magidi, I. C., Watanabe, L. G., Inai, N., Balooch, M., Kinney, J. H., and Marshall, S. J. (1998) Effect of citric acid concentration on dentin demineralization, dehydration, and rehydration: atomic force microscopy study. *J. Mater. Res.* **42,** 500–507.
15. Oliveira, S. S.A., Hilton, J. F., Marshall, S. J., and Marshall, G. W. (2002) Etching kinetics of a self-etching primer. *Biomaterials* **23,** 4105–4112.
16. Marshall, G. W., Saeki, K., Gansky, S. A., and Marshall, S. J. (1999) AFM study of citric acid-ferric chloride etching characteristics of dentin. *Am. J. Dentistry.* **12,** 271–276.
17. Saeki, K., Marshall, S. J., Gansky, S. A., and Marshall, G. W. (2001) Etching characteristics of dentin: effect of ferric chloride in citric acid. *J. Oral Rehabil.* **28,** 301–308.
18. Nakabayashi, N. and Pashley, D. H. (1998) *Hybridization of Dental Hard Tissues*, Quintessence Publishing Co., Ltd., Tokyo. p. 18.
19. White, J. M., Goodis, H. E., Marshall, S. J., and Marshall, G. W. (1994) Sterilization of teeth by gamma radiation. *J. Dental Res.* **73,** 1560–1567.
20. Marshall, G. W., Jr., Chang, Y. J., Saeki, K., Gansky, S. A., and Marshall, S. J. (2000) Citric acid etching of cervical sclerotic dentin lesions: An AFM study. *J. Mater. Res.* **49,** 338–344.
21. Marshall, G. W., Chang, Y. J., Gansky, S. A., and Marshall, S. J. (2001) Demineralization of caries-affected transparent dentin by citric acid: An atomic force microscopy study. *Dental Mater.* **17,** 45–52.

22. Oliver, W. C. and Pharr, G. M. (1992) An improved technique for determining hardness and elastic modulus using load and displacement sensing indentation experiments. *J. Mater. Res.* **7,**1564–1583.
23. Habelitz, S., Marshall, S. J., Marshall, G. W., Jr., and Balooch, M. (2001) The functional width of the dentino-enamel junction determined by AFM- Based nanoscratching. *J. Struct. Biol.* **135,** 294–301.
24. Marshall, G. W., Habelitz, S., Gallagher, R., Balooch, M., Balooch, G., and Marshall, S. J. (2001) Nanomechanical properties of hydrated carious human dentin. *J. Dent. Res.* **80,** 1768–1771.

12

Applying Atomic Force Microscopy to Studies in Cardiac Physiology

Jason J. Davis, Trevor Powell, and H. Allen O. Hill

1. Introduction

At the present time there exists a great deal of interest in the application of scanning probe microscopy methods to the imaging of cellular systems ***(1,2)***. It would now not be an exaggeration to state that atomic force microscopy (AFM), in particular, represents perhaps the most powerful means of structural/functional analysis at the level of a single live cell. In recent years this technology has been applied, amongst many other systems, to studies of bacterial flagella ***(3)***, erythrocytes ***(4)***, human platelets ***(5)***, endothelial cells ***(6)***, skin fibroblasts ***(7)***, plant cuticles ***(8)***, and cardiac myocytes ***(9)***. In resolution terms, perhaps the most impressive work is that of Engel et al. ***(10)***. Although not on whole cells (thereby greatly simplifying the experiment), molecular-level images of isolated cellular gap junctions, which play an important role in intracellular communication and signal transduction, have been obtained. More recently, experimental protocols have advanced to the point where it is possible to monitor, simultaneously, both cellular topography and ion channel flux ***(11)***. The ability to characterize functionally active cellular systems at a nanometre resolution under controlled fluid conditions has also been used in the monitoring of time-dependent cellular change ***(12,13)***.

Importantly, it is now generally accepted that, under appropriate imaging conditions, nanometre-resolved AFM experiments can be conducted with negligible levels of cellular damage ***(14)*** or, indeed, impaired cell physiological function ***(15)***. Despite this, however, under normal operational forces, one generally resolves submembrane structure rather than the structure of the membrane itself though the tip is only in direct contact with the latter. The plasma membrane offers little resistance to the loading force exerted by the scanning tip and is accordingly deformed as the tip traces out underlying internal struc-

From: *Methods in Molecular Biology, vol. 242: Atomic Force Microscopy: Biomedical Methods and Applications*
Edited by: P. C. Braga and D. Ricci © Humana Press Inc., Totowa, NJ

ture. Although this surface indentation has hindered high-resolution imaging of the extracellular surface, it can be used in the spatial characterization of internal cellular components. In summary, scanning probe methods, especially when combined with optical systems (confocal, total internal reflection, epifluorescence) provide a very powerful means of resolving the three-dimensional structure and dynamics of cellular systems under ambient and near-physiological conditions.

1.1. Cell Immobilization/Pretreatment

For any biological structure to be imaged satisfactorily by scanning probe methods, it must be immobile on an underlying substrate surface, under the typical lateral forces imparted by the scanning probe, at least for the duration of the scan. A range of methods has been developed for cellular immobilization. Most simply, the cells are dried down onto, or grown on, a suitable flat substrate surface; commonly mica (an aluminosilicate) or glass microscope slides. Nonspecific or electrostatic coatings, such as laminin or poly-L-lysine, are commonly applied to the bare surface to enhance the immobilization stability ***(16,17)***. Perhaps most simply, cells can be grown directly onto a substrate surface; these typically adhere robustly, although their structures are commonly perturbed (they may appear, for example, to be somewhat "spread" on the surface—a common observation with strong cell–substrate adhesion). Cells have also been entrapped in flexible, porous media ***(18,19)*** or imaged while embedded in a resin ***(20)***. It can be useful to adjust cellular mechanical properties (particularly in terms of membrane flexibility) by fixation (such as with glutaraldehyde). Such cell pretreatment generally enhances image resolution of the cytoskeleton. Related to this, the advantages associated with lowering imaging temperature, in terms of improved cellular robustness, have been noted ***(21)***.

1.2. Basic AFM Requirements

The substrate should have a surface roughness well below the vertical dimensions of the cell (and typically to be flat on a nanometre scale). In both contact and tapping force imaging it is commonly useful, if not critical, to quantify the forces imparted by the scanning tip (usually for the purposes of minimizing structural deformation of the sample). This is achieved, once the spring constant is determined (or estimated), through the generation of force–distance or amplitude–distance curves. The process of acquiring force–distance data over a cell surface can indeed be used to map cell mechanical properties with high spatial resolution ***(22,23)***. Note also that, under solution, it can be instructive to consider the effects of pH and ionic strength in minimizing electrostatic contributions to imaging force. Tip-sample adhesion forces are also highly dependent on the chemistry at the probe surface (be this silicon, silicon

nitride, or gold) and tip cleaning in oxidizing acids, or oxygen plasmas can be an effective way of attaining a reproducible behavior.

1.3. Cardiac Myocytes

The human heart is shaped like a blunt cone and is the size of a clenched fist, being some 12 cm long and 9 cm wide on average and weighs between 250 to 390 g in an adult male and about 200 to 250 g in a female. The mammalian heart is a hollow organ, containing four chambers, with a wall of muscle (or septum) dividing the organ vertically into a right and left heart. At the top of each half is an atrium (porch or antichamber) whereas below on each side is a ventricle (little belly). Within the walls of the heart are cells that both conduct electrical impulses and contract intermittently to raise blood pressure in the atria and ventricles. Particularly within the ventricular walls, these myocytes are arranged in bands as either spirals (like a turban) or in horizontal layers. The overall geometry of this contractile machinery subserves the function of impelling the blood from the left ventricle, or squeezing it out of the right half of the heart, into either the systemic or pulmonary circulations. The left ventricular wall is made up primarily of powerful circular musculature, sandwiched between layers of spiral muscles running from base to apex. The right ventricular wall consists almost exclusively of spiral muscles. This intricate myocardial anatomy, coupled with the distinct morphology and function of specialized component cells, often presents acute problems in the interpretation of experimental data obtained from the whole organ. Over the last 25 yr, individual myocytes isolated from the adult heart have become an important model system for a vast range of investigations concerning cardiac function in both the normal and diseased states. We shall demonstrate here that these myocytes are proving very useful in structure–function studies at resolutions obtainable with AFM.

2. Materials

1. High-purity buffer reagents; *N*-hydroxyethylpiperazine-*N*'-2-ethanesulfonate (HEPES), Dulbecco's minimal essential medium (DMEM).
2. Phosphate-buffered saline (PBS); (Sigma-Aldrich, cat. no P 0261).
3. High-purity water; 18.2 MΩ cm (Elga, UK).
4. 0.2 μm Syringe filters (Sterelin, UK).
5. Cleavable mica substrate (Agar Scientific, UK).
6. Glass microscope slides (Agar Scientific, UK).
7. Optical microscope (preferably of the Inverted configuration, with 60 to 100× objectives).
8. Scanning probe microscope capable of ambient and fluid contact and noncontact imaging.
9. Etched silicon and silicon nitride probes of appropriate spring constant and resonance frequency.

10. Perfusion apparatus; standard system for retrograde coronary perfusion (*see* **ref. *24*** for details).
11. DMEM solution (Life Technologies, UK).
12. Serum substitute; Ultroser G (Life Technologies, UK, cat. no. 81-003).
13. Collagenase; Worthington Type CLS I (Lorne Laboratories, UK).
14. Glutaraldehyde (Sigma-Aldrich).
15. 10-mL Sterile tubes (Sigma-Aldrich, cat. no. C-3084).

Centrifuge Note: with heart cells, small benchtop centrifuges are not to be recommended because their rapid acceleration can damage myocytes. Much better are the larger free-standing cooled types, such as the Mistral 4L.

3. Methods

The methods described below outline the process of (1) cell preparation, isolation, and electron microscopy characterization and (2) scanning force characterization.

3.1. Cell Preparation and Electron Microscopy Characterization

The detailed tissue dissociation protocols for the adult heart ***(24)*** will provide isolated myocytes suspended in Dulbecco's modified Eagle's medium supplemented with pyruvate and 10 m*M* HEPES to which has been added 2% (v/v) serum substitute. It is convenient to store cells at room temperature in sterile 10-mL tubes from Sigma-Aldrich. As long as standard precautions have been taken during isolation, these myocytes can be used for up to 24 h without any antibiotics. When incubation at 37°C is used (100% O_2 with HEPES media or 95 % O_2/5% CO_2 v/v if bicarbonate buffered only) then antibiotics must be added. Myocytes can be plated directly on to cover slips. Alternatively, cells can be fixed by first resuspending in Krebs' buffer (NaCl, 134.1; KCl, 5.4; $NaH_2PO_4.2H_2O$, 0.3; $MgCl_2$, 1; Na acetate.$3H_2O$, 5; Na pyruvate, 5; glucose, 11.1; HEPES, 5; all m*M*, pH adjusted to 7.4 with NaOH) and then adding 1 volume of myocytes to 2.5 % v/v glutaraldehyde in 1/3 Krebs' buffer. Though fixation is rapid, the cells are typically left for at least 30 min, then resuspended in phosphate-buffered saline and stored at 4°C. This fixative procedure has been designed to reduce the osmotic strength of the fixation solution and thereby reduce cell shrinkage.

High yields of ventricular myocytes from adult mammalian hearts are obtainable using retrograde (Langendorff) coronary perfusion of the whole organ, with fluids low in calcium, containing collagenase and protease. Details of the procedures have been presented elsewhere (*see*, for example, **ref. *24***; *see* **Note 1**). Examination of suspensions of isolated myocytes by bright-field light microscopy showed two distinct cell types; a dominant rod-shaped form together with a population of rounded cells (**Fig. 1**). It is clear from a number

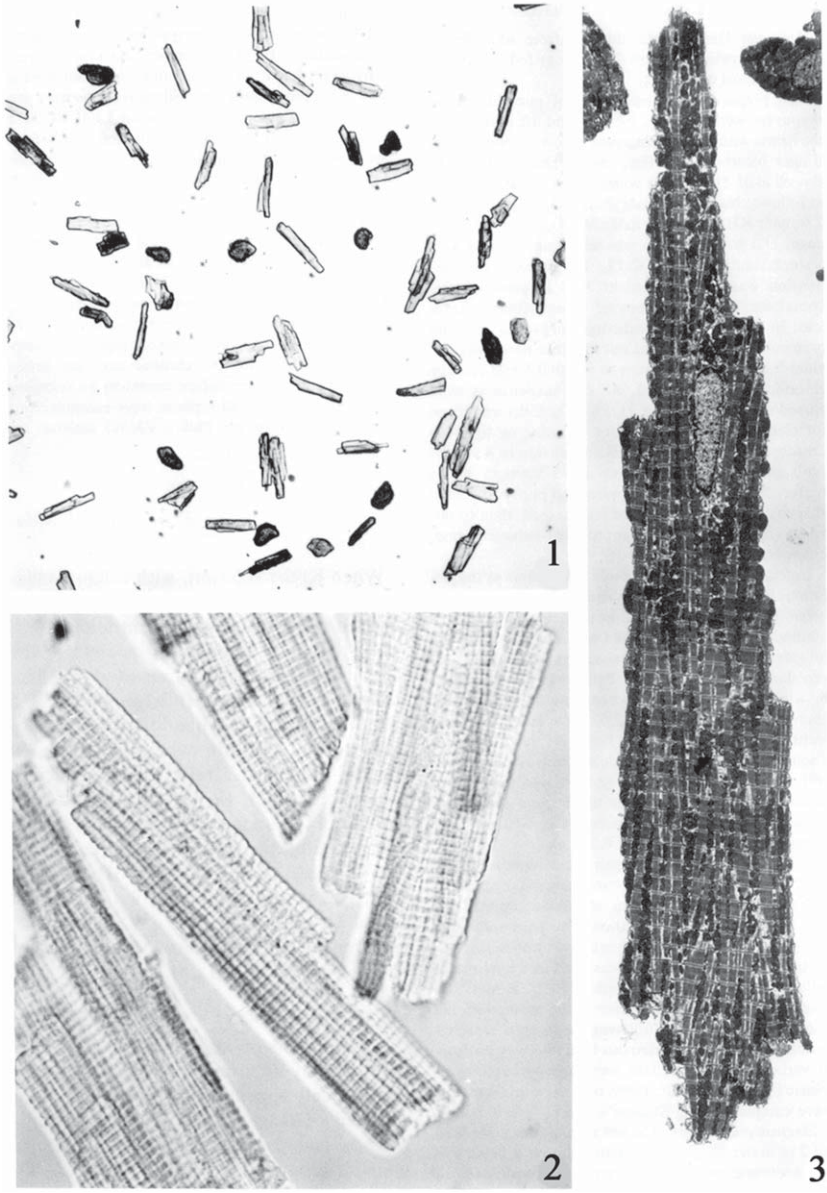

Fig. 1. **(1)** Bright-field survey view of a preparation of isolated ventricular myocytes. Damaged cells appear dark and round and are easily distinguished from the intact rod-shaped cells. (magnification ×100). **(2)** Light microscope view at higher magnification (×800) showing the structural details of rod-shaped cells. **(3)** Electron micrograph of a longitudinal thin-section through an isolated rod-shaped myocyte. Characteristic banded-structure myofilament bundles alternate between rows of mitochondria. In this example, there are 64 sarcomeres along the length of the cell. (magnification ×1500). From **ref. *25***, with permission from Elsevier.

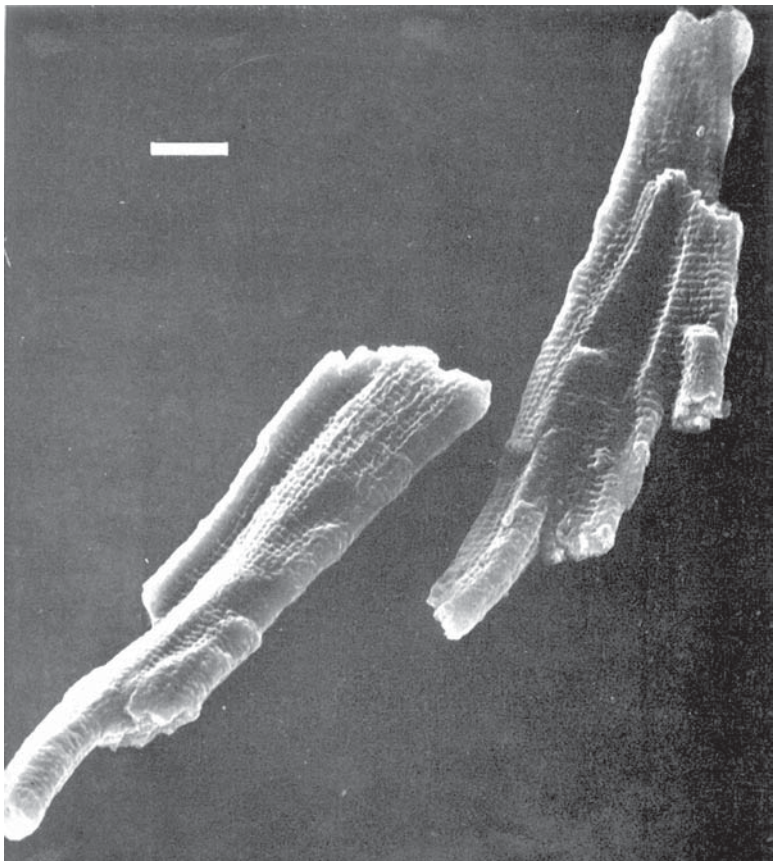

Fig. 2. The typical transverse ridges and longitudinal grooves of heart muscle cells, obtained with scanning electron microscopy. Scale bar, 10 μm (magnification ×1158). From **ref. *26***, with permission from Elsevier.

of tests (dye exclusion, morphology from low-power light microscopy and electron microscopy) that the rounded cells are myocytes damaged by the dissociation protocols. Standard purification procedures can reduce the round cell population to <10 % of the total. Of major interest are the rod-shaped cells, which display many of the gross morphological characteristics expected from studies of whole cardiac tissue. Isolated myocytes are more rectangular than cylindrical with irregular profiles, and also large, being some 80–180 μm long, 8–20 μm wide, and 8–16 μm thick. This wide range of sizes reflects the complex ventricular ultrastructure, which is illustrated more clearly by scanning electron microscopy, where individual cells are seen to be most irregular in shape (**Fig. 2**) with longitudinal grooves. On occasion, very flat cells are also

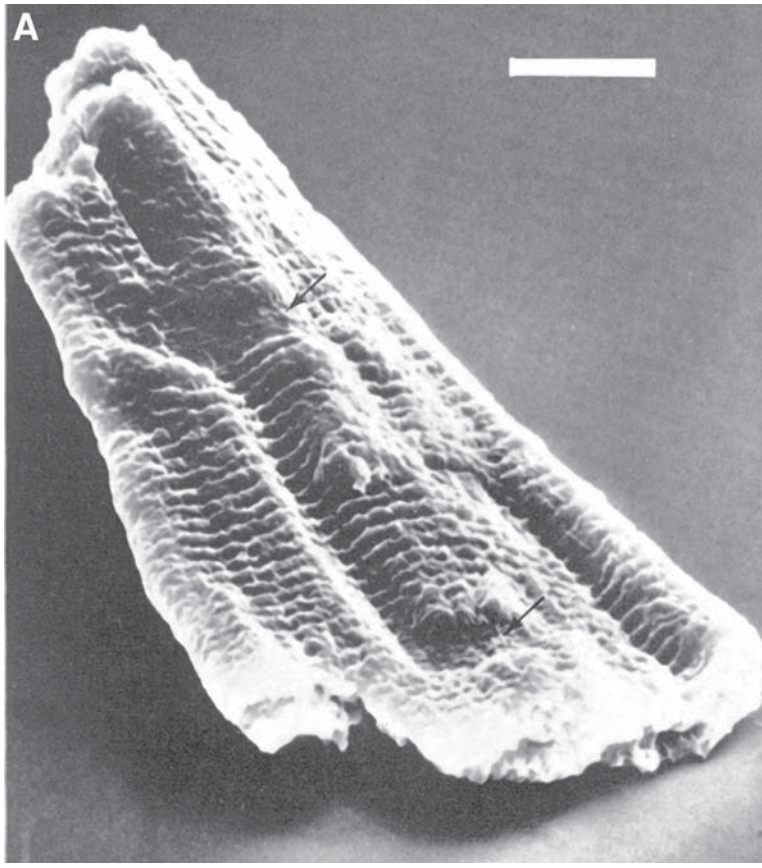

Fig. 3. **(A)** Scanning electron micrograph of cell having flatter profile than those shown in **Fig. 2**. Scale bar, 10 μm (magnification ×1158). From **ref. *26***, with permission from Elsevier.

observed (**Fig. 3A**). If it were possible to fit the cells back together again, then it becomes clear how the spiraling and horizontal bands of whole muscle (see above) arise from the complex interdigitation of myocytes with grossly varying shapes. Also apparent in **Fig. 2** are the regular transverse ridges on the surface of each cell. These reflect the action of the underlying contractile proteins, which run longitudinally within each myocyte and partially overlap, giving rise to the striated appearance of cardiac muscle, when longitudinal sections are viewed with the electron microscope (**Fig. 1**, Plate 3). As will be seen below, these general morphological features of cardiac ventricular myocytes are apparent at magnifications comfortably achievable by AFM.

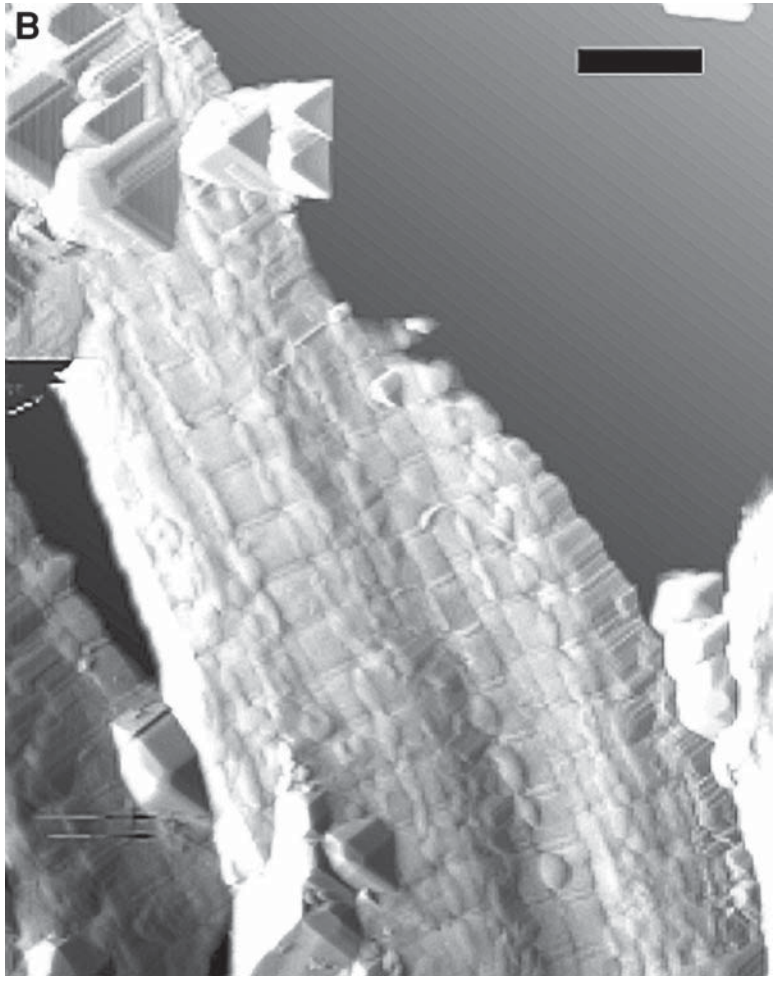

Fig. 3. **(B)** Large-scale deflection AFM micrograph of a single isolated cardiac myocyte immobilized on mica substrate. Note the intercalated disc region evident on the right-hand-side of the cell. Scale bar, 5 μm. From **ref. *9***, with permission from Elsevier.

The scalloped appearance of the surface membrane is seen in more detail in **Fig. 4A**. Evident at these levels of magnification are the regular apertures in the surface sarcolemma, the mouths of tubules dipping transversely into the cell. These T-tubules conduct the wave of electrical depolarization traveling across the myocyte surface down into the cell, so that contraction is triggered synchronously throughout the cell interior during each heartbeat. These scan-

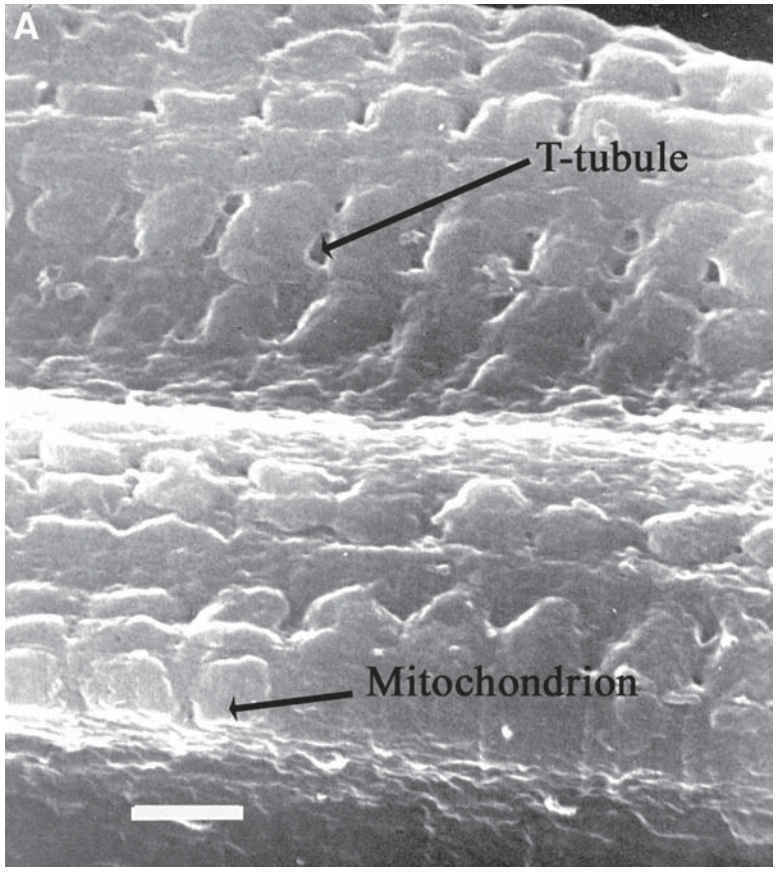

Fig. 4. **(A)** Scanning micrograph showing array of T-tubule openings, which have both ovoid and circular cross-sectional geometry. Scale bar, 2 μm (magnification ×8000). From **ref. *26***, with permission from Elsevier.

ning electron micrographs, taken on air-dried specimens of fixed myocytes, are directly relevant to observations made by AFM (see paragraphs following and **Note 2**).

Under these conditions, the surface membrane is forced down on the underlying structures, and in **Fig. 4A** there are seen rectangular "packets" at the periphery of the cell, lying along what appears to be a cylindrical structure within the cell. These packets are mitochondria, the oxidative motors in the heart, providing the aerobic production of ATP for the contractile proteins, which is essential for a normal mechanical output from each ventricle in the whole organ. It follows that if scanning force microscopy is applied to

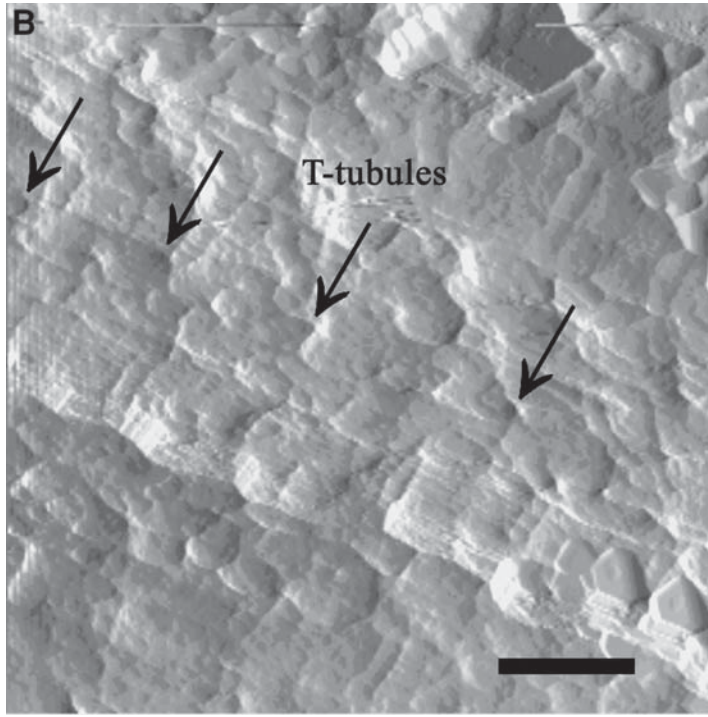

Fig. 4. **(B)** Deflection AFM micrograph of a myocyte surface in which T-tubule openings are indicated by arrows. Compressed between the contractile machinery are mitochondria. Scale bar, 2 μm. From **ref. *9***, with permission from Elsevier.

myocytes prepared using the same protocols, similar subsurface structures should be apparent (*see* **Note 3**).

Figure 5 demonstrates that all the normal features of sarcolemmal structure, including the glycocalyx, are preserved in these isolated cells. The structure of intracellular membranes and organelles also shows excellent preservation, indistinguishable from that reported in cells of the intact heart. A network of tubules in the M region, the M rete (MR), is connected by longitudinal elements (L) to a z tubule (ZT_L) seen here in longitudinal section. Examples of transversely sectioned z tubules, seen elsewhere, are indicated by ZT_T. Junctional sarcoplasmic reticulum (JSR) is continuous with the free SR (arrow) and consists of flattened cisternae closely apposed to the sarcolemma. Peripheral junctional SR (JSR_p) occurs in association with the surface sarcolemma, and interior junctional SR (JSR_I) occurs against transverse-tubule membrane. The latter may take the form of dyads (D), which consist of a transverse tubule plus one JSR cisterna, or triads (T), which consist of a transverse tubule sandwiched

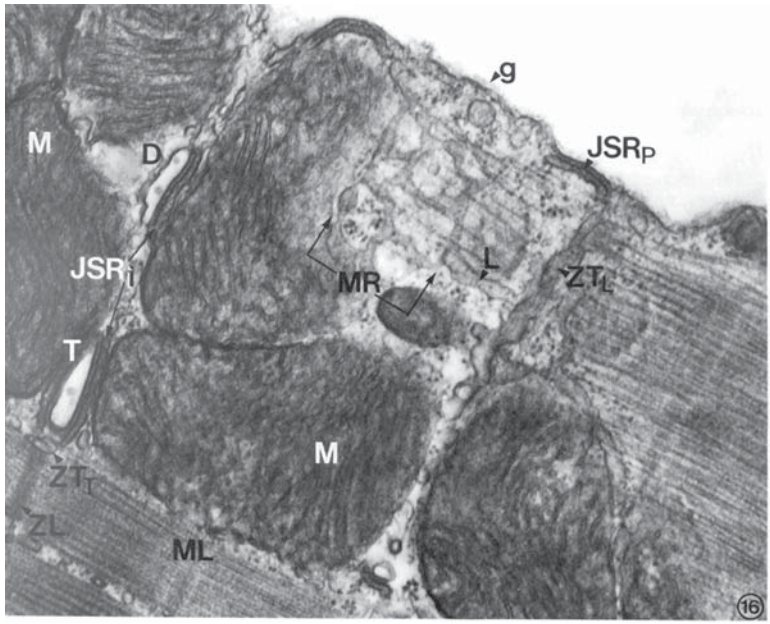

Fig. 5. Electron micrograph detailing the structural complexity of the interior of mammalian ventricular heart cells. See text for further description and abbreviations. (magnification ×50 000). D, dyad; M, mitochondria; JSR, junctional sarcoplasmic reticulum; JSR_p, peripheral JSR; L, longitudinal elements; ZT_T, transversely sectioned Z tubules; ZL, Z line; ZT_L, longitudinally sectioned Z tubule; ML, M line; g, glycalyx. From **ref. *26***, with permission from Elsevier.

between two JSR cisternae. The JSR lumen is characteristically bisected by an electron-dense line, and regularly spaced electron-dense feet project from the membrane facing the sarcolemma. Mitochondria (M) show well-preserved membranes and cristae.

Finally, if the plasma membrane is freeze-fractured, intramembrane particles can be observed (**Fig. 6**) reflecting aggregations of membrane proteins involved in cellular function; the density of these particles in isolated myocytes is very similar to that observed in whole hearts (**Fig. 7**). Note that the scale bar for these measurements (100 nm) is approaching the range more usually associated with scanning force microscopy. Clearly, freeze-fractured membranes would make most interesting specimens for AFM imaging. From the evidence presented here, and from many other studies, of those myocytes surviving the dissociation procedures, the structure of intracellular membranes and organelles shows excellent preservation, indistinguishable from that reported in cells of the intact heart.

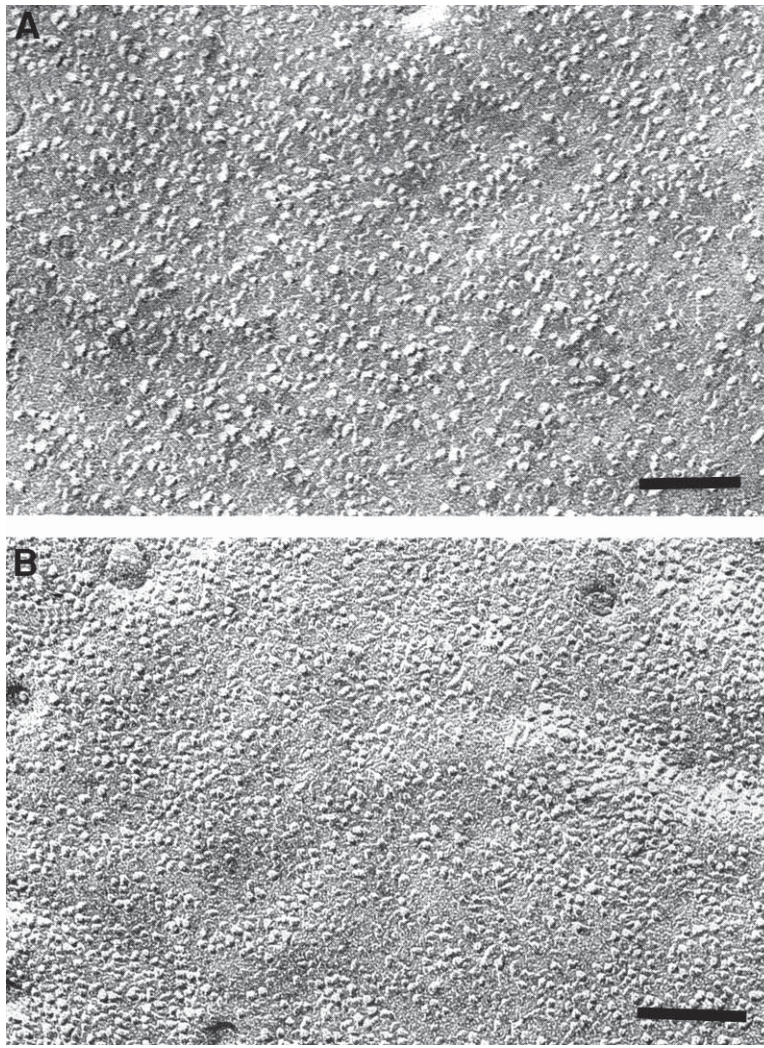

Fig. 6. **(A)** P-face view of isolated myocyte sarcolemma. **(B)** P-face view of myocyte sarcolemma from intact left-ventricular myocardium. Scale bars 0.1 µm. Taken From **ref. *27***, with permission from Elsevier.

3.2. AFM (see Notes 4–6)

Aliquots of myocytes (approx 100 µL of cell suspension) were added to a freshly cleaved mica (Agar Scientific, Cambridge, UK) surface. The sample was then gently blown dry with high purity argon or allowed to dry overnight

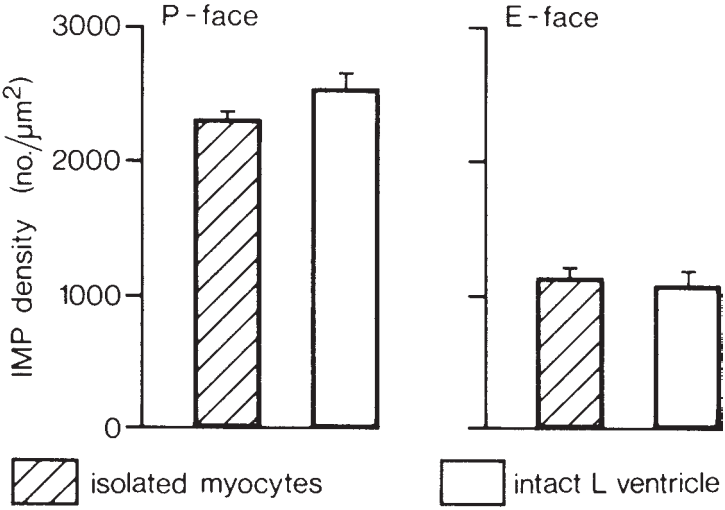

Fig. 7. Numerical density of membrane particles (expressed as numbers per square micrometer) for isolated myocytes and intact myocardium. From **ref. *27***, with permission from Elsevier.

at 5°C. Experiments were performed with a Digital Instruments MultiMode microscope in conjunction with a Nanoscope IIIa control system. A "J" scanner (with a lateral range of approximately 125 μm) was used. Etched silicon probes, attached to triangular cantilevers 100–200 μm in length, were used (Digital Instruments, UK Ltd, model TESP) operated at resonances in the 300–400 KHz range (nominal force constant 20–100 N/m). Drive amplitude was adjusted so as to give the sharpest resolution at the minimum amplitude (typically 1–2 V rms). Integral and proportional gains were balanced so as to allow simultaneous acquisition of sharp, noise-free, height and amplitude data sets. With the aid of a ×30 magnification eyepiece, the scanning cantilever was positioned directly above a surface-immobilized cell (*see* **Note 4**). Because the vertical dimensions of the cells exceed the full vertical range of the scanner (ca. 4 μm), scanning laterally into a cell commonly led to destruction of the probe. Vibrational/acoustic shielding was achieved by mounting the microscope in a PicoIsolation chamber (Molecular Imaging Co) during scanning. Height, amplitude and phase data were simultaneously collected, the latter with a Digital Instruments Phase Extender Module. Data sets were subject to a first order flattening and low band pass filtering only when stated. Thermal noise levels were estimated to be approx 0.4 Å.

As shown in **Fig. 3**, whole-cell images obtained by AFM methods compare very favorably with scanning electron micrographs. Even at this relatively low

magnification, both the cellular cross-striations and the step-like morphology of the intercalated disc regions are clearly evident. Fine details of the subsurface structure were, in general, more easily observed in deflection mode than height mode, though imaging was somewhat sensitive to the scanning set point and drive amplitude (equivalent to energy dissipation by the probe rather than the imaging force directly; *see* **Note 5**). Scanning at high amplitude produced no noticeable structural damage (though increased deformation of the plasma membrane is likely as the drive amplitude is increased), that is, when the same area was subsequently reimaged at lower drive no significant image deterioration was observed. The fact that cell dimensions exceeded the full vertical range of the scanners prevented a quantification of the effect of increased dissipation on cell height though changes in surface roughness were minimal across the range of values used. At increased magnification, the general morphology of working ventricular myocytes can be seen in more detail (**Fig. 8**). This AFM image strikingly reveals all the major characteristics of cellular morphology that have been discussed previously in reference to electron microscopy (*see* **Note 6**). The parallel arrays of longitudinal contractile machinery, separated by embedded organelles and transversed by regular tubular structures to demarcate sarcomeres, all reflect the integrated structure to be expected of this syncytial tissue.

The scalloped nature of the external sarcolemma, with the grooved surface structure reflecting the underlying contractile apparatus alternating between rows of mitochondria, is shown in **Fig. 4B**, which is presented with a corresponding scanning electron micrograph to emphasize the remarkable similarity in the two images. Z grooves, which run at right angles to the long axis of the myofilaments, mark the sarcomeres from one Z line to the next and can be quite deep and narrow, especially in contracted tissue. It is clear that there is a consistent relationship between these grooves and the Z lines, suggesting strongly that the Z line material must be attached firmly to the interior face of the plasmalemma. Using such images, resting sarcomere length is measured as 1.6–2 μm and T-tubules of diameter 200–260 nm are present in rows at approximately every 1.8–1.9 μm. The measured lateral spacing between T-tubule openings (**Fig. 4B**) is 2–2.3 μm. These dimensions are comparable to those reported for fixed ventricular cells.

4. Notes

1. It is clear that to exploit the many advantages that AFM imaging has to offer for the study of heart cells, the obvious prerequisite is a preparation of stable, isolated myocytes. Though more than 30 yr have elapsed since dissociation techniques were first reported, this initial step remains one of the most difficult. Much has been written about isolation protocols (*see* references in ***24***) and here we can

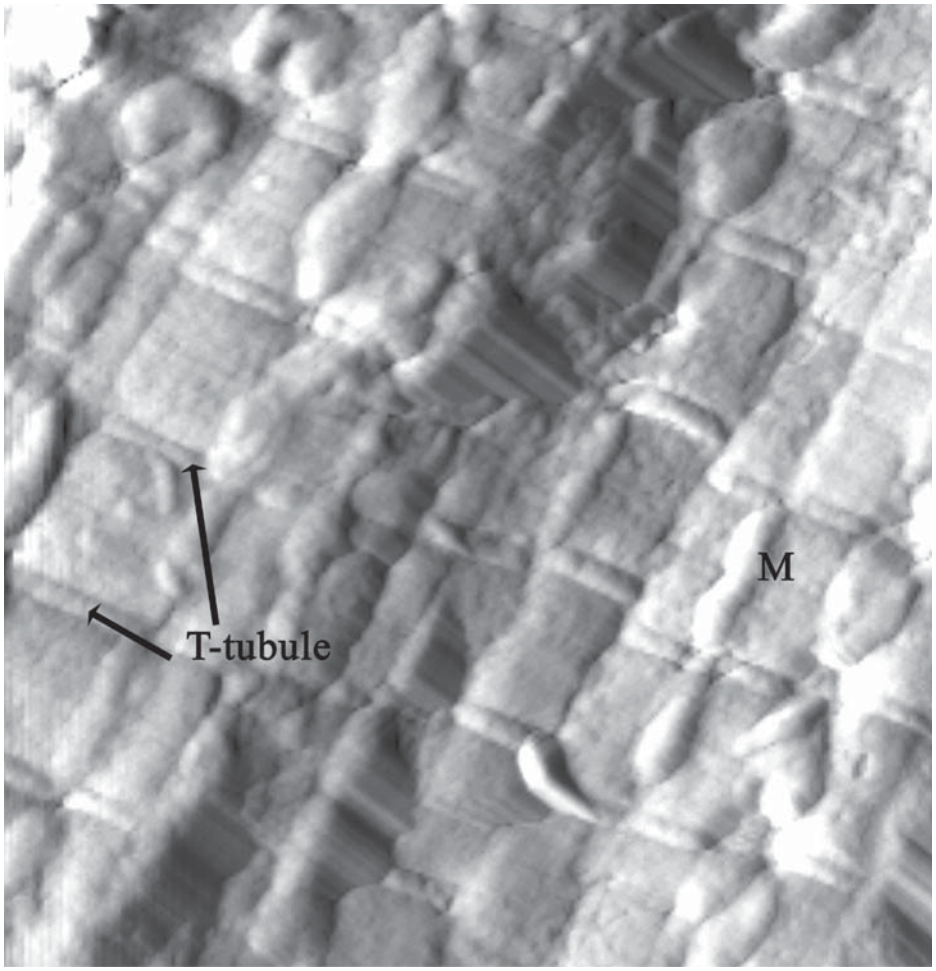

Fig. 8. High-resolution deflection AFM micrograph of a myocyte cell surface. Longitudinal columns of underlying contractile proteins, separated by valleys having regular transverse grooves. The globular features evident (M and elsewhere) are subsurface mitochondria. Also evident are the invaginations of the surface membrane by transverse tubules. Scale bar, 2 μm. From **ref. *9***, with permission from Elsevier.

give only a few of the main stumbling blocks that might prevent successful dissociation of heart tissue. The first very important procedure is retrograde coronary perfusion of the whole heart. A simple alternative would be to chop the organ and incubate the tissue chunks in the appropriate solutions, but this produces very low yields of poor quality myocytes. Cardiac tissue is predominantly aerobic, so any delay in excising and mounting the organ for in vitro perfusion can cause

irreversible damage to the constituent cells. Experience has shown that the highest-quality reagents should be used in the perfusion fluids (but not generally of spectroscopic grade) made up with high quality distilled water. Ideally, the whole dissociation protocol should be conducted in a sterile environment and the cells stored under tissue culture conditions, but as long as standard levels of cleanliness are observed, this should not be a limiting condition. Like most physiological investigations, living tissue is very susceptible to minor changes in buffer quality; therefore, new reagents should be screened before routine use. We, for example, purchase enzymes and serum albumin in bulk to minimize any major variations in myocyte quality.

2. The cells of choice should be immobilized on a flat, stable, and (ideally) optically transparent substrate surface. This may require pretreatment of cell and/or substrate surface.
3. The scanning force microscope is set up with a low spring, sharp lever and allowed to stabilize. High-powered inverted optics are used to locate the cells and carefully position the scanning probe above the one of choice. This is of particular importance with very large cells, such as cardiac myocytes, as they are typically about 8 μm thick. Tapping Probes, in particular, are expensive and easily damaged during alignment or if scanning is initiated when the tip lies to the side of a cell.
4. Surface-dried isolated myocytes are easily visible in the bright field. The cells become opaque and considerably more difficult to see in bright field on immersion in fluid. Higher optical magnification (>500×) under such conditions is of considerable benefit.
5. It is important that the cells be mechanically stable under the lateral forces imparted by the scanning probe. The worst-case scenario is when the cell is dragged across the supporting surface as scanning starts. Several imaging modes should, ideally, be available, for example, contact, noncontact, "tapping," magnetic AC ("MAC"). Each has its advantaged and disadvantages and selection should be based on maximizing resolution at minimal cellular perturbation. Occasionally, and especially in fluid, imaging will suddenly deteriorate as matter adsorbs to the scanning tip. Though commonly terminal (in terms of the tips usefulness), it may be possible to clean the probe using oxygen plasma.
6. Although surprisingly underused by physiologists and cell biologists, it is clear that AFM imaging techniques can be adapted for a large variety of cellular studies and, in terms of three-dimensional topographic resolution, compete well with classic scanning electron microscopy. By integrating AFM technology with commercially available (or adaptable) optical microscopes (such as the Nikon TE2000 inverted) one can generate a powerful imaging and characterization system. Such multiport systems can incorporate, rather straightforwardly, epi-fluorescence and confocal microscopy (with electronic motorized transfer between the two) and do not require complex set-up and alignment procedures. By integrating characterization systems in this way, it should be possible to address important questions of structure–function relationships in living cellular systems or preparations.

Acknowledgments

The authors thank The Royal Society (JJD), Abbott Diagnostics, and the EPSRC (HAOH). JJD also acknowledges The Queen's College, Oxford for an Extraordinary Junior Research Fellowship. TP is supported by the British Heart Foundation.

References

1. Kasas, S., Gotzos, V., and Celio, M. R. (1993) Observation of living cells using the atomic force microscope. *Biophys. J.* **64,** 539–544.
2. Lehenkari, P. P., Charras, G. T., Nykanen, A., and Horton, M. A. (2000) Adapting atomic force microscopy for cell biology. *Ultramicroscopy* **82,** 289–195.
3. Gunning, P. A., Kirby, A. R., Parker, M. L., Gunning, A. P., and Morris, V. J. (1996) Comparative imaging of *Pseudomonas putida* bacterial biofilms by scanning electron microscopy and both dc contact and ac non-contact atomic force microscopy. *J. Appl. Bacteriol.* **81,** 276–282.
4. Zhang, P., Bai, C., Huang, Y., Zhao, H., Fang, Y., Wang, N., and Li, Q (1995) Atomic force microscopy study of fine structures of the entire surface of red blood cells. *Scanning Microscopy* **9,** 981–988.
5. Siedlecki, C. A. and Marchant, R. E. (1998) Atomic force microscopy for characterization of the biomaterial interface. *Biomaterials* **19,** 441–454.
6. Barbee, K. A. (1995) Changes in surface topography in endothelial cells imaged by atomic force microscopy. *Biochem. Cell. Biol.* **73,** 501–505.
7. Braet, F., Seynaeve, C., de Zanger, R., and Wisse, E. (1998) Imaging surface and submembraneous structures with the atomic force microscopy: A study on living cancer cells, fibroblasts and macrophages. *J. Microscopy* **190,** 328–338.
8. Canet, D., Rohr, R., Chamel, A., and Guillian, F. (1996) Atomic force microscopy study of isolated ivy leaf cuticles observed directly and after embedding in Epon. *New Phytol.* **134,** 571–577.
9. Davis, J. J., Hill, H. A. O., and Powell, T. (2001) High resolution scanning force microscopy of cardiac myocytes. *Cell Biol. Int.* **25,** 1271–1277.
10. Hand, G. M., Muller, D. J., Nicholson, B. J., Engel, A., and Sosinsky, G. E. (2002) Isolation and characterization of gap junctions from tissue culture cells. *J. Mol. Biol.* **315,** 587–600.
11. Schar-Zammaretti, P., Ziegler, U., Forster, I., Groscurth, P., and Spichiger-Keller, U. E. (2002) Potassium-selective atomic force microscopy on ion-releasing substrates and living cells. *Anal. Chem* **74,** 4269–4274.
12. Braunstein, D. and Spudich, A. (1994) Structure and activation dynamics of RBL-2H3 cells observed with scanning force microscopy. *Biophys. J.* **66,** 1717–1725.
13. Schoenberger, C. A. and Hoh, J. H., (1994) Slow cellular dynamics in MDCK and R5 cells monitored by time-lapse atomic force microscopy. *Biophys. J.* **67,** 929–936.
14. Schauss, S. S. and Henderson, E. R. (1997) Cell viability and probe-cell membrane interactions of XR1 glial cells imaged by atomic force microscopy. *Biophys. J.* **73,** 1205–1214.

15. Haydon, P. G., Lartius, R., Parpura, V., and Marchese-Ragona, S. P. (1996) Membrane deformation of living glial cells using atomic force microscopy. *J. Microscopy* **182,** 114–120.
16. Klebe, R. J., Bentley, K. L., and Schoen, R. C. (1981) Adhesive substrates for fibronectin. *J. Cell. Physiol.* **109,** 481–488.
17. Butt, H. J., Wolff, E. K., Gould, S. A. C., Northern, B. D., Peterson, C. M., and Hansma, P. K. (1990) Imaging cells with the atomic force microscope. *J. Struct. Biol.* **105,** 54–61.
18. Kasas, S. and Ikai, A. (1996) A method for anchoring round shaped cells for atomic force microscope imaging. *Biophys. J.* **68,** 1678–1680.
19. Gab, M. and Ikai, A. (1996) Method for immobilizing microbial cells on gel surface for dynamic AFM studies. *Biophys. J.* **69,** 2226–2233.
20. Yamashina, S. and Shigeno, M. (1995) Application of atomic force microscopy to ultrastructural and histochemical studies of fixed and embedded cells. *J. Electron Microsc.* **44,** 462–466.
21. Zhang, Y., Sheng, S. J., and Shao, Z. (1996) Imaging biological structures with the cryo atomic force microscope. *Biophys. J.* **71,** 2168–2176.
22. Hoh, J. H. and Schonenberger, C. A. (1994) Surface morphology and mechanical properties of MDCK monolayers by atomic force microscopy. *J. Cell. Sci.* **107,** 1105–1114.
23. Domke, J., Parak, W. J., George, M., Gaub, H. E., and Radmacher, M. (1999) Mapping the mechanical pulse of single cardiomyocytes with the atomic force microscope. *Eur. Biophys. J. Biophys Lett.* **28,** 179–186.
24. Powell, T., Noma, A., and Severs, N.J. (1998) Isolation and culture of adult cardiac myocytes, in *Cell Biology: A Laboratory Handbook*, 2nd ed, vol. 1 (Celis, J. E., ed). Academic Press, San Diego, CA, 1pp. 25–132:
25. Severs, N. J., Slade, A. M., Powell, T., Twist, V. W., and Warren, R. L. (1982) Correlation of ultrastructure and function in calcium-tolerant myocytes isolated from the adult rat heart. *J. Ultrastruct. Res.* **81,** 222–239.
26. Powell, T., Steen, E.M., Twist, V.W., and Woolf, N. (1978) Surface characteristics of cells isolated from adult rat myocardium. *J. Mol. Cell. Cardiol.* **10,** 287–292.
27. Slade, A. M., Severs, N. J., Powell, T., Twist, V. W., and Jones, G. E. (1985) Morphometric analysis of calcium-tolerant myocytes isolated from the adult rat heart, in *Advances in Myocardiology*, vol. 6 (Dhalla, N. S. and Hearse D. J., eds.), Plenum Publishing Corporation, New York, pp. 3–12.

13

Imaging Bacterial Shape, Surface, and Appendages Before and After Treatments With Antibiotics

Pier Carlo Braga and Davide Ricci

1. Introduction

Bacteria are typically smaller than eukaryotic cells. The average diameter of *Staphylococcus aureus* is 1 ± 0.5 μm, whereas *Escherichia coli* is on average 0.5×1.5 μm. The bacterial cell is also characterized by the presence of a complex external rigid structure called cell wall, which protects the internal protoplast and gives also the cellular shape, that generally falls into one of the, three basic morphologic categories, spherical (cocci), rod-shaped (bacilli), and spiral. Some bacteria show an atypical bacterial shape.

Bacteria are also able to extrude some material that collects outside the cell wall to form an additional, surface layer. Many genera of bacteria possess also filamentous structures projecting through the cell wall to form the so-called surface appendages. The most commonly observed bacterial appendages are flagella, fimbriae or pili, and filaments.

Antibiotics are particular type of drugs able to interfere in different ways to the metabolic pathways of bacteria. This causes also changes directly or indirectly in the structure of cell wall and consequent alterations in the shape of bacteria. The integrity of cell wall and bacterial shape are important to maintain the vitality and the virulence of bacteria. Morphostructural alterations not only cause bacteria to loose cytoplasm but also to be more easily phagocytized and killed by human phagocytic cells. A large amount of basic and clinical researches in microbiology, chemotherapy, and infectious diseases have been performed to investigate the morphology and structure of bacteria. These studies have been previously conducted by means of optical microscopy and scanning electron microscopy (SEM).

From: *Methods in Molecular Biology, vol. 242: Atomic Force Microscopy: Biomedical Methods and Applications*
Edited by: P. C. Braga and D. Ricci © Humana Press Inc., Totowa, NJ

Optical and scanning (or transmission) electron microscopes are classified as far-field microscopes because the distance between the sample and the point at which the image is obtained is long in comparison with the wavelengths of the photons or electrons involved. In this case, the image is a diffraction pattern and its resolution is wavelength limited ***(1,2)***: in optical microscopy, resolution is determined by the Nyquist relation to the wavelength of the light used (typically about 1 μm); in a general purpose SEM, it is limited by the properties of the electromagnetic lenses (typically about 50 Å; **ref. *3***).

In 1986, a completely new type of microscopy was proposed: without lenses, photons, or electrons, it involved the mechanical scanning of samples ***(4)*** and opened up unexpected possibilities for the surface analysis of biological specimens. Initially called the scanning force microscope (SFM), it was a development of the previous scanning tunneling microscope ***(5)***, which provided information at atomic resolution of specimens that are electrically conducing. Because SFMs involve interactions between atomic forces (about 10^{-9} Newton), they are also and more frequently called atomic force microscopes (AFMs; **ref. *3***).

These new types of scanning probe microscopes (SPMs) are based on the concept of near-field microscopy, which overcomes the problem of the limited diffraction-related resolution inherent in conventional microscopes. Located in the immediate vicinity of the sample itself (usually within a few nanometers), the probe records the intensity and not the interference signal, and this greatly improves resolution ***(1)***.

As shown in **Fig. 1**, AFM explores the surface of a sample not by means of a system of lenses that form an image using the diffraction patterns of rays of different wavelengths but by means of a very small sharp-tipped probe located at the free end of a cantilever driven by the interatomic repulsive or attractive forces (van der Waals forces) between the molecules at the probe tip and those on the surface of the specimen. This can be done by scanning the sample laterally (x, y) while a closed loop control system keeps the tip in proximity to the surface by adjusting the z position of the sample. In most AFMs, tip movements are monitored by reflecting a laser beam from the back of the cantilever on to a position-sensitive photodiode ***(6)***.

AFM is extremely useful for analyzing the three-dimensional structure of the surface of biological specimens, particularly bacteria. Although SEM is still frequently used, the introduction of the AFM technique offers substantial benefits in real quantitative data acquisition in three dimensions, minimal sample preparation times, flexibility in ambient operating conditions (i.e., no vacuum is necessary), and effective three-dimensional magnification at the submicron level ***(7,8)***.

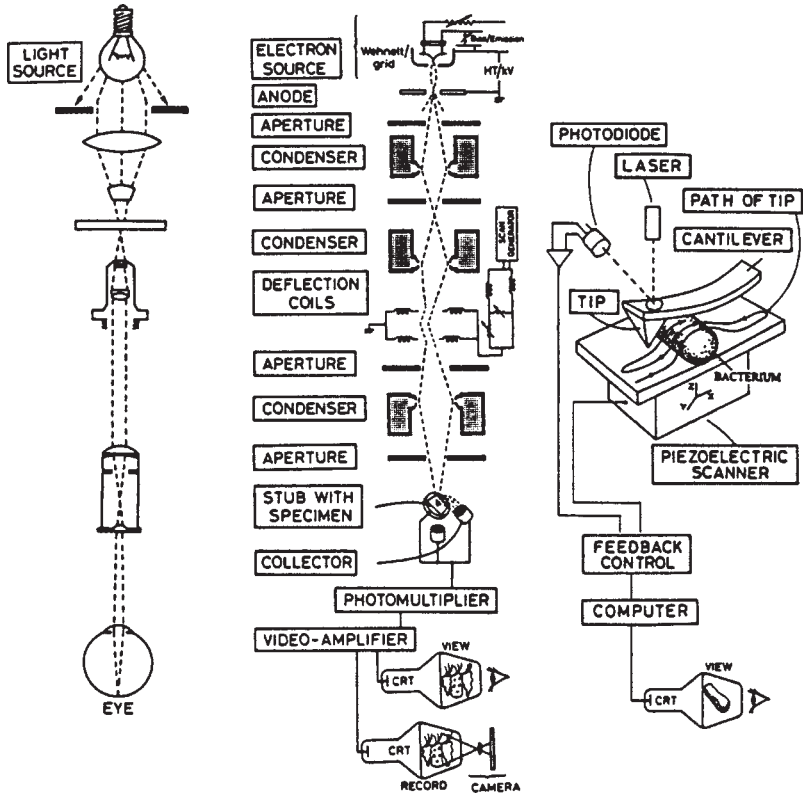

	LIGHT MICROSCOPE	SCANNING ELECTRON MICROSCOPE	ATOMIC FORCE MICROSCOPE
•SAMPLE			
-preparation	none/ little	freeze drying gold sputtering vaccuum	none/ little
-characteristics:	thin/ trasparent	vacuum compatible	not excessive variation in height
-operating environment	dry/liquid/ vacuum	vacuum	dry/liquid/ vacuum
•BIOLOGICAL APPLICATION	many	surface analysis	surface analysis
•FOCUS (depth)	medium	small	small
•FIELD (depth)	small	large	medium
•RESOLUTION			
xy axis	1.0 μm	5 nm	0.1-1.0 nm
z axis	——	——	0.01 nm
•MAGNIFICATION	$1\text{-}2\text{x}10^3$	$10\text{x}10^6$	$5\text{x}10^2\text{-}10^6$

Fig. 1. Comparative schematic view of the elements characterizing light microscopy, scanning electron microscopy, and atomic force microscopy, together with their specific technical parameters.

To investigate the shape and the surface of bacteria offers the possibility of investigating the efficacy and the mechanism of action of antibiotics that disrupt this structure as an epiphenomenon of internal biochemical action ***(9–13)*** and at the same time the possibility of investigating their lack of activity, as in the case of resistance.

2. Materials

1. Test organisms. Both Gram-positive and Gram-negative bacteria are suitable for AFM.
2. Tryptic soy broth or other suitable medium.
3. Phosphate buffer saline (PBS): 0.02 *M* phosphate and 0.15 *M* NaCl, pH 7.3.
4. Glutaraldehyde: 2.5%.in 0.1 *M* cacodylate buffer, pH 7.0.
5. Graded alcohols (60, 70, 80, 90, and 100%).
6. Incubator.
7. Centrifuge.
8. Micropipette and sterilized disposables for culturing bacteria.
9. Round glass coverslides, diameter 6–7 mm (or mica).
10. AFM (including probe-tips, software for processing signals and three-dimensional rendering, and computer).

3. Methods

1. Prepare the cultures of chosen microorganism according to common standard procedures.
2. Wash the test microorganism from the suspension in broth (i.e., 10^6 cells/mL) three times with PBS.
3. Resuspend the final pellet in 1–2 mL of PBS.
4. Collect 0.1 mL (or less) of this suspended bacteria with a micropipet and place it on round glass coverslide (*see* **Note 1**).
5. Dry the coverslip in air.
6. Fix with 2.5% glutaraldehyde in 0.1 *M* cacodylate buffer (pH 7.1).
7. Dehydrate in graded alcohols.
8. Dry the coverslip in air (*see* **Note 2**).
9. Repeat steps 1–8, incubating bacteria with various supra-minimum inhibitory concentrations (MICs) or sub-MICs of antibiotic.
10. AFM observation (*see* **Notes 3** and **4**). A typical AFM imaging session begins by firmly fixing the sample cover slide to the microscope holder to avoid even the slightest movement (*see* **Note 5)** and then positioning it under the probe tip and locating the area of interest by moving the *x*–*y* table.
11. A good-quality on-axis optical microscope is essential to be able to position the probe tip in the proximity of a bacterium to be imaged by AFM. Because bacteria are about 1 μm in size, it is necessary to have appropriate lighting conditions to distinguish them from any debris on the slide surface. In the experiments described here, a reflection optical microscope equipped with long-range objec-

tives was used. Although the cantilever bearing the probe partially obstructs the optical view of the underlying bacteria, it does allow the probe to be positioned sufficiently accurately in the area of interest (*see* **Notes 6** and **7**). Commercial AFM instrumentation coupled to a transmitted light optical microscope offers a higher degree of precision in the first approach of the probe to the sample (*see* **Note 8**).

12. Once an area has been located after the tip-to-sample approach, a first large scan (i.e., 30×30 µm) using a high scan speed and small number of pixels per line can be made in order to assess its exact position within the scanner coordinate system, identify the nature of the bacteria and select an interesting one. Further smaller scans may be necessary in order to position the bacterium exactly at the centre of the scanning area.
13. Record high-resolution images (*see* **Note 6**) by using appropriate instrument settings depending on the imaging mode selected (contact, intermittent contact, non-contact; *see* **Note 7**). In general, accurate feedback setting is necessary to obtain the maximum possible gain for the resolution of bacterial surface structures while avoiding oscillation when scanning along the cell sidewalls (*see* **Note 2**).
14. Acquire image (typically acquired at 512×512 pixels) and process by means of plane fitting, high-frequency filtering, and three-dimensional-shaded rendering (**Figs 2** and **3**).
15. Postprocessing analysis and the spatial representation of AFM-generated data are essential to extract all of the available information from the image dataset. Because the recorded data are an intrinsically three-dimensional digital matrix (the height of the sample recorded at each x, y coordinate), the software makes it easy to obtain numerical data of cross-sections of interesting features expressed with sub-nanometer accuracy (*see* **Note 8**). The same software allows three-dimensional rendering of the surface and rotation in space so that only one acquisition is needed to be able to observe the same object from many different points of view (*see* **Notes 9–11**).

4. Notes

1. It is better to use low concentrations of bacteria because they tend to concentrate in small areas during the air-drying phase, whereas a single bacterium provides a clearer image. Be sure to mark the location of your specimen on the upper surface of your round glass coverslide to avoid wasting time investigating the wrong side.
2. If the sample is kept dry, repeated sessions could generally be performed without any loss of resolution.
3. Bacterial sample preparation for AFM is very simple and rapid. There is no need for critical point drying, which also avoids shrinkage effects; there is no need for gold sputtering, a procedure that covers and smooths fine surface details. There is no need for vacuum conditions, as with SEM.
4. A recent technical evolution has also opened up the possibility of using AFM on wet samples, that is, living cells immersed in biological fluids in culture chambers ***(14,15)***.

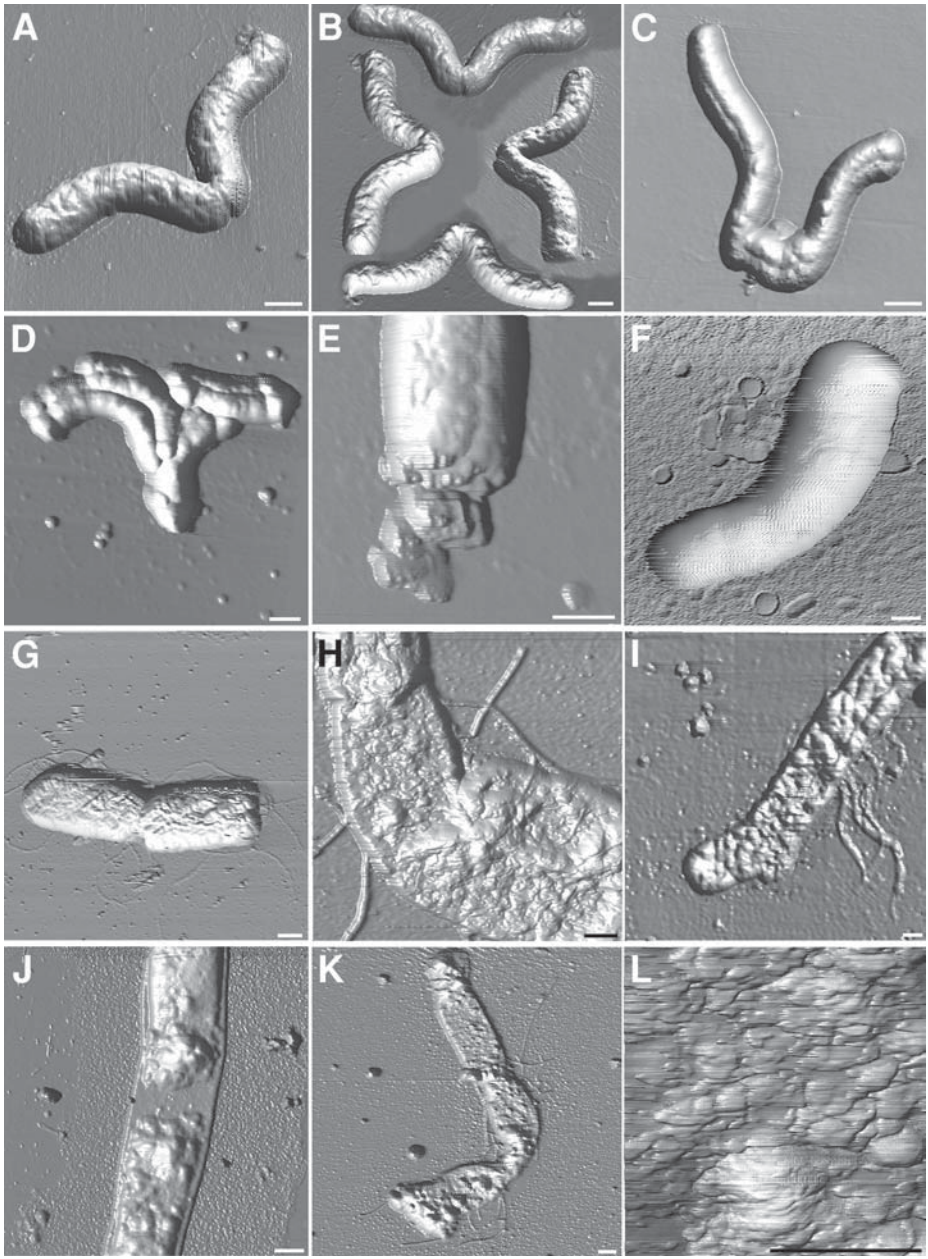

Fig. 2. Atomic force pictures of *Helicobacter pylori* and *E. coli*. The bar at the bottom right of each picture corresponds to 500 nanometers. **(A)** Common morphology of *H. pylori* without exposure to antibiotic. **(B)** Example of the different perspectives obtained by means of computer processing **(C–E)** Different alterations induced in *H. pylori* by

5. Care must be taken when choosing the adhesive used for fixing the glass slide to the sample holder. Avoid using thick double-sided adhesive tape, as this can expand for a long time after pressure and thus cause instability in the vertical position of the tip. The specially produced sticky tabs made by different manufacturers are fine.
6. To obtain the best results, it is necessary to be thoroughly familiar with the characteristics of different cantilevers and tips, how these can be used and how they suit to the different kinds of samples investigated. For high-resolution work, tip sharpness is essential: tip properties can vary significantly within the same batch of cantilevers. Fine tuning of the feedback loop and set point, together with the chosen scan speed, is critical for good surface tracking.
7. As mentioned above, AFM offers different imaging modes for investigating the sample. There is the contact mode in which the tip of the probe makes soft physical contact with the sample, which should be used with harder and stiffer materials than biological samples as it can easily give rise to undesirable effects as the result of tip-to-sample interactions (**Fig. 2L**). Tip pressure can indent and deform the sample surface, and lateral forces can stretch the sample, drag away loosely bound fragments, or even detach the whole bacterium from the substrate ***(3)***. These drawbacks of the contact AFM mode are overcome by using the intermittent-contact mode, also called tapping mode. In this case, the AFM feedback loop constantly dampens the high-frequency oscillations of the vibrating cantilever due to the tip coming into contact with the surface for a very short time ***(16)***. For this reason, indentation effects are less invasive, lateral forces are greatly reduced, and a high lateral resolution can be maintained. In the third noncontact mode, small amplitude and high-frequency oscillations induced on the cantilever allow the feedback control loop to maintain the tip-to-sample distance within the range of attractive Van der Waals forces. Tip-to-sample interactions are greatly reduced at the expense of lateral resolution and the scanning speed ***(2)***. For biological specimens the noncontact and intermittent contact are the most suitable, although the contact mode may be used for high-resolution work on very small areas.
8. To make accurate dimensional measurements, the calibration of the AFMs piezoelectric scanner has to be periodically checked. The procedures are usually described in the instrument manual. Lateral dimension calibration is relatively straightforward, but special care must be taken when calibrating height. We used a VLSI standard calibration grid (NIST traceable) with a 100-nanometer nominal step height and an in-house developed statistical analysis procedure for calibration.

Fig. 2. *(continued)* exposure to sub-MICs and supra-MICs of rokitamycin. **(F)** Example of artifacts. High-frequency oscillations and lack of bacterium surface detail can be caused by feedback instabilities induced by an electrostatically charged sample. **(G)** Common morphology of *E. coli* without exposure to antibiotic. **(H–K)** Different alterations induced in *E. coli* by exposure to sub-MICs and supra-MICs of cefodizime. **(L)** Example of artefact produced by excessive tip-to-sample interactions in contact mode.

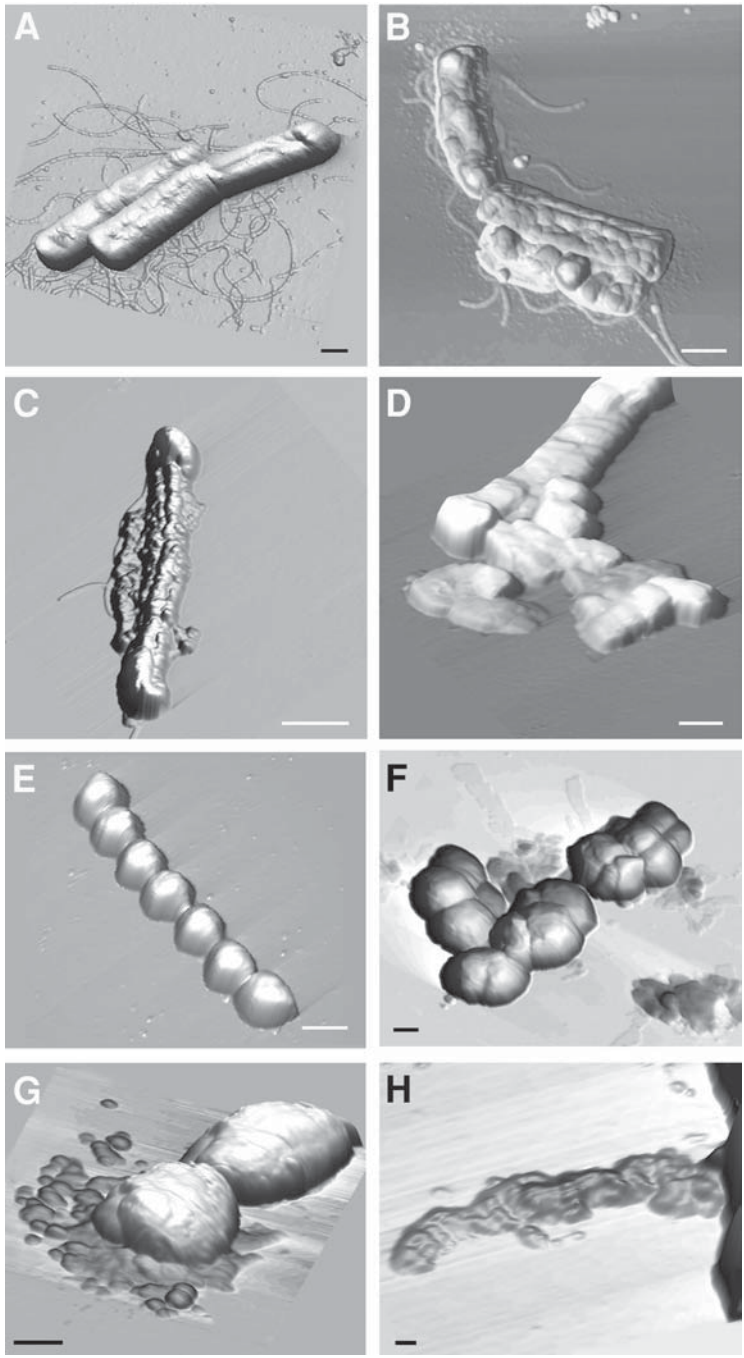

Fig. 3. Atomic force pictures of *Bacillus cereus* and *Streptococcus pyogenes*. The bar at the bottom right of each picture corresponds to 1 μm. **(A)** Example of untreated common rod-shaped morphology with flagella of *B. cereus*. **(B)** Morphostructural

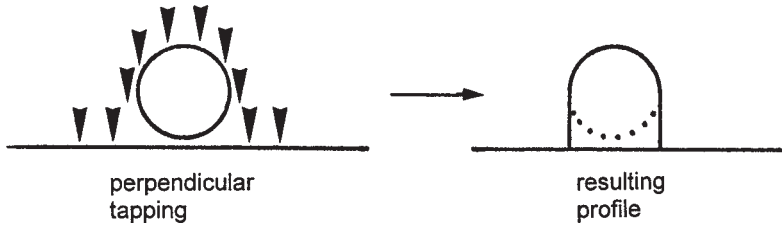

Fig. 4. Example of the AFM rendering of a spherical bacterium.

9. The images may sometimes be blurred as a result of poor washing procedures, an electrostatic charge on the specimen, improper feedback parameter settings, debris on the tip, or an eroded tip (**Fig. 2F**).
10. The images of spherical bacteria, such as *S. aureus*, will suffer from little lateral resolution along the perimeter because of the perpendicular direction of analysis. In general, the shape of the tip and its lateral walls will limit the detection of steep elevated features (**Fig. 4**).
11. After image acquisition, the built-in software allows the rendering of the picture to be greatly improved by means of shadowing, rotation, different illumination, and different points of view (**Fig. 2B**).

Acknowledgments

We would like to thank M. Dal Sasso for preparing the bacterial samples. This study was partially supported by a grant from MIUR (60%).

References

1. Heckl, W. M. (1995) Scanning the thread of life, in *The human genome* (Fisher, E. P. and Klose, S., eds.), R. Piper GmbH & Co. KG, Munchen, pp. 99–146.
2. Braga, P. C. and Ricci, D. (1998) Atomic force microscopy: Application to investigation of *Escherichia coli* morphology before and after exposure to cefodizime. *Antimicrob. Agents Chemother.* **42,**18–22.
3. Strausser, Y. E. and Heaton, M. G., (1994) Scanning probe microscopy technology and recent innovations. *Am. Laboratory*, May, 1–7.
4. Binning, G., Quate, C. F., and Gerber, C. (1986) Atomic force microscope. *Whys. Rev. Lett.* **12,** 930–933.

Fig. 3. *(continued)* alterations of *B. cereus* after 2-h incubation with daptomycin at 8× MIC. **(C)** Example of alterations induced in *B. cereus* after 4-h incubation with daptomycin 8 × MIC. **(D)** Lateral view of altered structure of *B. cereus* after 8-h incubation with daptomycin 4× MIC. **(E)** Example of common morphology of *S. pyogenes* phenotype M without exposure to antibiotic. **(F–H)** After 6-h of incubation with rokitamycin (2 µg/mL, abnormally enlarged cells, loss of typical chain structure, formation of clusters, flattening of the cells, and ghost formation were present.

5. Binnig, G. and Rohrer, H. (1982) Scanning tunneling microscopy. *Helv. Phys. Acta.* **55,** 726–735 .
6. McDonnel, L. and Phelan, M. (1998) The scanned cantilever AFM: A versatile tool for industrial application. *Microscopy Anal.* **52,** 25–27.
7. Ratneshwar, L. and Scott, A. J. (1994) Biological applications of atomic force microscopy. *Am. J. Physiol.* **266,** C1–C21.
8. Campbell, P. A., Gordon, R., and Walmsley, D. G. (1998) Active surface modification by scanning tunneling microscopy. *Microscopy Anal.* **56,** 25–27.
9. Lorian, V. (1986) Effect of low antibiotic concentrations on bacteria: effects on ultrastructure, their virulence and susceptibility to immunodefenses, in *Antibiotics in Laboratory Medicine* (Lorian, V., ed.), The Williams & Wilkins Co., Baltimore, pp. 596–668.
10. Lorian, V., Atkinson, B., Walushacka, A., and Kim, Y. (1982) Ultrastructure, in vitro and in vivo, of staphylococci exposed to antibiotics. *Curr. Microbiol.* **7,** 301–304.
11. Braga, P. C. and Ricci, D. (2000) Detection of rokitamycin-induced morphostructural alterations in *Helicobacter pylori* by atomic force microscopy. *Chemotherapy* **46,** 15-22.
12. Braga, P. C. and Ricci, D. (2002) Differences in the susceptibility of *Streptococcus pyogenes* to rokitamycin and erythromycin revealed by morphostructural atomic force microscopy investigation. *J. Antimicrob. Chemother.* **50,** 457–460.
13. Braga, P. C., Ricci, D., Dal Sasso, M. and Thorne, G. (2002) *Bacillus cereus* morphostructural damage by daptomycin: atomic force microscopy investigation. *Chemotherapy* **14,** 336-341.
14. Nagao, E. and Dvorak, J. A. (1999) Developing the atomic force microscope for studies of living cells. *Intern. Lab.* January, 21–23.
15. Schaus, S. S., and Henderson, E. R. (1997) Cell viability and probe-cell membrane interactions of XR1 glial cells imaged by atomic force microscopy. *Biophys. J.* **73,** 1205–1214
16. Howland, R. and Benatar, L. (1997) *A Practical Guide to Scanning Probe Microscopy*. Park Scientific Instrument, Sunnyvale, CA, pp. 1–73.

14

Visualizing Nuclear Structure *In Situ* by Atomic Force Microscopy

Luis Felipe Jiménez-García and María de Lourdes Segura-Valdez

1. Introduction

The cell nucleus is an organelle where molecules involved in gene expression are highly compartmentalized ***(1)*** in very dynamic ***(2)*** territories. This current notion of functional organization has been possible because of many studies of this organelle that included its cell and molecular organization, and where microscopy played an important role. Light and electron microscopy in conjunction with molecular approaches, such as the construction of both antibodies and nucleic acid probes, as well as molecular construction of genes with green fluorescent protein and fluorescence recovery after photobleaching technology, in addition to high-resolution *in situ* hybridization and immunocytochemistry now offer a more complete knowledge.

Structurally, the mammalian cell nucleus is organized as an organelle surrounded by a double layer of phospholipids called the nuclear envelope, which is interrupted by the nuclear pores. It is covered in the interior by the nuclear lamina. Within the cell nucleus, a nuclear matrix is present as a nuclear skeleton made of several different proteins. DNA is organized as euchromatin and heterochromatin. The ribonucleoproteins are distinguished by their participation in pre-mRNA or pre-rRNA metabolism. In the first case, ribonucleoproteins are visualized as nuclear speckles by light microscopy, which correspond to interchromatin granule clusters and perichromatin fibers observed by electron microscopy. In addition, perichromatin granules are also present. All these structures are related to transcription and splicing of pre-mRNA and transport or storage of intranuclear mRNA. The nucleolus, however, is involved in pre-rRNA transcription and processing as well as ribosome assembly. There are other nuclear structures, such as the Cajal bodies, which contain factors

From: *Methods in Molecular Biology, vol. 242: Atomic Force Microscopy: Biomedical Methods and Applications*
Edited by: P. C. Braga and D. Ricci © Humana Press Inc., Totowa, NJ

involved in both pre-mRNA and pre-rRNA metabolism ***(1–8)***. In plants, there are two major classes of nuclei: (1) the chromocentric and (2) the reticulated types, depending on the arrangement of heterochromatin fibers ***(9–12)***. In the first type, DNA is organized as discrete clumps within the nucleoplasm. In the second one, DNA forms a reticulated strand.

Lacandonia schismatica is a rare plant whose most important feature is the inverted position of the sexual organs, with the androecium in the center, surrounded by the gynoecium ***(13,14)***. In studying the biology of this species, we have analyzed the cell biology, including the interphase cell nucleus, which we have published previously ***(15–20)***. The cell nucleus of *L. schismatica* is reticulated.

To explore the possibility of studying the interphase cell nucleus with high resolution, while at the same time of working in solution, we have been studying the nuclear structure by using an approach whereby a sample is prepared for transmission electron microscopy (TEM) and the surface of the unstained semithin sections is explored with an atomic force microscopy working in contact mode ***(17,19)*** to visualize the interior of the cell. It is a common observation when sectioning with an ultramicrotome that trimming of the plastic blocks to get thin sections many times reveals the profile of the embedded cells over the surface. This observation suggested that even very flat surfaces have a texture corresponding to cell organelles, and indeed this is the case. Therefore, because the microscope is an instrument to analyze surfaces, the surface of each section can be visualized as a representative sample of a portion of the cell interior. Similar approaches also have been used previously ***(21,22)*** to study cell structure *in situ*. As a first step, we have been validating this approach by observing and generating images of already known material. For these purposes we have been visualizing the nuclear structure of *L. schismatica* by using the protocols described in **Subheading 3.** ***(17,19)***.

2. Materials

2.1. Sample Preparation

1. 70% Glutaraldehyde (Polysciences). Toxic. Wear gloves, goggles and work in a chemical fume hood. Store at 4°C.
2. 2% Osmium tetroxide. Toxic. Wear gloves, goggles and work in a chemical fume hood. Store at 4°C. Protect from light.
3. Phosphate-buffered saline (PBS) 0.01 *M*, pH 7.4. Store at 4°C.
4. Deionized water.
5. 100% Ethanol, electron microscopy grade.
6. 100% Propylene oxide, electron microscopy grade.
7. Epoxy resin (glycidether 100, Merck). Plastic resin.
8. DDSA (dodecenylsuccinic anhydride) hardener (Merck).

9. NMA (methylnorbornene-2,3-dicarboxylic anhydride) plasticizer (Merck)..
10. DMP (2, 4, 6-Tris[dimethyl-aminomethyl]phenol) accelerator (Merck)..
11. Toluidine blue.
12. Clean glass slides. Keep within a chamber to avoid dust.
13. Ultramicrotome (Reicher-Jung).
14. Glass knives.
15. Diamond knife.

2.2. Microscope

1. BioScope (Digital Instruments, Santa Barbara, CA).
2. NanoScope IIIa (Digital Instruments, Santa Barbara, CA) control system and the software.
3. Inverted Diaphot 200 microscope (Nikon, NY).
4. Silicone nitride tips, 20–60 nm radius of curvature (model NP).
5. 100-µm Atomic force microscope scanner.
6. Proscan software (version 3.1, Park Scientific, 1997)

3. Methods

3.1. Sample Preparation

Samples are prepared as for standard TEM or histology. For TEM, we have used several protocols, including different types of fixation with aldehydes such as glutaraldehyde or paraformaldehyde at different concentrations, or with embedding media such as glycol methacrylate, London resin white, Lowicryl®, and epoxy resin. Here, we describe the regular protocol for TEM ***(15,23–25)*** because it produced thus far the best results as far as morphology is concerned.

1. Samples are fixed with freshly made 6% glutaraldehyde from 70% vials, buffered with 0.01 *M* PBS at pH 7.4 for 2–6 h at room temperature. PBS is prepared as follows ***(23)***: dissolve 8 g of NaCl, 0.2 g of KCl, 1.44 g of Na_2HPO_4, and 0.24 g of KH_2PO_4 in 800 mL of distilled water. Adjust pH to 7.4 with HCl. Add water to 1 L. Sterilize by autoclaving.
2. After fixation, samples are washed with PBS for three times 10 min each.
3. Postfixation is performed with 1% osmium tetroxide in bidistilled water for 1–2 h. Prepare from a stock solution of 2% made from crystals in bidistilled water.
4. Dehydration is conducted with a series of graded concentration of ethanol, 10 min each of 30, 50, 70, 80, 90, and 96, and three changes of 100% ethanol. Propylene oxide is then used for three times for 10 min each.
5. For preembedding, samples are placed in a mixture of 1:1 of propylene oxide and epoxy resin during 16 h at room temperature. The epoxy resin is made as a stock solution. A recommended proportion of the components for working with plants can be taken from the references ***(23)*** and will contain 9.44 g of epoxy resin, 5 g of DDSA, 10 g of NMA, and 0.2 mL of DMP.

Mix the components thoroughly with a glass rod avoiding making bubbles. Store at 4°C in a small jar avoiding the penetration of air by sealing with parafilm. Prepare in the chemical fume hood. Avoid contact with the skin and to inhale. *See* **Note 1.**

6. Embedding is conducted with epoxy resin for 16 h at 60°C.
7. Semithin sections of about 150–250 nm width are obtained with an ultramicrotome working with glass or diamond knives. *See* **Note 2.**
8. Two sets of sections are placed onto an ethanol-cleaned glass slide. The sections are transferred by placing a platinum loop onto a drop of water. The sections are placed onto a glass slide. Sections are fixed to the glass by gently heating the slide. One set of sections is stained with toluidine blue and rinsed thoroughly with bidistilled water. Toluidine blue stain is prepared as a stock solution by dissolving 1% toluidine blue in 1% sodium borate, to stain the sections but not the plastic. For staining, once the slide reaches room temperature after fixing to the glass, cover the section with one or two drops of the stain and place it on a hot plate until stain starts to dry and obtain a metallic green color at the borders. Rinse the excess stain off the slide with bidistilled water. Sections are stored in a chamber to avoid dust.

3.2. Atomic Force Microscopy

An atomic force microscope model Bioscope (Digital Instruments) is used for observations. The microscope is mounted on an inverted light microscope Diaphot 200 (Nikon). Observations are made in contact mode. The scan size are from 100 to 5 µm at a scan rate varying from 1.969 to 1.285 Hz. Images were generated with the NanoScope IIIa control system. Alternatively, an atomic force microscope from Park Scientific has been used ***(17,19)***. In that case, the microscope is equipped with a scanner of 100 µm and a 100-Å radius silicone nitride tip, mounted on a cantilever of 0.6 µm. A scan rate of 2–3 Hz, a force of 10 nN, and a gain of 0.5 arbitrary units have been used. Images are then generated with Proscan. (*See* **Note 3.**) For the BioScope model, it is suggested to follow the next steps:

1. Fix the slide onto the stage by using the vacuum system provided.
2. Localize the sample with the bright field microscope using a low-magnification objective.
3. Approach the head of the microscope manually.
4. Visualize the cantilever and the tip with the light microscope and align the tip (*see* **Note 4**).
5. Adjust parameters as scan size to 100 µm, scan rate to about 1.5 Hz, and data scale to about 400 nm.
6. Engage the microscope and scan the sample (*see* **Note 5**).
7. Generate the images using the Nanoscope IIIa software provided (**Figs. 1** and **2**; (*see* **Notes 6** and **7**).

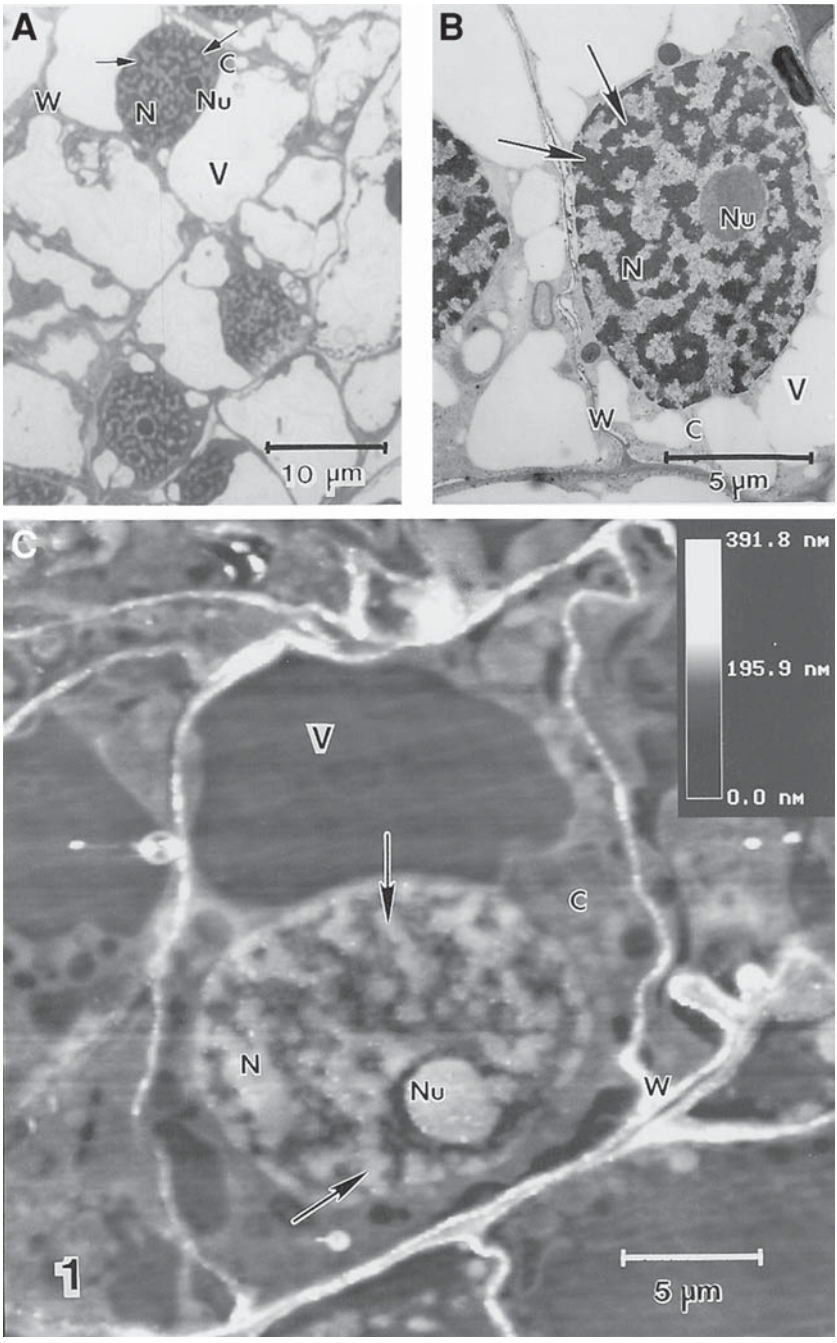

Fig. 1. Light **(A)**, electron **(B)**, and atomic force **(C)** microscopy of cell nuclei from the tegument cells from an ovary of a flower of the plant *Lacandonia schismatica*. The three types of microscopes generate a similar image of the cell nuclei. However, the resolution in every case varies according to the instrument. N, nucleus; Nu, nucleolus; arrows, reticulated compact chromatin; W, cell walls; V, vacuoles; C, cytoplasm.

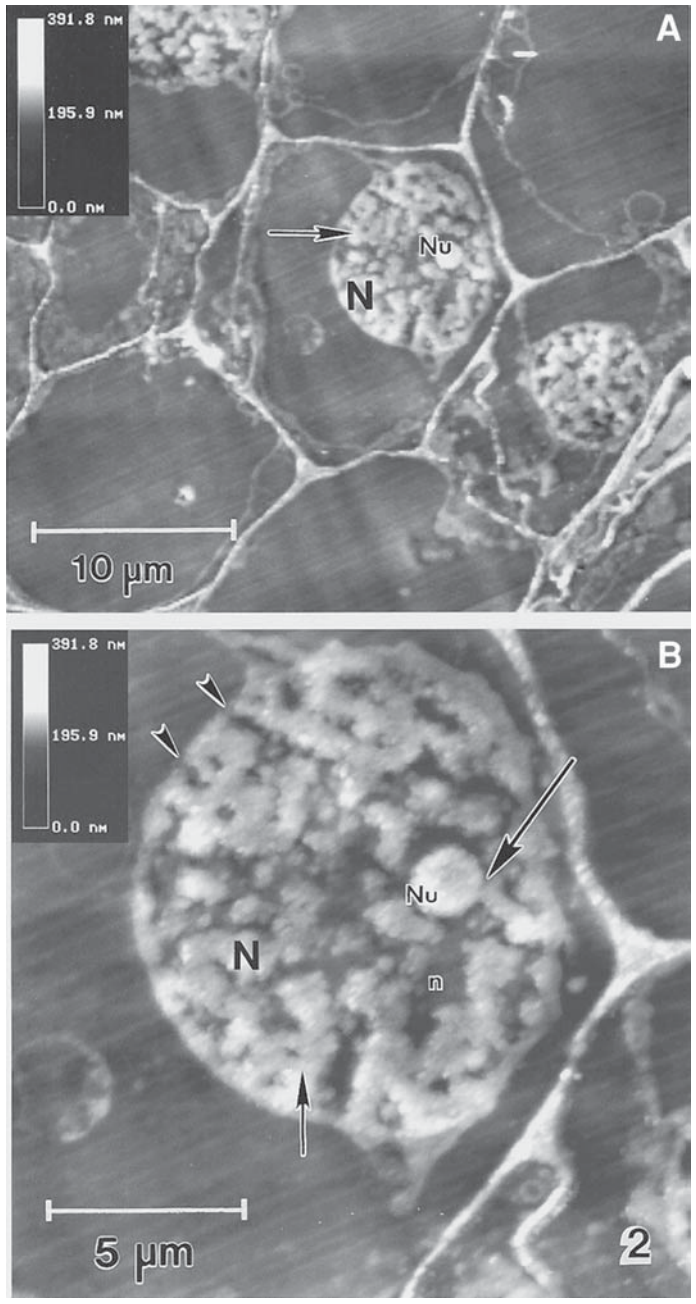

Fig. 2. Atomic force microscopy at low **(A)** and high **(B)** magnification of a *L. schismatica* cell nucleus. N, nucleus; Nu, nucleolus; small arrow, reticulated compact chromatin. In (B), nuclear pores (arrowheads) are observed as discontinuities of the nuclear envelope. The nucleolar organizer region (large arrow) is observed as a portion of compact chromatin strand that makes contact with the nucleolus. The nucleoplasm (n) is seen as texturized material among chromatin strands.

4. Notes

1. Regarding the epoxy resin for embedding, it is better to prepare the hardest mixture, by varying the concentration of the components such as the hardener (DDSA).
2. For obtaining sections it is better to use a diamond knife, although a glass knife also produces good quality material. Use only very clean water during the sectioning.
3. Before observation, it is recommended to place two sets of semithin sections onto the glass slide. One set is intended for staining with toluidine blue and the other will remain unstained. Under a bright-field microscope, the stained sections will be useful in recognizing the area to be scanned with the atomic force microscope on the unstained sections, which will be placed close by the stained sections. After staining, rinse the sections thoroughly with bidistilled water and air dry them.
4. Because the slide is placed sample side up, the sections face the cantilever and the tip of the atomic force microscope. However, the 10, 16, 20, and 40× objectives will image the sample through the width of the slide. Moreover, a fiberglass light will be used to illuminate the sample laterally. In an inverted microscope, it will not be possible to observe with the atomic force microscope and simultaneously perform bright field illumination according to Köhler, because the BioScope microscope is mounted on a special stage and it will interfere with the light path of a halogen lamp. Therefore, although the image visualized under the 10, 16, and 20× objectives will be of relatively good quality, when using the 40× objective, the image will be fuzzy as a result of the width of the glass. In general, however, it will not be necessary to use the 40× objective to localize particular areas of interest.
5. A scanning field of about 100 µm is recommended at the beginning, in order to easily recognize structures at low magnification. Once a good area of interest is obtained, smaller areas can be analyzed. It is better to approach smaller areas of scanning gradually.
6. It is a common practice in our laboratory to generate images of both stained and corresponding unstained samples for comparison.
7. To operate the microscope, it is reccommended to start using the parameters as scan size accordingly (from 100 to 5 mm) The scan rate will be around 1.285, whereas the image data will remain at height and the data scale around 400 nm.

Acknowledgments

This work was supported by CONACyT 28002N and DAGAPA-UNAM IN221202, and SEMARNAT2002-COI-0435. We thank E. Ubaldo for technical assistance.

References

1. Spector, D. L. (1993) Macromolecular domains within the cell nucleus. *Annu. Rev. Cell Biol.* 9, 265–315.
2. Misteli, T. (2001) Protein dynamics: implications for nuclear architecture and gene expression. *Science* **291,** 843–847.

3. Fakan, S. (1994) Perichromatin fibrils are *in situ* forms of nascent transcripts. *Trends Cell Biol.* **4,** 86–90.
4. Vázquez-Nin, G. H. and Echeverría, O. M. (1996) The polytene nucleus in morphological, cytochemical, and functional studies of messenger RNA transcription, processing and transportation. *Eur. J. Histochem.* **40,** 7–16.
5. Lamond, A. I. and Earnshaw, W. C. (1998) Structure and function in the nucleus. *Science* **280,** 547–553.
6. Matera, A. G. (1999) Nuclear bodies: Multifaceted subdomains of the interchromatin space. *Trends Cell Biol.* **9,** 302–309.
7. Lewis, J. D. and Tollervey, D. (2000) Like attracts like: Getting RNA processing together in the nucleus. *Science* **288,** 1385–1389.
8. Gall, J. G. (2000) Cajal bodies: The first 100 years. *Annu. Rev. Cell Dev. Biol.* **16,** 273–300.
9. Lafontaine, J. G. (1974) Ultrastructural organization of plant cell nuclei, in *The Cell Nucleus* (Busch, H., ed.), Academic Press, New York, pp. 24–59.
10. Jordan, E. G., Timmis, J. N., and Trewavas, A. J. (1980) The plant nucleus, in *Biochemistry of Plants* (Tolbert, N. E., ed.), Academic Press, New York, pp. 489–588.
11. Nagl, W. (1985) Chromatin organization and the control of gene activity. *Int. Rev. Cytol.* **94,** 21–56.
12. Moreno Díaz de la Espina, S., Mínguez, A., Vázquez-Nin, G. H., Echeverría, O. M. (1992) Fine structural organization of a non-reticulated plant cell nucleus. An ultracytochemical and immunocytochemical study. *Chromosoma* **101,** 311–321.
13. Martínez, E. and Ramos, C. H. (1989) Lacandoniaceae (Triuridales): Una nueva familia de México. *Ann. Miss. Bot. Gard.* **76,** 128–135.
14. Márquez-Guzmán, J., Engleman, E. M., Martínez-Mena, A., Martínez, E., and Ramos, C. H. (1989) Anatomía reproductiva de *Lacandonia schismatica* (Lacandoniaceae). México. *Ann. Miss. Bot. Gard.* **76,** 124–127.
15. Jiménez-García, L. F., Agredano-Moreno, L. T., Segura-Valdez, M. de L., Echeverría, O. M., Ramos, C. H., Martínez, E., et al. (1992) The ultrastructural study of the interphase nucleus of *Lacandonia schismatica* (Lacandoniaceae:Triuridales) reveals a non-typical extranucleolar particle. *Biol. Cell* **62,** 5–14.
16. Agredano-Moreno, L. T., Jiménez-García, L. F., Echeverría, O. M., Martínez, E., Ramos, C. H., and Vázquez-Nin, G. H. (1994) Cytochemical and immunocytochemical study of nuclear structures of *Lacandonia schismatica*. *Biol. Cell* **82,** 177–184.
17. Jiménez-García, L. F., Reynoso-Robles, R., Fragoso-Soriano, R., Agredano-Moreno, L. T., Segura-Valdez, M. de L., González-Moreno, S., et al. (1998) Biología celular de *Lacandonia schismatica*. Análisis por microscopía electrónica y de fuerza atómica. *Bol. Soc. Bot. México* **62,** 5–14.
18. Agredano-Moreno, L. T. and Jiménez-García, L. F. (2000) New evidence that *Lacandonia* granules are ultrastructurally related to perichromatin and Balbiani ring granules. *Biol. Cell* **92,** 71–78.
19. Jiménez-García, L. F., and Fragoso-Soriano, R. (2000) Atomic force microscopy of the cell nucleus. *J. Struct. Biol.* **129,** 218–222.

20. Agredano-Moreno, L. T., González-Jiménez, M. A., Segura-Valdez, M. de L., Ubaldo, E., Ramos, C. H., Martínez, E., et al. (2001) Further ultrastructural characterization of the intranuclear ring-shaped bodies of the plant *Lacandonia schismatica*. *J. Struct. Biol.* **136,** 1–6.
21. Mariani, T., Musio, A., Frediani, C., Sbrana, I., and Ascoli, C. (1994) An atomic force microscope for cytological and histological investigations. *J. Microsc.* **176,** 121–131.
22. Morris, V. J., Kirby, A. R., and Gunning, A. P. (1999) *Atomic Force Microscopy for Biologists*, Imperial College Press, London.
23, Spector, D. L., Goldman, R. D., and Leinwand, L. A. (1998) *Cells: A Laboratory Manual*, Cold Spring Harbor Laboratory Press, Cold Spring Harbor, New York.
24. Vázquez Nin, G. H. and Echeverría, O. (2000) *Introducción a la microscopía electrónica aplicada a las ciencias biológicas*, Universidad Nacional Autónoma de México-Fondo de Cultura Económica, México.
25. Bozzola, J. J. and Russell, L. D. (1992) *Electron Microscopy*, Jones and Bartlett Pub, Boston.

15

Imaging Surface and Submembranous Structures in Living Cells With the Atomic Force Microscope

Notes and Tricks

Filip Braet and Eddie Wisse

1. Introduction

In 1986, Binnig et al. ***(1)*** revolutionized microscopy through the invention of the atomic force microscope (AFM). Subsequently, commercial instruments of this new imaging technique began to appear in the 5 yr after its discovery. In the early 1990s, Henderson et al. ***(2)*** and Radmacher et al. ***(3)*** both illustrated the potential of the instrument to image biological preparations in real time under nearby physiological conditions with nanometer resolution. From that point onwards the AFM has attracted biologists and the number of publications describing biological applications of AFM have grown rapidly ***(4)***.

A range of materials, methods, and notes have been described for imaging cultured cells with the AFM ***(5)***. In general, maintenance of steady-state culture conditions involve a high degree of thermal stability (37°C ± 0.5), continual renewal of the culture medium (osmolarity of ± 320 mOsmol/kg/H_2O), and a neutral pH (7.4 ± 0.3), stabilized by the use of 20 m*M* *N*-Hydroxyethylpiperazine-*N*'-2-ethanesulfonate (HEPES) buffer and/or a flow of CO_2 through the AFM cell chamber to maintain a steady-state concentration of 5%. It is well known that fluctuations in temperature, osmotic pressure, and pH have severe affects on cell viability and structure making consistent AFM imaging difficult ***(6)***. Commercial liquid cells for studying biological samples under controlled conditions are available but only useful for a limited number of special application problems. Therefore, biologists designed their own set-ups and as a consequence a variety of homemade systems exist and differs from laboratory to laboratory when reviewing the literature.

From: *Methods in Molecular Biology, vol. 242: Atomic Force Microscopy: Biomedical Methods and Applications*
Edited by: P. C. Braga and D. Ricci © Humana Press Inc., Totowa, NJ

In our AFM studies we used: 1) the Topometrix Explorer TMX equipped with a 100 µm XY/12 µm Z TrueMetrix Linearized Liquid Scanner installed on a Zeiss IM 35 inverted microscope with a homemade XY specimen stage adaptation and 2) a homemade fluid cell in combination with a heating stage. This design allows positioning of the cantilever in the optical axis of the inverted microscope, movement of the sample via the inverted microscope independently of the AFM, and minimizes cantilever drift by controlling temperature-induced variations. Time lapse images of living cells in contact ***(7–9)*** or noncontact mode ***(9,10)*** were obtained over a period of 2–3 h before peripheral parts of the cytoplasm started to detach from the substrate or before cell viability started to decrease as determined by the trypan blue exclusion test ***(11)***.

In this chapter we will give a short survey of our past research with the AFM on various (liver) cell types (**Figs. 1–5**). Moreover, the Methods and Notes sections address the most common problems and artifacts we encountered in AFM imaging when membranous and submembranous structures of cells wanted to visualized.

2. Materials

2.1. Surface Coating for Nonadherent Cells

1. Collagen-S solution (Boehringer Mannheim, cat. no. 1098292; *see* **Note 1**).
2. Sterile water.
3. RPMI-1640 with 25 m*M* HEPES (Gibco BRL, cat. no. 52400-025).

2.2. Growth Medium and Reagents

1. For slow-growing or nondividing cells ***(7,9)***: RPMI-1640 with 25 m*M* HEPES (*see* **Note 2**), 2 m*M* L-glutamine (Gibco BRL, cat. no. 25030-024), 100 U/mL penicillin, 100 mg/mL streptomycin (Gibco BRL, cat. no. 15140-122), and 2% heat-inactivated fetal calf serum (Gibco BRL, cat. no. 10270-098).
2. For fast-growing cells or cells with a high metabolic rate ***(7,8)***: DMEM with 25 m*M* HEPES (Gibco BRL, cat. no. 32430-027), 2 m*M* L-glutamine, 100 U/mL penicillin, 100 mg/mL streptomycin, and 10% heat-inactivated fetal calf serum.
3. Trypan blue stain 0.4% (Gibco BRL, cat. no. 15250-061).

2.3. Apparatus

1. LifeSciences SPM Explorer TMX (ThermoMicroscopes, cat. no. SPM 4400-11).
2. TrueMetrix 100 µm XY/12 µm Z Linearized Liquid Scanner (ThermoMicroscopes, cat. no. 5180-00).
3. Zeiss IM 35 inverted microscope (Zeiss, Germany, cat. no. IM35) with a homemade XY specimen-stage adaptation.
4. 150-W Fiber light source (Schott, Mainz, Germany, cat. no. KL 150 B).
5. Linkam heating device (Linkam Scientific Instruments, cat. no. CO102, UK).
6. Video camera (Pulnix, cat. no. TM-300 CCD miniature).

7. Video monitor (Philips,, The Netherlands, cat. no. CM8833 Personal Monitor).
8. Video recorder (JVC, UK, cat. no. SR-5970E time-lapse SVHS-VCR).

2.4. Tip Specifications

1. For contact imaging ***(12)***: Standard silicon nitride tips (TopoMetrix SFM-Probes, Ref 1520-00) with an arm length of 200 µm, a spring constant of 0.032 N/m and a 4 µm on 4-µm pyramidal base are preferred (*see* **Note 3**).
2. For noncontact imaging ***(10)***: Standard silicon nitride tips (Topometrix SFM-Probes, Ref 1530-00) with an arm length of 100 µm, a spring constant of 0.5 N/m, and a 4 µm on 4-µm pyramidal base are preferred.

3. Methods

3.1. Surface Coating for Nonadherent Cells (see Note 4)

1. Mix 30 µL of Collagen-S solution with 270 µL of sterile water.
2. Equally distribute this solution on a 35-mm Petri dish with the aid of a melted Pasteur pipet.
3. Incubate under sterile conditions for 18 h at 4°C.
4. Rinse twice with growth medium.
5. Incubate the Petri dish for 20 min at 37°C (*see* **Note 5**).
6. Seed the cells and culture for at least 4 h to allow adherence and spreading of the cells on the substrate (*see* **Note 6**).

3.2. Contact Imaging

1. The TopoMetrix Explorer (Santa Clara, CA) equipped with a 100-µm XY/12- µm Z TrueMetrix Linearized (*see* **Note 7**) Liquid Scanner and a homemade fluid cell were used (*see* **Note 8**).
2. The cantilever of the AFM was positioned in the optical axis of a Zeiss IM 35 inverted microscope with a home made adaptation (*see* **Note 9**; **Fig. 1**).
3. The temperature of the instrument was set at 37 ± 0.5°C by using the heating device.
4. Align the laser beam on the desired cantilever (*see* **Note 10**).
5. The sample was placed into the homemade sample holder (*see* **Note 11**).
6. Noise-free images were recorded (*see* **Note 12**) according to the guileless of the manufacturer until the viability of the cell cultures started to decrease (*see* **Note 13**).
7. Typical loading forces to be used for imaging living cells should vary between 2 and 4 nN (*see* **Note 14**).
8. Optimize the scan rate during scanning (*see* **Note 15**).
9. Optimize feedback parameters during scanning (*see* **Note 16**).

3.3. Noncontact Imaging

1. Follow **steps 1** to **6** as described under **Subheading 3.2.**
2. Use the appropriate noncontact tips as described under **Subheading 2.3.**

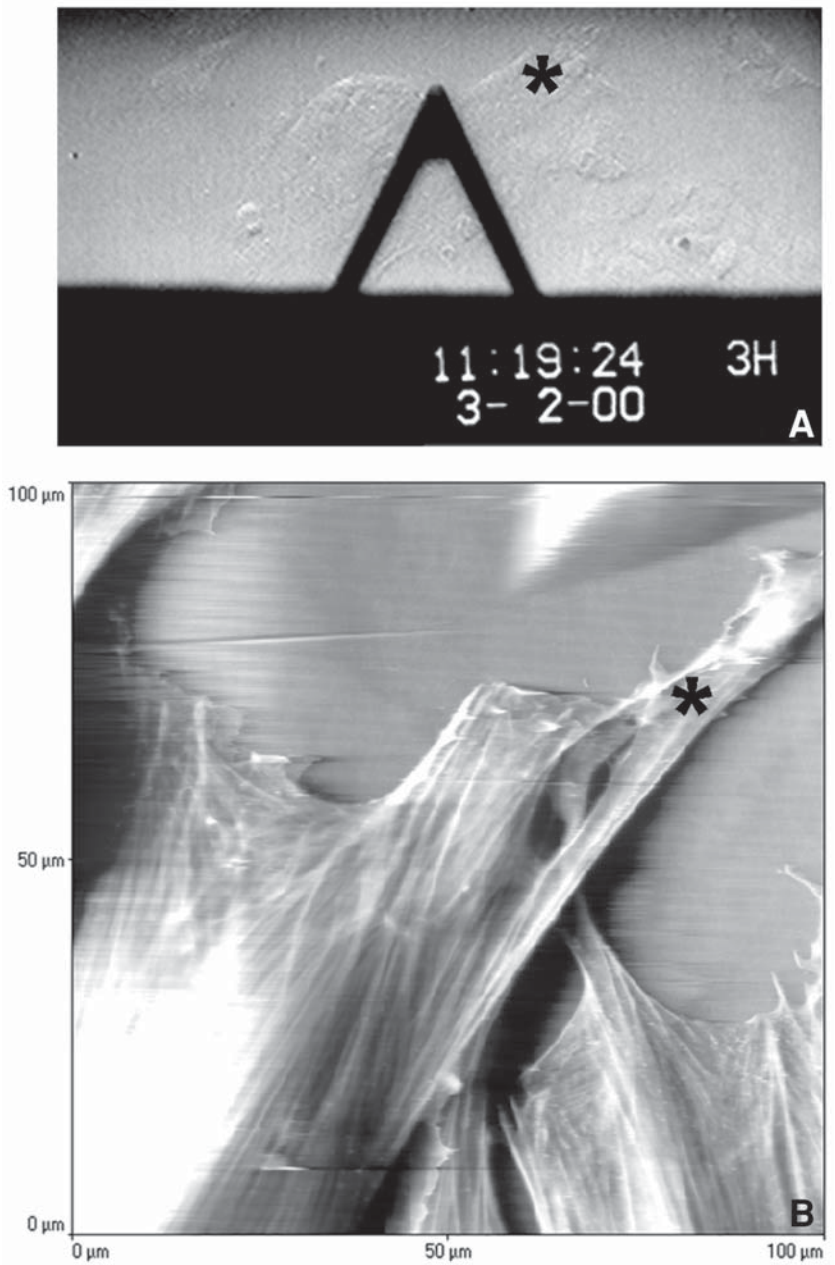

Fig. 1. **(A)** Light microscopic image obtained with a 20× objective lens mounted on a Zeiss IM 35 inverted microscope. The optical path of the eyepieces is connected to a video camera and video monitor allowing easy positioning of the cell of interest under the tip and real time observation of the AFM scanning process. In this

3. For living cells, a low resonance frequency of 38–78 kHz (depending on the appropriate spectrum frequency range of the cantilever used) and a ± 50% free-oscillation amplitude damping are preferred (*see* **Note 17**).
4. Optimize feedback parameters during scanning (*see* **Note 18**).

3.4. Viability Assessment

1. Add 0.3 mL of 0.4% Trypan Blue Stain into the 35-mm Petri dish with the aid of a Pasteur pipette and mix thoroughly. The amount of growth medium in the 35-mm Petri dish is 1.7 mL.
2. Allow to stand 5 min at 15 to 30°C.
3. Observe under the inverted microscope. Nonviable cells stain blue and viable cells exclude the stain *(11)*.

3.5. Imaging and Image Interpretation During Scanning

3.5.1. Z-Height Limitations

AFM imaging can result in artifactual images because of the limited range of the z piezo (**Fig. 2**). For example, in **Fig. 2**, the cells respond to a drug, which causes nuclear swelling in time, resulting in an increase of cell height that exceeds the limits of the z piezo (**Fig. 2C**). As a consequence, some nuclei have heights greater than the tip and image the structure of the whole cantilever. This can be avoided by changing the feedback parameters during imaging (*see* **Note 16**, **Fig. 2D**). Therefore, the use of the AFM is in some cases limited when the dimensions of biological structures exceed the available z displacement of the piezoelectronic scanner *(7)*.

3.5.2. Loading Forces

Using different loading forces on the same sample will result in images with different information (**Fig. 3**). As outlined in **Fig. 3**, applying low imaging forces will result in a more accurate surface visualization (**Fig. 3B**), whereas increasing the force will result in obscuring of fine membranous details (**Fig. 3C**). However, submembranous structures become apparent when higher loading forces are applied. This submembranous imaging originates from local variations in stiffness when the AFM-tip palpates the cell membrane.

Fig. 1. *(continued)* video image the cantilever with an arm length of 200 µm is positioned above a cluster of rat skin fibroblasts. **(B)** Concordant AFM image of rat skin fibroblasts. Compare with 1A and notice the small cytoplasmic processes (*) as observed under the light microscope and AFM. The white bump in B correspondents with the nuclear area and the surrounding cytoplasmic area contains fine and parallel organized cytoskeleton fibers, probably representing stress fibers, 100 µm × 100 µm.

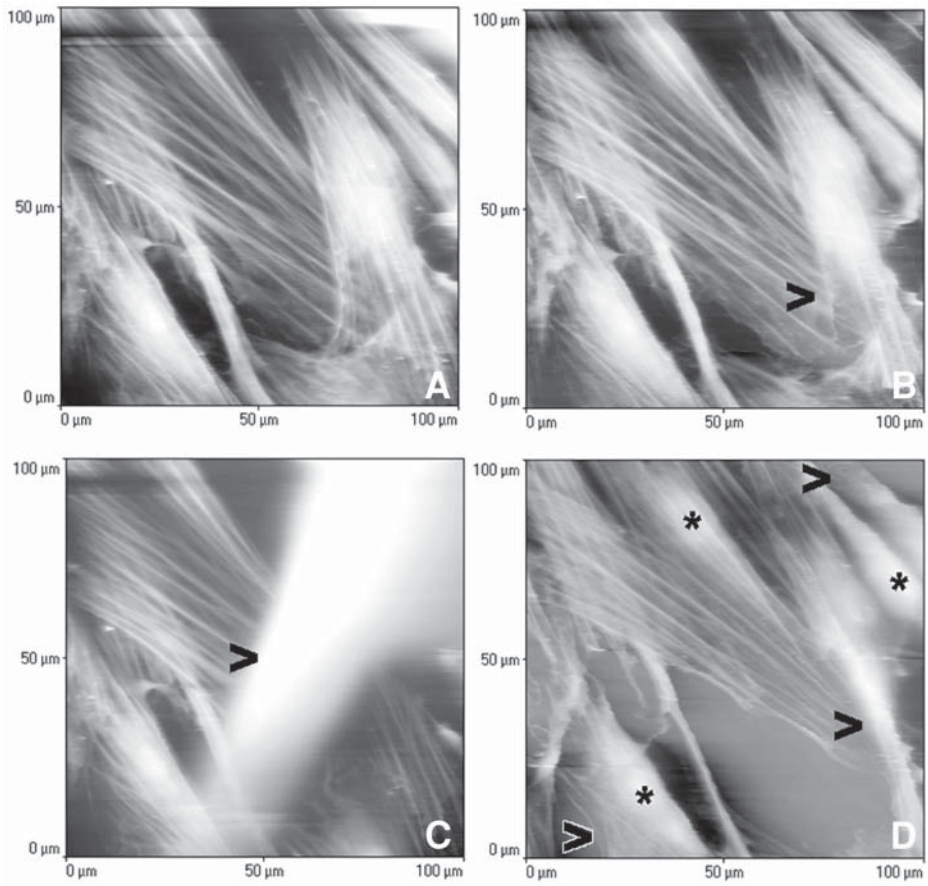

Fig. 2. Time-lapse AFM series of jasplakinolide A-induced microfilament disruption in rat skin fibroblasts (*see also* **ref. 7**). **(A)** Untreated fibroblasts show a parallel fiber orientation. Right after the acquisition of **(A)**, 200 n*M* jasplakinolide A was added and subsequently three sequential images of the same area were recorded (recording time 1 image ~ 15 min). **(B)** In the middle of the image the first signs of microfilament disruption could be noticed (>). **(C)** The cantilever is depicted instead of the cells. Jasplakinolide A induces an accumulation of filamentous actin around the nucleus and results in an increase of the nuclear height (from 8 to 12 µm; data not shown). In this case the sample visualizes the cantilever (>), rather than vice versa. **(D)** Increasing the integral gain (*see* **Note 16** during imaging resulted in an artifact-free image and reveal typical jasplakinolide-induced changes, that is, a loss of jasplakinolide A-sensitive fibers (>) and nuclear swelling (*). 100 µm × 100 µm.

A great help in interpreting results in relation to the forces used is the application of glutaraldehyde which increases the rigidity or stiffness of cells,

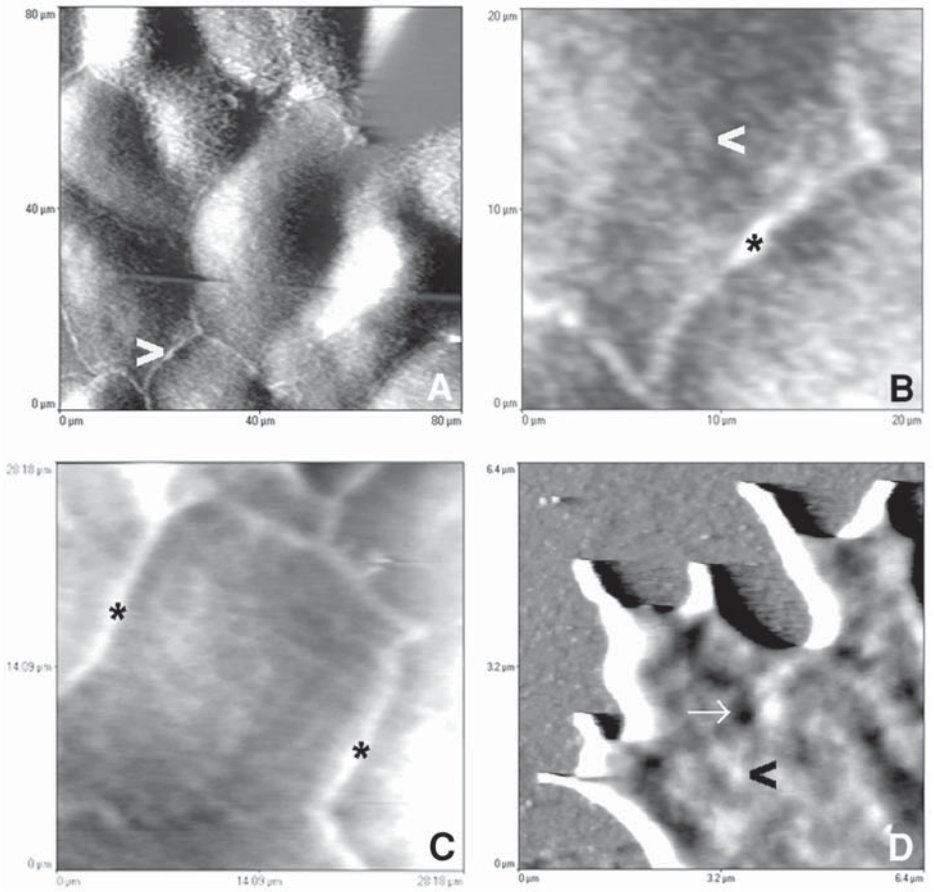

Fig. 3. AFM micrographs of colon carcinoma cells (*see also* **ref. 7**). **(A)** Low magnification showing central lying nuclei (white bumps) and clearly depicted cell borders (>), 80 µm × 80 µm. **(B)** Higher magnification of the cytoplasm obtained with a loading force of 2 nN showing fine membranous detail in the form of microvilli (>). Cell border (*), 20 µm × 20 µm. **(C)** Increasing the loading force with a factor 10 resulted in the disappearance of fine membranous detail and in clearly depicted cell borders (*), 20 µm × 20 µm. **(D)** High-magnification AFM image after glutaraldehyde fixation, confirming the presence of granular membranous elevations (>). Round membranous indentations (→) could be visualized as well which could not be imaged in the living state, 6.4 µm × 6.4 µm.

resulting in images dominated by surface details (**Fig. 3D**). This can be explained by the fact that the stiffness of the cell membrane is enhanced by fixation relative to the spring constant of the AFM-cantilever, resulting in less deformation of the membrane around rigid submembranous structures.

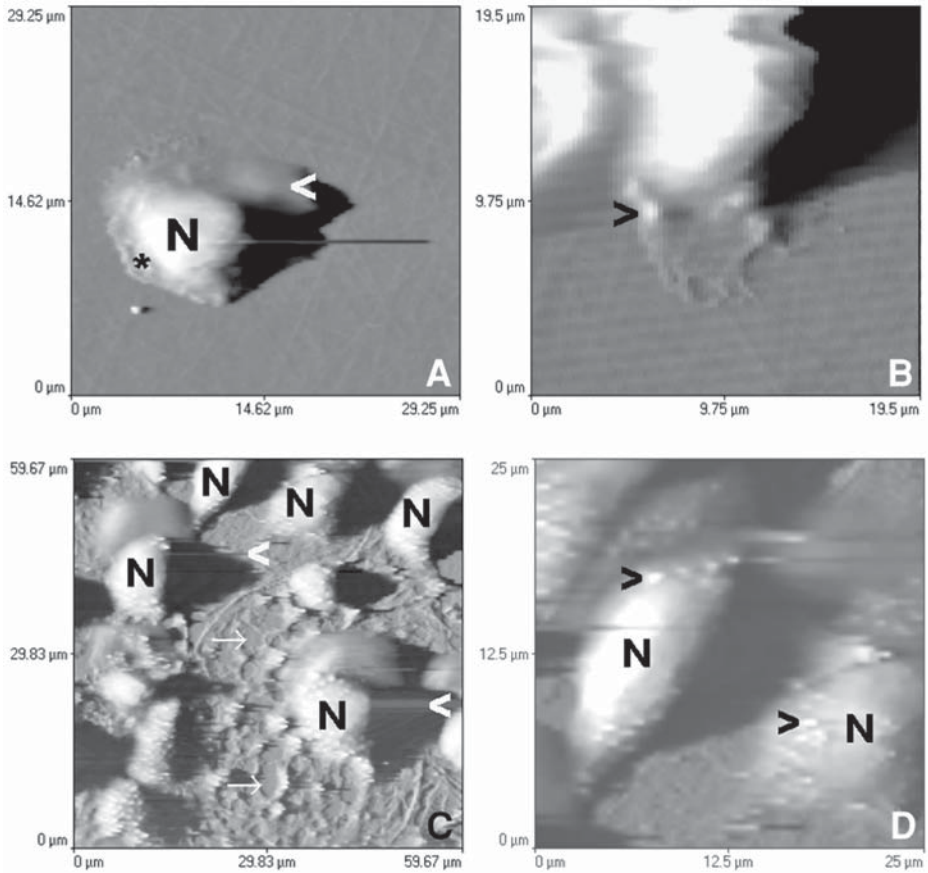

Fig. 4. AFM contact imaging of intracellular organelles in hepatic natural killer (**A** and **B**; *see also* **ref. *9***) and endothelial cells (**C** and **D**; *see also* **ref. *8***). **(A)** Overview of one cell showing the bulging nucleus (N) and surrounding cytoplasmic margins. Note the well-attached cytoplasm (*). At the other side of the cell the scanning process apparently deformed the cytoplasm, thereby showing less detail (>). This indicates that the tip sweeps these parts of the cytoplasm along the scan direction, illustrating that these structures do not attach well to the substrate. Therefore, this part of the cell probably corresponds to the pseudopodium or leading edge of the moving cell, 29 µm × 29 µm. **(B)** Detailed image of a part of the well attached cytoplasm, showing clearly the grain-like projections (>), 19.5 µm × 19.5 µm. **(C)** Low-magnification AFM image of living hepatic endothelial cells showing well-spread cells and bulging nuclei (N) which are prominently present. Artefactual smearing by the tip (<) is evidently present. Artifactual large gaps (→) within the cells could be noticed and probably originates from the removal of parts of the cytoplasm by the tip, 60 µm × 60 µm. **(D)** At higher magnification small white dots (>) could be observed around the nuclei (N), illustrating the presence of intracytoplasmic vacuoles (as known by correlative TEM studies), 25 µm × 25 µm.

3.5.3. Tip-Induced Smearing

In general, the lateral force can wipe away or smear out surface features, whereas the constant force can deform soft biological samples (**Fig. 4**). Because of these tip–specimen interactions, artifactual AFM images can be obtained, that is, 1) streaks in the scan, indicating that material is being removed by the tip (**Fig. 4A** and **C**) and 2) high corrugated regions are imaged as white bumps (**Fig. 4B** and **D**), illustrating smearing or lateral deformation which is probably caused by the cantilever indenting the cell surface.

Figure 4A and **B** are AFM images of cells moving along the substrate, showing scanning-deformed membrane sheets with less detail. This indicates that the tip sweeps these parts of the cytoplasm along the scan direction, at the same time illustrating that these structures do not attach well to the substrate. Whereas, the scanning of firmly attached protrusions reveals the presence of submembranous granular projections underlying the cell membrane. In this case, the artifactual tip-induced smearing helps to interpret the activity of the cells, where the deformed membrane sheets probably represent the pseudopodium or leading edge of the moving cell. In another example, firmly attached cells show severe effects as a result of the tip–sample interactions. In this case the tip interacts with the soft cytoplasm of the cell, resulting in the formation of large artefactual gaps (**Fig. 4C**). However, the stiffer nuclear area facilitates imaging of perinuclear details, such as storage vacuoles (**Fig. 4D**).

3.5.4. Cell Type Limitations

It happens that the cell type of interest bears extreme phagocytotic activities (**Fig. 5**). In our studies we used liver macrophages, also called Kupffer cells (**Fig. 5A**), which have a high phagocytotic capacity for latex beads (**Fig. 5B**) and at the same time for the silicon nitride tip (**Fig. 5C**). Attempts to compose time–lapse series of images during the process of phagocytosis partly failed. Because the cells rounded up during phagocytosis and, as a consequence, the higher parts of the cells were depicted as saturated images (**Fig. 5B**, *see also* **Subheading 3.5.1.**). Moreover, during the first seconds of tip contact, as observed in the inverted light microscope, it occurs that phagocytotic cells start to react against the cantilever in an attempt to phagocytose the tip, resulting in a image of the cantilever bottom side (**Fig. 5C**) or in pyramidal tip images (**Fig. 5D**). These pyramidal tip images are probably derived from the fine cytoplasmic protrusions, which have sharper contours than the AFM tip. In other words, the fine-edged protrusions, which are trying to embrace the tip, image the tip; rather than vice versa.

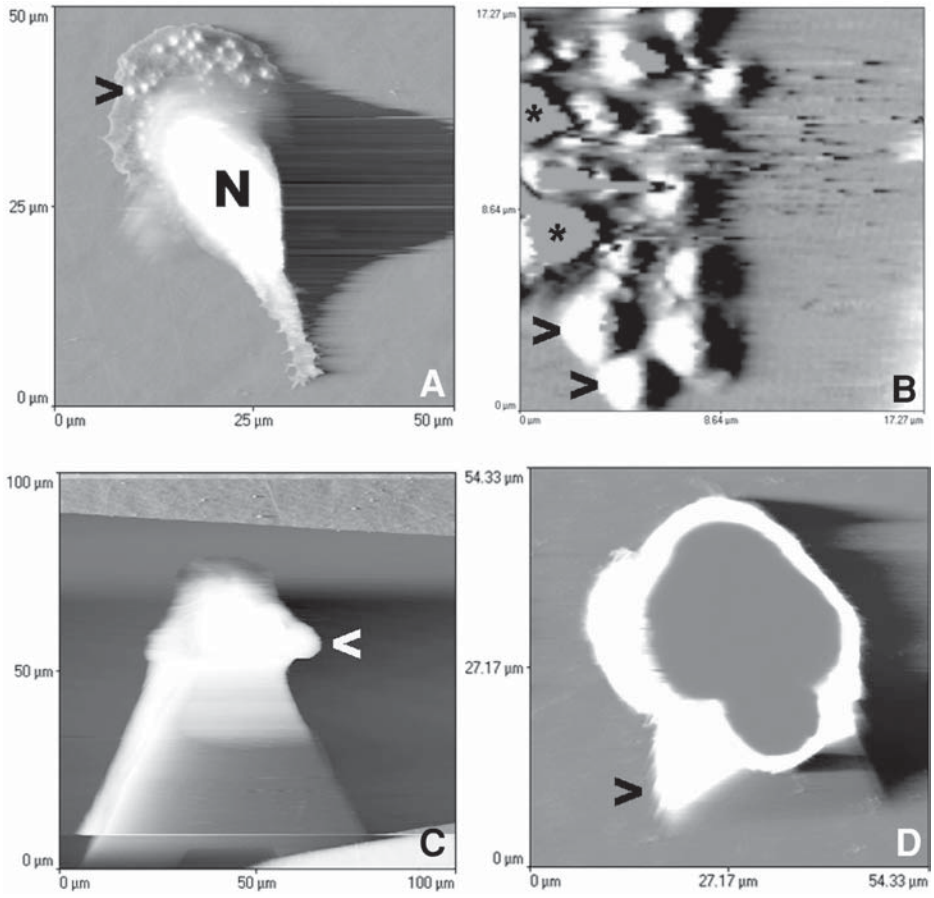

Fig. 5. Set of AFM micrographs of living liver macrophages, also called Kupffer cells (*see also* **ref. 7**). **(A)** Low magnification showing filopodial (below image) and lamellipodial (top image) spreading 20 min after seeding of the Kupffer cells. Notice numerous membrane projections (>), nucleus (N), 50 µm × 50 µm. **(B)** Living liver macrophages after phagocytosis of latex beads of 3 µm diameter. Only beads in the peripheral parts of the cells could be imaged (>). Most of the beads were depicted with saturated image information (*) because the height of the cells after phagocytosis exceeded the limits of the z piezo, 17.3 µm × 17.3 µm. **(C)** AFM image showing at the end of the cantilever a Kupffer cell (<), which is trying to phagocytose the tip and as a consequence loosing grip with the substrate, 100 µm × 100 µm. **(D)** In some cases macrophages do not attach well to the substrate and probably forms structures on top of their surface, which have sharper contours than the AFM tip. As a consequence, these structures give rise to artefactual pyramidal tip images (>), 54 µm × 54 µm.

4. Notes

1. Collagen solution PC-3 (ICN, cat. no. 152391) can be used as an alternative for collagen-S.
2. The pH of the medium during AFM imaging was stabilized in the physiological range of pH 7.4 by using growth medium enriched with 25 m*M* HEPES. When HEPES is used in combination with exogenous gas, it is important that the HEPES concentration must be more than double for adequate buffering, that is, 2% CO_2 approx 10 m*M* HEPES vs 5% CO_2–50 m*M* HEPES. Importantly, concentrations higher than 25 m*M* are in general toxic for cells and HEPES should be added in addition to, not in place of, sodium bicarbonate.
3. For very soft cells, such as living liver endothelial cells, which have an elastic modulus of 1 kPa ***(13)***, cantilevers with the lowest force constant (i.e., 10 mN/m, loading force 500 pN) should be used when the maximum resolution has to be achieved. The expected theoretical resolution for a loading force of 500 pN is 300 nm, 100 nm, and 30 nm if the sample softness is 1 kPa, 10 kPa, and 100 kPa, respectively ***(6)***. However, these low-force constant cantilevers have an arm length of 320 µm, making optimal laser alignment difficult for some commercial instruments and resulting in poor feedback.
4. Spontaneous adherence to and spreading on to the bottom of culture dishes is restricted to (some) hemopoietic cells, (some) tumor cell lines, and a few other selected cell types (fibroblasts) or cell lines. Therefore, the cells to be visualized by AFM have to be checked whether they are anchorage-dependent (e.g., freshly isolated rat liver endothelial cells need an addition to the substrate) vs anchorage-independent (e.g., immortomouse liver endothelial cells can be cultured directly on glass or plastic; **ref. *8***).
5. Prewarming the dishes before seeding accelerates the process of cell spreading.
6. It is advised to use well adhering and well spread cell cultures which can be easily judged by using a routine inverted microscope. Less-adherent cells can desorb off the substrate when they become in contact with the tip, and therefore become impossible to image. However, crawling cells are an appealing topic for AFM studies ***(9)***, but precautions regarding the scan rate should be taken when studying them with the AFM (*see* **Note 15**).
7. The piezoelectric ceramics are used to generate and control scanner motion. Ideally, piezoelectric ceramic distortion is linear with applied voltage (equals linearized scanner). In principle, the present commercial scanners are corrected for nonlinear behavior. However, the scanner should be checked regularly by measuring a known sample. If nonlinearity occurs, the software of the scanner should be reinstalled or display parameters should be recalculated and adapted with the aid of a calibration sample. For more detail, all instruments contain an extended "calibration software" program in combination with a "verify calibration function." Sometimes, nonlinearities in the piezoelectric ceramics can be discovered when an image is zoomed. In this case, the image shifts from that which is desired.

8. The main advantage of imaging in liquid is the reduction of the total force that the tip exerts on the sample, since the large capillary force is isotropic in liquid. Therefore, it is important that the cantilever is completely submerged in the growth medium. For 35 Petri dishes we advise using 1.7 mL of liquid. Another obvious advantage of liquid imaging is the reduction in vibration caused by acoustic waves (e.g., voices; *see* **Note 12**).
9. The combined AFM/inverted microscope is preferred when AFM imaging of living cells is to be performed. This set-up allows movement of the sample via the inverted microscope independently of the AFM and enables the user to easily locate and identify the cells or areas of interest. Moreover, correlative information is obtained and therefore improves the understanding of both microscopies, providing a limit of confidence for AFM imaging of living cells. Finally, the use of a video camera installed on the eyepieces of the inverted microscope in combination with a TV monitor and a (time-lapse) video recorder is advised, but is not obligatory. Note that laser filters should be placed in the optical path to prevent laser light accidentally entering the user's eyes through the oculars. Moreover, to prevent light-induced damage to the cells, a broad-spectrum green interference filter should be placed in the light path of the microscope. This filter blocks the light with a wavelength below 510 nm, which is extremely toxic for cells and therefore prevents a decrease in cell viability. Because of the fact that the scan head is positioned in the light path of the microscope, a very simple way of illumination was chosen by the use of a fiber light source illuminating the close proximity of the objective.
10. It is advised to align always first the laser beam by using a blank 35-mm Petri dish (without cells) filled with growth medium before you start AFM imaging on a real biological sample. By doing so, the most common pitfalls can be discovered beforehand, such as false contact, thermal drift, oscillation, and vibration. Importantly, sometimes air bubbles might become trapped between the tip and glass sight-plate during mounting the tip on the liquid scanner. This can manifest in the impossibility to find the reflected laser spot when the liquid has been added in the liquid cell or the reflected laser spot can be found but appears to flicker, resulting in a rapidly varying sum signal from the photo-diode.
11. The Petri dish holder of the microscope can fit 35-mm dishes and is connected to the homemade XY specimen stage. The XY specimen stage and holder is made of stainless steel and could be heated by the heating device, which is placed on the saving of the XY specimen stage. To allow complete temperature equilibration it is advised to warm up the stage and holder one hour before imaging. By doing so, temperature fluctuations during imaging are avoided which can cause cantilever drift. For the same reason, the microscope, the laser and the electronic control units has to be switched on beforehand as well. Ideally, the whole instrument should be placed in a constant-temperature environment to avoid drift problems.
12. Vibration is the greatest source of image noise in AFM. This can be easily determined when the instrument is in feedback, that is, the internal feedback signal should be stable and noise-free (equals flat line). Therefore, to obtain the highest

resolution, the AFM scan head together with the inverted microscope must be maintained in a vibration-free environment. Special vibration isolation tables are commercially available and isolate the AFM instruments from the ground-floor laboratory. In addition, it is advised to place the microscopic stage on a table separate from the rest of the system. Moreover, also acoustic waves can excite vibrations in the stage and should be minimized by using a plexiglas box around the scan head for example. Sometimes, the mechanical components of the sample holder and the XY specimen stage can give rise to vibrations. Therefore, attention should be paid to make the combination of scan head and XY specimen stage as rigid as possible to avoid mechanical vibration. Vibration can also be caused by the sample holder. In this case, one or two drops of corn oil between the edges of the sample and the base plate of the microscope can solve the vibration problems.

13. To assure an optimal viability of the cells, scanning of the sample should be carried out for a maximum of 2-3 hours, after which the sample should be replaced. At the end of the experiment, the viability should be checked routinely with the aid of the trypan blue (*see* **Subheading 3.4.**, **ref. *7***) and/or the propidium iodide test ***(14)***. In our combined AFM-light microscope set-up, the overall viability usually drops with $5.8 \pm 2.1\%$ every hour. In addition, the combined AFM / inverted microscope allows the cell and AFM tip to be seen by the optical microscope at all times during the scanning process (*see* **Fig. 1** and **Note 9**). By doing so, the morphology of the cells during AFM imaging can be easily judged and tip-induced alterations such as detachment of removal of the peripheral parts of the cytoplasm can be easily observed. These tip-induced changes are typical morphological signs for the onset of a decreased cell viability ***(15)***.
14. The loading forces should be kept as low as possible under all imaging conditions. A general idea about the force applied can be obtained by multiplying the force conversion factor (feedback) with the set point value, for example, 0.208 nN/nA $\times$ 30 nA = 6 nN. The application of high loading forces become apparent when an enhanced number of streaks are observed. This type of artifact is caused by the interaction of the tip and the sample surface and may damage your preparation. Streaking can be easily diagnosed by changing the scan direction, which should result in concomitant streaking. Streaking is more frequent when the samples are imaged under air and dry conditions resulting from the supplementary capillary forces ***(16–18)***.
15. Optimize the scan rate during scanning to avoid smearing artefacts due to tip-sample interaction. Sometimes it is possible to scan a sample so fast that the z piezo cannot react quickly enough to the motion of the cantilever. Therefore, typically the scan rate is set to two times the scan range, for example, for a scan range of 10 µm, the scan rate would be set to 20 µm/s. For moving cells ***(9)*** or less-adherent ***(19)***, cells the scan range should be set ideally on half of the scan range, for example, for a scan range of 10 µm, the scan rate is 5 µm/s. In addition, feedback parameters should be optimized as well (*see* **Note 16**).
16. It is of great importance to adjust feedback (proportional, integral, and derivate) and scan (rate, size, set point) parameters to optimize image acquisition. The

optimum settings are largely dependent on the sample properties and therefore need to be determined experimentally. Adjusting the integral, controlling the response of the cantilever and z piezo to the largest topographical features induces the most noticeable improvement in image quality. Lowering this parameter too much, results in a smear out of the sample, whereas increasing results in a optimal image acquisition with regard to the size and shape. However, in our experience, changing the proportional gain, which controls how the z piezo will respond to fine structural details, did not affect the image quality. It is known that the effects of the proportional gain are more significant for smaller scan ranges (1–2 μm). Also the derivate gain was of secondary importance when cells wanted to be visualized. Although when relatively large topographic cells wanted to be visualized the derivate gain acts as a stabilizing parameter. Raising this parameter reduces unwanted oscillation and allows a higher integral gain setting. The optimal value is best determined experimentally and varies from cell to cell type and scan rate used.

17. Once in feedback, the signal should be stable and have no noise. If not, move the tip away from the cells by increasing the set point (>60%). Alternatively, move the tip closer the cells by decreasing the set point (<40%). Decreasing the set point below 20% risks tip (and cell) damage.
18. Noncontact AFM takes place without physical contact between the tip and the sample and for this reason it is the AFM mode of choice for scanning soft samples (1–10 kPa), such as living cells. Another advantage of this imaging mode is the reduction of the lateral forces that can push the sample around or smear out surface features. It has to be emphasized that the mean drawback of non-contact imaging is the increased acquisition time necessary when (fast) dynamic biological processes are to be visualized. For living cells, the scan rate (*see* **Note 15**) and integral gain (*see* **Note 16**) are the critical parameters for noncontact imaging ***(10,17)***.

Acknowledgments

This work was supported by the Fund for Scientific Research–Flanders, Grant No. 1.5.411.98 and partially by the Free University of Brussels (Ignace Vanderscheuren Price–Biomedicine 2000). F. Braet is a postdoctoral fellow of the Fund for Scientific Research - Flanders. Our AFM work would have been impossible without the collaboration with other departments. Special thanks to Dr. Wouter Kalle (Waga Waga, Australia) and Prof. Dr. Manfred Radmacher (Georg-August Universität Göttingen, Germany) for introducing us in the world of AFM. The authors would also like to thank TopoMetrix Santa Clara, California (Dr. Steffan Kämmer), the Laboratory for Cytochemistry and Cytometry of the State University of Leiden (Prof. Hans J. Tanke), and the Department of Applied Physics of the Technical University of Twente (Prof. Bart G. de Grooth) for their valuable collaboration, advice, and technical support.

References

1. Binnig, G., Quate, C. F., and Gerber, C. H. (1986) Atomic force microscope. *Phys. Rev. Lett.* **56,** 930–933.

2. Henderson, E., Haydon, P. G., and Sakaguchi, D. S. (1992) Actin filament dynamics in living glial cells imaged by atomic force microscopy. *Science* **257,** 944–1946.
3. Radmacher, M., Tillman, R. W., Fritz, M., and Gaub, H. E. (1992) From molecules to cells: imaging soft samples with the atomic force microscope. *Science* **257,** 1900–1905.
4. Lillehei, P. T. and Bottomley, L. A. (2000) Scanning probe microscopy. *Anal. Chem.* **72,** 189R–196R.
5. Nagao, E. and Dvorak, J. A. (1998) An integrated approach to the study of living cells by atomic force microscopy. *J. Microsc.* **191,** 8–19.
6. Radmacher, M. (1997) Measuring the elastic properties of biological samples with the AFM. *IEEE. Eng. Med. Biol. Mag.* **16,** 47–57.
7. Braet, F., Seynaeve, C., De Zanger, R., and Wisse, E. (1998) Imaging surface and submembranous structures with the atomic force microscope: A study on living cancer cells, fibroblasts and macrophages. *J. Microsc.* **190,** 328–338.
8 Braet, F., De Zanger, R., Seynaeve, C., Baekeland, M., and Wisse, E. (2001) A comparative atomic force microscopy study on living skin fibroblasts and liver endothelial cells. *J. Electron Microsc. (Tokyo)* **50,** 283–290.
9. Braet, F., Vermijlen, D., Bossuyt, V., De Zanger, R., and Wisse, E. (2001) Early detection of cytotoxic events between hepatic natural killer cells and colon carcinoma cells as probed with the atomic force microscope. *Ultramicroscopy* **89,** 265–273.
10. Braet, F., De Zanger, R., Kämmer, S., and Wisse, E. (1997) Noncontact versus contact imaging: An atomic force microscopic study on hepatic endothelial cells in vitro. *Int. J. Imaging Syst. Technol.* **8,** 162–167.
11. Freshney, I. (1987) Measurement of cytotoxicity and viability, in *Culture of animal cells—A Manual of Basic Techniques* (Freshney, I., ed.), A. Liss, New York, pp. 245–256.
12. Braet, F., Kalle, W. H. J., De Zanger, R., de Grooth, B. G., Raap, A. K., Tanke, H. J., et al. (1996) Comparative atomic force and scanning electron microscopy: An investigation on fenestrated endothelial cells in vitro. *J. Microsc.* **181,**10–17.
13. Braet, F., Rotsch, C., Wisse, E., and Radmacher, M. (1998) Comparison of fixed and living liver endothelial cells by atomic force microscopy. *Appl. Phys. A* **66,** S575–S578.
14. Weyn, B., Kalle, W., Kumar-Singh, S., Van Marck, E., Tanke, H., and Jacob, W. (1998) Atomic force microscopy: Influence of air drying and fixation on the morphology and viscoelasticity of cultured cells. *J. Microsc.* **189,** 172–180.
15. Schaus, S. S. and Henderson, E. R. (1997) Cell viability and probe-cell membrane interactions of XR1 glial cells imaged by atomic force microscopy. *Biophys. J.* **73,** 1205–1214.
16. Braet, F., De Zanger, R., Kalle, W. H. J., Raap, A. K., Tanke, H. J., and Wisse, E. (1996) Comparative scanning, transmission and atomic force microscopy of the microtubular cytoskeleton in fenestrated endothelial cells. *Scan. Microsc.* **10,** 225–236.
17. Kalle, W. H. J., Braet, F., Raap, A. K., de Grooth, B. G., Tanke, H., and Wisse, E (1997) Imaging of the membrane surface of sinusoidal rat liver endothelial cells

by atomic force microscopy, in *Cells of the Hepatic Sinusoid 6* (Wisse, E., Knook, D. L., Balabaud, C., eds.), Kupffer Cell Foundation, Leiden, pp. 94–96.
18. Braet, F., De Zanger, R., and Wisse, E. (1997) Drying cells for SEM, AFM and TEM by hexamethyldisilazane: A study on hepatic endothelial cells. *J. Microsc.* **186,** 84–87.
19. Rotsch, C., Braet, F., Wisse, E., and Radmacher, M. (1997) AFM imaging and elasticity measurements on living rat liver Kupffer cells. *Cell Biol. Int.* **21,** 685–696.

16

Atomic Force Microscopy of Protein Complexes

Olga I. Kiselyova and Igor V. Yaminsky

1. Introduction

Scanning probe microscopy (SPM) is a rather new family of surface studies methods, having broad applications to biomedical science. The main advantage of SPM over conventional microscopic techniques (i.e., scanning and transmission electron microscopy) is its ability to study living objects in their natural environment and, therefore, the ability to observe dynamical processes occurring to them with subnanometer resolution. Here, we will discuss one of its family members, atomic force microscopy (AFM), which has yielded fascinating results for the past decade.

AFM is a surface science technique and, thus, requires the immobilization of the studied object on a flat rigid support (substrate). A crystalline microtip attached to a cantilever is brought in contact with the investigated surface. The deflection of the cantilever is roughly proportional to the force of interaction between the tip and the surface. It can be registered by the deflection of a laser beam directed to the reflective surface of the cantilever. The electronic system maintains the constant force value, whereas the cantilever is scanning over the sample. Registration of the cantilever position normal to the sample gives the 3D surface profile. In the dynamical (or resonance) regime of registration the cantilever oscillates near the surface and the amplitude is modulated by the tip–sample interaction force. The surface profile roughly coincides with the surface of equal oscillation amplitude. (For detailed description of the AFM technique, *see* **refs. *1*** and ***2***). Probe microscopy technique does not necessarily involve the sample–light interaction and, therefore, the $\lambda/2$ restriction on resolution is removed.

Although AFM can attain the atomic resolution on inorganic crystals, on biological objects it is up to date restricted to molecular one. For that reason,

From: *Methods in Molecular Biology, vol. 242: Atomic Force Microscopy: Biomedical Methods and Applications*
Edited by: P. C. Braga and D. Ricci © Humana Press Inc., Totowa, NJ

the main fields of AFM morphological studies of proteins is the formation of nucleic acid–protein and protein–protein complexes, oligomerization, and the organization of protein molecules in biological membranes and Langmuir films (for review, *see* **ref. *3***).

Here, for an example of AFM observation of the protein oligomerization and complex formation, we reproduce the experiments in a system of membrane proteins (cytochrome P450–cytochrome P450 NADH-reductase), which we had previously reported ***(4)*** and give detailed explanations of the experimental procedure and data interpretation.

2. Materials

1. AFM with tapping mode regime (e.g. Nanoscope, Digital Instruments).
2. Cantilevers (e.g., Nanoprobe, MicroMash).
3. Liquid cell for tapping mode.
4. Supports: highly oriented pyrolytical graphite (HOPG), mica.
5. Protein solution.
6. Tridistilled water.
7. Buffers for the protein under consideration.
8. Double-sided adhesive tape.
9. Metal discs.
10. Filter paper.

3. Methods

The cornerstone of successful imaging by AFM is a proper sample preparation, which can be considered as a sort of art. Preparation technique includes the correct choice of the substrate for immobilization, the adjustment of specimen concentration and buffer ionic strength, drying conditions (if necessary).

3.1. Choosing the Substrate

The main properties a good substrate should posses is flatness (a monocrystal plane would be ideal), rigidity and the studied objects' high adhesion to it. The choice of the substrate material is usually guided by the a priori information about the object's properties. Moreover, for biological research it is favorable to have a set of substrates with different hydrophobicity and surface charge of different sign. Comparing the images of the same object fixed on substrates with hydrophillic and hydrophobic surfaces one can reveal its surface properties. The strength of adhesion and the distribution on the substrate show whether the object's surface is polar, hydrophobic, or positively/negatively charged. This information is of special importance in complex formation studies, indicating which parts of molecules are in contact with each other, and which, with the solvent.

In biological SPM research, two substrates are the most widely used and are the simplest to handle: HOPG and mica. These two materials do not require any preliminary cleaning because simple cleavage (using tweezers or adhesive tape) yields atomically flat crystalline planes of considerable area (tens and hundreds of square microns) practically devoid of defects. Subsequent cleavage of the used plate allows reusing it many times.

HOPG has hydrophobic neutral surface, composed of flat terraces separated by steps. After anodization, the HOPG surface becomes hydrophilic and can be used for covalent binding of proteins (**Note 1**; **refs. *5–7*).**

The surface of mica is, on the contrary, polar, negatively charged, and has high adhesion to many biological specimens. Unfortunately for microscopists, a material with similar properties, but with positively charged surface, has not been found yet. To recharge mica surface, a variety of procedures has been elaborated. The simplest are based on divalent cationic treatment ***(8,9)***, others imply more complicated lipid monolayer application ***(10,11)***, or one of the most progressive techniques of silanization ***(12,13)***. Polypeptide coating produces rough surface and can be used for visualization of whole cells or organelles ***(14,15)***. Description of other possible substrates, such as silicon wafers ***(16)***, evaporated gold films ***(17)***, and Au(111) facets ***(18)***, can be found elsewhere (**Note 2**).

3.2. Applying the Sample

The visualization of proteins requires special attention to be paid to the application of material onto the substrate and to related aspects of the sample purity and possible contamination artifacts. The two main techniques of application of protein molecules onto the substrate are direct adsorption and Langmuir film transformation. The latter technique, having certain advantages for amphiphylic molecules, for example membrane proteins, is described elsewhere ***(19,20)***. Covalent binding of the proteins to previously applied lipid films or silanized surfaces is specimen specific and requires a detailed description, which can be found elsewhere ***(21,22)***. Electrochemical deposition ***(23)*** and covalent binding ***(5)*** of protein molecules onto anodized HOPG surface are used mainly in scanning tunneling microscopy.

The direct adsorption technique implies, as can be understood from its name, a direct application of the protein solution droplet (several microliters) onto the prepared substrate. Then it is left to adsorb for several minutes, after which the unbound material is rinsed by the same buffer as containing the protein. The exact time of exposition depends on the protein concentration and the adhesion rate and should be adjusted experimentally. Typically used protein concentrations range between 1 μg/mL and 1 mg/mL. After adsorption the

researcher has two choices: to place the sample into the liquid cell of the microscope, add more buffer if necessary and start *in situ* imaging or to dry the sample first and image in air.

Although the second choice does not profit all the AFM potential, it is much easier to perform, and we can recommend it to beginners or as a first step of the experiment. Dried material better adheres to the substrate and cantilever tuning is much easier as well. After drying of the buffer solution, all contaminants and salts containing the drop bulk remain on the surface, sophisticating the objects' identification. Working in liquid facilitates this problem, but on the other hand decreases adhesion stability of the molecules on the substrate. For that reason, before drying, the samples are rinsed with distilled water. The remaining water can be removed by the airflow, then contaminants of the solution will also leave the surface.

Despite all that precautions artifacts are quite often registered in AFM images of the adsorbed proteins, obtained both in liquid and air. Typically, these artifacts are all images of residual contaminants and have the shape of protrusion 3–5 nm in diameter and can be easily mistaken for protein molecules themselves. It is usually the height of the artifacts (1 nm and less) that allows one to distinguish them from the adsorbed protein molecules (**Note 3**).

3.3. AFM Imaging

AFM measurements start with cantilever tuning. In tapping mode lateral tip–sample forces are minimized, which helps to avoid sweeping of the adsorbed material by the tip during scanning. Contact mode silicon nitride cantilevers (Nanoprobe) with a force constant of 0.3–0.6 N/m or Ultrasharp cantilevers of NSC17 series (MicroMash, Estonia) give reliable results for tapping mode imaging of protein molecules in liquid. Samples dried in airflow can be imaged with NanoSensors tapping mode etched silicon probes or cantilevers from noncontact series produced by other manufacturers. The set of parameters is individual for each system. The oscillation amplitude depends on the cantilever's resonant properties. The amplitude of free resonant oscillations A_0 can be chosen between 10 and 50 nm. The aspect ratio of loaded vs free oscillation amplitude A_S/A_0 should be kept in the interval of 0.8–0.9 for air imaging and 0.90–0.95 for imaging in liquid.

Scan rates in tapping mode are relatively low (1–3 Hz, depending on the field size). For imaging individual protein molecules, it is recommended to get several 2×2 μm^2 images first (to get the idea of coverage density and choose an appropriate area) and then proceed to more detailed 0.5×0.5 μm^2 ones (**Note 4**; **ref. *24***).

3.4. Image Interpretation

In SPM the interpretation of images is a key role task, more complicated than obtaining the images. The registered objects are not "labeled" and it is normally their shape and size that serves as criterion to distinguish between them.

It is well established that apparent lateral dimensions of all AFM-imaged objects are overestimated as a result of the influence of the geometry of the probe tip, that has finite size, typically 5–10 nm, that is, the same order that a protein molecule. This can be illustrated by a simple geometrical example (**Fig. 1A**; **ref. *25***).

$$d = 2\sqrt{r^2 + 2Rr}$$

Here, we roughly consider a protein molecule as a sphere with radius r and the probe having a spherical tip with radius R. The depicted trajectory of the tip during scanning and thus the image profile has bell-like shape. Evidently, the apparent diameter d measured at half height does not coincide with the real diameter of the molecule. A real cross-section profile taken from the AFM image of a protein molecule (cytochrome P450) is shown in **Fig. 1B**. Simple geometrical calculations yield the formula for this "tip-broadening" effect.

Knowing the tip radius R one can estimate the real diameter of molecule D

$$D = 2r = 2\left(\sqrt{R^2 + d^2/4} - R\right)$$

In practice, the tip is not an ideal sphere of radius R, and its dimensions are usually not known precisely and differ from tip to tip. Moreover, real molecules are not spherical and can be deformed, which makes the above-mentioned calculations very approximate. For this reason, single objects' lateral dimensions are seldom used in analytical measurements, whereas vertical dimensions are preferable in calculations. A more complicated model of elliptical sample is described elsewhere ***(26)***.

A successful AFM image of adsorbed globular protein molecules is a set of dots (*see* **Fig. 2**). Assuming the protein does not oligomerize and the shape is roughly spherical, the dots are round and of equal size. The histogram of height distribution shows a single peak (**Fig. 3A**). In this article we will use the molecules height, measured on the cross-section made along the scan line (*see* **Fig. 1B** for example of cross-section). Apparent diameter measured at half height, D, can be used for general description or rough estimation of the lateral dimensions. If the molecules are spherical, the peak is very narrow, because all the molecules are identical. If the shape is asymmetric, the peak is widened. The

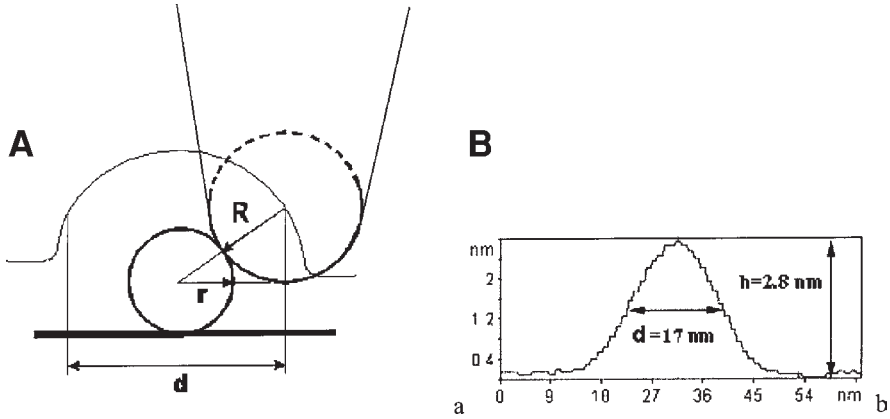

Fig. 1. **(A)** Illustration of the tip-broadening effect resulting from the tip geometry. R, tip radius, r, molecule radius; d, apparent molecule diameter. **(B)** A real cross-section profile taken from the AFM image of a protein molecule (cytochrome P450).

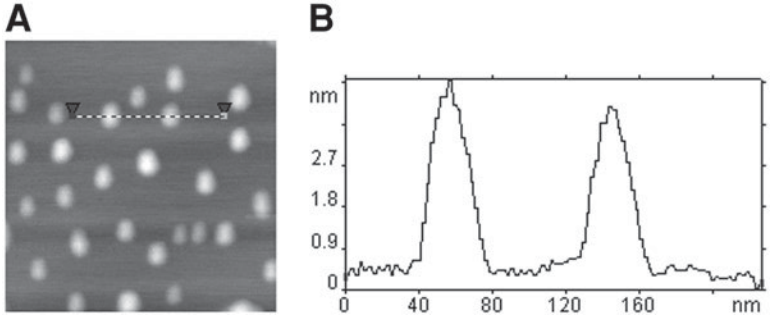

Fig. 2. Molecules of Fp in monomer form adsorbed on HOPG surface **(A)**. Image size 0.3×0.3 μm^2; **(B)** cross-section made along the marked line in **(A)**.

molecules can adhere to the substrate with different sites, and therefore, different parts contribute to the height measurements (*see* **Fig. 4**).

If the asymmetry is considerable, for example one deals with dimers composed of two spherical globules, the histogram might show several peaks *(27)*. Comparing the relative heights of the peaks one can calculate the probability of adsorption on this or that part and the free energy of binding (**Note 5**).

When transmembranous proteins are extracted from their native membrane surrounding, their molecules form oligomers. The investigation of oligomerization and protein complexes formation by X-ray and diffraction methods is problematic because it requires crystallization of the sample. Meanwhile, the

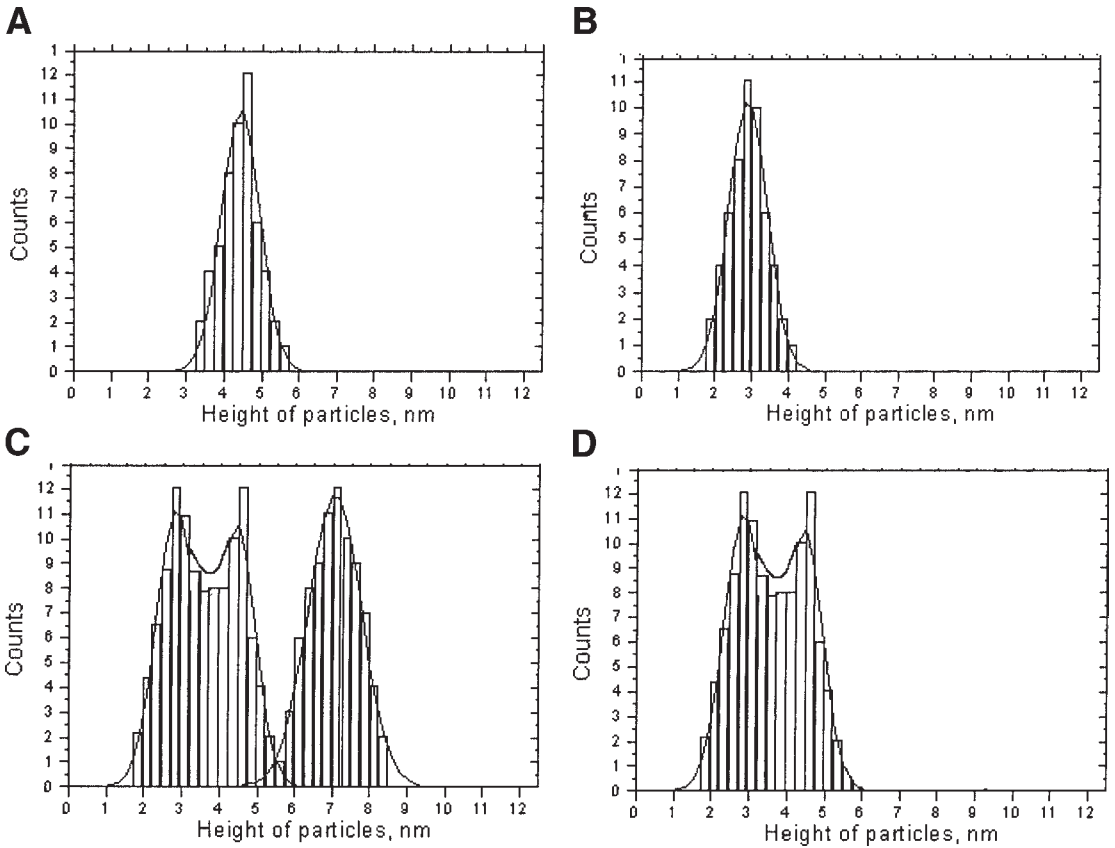

Fig. 3. Histograms of heights distribution of adsorbed proteins. **(A)** Fp; **(B)** cytochrome P450; **(C)** mixture of Fp and cytochrome P450; **(D)** mixture of noninteracting proteins.

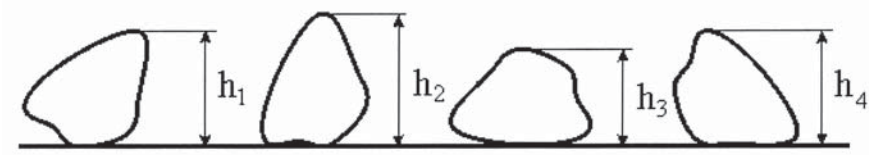

Fig. 4. Possible orientation of a protein molecule adsorbed on a flat substrae.

crystallization of transmembrane proteins is one of the most difficult crystallographic tasks.

In this chapter we describe the results on AFM studies of oligomerization and complex formation for the system of two membrane proteins: cytochrome P450 2B4 ***(28)*** and NADPH–cytochrome P450 reductase (Fp) from rabbit liver ***(29)***. These proteins are part of the microsomal monooxigenase system, playing the key role in the metabolism of drugs, cancerogenes, mutagens, and xenobiotics. Both proteins oligomerize when extracted from microsomal membranes ***(30,31)***.

AFM demonstrates the efficiency of the monomerization procedure previously described ***(4)*** for these proteins. **Fig. 2** depicting individual Fp molecules adsorbed on HOPG is a typical example of AFM image of adsorbed protein in monomer form. The distribution of heights is reflected by the histogram (**Fig. 3A**). The height of the molecules is 4–5 nm, the apparent diameter *d* is 20–22 nm. The histogram consists of a single peak, which indicates that one is dealing with one sort of particles. In order to confirm the fact that Fp is in the monomer form, one should compare the obtained dimensions with independent data. Despite the lack of crystallographic data, the average radius of a protein globule *r* in Angströms can be roughly estimated using a simple formula for spherical molecules cited by ***(19)***:

$$r = 0.717\ M^{1/3},$$

where *M* is the protein's molecular weight in Daltons.

For the Fp with molecular weight of 60 kDa, it yields $r = 2.8$ nm. Therefore, the expectation for the average height in AFM image is 5.6 nm. The registered value of 4.5 nm is quite close. The experimental value of height may be underestimated due to the deformation, caused by the tip's pressure ***(32)***. Thus, we can be sure that the obtained image demonstrates Fp monomers. Following the same procedure, the AFM image of cytochrome P450 2B4 on HOPG can be obtained (data not shown). The overall appearance of most globular proteins AFM images is very similar and the measurements of heights are necessary for their sizes evaluation. Height distribution histogram for cytochrome P450 is presented in **Fig. 3B** (**Note 6**).

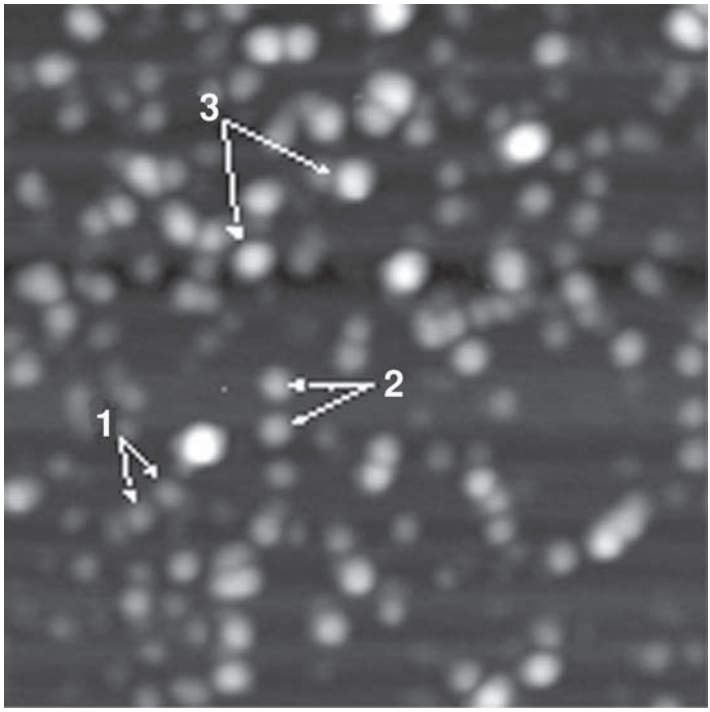

Fig. 5. Mixture of Fp and cytochrome P450 molecules in monomer form adsorbed on mica surface. Image size 540 × 540 nm^2. Arrows indicate: 1, cytochrome P450; 2, cytochrome P450 NADPH-reductase (Fp); 3, complexes of cytochrome P450 2B4 with Fp (P450/Fp).

Complexes of cytochrome P450 2B4 and NADPH-cytochrome P450 reductase (2B4/Fp) were obtained by mixing respective solutions of monomer proteins of the same molar concentrations. After the incubation, the mixture was diluted and applied onto the substrate.

The AFM image of the mixture applied onto mica substrate is depicted in **Fig. 5**. The image represents a variety of dots of different sizes, which visually seem chaotic. Because the initial mixture contained Fp monomers and cytochrome P450 monomers, the AFM image can represent those and, possibly, the product of their interaction, that is, complexes. The identification of the observed particles is based on the heights distribution.

The histogram of heights' distribution consists of three peaks (**Fig. 3C**). The position of the first peak (2.5–3.0 nm) coincides with that of the peak at the histogram for cytochrome P450 2B4 (**Fig. 3B**), that is, it represents cytochrome P450 2B4 monomers. The second one (the height of 4–5 nm) corresponds to

Fp monomers (compare with **Fig. 3A**). If the two proteins did not interact, the histogram of the mixture would be the sum of the two independent ones and would contain two peaks (**Fig. 3D**). But the experimental histogram (**Fig. 3C**) shows the third peak, located at 6–8 nm, corresponding to complexes of cytochrome P450 2B4 and NADPH-cytochrome P450 reductase (2B4/Fp). The molecules of cytochrome P450, Fp, and 2B4/Fp are indicated by arrows with respective numbers in **Fig. 5**.

Using the technique described above, one can investigate the oligomerization of each of the two proteins in the absence of detergent and qualitatively reveal the dependency of the oligomerization percent versus the protein concentration and buffer ionic strength. AFM image of the oligomers of cytochrome P450 (**Fig. 6A**) is apparently similar to that of P450/Fp mixture. Individual monomers within oligomers are not resolved. For the estimation of oligomers percentage one can make height distribution histograms and determine the size of oligomers (**Fig. 6B**; **Note 7**). Determination of the number of particles in each oligomer requires a geometrical model. The choice of the model depends on the ratio of sizes and *a priori* knowledge of the molecule properties.

4. Notes

1. If steps are not seen in the image of $10 \times 10\ \mu m^2$, either the user is very lucky to have an extremely high quality material, or the feedback system of the microscope is not working properly). When using HOPG one has to be careful about artifacts, which are now well established ***(6,7)***.
2. Because long contact with the atmosphere contaminates the substrate surface, cleavage should be performed right before the application of the sample. Before using a certain substrate for a biological experiment it is strongly recommended to get a few images of it to check for possible defects and artifacts.
3. It is strongly recommended to get several control AFM images of the buffer solution used (using the preparation technique described above) and compare them to protein molecules images, in order to reveal possible contamination artifacts. Much attention should be paid to the purity of water and chemicals.
4. It is important to bear in mind that A_0 and A_s/A_0 parameters might influence the apparent height of the biological objects imaged, introducing up to 15% error (for details, *see* **ref. *24***). Therefore, for analytical measurements it is recommended to use the same parameters for images one is going to compare. Using the same cantilever would be the best.
5. If the tip happens to be asymmetric, the AFM image of a spherical particle reflects the tip's shape and can be triangle, elliptical, or other. If so, the orientation of the figure is the same for all particles registered in the field. It is recommended to rotate the sample manually and see if the pattern rotates, too. If it is due to the

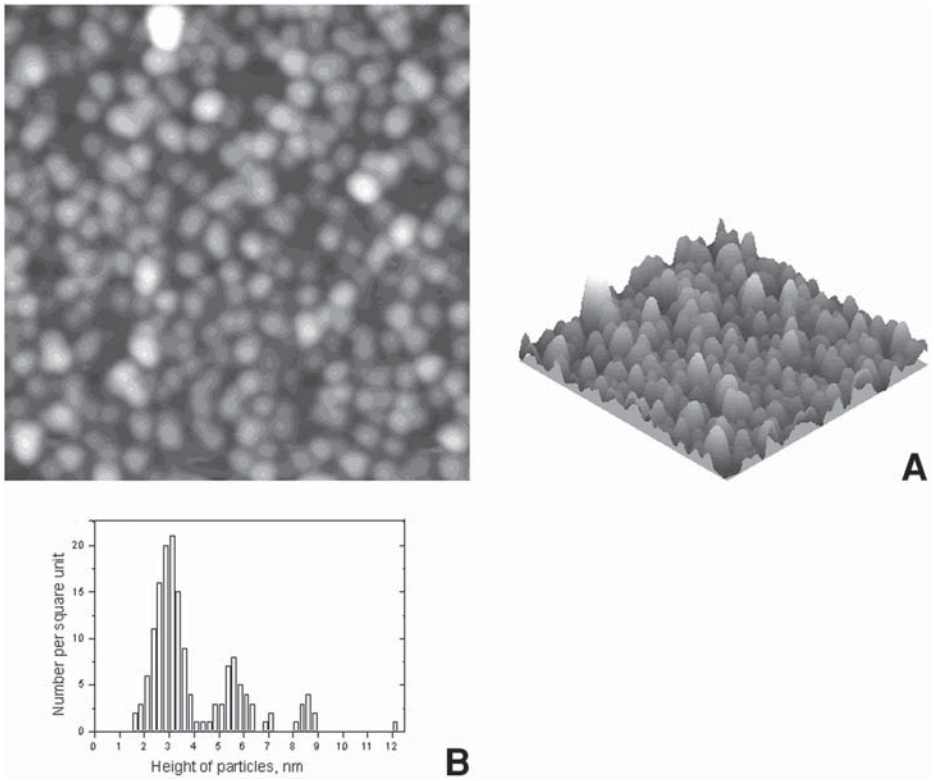

Fig. 6. **(A)** Molecules of cytochrome P450 in oligomer form adsorbed on mica surface, 2D and 3D images, respectively. Image size is 480×480 nm^2. **(B)** Histogram of height distribution shows three peaks. The first (approx 3 nm) corresponds to monomers, the second (approx 5.5 nm) and the third (8.5 nm), presumably octamers and 12–30-mers, respectively.

tip's asymmetry, the orientation of figures does not change.

6. Here and further in that chapter we imaged dried samples. Such an approach is justified because the monomer–oligomer state is believed not to change upon drying. Detergents containing in the buffer often produce foam, and the bubbles do not allow imaging with a microscope with light detection of cantilever position.
7. The two proteins and their complex may have different adsorption rate to the substrate used. Therefore, one has to be careful when using the height of peaks at the histogram for the estimation of the relative part of complexes formed. If such estimations are really essential, it is recommended to calculate the amount of single molecules of one of the proteins and compare it to that adsorbed from this protein solution of the same concentration on the same area. The difference will indicate the amount, forming the complex.

Acknowledgments

This work was supported by INTAS (grant no. 01-0045), Russian Foundation for Basic Research (Grant nos. 00-04-55020 and Russian Ministry of Science and Technology (Grant no. 40.012.1.1.1151).

References

1. Binnig, G., Quate, C. F., and Gerber, Ch. (1986) Atomic force microscope. *Phys. Rev. Lett.* **56,** 930–933.
2. Meyer, G., and Amer, N. M. (1988) Novel optical approach to atomic force microscopy. *Appl. Phys. Lett.* **53,** 1045–1047.
3. Kiselyova, O. I., and Yaminsky, I. V. (1999) Proteins and membrane-protein complexes. *Colloid J.* **61,** 1–19.
4. Kiselyova, O. I., Yaminsky, I. V., Ivanov, Yu., D., Kanaeva, I. P., Kuznetsov, V. Yu., et al. (1999) Study of membrane proteins, cytochrome P450 2B4, and NADPH-cytochrome P450 reductase and their complex formation. *Arch. Biochem. Biophys.* **371,** 1–7.
5. Zhang, J., Chi, Q., Dong, S., and Wang, E. (1996) In situ electrochemical scanning tunneling microscopy investigation of structure for horseradish peroxidase and its electrocatalytic property. *Biochem. Bioenergetics* **39,** 267–274.
6. Chang, H. and Bard, A. J. (1991) Observation and characterization by scanning tunneling microscopy of structures generated by cleaving highly oriented pyrolytic graphite. *Langmuir* **7,** 1143–1153.
7. Dunlap, D. D. and Bustamante, C. (1989) Images of single-stranded nucleic acids by scanning tunneling microscopy. *Nature* **324,** 204–206.
8. Bustamante, C., Vesenka, J., Tang, C. L., Lees, W., Guthhold, M., and Keller, R. (1992) Circular DNA molecules imaged in air by scanning force microscopy. *Biochemistry* **31,** 22–26.
9. Vesenka, J., Guthhold, M., Tang, C. L., Keller, R., Delaine, E., and Bustamante, C. (1992) Substrate preparation for reliable imaging of DNA molecules with the scanning force microscope. *Ultramicroscopy* **42–44,** 1243–1249.
10. Onishi, S., Hara, M., Furuno, T., Okada, T., and Sasabe, H. (1993) Direct visualization of polypeptide shell of ferritin molecule by atomic force microscopy. *Biophys. J.* **65,** 573–577.
11. Kacher, C. M., Weiss, I. M., Stewart, R. J., Schmidt, C. F., Hansma, P. K., Radmacher, M., et al. (2000) Imaging microtubules and kinesin decorated microtubulesusing tapping mode atomic force microscopy in fluids. *Eur. Biophys. J.* **28,** 611–620.
12. Lyubchenko, Yu., L., Shlyakhtenko, L. S., Harrington, R. E., Oden, P. I., and Lindsay, S. M. (1993) Atomic force microscopy of long DNA: Imaging in air and under water. *Proc. Natl. Acad. Sci. USA* **90,** 2137–2140.
13. Shlyakhtenko, L. S., Potaman, V. N., Sinden, R. R., and Lyubchenko, Yu, L. (1998) Structure and dynamics of supercoil-stabilized DNA crusiforms. *J. Mol. Biol.* **280,** 61–72.

14. Bolshakova, A. V., Kiselyova, O. I., Filonov, A. S., Frolova, O., Yu., Lyubchenko, Y. L., and Yaminsky, I. V. (2001) Comparative studies of bacteria with atomic force microscopy operating in different modes. *Ultramicroscopy* **68,** 121–128.
15. Vater, W., Fritzsche, W., Schaper, A., Bohm, K. J., Unger, E., and Jovin, T. M. (1995) Scanning force microscopy of microtubules and polymorphic tubulin assemblies in air and in liquid. *J. Cell Sci.* **108,** 1063–1069.
16. Mazeran, P.-E., Loubet, J.-L., Martelet, C., and Theretz, A. (1995) Under buffer SFM observation of immunospecies adsorbed on a cyano grafted silicon substrate. *Ultramicroscopy* **60,** 33–40.
17. Andersen, J. E.T., Moller, P., Pedersen, M. V., and Ulstrup, J. (1995) Cytochrome c dynamics at gold and glassy carbon surfaces monitored by in situ scanning tunnel microscopy. *Surface Sci.* **325,** 193–205.
18. Leggett, G. J., Davies, M. C., Jackson, D. E., Roberts, C. J., Tendler, S. J. B., and Williams, P. M. (1993) Studies of covalently immobilized protein molecules by scanning tunneling microscopy: The role of water in image contrast formation *J. Phys. Chem.* **97,** 8852–8854.
19. Guryev, O. L., Dubrovsky, T., Chernogolov, A., Dubrovskaya, S., Usanov, S., and Nicolini, C. (1997) Orientation of cytochrome P450scc in Langmuir-Blodgett monolayers. *Langmuir* **13,** 299–304.
20. Kiselyova, O. I., Guryev, O. L., Krivosheev, A. V., Usanov, S. A., and Yaminsky, I. V. (1999) Atomic force microscopy studies of Langmuir-Blodgett films of cytochrome P450 scc (CYP11J1): Hemoprotein aggregation states and interaction with lipids. *Langmuir* **15,** 1353–1359.
21. Weisenhorn, A. L., Drake, B., Prater, C. B., Gould, S. A. C., Hansma, P. K., Ohnesorge, F., et al. (1990) Immobilized proteins in buffer solution at molecular resolution by atomic force microscopy. *Biophys. J.* **58,** 1251–1258.
22. Karrasch, S., Hegerl, R., Hoh, J. H., Baumeister, W., and Engel, A. (1994) Atomic force microscopy produces faithful high-resolution images of protein surfaces in an aqueous environment. *Proc. Natl. Acad. Sci. USA.* **91,** 836–838.
23. Zhang, J., Chi, Q., Dong, S., and Wang, E. (1995) STM of folded and unfolded haemoglobin molecules electrochemically deposited on highly oriented pyrolytic graphite. *J. Chem. Soc. Faraday Trans.* **91,** 1471–1475.
24. Kiselyova, O. I., Galyamov, M. O., Nasikan, N. S., Yaminsky, I. V., Karpova, O. V., and Novikov, V. K. (2002) Scanning probe microscopy of biomacromolecules: nucleic acids, proteins and their complexes, in *Frontiers of Multifunctional Nanosystems* (Buzanaeva, E. V., and Scharff, P., eds.), Kluwer Academic Publishers, Dordrecht, pp. 321–330.
25. Stemmer, A. and Engel, A. (1990) Imaging biological macromolecules by STM: quantitative interpretation of topographs. *Ultramicroscopy* **34,** 129–140.
26. Gallyamov, M. O., and Yaminskii, I. V. (2001) Quantitative methods for restoration of true topographical properties of objects using the measured AFM-images. 2. The effect of broadening of the AFM-profile. *Surface Invest.* **16,** 1135–1141.
27. Waner, M. J., Gilchrist, M., Schindler, M., and Dantus, M. (1998) Imaging the molecular dimensions and oligomerization of proteins at liquid/solid interfaces. *J. Phys. Chem. B.* **102,** 1649–1657.

28. Imai, Y., Hashimoto, Y. C., Satake, H., Garardin, A., and Sato, R. (1980) Multiple forms of cytochrome P450 purified from liver microsomes of phenobarbital- and 3-methylcholantrene-pretreated rabbits. *J. Biochem.* **88,** 489–503.
29. Kanaeva, I. P., Skotselyas, E. D., Kuznetsova, G. P., Antonova, G. N., Bachmanova, G. I., and Archakov A. I. (1985) Reconstruction of a membrane monooxygenase cytochrome P 450-containing system in the liver using detergents in solution. Biokhimia **50,** 1382–138.
30. Dean, W. L. and Gray, R. D. (1982) Relationship between state of aggregation and catalytic activity for cytochrome P-450LM2 and NADPH-cytochrome P-450 reductase. *J. Biol. Chem.* **257,** 14679–14695.
31. Wagner, S. L., Dean, W. L., and Gray, R. D. (1984) Effect of a zwitterionic detergent on the state of aggregation and catalytic activity of cytochrome P-450LM2 and NADPH-cytochrome P-450 reductase. *J. Biol. Chem.* **259,** 2390–2395.
32. Gallyamov, M. O. and Yaminsky, I. V. (2001) Quantitative methods of restoration of true topographical properties of the objects by measurement of AFM-images. 1. Contact deformations of the probe and the specimen. *Surface Invest.* **16,** 1127–1134.

17

Atomic Force Microscopy of Interfacial Monomolecular Films of Pulmonary Surfactant

Kaushik Nag, Robert R. Harbottle, Amiyo K. Panda, and Nils O. Petersen

1. Introduction

Pulmonary surfactant (PS) is a lipid protein complex secreted at the terminal airways of the lung. The material is secreted as lipid rich multilamellate bodies, which transforms into lipid–protein tubules, planar bilayers, and monomolecular films at the alveolar air–aqueous interface ***(1,2)***. The films reduce the surface tension of the interface and prevents lung collapse during end expiration ***(3)***. PS layers also act as a protective barrier against inhaled particles and bacteria and keeps the upper airways or bronchioles open during respiration ***(3)***. Dysfunction of PS has been implicated in various lung diseases, such as asthma, acute respiratory distress syndrome, cystic fibrosis, and pneumonia ***(4)***. The composition of PS is conserved in most air-breathing species; however, its high content of saturated phosphatidylcholine (PC) and phosphatidylglycerol (PG) is unique compared with other secretory materials and cell membranes, which lack these phospholipids ***(1,5)***. Specifically, PS contains significant amounts of dipalmitoylphosphatidylcholine (DPPC), palmitoyl-oleyl-PC (POPC) and PG (POPG), cholesterol, and small amounts (10%) of surfactant proteins SP-A, SP-B, SP-C, and SP-D ***(1)***. It is not clear to date how this lipid–protein complex functions by forming alveolar films or barrier *in situ* because such fragile and dynamic films are difficult to preserve for traditional electron microscopy ***(2,3)***. In vitro studies have focused on model lipid–protein films of PS and also by extracting the material out of lungs and studying interfacial properties of surface tension of such material using Langmuir and other surface balances ***(6–8)***. We have taken an approach of studying such surfactant films from lungs of normal as well as those in dis-

From: *Methods in Molecular Biology, vol. 242: Atomic Force Microscopy: Biomedical Methods and Applications*
Edited by: P. C. Braga and D. Ricci © Humana Press Inc., Totowa, NJ

eased states using a combination of fluorescence and atomic force microscopy (AFM) ***(9)***.

Monolayer films have also become a standard model for studying lipid–protein interactions and associations in biological membranes ***(10)***. Models of interactions of enzymes with lipid membranes, two-dimensional crystallization of proteins, the binding kinetics of soluble proteins with a substrate, and biosensor developments have also been studied using monolayer films ***(10)***. Lipid films undergo a lateral phase separation from gas to fluid to gel-like phase with increasing surface packing density driven by increasing lateral pressure ***(11)***. The inherent changes of packing the lipid in a film undergoing lateral phase separation allows for the imaging of the structures and processes associated with formation of gas, fluid, gel, and solid domains, as well as supramolecular aggregates ***(10)***. The domain structures can be imaged using fluorescence and Brewster angle microscopy directly at the air–water interface. By depositing them on solid substrate using Langmuir–Blodgett technique***(12)***, it is also possible to image them by AFM ***(12,13)***. The contrast in AFM image of these domains arises from differences in the molecular tilt and density of the lipids in the separate phases. Typical vertical height profiles, or topography, of films deposited on an atomically flat surface vary on the nanometer level ***(14–17)***. Thus AFM at an atomic resolution show fatty acid chains and lattice spacing of single molecules of DPPC within films ***(17)***. These and other AFM studies have demonstrated that mono-molecular films can be used to study the molecular structure–function properties of PS and biomembrane components ***(13,16)***. This chapter focuses on the methodology for preparation and imaging monolayer films using AFM to study lung surfactant and suggests a relatively simple method to study molecular organization and disorganization (during dysfunction ***(18)***) of lipid–protein systems at an interface.

AFM uses a sharp tip to scan the surface of materials, which are rough at the nanometer or atomic level. Because of the interactions and deflections of the tip with the corrugated surface, real-time imaging and physical properties (friction) of such surfaces are possible in air and in liquid ***(12,13)***. However, AFM imaging of lipid films with phase transitory structures is only possible in air because the amphipathic lipids phase transition or domain formation arise from the differences in tilt of the hydrocarbon chains in air. This phase heterogeneity of packing is not observed in bilayers or monolayers, from the polar headgroups in water ***(11,15)***. However, protein–lipid interactions, binding, and crystallization processes of the proteins are better imaged in AFM in the polar head-group region because in a number of situations such processes occur in a polar environment ***(12,13)***. It is also possible to image soluble or hydrophobic proteins inserted into lipid films by AFM in air because such proteins interfere

with the lipid packing ***(19)***. In case of dysfunction of surfactant as in respiratory disease, such as acute respiratory distress syndrome, leaked plasma proteins can enter the films from the lung aqueous interface and disrupt the surface activity of PS ***(4,18)***. We have used surfactant from a bovine source (bovine lipid extract surfactant, or BLES) and surfactant from a normal and ventilation injured rat lungs (dysfunctional surfactant), and studied them in planar films using AFM. The methods to form and study such films by AFM, and specific information about lipid packing of surfactant at an air–water interface obtained using AFM are discussed.

2. Materials

1. Synthetic phospholipids of high purity, such as DPPC, POPC, and a fluorescent probe 1-palmitoyl, 2-nitrobenzo-dioxo-dodecanoly phosphatidylcholine (NBD-PC) are available from Avanti Polar Lipids (Birmingham, AB) ***(6)***. These lipids are required to measure and standardize the surface pressure-area isotherms of films and to image structure formation as a model for surfactant ***(8,14,19)***.
2. Commercial clinical preparations of pulmonary surfactant, such as BLES (BLES Pharmaceuticals, London, Ontario, Canada), or calf lipid surfactant extract (ONY Inc., Amherst, NY) are available. These surfactants are used mainly in clinical trials and are commercially available as a pharmaceutical product for research. They contain most of the lipid and hydrophobic protein components of natural surfactant extracted from animal lungs, except the water soluble proteins SP-A and SP-D ***(1)***. We have also obtained surfactant from ventilation injured rat lungs ***(18)***, however a simple model for such surfactant can be prepared from a clinical source or similar materials can made from 10:1 wt/wt of (lipid/protein ratio) of BLES:serum protein mixtures.
3. High-purity organic solvents (99.1% high-performance liquid chromatography grade) chloroform and methanol are needed for solubilizing surfactant for film formation. Also small volumes of fluorescent probe NBD-PC in 2-5 micro liter (μL) of methanol can be directly added to the emulsion of the surfactant to form adsorbed films at the air-water interface. We have applied this method in conjunction with solvent spreading, and find both techniques yield similar film microstructures in the compressed films ***(19)***.
4. Doubly glass distilled and deionized water of resistivity above 18 MΩ (megaohms) is required. The second distillation in this case can be performed using dilute $KMnO_4$ to remove mainly organic surface-active contaminants. It is absolutely necessary for reproducible results (**Note 1**). Surface tension of such clean water can be measured using the surface balance and should be close 72 mN/m at 23 ± 1°C (*see* **Subheading 3.11.**).
5. Cleaned glass and mica slides are required for film deposition for AFM imaging. The glass slides can be 1 cm diameter coverslips that can fit the AFM magnetic base or freshly cleaved mica of the same dimension. In case of the glass cover slips, they need to be washed first with chloroform:methanol (2:1, vol/vol) and then rinsed in chromo-sulphuric acid and doubly distilled water. Such mica and

glass are to be dried in air and preserved in covered Petri dish and used directly during film deposition to avoid contaminants in the surrounding air from coming in contact with the surface on which the film is to be deposited.

6. A dedicated Langmuir–Wilhelmy surface balance with fluorescence imaging attachments was used in all experiments. Design and construction of such a balance is discussed in details elsewhere ***(20)***. Ours is a commercially available model (Kibron Scientific, Helsinki, Finland).
7. Scanning probe or an AFM with Silicon Nitride probes is required for film imaging ***(2,9)***. In our studies we use a DI Nanoscope IIIa (Digital Instrument, Santa Barbara, CA) scanning probe microscope with contact, tapping and tunneling mode abilities. However, other commercially available AFMs also can be used with minor alterations of the methods discussed below for films imaging. Gold-coated SiN_3 cantilevers (Wafer-113-135-22 Nanoprobe SPM tips, DI) with nominal spring constants of 0.06 or 0.38 N/m was used for contact and lateral force (friction) imaging with either a J (normal resolution) or E (high resolution) scanner.

3. Methods

3.1. Film Preparation

1. The Langmuir trough is filled with doubly distilled water, and the surface activity of this water is measured with a Wilhelmy dipping plate ***(20)***.
2. The open water interface is compressed from maximal to minimal surface area, and any surface tension drop is monitored below 72 mN/m (milli Newton/ meter) or that of a clean air-water interface. Using a suction apparatus with a sharp nozzle (Pasteur pipet), the surface contaminants are removed until the surface pressure reaches 0 mN/m or surface tension reaches 72 mN/m (*see* **Note 1**).
3. DPPC dissolved in chloroform:methanol (3:1 vol/vol) is applied drop-wise on this clean water interface using a micro-calibrated Hamilton syringe (10–50 μL) to form the monomolecular film. A total of 20 nM of phospholipid is applied, if the surface area of the trough is close to 120 cm^2 to give an area per molecule of DPPC to be 100 $Å^2$.$molecule^{-1}$ ***(6,20)***. Lung surfactant or BLES films can also be formed using exactly the same technique except because BLES is a complex lipid mixture an arbitrary or average area per molecule is calculated based on the average molecular weight of the material of 750 Da. The fluid phospholipid POPC should also have similar area per molecule as those of BLES. In case of adsorbed films (**Subheading 2.3.**), similar amounts of the surfactant solution is injected from the syringe just below the air-water interface resulting in an initial surface pressure raised to 2 mN/m. Most Langmuir surface balance software allows for automatic calculations of such film area and details of specific calculations on surfactant films are discussed elsewhere ***(6,8)***.
4. The DPPC film is rapidly compressed and the surface pressure–area profile monitored (**Fig. 1**). The phospholipid undergoes a two-dimensional phase transition, and this is seen in the pressure-area isotherms as a broad plateau around 5-8 mN/m (**Fig. 1A**). If this plateau does not occur then either the surface has not been cleaned enough, or the solvent or phospholipids contains contaminants.

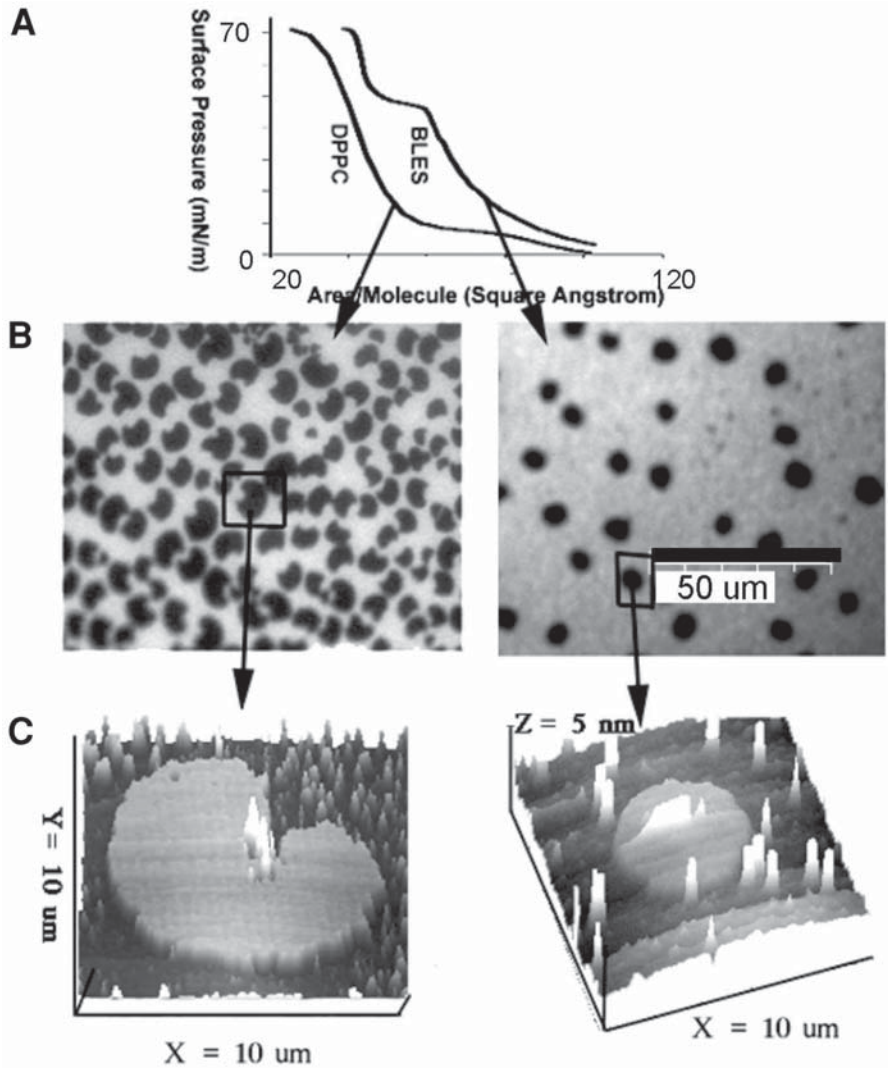

Fig. 1. Surface pressure–area isotherms of DPPC and BLES films **(A)** and typical fluorescence **(B)** and atomic force **(C)** microscope images of such films at the phase coexistence region of the isotherms (surface pressure of 16 mN/m). The plateau region of the DPPC isotherm in **(A)** suggests an expanded to condensed phase transition occurring at 4–8 mN/m. The plateau in BLES (at 45 mN/m) isotherm is possibly a higher order transition, considering that the fluid-gel transition occurs at lower pressures of 10–40 mN/m ***(6)***. The black regions in the fluorescence images **(B)** represent the gel or condensed phase and the lighter region the fluid or expanded phase, upon which the probe partitions. The gel regions have higher height than the surrounding fluid phase as seen in the deposited film shown in **(C)**, and this allows for topographical imaging of films via AFM.

5. BLES films will not show any plateau-like region below 45 mN/m (**Fig. 1A**), however a broad phase transition does occur between 5 and 45 mN/m. The BLES film isotherm would look similar to the one of POPC compressed at the same rate and initial area. This phase transition in BLES or DPPC films can be visually observed either by depositing the films and imaging them via AFM or using small amounts of fluorescent probe incorporated in the films and imaging them by fluorescence microscopy ***(20)***. Typical images taken from a DPPC and BLES films using fluorescence microscopy are shown in **Fig. 1B**. The black regions in the images are gel-phase domains coexisting with the homogeneously fluorescent fluid or bright regions.
6. Films are deposited on clean glass (**Subheading 2.5.**) or mica slides (*see* **Note 2**) by Blodgett deposition. The process requires a slow 0.2–10 $mm^2 \cdot s^{-1}$ up-stroke or vertically lifting of the slides from the subphase to air, termed as Blodgett deposition ***(14–16)***. The slides are originally placed into the subphase before spreading of the films from the solvent. The deposited films can be kept on a Petri dish with wet filter paper, for up to 2 days depending on the substrate of deposition. Films on glass substrates are more stable than mica, however other complications may arise using glass substrates (**Note 2**). Comparative AFM of the deposited films (from fluorescence imaging) showing single gel domains for DPPC and BLES are shown in **Fig. 1C**.

3.2. Film Imaging by AFM

1. Set the mode for imaging in the Nanoscope IIIa AFM to contact mode.
2. The glass or mica slide with the films are to be attached firmly to the magnetic disk or AFM base of the E (12 μm) or J (120 μm) scanner. Mount the disk onto the scanner head.
3. Attach the tip-cantilever to the metallic head of the AFM.
4. Adjust the laser to focus on the center of the tip. This is generally performed by observing the tip under an optical microscope or camera focused on the tip from above the scanner. General methodology for this is available in the manual supplied with the instrument.
5. Turn on the software program to online mode, and allow the tip to come in contact with the films surface. Set initial scan parameters to Integral Gain–2 and Proportional Gain–3, beginning with the 0 settings recommended for the instrument.
6. Perform a force calibration plot for the tip extracting and retracting at a z scan setting of 1 μm, set point = 0 volts, z-scan rate of 4–5 Hz, and *z* range to 1 μm. The tip deflection should read close 0.10 μm/div (*see* **Note 3**).
7. Open three separate channels for imaging the films in contact mode, such as channel 1, height; channel 2, deflection; and channel 3, friction. Set *x*/*y* range or scan size initially to 50 μm, and a *z* or height range to 10 nm.
8. Scan the film surface at a rate of 0.5–1 Hz (J scanner, 50–10 μm) or 2–10 Hz (E scanner 1 μm to 5 nm). The image in J scanner should appear as those shown in **Fig. 2A**. If no images appear at these settings and scanning method, adjust the integral and proportional gain in the software (*see* **Note 4**). These parameter set-

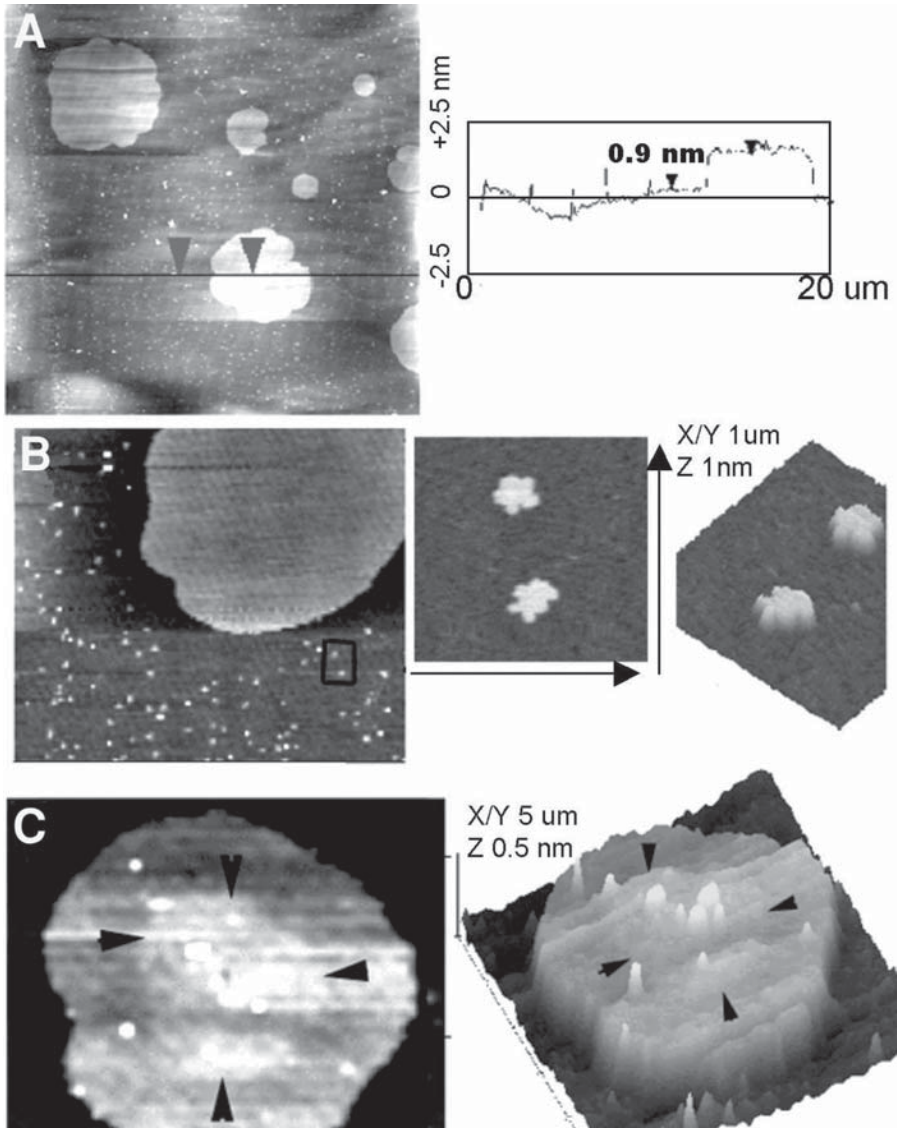

Fig. 2. AFM height mode images of solvent-spread BLES films deposited on mica. The line section analysis of the image in **(A)** suggests that the gel phase is 0.95 nm higher than the surrounding fluid phase, due to a different tilt of the phospholipid molecules in that phase compared with the fluid (*see* **Note 5**). The images in **(B)** shows that the fluid phase is not completely homogenous but has variety of micro-domains (<1 μm) as revealed by AFM and not seen in fluorescence (as in **Fig. 1B**). The gel domain **(C)** also has internal structures (region with arrows) and are possibly made with DPPC plus other saturated lipids of surfactant with differing chain lengths.

tings and methods can be found in further details in the nanoscope operation manual and has been discussed by others in details ***(13,21,22)***.

9. Save the first images and exact parameters used in files, and then zoom into various areas of the films. The zooming should be performed on the center of the condensed domains, in the fluid like phase, and at the edges of the gel-fluid regions, as shown in **Fig. 2B**. This can reveal various microstructures observed in such films beyond the gel and fluid like phase, such as smaller microstructures or domains (possibly surfactant proteins and protein–lipid aggregates) as shown in the right panel of **Fig. 2B**. The gel or condensed domains are not completely homogenous and show corrugation inside the domains as shown in **Fig. 2C**.

3.3. Structural Analysis and Interpretation of AFM Images

1. Change the setting of the software to off-line mode and choose the height mode image first.
2. The saved images in the height mode are then flattened. During flattening alter the z height between 10, 5, and 1 nm until the sharpest possible contrast between the gel and fluid phase is observed, as in **Fig 2A** the height was set to 5 nm.
3. Take a quick three-dimensional (3D) view of the image, and the gel-phase domains should be higher (brighter) than the fluid phase in such image (**Fig. 2C**).
4. Using the 2D flattened image perform a line section of the image in the vertical direction. The line should at least pass across a domain. The difference of this height between the gel and fluid phase should be around 0.8 to 1.3 nm. These height difference can reflect the molecular tilt of the phospholipids in the films (*see* **Note 5**) and are typical of the gel–fluid phase height differences as in other lipid films ***(7,14–16)***. For BLES films the height difference is about 1.3 nm and for DPPC films it is about 0.8 nm (**Figs. 1** and **3**).
5. In case of adsorbed films of rat surfactant (**Fig. 3A** and **B**) other regions of protein rich areas larger than gel or fluid domains are observed (shown by arrow). These domains are possibly adsorbed soluble proteins (**Fig. 3B**, the circular region), which has inserted into the monolayers, and interfere with the lipid pack-

---

Fig. 3. *(opposite page)* AFM height and deflection mode images of adsorbed films of (dys)functional surfactant from rat lungs. The image in **(A)** is from a film of normal rat (lung–lavage) surfactant and the one in **(B)** from the dysfunctional surfactant, in which the rat lungs underwent hyperventilation injury (*see* **Subheading 1.**) ***(18)***. The fluorescence microscopy images shown in the right side of each panel was obtained from the deposited films. The fluorescence image suggests that the edge of the gel domains (indicated by letter C in the images) in **(A)** are not smooth but contain different filamentous structure and microdomain (arrow) protruding from such domains as shown in the AFM. The large circular region or domain in **(B)** (arrow) is of different height and deflection profile compared to the fluid or gel phase, suggesting that these regions are possibly made of protein rich phase (since the estimates of soluble serum proteins in the dysfunctional surfactant was three times higher than those from normal surfactant ***[18]***).

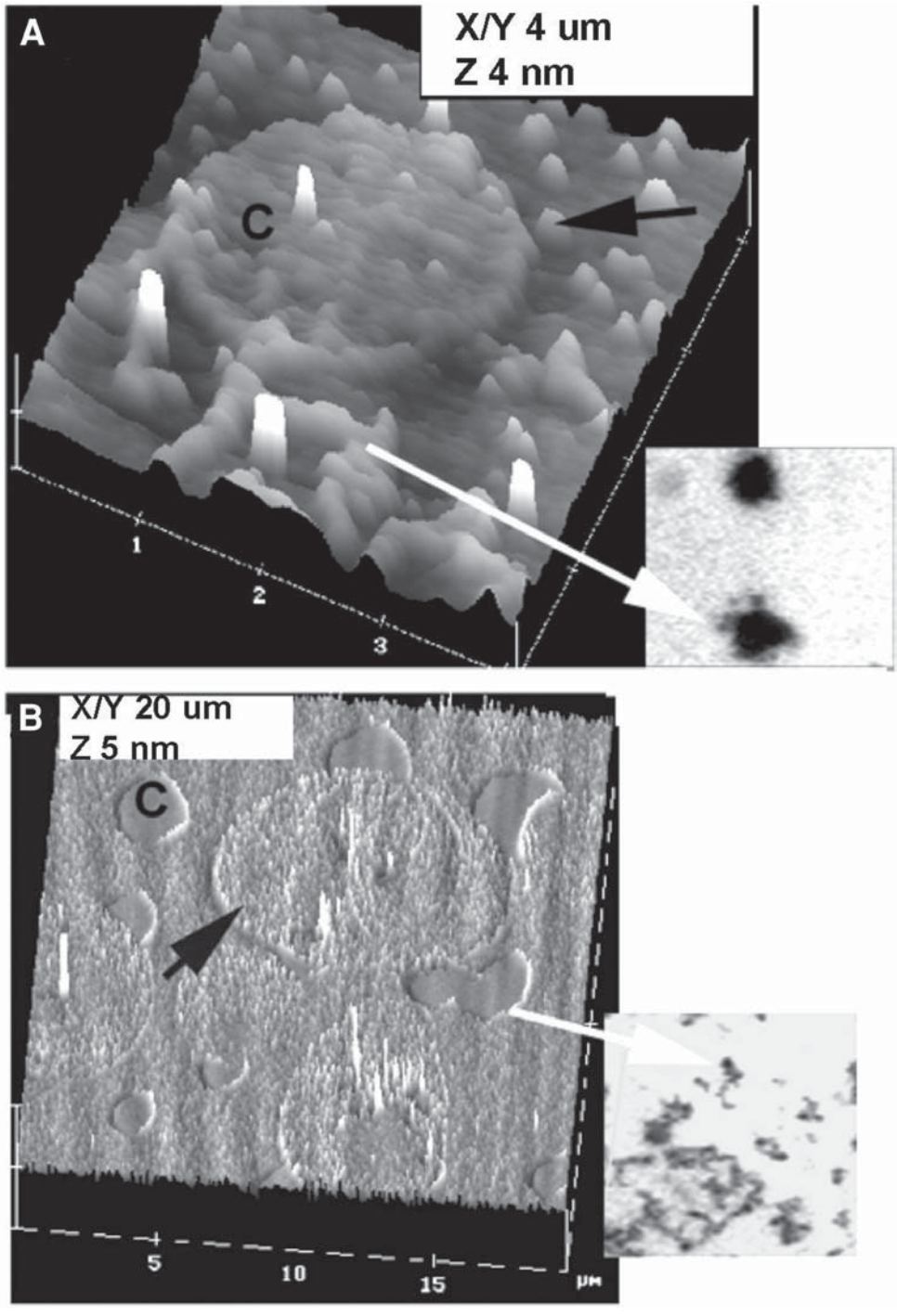
A
X/Y 4 um
Z 4 nm
C
1
2
3
B
X/Y 20 um
Z 5 nm
C
5
10
15
μm

ing. The effect of lipid packing efficacy can be monitored by measuring the gel domain diameters and height from normal vs dysfunctional surfactant films.

6. Because surfactant contains a host of other lipids and small amounts of hydrophobic proteins, various micro-heterogenous structures can be observed in the fluid-like phase. After selecting a heterogenous area, a 2D Spectral analysis using fast Fourier transform mode should be performed to observe any possible periodicity for these structures.
7. Save such analyzed images in a TIFF file (after the originals have been saved in the Nanoscope format) by exporting them for further display in normal image processing and display software for publication, image analysis and processing not supported by the AFM software. The AFM software normally allows for section analysis (line section, **Fig. 2A**), 2D Spectral and Grain size and fast Fourier transform analysis among others. Normally Adobe Photoshop, CorelDraw or NIH Imaging can allow further analysis and processing of the images.

4. Notes

1. For studies on interfacial film structures it is absolutely critical that a clean interface or water surface is maintained for all experiments. Although by doubly distilling (DDW) or deionizing the water using standard laboratory deionizers/distillation apparatus, it is possible to remove the inorganic components from water (resistivity ≈18 MΩ). However, we have observed certain surface-active (possibly organic) components enter the water during the distillation process or from the surrounding ambient laboratory environment. From our experience a second distillation of most laboratory distilled water using dilute potassium permanganate (0.01 m*M*) dissolved in this singly distilled water before the second distillation allows for quite high quality "clean" water interface. This can be easily monitored in a sensitive surface balance, by compressing the open surface of the DDW or so called "clean" interface and monitoring any change of surface tension or pressure at maximal compression or minimal surface area. Normally if there are any surface contaminants the surface pressure would increase by 2–5 mN/m at minimal surface area. At this stage, the surface can be cleaned by suction of the interface until the surface pressure drops to 0 mN/m. This clean surface is expanded further to the original surface area of the trough to 100%, and the film materials spread on this surface. Also a DPPC isotherm of a film on such a subphase, would show a sharp fluid to gel phase transition profile (*see* **Fig. 1A**) in the compression isotherm between 4–8 mN/m, if the DDW surface is clean. Surface contaminants tend to make the sharp transition more diffuse and sometimes may abolish them altogether, and can alter the typical size and shapes of the gel domains, by affecting the line tension of the gel–fluid domain boundaries ***(11,15)***.
2. It is still debated in the literature about the choice (pros and cons) of the best solid substrate to be used for film deposition for AFM ***(12,16)***. Both mica and glass surfaces are hydrophilic and therefore allow the polar regions of the films (or lipid head groups) to be deposited when they come in contact with either substrate. Although freshly cleaved mica is atomically flat and gives the best and

more accurate topographical profile of film structure at an sub-molecular resolution up to the atomic level ***(17)***, it does produce artifacts on film structures over time due to drying, since such films are scanned in air. Glass cover slips typically have surface heterogeneity (troughs and crevices) with depths exceeding 2–5 nm and therefore allow for a certain amount of the water to be trapped in the surface with the film during deposition ***(16)***. From our experience the glass substrate allows for imaging of such films for up to 3 days after deposit without any major changes of the gel or fluid domain structures of the films (as observed by fluorescence microscopy in **Fig. 1**). However the same films deposited on mica changes structure with an appearance of microstructures (smaller domains appearing in the fluid phase) within 2–-4 h of film deposit. Therefore depending on how quickly the films are scanned after deposit and the range of height resolutions required (<20 nm to >1 nm), glass or mica substrates should be chosen accordingly.

3. The parameters suggested here are the ones we use for scanning the films with our DI AFM. These can be altered depending on the instruments used; however, there are limits to how much force the tip can apply on the film before degrading the soft film structures. We find that the films can withstand forces ranging from 10 to 50 nN for imaging; however, others have used higher force >100 nN ***(16)***. Details of force–distance calibrations as applied to organic thin films have been discussed by others in details ***(12,13,22)***.
4. The imaging of the films using AFM depends only if the deposited films have the microstructures preserved as observed directly from the air–water interface using fluorescence microscopy (**Fig. 1A**). Other problems may occur if higher forces (<80 nN) are used during scanning, which can alter the film architecture and even remove the film from the area being scanned, by strong tip-film interactions. It is necessary therefore to image at least a DPPC film using fluorescence microscopy before and after deposit for preparing them for AFM imaging. The glass and mica slides containing the deposited film should be wiped on one surface for fluorescence imaging. Because the film deposits on both surfaces of the substrate, one of the surfaces (with film) should be cleaned by gently wiping this surface with a tissue paper or kim-wipe dipped in chloroform. This would remove the film from one surface and not allow for fluorescence from both surfaces to interfere during fluorescence imaging. From our experience we have noticed that many hours of AFM time is wasted in scanning a glass surface with broken or no films at all, since the fluorescence step was omitted. The fluorescent probe NBD-PC used below 1 mol% of the lipid do not significantly alter the film architecture, as confirmed at the air–water interface using lower-resolution Brewster angle microscopy, which do not require probe for imaging ***(8)***. If after using the fluorescence method, the AFM images cannot be observed, retract the tip from the surface and repeat procedure 6 through 9 (**Subheading 3.2.**) on a different region of the films.
5. The condensed or gel phase in BLES or DPPC films are formed as a result of the fatty acid chain being more perpendicular to the plane of the air–water interface compared to those in the fluid or expanded phase ***(23)***. This allows for the gel or

condensed phase to be imaged and the gel phase is considered as a tilt-condensed phase ***(11,23)***. However, AFM height differences between the gel–fluid phase do not give accurate numbers for the exact degree of tilt of the molecules in the gel compared with the fluid phase because the depression of the tip in a softer fluid phase varies depending on the composition of this phase. In case of BLES, a number of fluid phospholipid and surfactant proteins SP-B/C are present in the fluid phase (as determined from various model film studies ***[7,14]***). Therefore the exact degree of chain tilts are actually deduced using other techniques such as grazing angle incidence X-ray diffraction from such films ***(11)***. These results are in close agreement with AFM results obtained by line section of the domain boundaries (**Fig. 2A**). The AFM images in the friction mode can indicate regions of higher tip-surface interactions or the viscoelasticity of the gel or fluid phase, as suggested in the micro-heterogenous areas in Fig. 3B, with very small height differences observed in the deflection mode ***(15)***.

Acknowledgments

This work was supported by a collaborative health research grant from the National Scientific and Educational Research Council/Canadian Institute of Health Research (NSERC/CIHR). A.K.P. is a recipient of a Department of Science and Technology of India postdoctoral fellowship. We also gratefully acknowledge the valued advice and discussion of the data in this project with Dr. C. Yip, University of Toronto. K.N. is a CIHR-New Investigator at Memorial University.

References

1. Possmayer, F, Nag, K., Rodriguez, K., Quanbar, R., and S. Schürch (2001) Surface activity in vitro: Role of surfactant proteins. *Comp. Biochem. Physiol. A.* **129,** 209–320.
2. Nag, K, Munro, J. G., Hearn S. A., Rasmusson, J., Petersen N. O., and Possmayer, F. (1999) Correlated atomic force and transmission electron microscopy of nanotubular structures in pulmonary surfactant. *J. Struct. Biol.,* **126,** 1–15.
3. Goerke, J (1998) Pulmonary surfactant: Functions and molecular composition. *Biochim. Biophys. Acta* **1408,** 79–89.
4. Greise, M. (1999) Pulmonary surfactant in health and lung disease: State of the art. *Eur. Respir. J.* **13,** 1455–1476.
5. Veldhuizen, R. A. W., Nag, K, Orgeig, S., and Possmayer, F. (1998) The role of lipids in pulmonary surfactant. *Biochim. Biophys. Acta* **1408,** 90–108.
6. Nag, K, Perez-Gil, J., Ruano, M.L.F., Worthman, L. A. D., Stewart, J., Casals, C., and Keough, K. M. W. (1998) Phase transitions in films of lung surfactant at the air-water interface. *Biophys. J.* **74,** 2983–2995.
7. Von Nahmen, A., Schenk, M., Seiber, M., and Amrein, M. (1997) The structure of model surfactant as revealed by scanning force microscopy. *Biophys. J.* **72,** 463–469.

8. Piknova, B., Scheif, W.R., Vogel, V., Discher, B. M., and Hall, S. B. (2001) Discrepancy between phase behavior of lung surfactant phospholipids and the classical model of surfactant function. *Biophys. J.* **81,** 2172–2180.
9. Nag, K., Harbottle, R. R., and Panda, A. K. (2000) Molecular architecture of a self-assembled bio-interface: Lung surfactant. *J. Surface Sci. Technol.* **16,** 157–170.
10. Brockman, H. (1999) Lipid monolayers: why use half a membrane to characterize protein-membrane interactions? *Curr. Opin. Struct. Biol.* **9,** 438–443.
11. Kaganer, V.M, Möhwald, H, and Dutta, P. (1999) Structure and phase transition in Langmuir monolayers. *Rev. Mod. Phys.* **71,** 779–819.
12. Radmacher, M, Tillman, R.W., Fritz, M., and Gaub, H. E. (1992) From molecules to cells: Imaging soft samples with atomic force microscope. *Science* **257,** 1900–1905.
13. Zasadzinski, J. A. N., and Hansma, P. K. (1990) Scanning tunneling microscopy and atomic force microscopy of biological surfaces. *Ann. NY Acad. Sci.* **589,** 476–491.
14. Ding, J, Takamoto, D. Y, VonNahmen, A, Lipp, M.M., Lee, K.Y.C., Waring, A., and Zasadzinski, J. A. (2001) Effects of lung surfactant proteins, SP-B and SP-C and palmitic acid on monolayer stability. *Biophys. J.* **80,** 2262–2272.
15. Chi, L. F., Anders, F, Fuchs, H, Jhonston, R. R., and Ringsdorf., H. (1993) Domain structures in Langmuir-Blodgett films investigated by atomic force microscopy. *Science* **259,** 213–216.
16. Mikrut, J. M., Dutta, P., Ketterson, J. B., and MacDonald, R. C. (1993) Atomic-force and fluorescence microscopy of Langmuir–Blodgett monolayers pf 1,2,-dimyristoyl-phosphatidic acid. *Phys. Rev. B.* **48,** 14,479–14,487.
17. Zhai, X and Kleijn, J. M. (1997) Molecular structure of dipalmitoylphosphatidylcholine Langmuir–Blodgett monolayers studied by atomic force microscopy. *Thin Solid Films* **304,** 327–332.
18. Veldhuizen, R. A. W., Welk, B., Harbottle, R., Hearn, S., Nag, K., Petersen, N. O., and Possmayer, F (2001) Mechanical ventilation of isolated rat lungs changes the structure and biophysical properties of surfactant. *J. Appl. Physiol.* **92,** 1169–1175.
19. Nag, K, Perez-Gil, J., Cruz, A., Rich, N. H., and Keough, K. M. W. (1996) Spontaneous formation of interfacial lipid-protein monolayers from adsorption from vesicles. *Biophys. J.* **71,** 1356–1363.
20. Nag, K, Boland, C, Rich, N. H., and Keough, K.M.W. (1990) Design and construction of an epifluorescence microscopic surface balance for the study of lipid monolayer phase transition. *Rev. Sci. Instrum.* **61,** 3425–3430.
21. Gibson, C.T., Watson G. S., and Myhra, S. (1996) Scanning force microscopy-Callibrative procedures for "best practice." *Scanning* **19,** 564–581.
22. Gibson, C. T., Watson G. S., Mapledoram, L. D., Kondo, H., and Myhra, S. (1999) Characterization of organic thin films by atomic force microscopy:application of force vs distance analysis and other modes. *Appl. Surf. Sci.* **144/145,** 618–622.
23. Scheif, W. R., Touryan, L., Hall, S.B., and Vogel, V. (2000) Nanoscale topographic instabilities of a phospholipid monolayer. *J. Phys. Chem.* **104,** 7388–7393.

18

High-Resolution Analysis of the 3D Organization of Human Metaphase Chromosomes

Stefan Thalhammer, Pietro Gobbi, Mirella Falconi, Giovanni Mazzotti, and Wolfgang M. Heckl

1. Introduction

The detailed understanding of the nuclear cell functions requires an accurate knowledge of the spatial organization of their structures. For many years the study of human metaphase chromosomes was conducted with light microscopy after staining protocols disturbing the native chromosomal structure. The approach by scanning electron microscopy (SEM) provides higher resolution as compared with light microscopy and permits surface analysis of the chromosomal structure, which cannot be adequately obtained from transmission electron microscopy. Nevertheless, to obtain high resolution in SEM observations, the use of a high electron accelerating voltage (up to 30 kV) is required ***(1)***. With these experimental conditions, the sputter coating or a conductive staining of the samples is generally required ***(1,2)***. Both procedures allow electron-charging dispersion from the sample but may obscure fine details and produce sample alterations ***(3)***.

The field emission in lens scanning electron microscope (FEISEM; *see* **Fig. 1A**) represents a special kind of SEM, fitted with a cold cathode field emission electron gun ***(4,5)***, that can operate at low accelerating voltage with reduced electron charging of the sample. In fact, the low-voltage and low-current electron beam of the FEISEM together with a liquid nitrogen anti-contamination device in correspondence to the specimen area and an "in lens" assembly of the electron-optic column allows for high-resolution imaging of the biological sample without any conductive staining or metal coating. Nevertheless, contamination of the specimen is highly reduced as compared to conventional SEM ***(4)***.

The sample location between the objective pole piece limits the dispersion of the secondary electrons collected by the magnetic field of the lens. To sum-

From: *Methods in Molecular Biology, vol. 242: Atomic Force Microscopy: Biomedical Methods and Applications*
Edited by: P. C. Braga and D. Ricci © Humana Press Inc., Totowa, NJ

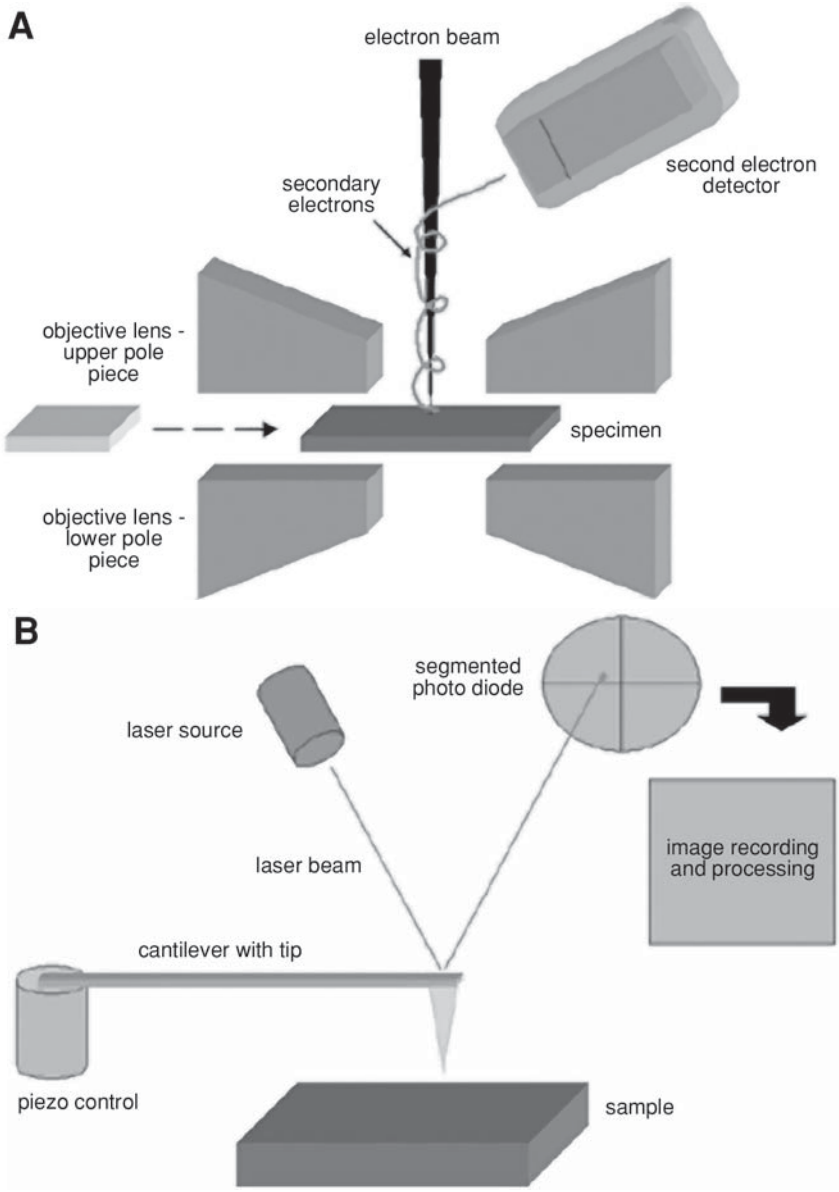

Fig. 1. **(A)** Schematic setup of a FEISEM: the specimen is brought between the upper and lower pole piece; the secondary electron beam moves in a spiral motion to a detector. **(B)** Schematic setup of an AFM with beam-bounce detection: the laser beam is deflected from the back of the cantilever according to the topographic properties of the sample. The laser beam displacement is measured with a segmented photo diode, recorded, and processed line by line.

marize, these characteristics allow the observation of uncoated biological samples with a higher resolution as compared with conventional SEM ***(6–9)***.

Since its invention in 1986, the use of the atomic force microscopy (AFM) has become a standard technique on various biological applications, including chromosomes ***(10–12)***, not requiring, especially in contact mode analysis, any particular treatment of the sample. The AFM allows imaging of chromosomes in ambient as well as in physiological conditions but with lower resolution compared with electron microscopy approaches ***(13–15)***. The schematic setup of an atomic force microscope is shown in **Fig. 1B**.

The combination of two different technical approaches shows a high correlation of the respective morphological information, both in normal and treated samples. The high-resolution potential of the FEISEM, together with the possibility to observe hydrated samples and/or to nanomanipulate the specimen with the AFM, confirms morphological data and offers an enhanced information on their biological significance ***(16)***. **Table 1** summarizes the necessary conditions of the different microscopes for the observation of biological samples.

The methods described here are aimed at producing the best possible samples obtainable from a starting material of peripheral blood lymphocytes to the final correlative observations using FEISEM and AFM.

2. Materials

1. 3× 6 mm ITO glass (Indium Thin Oxide) with 100 Ω surface resistance
2. AFM cantilevers: stiff cantilevers: spring constant, c = 0.3 N/m, nominal tip radius, $r < 10$ nm (Dr. Olaf Wolter GmbH, Germany).
3. Metaphase chromosomes: Human whole blood; Gibco Chromosome Medium 1A (Gibco/BRL); colchicine (10 µg/mL; Sigma); 0.075 *M* KCl (hypotonic solution); methanol/acetic acid (3:1); andalcoholic series (25, 50, 70, 90, and 100%).
4. GTG banding: 0.05% trypsin solution (Difco), 5% Giemsa staining solution, and 1X phosphate-buffered saline (PBS).
5. CBG banding: 0.2 *N* HCl; 5% $Ba(OH)_2$; 2X SSC buffer; and 5% Giemsa staining solution.
6. Protein digestion: Protease K (10 mg/mL; Roche); 3 *M* Na–acetate; 20% SDS.
7. FEISEM preparation: conductive carbon paint or colloidal graphite in Isopropanol (JEOL), and conductive tape (JEOL).

3. Methods

3.1. Cell Culture and Chromosome Preparation

1. Cultivate 0.4 mL human whole blood with 10 mL of Gibco Chromosome Medium 1A at 37°C for 72 h. Thirty minutes before preparation, the cells are arrested by adding colchicine (10 µg/mL) for 30 min.

Table 1
Comparison of Different Microscopic Techniques to Measure the Sample Topography

	Optical microscopy	SEM	FEISEM	AFM
Microscopic environment	Ambient Liquid Vacuum	Vacuum	Vacuum	Ambient Liquid Vacuum
Field depth	Small	High	Medium	Medium
Focus depth	Medium	Small	Very small	Small
Resolution	100 nm	5 nm	0.7 nm	0.1–1.0 nm
x, *y*, *z*	n/a	n/a	n/a	0.01 nm
Magnification	1x–2×10^3x	10x–10^6x	9x–10^5x	5×10^2x–10^8x
Necessary sample preparation	Low	Critical point drying or freeze-drying, metal coating	Critical point drying if necessary	Low
Necessary sample properties	Samples do not have to be completely transparent for visible light	Samples should not charge and have to be vacuum compatible	Vacuum compatibility	Samples do not have excessive changes in height in dependence to tip geometry

2. Spin down at **325*g*** for 10 min. Discharge supernantant and resuspend pellet in 10 mL of hypotonic solution containing 0.075 *M* KCl. Incubate at 37°C for 15 min (*see* **Note 1**).
3. After the incubation add two drops of the ice cold fixative containing methanol/acetic acid solution (3:1) and spin down at **325*g*** for 10 min (*see* **Note 1**).
4. Remove supernantant and resuspend pellet in 10 mL of ice-cold fixation mix.
5. Spin down at **325*g*** for 10 min and remove supernantant, and resuspend pellet in 10 mL of ice-cold fixative, repeating twice.
6. Spin down at **325*g*** for 10 min and resuspend pellet in 1 mL of fixative. Store at –20°C or proceed to **step 7**.
7. Resuspend the pellet and perform a drop fixation in the middle of the ITO-glass (*see* **Note 2**).

3.2. GTG Banding

1. Take 1 d or overnight aged chromosome preparations and incubate the slides at 37°C for 15 s in 0.05% trypsin-solution (Difco).
2. Rinse the slides briefly in PBS and staining and stain the treated slides in 5% Giemsa solution for 8 min.
3. Rinse the slides with water and allow to dry.

3.3. CBG Banding

1. For CBG banding use, 1- or 2-wk-old glass slides.
2. Incubate the slides in a 0.2 *N* HCl for 1 h at room temperature. Rinse briefly in deionized water and allow to dry.
3. After drying, treat the slides in a 5% $Ba(OH)_2$ at room temperature for 5 min, rinse them in deionized water, and pass through a alcoholic series and allow to dry.
4. After drying, incubate the slides in 2X SSC buffer (3 *M* NaCl, 300 m*M* Na–citrate) at 55°C for 1 h, followed by rinsing in deionized water and air drying.
5. Stain the slides in 5% Giemsa solution at room temperature for 45 min, rinse with water, and allow to dry.

3.4. Protein Digestion

1. After washing three times in 3:1 cold methanol: acetic acid, chromosome spreads were made by dropping the suspension onto the conductive surface of perfectly cleaned and degreased 3 × 6 mm ITO (Indium Thin Oxide) glasses. Metaphases were then air dried, dehydrated with an ethanol series (70, 90, 100%), air dried, and stored in a dry chamber until use.
2. Subsequently, the cleaning solutions are used alternatively. The treatment is a mix of 1 mL of 3 *M* Na–acetate, 20 µL of protease K (10 mg/mL) and 20 µL of 20% SDS for 2 min at 50°C.
3. After the cleaning procedure the ITO glass with the metaphases spreads is washed 2 min in distilled water, dehydrated in an ethanol series (25, 50, 70, 90, and 100%) and air dried.
4. The ITO glass is transferred to FEISEM microscopy.

3.5. FEISEM Microscopy

Cleaned and uncleaned metaphase spreads on ITO glasses are mounted onto the microscope specimen holders and observed without any conductive coating. Follow the instructions described in the microscope manual. We performed our experiments on a JEOL JSM-890 FEISEM (Jeol ltd. Japan) at 7k V accelerating voltage (1×10^{-11}. A probe current and 0° to 45° tilt angle. **Figure 2** shows two FEISEM images of metaphase chromosomes in low and high resolution. To unmount the ITO glass from the specimen holder cut the conductive glue and tape with a scalpel below the ITO glass, as shown in **Fig. 3**.

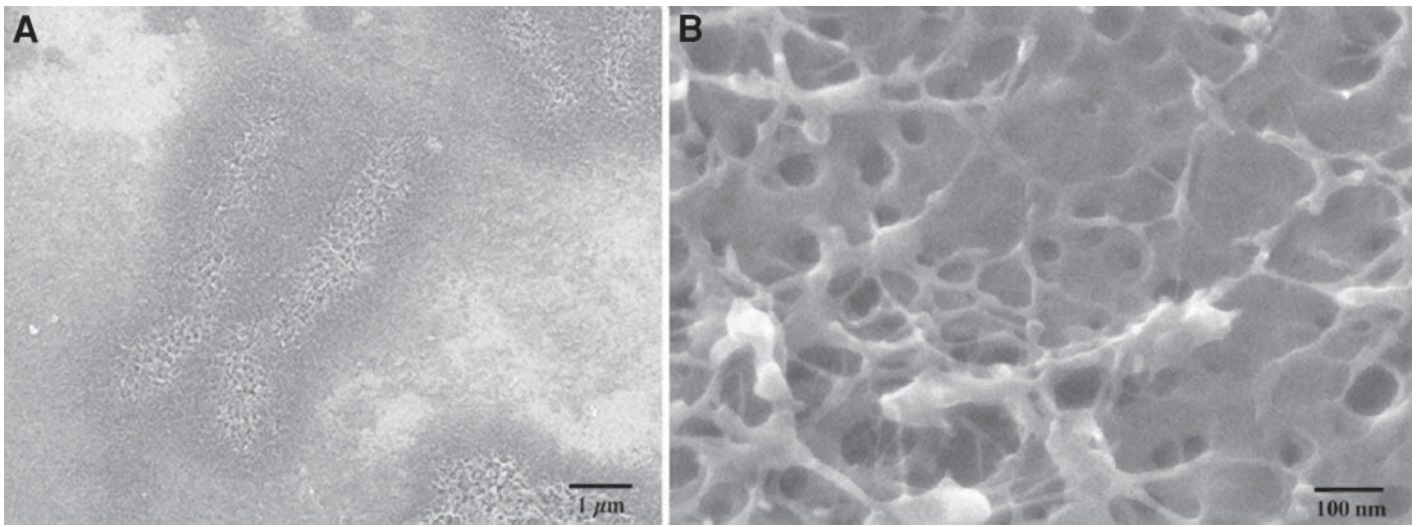

Fig. 2. FEISEM analysis of human metaphase chromosomes after protease K treatment. **(A)** The centromeric region and the chromatids are well recognizable. A dark halo surrounds the entire chromosome. Scale bar, 1 μm. **(B)** The chromosomal surface appears to be constituted of a network. Some fibrillar structures are well detectable. Scale bar, 100 nm.

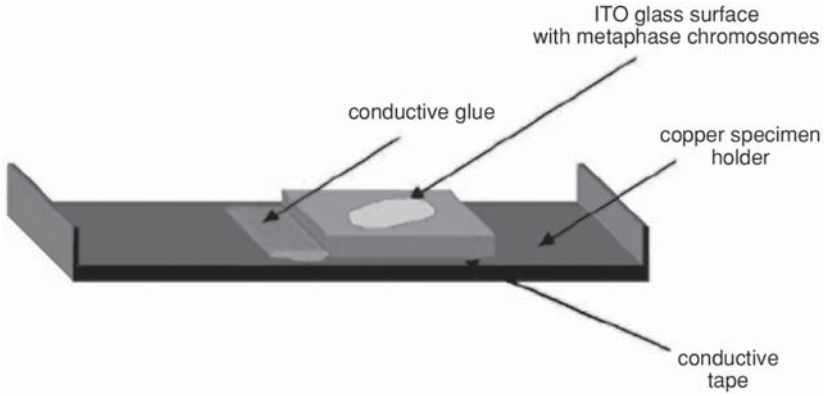

Fig. 3. Dismounting the ITO glass from the FEISEM specimen holder: to remove the ITO glass from the specimen holder, use a scalpel and cut below the conductive glue. Without any further treatment, the ITO glass can be used for AFM microscopy.

3.6. AFM

The unmounted ITO glass pieces with the metaphase chromosomes can be observed with AFM without any further treatment. Before imaging with the AFM, check the conductive side of the ITO glass (*see* **Note 2**). Please follow the recommended instructions of your AFM manual. In our experiments we used an AFM (Topometrix Explorer) with 130 µm *x*,*y*-scan range and 10 µm *z* scanner. The AFM was mounted on top of an inverted microscope to select the metaphase spreads. Observations of the human chromosomes in ambient conditions were conducted by means of stiff cantilevers in contact mode. The loading forces during AFM measurements were 10–20 nN in ambient conditions. **Figure 4** shows AFM images of metaphase chromosomes after protease K treatment. Some fibrillar structures are well detectable and the recorded chromosomal structures are comparable with the FEISEM images (*see* **Fig. 2**).

For imaging the GTG- and CBG-banded metaphase chromosomes in contact mode, we used stiff cantilevers. The loading forces during AFM measurements were 10–20 nN. The methodical properties are summarized in **Table 2**.

The scanning procedure of the AFM is controlled by the software SPMlab 3.06. The topographic and error signal image were recorded. The representation of the topographic image was done in gray scale with subsequent inversion of the image for easy comparison with known optical microscopy karyotypes. **Figure 5** shows AFM images of a GTG-banded chromosome imaged in contact mode, the corresponding error signal image, and a CBG-banded chromosome.

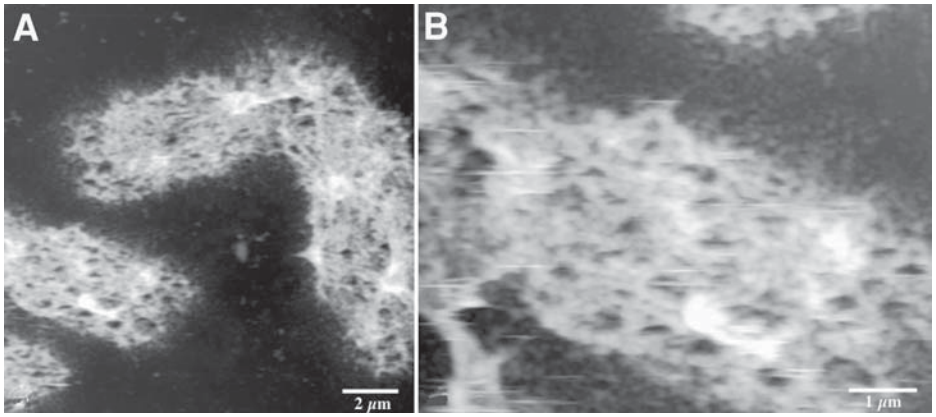

Fig. 4. The chromosomal surface presents a defined network structure after protease K treatment. Some fibrillar structures are well detectable, and the recorded chromosomal structures are comparable with the FEISEM images. Scale bar shown on Figures.

Table 2
Methodical Properties of the Different Operation Modes in AFM for High-Resolution Imaging and Manipulation of Metaphase Chromosomes

Operation mode	Contact mode	Noncontact mode	Tapping-mode
Tip loading force	Low → high	Low	Low
Contact with sample surface	Yes	No	Periodical
Manipulation of sample	Yes	No	Yes
Contamination of AFM tip	Yes	No	Yes
Microdissection	Yes	No	No

4. Notes

1. It is important to ensure that the hypotonic solution is removed from the cells immediately. By adding the fixative before spinning, the cells will be easier to resuspend. Remove all but a little of the supernatant and resuspend in the remaining solution before adding the fixative for the first time. Be sure not to leave too much hypotonic solution; this will cause a lot of cytoplasm to remain with the chromosome spreads; however, not leaving enough makes the cells difficult to resuspend.

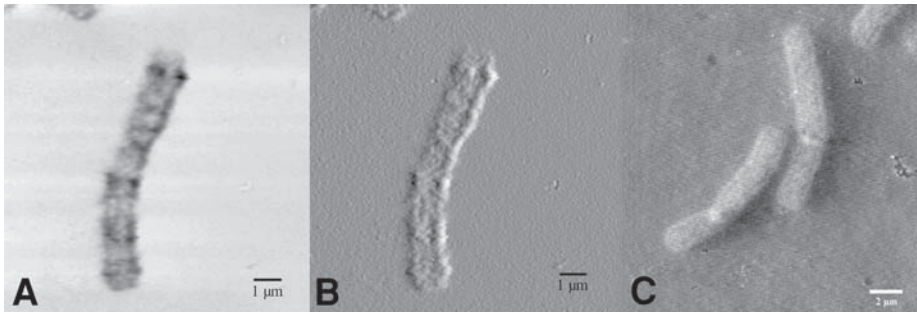

Fig. 5. **(A)** AFM image of a GTG-banded human metaphase chromosome 7. Imaging was performed in contact mode; it is a topographic image, and the single bands are well detectable. Scale bar, 1 µm. **(B)** Corresponding error signal image. **(C)** AFM image of CBG-banded human metaphase chromosomes: topographic image. Scale bar, 2 µm.

2. To check the conductive site of the ITO glass, use a voltage multimeter and make a resistance measurement. The conductive site will show a resistance, which has to be about 100 Ω.
3. To increase the contrast between sample surface and metaphase chromosomes for FEISEM microscopy a further fixation step and critical point drying can be performed. Our studies showed that this is not necessary. The fixation consists of a washing step 2 minutes in 1 × PBS buffer at room temperature, followed by a 30-min fixation in 1% glutaraldehyde in 1X PBS buffer. Please work under a hood. After a washing step in 1× PBS buffer for 2 min at room temperature the samples are fixed in 1% osmiumtetraoxide (OsO_4) in 1 × PBS buffer or in Veronal buffer (*see* **Note 4**). Wash the samples for 2 min in 1 × PBS buffer at room temperature and dehydrate the sample in an alcoholic series 70, 90, and 100% for 3 min at room temperature. Repeat the dehydration step three times and transfer the samples to critical point drying.
4. To prepare the 1% OsO_4 in 1X PBS buffer or in Veronal buffer, while working in the hood, brake two osmium crystals enclosed in a glass vessel into 100 mL of distilled water and dissolve osmium in a warm water bath for 1 d. Take an aliquot of the dissolved osmium and dilute in 1X PBS or Veronal buffer. Store the solution in a dark bottle at 4°C and fix the bottle additionally with parafilm to avoid evaporation.

References

1. Sumner, A. T., Ross, A. R., and Graham, E. (1994) Preparation of chromosomes for scanning electron microscopy. *Methods Mol. Biol.* **29**, 41–50.
2. Wanner, G. and Formanek, H. (1995) Imaging of DNA in human and plant chromosomes by high-resolution scanning electron microscopy. *Chromosome Res.* **3,** 368–374.

3. Hermann, R. and Müller, M. (1992) Towards high resolution SEM of biological objects. *Arch. Histol. Cytol.* **55**, 17–25.
4. Nagatani, T., Saito, S., Sato, M., and Yamada, M. (1987) Development of an ultra high resolution scanning electron microscope by means of a field emission source and in-lens system. *Scanning Microsc.* **1,** 901–909.
5. Pawley, J. (1997) The development of field-emission scanning electron microscopy for imaging biological surfaces. *Scanning* **19**, 324–336.
6. Rizzoli, R., Rizzi, E., Falconi, M., Galanzi A., Baratta B., Lattanzi, G., et al. (1994) High resolution detection of uncoated metaphase chromosome by means of field emission scanning electron microscopy. *Chromosoma* **103**, 393–400.
7. E., Falconi, M., Baratta, B., Manzoli, L., Galanzi, A., Lattanzi, G., et al. (1995) High-resolution FEISEM detection of DNA centromeric probes in HeLa metaphase chromosomes. *J. Histochem. Cytochem.* **43**, 413–419.
8. Lattanzi, G., Galanzi, A., Gobbi, P., Falconi, M., Matteucci, A., Breschi, L., et al. (1998) Ultrastructural aspects of the DNA polymerase distribution during the cell cycle. *J. Histochem. Cytochem.* **46**, 1435–1442.
9. Gobbi, P., Falconi, M., Vitale, M., Galanzi, A., Artico, M., Martelli, A. M., et al. (1999) Scanning electron microscopic detection of nuclear structures involved in DNA replication. *Arch. Histol. Cytol.* **62**, 317–326.
10. Binnig, G., Quate, C. F., and, Gerber, C. H. (1986) Atomic force microscopy. *Phys. Rev. Lett.* **56**, 930–933.
11. Mariani, T., Musio, A., Frediani, C., Sbrana, I., and Ascoli, C. (1994) An atomic force microscope for cytological and histological investigations. *J. Microsc.* **176**, 121–131.
12. Ushiki, T., Hitomi, J., Ogura, S., Umemoto, T., and Shigeno, M. (1996) Atomic force microscopy in hystology and cytology. *Arch. Histol. Cytol.* **50**, 421–431.
13. Putman, C. A.J., Van der Werf, K. O., De Grooth, B. G., Van Hulst, N. F., Segerink, F. B. and Greve, J. (1992) Atomic force microscope featuring an integrated optical microscope. *Ultramicroscopy* **42/44**, 1549–1552.
14. Musio, A., Mariani, T., Frediani, C., Ascoli, C., and Sbrana, I. (1997) Atomic force microscope imaging of chromosome structure during G-banding treatments. *Genome* **40**, 127–131.
15. Thalhammer, S., Köhler, U., Stark, R., and Heckl, W. M. (2000) GTG banding pattern on human metaphase chromosomes revealed by high resolution atomic-force microscopy. *J. Microsc.* **202,** 464–467.
16. Gobbi, P., Thalhammer, S., Falconi, M., Stark, R., Heckl, W. M., Mazzotti, G. (2000) Correlative high resolution morphological analysis of the three-dimensional organization of human metaphasechromosomes. Scanning **22**, 273-281.

19

Shape and Volume of Living Aldosterone-Sensitive Cells Imaged with the Atomic Force Microscope

Stefan W. Schneider, Rainer Matzke, Manfred Radmacher, and Hans Oberleithner

1. Introduction

The steroid hormone aldosterone, which is synthesized in the suprarenal glands and secreted in response to a reduction in circulating blood volume, increases water and sodium reabsorption in the kidney ***(1,2)***. Although kidney is the major target organ, various other cell types, including different epithelia, smooth muscle, and endothelium, respond to the hormone ***(3–6)***. The acute aldosterone-induced responses of target cells are an intracellular calcium change and an intracellular pH increase ***(3,7,8)*** along with activation of plasma membrane Na^+/H^+ exchange and plasma membrane proton conductance ***(9,10)***. Therefore, it is not surprising that researchers have postulated that these acute transmembrane shifts of electrolytes are accompanied by cell swelling ***(2,11)***. Cell swelling or shrinkage plays a critical role in endothelial cell (EC) function. ECs tightly coat the luminal surface of blood vessels, playing an important role in the regulation of vascular tone, in vascular remodeling, in the pathogenesis of arteriosclerosis, and in arterial hypertension of humans ***(12)***. It has been shown that swelling of EC may disturb cell-to-cell interactions, resulting in an increase of transendothelial permeability, a precursor mechanism in the development of arteriosclerosis ***(13,14)***. Moreover, environmental stress (e.g., mechanical forces or hyperosmolarity) induces changes in cell volume and stimulates tissue plasminogen activator synthesis ***(15–18)***. Direct evidence for the importance of cell-volume regulation of endothelial cells is the existence of a volume-sensitive protein kinase ***(19)***.

There are different methods to measure cell volume. A simple technique is to measure cell volume by Coulter counter, which is commonly used for blood cells in suspension. In contrast with spherical cells in suspension, ECs under

From: *Methods in Molecular Biology, vol. 242: Atomic Force Microscopy: Biomedical Methods and Applications*
Edited by: P. C. Braga and D. Ricci © Humana Press Inc., Totowa, NJ

physiological conditions adhere to a substrate and develop a complex morphology (i.e., they polarize, form tight junctions and gap junctions, and develop monolayers). Thus, more sophisticated techniques must be applied. One is optical sectioning using quantitative differential interference contrast light microscopy ***(20,21)***. Here, we present an alternative new method using atomic force microscopy (AFM) for measuring cell volume in individual ECs with femto-liter resolution ***(22–25)***. AFM enables measurement of cell volume and cell-volume fluctuations in living adherent cells irrespective of the cell shape changes that occur during time-lapse measurements ***(26)***. Because surface topography and cell volume are simultaneously recorded, localized volume changes become visible within a single cell.

This chapter describes the protocol for the measurement of cell volume of living, adherent endothelial cells upon aldosterone stimulation. We used the BioScope® (DI, St. Barbara, CA.) in combination with an inverted microscope (Axiovert 100, Zeiss, Jena Germany) in two different scanning modes (contact and force volume modes) and with commercially available scanning tips (Microlever, Park Scientific, Sunnyvale, CA).

2. Materials

2.1. Chemicals

1. Aldosterone (Sigma, Taufkirchen, Germany) soluble in ethanol (stock solution = 10 μ*M*, stored at 4°C for 2 wk). Experimental concentration 10–0.1 n*M* (ethanol concentration less than 0.1%).
2. HEPES-buffered solution (140 m*M* NaCl, 5 m*M* KCl, 1 m*M* $MgCl_2$, 1 m*M* $CaCl_2$, 5 m*M* glucose, 10 m*M* HEPES (*N*-2-hydroxyethylpiperazine-*N*'-2-ethanesulfonic acid); pH, 7.4 further referred to as HEPES-buffered Ringer solution (HBRS).
3. Medium for endothelial cells (M199, Gibco, Karlsruhe, Germany).

2.2. AFM

1. BioScope (Digital Instruments, St. Barbara, CA), including software for volume analysis and force volume measurements.
2. Cantilever (Microlever, spring constant = 0.01 N/m, Park Scientific, Sunnyvale, CA).
3. Perfusion and heating chamber (homemade for continuous cell superfusion at 37°C); "Heparin perfusor" (Perfusor E; B. Braun, Melsungen, Germany) to control the flow rate (approx 1–5 mL/h). Consider that the superfusion as well as the heating chamber may cause electrical and mechanical noise.
4. The BioScope is placed on a homemade antivibration table. The whole setup is placed in a homemade box (Faraday cage), which is insulated (with foamed matter) against outside noise.
5. Heating lamp, fixed inside the box, to increase the ambient temperature to about 30°C (this avoids large thermal fluctuations in the bath solution which is maintained at 37°C).

2.3. Endothelial Cells

1. We use freshly prepared bovine (aorta) or human endothelial cells from the umbilical vein (HUVECs). For preparation protocol, please *see* **ref. *27***.
2. The culture medium (M199, Gibco, Karlsruhe, Germany) contains 10% heat-inactivated fetal calf serum (Boehringer Mannheim, Mannheim, Germany), antibiotics (penicillin 100 U/mL, streptomycin 100 µg/mL), 5 U/mL heparin (Biochrom, Berlin, Germany), and 1 mL/100 mL growth supplement derived from bovine retina as described ***(28)***.
3. Cells are cultivated first in T25 Petri dishes coated with 0.5% gelatin (passage p0). After reaching confluency cells are split using trypsin and then cultivated (passage p1) on glass cover slips (coated with 0.5% gelatin and fixed with 2% glutaraldehyde). Only living cells of passage p1 are used for experiments.
4. For AFM experiments the glass cover slip with cells is mounted in the perfusion chamber and superfused with 37°C HBRS.
5. Important: always keep cells in solution!

3. Methods

3.1. AFM Handling

Follow the AFM manual to get started. All experiments (on glass and on cells) are performed in contact mode.

3.2. Calibration of the Cantilever on a Glass Cover Slip

1. Start to scan a clean glass cover slip in fluid. This will help you to evaluate your cantilever and AFM setup. Moreover, you have to calibrate your force curve on glass before imaging cells.
2. For a high-quality image (i.e., integral and proportional gains as high as possible) you should use cover slips that are at least 0.8 mm thick. Important: Thin glass cover slips may oscillate and cause mechanical noise. When glass oscillations occur, gain values above one are not advisable (a further increase in gain values will cause piezo oscillations).
3. Before you mount the cantilever in the holder, dip the cantilever in a 37°C buffer solution. The procedure avoids air bubbles at your cantilever.
4. Mount the BioScope head with the cantilever holder on your inverted microscope. The cantilever should be close to the glass surface and submerged in a 37°C buffer solution.
5. Never let fluid get into the piezo!
6. Focus the laser on the cantilever to get a sharp laser spot in the photo diode. You should get a sum signal of at least 2 V. Bring the laser spot on the display to the center (see manual for details).
7. Before imaging glass or a cell, acclimatethe cantilever to the 37°C warm HBRS (this may take up to 1 h). As long as the vertical detection signal is not stable (more than ±0.01 V/s), you should not start your experiment.

8. Air bubbles may be seen at the cantilever in solution. To eliminate the air bubbles lift the BioScope head and dry the cantilever with filter paper tissue (if necessary repeat this procedure "dry-wet" for a few times). Do not touch the cantilever and the tip; just hold the paper on the chip that carries the cantilevers.
9. Initial parameter settings are: scan size: 0 µm (during AFM tip approach), 1 µm (after successful AFM tip engagement); scan speed: 1 Hz, scan angle: 90°; integral gain: 3; proportional gain: 5; scan lines: 256, input attenuation: 8.
10. Bring the AFM tip in contact with the glass cover slip by using computer-controlled options.
11. After AFM tip engagement with the glass surface switch to the force calibration curve to calibrate the cantilever sensitivity (see manual for details). Measure your loading force. The loading force can be calculated by measuring the distance between the noncontact part of the force curve and the set-point line. This value (in nm) multiplied by the spring constant gives the loading force (for details, *see* Appendix). You should not exceed a loading force of 1 nN when working with living cells. Start with a loading force of 0.5 nN and then switch to the image mode. If the cantilever is in contact with the glass surface increase the integral and proportional gains until the piezos start oscillating. Decrease the integral and/or the proportional gain until oscillations stop. Gains should be as high as possible without piezo oscillations. If 0.5 nN is not sufficient to maintain the contact between cantilever and glass surface increase the loading force stepwise (+0.1 nN steps) and repeat gain settings. Good values are: loading force below 1 nN, an integral gain above 3, and proportional gain above 5. After each single image switch to the force calibration mode to see whether the loading force is constant. A constant force curve is reflected by the same loading force at a given set point. Another way to test the stability of your loading force is to look at the vertical movement of your force calibration curve. A small vertical movement of the force calibration curve (approx 0.01 nN/min) cannot be avoided (because of thermal drift).
12. After getting reproducible and stable images (no piezo oscillations and a small cantilever drift) on glass (no cells), store a force curve and an image. Lift the BioScope head and replace the empty glass cover slip with a cover slip with cells.
13. The cantilever should be exchanged after each experimental session. Use only new cantilevers with clean AFM tips. When you are imaging living cells, you should put the cantilever chip under UV-light for several minutes to sterilize the tip before you mount it in the holder. A simple way to check if the tip is "dirty" is checking the quality of an image of the glass surface. Another possibility is to perform a force curve on glass. The force curve should show a sharp bend where it contacts the surface. A shallow transition from the noncontact part to the contact part is a hint that the tip has picked up some soft junk. It is a good idea to use a new cantilever for a new day you are doing experiments.
14. To clean the cantilever holder just use distilled water and soap. Dry the holder in a nitrogen jet stream. Be careful not to scratch the holder. Before you mount a new cantilever, the holder has to be dry.

3.3. EC Preparation for AFM

1. Isolate HUVECs and grow in culture as described *(27)*. For experiments, we use confluent endothelial cells not older than 14 days (passage 1) cultured on a thick (1 mm) glass cover slip (Important: a thick glass cover slip reduces glass vibrations during scanning).
2. Cells are washed with 37°C HBRS to clean the surface of cell debris.
3. The glass cover slip must be mounted firmly in the perfusion chamber. We use Superglue (Uhu GmbH, Bühl, Germany) to fix the glass cover slip in the chamber. For firm gluing, it might be necessary to dry the bottom of cover slip. Take care to ensure that cells never get dry. After glass cover slip fixation, start superfusion with 37°C HEPES-buffered solution (flow velocity: 1–5 mL/min). Cells are bathed in about 2 mL of solution. Alternatively, you can culture cells in a Petri dish, which can be mounted in the perfusion chamber. Make sure that the fluid level is not too high in order to avoid salt solution creeping into the piezos of the AFM head (*see* manual for details).

3.4. Single-Cell Volume Measurement in a Living Cell

1. Bring the cantilever close to the cell and allow adaptation to the 37°C warm HBRS. Start the perfusion. To avoid thermal fluctuations heat the perfusion chamber (37°C) and the solutions to 37°C. It may be even helpful to warm up your whole equipment in the box (approx 30°C).
2. To get a good image of your cells keep the loading force as low as possible. Therefore, follow the first contact between the cantilever and the cell immediately with force calibration. Initial parameter settings are as follows:
   scan size: initially 0 µm (approach), then (after contact) increase to 1 µm; scan speed: 1 Hz; scan angle: 90°;integral gain: 3; proportional gain: 5; input attenuation: 8; scan lines: 256; no offline plane fit or flattening!
3. After the AFM tip engages the cell surface (**Fig. 1**), switch to the force calibration curve to measure the loading force. Do not exceed a loading force of 1 nN. Start with a loading force of 0.5 nN and then switch to the image. When the cantilever is in contact with the cell surface, increase the integral and proportional gains until piezo oscillations occur. Then, decrease gains slightly. If 0.5 nN is not sufficient to keep the contact between cantilever and cell surface increase the loading force step by step (+0.1-nN steps).
4. After obtaining a reproducible image try to increase the scan size (in 10-µm steps) up to 50 µm. You may have to increase the loading force by 0.1–0.3 nN. Now you should see a whole cell appearing on the screen (**Figs. 2** and **3**). Then you may increase the scan size to 100 µm for imaging larger areas. For an accurate volume analysis in the offline mode (*see* **Subheading 3.7.**) you need to have a small glass area as a reference level in your image. It should be visible between the cells. Thus, use a subconfluent cell monolayer. Over the entire course of the experiment, always try to reduce the loading force by decreasing the set point. As soon as you loose contact with the cell surface increase the set point until contact

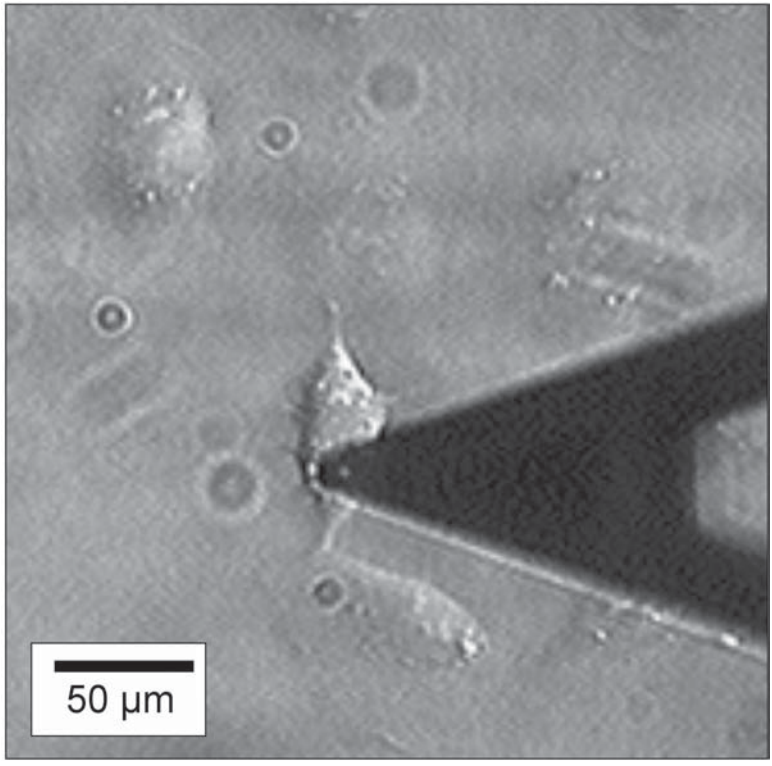

Fig. 1. Light microscopy image showing the cantilever located above the plasma membrane of a living cell. Scanning occurs in parallel to the longitudinal cell axis.

is restored. After using the lowest possible loading force try to increase the integral and proportional gain until the piezos start oscillating. Try to increase your scan speed to 2 Hz. Scan speed is also limited by piezo oscillations.

5. If the piezo reaches its limits, use the step motor function and retract the piezo from the surface (0.5-µm steps). The piezo should be almost completely extended when the AFM tip is scanning the glass substrate. To achieve this, move the AFM-tip to a cell-free site on the glass cover slip and adjust the scan offset values. Set the scan size to zero. The piezo should be completely extended. (Check the white bar in piezo position.)
6. Store the images. Control the loading force after each image.
7. Before switching to the aldosterone solution, store the force calibration curve.
8. To measure cell swelling upon aldosterone stimulation switch to a perfusion solution containing 1 n*M* aldosterone (**Fig. 2**). One image takes about 2–4 min (*see* **Notes 1–6**). So, before switching to an aldosterone-containing solution, make sure that you activate the movie capture mode (images will be continuously stored). Do not forget to store force calibrations curves.

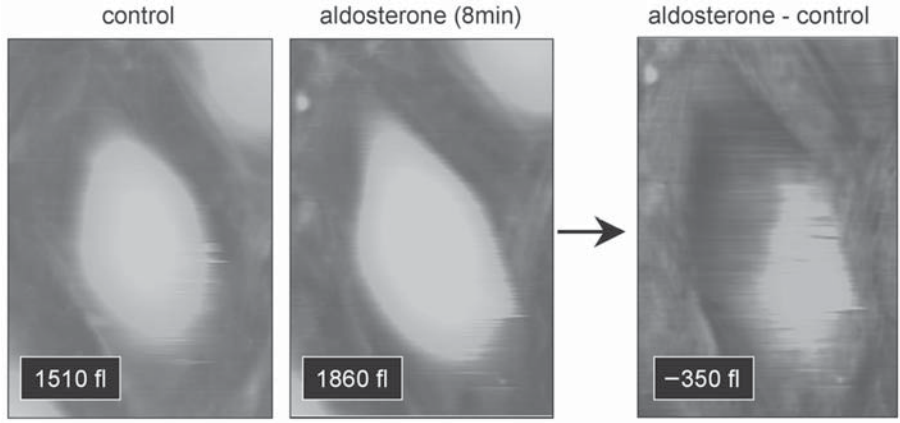

Fig. 2. Rapid endothelial cell swelling in response to aldosterone. One living EC is visible. Different brightness relates to different heights within the cells. After addition of aldosterone, the EC volume increases within 8 min. The cell changes its morphology because of the volume increase, shown by a change of the brightness pattern. Subtraction image (aldosterone – control) shows localized cell swelling within the cell (net volume change). Note that cell swelling occurs where the cell nucleus is located. This is typical for steroid hormone action.

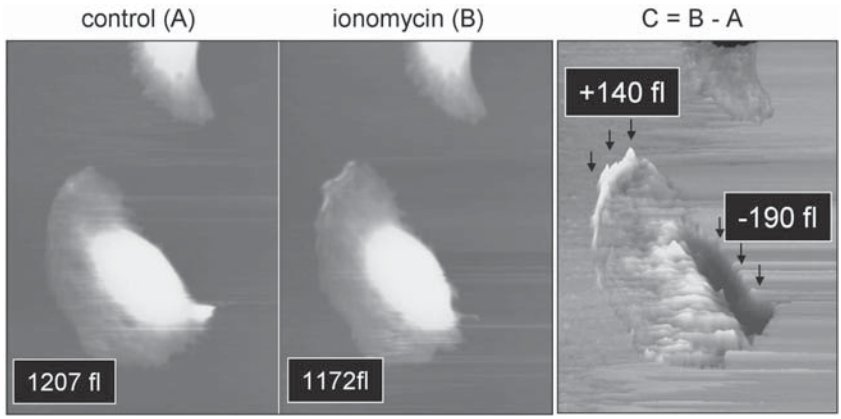

Fig. 3. Cell volume measurement in a migrating transformed kidney (Madin-Darby canine kidney [MDCK]) cell (migration direction: to upper left corner) before **(A)** and after **(B)** addition of ionomycin. Ionomycin increases intracellular calcium and thereby activates a potassium channel at the rear end of the cell and the Na^+/H^+ exchanger at the lamellipodium (front of the cell). The Na^+/H^+ exchanger activity increases cell volume. The potassium channel decreases cell volume. Image C represents the net volume change (volume increase at the front and volume decrease at the rear end of the cell) by subtracting both images (**C = B – A**).

9. After about 15–30 min, switch back to the control solution, store the images, and then stop the experiment.
10. Calibrate the cantilever again on glass (see **step 5**). Compare the sensitivities. If sensitivity is different at the end of your experiment compared with the initial sensitivity value take the mean value of both to calculate the loading force of the past experiment.

3.5. Single-Cell Volume Measurement in a Nonliving, Fixed Cell

In addition to cell volume measurements on living cells, it is also possible to image and analyze the volume of fixed cells (**Fig. 4**). Fixed cells are much easier to measure because of there is an increase in stiffness after fixation (higher resolution, less indentation by the loading force), the work can be done at room temperature, and cell activity, such as migration, is eliminated. However, paired experiments are not possible as well as the continuous monitoring of volume fluctuations. Moreover, fixation may cause volume and topography artifacts. For cell fixation we use 4% paraformaldehyde dissolved in 100 m*M* sodium-phosphate supplemented with 4% sucrose; pH 7.4; incubation time is 12 h at 4°C. After fixation cells are washed with 100 m*M* sodium phosphate buffer with 4% sucrose (personal communication by R. Ossig). Always keep cells under fluid. Mounting the glass cover slip in the perfusion chamber and imaging procedures are identical to the one described in **Subheading 3.4.**. It is not necessary to work at 37°C and under constant buffer perfusion, reducing electrical, mechanical, and thermal noise. For further fixation protocols, check *Current Protocols in Cell Biology* ***(29)***.

3.6. Visualization of Local Intracellular Volume

To visualize the local volume change upon stimulation of a single living cell you can subtract two subsequent images from each other. You have to make sure that in both images the scan area and cell localization within this area are identical. Go into the browse menu, select the two images and subtract them from each other. The new image shows the "net volume" change within a single cell. In case of localized volume changes you can detect intracellular compartments that undergo volume changes (**Figs. 2** and **3**).

3.7. Single-Cell Volume Off-Line Analysis

Cell volume analysis is based on the following principle: Each pixel includes information on three dimensions (i.e., on *x*, *y*, and *z* axes). The *x* and *y* parameters are given by the size of the scan area and by the number of scan lines per image. The *z* (height) information is given by the specific gray level of each pixel.

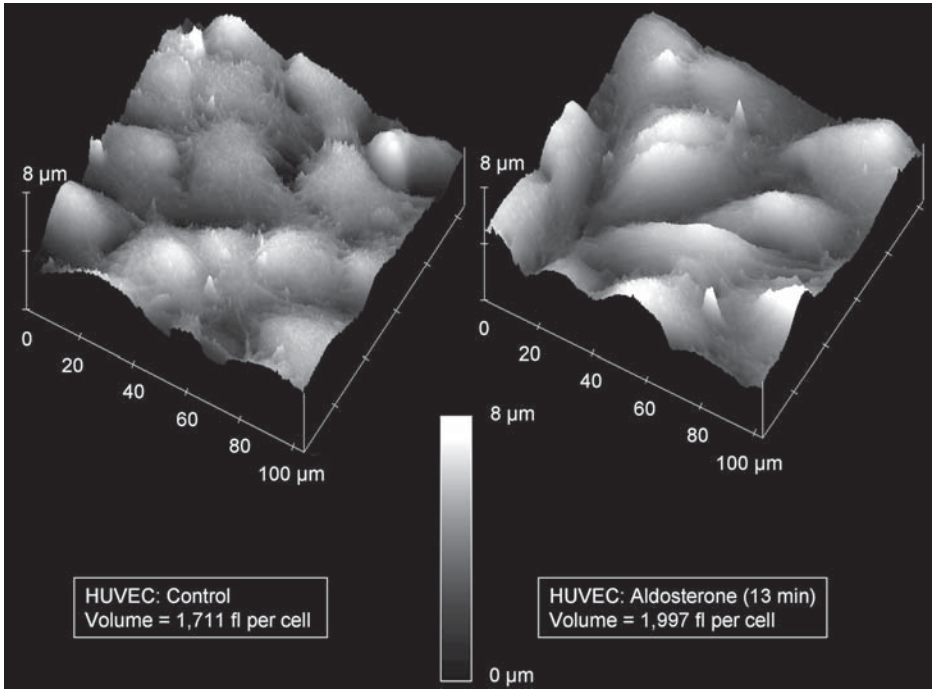

Fig. 4. Fixed endothelial cells (HUVEC) imaged in fluid in the absence (control) and 13 min after addition of aldosterone. Cells are grown on gelatin-coated glass and fixed in physiological conditions directly in the incubator, i.e. in culture medium supplemented with serum at 5% CO_2 at 37°C. Fixation was performed by gently adding the fixative (glutaraldehyde) to the cells to reach a final concentration of 0.5%.

1. Bring the image into a "correct" horizontal plane by using plane fit, order one. Glass surface visible between the endothelial cells helps to show if the cell layer is in a correct horizontal position.
2. The software provides an analysis tool "bearing" (**Fig. 5**). Drawing a square on the image gives the total volume (μm^3, equivalent to 10^{-15} L or 1 fL) inside the square. Move the marker (triangle) in the bearing area graph to 100%. The software uses the lowest point in the image as a reference for volume calculation. The best reference level is the glass surface.

3.8. CAVE

For contact mode imaging, it is necessary to apply a (minimal) loading force to the cell. Because cells are soft, it is unavoidable that plasma membranes will be indented by the AFM tip, even if the loading force is at the minimum necessary for successful contact mode imaging. This indentation

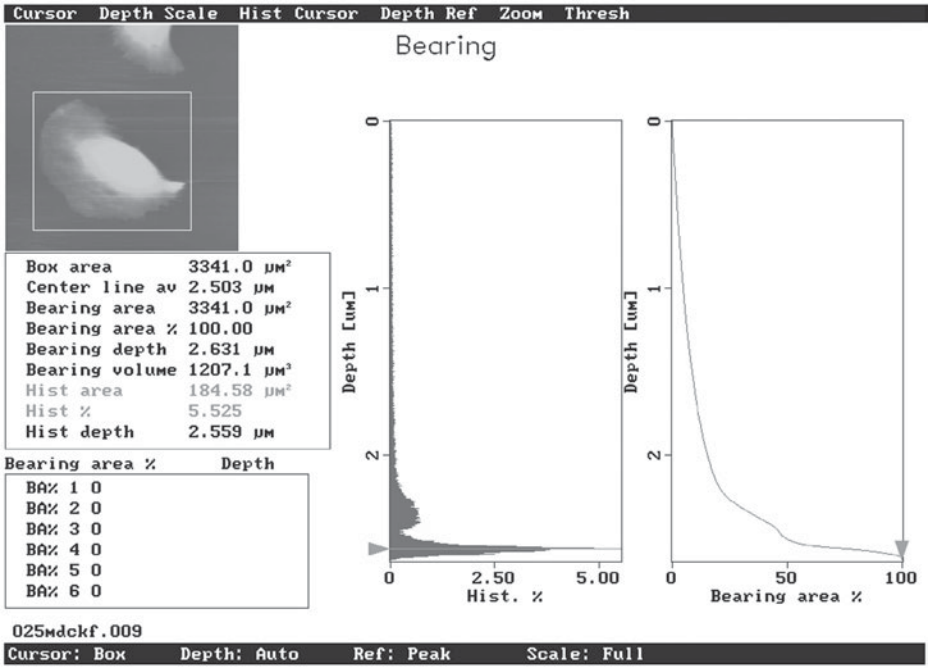

Fig. 5. Single-cell volume offline analysis. Using the bearing feature of the software package, it is possible to measure single-cell volume (1 μm^3 = 1 fL). The white box in the image limits the area used for volume calculations. Draw the box around the cell including the substrate (i.e., glass) to have a reference level. Displace the marker (triangle) in the bearing area graph to 100%. The volume is given as bearing volume in μm^3. The cell volume of the presented example is 1207 fL. In addition to cell volume calculation the program provides a height histogram (Depth [µm] vs Hist. %).

leads to an underestimation of the cell height and therefore to an underestimation of the cell volume. The physical parameter that describes the stiffness of a material is the elastic modulus E (also called Young's modulus). Typical values for living cells are 1–10 kPa , for fixed cells, 10–100 kPa. (Compare with rubber: 1.5 MPa; with glass: 1 GPa; **ref.** ***30***). For example: a loading force of 0.5 nN applied to a cell with a Young's modulus of 5 kPa causes a cell indentation of 400 nm. If we propose an actual cell height of 4 µm, the volume measurements in contact mode underestimate the cell volume by about 10% (**Fig. 6**). The indentation varies also strongly with the applied loading force. Therefore, it is necessary to keep the loading force constant to obtain reliable volume measurements.

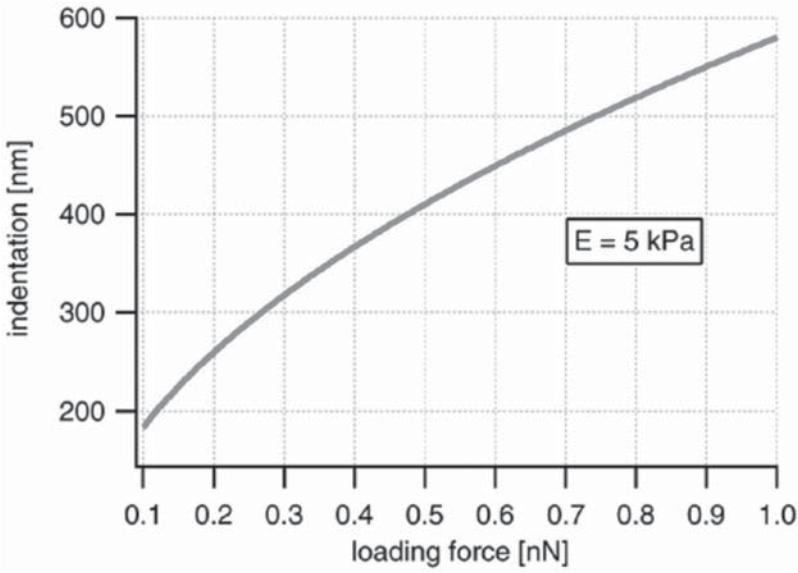

Fig. 6. Indentation of a soft sample with an elastic modulus of $E = 5$ kPa (a typical value for living cells) as a function of the applied loading force for the geometry of a typical AFM tip. Typical loading forces (several 100 pN) used for contact mode imaging cause indentations from 200 to 600 nm. Because the height of cells is in the range of only a few micrometers (typical value 4 μm), such indentations are significant. The indentation also varies strongly with the loading force. Therefore, it is necessary to keep the loading force constant to obtain reliable volume measurements. The Hertz model for a conical indenter with a half opening angle of 35° was used for this calculation.

Another problem is that the biochemical stimulus used to change the cell volume might also change the elastic properties of the cell. Such changes will also change the indentation, even if the loading force is kept constant (**Fig. 7**). Because of the elastic indentation of the cell by the AFM tip, cell volume measurements in contact mode lead to an underestimation of the absolute cell volume. However, relative changes can be measured if the loading force is constant during the measurement and if the elastic properties of the cell do not change. As long as these parameters remain constant volume underestimation is a systematic error and relative volume changes upon cell stimulation are virtually correct.

In practice, it is not easy to keep the loading force constant because thermal fluctuations cause a bending of the cantilever and therefore alter the force. This bending is caused by the bimetallic construction of the cantilever and even very small changes in temperature can change the loading force by several

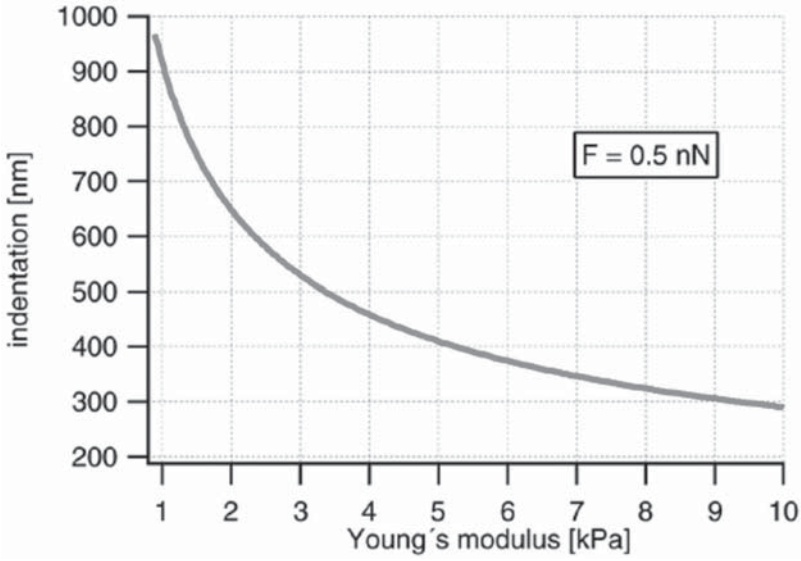

Fig. 7. Indentation of a soft sample at a constant loading force of 0.5 nN as a function of the elastic modulus of the sample. The Hertz model for a conical indenter with a half opening angle of 35° was used for this calculation.

hundred pN, a change that alters the indentation significantly (**Fig. 6**). Another consideration is that changes in cell elasticity may occur that will change the indentation significantly (**Fig. 7**). For example, the stimulation of endothelial cells with thrombin (a mediator of inflammation that increases the permeability of the endothelial monolayer) changes the cell elasticity by a factor of 5 (unpublished data by R. Matzke). A third point is that it is desirable to obtain quantitative volume data. A method to circumvent the above mentioned problems is to operate the AFM in the force-mapping mode (also called force-volume mode; **ref.** ***31***). This method allows a quantification of the unindented cell volume, independent of the loading force and independent of the elastic modulus of the cell. It allows a measurement and quantification of the local cell elasticity. The BioScope can be operated in the force volume mode. Therefore, it would be possible to calculate actual cell height and cell volume irrespective of cell stiffness. The BioScope software permits a qualitative analysis of the elastic properties of the sample, but features to calculate the unindented height and to quantify the elastic modulus are missing. In other words, it is possible to record all the data necessary for a actual cell volume measurement, but we cannot analyze the data with the current BioScope software. A group of researchers, M. Radmacher, C. Rotsch and R. Matzke (Departments of Physics; Universities of Munich and Göttingen, Germany) wrote a program in IGOR

PRO (Wavemetrics, Lake Oswego, OR) to analyze the force volume data. Please, check the Appendix and the literature ***(30–36)*** for further information.

3.9. Appendix

Force Mapping ***(31)*** allows a quantification of the unindented cell volume, independent of the loading force and independent of the elastic modulus of the cell. The following section explains the analysis of the data and gives practical hints for data acquisition.

3.9.1 Force Mapping

A force map is a 2D array of force curves. (You already know a single force curve from the force calibration menu of the BioScope.) In a force curve, the force acting on the AFM tip is measured as the tip approaches and retracts from the surface of a sample (**Fig. 8**). Typically, the cantilever starts the approach from a point where it is not in contact with the surface. After contact, it can be further approached until a maximal loading force is reached. Then the cantilever is retracted from the surface until the tip is free again. The deflection and the vertical position of the z piezo are recorded in such a force curve. According to Hooke's law, the loading force, F, can be calculated by multiplying the measured deflection, d, with the spring constant, k_C, of the cantilever.

$$F = k_C \times d \tag{1}$$

A force curve consists of two parts: the noncontact part and the contact part. When the tip is not in contact with the surface, the deflection will be constant. A further motion down after contact will deflect the cantilever. On a stiff sample, this deflection is equal to the travel of the z piezo after the contact point because the stiff sample cannot be indented (**Fig. 8**). However, a soft sample will be indented by the tip. Thus, the force curve will be shallower than on a stiff sample (**Fig. 9**). The indentation, δ, at a certain loading force can be calculated as the travel of the z piezo, z, after the contact point minus the deflection of the cantilever.

$$\delta = z - d \tag{2}$$

The unindented height of the sample can be calculated by finding the contact point. The contact point can be found rather easily in the case of a stiff sample since the force curve shows a sharp bend there (**Figs. 8** and **9**). In the case of a soft sample, the exact position of the contact point is often hard to determine since the transition between noncontact part and contact part is very shallow (**Fig. 9**). The contact point may also be hidden by thermal noise. A method to determine the contact point on a soft sample is described below. From the contact part of a force curve the elastic modulus can be calculated

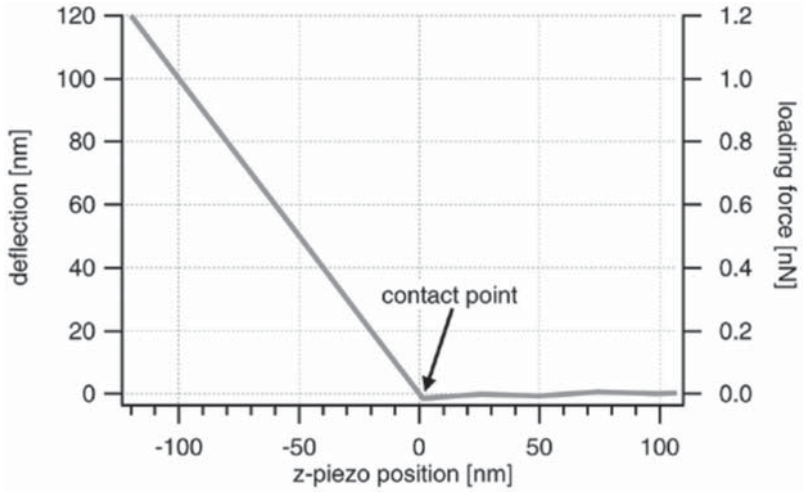

Fig. 8. Force curve on a stiff sample. Only the approach part is shown. The force curve consists of two parts: the noncontact part and the contact part. As long as the tip is not in contact with the surface, the deflection (and therefore the loading force) is constant. The tip contacts the surface in the contact point. In the contact part, a further approach deflects the cantilever. Because the stiff sample cannot be indented by the tip, the deflection equals the travel of the z piezo after the contact point.

by analyzing the force dependent indentation. This analysis will also be described below.

By recording a 2D array of force curves on a cell, a map of the unindented height and a map of the local elastic properties can be calculated (**Fig. 10**).

3.9.2. Calculation of the Contact Point and of the Elastic Modulus

The contact part of a force curve on a soft sample is nonlinear because the compliance of the sample becomes higher for larger loading forces. This is attributable to a geometrical effect. AFM tips are approximately conical and therefore the contact area increases with the increasing indentation. This process was treated analytically first by Hertz *(37)* and a more general solution was obtained by Sneddon *(38)*. For the geometry of a conical tip indenting a flat sample (which is most appropriate here) the relation between the indentation, δ, and the loading force, F, is given by the following:

$$F = \delta^2 \times (2/\pi) \times [E/(1-\nu^2)] \times \tan(\alpha) \quad (3)$$

where ν is the Poisson ratio, E is the elastic modulus, and α is the half opening angle of the conical tip. For incompressible materials (as assumed for cells), the Poisson ratio is 0.5. The half opening angle for Microlever (Park Scien-

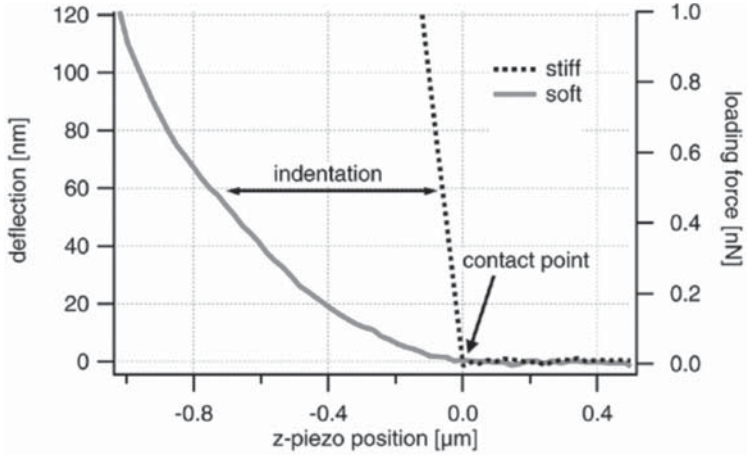

Fig. 9. Force curves on a soft and on a stiff sample. Only the approach parts are shown. The curve on the soft sample is shallower because sample is indented by the tip. The indentation is the travel of the z piezo after the contact point minus the deflection. The curve is nonlinear because the compliance becomes higher for larger loading forces. This is the result of a geometrical effect: AFM tips are (approximately) conical and therefore the contact area increases with the indentation. The contact point can very easily be determined on the stiff sample since the force curve shows a sharp bend there. On the soft sample, the determination of the contact point is more difficult since the transition between noncontact part and contact part is very shallow. *See* text for how to find the contact point on a soft sample.

tific) is 35°. The loading force can be calculated by Eq. 1 and the indentation can be calculated by Eq. 2. This gives the following:

$$k_c \times d = (z - d)^2 \times (2/\pi) \times [E/(1 - \nu^2)] \times \tan(\alpha) \quad (4)$$

Thus, the elastic modulus can be calculated by the measured deflection and z-piezo position. However, in measured data the deflection of the noncontact part of the force curve is not necessarily zero (**Fig. 11**). Therefore, the deflection, d, must be replaced by the following:

$$d \rightarrow d_i - d_0 \quad (5)$$

where d_0 is the deflection offset and d_i is a measured deflection value.

Eq. 3 is only valid for the contact part of the force curve. Thus, the contact point z_0 must be subtracted from a measured z-piezo value, z_i. Because the BioScope® stores force curves inverted (i.e., the point with the maximal deflection has the z-value 0 and the starting point of the approach has the maximum z value, **Fig. 11**), z must be replaced by the following:

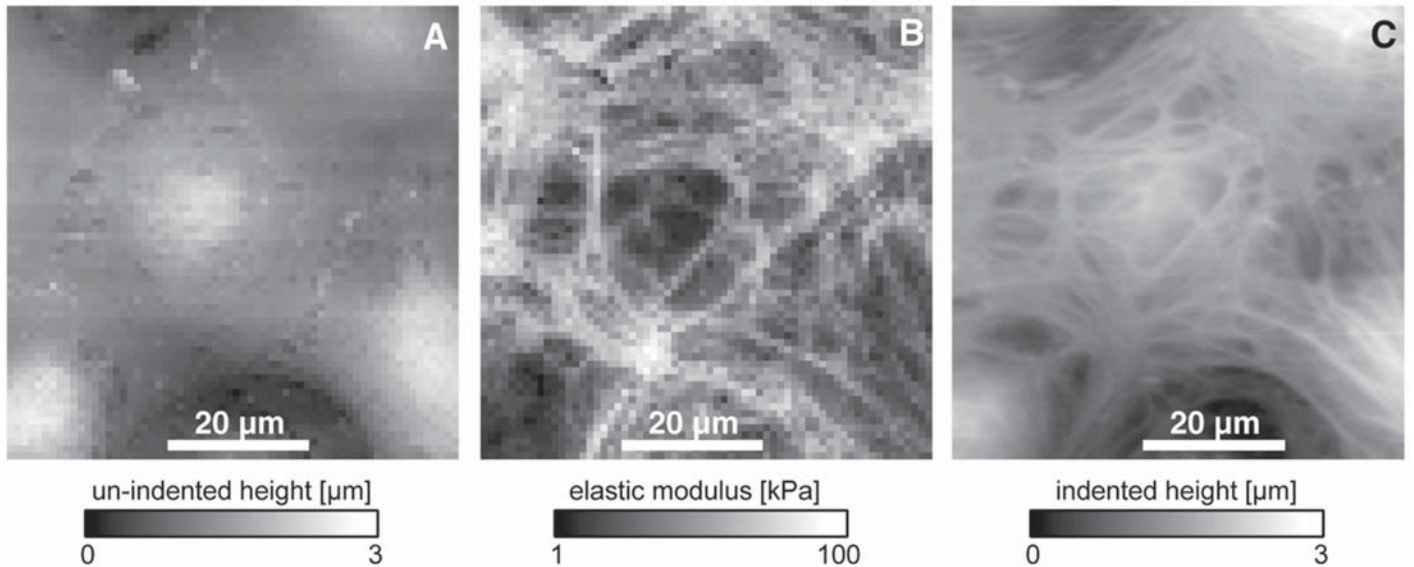

Fig. 10. Force maps of a living endothelial cell (HUVEC). **(A)** unindented height, **(B)** elastic modulus, and **(C)** contact mode image of the same cell. The unindented height image **(A)** shows a smooth cell surface, whereas the contact mode image shows height fluctuations **(C)**. This is because the indentation depends on the local elastic properties; soft regions will be more indented than stiffer regions. The cytoskeleton is a structured polymeric network with very different local elastic properties, as shown in the elasticity map **(B)**. The elastic indentation leads to an underestimation of the cell volume.

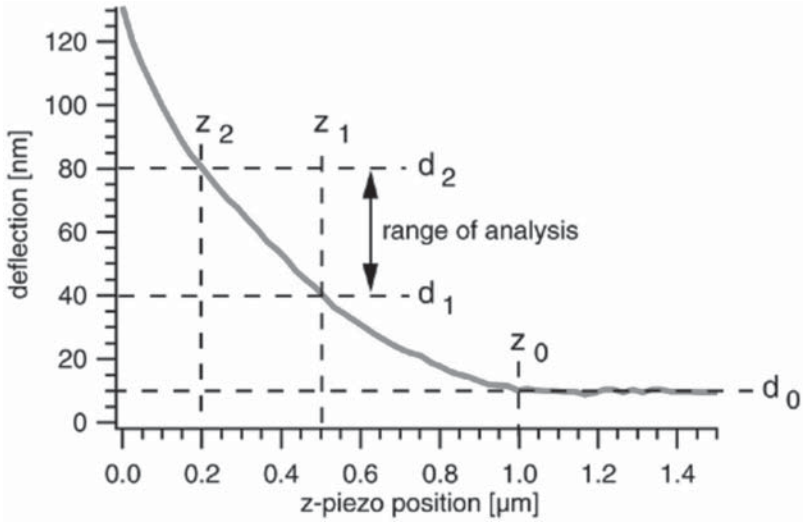

Fig.11. Parameters used for the calculation of the contact point and the elastic modulus. The two deflection values d_1 and d_2 and their corresponding z-piezo positions z_1 and z_2 define the range of analysis. The deflection-offset d_0 is given by the noncontact part of the force curve. With these values and **Eqs. 9** and **10**, the contact point z_0 and the elastic modulus can be calculated. In this example, $d_0 = 10$ nm, $d_1 = 40$ nm, $d_2 = 80$ nm, $z_1 = 0.5$ µm, $z_2 = 0.2$ µm, and $z_0 = 1$ µm.

$$z \rightarrow z_o - z_i \tag{6}$$

where z_0 is the z-piezo value of the contact point and z_i is a measured z-piezo position value (**Fig. 11**).

Eqs. 5 and 6 inserted in Eq. 4 gives the following:

$$k_c \times (d_i - d_0) = [(z_0 - z_i) - (d_i - d_0)]^2 \times (2/\pi) \times [E/(1 - \nu^2)] \times \tan(\alpha) \tag{7}$$

In this equation, we have three unknown parameters: the deflection offset, d_0, the contact point, z_0, and the elastic modulus, E. The deflection offset can easily be determined by the noncontact part of the force curve. As mentioned above, the transition from noncontact to contact part is very shallow and therefore the contact point cannot be determined by easy means. Unfortunately, Eq. 7 is of such a form that an analytical least squares fit to determine E and z_0 cannot be performed. One possibility is to perform a Monte-Carlo fit with reasonable starting values. However, the two missing parameters can be obtained more easily. Since the signal-to-noise ratio of measured data is very good (because thermal noise is reduced when the tip contacts the cell), we can

take two measured deflection values, d_1 and d_2, and their corresponding z-piezo values, z_1 and z_2, of the contact part of the force curve and insert them in Eq. 7. This gives two equations with two missing parameters, E and z_0:

$$k_c \times (d_1 - d_0) = [(z_0 - z_1) - (d_1 - d_0)]^2 \times (2/\pi) \times [E/(1 - \nu^2)] \times \tan(\alpha) \quad (8a)$$

$$k_c \times (d_2 - d_0) = [(z_0 - z_2) - (d_2 - d_0)]^2 \times (2/\pi) \times [E/(1 - \nu^2)] \times \tan(\alpha) \quad (8b)$$

The contact point can be calculated by solving Eq. 8a for E and inserting E in Eq. 8b:

$$z_0 = \frac{(z_2 + d_2)\sqrt{d_1} - (z_1 + d_1)\sqrt{d_2}}{\sqrt{d_1} - \sqrt{d_2}} \quad (9)$$

The elastic modulus can now be calculated by inserting z_0 in Eq. 8a or 8b.

A better method to calculate the elastic modulus is to apply an analytical least squares fit (this is possible now because z_0 is known) to all the data points (d_i/z_i) in the range of analysis (**Fig. 11**) that is limited by (d_1/z_1) and (d_2/z_2):

$$E = \frac{\sum_i F_i \delta_i^2}{\sum_i \delta_i^4} \times \frac{\pi \cdot (1 - \nu^2)}{2 \cdot \tan(\alpha)} \quad (10)$$

where $\delta_i = (z_0 - z_i) - (d_i - d_0)$.

The BioScope stores force curves in the force volume mode in a relative manner. This means that the absolute position of the z piezo is not recorded in the force curve itself and every force curve starts with $z = 0$. The force volume data consists of two separate datasets, one that contains the array of force curves, and another, in which the absolute height information is stored. Each pixel of the height image represents the absolute z-piezo value when the corresponding force curve switches from approach to retract (i.e., the point with the maximal loading force). Therefore, to calculate the unindented height, H_0, we have to add the calculated contact point, z_0, to the height at maximal loading force, H:

$$H_0 = H + z_0 \quad (11)$$

3.9.3. How to Access the Force Volume Data from the BioScope File

A force volume measurement consists typically of 64 × 64 force curves. Because of the amount of data, it is convenient to write a computer algorithm to analyze the data. Unfortunately, the BioScope software cannot export force volume data in a standard data format like ASCII. However, there is data analysis software (like IGOR PRO) that can read the binary information of the BioScope data file. At this time, it is difficult to give general advice on how to reconstruct the data from the binary file since the file format has changed in the past rather frequently for the various BioScope software versions. Please refer

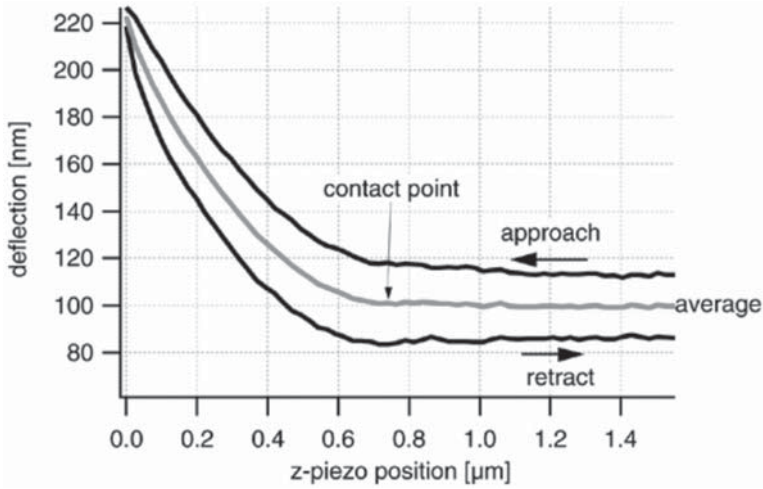

Fig. 12. Force curve on a living cell in liquid medium. The approach and retract parts are separated by hydrodynamic drag that adds a constant external force to the loading force of the cantilever. This force-offset is speed dependent (the faster the scan speed the bigger the force-offset; data not shown here) and changes its sign when the direction of movement is reversed from approach to retract. One way to deal with this force-offset is to average the approach and retract part point by point and to analyze the resulting average force curve.

to the manual of your software version to get information about the file and data structure.

When you are measuring living cells, the AFM is operated in liquid. In this case, the approach and retract part of the force curves are separated from each other (**Fig. 12**). This separation is caused by hydrodynamic forces as the cantilever is dragged through the fluid medium ***(34)***. This causes a force offset that depends on the speed of the z piezo, and the sign of that offset changes when the direction of movement is reversed between approach and retract. One way of dealing with this force offset is to average point by point the approach and retract part of the force curve and use this average for further analysis.

3.9.3.1 Notes

The Hertz model applied in the analysis is valid on condition that the sample is thick compared with the indentation, is homogeneous, and is flat, and that the geometry of the tip is a cone. The real situation fits these requirements only partly. The typical height of cells in the region of the nucleus is 4 µm. Here the height is sufficiently large versus the indentation (approx 400 nm). In the region of the thin lamellipodium, this condition is not fulfilled. With increasing indentation, the tip will feel the underlying stiff substrate and the force curve

will be initially the shape of a curve for a soft sample, but it will become linear and appear like a curve for a stiff substrate at higher deflection values ***(36)***. For the analysis of force curves taken on thin cell regions, it is therefore necessary to choose a fit range with sufficiently small deflection values ***(32)***. At small indentation values, the geometry of the AFM tip on nano-meter scale will become important. AFM tips look like a pyramid whose top is formed by a half sphere. The radius of that sphere is typically in the range of 50 nm. The Hertz model for the cone is no longer appropriate here. A better description of the data is the Hertz model for a sphere indenting a flat surface:

$$F = \frac{4}{3} \times \frac{E}{1 - \nu^2} \times \delta^{3/2} \times \sqrt{R} \tag{12}$$

where R is the radius of the tip ***(35)***.

Because the area of the cell surface is large, compared to the radius of the tip, one can assume as an approximation that the sample is flat, and thereby satisfy the Hertz model.

Cell material is not at all homogeneous. The cytoskeleton is a polymeric network that consists of polymers with very different elastic properties. There might also be contributions to the measured elastic modulus from the lipid membrane or from tension in the cytoskeleton. However, the scope of this article is the determination of the cell volume and not the quantification of the elastic modulus. Inhomogenieties may lead to an apparent elastic modulus, i.e., an average of all elastic components that contribute to the measured value. In practice, the contact point can be determined with sufficient precision despite this problem. If the elastic modulus changes with the depth of indentation (as with thin lamellipodia where the tip "feels" the underlying stiff substrate or when the elastic properties vary with the depth of indentation), one should take care that the data are analyzed in a fit range with small deflection values. Jan Domke (unpublished observation) showed by calculating simulations that the analysis of the cell height with the Hertz model gives reasonable values. There is only a systematic underestimation in the order of the tip radius.

3.9.4. How to Record a Force Map

Typical settings are trigger mode: relative; trigger threshold: 100 nm; z-scan size: 1.5 µm; z-scan speed: 10 Hz; 64 points per force curve, 64 × 64 points per image.

3.9.4.1 Comments

"Trigger mode: relative" means that the tip is approached to the sample until the cantilever reaches a deflection of "trigger threshold" (in our example 100 nm), relative to the deflection offset of the force curve given by the noncontact

part of the curve. This ensures that the deflection (and therefore the loading force) does not exceed the value given by trigger threshold. This prevents cell damage caused by high loading forces and ensures that the contact part of the scan will be long enough to find good deflection values for the data analysis. You can compare the relative trigger threshold with the set point in the contact mode, where the loading force can be adjusted by the set point. For the determination of the deflection offset, the force curve must contain a clear noncontact part (typically one-fourth of the total length of the force curve). In the BioScope, the tip is being approached until the deflection equals the trigger threshold. Then the z piezo moves upward the length given by the z-scan size. To get a distinct noncontact part, the z-scan size must be long enough for the tip to become free. A good starting value is 1.5 µm on living cells. With high cells, it might be difficult (or even impossible) to measure the topmost region of the cell since the necessary piezo travel range of the BioScope (6 µm) might be smaller than the height of the cell plus the z-scan range. New BioScope versions offer piezos with extended range. The z-scan speed is limited since hydrodynamic drag will cause a speed-dependent force offset. On the other hand, slow scan speed increases the time necessary to record a complete force map. A good compromise is a scan speed of 10 Hz. It will then take about 13 min to record a force map with 64×64 pixels. The number of pixels determines the lateral resolution. Of course, a small number will speed up data acquisition but decrease lateral resolution. However, you should consider the motion of the tip in the force-mapping mode: after recording one force curve, the tip moves laterally to record the next force curve. The lateral step size is given by the total lateral scan size divided by the number of pixels. With large step sizes, it might happen that the tip or cantilever bumps against the cell when it moves to the side because the tip is not far enough above the cell than the height of the cell increases. If possible, you can either increase the z-scan size or increase the number of pixels. Note that the BioScope cannot store more than $64 \times 64 \times 64$ data points (64 lines $\times$ 64 columns $\times$ 64 points in the force curve). When you increase the length of the force curve, the force resolution of the curve will become worse. Smaller lateral pixel numbers permit more points in the force curve (for example, $16 \times 16 \times 512$).

4. Notes

1. How to increase your time resolution: If it is not necessary to record all three dimensions (*x*-, *y*-, and *z*-axis) of the cell you can increase time resolution (up to 100 ms/line) by imaging only two dimensions (*x*- and *z*-axis). Switch the mode from slow axis enable to slow axis disable (= line scan) in your software menu. The cantilever is now moving back and forth along the same scanning line (*x*-axis). The *y*-axis will not be recorded. Fast volume fluctuations upon cell stimulation are now visible as a height increase or decrease.

2. Before starting cell imaging, make sure that your system provides good and stable images on a clean glass cover slip under fluid. This will help you to distinguish between problems that arise from the microscope (AFM tip damaged, air bubbles stuck to the cantilever, mechanical vibrations) or problems caused by the cells (membrane blebbing, cell detachment, etc.).
3. ECs that are under scanning should not change their morphology. You can observe the cells constantly through the light microscope.
4. The temperature of the environment (in the box) should be close to 37°C (in practice: approx 30°C) to minimize temperature alterations. Any increase or decrease of the temperature in the bath solution (which must have 37°C) is followed by artificial cantilever deflections.
5. Avoid acoustical or mechanical noise (speaking or walking) during the experiment.
6. If you cannot get an image or if you cannot increase the integral gain above 1 and the proportional gain above 2, check or modify the following parameters:
   a. Increase the loading force.
   b. The glass cover slip is too thin (<0.8 mm);
   c. There is a lot of noise or vibrations in your laboratory. Switch off: heating chamber, microscopy lamps, perfusion system, etc. Install the BioScope computer some distance away from the scanner and make sure that its fan does not blow in the direction of the scanner;
   d. The temperature of the bath solution is not constant;
   e. There are air bubbles stuck to the cantilever;
   f. The AFM tip is dirty;
   g. The cells detach from the glass surface (e.g., temperature above 37°C);
   h. The cells show membrane blebbing (a hint that the cells are in a bad condition and/or get damaged by the scanning tip);
   i. The glass cover slip (with the cell layer) is not firmly fixed in the perfusion chamber and thus comes off;
   j. Cell height is beyond the *z* piezo range of the instrument. Decrease the scan size or try to image a flat cell surface area (i.e. lamellipodium or cell–cell contact area). Adjust the piezo height with the step motor.

Acknowledgments

This work was supported by the VW-Stiftung (AZ I/77299) and the Interdisziplinäre Zentrum für Klinische Forschung (IZKF, TP I/90).

References

1. Harvey, B. J. , Condliffe, S., and Doolan, C. M. (2001) Sex and salt hormones: rapid effects in epithelia. *News Physiol. Sci.* **16,** 174–177.
2. Wehling, M., Käsmayr, J., and Theisen, K. (1991) Rapid effects of mineralocorticoids on sodium exchanger: Genomic or nongenomic pathways? *Am. J. Physiol.* **260,** E719–E726.
3. Wehling, M., Ulsenheimer, A., Schneider, M., Neylon, C., and Christ, M. (1994) Rapid effects of aldosterone on free intracellular calcium in vascular smooth

muscle and endothelial cells: subcellular localization of calcium elevations by single cell imaging. *Biochem. Biophys. Res. Commun.* **204,** 475–481.
4. Gekle, M., Silbernagl, S., and Oberleithner, H. (1997) The mineralocorticoid aldosterone activates a proton conductance in cultured kidney cells. *Am. J. Physiol.* **273,** C1673–C1678
5. Schneider, S. W., Yano, Y., Sumpio, B. E. , et al. (1997) Rapid aldosterone-induced cell volume increase of endothelial cells measured by the atomic force microscope. *Cell Biol. Int.* **21,** 759–768.
6. Vaupel, P., Kelleher, D. K., and Hockel, M. (2001) Oxygen status of malignant tumors: pathogenesis of hypoxia and significance for tumor therapy. *Semin. Oncol.* **28,** 29–35.
7. Winter, D. C., Schneider, M. F. , O'Sullivan, G. C. , Harvey, B. J., and Geibel, J. P. (1999) Rapid effects of aldosterone on sodium-hydrogen exchange in isolated colonic crypts. *J. Membr. Biol.* **170,** 17–26.
8. Urbach, V. and Harvey, B. J. (2001) Rapid and non-genomic reduction of intracellular [Ca(2+)] induced by aldosterone in human bronchial epithelium. *J. Physiol.* **537,** 267–275.
9. Oberleithner, H., Weigt, M., Westphale, H.-J., and Wang, W. (1987) Aldosterone activates Na+/H+ exchange and raises cytoplasmic pH in target cells of the amphibian kidney. *Proc. Natl. Acad. Sci. USA* **84,** 1464–1468.
10. Paccolat, M. P., Geering, K., Gaeggeler, H. P., and Rossier, B. C. (1987) Aldosterone regulation of Na+ transport and Na+-K+-ATPase in A6 cells: role of growth conditions. *Am. J. Physiol.* **252,** C468-C476
11. Schneider, S. W., Pagel, P., Storck, J., et al. (1998) Atomic force microscopy on living cells: aldosterone-induced localized cell swelling. *Kidney Blood Press. Res.* **21,** 256–258.
12. Cines, D. B., Pollak, E. S. , Buck, C. A., et al. (1998) Endothelial cells in physiology and in the pathophysiology of vascular disorders. *Blood* **91,** 3527–3561.
13. Phillips, P. G. and Tsan, M. F. (1988) Hyperoxia causes increased albumin permeability of cultured endothelial monolayers. *J. Appl. Physiol.* **64,** 1196–1202.
14. Shepard, J. M., Goderie, S. K., Brzyski, N., Del Vecchio, P. J. , Malik, A. B., and Kimelberg, H. K. (1987) Effects of alterations in endothelial cell volume on transendothelial albumin permeability. *J. Cell Physiol.* **133,** 389–394.
15. Barbee, K. A., Mundel, T., Lal, R., and Davies, P. F. (1995) Subcellular distribution of shear stress at the surface of flow- aligned and nonaligned endothelial monolayers. *Am. J. Physiol.* **268,** H1765–H1772.
16. Levin, E. G., Santell, L., and Saljooque, F. (1993) Hyperosmotic stress stimulates tissue plasminogen activator expression by a PKC-independent pathway. *Am. J. Physiol.* **265,** C387–C396.
17. Iba, T. and Sumpio, B. E. (1992) Tissue plasminogen activator expression in endothelial cells exposed to cyclic strain in vitro. *Cell Transplant.* **1,** 43–50.
18. Iba, T., Shin, T., Sonoda, T., Rosales, O., and Sumpio, B. E. (1991) Stimulation of endothelial secretion of tissue-type plasminogen activator by repetitive stretch. *J. Surg. Res.* **50,** 457–460.

19. Klein, J. D., Perry, P. B., and O'Neill, W. C. (1993) Regulation by cell volume of Na(+)-K(+)-2Cl- cotransport in vascular endothelial cells: role of protein phosphorylation. *J. Membr. Biol.* **132,** 243–252.
20. Marsh, D. J., Jensen, P. K., and Spring, K. R. (1985) Computer-based determination of size and shape in living cells. *J. Microsc.* **137,** 281–292.
21. Timbs, M. M. and Spring, K. R. (1996) Hydraulic properties of MDCK cell epithelium. *J. Membr. Biol.* **153,** 1–11.
22. Oberleithner, H., Brinckmann, E., Schwab, A., and Krohne, G. (1994) Imaging nuclear pores of aldosterone sensitive kidney cells by atomic force microscopy. *Proc. Natl. Acad. Sci. USA* **91,** 9784–9788.
23. Oberleithner, H., Giebisch, G., and Geibel, J. (1993) Imaging the lamellipodium of migrating epithelial cells in vivo by atomic force microscopy. *Pflügers Arch.* **425,** 506–510.
24. Radmacher, M., Tillmann, R. W., Fritz, M., and Gaub, H. E. (1992) From molecules to cells: imaging soft samples with the atomic force microscope. *Science* **257,** 1900–1905.
25. Schneider, S. W. (2001) Kiss and run mechanism in exocytosis. *J. Membr. Biol.* **181,** 67–76.
26. Schneider, S. W., Pagel, P., Rotsch, C., et al. (2000) Volume dynamics in migrating epithelial cells measured with atomic force microscopy. *Pflügers Arch.* **439,** 297–303.
27. Jaffe, E. A., Nachman, R. L., Becker, C. G., and Minick, C. R. (1973) Culture of human endothelial cells derived from umbilical veins. Identification by morphologic and immunologic criteria. *J. Clin. Invest.* **52,** 2745–2756.
28. Langer, F., Morys-Wortmann, C., Kusters, B., and Storck, J. (1999) Endothelial protease-activated receptor-2 induces tissue factor expression and von Willebrand factor release. *Br. J. Haematol.* **105,** 542–550.
29. Peters, P. J. (1999). Current protocols in cell biology 4.7.1–4.7.12, Wiley, New York.
30. Radmacher, M. (1997) Measuring the elastic properties of biological samples with the AFM. *IEEE Eng. Med. Biol. Mag.* **16,** 47–57.
31. Radmacher, M., Cleveland, J. P., Fritz, M., Hansma, H. G., and Hansma, P. K. (1994) Mapping interaction forces with the atomic force microscope. *Biophys. J.* **66,** 2159–2165.
32. Rotsch, C., Jacobson, K., and Radmacher, M. (1999) Dimensional and mechanical dynamics of active and stable edges in motile fibroblasts investigated by using atomic force microscopy. *Proc. Natl. Acad. Sci. USA* **96,** 921–926.
33. Matzke, R., Jacobson, K., and Radmacher, M. (2001) Direct, high-resolution measurement of furrow stiffening during division of adherent cells. *Nat. Cell Biol.* **3,** 607–610.
34. Radmacher, M., Fritz, M., Kacher, C. M., Cleveland, J. P., and Hansma, P. K. (1996) Measuring the viscoelastic properties of human platelets with the atomic force microscope. *Biophys. J.* **70,** 556–567.
35. Radmacher, M., Fritz, M., and Hansma, P. K. (1995) Imaging soft samples with the atomic force microscope: gelatin in water and propanol. *Biophys. J.* **69,** 264–270.

36. Domke, J. and Radmacher, M. (1998) Measuring the elastic properties of thin polymer films with the atomic force microscope. *Langmuir* **14,** 3320–3325.
37. Hertz, H. (1882) Über die Berührung fester elastischer Körper. *J. Reine Angew. Mathematik* **92,** 156–157.
38. Sneddon, I. N. (1965) The relation between load and penetration in the axisymmetric Boussinesq problem for a punch of arbitrary profile. *Int. J. Eng. Sci.* **3,** 47–57.

20

Localization of Epithelial Sodium Channels by Atomic Force Microscopy

Peter R. Smith and Dale J. Benos

1. Introduction

Epithelial sodium channels (ENaC) mediate Na reabsorption across a variety of sodium reabsorbing epithelia, such as the kidney, distal colon, and airway. Normal function of these channels is critical for processes as diverse as blood volume control and airway fluid homeostasis. The molecular cloning of ENaC from a variety of epithelial cells has revealed that they are composed of three homologous subunits, such as α, β, and γ ***(1)***.

Each subunit consists of intracellular N and C termini, two membrane transmembrane domains, and a large extracellular loop (**Fig. 1**; **ref. *1***).

We have previously used atomic force microscopy (AFM) for high-resolution imaging of the apical distribution of endogenously expressed ENaC in *Xenopus* A6 renal epithelial cells ***(2)***. A6 cells are a well-characterized and widely used model of a Na^+ reabsorbing epithelium. A6 cells were grown on cover slips and surface labeled with an antibody generated against an epithelial sodium channel complex purified from bovine renal medulla that had been coupled to 8-nm colloidal gold particles before preparation for AFM ***(2)***. We were successfully able to image ENaC on the cell surface of intact cells because the antibody recognized an extracellular epitope in the channel complex. However, this antibody is no longer available and the anti-ENaC antibodies that are currently commercially available have been generated against intracellular (N and/or C termini) epitopes of the subunits. Insertion of epitope tags into the extracellular domains of transmembrane proteins is a widely used approach for analysis of the cell surface distribution of heterologously expressed transmembrane proteins. Here we describe methods that can be used for AFM imaging of the cell surface distribution of heterologously expressed epitope tagged ENaC.

From: *Methods in Molecular Biology, vol. 242: Atomic Force Microscopy: Biomedical Methods and Applications*
Edited by: P. C. Braga and D. Ricci © Humana Press Inc., Totowa, NJ

2. Materials

1. α, β, and γ ENaC subunit cDNAs in a mammalian expression vector such as pcDNA3.1 (Invitrogen).
2. Standard molecular biological equipment including thermal cycler and agarose and sequencing gel equipment.
3. Gold chloride ($HAuCl_4$).
4. Trisodium citrate ($C_6H_5Na_3O_7 \cdot 2H_2O$).
5. Tannic acid.
6. Bovine serum albumin (IgG free).
7. Polyethylene glycol.
8. Sodium azide.
9. Anti-FLAG monoclonal antibody (M2-Sigma) or anti-HA monoclonal antibody (Roche, 3F10).
10. Control mouse IgG (Jackson Immunoresearch; West Grove, PA).
11. Lipofectamine 2000 (Invitrogen), FuGENE 6 (Roche), or a similar cationic lipid transfection reagent.
12. HEK 293 cells (ATCC # CRL-1573).
13. Thermanox cover slips (13 mm in diameter; Nunc).
14. Serum-free media for transfection, such as OPTI-MEM 1 (Gibco-BRL).
15. Amiloride.
16. Glutaraldehyde.
17. Sodium cacodylate.

3. Methods

The methods described below outline: (1) the construction of epitope-tagged ENaC plasmids, (2) preparation of colloidal gold-anti-epitope tag antibody conjugates, (3) heterologous expression of epitope-tagged ENaC, (4) antibody labeling of ENaC expressing cells, and (5) AFM imaging of ENaC-expressing cells.

3.1. Construction of Epitope-Tagged ENaC Plasmids

To allow detection of ENaC expressed at the cell surface, the α, β, and γ ENaC subunits are tagged in their extracellular loops at the regions shown in **Fig. 1** with either the FLAG peptide (DYKDDDDK) or the HA peptide (YPYDVPDYA). These regions were initially chosen because they show a high degree of sequence divergence between ENaC subunits of *Xenopus*, rat, mouse, and human ***(3)***. Insertion of either the FLAG or HA epitope tag into these regions does not affect channel assembly or function ***(3,4)***.

Introduction of FLAG or HA peptides into the extracellular loops of α, β, and γ ENaC (*see* **Note 1**) is performed by polymerase chain reaction-based methods as described by Ausbel et al. ***(5)***. In α and γ ENaC, this involves the replacement of amino acids in the extracellular loop with the FLAG or HA epitope and in β ENaC, it involves the insertion of the FLAG or HA epitope

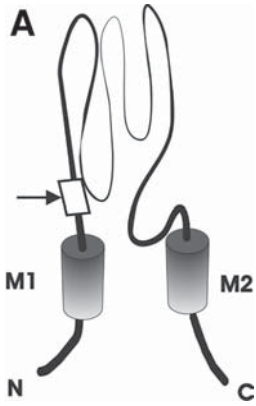

B

α

	Replacement	**DYKDDDDK/ YPYDVPDYA**
α rat/mouse ENaC	^{191}NSSY**TRQAG(A/G)RR**RSSR^{205}	
α human ENaC	^{165}SSFT**TLVAGS . .** RSRR^{178}	
α *Xenopus* ENaC	^{129}NGTG**VQGWIPNN**QRVK^{144}	

β

	Insertion	**DYKDDDDK/ YPYDVPDYA** ↓
β rat/mouse ENaC	^{135}NT . . . . . T(S/N)TLN^{141}	
β human ENaC	^{135}NA . . . . . TRNLN^{141}	
β *Xenopus* ENaC	^{141}NTFHNNQTRQNVTLVD^{156}	

γ

	Replacement	**DYKDDDDK/ YPYDVPDYA**
γ rat/mouse ENaC	^{139}EAGS**MPSTLEGT**PPRF^{154}	
γ human ENaC	^{139}EAES**WNSVSEGK**QPRF^{154}	
γ *Xenopus* ENaC	^{140}KRDV**GVNVENST** EDI F^{155}	

Fig. 1. Placement of the FLAG and HA epitope into the extracellular domains of α, β, and γ ENaC. **(A)** Schematic diagram of an ENaC subunit illustrating the region (arrow) of the extracellular domain that is modified by the replacement or insertion of the epitope tag. **(B)** Sites of replacement (α and γ subunit) and insertion (β subunit) of the FLAG (DYKDDDDK) or HA (YPYDVPDYA) epitope tags into the amino acid sequence of the extracellular domains of ENaC subunits. The nine amino acids that are replaced in α and γ subunits are indicated in bold. For insertion of the HA eptiope, an additional amino acid (underlined) is replaced. The site of insertion of the epitope tag into the β subunit is indicated by the arrow. Based upon **ref. *3***.

into the extracellular loop as shown in **Fig. 1**. The accuracy of the constructs must be verified by restriction enzyme digestions and DNA sequencing. If the

ENaC subunit cDNAs are not in a mammalian expression vector, the cDNAs can be subloned into a suitable expression vector, such as pcDNA3.1, using standard molecular biological techniques. The constructs should be verified by restriction enzyme digestions and DNA sequencing before their expression is attempted.

3.2. Preparation of Colloidal Gold Anti-Epitope Tag Antibody Conjugates

Putnam and coworkers originally described the use of immunogold labels as cell surfaces markers in atomic force microscopy ***(6)***. We have found that 8-nm colloidal gold particle antibody conjugates work well for the detection of ENaC at the cell surface by AFM ***(2)***. Below, we describe the preparation of 8-nm colloidal gold particles after the tannic acid methods of Slot and Geuze (*see* **Note 2**; **ref. *7***) and the conjugation of the colloidal gold particles to anti-eptiope tag antibody or control IgG.

1. Prepare solution A consisting of 1 mL of 1% $HAuCl_4$ and 79 mL of distilled water.
2. Prepare solution B consisting of 4 mL of 1% $C_6H_5Na_3O_7 \cdot 2H_2O$, 15.5 mL of distilled water, and 0.25 mL of 1% tannic acid.
3. Warm solutions A and B to 60°C, mix rapidly, and heat with stirring until boiling.
4. Stabilize the conjugates by the addition of polyethylene glycol to a final concentration of 0.5% before adjusting the pH of the gold solution to 9.0 with 200 m*M* K_2CO_3. It is critical that the solution be stabilized before adjusting the pH because the unstabilized gold solution will destroy the pH electrode.

Next, the colloidal gold particles should be conjugated to the anti-eptiope tag antibody or control IgG following the protocol of Hartwig ***(8)***.

1. Dialyze anti-epitope tag antibody (anti-FLAG epitope or anti-HA epitope monoclonal antibody) and matched control mouse IgG (approximate concentration of 1 mg/mL) against 2 m*M* $Na_4B_4O_7$, pH 9.0.
2. Add either anti-epitope tag antibody or control IgG (120 µg) to 20 mL of stabilized colloidal gold solution, pH 9.0 and rapidly stir for 20 min.
3. Stabilize conjugates by the addition of 250 µL of 8% bovine serum albumin (IgG free) and 20 µL of 5% polyethylene glycol.
4. Collect colloidal gold IgG conjugates by centrifugation at 50,000*g* for 1 h (4°C).
5. Resuspend pellet in 1 mL of 150 m*M* NaCl, 20 m*M* Tris, 1% bovine serum albumin, and 0.1% sodium azide, pH 8.3, and remove aggregates by centrifugation for 10 min at full speed in a microcentrifuge
6. Store conjugates at 4°C. They remain stable for several months.

3.3. Heterologous Expression of Epitope-Tagged ENaC

Next, the epitope-tagged ENaC subunits are transiently expressed in a well-characterized mammalian cell line, such as HEK 293 cells (*see* **Note 3**).

1. HEK 293 cells to be transfected are plated on a Thermanox circular cover slip placed in either a 35-mm tissue culture dish or a single well of a 6-well tissue culture dish. The day before transfection, trypsinize and count to determine the plating density. Cells should be 80–90% confluent on the day of transfection. Plate cells in normal growth medium containing serum but without antibiotics.
2. Transfect cells with epitope tagged α, β, and γ ENaC (start with 0.3 μg of each plasmid/cover slip) or an equivalent concentration of empty vector to serve as a control following the manufacturer's directions for the cationic lipid transfection reagent chosen (i.e., Lipofectamine 2000, FuGENE 6; *see* **Note 4**). Use a serum-free medium, such as OPTI-MEM 1, for the transfection procedure. Replace the media containing the transfection complexes 3–6 h after transfection with fresh complete media (containing serum and antibiotics). Supplement the media with 10 μ*M* amiloride to prevent cell swelling and lysis as a result of ENaC expression.
3. Cells are ready for antibody labeling 24–48 h after transfection.

3.4. Antibody Labeling of ENaC-Expressing Cells

The next step in the process involves the labeling of the transfected cells with the antibody colloidal gold conjugates.

1. Wash cover slips bearing transfected cells in phosphate-buffered saline (PBS) 1 m*M* $CaCl_2$, 3 m*M* KCl, 1 m*M* K_2HPO_4; 2 m*M* $MgCl_2$, 140 m*M* NaCl, 8 m*M* Na_2HPO_4; pH 7.4 (2 × 5 min).
2. Depending upon the epitope tag used, incubate cover slips in either colloidal gold conjugated anti-FLAG or anti-HA tag antibody diluted in PBS for 45 min at 4°C to prevent internalization of the colloidal gold conjugates. Also incubate cover slips bearing transfected cells in colloidal gold-control IgG conjugates diluted in PBS to serve as controls. As additional controls, incubate cover slips bearing nontransfected cells and cells transfected with vector only in colloidal gold antibody and colloidal gold IgG conjugates. The optimal dilution of the colloidal gold antibody complexes will need to be determined for each conjugation. A suggested range of dilutions is 1:10 to 1:100.
3. Wash cover slips in PBS (4 × 5 min) at 4°C and then fix cells for 15 min in 0.25% glutaraldehyde in 0.1 *M* sodium cacodylate buffer, pH 7.5.
4. Wash cover slips in PBS (2 × 5 min). Cells are now ready for AFM imaging.

3.5. AFM Imaging of ENaC-Expressing Cells

Here, we briefly describe AFM imaging of the cells using a Nanoscope III (Digital Instruments) equipped with the "D" scanner (maximal *x*, *y* scan size 14 mm) and cantilevers with a spring constant of 0.6 N/m and estimated tip diameter of 10 nm (Digital Instruments).

1. Attach a cover slip to the metal AFM puck using double-sided adhesive tape and mount in the fluid cell. Image the sample in PBS.

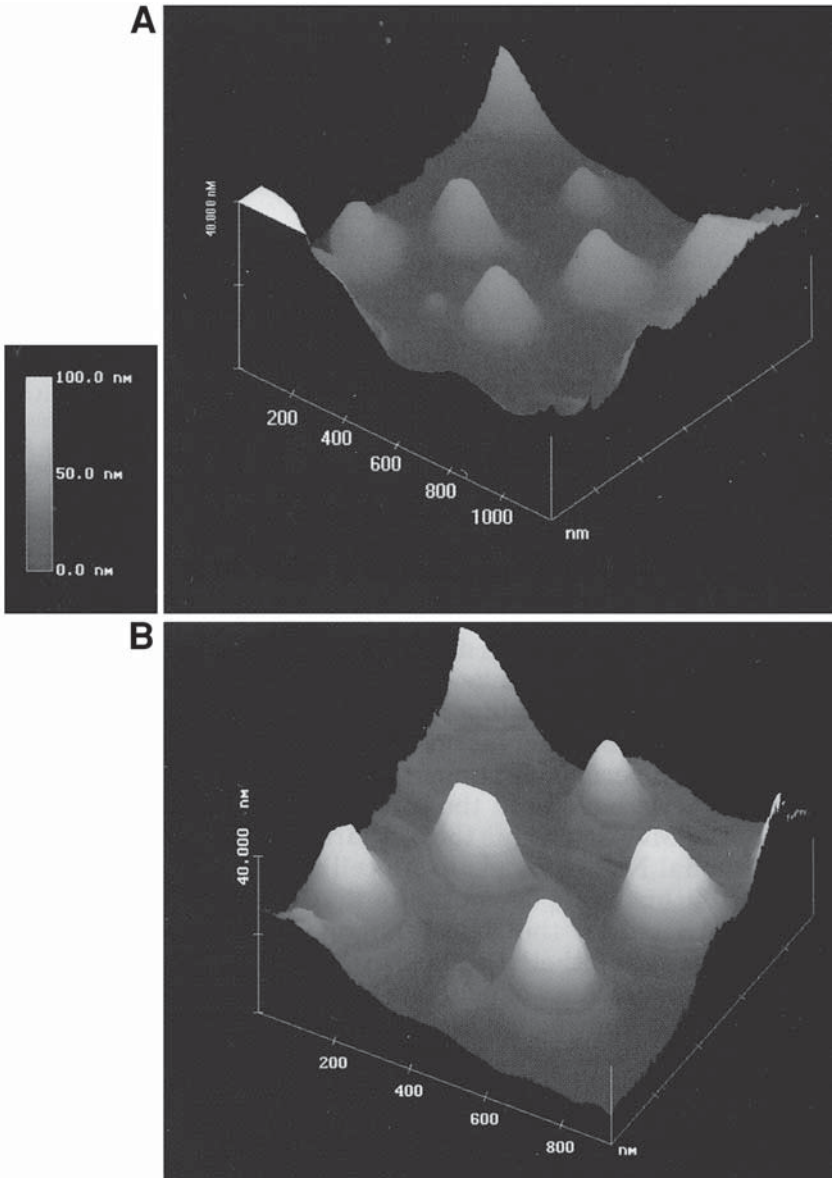

Fig. 2. Representative images illustrating the localization of epithelial sodium channels by AFM. **(A)** Image of the surface of an A6 renal epithelial cell labeled with colloidal gold particles conjugated to nonimmune IgG showing the microvilli. **(B)** Image of the surface of an A6 cell labeled with colloidal gold particles conjugated to an anti-epithelial sodium channel antibody showing localization of marker to the microvilli. Note marked increase in height of microvilli when compared to A. Reproduced with permission from the American Physiological Society from **ref. *2***.

2. Operate Bioscope in the contact mode. After engagement with the sample, adjust the scan force to values in the range of 5 nN. Record images with a display of 512 lines/screen (1 μm^2 scan area) at a constant force. (Typical area rate of 1–2 Hz.)
3. Scan multiple cells/cover slip and multiple cover slips labeled with both antibody and control IgG. Also scan cover slips bearing cells that were fixed but not labeled to obtain dimensions and surface topography of the cells before antibody treatment. Binding of colloidal gold antibody conjugates to the epitope-tagged ENaC results in a marked difference in height of the cell surface when compared to controls (*see* **Fig. 2**; **Note 5**).

4. Notes

1. cDNAs have been cloned for the α, β, and γ subunits of *Xenopus* ***(9)***, rat ***(10–13)***, mouse ***(14)***, and human ENaC ***(15–17)***. All species can be expressed heterologously in mammalian cells. Typically, the cDNAs are available upon request from the laboratories that cloned them. Subcloning of the subunits into a mammalian expression vector, such as pcDNA3.1, may be required. A number of laboratories have produced constructs for ENaC subunits with extracellular epitope tags that may be available upon request ***(3,4,18)***.
2. Although we produce colloidal gold particles following the method of Slot and Geuze ***(7)***, colloidal gold particles produced by this method are available commercially (Sigma; Electron Microscopy Sciences, Fort Washington, PA).
3. HEK 293 cells have been effectively used for the transient expression of ENaC ***(19,20)***. When HEK 293 cells are used with an expression vector that includes the CMV promoter, such as pcDNA 3.1, high levels of transcription are obtained. COS 7 cells ***(19)*** and Fisher rat thyroid cells, which form polarized monolayers ***(21)***, have also proven useful for the transient expression of ENaC. Alternatively, stably transfected cell lines expressing epitope-tagged α, β, and γ ENaC can be generated ***(18,20,22)***. The selection of an appropriate cell line and the use of transient or stable transfectants depends upon the objectives of the investigation.
4. For transient tranfection using liposome-mediated transfection reagents, we suggest starting with a plasmid concentration of 0.3 μg for each ENaC subunit. This, however, will need to optimized in each lab. Follow the manufacturer's directions for optimization of transfection efficiency and protein expression levels. To achieve high efficiency transfections, it is critical that the plasmid DNA used is of high quality and is free of contaminants.
5. For visualization of colloidal gold antibody conjugate on the cell surface, select small areas of interest during scanning and reduce the field to concentrate on these areas. In addition, small areas of interest can be selected from stored images, zoomed to full screen and analyzed using the Nanoscope III software. To control for bias during both scanning and analysis, it is recommended that a blind study be performed.

Acknowledgments

This work was supported by National Institutes of Diabetes and Digestive and Kidney Diseases Grants DK-37206 (Dale J. Benos) and DK-56596 (Peter

R. Smith). Peter R. Smith is the recipient of an Established Investigator Award from the American Heart Association.

References

1. Alvarez de la Rosa, D., Canessa, C. M., Fyfe, G. K., and Zhang, P. (2000) Structure and regulation of amiloride-sensitive sodium channels. *Ann. Rev. Physiol.* **62,** 573–594.
2. Smith, P. R., Bradford, A. L., Schneider, S., Benos, D. J., and Geibel, J. P. (1997) Localization of amiloride-sensitive sodium channels in A6 cells by atomic force microscopy. *Am. J. Physiol.* **272,** C1295–1298.
3. Firsov, D., Schild, L., Gautschi, I. Merillat, A. M., Schneeberger, E., and Rossier, B. C. (1996) Cell surface expression of the epithelial Na channel and a mutant causing Liddle syndrome: A quantitative approach. *Proc. Natl. Acad. Sci. USA* **93,** 15370–15375.
4. Konstas, A. A., Bielfeld-Ackermann, A., and Korbmacher, C. (2001) Sulfonylurea receptors inhibit the epithelial sodium channel (ENaC) by reducing surface expression. *Pflugers Arch.* **442,** 752–761.
5. Ausbel, F. M., Brent, R., Kingston, R. E., Moore, D. D., Seidman, J. G., Smith, J. A., et al. (1997) *Current Protocols in Molecular Biology*, J. Wiley and Sons, New York.
6. Putnam, C. A.J., deGrooth, B. G., Hansma, P. K., van Hulst, N. F., and Greve, J. (1992) Immunogold labels: cell-surface makers in atomic force microscopy. *Ultramicroscopy* **42,** 1549–1552.
7. Slot, W. and Geuze, H. J. (1985) A new method to make gold probes for multiple-labeling cytochemistry. *Eur. J. Cell. Biol.* **38,** 87–93.
8. Hartwig, J. H. (1992) An ultrastructural approach to understanding the cytoskeleton, in *The Cytoskeleton. A Practical Approach* (K. L. Carraway and C. A.C. Carraway, eds), IRL, New York.
9. Puoti, A., May, A., Canessa, C. M., Horisberger, J-D., Schild, L., and Rossier, B. C. (1995) The highly selective low-conductance epithelial Na^+ channel of *Xenopus* laevis A6 kidney cells. *Am. J. Physiol.* **269,** C188–C197.
10. Canessa, C. M., Horisberger, J.-D., and Rossier, B. C. (1993) Epithelial sodium channel related to proteins involved in neurodegeneration. *Nature* **361,** 467–470.
11. Canessa, C. M., Schild, L. Buell, G., Thorens, B., Gautschi, I, Horisberger, J.-D., et al. (1994) Amiloride sensitive epithelial Na^+ channel is made of three homologous subunits. *Nature* **367,** 463–467.
12. Linqueglia, E., Voilley, N., Waldmann, R., Lazdunski, M., and Barbry, P. (1993) Expression cloning of an epithelial amiloride-sensitive Na^+ channel. A new channel type with homologies to *Caenorhabdites elegans* degenerins. *FEBS Lett.* **318,** 95–99.
13. Lingueglia, E., Renard, S., Waldmann, R., Voilley, N., Champigny, G., Plass, H., et al. (1994) Different homologous subunits of the amiloride-sensitive Na^+ channel are differently regulated by aldosterone. *J. Biol. Chem.* **269,** 13736–13739.

14. Ahn, Y. J., Brooker, D. R., Kosari, F., Harte, B. J, Li, J., Mackler, S. A., et al. (1999) Cloning and functional expression of the mouse epithelial sodium channel. *Am. J. Physiol.* **277,** F121–129.
15. McDonald, F. J., Snyder, P. M., McCray, P. B., and Welsh, M. J. (1994) Cloning, expression, and distribution of a human amiloride-sensitive Na^+ channel. *Am. J. Physiol.* **266,** L728–L734.
16. McDonald, F. J., Price, M. P., Snyder, P. M., and Welsh, M. J. (1995) Cloning and expression of the β and γ subunits of the human epithelial sodium channel. *Am. J. Physiol.* **268,** C1157–C1163.
17. Voilley, N., Lingueglia, E., Champigny, G., Mattei, M.-G., Waldmann, R., Lazdunski, M., et al. (1994) The lung amiloride-sensitive Na^+ channel: biophysical properties, pharmacology, ontogenesis, and molecular cloning. *Proc. Natl. Acad. Sci. USA* **91,** 247–251.
18. Hanwell, D., Isikawa, T., Saleki, R., and Rotin, D. (2002) Trafficking and cell surface stability of the epithelial Na^+ channel expressed in epithelial Madin–Darby canine kidney cells. *J. Biol. Chem.* **277,** 9772–9779.
19. Prince, L. S. and Welsh, M. J. (1998) Cell surface expression and biosynthesis of epithelial Na^+ channels. *Biochem. J.* **336,**705–710.
20. Staub, O., Gautschi, I., Ishikawa, T., Breitschopf, K., Ciechanover, A., Schild, L., et al. (1997) Regulation of stability and function of the epithelial Na^+ channel (ENaC) by ubiquitination. *EMBO J.* **16,** 6325–633.
21. Snyder, P. M. (2000) Liddle's syndrome mutations disrupt cAMP-mediated translocation of the epithelial Na^+ channel to the cell surface. *J. Clin. Invest.* **105,** 45–53.
22. Shimkets, R. A., Lifton, R., and Canessa, C. M. (1998) *In vivo* phosphorylation of the epithelial sodium channel. *Proc. Natl. Acad. Sci, USA.* **95,** 3301–3305.

21

High-Resolution Imaging of Bacteriorhodopsin by Atomic Force Microscopy

Dimitrios Fotiadis and Andreas Engel

1. Introduction

In the last years the atomic force microscope (AFM; **ref. *1***) has become a powerful imaging tool for the biologist. The unique features like the possibility to image biological structures in their native environment (i.e., in buffer solution, at room temperature, and under normal pressure), the high lateral and vertical resolution, and the high signal-to-noise ratio of the topographs acquired by AFM make this instrument outstanding. It has made the observation of different single biomolecules at work and the monitoring of biomolecular interactions by time-lapse AFM possible (for recent reviews, *see* **refs. *2–4***).

This chapter focuses on the application of contact mode AFM to acquire high-resolution structural information of membrane proteins in buffer solution. In this scan mode the probing tip touches the surface with a constant force while scanning. To minimize possible damage of the biological specimen by the tip, soft cantilevers with spring constants around 0.1 N/m must be used and scanning must be performed at minimal tip force (approx 100–300 pN). Lateral resolutions down to 0.41 nm and vertical resolutions down to 0.10 nm have been achieved on biological membranes in solution ***(5)***. Alternative AFM modes to record topographies are the tapping mode ***(6–8)*** and the magnetically activated oscillating mode ***(9,10)***, better known as MAC mode. Both are similar and frequently used to image the surface topography of weakly immobilized biomolecules, that is, single proteins, fibrils, and chromosomes, and have in common that the AFM tip is oscillated vertically while scanning the sample. Thus, frictional forces are reduced by the oscillation of the tip avoiding deformation and displacement of the sample. However, for high-resolution imaging of biological membranes contact mode has shown to be the better choice pro-

From: *Methods in Molecular Biology, vol. 242: Atomic Force Microscopy: Biomedical Methods and Applications*
Edited by: P. C. Braga and D. Ricci © Humana Press Inc., Totowa, NJ

vided the imaging parameters, for example, force and imaging buffer, are adjusted correctly ***(11)***. To prevent deformation of the structure as a result of friction, the forces acting between tip and sample should not exceed 300 pN in contact mode. However, application of higher forces can sometimes be useful to perform precise and controlled dissections of biological samples by manipulation with the AFM tip ***(12)***.

As biological specimen for the AFM imaging experiment presented here, we have chosen bacteriorhodopsin (BR) membranes. This 26-kDa heptahelical transmembrane protein acts as a light-driven proton pump in the cell membrane of the bacterium *Halobacterium salinarum* ***(13,14)***. Photoisomerization of the covalently bound chromophore from all-*trans* to 13-*cis* retinal initiates proton translocation across the cell membrane ***(15,16)***. This establishes a proton gradient across the cell membrane for ATP synthesis and other energy requiring processes in the cell. BR molecules form highly ordered two-dimensional crystals ***(17)*** (trigonal lattice: $a = b = 6.2$ nm, $\gamma = 60°$) in the native membrane of *Halobacterium salinarum*, termed purple membrane for its color. Because of its crystallinity and flatness this sample is very suitable for AFM and cryo-electron microscopy. High-resolution three-dimensional structures of BR (**Fig. 1**) were determined by electron crystallography and X-ray diffraction (for a recent review, *see* **ref. *18***). In BR, the retinal (*see* **Fig. 1**; arrowhead) lies in the intramembrane cavity formed by the seven transmembrane α-helices generally denoted A to G. The main portions of BR that protrude out of the membrane are: The loops connecting the transmembrane α-helices A and B as well as E and F (AB and EF loops; **Fig. 1**) on the cytoplasmic side and the B-C interhelical loop (BC loop; **Fig. 1**) on the extracellular side. The latter forms a twisted antiparallel β-sheet and is more stable than the wobbly EF loop ***(19)***.

2. Materials

2.1. Preparation of Mica Supports for Sample Immobilization

1. Inoxydable and magnetic steel disks of 11 mm in diameter (internal services of the Biozentrum, Basel, Switzerland).
2. Teflon sheets of 0.25-mm thickness (Maag Technic AG, Birsfelden, Switzerland).
3. Mica sheets with a thickness between 0.3–0.6 mm (Mica House, 2A Pretoria Street, Calcutta 700 071, India).
4. "Punch and die" set from Precision Brand Products Inc. (Downers Grove, IL).
5. Ethanol (concentration 96% [v/v]).
6. Loctite 406 superglue from KVT König, Dietikon, Switzerland.
7. Araldit Rapid: Two-component epoxy glue from Ciba-Geigy, Basel, Switzerland.
8. Scotch tape.

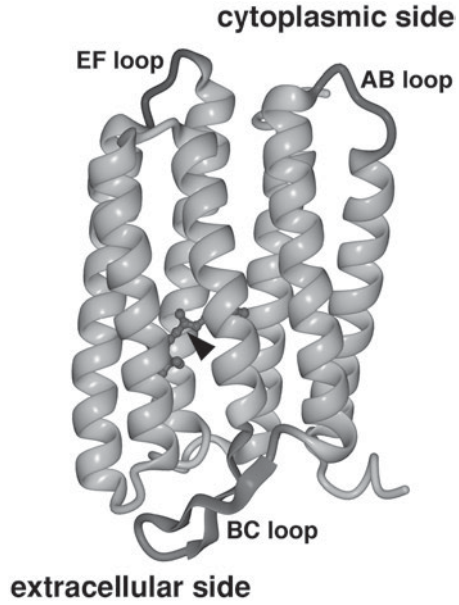

Fig. 1. Ribbon diagram of BR. The retinal chromophore (arrowhead) is displayed as a ball-and-stick model. This illustration of BR was calculated using the coordinates of Kimura et al. ***(28)*** and the three-dimensional visualization program DINO (http://www.dino3d.org/).

2.2. BR and Buffers (see *Note 1)*

1. Purple membranes of *H. salinarum*. Stock solution: 0.25 mg/mL in double distilled water containing 0.01% NaN_3. Store at 4°C and protect from unnecessary light irradiation.
2. Adsorption buffer: 20 m*M* Tris-HCl, pH 7.8, 150 m*M* KCl.
3. Imaging buffer for the extracellular side (ES imaging buffer): 20 m*M* Tris-HCl, pH 7.8, 150 m*M* KCl, 25 m*M* $MgCl_2$.
4. Imaging buffer for the cytoplasmic side (CS-imaging buffer): 20 m*M* Tris-HCl, pH 7.8, 150 m*M* KCl.

2.3. AFM and Accessories (see *Note 2)*

1. A commercial multimode AFM equipped with a 120-µm scanner (j-scanner) and a liquid cell (Digital Instruments, Veeco Metrology Group, Santa Barbara, CA).
2. Oxide-sharpened Si_3N_4 micro cantilevers of 100 µm in length and a nominal spring constant of k = 0.08 N/m (Olympus Optical Co., LTD, Tokyo, Japan).

3. Method

3.1. Preparation of Mica Supports for Sample Immobilization

1. Punch mica disks of 6 mm and Teflon disks of 13 mm diameter using the "punch and die" set and a hammer.
2. Clean the Teflon and steel disks with ethanol and paper wipes.
3. Glue a Teflon disk on a steel disk using Loctite 406.
4. Glue a mica disk on the Teflon surface of the Teflon-steel disk with the two-component epoxy glue.
5. Let the supports dry for at least 1 day.

3.2. Adsorption of BR to Mica

1. Dilute and mix 3 μL of purple membrane stock solution with 30 μL of adsorption buffer in an Eppendorf tube.
2. Cleave mica with Scotch tape.
3. Pipet the diluted purple membranes on the freshly cleaved mica support.
4. Adsorb BR for 15 to 30 min.
5. Wash away the purple membranes that are not firmly attached to the mica by removing approximately two thirds of the fluid volume from the mica surface and readding the same amount of the corresponding imaging buffer. Repeat this washing procedure at least three times.
6. Transport the support onto the piezo scanner.
7. Mount the AFM head containing fluid cell (without o-ring seal) and cantilever on the microscope.
8. Fill the space between the mica surface and the fluid cell with the corresponding imaging buffer to avoid drying of the protein.

3.3. Operation of the AFM (see *Notes 3–5*)

After thermal relaxation of the instrument, initial engagement of the tip is performed. Specimen deformation and contamination of the tip is minimized during the engagement process by setting the scan size to 0. Prior scanning the surface, the operating point of the instrument is set to forces below 1 nN. During scanning the forces are kept as small as possible (<300 pN) and corrected manually to compensate for thermal drift.

Two frames of 512 by 512 pixel are simultaneously recorded either showing topography or deflection signal in trace or retrace direction. Usually deflection and height signals are recorded at low magnification (frame size >1 μm) whereas height signals were acquired in both, trace and retrace direction at high magnification (frame size <1 μm).

This allows deformation of the sample in the fast scan direction to be detected and to be minimized by lowering the force applied to the stylus. Typically, the scan speed is set to 4.7–5.5 Hz (lines per second). At high magnification the scan range of the z piezo is reduced to avoid limitation of the axial

z-resolution by the digitalization of the signal (AD conversion). All measurements are carried out under ambient pressure and at room temperature.

3.4. Conclusion

Here we have presented materials and methods to image the native surface of bacteriorhodopsin at subnanometer resolution with the AFM in buffer solution (*see* **Note 6**). We have demonstrated that forces between stylus and sample as well as shape and geometry of the AFM tip play an important role for successful imaging of the biological sample (*see* **Note 7**). Additionally, it was shown that higher forces may be of advantage to study otherwise hidden features of a protein, that is, the AB loop in BR (*see* **Note 5**).

4. Notes

1. Buffer conditions for high-resolution AFM imaging: Topographs of native membrane proteins with a lateral resolution of 0.41 nm ***(5)*** can reproducibly be recorded with the AFM provided imaging force and buffer are adjusted correctly ***(11)***. In general, scanning is performed at minimal forces applied to the stylus to avoid friction and deformation of the biological sample. However, often even the smallest force adjustable by the instrument is too high for preventing deformation of the biomolecule.
   The effective interaction force acting between AFM stylus and specimen is the sum of the force applied to the stylus, the electrostatic repulsion and the van der Waals attraction between the two surfaces. By adjusting pH and ion strength of the imaging buffer van der Waals attraction and electrostatic repulsion between tip and sample can be balanced. Under these conditions the tip is assumed to surf on a cushion of electrostatic repulsion minimizing the deformation of the biomolecule. The best imaging conditions are determined by recording and analyzing force-distance curves between tip and sample in different buffers. Conditions that yield force curves with a small repulsive peak are ideal for high-resolution imaging. By this screening method the two slightly different imaging buffers for BR mentioned in **Subheading 2.2.** (CS and ES imaging buffer) were found. For further reading on this topic, *see* **ref. *11***.
2. Damping of vibrations: For high-resolution AFM imaging, an acoustic and vibration isolated set-up of the microscope is crucial. Antivibration and damping tables, or lead platforms supported by bungees offer excellent vibration damping. Acoustic isolation of the AFM can efficiently be achieved by a vacuum bell jar.
3. Morphology of BR crystals. **Figure 2** shows a typical overview (frame size 25 μm) of purple membranes adsorbed to freshly cleaved mica. The diameter of the BR sheets varies between 0.5–1.5 μm. The number of adsorbed membrane patches depends on the adsorption buffer, time and the concentration of the bacteriorhodopsin solution deposited on the mica. To avoid contamination of the tip, BR sheets were not adsorbed too densely on the support. At higher magnification (**Fig. 3**; frame size 3.67 μm) two different types of membranes can be

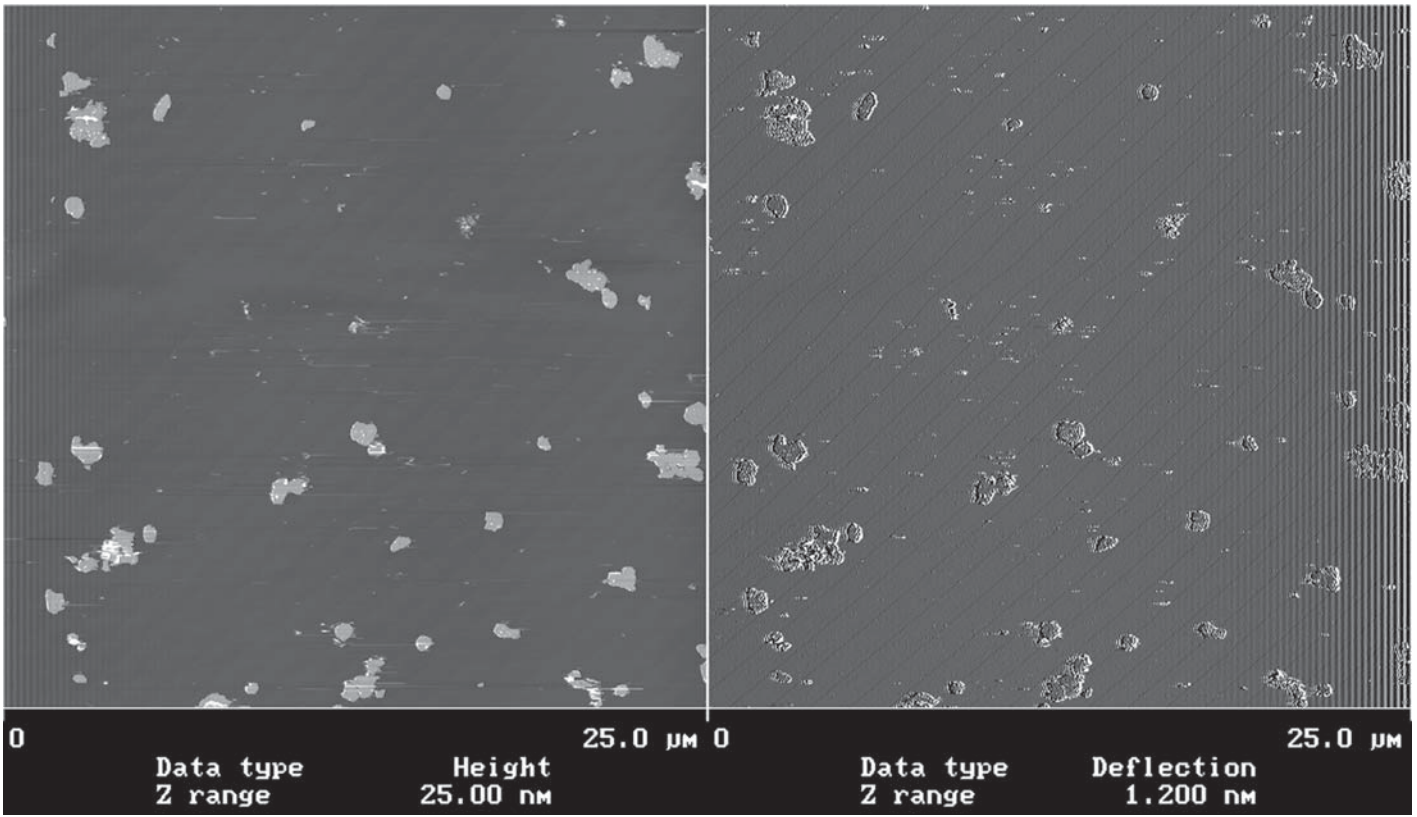

Fig. 2. Low-magnification AFM topograph (left) and deflection image (right) of purple membranes adsorbed to mica. The average height of the membranes was approx 6 nm under the given buffer conditions. Imaging buffer: 20 m*M* Tris-HCl, pH 7.8, 150 m*M* KCl.

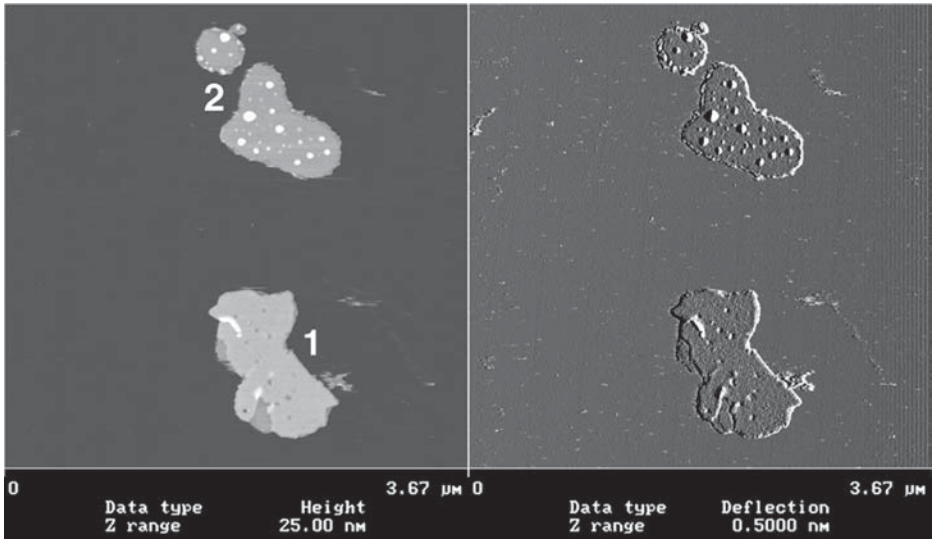

Fig. 3. Medium magnification AFM topograph (left) and deflection image (right) of two purple membranes exposing the extracellular (1) and the cytoplasmic (2) side. Imaging buffer: 20 m*M* Tris-HCl, pH 7.8, 150 m*M* KCl.

discerned. The extracellular side is characterized by small holes (**Fig. 3**, 1), whereas the cytoplasmic side by protruding bumps (**Fig. 3**, 2; **refs. *20*** and ***21***). A further feature that can be used to discriminate between the two sides is the small difference in thickness seen when scanning in CS imaging buffer. Purple membranes exposing the cytoplasmic side appear slightly lower than those exposing the extracellular one. As described by Müller et al. ***(22)*** ionic strength and pH affect the height measured between biological samples with different surface properties and their support.

4. The extracellular surface of BR: At high magnification the extracellular side of BR is characterized by protrusions extending 0.5 ± 0.1 nm out of the lipid bilayer (**Fig. 4**). The β-sheet in the loop connecting the transmembrane α-helices B and C constitutes the main part of the observed protrusion. For clarity a part of the image (17 nm × 17 nm frame) around the contoured trimer in **Fig. 4** was extracted and enlarged (see inset). An estimate of the resolution of this topograph is given below in **Subheading 4.6.**
5. The cytoplasmic surface of BR: Force-induced conformational changes: Imaging of the cytoplasmic surface is force-dependent because of the flexible EF loop ***(23,24)***. At approx 100 pN applied to the AFM stylus (**Fig. 5**; areas 1 and area in the inset above the broken line) the fully extended EF loops can be discerned as sharp protrusions of 0.8 ± 0.2 nm height. These become less prominent if the loading force is increased to approx 300 pN (**Fig. 5**; area 2 and area in the inset

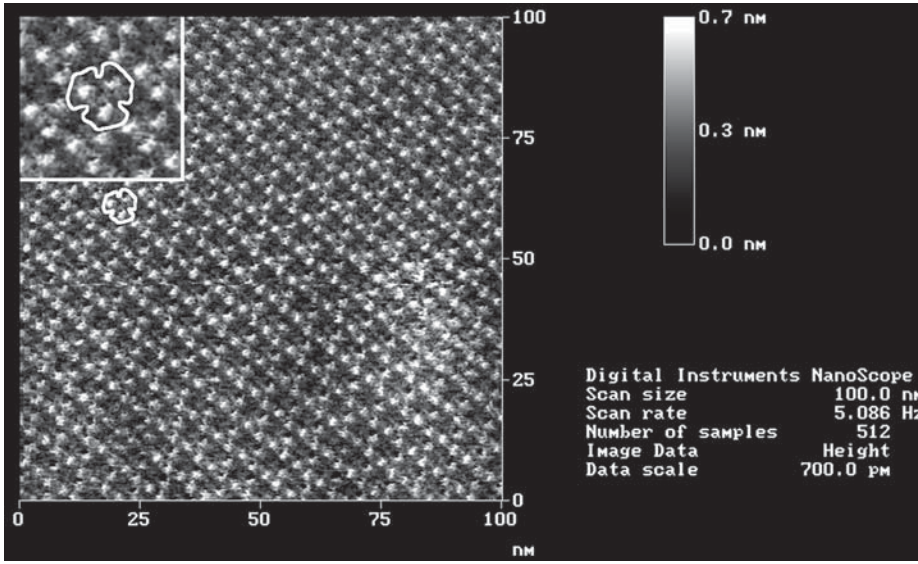

Fig. 4. High-magnification AFM topograph of the extracellular side of BR. For clarity, the square area (17 × 17 nm) around the contoured BR trimer was enlarged and is displayed in the inset. Imaging buffer: 20 m*M* Tris-HCl, pH 7.8, 150 m*M* KCl, 25 m*M* $MgCl_2$.

below the broken line). In the contoured trimer (inset) the two different states can clearly be seen: The upper two EF-loops are fully extended (above the broken line: applied force approx 100 pN) whereas the third one (below the broken line: applied force approx 300 pN) is pushed away by the tip and is therefore less prominent. Instead, the AB loops become visible at approx 300 pN applied to the AFM tip with a height of 0.6 ± 0.1 nm above the lipid bilayer. The advantage of such force induced conformational changes is that shorter loops covered by the bigger ones can be studied. If the applied force is further increased to approx 400 pN (**Fig. 5**; area 3) the BR trimers are hardly visible and horizontal streaks appear, indicating that the force is too high. When scanning at such high forces, care has to be taken because irreversible damages of the membrane may happen.

6. Estimating the resolution of AFM topographs: The resolution of a topograph containing a regular structure can be estimated from its powerspectrum. In the software package delivered with the AFM by Digital Instruments the option to calculate powerspectra of topographs is available. Otherwise various public domain programs like NIH image from the National Institutes of Health (Bethesda, MD) or SXM from the University of Liverpool (Liverpool, UK) have such algorithms implemented and can be downloaded for free (NIH image: http://rsb.info.nih.gov/nih-image/ and SXM: http://reg.ssci.liv.ac.uk/).

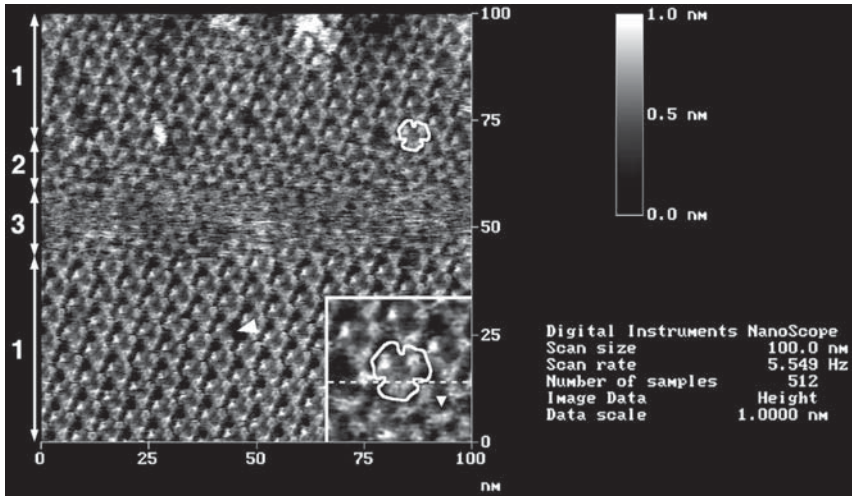

Fig. 5. Force-dependent AFM topography of the cytoplasmic side of purple membrane. At approx 100 pN (area 1) the EF loop is fully extended whereas at approx 300 pN (area 2) the loop is pushed away by the tip and is therefore not visible anymore. At approx 400 pN the BR trimers are hardly visible and streaks in the fast scan direction arise. This indicates that the applied force is too high and that irreversible damages may be inflicted to the membrane. For clarity, the square area (17×17 nm) around the contoured BR trimer was enlarged and is displayed in the inset. The broken line in the inset marks the force change from approx 100 to 300 pN. There, the contoured BR trimer contains both states of the EF loop: Two fully extended (above the broken line) and one where the loop was pushed away by the stylus (below the broken line). The triangle in the inset marks the threefold symmetry axis of a BR trimer recorded at approx 300 pN. Sometimes defective BR trimers with a monomer missing can be found (arrowhead). Imaging buffer: 20 m*M* Tris-HCl, pH 7.8, 150 m*M* KCl.

The calculated powerspectrum of the extracellular side (**Fig. 4**) is shown in **Fig. 6**. Diffraction patterns of this side of BR typically exhibit strong second order spots. The higher the order of the discernible spots, the higher is the resolution of the details preserved in the topograph. Here, sharp spots extend beyond the 1 nm resolution limit (see broken circle). The encircled spot (4,4) corresponds to a lateral resolution of 0.78 nm. To calculate the resolution at a selected diffraction spot (h,k) of such a trigonal lattice with lattice parameters: $a = b = 6.2$ nm and $\gamma = 60°$, Eq. (1) can be used. This formula is applicable to all lattice types, e.g., for orthorhombic lattices which also occur frequently in native and reconstituted two-dimensional crystals of membrane proteins (for further reading on crystallography, *see* **ref. *25***).

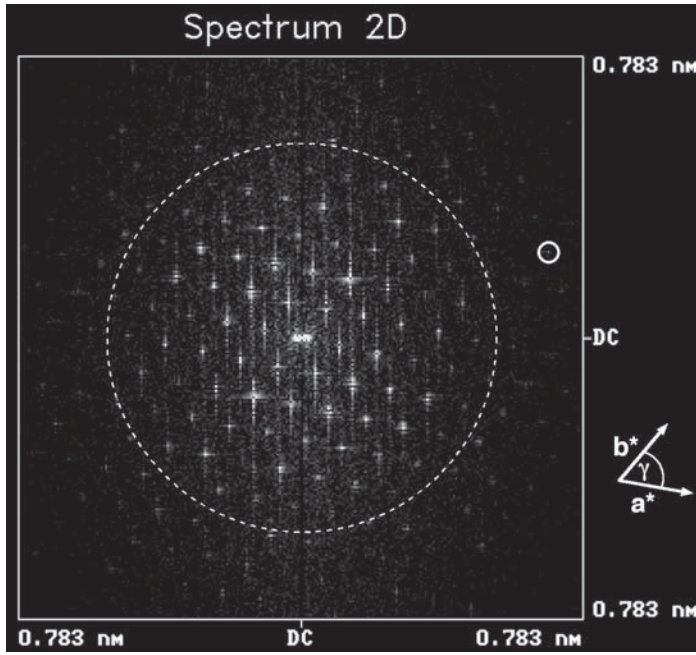

Fig. 6. Powerspectrum of the extracellular side of BR calculated from **Fig. 4**. Diffraction spot (4,4) represents a resolution of 0.78 nm (small circle). The broken circle represents the 1 nm resolution limit.

$$\delta = \frac{1}{|\vec{r}|} = \frac{\sin\gamma}{\sqrt{\frac{h^2}{a^2} + \frac{2 \cdot h \cdot k \cdot \cos\gamma}{a \cdot b} + \frac{k^2}{b^2}}}$$

where δ = resolution; a and b = basic lattice vectors; γ = angle between the basic lattice vectors; h and k = Miller indices; $\vec{r}$ = vector from origin to diffraction spot (h,k).

7. Tip effects and artifacts: At this time no commercial AFM tips are available with ideal point probes and perfect geometries in the subnanometer range. Therefore, tip effects and artifacts arising from the tip geometry are unavoidable and have to be considered when interpreting AFM topographies (for further reading on tip effects and artifacts, *see* **refs. *26*** and ***27***). Tip effects result when the probe interacts with the sample at different sites simultaneously, instead of at only one site. This leads to an AFM image of the sample features convoluted with the tip shape. To be sure of having acquired the correct surface structure and not an artifact, the same surface topography of the object being investigated has to be reproduced several times with different tips, from different batches. Tip artifacts can also be identified by changing the direction in which the AFM tip scans the sample (scan angle) because artifacts will rotate correspondingly ***(26)***. In addition, structures

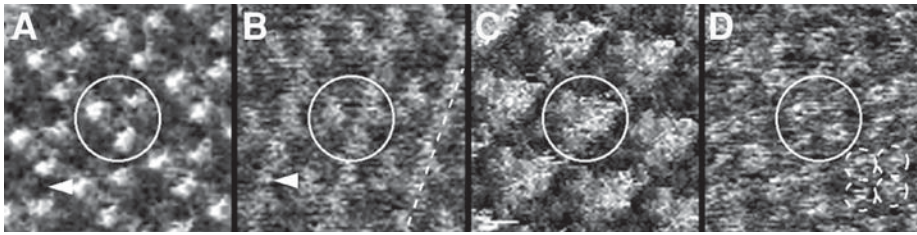

Fig. 7. Tip effects and artifacts. **A,** Artifact-free topography of the extracellular side of BR. **B** through **D,** Artifacteous topographies of the extracellular surface of BR. In all images the central trimers are encircled. In **A** (arrowhead) the lipid moiety separating the trimers is visualized whereas in **B** (arrowhead) not. The characteristic central depression in the BR trimer is completely missing in **C**. The broken circles in **D** mark four different protrusions instead of the three expected. The frame sizes in **A** to **D** are 17 nm. The heights are 0.7 nm **(A)**, 0.8 nm **(B)**, 1.2 nm **(C)**, and 0.7 nm **(D)**.

of samples that have been determined by other methods, for example, electron and X-ray crystallography for BR, can be used to further compare and confirm the observed AFM surface. The extracellular surface of BR recorded with an artifact-free tip is shown in **Fig. 7A** whereas **Fig. 7B** through **D** display images acquired with artifacteous tips. Tentative explanations of the observed artifacts are omitted because the statements would be too speculative. We restrict ourselves to a comparison of the artifacteous surfaces with the nonartifacteous one. Compared with **Fig. 7A**, the trimer in **Fig. 7B** has more the shape of an isosceles than an equilateral triangle indicating a distortion of the BR trimer. The lipid moiety that separates the neighboring trimers could not be visualized by the artifacteous tip (compare the areas marked by arrowheads in **Fig. 7A** and **B**). Along the broken line in **Fig. 7B** alternating heights between the prominent extracellular protrusions and the lipid moieties would be expected, but instead a rim of constant height is seen. In **Fig. 7C**, the depression at the threefold symmetry axis of the BR trimer is completely missing and the trimer seems to consist of a single plateau. The encircled BR trimer in **Fig. 7D** has lost its trigonal shape and resembles more a tetramer (the four protrusions constituting the tetramer are marked by broken circles). It should be noted that not the resolution of a topograph alone can be a figure of quality, but the crystallographic symmetry and the reproducibility must be considered as well.

Acknowledgments

This work was supported by the M. E. Müller-Foundation of Switzerland, the European Union-Quality of Life and Management of Living Resources Project (grant QLRT-2000-00778) and the Swiss National Center of Competence in Research "Nanoscale Science". The authors are indebted to Dr. Ansgar Philippsen for **Fig. 1**, to Dr. Patrick L. T. M. Frederix for fruitful discussions

and constructive comments on the manuscript and to Profs. Dieter Oesterhelt (Max-Planck-Institut für Biochemie, Martinsried, Germany) and Georg Büldt (Forschungszentrum Jülich, Jülich, Germany) for kindly providing us with BR.

References

1. Binnig, G., Quate, C. F., and Gerber, C. (1986) Atomic force microscope. *Phys. Rev. Lett.* **56,** 930–933.
2. Engel, A., Lyubchenko, Y., and Müller, D. J. (1999) Atomic force microscopy: A powerful tool to observe biomolecules at work. *Trends Cell Biol.* **9,** 77–80.
3. Stolz, M., Stoffler, D., Aebi, U., and Goldsbury, C. (2000) Monitoring biomolecular interactions by time-lapse atomic force microscopy. *J. Struct. Biol.* **131,** 171–180.
4. Engel, A. and Müller, D. J. (2000) Observing single biomolecules at work with the atomic force microscope. *Nat. Struct. Biol.* **7,** 715–718.
5. Stahlberg, H., Fotiadis, D., Scheuring, S., Rémigy, H., Braun, T., Mitsuoka, K., et al. (2001) Two-dimensional crystals: A powerful approach to assess structure, function and dynamics of membrane proteins. *FEBS Lett.* **504,** 166–172.
6. Zhong, Q., Inniss, D., Kjoller, K., and Elings, V. B. (1993) Fractured polymer/silica fiber surface studied by tapping mode atomic force microscopy. *Surf. Sci. Lett.* **290,** L688–L692.
7. Putman, C. A. J., Vanderwerf, K. O., de Grooth, B. G., Vanhulst, N. F., and Greve, J. (1994) Tapping mode atomic-force microscopy in liquid. *Appl. Phys. Lett.* **64,** 2454–2456.
8. Hansma, P. K., Cleveland, J. P., Radmacher, M., Walters, D. A., Hillner, P. E., Bezanilla, M., et al. (1994) Tapping mode atomic force microscopy in liquids. *Appl. Phys. Lett.* **64,** 1738–1740.
9. Han, W. H., Lindsay, S. M., and Jing, T. W. (1996) A magnetically driven oscillating probe microscope for operation in liquids. *Appl. Phys. Lett.* **69,** 4111–4113.
10. Han, W. H., Lindsay, S. M., Dlakic, M., and Harrington, R. E. (1997) Kinked DNA. *Nature* **386,** 563.
11. Müller, D. J., Fotiadis, D., Scheuring, S., Müller, S. A., and Engel, A. (1999) Electrostatically balanced subnanometer imaging of biological specimens by atomic force microscope. *Biophys. J.* **76,** 1101–1111.
12. Fotiadis, D., Scheuring, S., Müller, S. A., Engel, A., and Müller, D. J. (2002) Imaging and manipulation of biological structures with the AFM. *Micron* **33,** 385–397.
13. Oesterhelt, D. and Stoeckenius, W. (1973) Functions of a new photoreceptor membrane. *Proc. Natl Acad. Sci. USA* **70,** 2853–2857.
14. Oesterhelt, D. and Stoeckenius, W. (1971) Rhodopsin-like protein from the purple membrane of *Halobacterium halobium*. *Nat. New Biol.* **233,** 149–152.
15. Lanyi, J. K. (1993) Proton translocation mechanism and energetics in the light-driven pump bacteriorhodopsin. *Biochim. Biophys. Acta* **1183,** 241–261.
16. Khorana, H. G. (1988) Bacteriorhodopsin, a membrane protein that uses light to translocate protons. *J. Biol. Chem.* **263,** 7439–7442.

17. Blaurock, A. E. and Stoeckenius, W. (1971) Structure of the purple membrane. *Nat. New Biol.* **233,** 152–155.
18. Lanyi, J. K. and Luecke, H. (2001) Bacteriorhodopsin. *Curr. Opin. Struct. Biol.* **11,** 415–419.
19. Heymann, J. B., Müller, D. J., Landau, E. M., Rosenbusch, J. P., Pebay-Peyroula, E., Büldt, G., et al. (1999) Charting the surfaces of the purple membrane. *J. Struct. Biol.* **128,** 243–249.
20. Müller, D. J., Schoenenberger, C.-A., Büldt, G., and Engel, A. (1996) Immuno-atomic force microscopy of purple membrane. *Biophys. J.* **70,** 1796–1802.
21. Müller, D. J., Schabert, F. A., Büldt, G., and Engel, A. (1995) Imaging purple membranes in aqueous solutions at sub-nanometer resolution by atomic force microscopy. *Biophys. J.* **68,** 1681–1686.
22. Müller, D. J. and Engel, A. (1997) The height of biomolecules measured with the atomic force microscope depends on electrostatic interactions. *Biophys. J.* **73,** 1633–1644.
23. Müller, D. J., Sass, H.-J., Müller, S. A., Büldt, G., and Engel, A. (1999) Surface structures of native bacteriorhodopsin depend on the molecular packing arrangement in the membrane. *J. Mol. Biol.* **285,** 1903–1909.
24. Müller, D. J., Büldt, G., and Engel, A. (1995) Force-induced conformational change of bacteriorhodopsin. *J. Mol. Biol.* **249,** 239–243.
25. Misell, D. L. and Brown, E. B. (1987) Electron diffraction: An introduction for biologists, in *Practical Methods in Electron Microscopy*, vol. 12 (Glauert, A. M., ed.) Elsevier Science Publishers B. V., The Netherlands.
26. Xu, S. and Arnsdorf, M. F. (1994) Calibration of the scanning (atomic) force microscope with gold particles. *J. Microsc.* **173,** 199–210.
27. Schwarz, U. D., Haefke, H., Reimann, P., and Güntherodt, H.-J. (1994) Tip artefacts in scanning force microscopy. *J. Microsc.* **173,** 183–197.
28. Kimura, Y., Vassylyev, D. G., Miyazawa, A., Kidera, A., Matsushima, M., Mitsuoka, K., Murata, K., et al. (1997) Surface of bacteriorhodopsin revealed by high-resolution electron crystallography. *Nature* **389,** 206–211.

22

Measurement of Mechanical Properties of Intact Endothelial Cells in Fresh Arteries

Hiroshi Miyazaki and Kozaburo Hayashi

1. Introduction

Atomic force microscopy (AFM) has been successfully applied not only to the topography of biological specimens but also to the measurement of their local mechanical properties. This technique is very useful for imaging such biological specimens as cells, proteins, and DNA, because no special treatments of samples are required ***(1,2)***. The measurement of local mechanical properties in a living cell is achieved with a nanoindentation technique ***(3)***. The method has been applied to several kinds of cultured cells, including Madin-Darby canine kidney (MDCK) cells ***(4)***, myocytes ***(5)***, fibroblasts ***(6,7)***, and endothelial cells ***(8,9)***. However, morphology and properties are different between cells cultured in vitro on substrate and intact cells in vivo ***(10)***.

Vascular endothelial cells form a lining of the inner surface of blood vessel and are always exposed to blood flow. Because their morphology, internal structure, functions, and mechanical properties are closely related to each other and are strongly affected by hemodynamic factors, the measurement of the mechanical properties of the cells *in situ* is very important. Unlike the other cell types, endothelial cells are not embedded in tissues. Therefore, if a blood vessel is cut opened, we can observe intact endothelial cells and measure their mechanical properties with AFM ***(11)***.

This chapter explains an AFM method for the measurement of the local mechanical properties of intact endothelial cells in fresh arteries. The artery in living animals is exposed under anesthesia, and marked with stain dots on the outer surface along the axial direction. The distances between the dots and the external diameter of the artery are measured to give the in vivo axial and circumferential lengths, respectively. Immediately after sacrifice, the artery is excised, and temporarily stored in Hanks' balanced salt solution (HBSS) at 4°C.

From: *Methods in Molecular Biology, vol. 242: Atomic Force Microscopy: Biomedical Methods and Applications*
Edited by: P. C. Braga and D. Ricci © Humana Press Inc., Totowa, NJ

First, the sensitivity of the AFM system is determined using a cantilever for each measurement and a glass cover slip. Immediately before AFM observation, strip specimens are cut out from the artery. Each specimen is fixed on silicone rubber with the endothelial side up using pins at its in vivo axial and circumferential lengths. The specimen attached to the rubber is covered with HBSS of room temperature and is mounted onto the sample stage of the AFM. After the surface topograph of the endothelium is determined, force curves are obtained at various locations in each endothelial cell. Force–indentation relations are determined from the force curves. Stiffness is calculated from the force–indentation relations.

2. Materials

1. Living animal.
2. Pentobarbital sodium solution.
3. Gentian violet solution: dissolve gentian violet pellets in distilled water to make saturated solution; store the solution in a refrigerator at 4°C (*see* **Note 1**).
4. HBSS: mix 136.8 m*M* NaCl, 5.3 m*M* KCl, 0.3 m*M* $Na_2HPO_4 \cdot 12\ H_2O$, 0.4 m*M* KH_2PO_4, 0.5 m*M* $MgCl_2 \cdot 6H_2O$, 0.4 m*M* $MgSO_4 \cdot 7H_2O$, 1.3 m*M* $CaCl_2$, 4.2 m*M* $NaHCO_3$, and 5.6 m*M* dextrose in distilled water, filtrate with a membrane filter having the pore size of 0.2 μm, adjust the pH to 7.4, and store in a refrigerator at 4°C (*see* **Note 2**).
5. Silicone rubber: cut a 3-mm thick silicone rubber sheet into appropriate size (e.g., 5 × 5 mm). Ultrasonically wash it with acetone, ethanol, and then distilled water for 10 min for each, and dry it.
6. Stainless steel pin: cut an approximately 0.3-mm diameter stainless-steel wire into short pieces each having the length of about 4 mm and bend one end of each to an angle of about 90° to make an L-shape. Ultrasonically wash them in the same way as that for the silicone rubber, and dry (*see* **Note 3**).

3. Methods

3.1. Resection of Arterial Segment

3.1.1. Exposure of Artery Under Anesthesia

1. Induce general anesthesia to an animal by the injection of pentobarbital sodium into the vein or the abdominal cavity (*see* **Note 4**).
2. Shave and incise the skin.
3. Carefully expose an artery, and dissect it from the surrounding tissues using forceps (*see* **Note 5**).

3.1.2. Measurement of Arterial Dimensions

1. Measure the external diameter of the artery with a caliper (*see* **Note 6**).
2. Dot with gentian violet on the outer surface along the axial direction at 3- to 5-mm intervals.
3. Measure the distances between the dots with a caliper.

3.1.3. Resection of Arterial Segment and Storage

1. Inject an excess of pentobarbital sodium solution into the vein, and wait until cardiac arrest (*see* **Note 7**).
2. Immediately after sacrifice, cannulate the artery with a syringe needle, and gently flush it with HBSS of room temperature to wash out blood (*see* **Note 8**).
3. Ligate the artery at proximal and then at distal position with threads.
4. Resect an arterial segment with a surgical scissors between the ligations.
5. Immediately immerse the resected segment in HBSS of room temperature in a Petri dish and gently wash the segment (*see* **Note 9**).
6. Put the segment in a bottle with fresh HBSS room temperature and store it at 4°C.

3.2 Preparation of Arterial Wall Specimen

3.2.1. Cutting Out Specimen Strips

1. Transfer the arterial segment from the bottle to a Petri dish.
2. Measure the external diameter and the distance between the gentian violet dots on the outer surface. Calculate the in vivo circumferential and axial extension ratios (ratio of in vivo dimension to in vitro one).
3. Cut out rectangular specimen strips from the segment using a microscissors and a surgical blade (*see* **Note 10**).

3.2.2. Attachment of Specimen to Silicone Rubber

1. Place each specimen strip on a silicone rubber with the endothelial side up and cover the endothelium with a droplet of HBSS to keep wet.
2. Fix the specimen to the rubber with L-shaped stainless-steel pins, stretching to the in vivo axial and circumferential length.
3. Soak the specimen in HBSS of room temperature.

3.3. AFM

3.3.1. Mounting of Specimen on AFM Sample Stage

1. Mount a clean glass cover slip on the sample stage of AFM. Attach a cantilever to the cantilever holder of AFM and place it over the cover slip. After putting a drop of HBSS at room temperature on the cover slip and soaking the cantilever in the drop, adjust a laser beam from AFM head so as to strike the backside of the end part of the cantilever. Then, scan the cantilever or the cover slip, and obtain an image of the cover slip surface. Subsequently, determine the sensitivity of the system using the function of sensitivity measurement of AFM (*see* **Note 11**).
2. Input the values of the cantilever's spring constant and the above-determined sensitivity (**item 1**; *see* **Note 12**).
3. Obtain a force curve from the glass cover slip in the force curve mode of AFM, and confirm the suitability of the cantilever (*see* **Note 13**). Remove the cover slip from the sample stage.
4. Mount a specimen attached to the silicone rubber onto the sample stage of the AFM, and cover it with HBSS at room temperature (*see* **Note 14**).

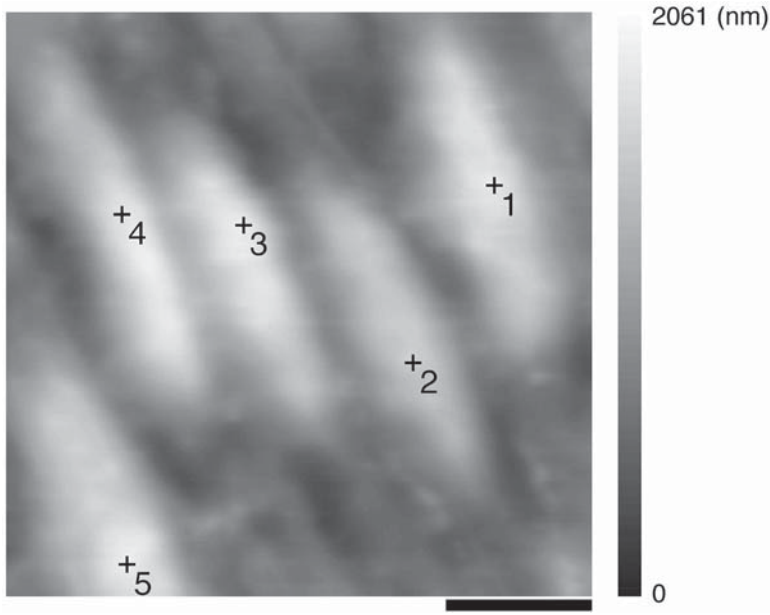

Fig. 1. AFM image of living endothelium in a rabbit abdominal aorta. Plus symbols indicate the highest points in individual endothelial cells. Black bar is 10 µm. Grey scale shows relative height.

3.3.2. Topography of Endothelial Surface

1. Set the *x-y* scanning range as large as possible.
2. Take a topograph of the endothelial surface in the contact mode at a low scanning rate (less than 1 Hz). Keep imaging force as low as possible to avoid the damage of endothelial cells. Change HBSS every 30 min.
3. Using the zoom function of AFM and monitoring the image, reduce the scanning size to the area of interest, and scan again to obtain a magnified image (*see* **Fig. 1** and **Note 15**).

3.3.3. Measurement of Force Curve

1. Obtain force curves from endothelial cells (*see* **Note 16**).
2. Force–indentation relation is determined from each force curve, where indentation is obtained from the difference between the vertical displacement of the piezo and the cantilever deflection (*see* **Fig. 2**). From the force–indentation relation, stiffness is determined (*see* **Note 17**).

4. Notes

1. The addition of very small amount of formaldehyde may help the stain attach to the adventitial surface of the artery.

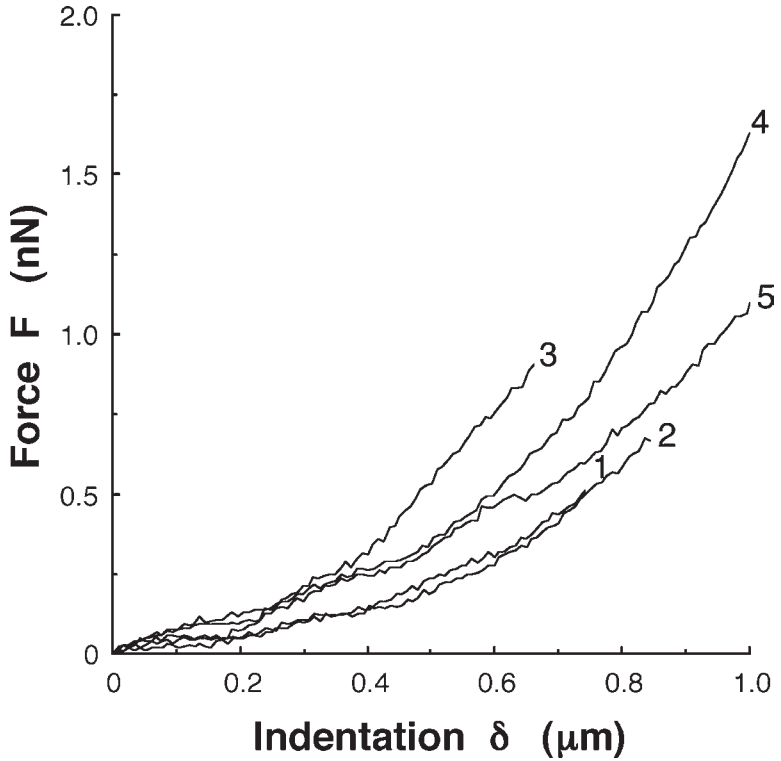

Fig. 2. Force–indentation curves obtained from the highest points in the endothelial cells shown in **Fig. 1.** The numbers attached to the curves correspond to the locations indicated in the AFM image.

2. HBSS is commercially available.
3. One of the tips of the wire should be made sharp so as to be easily pierced into the silicone rubber through the arterial wall.
4. Do not apply too much pentobarbital sodium to avoid respiratory failure. The dosage depends on animal species and weight. Inhalation anesthesia can also be used.
5. When exposing and resecting arterial segments, avoid bleeding as far as possible. Arteries contract when contacting with blood, which makes difficult to precisely measure the in vivo external diameter. Never grip arterial wall itself with forceps to avoid wall damage and detachment of endothelial cells. Rubbing and stretching of arterial wall also should be avoided as far as possible. Always keep the artery wet with HBSS at room temperature during the procedure.
6. If a noncontact measurement method is available, it is recommended.
7. If arteries for study are located in the legs or neck, they may be resected before sacrifice.

8. Do not flush the artery at high flow rate to avoid the detachment of endothelial cells.
9. When handling the arterial segment, hold loose fibers on the outer surface. Do not touch arterial wall itself. If blood remains inside the resected artery, gently wash it out.
10. Do not scrape the inner surface of the segment to prevent the detachment of endothelial cells. Always keep the specimen wet with HBSS.
11. Sensitivity defines a relation between the displacement of the cantilever tip (or the deflection of the cantilever) and the voltage applied to the piezo of the AFM, which is determined by pressing the tip against the cover slip using the piezo. The laser beam is reflected from the backside of the end part of the cantilever toward a segmented photodiode in the AFM head. The photodiode senses the shift of the reflected laser beam, which is induced by the displacement of the cantilever tip. The sensitivity is expressed as a relation between the output voltage from the photodiode and the voltage applied to the piezo. Thus, the displacement of the cantilever tip (or the deflection of the cantilever) can be obtained from the voltage output of the photodiode and the sensitivity. Because the sensitivity is changeable depending on the striking position of the laser beam on the cantilever, do not change the alignment of the beam until all force curve measurements are completed. The method for the determination of sensitivity is specified for each AFM apparatus and software.
12. A spring constant is given for each cantilever. Because the actual value may be slightly different from the nominal value, it is advisable to measure or calculate it in advance. There are several methods for the determination of the spring constant of a cantilever, including a thermal vibration method.
13. A force curve shows a relation between the force applied to a specimen and the displacement of the piezo. Force is calculated by multiplying the spring constant by the deflection of the cantilever (output voltage from the photodiode). The deflection of cantilever is obtained from the sensitivity and the voltage applied to the piezo as mentioned in **Note 11**. The force curve of a glass cover slip is obtained from pushing the cantilever tip against the cover slip by the drive of the piezo only in z direction at a constant rate. In case the initial linear portion of the curve is not clearly observed, discard the cantilever and use a new one. The method for the determination of force curve is different in each AFM apparatus and software. A large-area piezo scanner having the maximum x–y scanning range of about 100×100 μm and the z range of more than 10 μm should be used, partly because the length of endothelial cells is 20–50 μm and partly because the arterial wall is not flat even if it is pinned under tension. Select a soft cantilever having a spring constant of, for example, less than 0.1 N/m and a pyramidal or a conical tip.
14. The specimen should be firmly fixed to the sample stage to obtain a good image. The silicone rubber easily adheres to the surface of the sample stage without glue.
15. A clear image is necessary to obtain a good force curve. The cantilever should be withdrawn from the specimen surface before setting the new (smaller) scanning area, because the thickness of arterial wall is not uniform and the endothelial surface is not flat. If the cantilever tip remains in contact with the specimen sur-

face, it may scratch and destroy the endothelium, and debris from cells and/or tissue may stick to the tip. This should be avoided because good images and force curves cannot be obtained with such a contaminated tip.

16. All the measurements should be completed within 12 h after the sacrifice of animals to avoid the deformation and structural change of endothelial cells.
17. There are various methods for the analysis of force–indentation relations.

References

1. Hansma, H. G. and Hoh, J. H. (1994) Biomolecular imaging with the atomic force microscope. *Annu. Rev. Biophys. Biomol. Struct.* **23,** 115–139.
2. Lal, R. and John, S. A. (1994) Biological applications of atomic force microscopy. *Am. J. Physiol.* **266,** C1–C21.
3. Weisenhorn, A. L., Khorsandi, M., Kasas, S., Gotzos, V., and Butt, H. J. (1993) Deformation and height anomaly of soft surfaces studied with an AFM. *Nanotech.* **4,** 106–113.
4. Hoh, J. H. and Schoenenberger, C. A. (1994) Surface morphology and mechanical properties of MDCK monolayers by atomic force microscopy. *J. Cell Sci.* **107,** 1105–1114.
5. Shroff, S. G., Saner, D. R., and Lal, R. (1995) Dynamic micromechanical properties of cultured rat atrial myocytes measured by atomic force microscopy. *Am. J. Physiol.* **269,** C286–C292.
6. Ricci, D., Tedesco, M., and Grattarola, M. (1997) Mechanical and morphological properties of living 3T6 cells probed via scanning force microscopy. *Microsc. Res. Tech.* **36,** 165–171.
7. Sasaki, S., Morimoto, M., Haga, H., Kawabata, K., Ito, E., Ushiki, T., et al. (1998) Elastic properties of living fibroblasts as imaged using force modulation mode in atomic force microscopy. *Arch. Histol. Cytol.* **61,** 57–63.
8. Sato, M., Nagayama, K., Kataoka, N., Sasaki, M., and Hane, K. (2000) Local mechanical properties measured by atomic force microscopy for cultured bovine endothelial cells exposed to shear stress. *J. Biomech.* **33,** 127–135.
9. Mathur, A. B., Truskey, G. A., and Reichert, W. M. (2000) Atomic force and total internal reflection fluorescence microscopy for the study of force transmission in endothelial cells. *Biophys. J.* **78,** 1725–1735.
10. Ookawa, K., Sato, M., and Ohshima, N. (1993) Morphological changes of endothelial cells after exposure to fluid-imposed shear stress: Differential responses induced by extracellular matrices. *Biorheology.* **30,** 131–140.
11. Miyazaki, H. and Hayashi, K. (1999) Atomic force microscopic measurement of the mechanical properties of intact endothelial cells in fresh arteries. *Med. Biol. Eng. Comput.* **37,** 530–536.

23

Observation of Oxidative Stress on Yeast Cells

Ricardo de Souza Pereira

1. Introduction

Before the advent of the atomic force microscope (AFM), scanning electron microscopy (SEM) was used to obtain high-resolution visualizations of the surface of biological samples. Normally, to scan samples of yeast cells, each preparation was coated with a film of evaporated gold approx 20 nm in thickness ***(1,2)***. Although necessary for scanning, the application of gold to the sample resulted in distortions in its surface. In addition, the application of a conductive coating to the surface effectively masked all the information that can exist below the gold film. The AFM apparatus permits the observation of samples without the use of this mask (samples are uncoated and nonfixed). If we compare the thickness of the gold coating to the thickness of the yeast cell wall (*Saccharomyces cerevisiae* cell wall is about 25 nm; **ref. *3***), we find that they have approximately the same dimensions, which results in loss of resolution from the surface of the cells, including any changes that might occur on the cell wall. With improvements in AFM technology, it became possible to examine the surface of many preparations at much greater resolutions than previously described ***(4)***. Recently, it has become possible to observe, with AFM, that the surface of the cell wall of *S. cerevisiae* contains natural undulations (rugosities) never described when SEM was used ***(4)*** and that these cell walls contain pores along the surface that vary from strain to strain ***(4)***. With AFM is also possible to observe pores on membrane of others eukaryotic cells ***(5)***.

The ideas of pores on the surface of the yeast cell is not a novel idea, and in fact in previous studies ***(6–8)*** it has been shown that it is possible to transport genetic information (plasmids or genes) to the inside of these microbes using a technique called electroporation, which involves increasing the cell wall permeability via electric pulses ***(6,9–11)***. Values from 2–7 kV/cm having a duration of 5 ms are used to generate pores in the cell membrane or cell wall. It is

From: *Methods in Molecular Biology, vol. 242: Atomic Force Microscopy: Biomedical Methods and Applications*
Edited by: P. C. Braga and D. Ricci © Humana Press Inc., Totowa, NJ

believed that pore formation generated in this manner is reversible ***(7)***. Unfortunately, it has been demonstrated that these values of electric pulse induce formation of reactive oxygen species and, consequently, lipoperoxidation in biological membranes (oxidative stress condition), leading to the death of a considerable number of cells ***(12,13)***. Mihai and colleagues have shown that electroporation can be used to stimulate cell growth by as much as 50% in plant cells ***(14)***. All such studies were very empirical before AFM technology, and until then it had not been possible to visualize if such pores were directly formed when cells were under oxidative stress conditions (induced by a chemical such as diamide or *t*-butylhydroperoxide) or stimulated by electric pulses, or conversely, if these pores were permanently in the cell wall and expand in response to electrical or chemical stimulation. Then, as with other questions, AFM solved the doubts by providing visualization of the pores and demonstrating that some strains of *S. cerevisiae* cells are resistent to oxidative stress in contrast to others (*see* **Note 1**; ***15***).

1.1. Mechanism of Action of Diamide

Diamide, a prooxidant (**Fig. 1**), induces an increase in nonspecific pore formation in organelles and cells owing to the oxidation of cysteine sulfhydryl groups (SH residue) of proteins present in their membranes ***(16,17)***. The oxidation of SH to an S-S bridge also induces the formation of reactive oxygen species (ROS) and, as a consequence, lipid peroxidation in biological membranes (**Fig. 2**; **ref.** ***18***). Therefore, diamide and other prooxidants can act as electroporation agents, inducing ROS formation and pore opening. The mannoproteins, a constituent of yeast cell wall, have cysteine in their structure ***(19)*** and can suffer attack by diamide (and others prooxidants) and, consequently, alter the porosity of the cell wall, as observed before ***(15)***. This alteration of the porosity is reversible because of the antioxidant system of the cell, which is composed by adenine nucleotide in its reduced form (NADH; *see* **Fig. 3**). To induce an oxidative stress condition in the cells high quantities of prooxidant are necessary, for example, 10 m*M* (*see* **Notes 2** and **3**).

When diamide in high concentration (10 m*M*) is added to the medium with yeast, the antioxidant system is probably exhausted, leading to an oxidative stress condition for the cells (there are no NADH molecules in the cells). As a consequence, pore closure, which is possible when NADH is present in its reduced form, is not possible (**Figs. 2** and **3**). Surprisingly, there are some yeast strains in which it is not possible to observe this phenomenon. Probably, these cells have a good antioxidant system because of higher quantities of NADH relative to the others strains ***(15)***. Cell strains that produce higher NADH than others has been observed before ***(20–23)***. This good antioxidant system reduces the S-S bridge, inducing the closure of the pores. When the antioxidant system

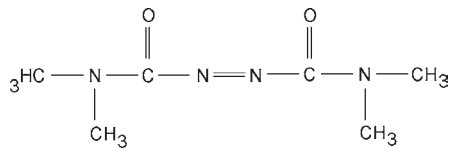

Fig. 1. Chemical structure of diamide.

is overcome, the S-S bridge is not reduced further and, in the presence of molecular oxygen, induces the formation of ROS. These ROS can oxidize further SH residues of proteins, leading to the formation of S-S bridges and inducing a chain reaction (**Fig. 2**).

These ROS induce lipid peroxidation in biological membranes, which increases the membrane permeability by opening nonspecific pores as is seen for mitochondria ***(18,24)***. By protecting sulphydryl groups from oxidation, membrane lipid peroxidation can be prevented or, at least, delayed ***(18,24)***, proving that oxidation of SH residues is directly involved with membrane permeability. If the protein has more than one SH residue in its primary structure, the oxidation of all SH present in this protein leads to the formation of an aggregation of proteins as seen before in sodium dodecyl sulfate polyacrylamide electrophoresis (**Fig. 2**; **ref. *17***); as a consequence, there is an increase in membrane permeability ***(17)*** and pore opening ***(15)***. The cell walls of *S. cerevisiae* contain polysaccharide mixed with proteins. Probably, this latter controls the influx of molecules into the periplasmic space ***(15)*** and can suffer attack by diamide or other prooxidants.

1.2. AFM as a Screening Tool

AFM technology proves to be a useful rapid screening process (45–60 min) to identify which yeast strains are oxidatively resistant, which groups of yeast are sensitive to oxidative stress, and which have pores that allow passage of macromolecules (plasmids or genes). This rapid screening tool may have direct applications in molecular biology (for example, in the transfer of genes to the interior of living cells) and biotechnology (in biotransformation reactions to produce chiral synthons in organic chemistry; **refs. *20*** and ***21***).

2. Materials

1. Industrial strains of *S. cerevisiae* (lyophilized).
2. Ultrapure water.
3. 100-µL Automatic pipet.
4. Si_3N_4 AFM tip.
5. Glass cover slips.
6. Diamide (from Sigma Chemical Co.).
7. $CaCl_2$.

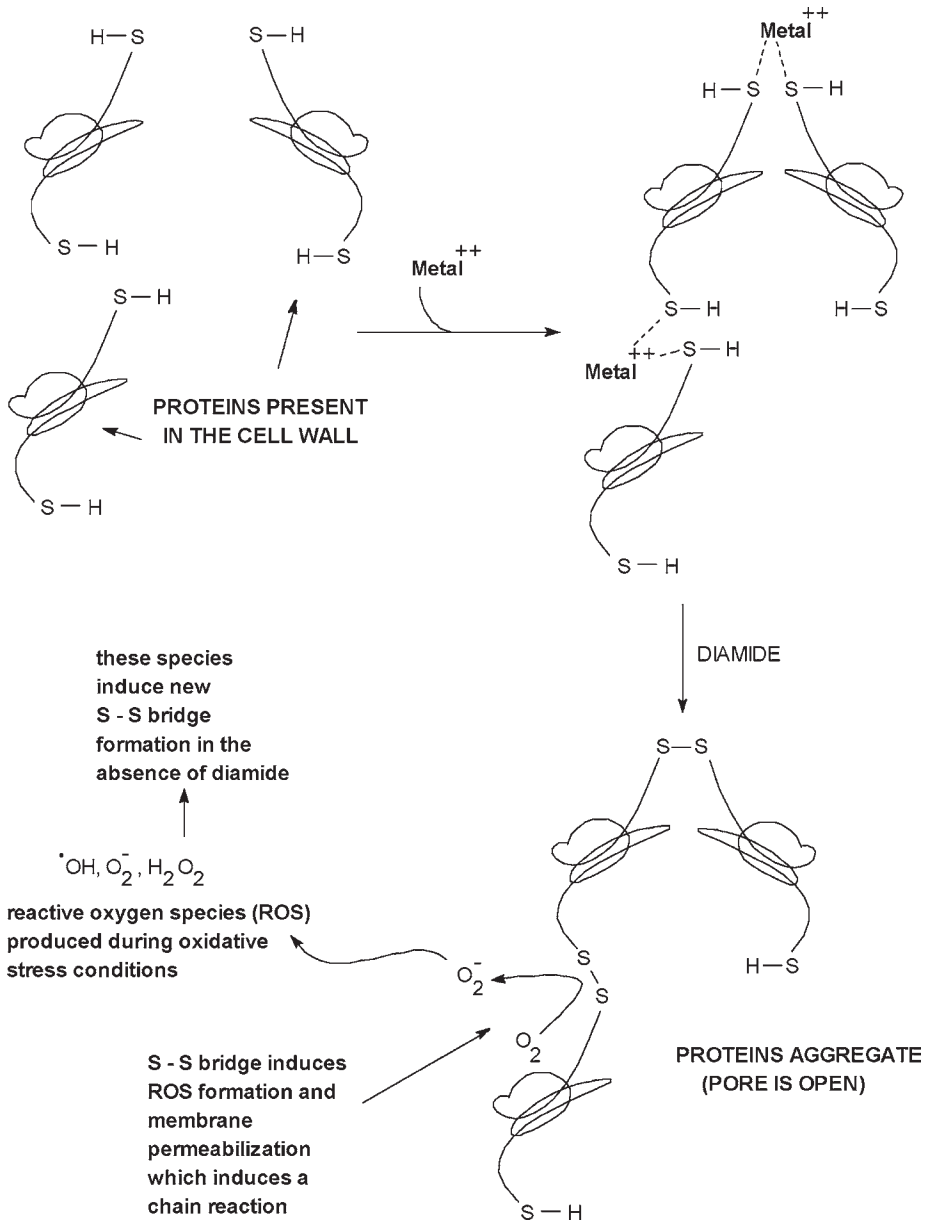

Fig. 2. Formation of S-S bridge induced by diamide and a divalent metal (metal^{++}, Ca^{2+}).

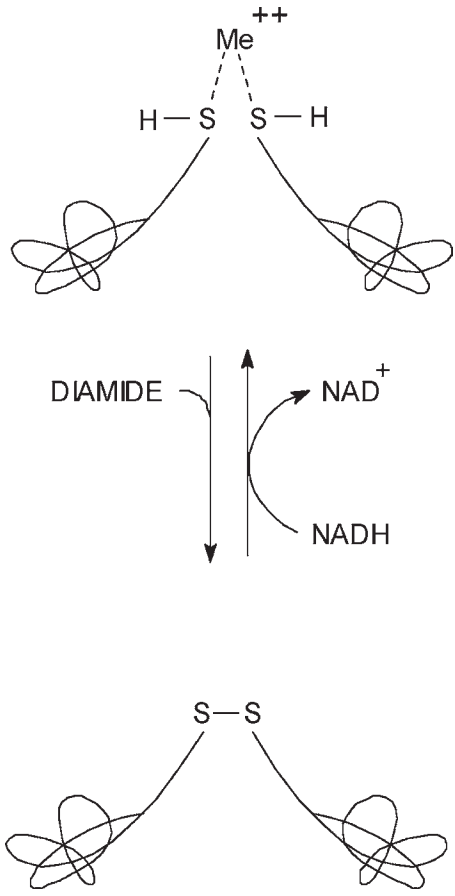

Fig. 3. Role of NADH in the reduction of S-S bridge.

3. Method

3.1. Stock Suspension and Solutions

The stock suspensions of yeast cells are prepared by adding 1.0 g of dry baker's yeast to 10 mL of water (double distilled and deionized) while stirring at room temperature and the cells were metabolically active as demonstrated previously ***(21)***.

3.2. Control Experiment

Sixty microliters of the suspension is placed on the surface of glass cover slip and excess water allowed to dry for 12 h in air at room temperature and the cells were metabolically active as observed before ***(4)***.

3.3. Addition of Diamide

Diamide is diluted in ultrapure water (stock solution has 10 m*M*). An aliquot of 60 µL of stock solution of diamide is mixed with 60 µL of yeast stock suspension and dried in air at room temperature from 30 min to 12 h before imaging.

3.4. AFM

A BioScope or BioProbe (AFM for biological area; VEECO Instruments) operating in contact mode is used in the experiments with Si_3N_4 Nanotips (VEECO Instruments) with a spring constant of 0.06 N/m. In some cases, the images are low-pass filtered to remove stray scan lines. All images are collected on the AFM using a scan speed of 2.5 Hz, and all imaging is done in air at room temperature as described before ***(4)***.

4. Notes

1. In the same sample, it seems that some populations of cells are affected by diamide and others are not. For this reason, it is necessary to begin by scanning an area of 50 μm^2 to know what area is suffering the attack of diamide.
2. To improve the effect of diamide, $CaCl_2$ at 300 µ*M* is added to the medium.
3. If EDTA is present in the medium, Ca^{2+} is chelated and the effect of diamide diminishes dramatically.

References

1. Mogren, H., Hedenskog, G., and Hofsten, A. (1973) The influence of heat processing and mechanical disintegration on yeast for single-cell protein. *Physiol. Plant.* **29,** 82–91.
2. Bowen, R. W., Sabuni, H. A.M., and Ventham, T. J. (1992) Studies of the cell-wall properties of *Saccharomyces cerevisiae* during fermentation. *Biotechnol. Bioeng.* **40,** 1309–1318.
3. Pereira, R. S., Durán, N., and Teschke, O. (1998) Observation of structures on *Saccharomyces cerevisiae* cell wall by atomic force microscope *Probe Microsc.* **1,** 277–282.
4. Pereira, R. S., Parizotto, N. A., and Baranauskas, V. (1996) Observation of baker's yeast strains used in biotransformation by atomic force microscopy. *Appl. Biochem. Biotechnol.* **59,** 135–143.
5. Danker, T., and Oberleithner, H. (2000) Nuclear pore function viewed with atomic force microscopy. *Eur. J. Physiol.* **439,** 671–681.
6. Costaglioli, P., Meilhoc, E., and Masson, J. M. (1994) High-efficiency electrotransformation of the yeast *Schwanniomyces occidentalis*. *Curr. Genet.* **27,** 26–30.
7. Wolf, H., Rols, M. P., Boldt, E., Neumann, E., and Teissie, J. (1994) Control by pulse parameters of electric field-mediated gene-transfer in mammalian-cells. *Biophys. J.* **66,** 524–531.

8. Gustafson, V. D., Baenziger, P. S., Mitra, A., Kaeppler, H. F., Papa, C. M., and Kaeppler, S. M. (1995) Electroporation of wheat anther culture-derived embryoids. *Cer. Res. Commun.* **23,** 207–213.
9. Muraji, M., Tatebe, W., and Berg, H. (1998) The influence of extracellular alkali and alkaline-earth ions on electropermeation of *Saccharomyces cerevisiae*. *Bioelectrochem. Bioenerg.* **46,** 293–295.
10. Teissie, J. (1998) Transfer of foreign receptors to living cell surfaces: The bioelectrochemical approach. *Bioelectrochem. Bioenerg.* **46,** 115–120.
11. Ganeva, V., Galutzov, B., and Teissie, J. (1995) Electric-field mediated loading of macromolecules in intact yeast-cells is critically controlled at the wall level. *Biochim. Biophys. Acta* **1240,** 229–239.
12. Benov, L. C., Antonov, P. A., and Ribarov, S. R. (1994) Oxidative damage of the membrane-lipids after electroporation. *Gen. Physiol. Biophys.* **13,** 85–97.
13. Maccarrone, M., Rosato, N., and Agro, A. F. (1995) Electroporation enhances cell-membrane peroxidation and luminescence. *Biochem. Biophys. Res. Commun.* **206,** 238–245.
14. Mihai, R., Cogalniceann, G., and Brezeanu, A. (1994) Control of *Nicotiana-Tabacum callus* growth by alternating and pulsed electric-field. *Electro-and Magnetobiol.* **13,** 195–201.
15. Pereira, R. S., and Geibel, J. (1999) Direct observation of oxidative stress on the cell wall of *Saccharomyces cerevisiae* strains with atomic force microscopy. *Mol. Cell. Biochem.* **201,** 17–24.
16. Fagian, M. M., Pereira-da-Silva, L., Martins, I. S., and Vercesi A. E. (1990) Membrane protein thiol cross-linking associated with the permeabilization of the inner mitochondrial membrane by Ca^{2+} plus prooxidants. *J. Biol. Chem.* **265,** 19955–19960.
17. Pereira, R. S., Bertocchi, A. P.F., and Vercesi, A. E. (1992) Protective effect of trifluoperazine on the mitochondrial damage induced by Ca^{++} plus prooxidants. *Biochem. Pharmacol.* **44,** 1795–1801.
18. Pereira, R. S. and Hermes-Lima, M. (1996) Can trifluoperazine protect mitochondria against reactive oxyen species? *Eur. J. Drug Metab. Ph.* **21,** 281–284.
19. Walker, G. M. (1998) *Yeast Physiology and Biotechnology*, John Wiley and Sons, Chichester, West Sussex, UK, pp. 22–25.
20. Pereira, R. S. (1995) Biological fermentation of baker's yeast (*Saccharomyces cerevisiae*) and its use in asymmetric synthesis. *Quím Nova* **18,** 452–459.
21. Pereira, R. S. (1995) Baker's yeast: Some biochemical aspects and their influence in biotransformations. *Appl. Biochem. Biotechnol.* **55,** 123–132.
22. Pereira, R. S. (1998) Comparison of biochemical effects produced by calcium ions and by monomers of polyacrylamide (acrylamide and bisacrylamide) on strains of *Saccharomyces cerevisiae* used for production of chiral synthons. *Mol. Cell. Biochem.* **178,** 33–40.
23. Pereira, R.S, and Durán, N. (1996) Variable influence of ferric and cupric ions on *Saccharomyces cerevisiae* strains used in asymmetric organic synthesis. *Biotechnol. Lett.* **18,** 857–862.
24. Bindoli, A., Cavallini, L., and Siliprandi, N. (1977) Effect of thiol oxidation on lipid peroxidation in rat liver mitochondria. *Chem. Biol. Interact.* **19,** 383–386.

24

Lymphoblastoid Cells Exposed to Low-Frequency Magnetic Fields

Study by Atomic Force Microscopy

Settimio Grimaldi, Marco Girasole, and Antonio Cricenti

1. Introduction

Since the appearance of the first pioneering article in the 1970s, particular efforts have been made to study the effect of exposure to electric and magnetic fields (EMFs) on living matter ***(1–10)***. The initial interest in radio frequency and microwaves has shifted to include the nonthermal, and essentially magnetic, effect of extremely low frequencies (ELF, 1–300 Hz), in particular the 50 and 60 Hz of the electric power system ***(3,4,9)***. The density of normal ELF fields is usually below 0.1 μT, but values of 0.5 μT may be found in front of television sets and computer monitors ***(11)*** as well as at a distance of 50 m from 300-kV high-voltage power lines ***(12)***. Values up to two to three orders of magnitude higher can be found near some domestic appliances or in some industrial processes, and pulsed magnetic fields in the range 1–10 mT are used in nuclear magnetic resonance imaging and for the therapy of soft tissue or nonhealing bone fractures ***(1)***.The increasing interest in ELF fields has been partially motivated by epidemiological reports of an increase in some types of cancer and leukemia in children ***(13,14)*** and workers exposed to high levels of ambient fields. Carcinogenesis is considered to be a multistep process consisting of initiation–promotion–progression stages ***(15)***. Although ELF magnetic fields are not considered sufficiently energetic to interact with DNA and initiate a cancerous process, they could, by acting on cellular receptors, affect cell proliferation and modulate the promotion or progression stage. Although exposure to a high-intensity, 50–60 Hz, magnetic field (MF) has been demonstrated to be effective in modifying the growth rate of cells ***(16)***, and a distur-

From: *Methods in Molecular Biology, vol. 242: Atomic Force Microscopy: Biomedical Methods and Applications*
Edited by: P. C. Braga and D. Ricci © Humana Press Inc., Totowa, NJ

bance of melatonin rhythm has also been found-supporting the hypothesis of melatonin-mediated breast cancer development ***(17)***-no final evidence of a link between tumor and field MF exposure has been reported. In light of this, however, particular attention must be paid to studies performed on cells of the immune system because of its fundamental barrier action against pathogens and cancer development.

One of the main difficulties in the study of electric and magnetic field interaction with cells and in the extension of the results to different biosystems arises from the strong dependence of the response pathway on such field parameters as intensity, exposure time, wave shape, and especially the nonlinear frequency dependence. Because the plasma membrane can be regarded as a (nonideal) capacitor with a fixed frequency curve ***(4)***, differences in the induced effects between low frequency fields, which can modify the membrane potential, and high frequency fields, which can easily penetrate cells, are expected. Less understandable is how and why specific frequency windows (sometimes as narrow as few Hz) seem to be particularly effective in producing biophysical or biochemical cell modifications. Little is known as well about the mechanism of action when the field intensity is close to the thermal noise limit. Another complication is the known fact that present inhibitory or stimulatory behavior depends on the cell line used.

Even though no theory has completely succeeded in describing the interaction between field and cells, different models have been proposed to explain the experimental results ***(2,9,18–20)***. These models converge in attributing a crucial role to Ca^{2+} ions, suggesting a change in transport and/or in reactivity of Ca^{2+} induced by particular frequencies of the applied field. Such changes can induce a nonphysiological concentration of these ions within the cell ***(21,22)*** that can trigger biochemical and genetic modifications ***(23)***. It is also accepted that the plasma membrane is one of the target sites of the field, so characterizing its modifications is important to understanding the nature of the interaction. A high-resolution surface-characterizing technique such as atomic force microscopy (AFM) can be a helpful tool in such a study. Recent reviews of this technique and some of its successes that justify its increasing prestige in the study of biological samples can be found in literature ***(24–29)***.

A large number of experimental studies have been done both in vivo and in vitro on this subject. With regard to in vivo experiments concerning immune system cells, it has been demonstrated that nonthermal ELF MF exposure can modify the number of leukocytes, the response to inflammations ***(30,31)***, as well as the activity of natural killer cells in blood ***(32)***. In vitro studies of ELF MF in the range of 1–10 mT have shown membrane surface modifications as evidenced by microscopy, as well as a decrease in conductivity induced by 2.5-mT, 50-Hz exposure in K562 cells ***(5,33)***. In addition, effects on calcium fluxes, DNA synthesis, and RNA transcription have been reported, such as an increase

in cytosolic Ca^{2+} concentration in HL-60 cells exposed to a 0.1-mT MF ***(21)***, the same effect on T lymphoblast cells ***(34)***, changes in protein kinase activity in Raji cells exposed to 2-mT, 50-Hz MF ***(10)***, an increase of uridine (RNA) uptake in HL-60 cells exposed to 1-mT, 60-Hz MF ***(35)***, and reduction in thymidine (DNA) uptake in human peripheral blood lymphocytes ***(36)*** exposed to 6-mT, 3-Hz (square wave) MF. It must be noted that some of the reported effects on DNA or RNA are in some way calcium-dependent or calcium-mediated so that a crucial role for calcium as target of ELF fields clearly emerges.

2. Materials

2.1. Exposure Solenoid

The MF was generated by a sinusoidal current flowing in a solenoid (height 40 cm, diameter 20 cm) made of 600 turns of 0.2-cm (diameter) copper wires wound around an asbestos tube and placed with its axis vertical, so that the magnetic flux was perpendicular to the sample ***(10)***. The sample holder consisted of a water jacket (temperature regulated) container suspended at the centre of the solenoid. The current was driven by a 50-Hz power supply through a variable autotransformer generating a flux of 2 mT (root mean square [rms]) for an applied voltage of 12 V (rms). With these parameters, the surface temperature of the solenoid during the experiment is always below 30°C; no warming of the sample is possible. In order to maintain a fixed temperature during the exposure and to avoid morphological modifications induced by temperature variations ***(37)***, the sample was carefully maintained at a constant temperature of 37 ± 0.3°C by the temperature control system. The field intensity (measured with a calibrated Hall probe) varied within 5% of its central value inside the cylindrical exposure space.

The presence of a homogeneous electric field component parallel to the applied MF is very much debated in experiments with electromagnetic radiation because some researchers report effects induced by weak electric fields (although this still in discussion) ***(38)***.

Surely one way to bypass such a problem is to use EMFs in which one of the components is clearly predominant with respect to the other. This is achieved in experiments with ELF fields in which the magnetic component is in the mT range. For instance, in our experiments we estimated that the residual electric component ***(10)*** on the sample was below 80 μV/cm, which is very close to the minimum theoretical electric field to which a cell may respond ***(38)***, and its putative contribution can be considered negligible compared to the magnetic component.

2.2. Sample Preparation

1. Lymphocyte B cells transformed by Epstein-Barr virus.
2. RPMI (Gibco Laboratories).

3. Trypan blue dye.
4. Poly-lysine-treated glass.

The cell line used was lymphocyte B cells transformed by the Epstein–Barr virus ***(39)***, also known as Raji cells (from ATCC; Rockville, MD), grown at 37°C in RPMI (from Gibco Laboratories; Paisley, Scotland UK) supplemented with 10% fetal calf serum (Gibco), penicillin (110 U/mL), streptomycin (100 µg/mL), and perfused with 5% CO_2 as carbon source (which was provided also during the MF exposure). At confluence, the cells were divided into two samples and placed in 25-mL Corning flasks filled with the above mentioned medium. One sample was exposed to the sinusoidal MF continuously for 9, 15, 24, 44, and 64 h; the sham sample (control) was placed under the same conditions in a solenoid with no field. After the exposure, cell viability was determined by Trypan blue dye exclusion. This invariably showed a negligible amount of dead cells. Exposed and non-exposed cells were attached to poly-lysine treated glass cover slides, fixed in paraformaldehyde (2% for 10 min), washed with a physiological solution, washed again with distilled water to avoid salt deposition, air dried, and finally observed in air by AFM.

This way of preparing dried samples is often used in air performed microscopy experiments to reduce as much as possible any artifact on cell morphology or viability. It allows good and reproducible results ***(40,41)*** because the samples are not damaged or weakly stressed, and they remain stable for long periods of time. Moreover, to distinguish between real effects and artifacts, a control sample was prepared for each exposed sample.

2.3. AFM Instrument and Data Analysis

Our homemade AFM instrument was described in detail elsewhere ***(42)***; briefly, it consists of a stainless-steel unit made of two separable cylindrical supports equipped with a vibration isolating system. The lower unit contains the sample holder mounted at the top of a piezo electric scanner that allows a maximal scan size of $40 \times 40 \times 6$ µm. Additionally an *x-y-z* motor-controlled translator is used to select suitable areas of the sample. The upper unit contains the cantilever holder, the mirror deflection system, and a four-sector position-sensitive photodiode used as deflection detector. An electronic feedback loop is used to integrate the optical signal and maintain a constant cantilever deflection during the data acquisition. Our instrument has been previously successfully used for imaging biological samples ***(29,43,44)***; the typical lateral resolution is about 10 nm and around 0.1 nm in the *z* direction (for a sample placed on a flat surface; **ref. *29***). In the present work, several reported images have a relatively low lateral resolution because of the large range required to observe a whole cell and because of the characteristics of our acquisition soft-

ware, which allows a maximum of 256 points per row (regardless of the range of the image). However, a number of smaller images were acquired (data not shown) in which features as small as 20 nm or less were distinguishable.

The AFM measurements were performed in air (at room temperature), with the microscope working in the weak repulsive regime of contact mode with a force of less than 1 nN from zero cantilever deflection. Gold-coated Si_3N_4 (Park Scientific Instruments; Sunnyvale, CA) microlevers with a spring constant of 0.023 N/m and an expected statistical apical radius of 5–30 nm were used. Constant force and lateral friction images were acquired simultaneously with a typical scan rate of 3–4 s/row (256 points/row). The lateral friction-imaging mode has been found very powerful in this work because of its sensitivity to small structures, such as microvilli, that protrude from a large and corrugated surface.

The raw data were treated only using background subtraction and the reproducibility of data (including the absence of sample damage attributable to the measurement procedure) was successfully tested by imaging the same cells on different days. In relation to the still open question of the elastic deformation of soft biological samples because of the contact mode measurement method, it should be noted that the probe force (which was the same in all the samples analyzed) is very small and in the range commonly reported in the literature for similar contact mode experiments. Anyway, a rough estimation ***(24)*** of the elastic compression of a protein characterized by a Young's modulus of about 20 kg_f/cm^2 (i.e., well below the value expected in the case of a whole cell) carried out a value of elastic deformation that is largely inside the experimental error reported by us. The fit of data was calculated using the Kaleidagraph for Windows (Synergy Software version 3.08) software package.

3. Methods

3.1. Image Collection and Interpretation

In **Figs. 1** and **2**, AFM topological and lateral friction images, respectively, of typical cells unexposed (**Figs. 1A** and **2A**) and exposed continuously for 9, 24, and 64 h to MF (**Figs. 1B–D** and **2B–D**, respectively) are shown. Unexposed cells (**Figs. 1A** and **2A**) show a characteristic domed shape and have height values (defined as top cell height minus cell background) ranging between 2.1 and 2.5 μm. The cells appear highly structured and covered by microvilli, which are recognized both in the topographic (**Fig. 1A**) and lateral friction (**Fig. 2A**) images. Microvilli are protrusions, mainly composed of actin polymers, of the lymphocyte membrane known to be very sensitive to environmental variations ***(36,45,10)*** and important in the recognition of inflammations sites. In the untreated sample it is also possible to see, on the

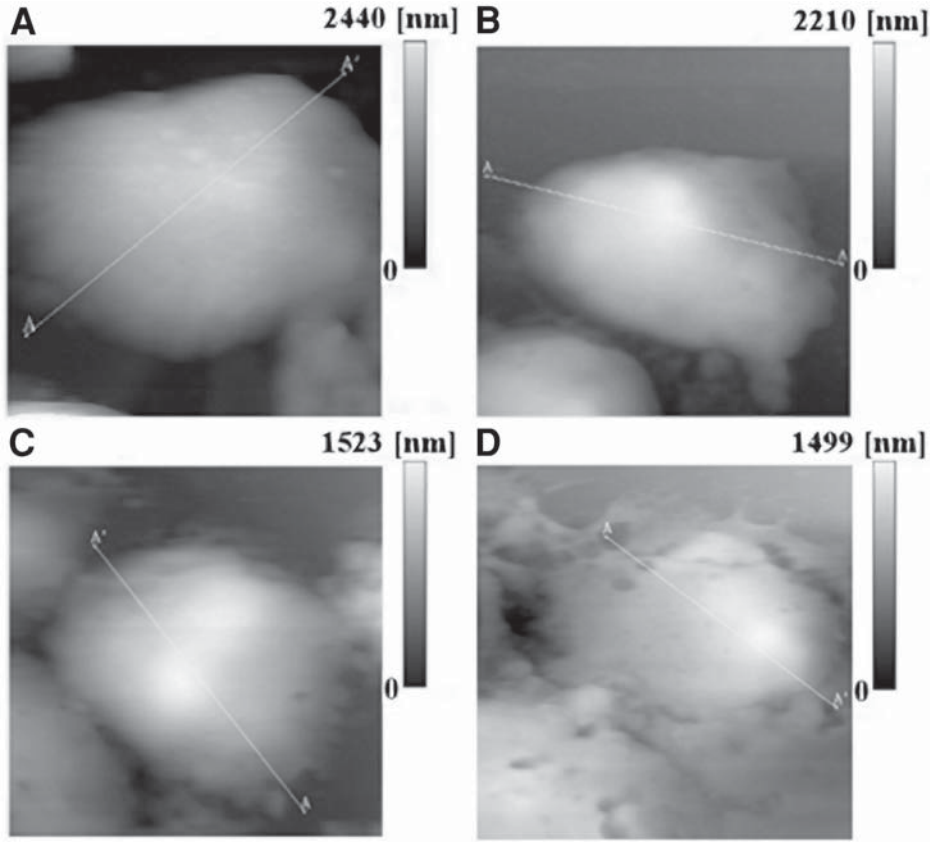

Fig. 1. Constant force AFM images of untreated (**A**, 10 × 10 μm) and, respectively, 9 h (**B**, 13 × 13 μm), 24 h (**C**, 14 × 14 μm), and 64 h (**D**, 13 × 13 μm)-exposed Raji cells. The gray scale is defined so that lighter colors correspond to higher corrugations. It is worth noting that the top height reported for the cells progressively decreases at increasing exposure. In **(A)**, microvilli are visible as a lighter spot on the cell membrane that are no more recognizable after 9–15 h **(B)**. At very long exposure the cell surface become characterized by several "furrows" and infolding **(D)**. A cross-section of these cells, taken along the white line A–A', is shown in **Fig. 4**.

border of the cells, anchoring structures named pseudopodia that are, similarly to microvilli, involved in cell migration.

Cells exposed for 9 h (**Fig. 1B** and **2B**) to MF show clear differences compared to untreated cells: in this case, the microvilli have almost completely disappeared from the surface of the cells and also pseudopodia are hardly detectable.

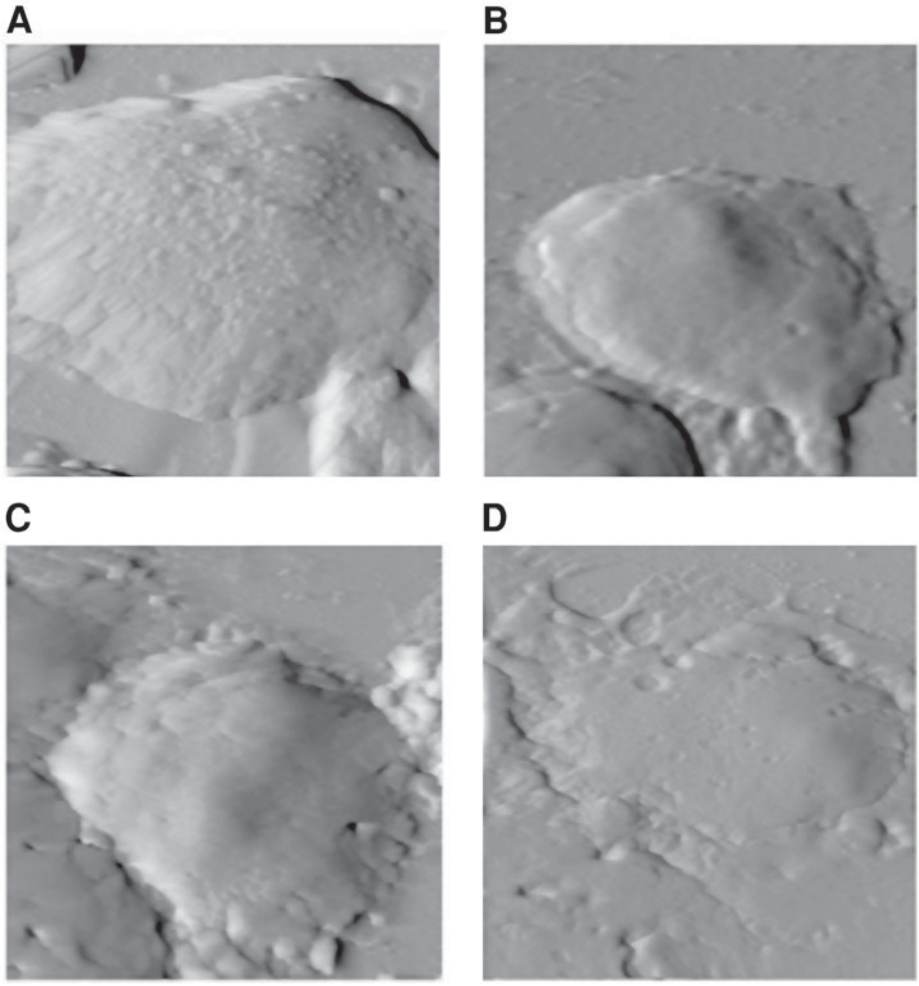

Fig. 2. Lateral friction AFM images of the same cells shown in **Figs. 1A–D**, respectively. Lateral friction images (collected simultaneously to topography) are very sensitive to small structures protruding from a large and corrugated surface so that they are very suitable for describing microvilli **(A)**, as well as the fine surface modifications induced by MF exposure (for instance the pits structure in **D**).

3.2. Cell Membrane Features

The cell membrane, which because of the microvilli could not be directly observed in untreated samples, appears quite smooth with no structures or protrusions on the surface. In cells exposed for 15 h to MF (not shown) both microvilli and pseudopodia can no longer be recognized whereas, as in samples

exposed for a shorter time, the dome shape is essentially unchanged. After 24 h of exposure to MF (**Figs. 1C** and **2C**), a slow membrane change is still going on as revealed by the presence, in some cases, of ripples on the surface (better recognized in the lateral friction image) and by a progressive flattening of the cells. Such a membrane modification is accompanied, in cells exposed for 44 h, by the appearance of "furrows" and pit-like structures (narrow membrane infolding) that become more common in lymphoblasts exposed for 64 h to the field (**Figs. 1D** and **2D**). These features could be considered as markers of the long exposure effect. After 64 h of exposure another important change in cell structure, namely the loss of the spherical shape of the cell, becomes evident. It is worth noting that, in some cases, this change can already be found after 44 h of exposure.

The noticeable modifications of the membrane surface because of MF exposure are shown in the high resolution (3×3 μm) 3D images of **Fig. 3**, in which the surface of an unexposed cell is compared with that of cells exposed for 9, 44, or 64 h. A comparison between **Fig. 3A** and **3B** clarifies the effect of short time exposure, which essentially results in the loss of microvilli.

3.3. Microvilli and Adhesion

An interesting question regards the possibility that the magnetic field exposure changes the proportion of cells adhering to the substrate through the disappearance of microvilli that are involved in cell adhesion and migration: we did not find changes in adhesion although it is not possible to completely exclude such an effect.

3.4. Surface Modification Analysis

The surface modifications after longer exposure are shown in **Figs. 3C** and **3D**, consisting in a slow "aging" of the membrane, which becomes progressively more ruffled and characterized by several narrow introflections easily recognizable in samples exposed for 44 and 64 h.

Figure 4 shows the profiles, taken along the white lines drawn in **Fig. 1**, of the four cells shown in **Figs. 1** and **2**. These data allow at least two important observations about the overall morphological changes of the cells. The first one is the progressive and relevant decrease in the maximum height of the cell with increasing exposure. During the first 9–15 h, such a decrease can be related to the observed loss of microvilli, but the residual changes must reflect modifications of other cellular structures. The second observation regards the cell's domed shape. In fact, unexposed or briefly exposed cells have high dome (**Fig. 4A** and **B**), whereas a loss of the spherical shape starts to be detectable after about 44 h (data not shown) and reaches a maximum after 64 h of exposure. Observing the profile reported in **Fig. 4D**, it is quite evident how this loss

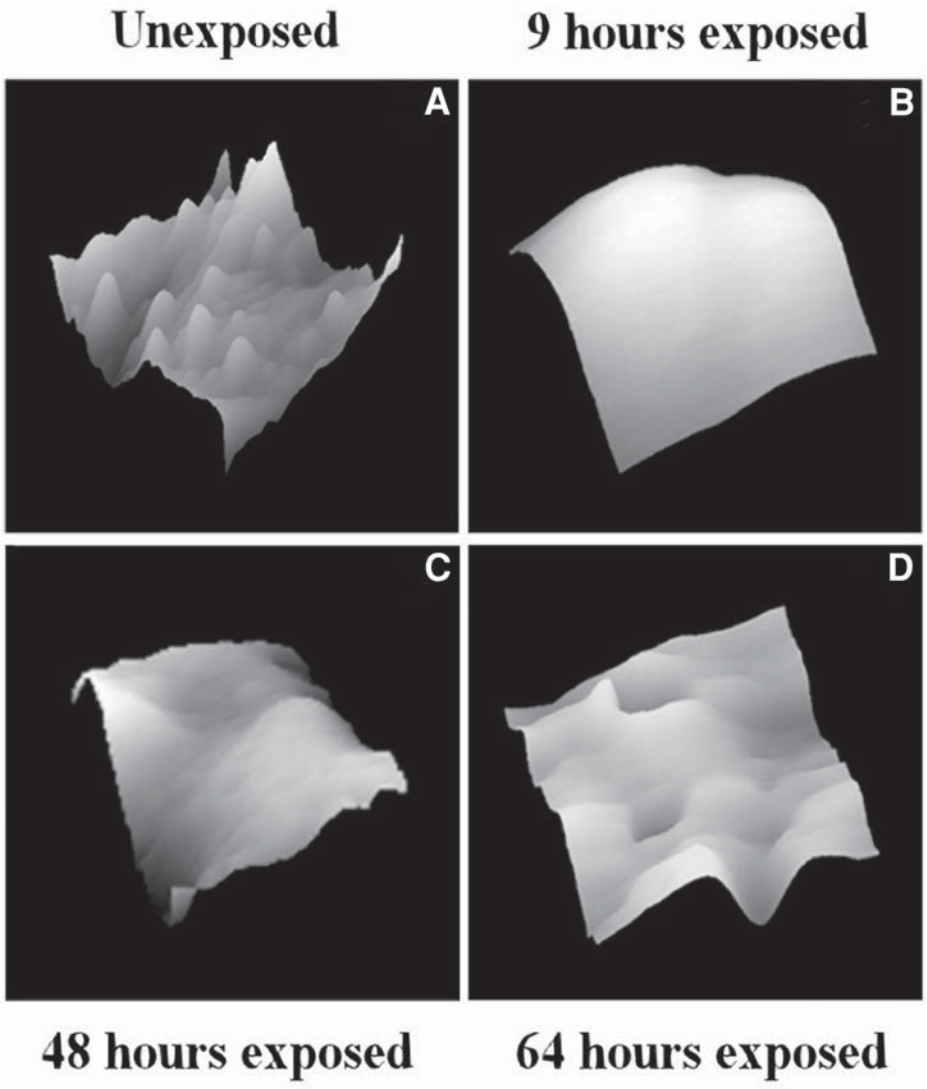

Fig. 3. Constant force images (4 × 4 μm) in a side view 3D representation of the membrane surface of an untreated cell **(A)**, after 9 h **(B)**, 48 h **(C)** and 64 h **(D)** of exposure to MF. The noise in these images is 0.1–0.3 nm. Microvilli are clearly visible in the untreated sample, whereas after 9 h exposure the surface shows flat and smooth. The progressive membrane ageing revealed by surface rippling and the appearance of pit-like structures is evident in images **(C)** and **(D)**.

of spherical shape is the result of a weakening of the support exerted by the cytoskeleton, the cellular structure responsible for the maintenance of the cell shape.

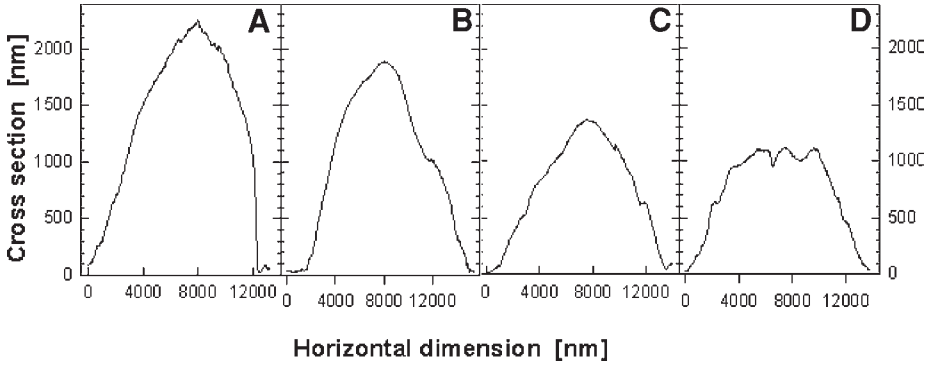

Fig. 4. Cross-sections of the four cells presented in **Fig. 1A–D**, respectively (the profiles are taken along the white line A–A'). This picture clearly shows the main morphological modifications induced by MF. They consist in the (maximum) cell height decreasing at increasing exposure as well as in the loss of cell shape taking place after long time exposure **(D)**. The decrease in height is about complete after 24 h whereas the spherical shape is essentially conserved. At longer exposure, the residual modifications affect only the domed shape of the cell **(D)**. A comparison of the cross-sections of **(C)** and **(D)** shows clearly that the loss of the dome shape arises from loss of support exerted by the cytoskeleton, that is, from a breakdown of this structure.

It seems important to comment the possibility that drying might affect differently the surface structure of control and treated cells: the control cells were treated in exactly the same way as the exposed samples (except, of course, for the exposure). In this way, any difference after drying could only be caused by the exposure. A slightly higher, drying-induced, ruffling of the membrane in cells exposed for 44 or 64 h to MF cannot be excluded because of the changes in the cytoskeleton in those cells. However, we believe that this effect also, if it exists at all, has to be ascribed to the MF-induced modification of the cytoskeleton and not to the drying procedure.

3.5. Artifacts

Another point regards the possibility that while fixing and drying samples many changes might occur in the cell membrane: in the present study, we prepared air-dried samples with a weakly stressing method in order to reduce, as much as possible, any morphological artifact or effect on cell viability. Of course it would be better to study the living cells with the AFM, even though we consider that important information can also be obtained on dried samples. For instance, on dried neurones, there are many aspects that have been studied with ultra-high-vacuum techniques such as spectromicroscopy with synchrotron radiation (*see*, for instance, **refs. *40*** and ***41***).

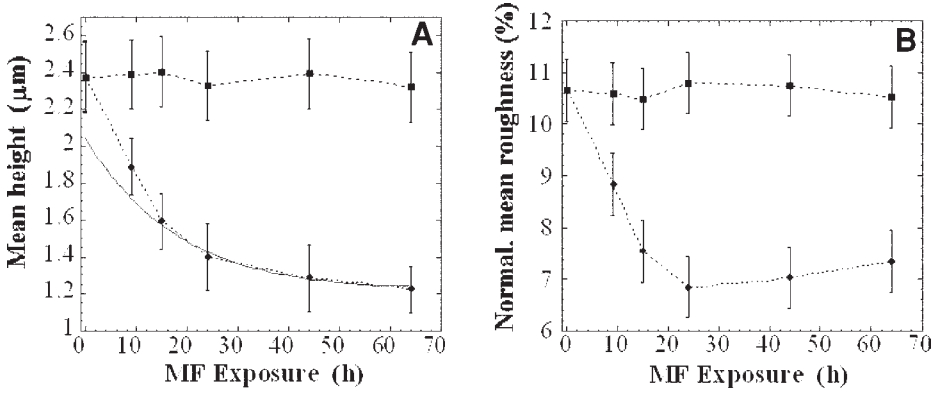

Fig. 5. Normalized roughness **(B)** and mean cell height **(A)** plotted as function of exposure time. Each point is the average of about 50 cells. In both graphs the square symbols represent the control samples and the circles refers to the exposed cells. The controls only show variations within the experimental error. In **(A)**, we report (solid line) the fit executed on the last four data points (the ones free from effects on microvilli). The best fit was obtained with the function $y = m1 + m2 \times e^{-t/18}$ with the following parameters: $m1 = 1.20$; $m2 = 0.84$; $\Delta m1 = 0.06$; $\Delta m2 = 0.03$. The extrapolated value of $H0$ (the zero exposure cells height that does not take into account the microvilli) is 2.04 μm. The results of the fit are discussed in the text.

Concerning cell height and roughness, the results indicate that during the first 24 h both trends are very similar and give rise to a fast and large decrease of the parameters. We suggest that these changes are characterized by two simultaneous effects of MF on microvilli and cytoskeleton respectively. During the following 49 h, the trends become different: in fact decrease in height continues, although very weakly, while the normalized cell roughness undergoes a small increase in agreement with the progressive rippling and appearance of pit structures on the membrane surface.

3.6. Quantitative Evaluation

To allow a more quantitative evaluation of the MF-induced effects, we performed a statistical analysis of the relation between cell modification and exposure time. The results, in terms of mean cell height and normalized roughness (defined as the ratio between the height variance and the mean height value on the portion of surface analyzed), are shown in **Fig. 5A** and **B**. During the first 15–24 h, in which the main part of the MF-induced effect takes place, both graphs show similar decreasing trends. The similarity between the trends in this time frame also implies that the two phenomena of decrease in cell height and loss of structure of the membrane surface occur simultaneously. At longer exposure times, however, the trends of mean height and normalized roughness differ. The height decrease continues, although very weakly, while

the roughness, after reaching a minimum value, shows a small but significant increase. This behavior is not surprising compared with the morphological data of **Fig. 3**, which, in fact, suggest a small increase of the roughness after long exposure in agreement with the progressive membrane rippling and formation of pit structures. This observation demonstrates the sensitivity of our statistical analysis to fine morphological modifications.

In the graph of cell height two different rates of variation are recognizable: a faster one during the first 15 h and a slower one after longer exposure. Because the height decrease continues even after the disappearance of microvilli, an important but time-limited phenomenon, it is clear that the MF acts also on other cellular structure. This structure is the cytoskeleton, subject to a slow but continuous modification. During the first 15 h, the superposition of these two effects causes the faster rate of height variation that is one of the most important results reported.

To avoid the possible interpretation that the data results from a decrease in cell volume, we measured the (apparent) cellular volume individually using an approximation of the cells as spheres or hyperboloids. The results (not shown) reveal volume changes within the experimental error, which means that as height decreases the cells become progressively wider at increasing exposure.

3.7. Role of Calcium

An interpretation of the effects we observed brings into play the role of calcium. Microvilli and pseudopodia are in fact dynamic structures, mainly composed of poly-actin filaments, that can be rapidly created and destroyed ***(46)*** because of Ca^{2+} concentration fluctuations that are known to be induced by exposure to MF ***(3,4,21,22)***. Because actin is present both in the microvilli and in the rest of the cytoskeleton, it is reasonable to believe that the cytoskeleton undergoes the same depolymerization effect observed in the microvilli. However, in the case of the cytoskeleton, the effect is expected to be smaller because of the rigidity of this structure, and it can be unequivocally identified only after long MF exposure (i.e., when the microvilli have already disappeared).

3.8. Estimation of the Effect Induced by MF on the Cytoskeleton

A possible, although rough, estimate of the effect induced by MF on the cytoskeleton during the first 15 h may be attempted by fitting the last four points of the height curve, which are the ones completely free from effects on microvilli. The result of the proposed fit, performed with a simple mono-exponential function (**Fig. 5A** and its caption) show the two rates of the phenomenon. In fact, the best fit obtained, which does not take into account the microvilli, describes very well the range of 13–64 h (for construction) but

clearly indicates a rate of height variation slower than the experimental one in the first hours of exposure. The difference between these two rates of height variation can be ascribed (in large part, at least) to the effect on microvilli.

The use of the fit also allows extrapolation of a zero exposure height value (H0) that takes into account only the effect on the cytoskeleton. The total height variation during the first 9–15 h of exposure can be written as follows:

$$\Delta H_{tot} = \Delta H_c + \Delta H_m \quad (1)$$

where ΔH_{tot} is the total height variation; ΔH_c is the contribution to the height variation because of the cytoskeleton and ΔH_m is the contribution to the height variation attributable to the microvilli.

At $t = 0$ ΔH_c can be estimated by the zero exposure fit extrapolation $H0$ (equal to 2.04 µm) and the contribution because of the microvilli ($\Delta H_m = \Delta H_{total} - \Delta H_c$) results to be about 0.34 µm (with an error of 0.09), a value close to the 0.4 µm suggested by Knutton et al. ***(47)***. It is worth noting that this value should be considered as an independent estimation of the size of microvilli in the sample analyzed.

3.9. Comparison With SEM and Fluorescence Microscopy

It is worth noting that our results are in agreement with previous data of Santoro et al. ***(10)*** that report, by scanning electron microscopy of lymphoblastoid cells, the loss of microvilli after 72 h exposure to 50 Hz, 2 mT MF and also show, by fluorescence microscopy analysis, a rearrangement of actin subsequent to (72 h) exposure. This supports the interpretation of our data with regard to effects on the cytoskeleton. In the same paper the authors also provide Laurdan spectroscopy evidence of a membrane fluidity variation that can be related to the progressive modification of the membrane leading to the appearance of rippling and pit-like structures reported here.

In this view, our data enable us to extend, and roughly quantify, the detection of cytoskeletal modifications during the first hours of exposure and to add a 3D description of the MF-induced changes. We can also introduce an experimental correlation between exposure time and morphological parameters such as cell height, shape, membrane roughness, and carry out the variation kinetics of these parameters to determine markers of long MF exposure.

4. Comments

The AFM images reported here demonstrate the existence of an exposure-dependent MF-induced morphological effect on immune system cells (Raji). This effect can roughly be divided as follows: within the first 10–15 h there is a large decrease of cell height and roughness related to the disappearance of microvilli with a minor simultaneous effect on the cytoskeleton. At longer

exposure time the plasma membrane appears to become completely free of microvilli and the weak residual variation, which can be completely ascribed to the cytoskeleton, leads to a less domed and wider cell shape and to the appearance of ripples and pit structures on the membrane surface.

The reported data allow us to speculate that in such treated cells some functional alteration occurs (for instance in cell motility or target recognition). However, the very large diffusion in intensity and frequency of the MF used in our study requires caution in drawing conclusions about a possible health hazard.

Further information about actual cell damage induced by MF will come from the characterization of the degree and the kinetics of reversibility of the morphological changes, and also from the study of the correlation of morphological changes to biochemical modifications and cellular dysfunction. It could also be interesting to establish the threshold value of the field intensity below which no morphological modification is detectable. Specific studies are in progress to extend the experiment to different cell lines that, because of the known specificity of the MF-induced effect, could present a different response pathway.

Acknowledgment

This work has been partially supported by a grant from Istituto Superiore Prevenzione E Sicurezza del Lavoro (ISPESL).

References

1. Bassett, C. A. L., Mitchell, S. N., and Gaston, S. R. (1982) Pulsing electromagnetic field treatment in ununited fractures and failed arthrodeses. *JAMA* **247,** 623–628.
2. Liboff, A. R. (1985) Cyclotron resonance in membrane transport, in *Interaction Between Electromagnetic Fields and Cells* (Chiabrera, A., Nicolini, C., and Schwan, H. P., eds.) NATO ASI, series A 97, Plenum Press, New York, pp 281.
3. Walleczeck, J. (1992) Electromagnetic field effect on cells of the immune system: the role of calcium signaling. *FASEB J.* **6,** 3177–3185.
4. Glaser, R. (1992) Current concepts of the interaction of weak electromagnetic fields with cells. *Bioelectrochem. Bioenerg.* **27,** 255–268.
5. Paradisi, S., Donelli, G., Santini, M. T., Straface, E., and Marloni, W. A. (1993) A 50 Hz magnetic field induces structural and biophysical changes in membranes. *Bioelectromagnetics* **14,** 247–255.
6. Tenforde, T. S. (1995) Interaction of extremely low frequency electric and magnetic fields with humans, in *Handbook of Biological Effects of Electromagnetic Field*, 2nd ed, Chapter 4 (Polk, C. and Postow, E., eds.) CRC Press, Boca Raton, FL, pp. 185–230.
7. Polk, C. (1995) Electric and magnetic fields for bone and soft tissue repairs, in *Handbook of Biological Effects of Electromagnetic Field*, 2nd ed., Chapter 5 (Polk, C. and Poston, E., eds.) CRC Press, Boca Raton, FL, pp. 231–246.

8. Stevens, R. G. (1995) Epidemiological studies of electromagnetic fields and health, in *Handbook of Biological Effects of Electromagnetic Field*, 2nd ed., Chapter 7 (Polk, C. and Poston, E., eds.) CRC Press, Boca Raton, FL, pp. 275–294
9. Kaiser, F. (1996) External signals and internal oscillation dynamics: Biophysical aspects and modelling approaches for interactions of weak electromagnetic fields at the cellular level. *Bioelectrochem. Bioenerg.* **41,** 3–18.
10. Santoro, N., Lisi, A., Pozzi, D., Pasquali, E., Serafino, A., and Grimaldi S (1997) Effect of extremely low frequency magnetic field exposure on morphological and biophysical properties of human lymphoid cell line (Raji). *Biochem. Biophys. Acta* **1357,** 281–290.
11. Tofani, S. and D'Amore, G. (1991) Extremely low frequency and very low frequency magnetic fields emitted by video display units. *Bioelectromagnetics* **12,** 35–45.
12. Vistnes, A. I., Ramberg, G. B., Bjornevik, L. R., Tynes, T., and Haldorsen T. (1997) Exposure of children to residual magnetic fields in Norway: Is proximity to power lines an adequate predictor of exposure? *Bioelectromagnetics* **18,** 47–57.
13. Savitz, D. A., John, E. M., and Kleckner, R. C. (1990) Magnetic field exposure appliances and childhood cancer. *Am. J. Epidemiol.* **191,** 763–773.
14. Coghill, R. W. (1996) Low frequency electric and magnetic fields in the bedplace of children with leukaemia. *Biophysics.* **41,** 809–816.
15. Kavet, R. (1996) EMF and current cancer concept. *Bioelectromagnetics* **17,** 339–357
16. Rosenthal, M. and Obe, G. (1989) Effects of 50-Hertz electromagnetic fields on proliferation and chromosomal alterations in human peripheral lymphocytes untreated or pretreated with chemical mutagens. *Mutat. Res.* **210,** 329–335.
17. Loscher, W. and Mevissen, M. (1995) Linear relationship between flux density and tumor co-promoting effect of prolonged magnetic field exposure in a breast cancer model. *Cancer Lett.* **96,** 175–179
18. Blank, M. (1987) The surface compartment model: a theory of ion transport focused on ionic processes in the electric double layers at membrane protein surface. *Biochem. Biophys. Acta* **906,** 277–294
19. Lednev, V. V. (1996) Bioeffects of weak combined, constant and variable magnetic fields. *Biophysics* **41,** 241–252.
20. Barnes, F. S. (1996) Effect of electromagnetic fields on the rate of chemical reactions. *Biophysics* **41,** 801–808.
21. Carson, J. J. L., Prato, F. S., Drost, D. J., Diesbourg, L. D., and Dixon, S. J. (1990) Time varying magnetic fields increase cytosolic free Ca^{2+} in HL-60 cells. *Am. J. Physiol.* **259,** 687–692.
22. Cadossi, R., Bersani, F., Cossarizza, A., et al. (1992) Lymphocytes and low frequency electromagnetic fields. *FASEB J.* **6,** 2667–2674.
23. Alipov, Y. D. and Belyaev, I. Y. (1996) Difference in frequency spectrum of extremely low frequency effects on the genome conformational state of AB1157 and *E. coli* cells. *Bioelectromagnetism* **17,** 384–387.

24. Shao, Z., Mou, J., Czajkowsky, D. M., Yang, J., and Yuan, J. Y. (1996) Biological atomic force microscopy: What is achieved and what is needed. *Adv. Phys.* **45,** 1–86.
25. Butt, H. J., Wolff, E. K., Gould, S. A. C., Dixon Nothern, B., Peterson, C. M., and Hansma, P. K. (1990) Imaging cells with the atomic force microscope. *J. Struct. Biol.* **105,** 54–61.
26. Gould, S. A. C., Drake, B., Prater, C. B., et al. (1990) From atoms to integrated chips, blood cells and bacteria with the atomic force microscope. *J. Vac. Sci. Tecnol. A.* **8,** 369–373.
27. Bustamante, C., Vesenka, J., Tang, C. L., Rees, W., Guthold, M., and Keller, R. (1992) Circular DNA molecules imaged in air by scanning force microscopy. *Biochemistry* **31,** 22–28.
28. Henderson, E., Haydon, P. G., and Sakaguchi, D. S. (1992) Actin filament dynamics in living glial cells imaged by atomic force microscopy. *Science* **257,** 1944–1946.
29. Cricenti, A., De Stasio, G., Generosi, R., Perfetti, P., Ciotti, M. T., and Mercanti D (1995) Atomic force microscopy of neuron networks. *Scanning Microsc.* **9,** 695–700.
30. Zecca, L., Dal Conte, G., Furia, G., and Ferrario, P (1985) The effect of alternating magnetic field on experimental inflammation in the rat. *Bioelectrochem. Bioenerg.* **14,** 39–43.
31. Stuchly, M. A., Ruddick, J., Villeneuve, D., et al. (1988) Teratological assessment of exposure to time-varying magnetic field. *Teratology* **38,** 461–466.
32. McLean, J. R. N., Stuchly, M. A., Mitchel, R. E. J., et al. (1991) Cancer promotion in a mouse skin model by 60-Hz magnetic field: II. Tumor development and immune response. *Bioelectromagnetics* **12,** 273–287.
33. Santini, M. T., Cannetti, C., Paradisi, S., et al. (1995) A 50 Hz sinusoidal magnetic field induces changes in the membrane electrical properties of K562 leukaemic cells. *Bioelectrochem. Bioenerg.* **36,** 39–45.
34. Weiss, A. and Imboden, J. B. (1987) Cell surface molecules and early events involved in human T lymphocyte activation. *Adv. Immunol.* **41,** 1–38.
35. Greene, J. J., Skowronski, W. J., Mullins, J. M., Nardone, R. M., Penafiel, M., and Meister, R. (1991) Delineation of electric and magnetic field effects of extremely low frequency electromagnetic radiation on transcription. *Biochem. Biophys. Res. Commun.* **174,** 742–749.
36. Conti, P., Gigante, G. E., Alesse, E., Cifone, M. G., Fieschi, C., Reale, M., and Angeletti, P. U. (1985) A role for calcium in the effect of very low frequency electromagnetic field on the blastogenesis of human lymphocytes. *FEBS Lett.* **181,** 28–32.
37. Lin, P. S., Wallach, D. F. H., and Tsai, S. (1973) Temperature induced variations in the surface topology of cultured lymphocytes are revealed by scanning electron microscopy. *Proc. Nat. Acad. Sci. USA* **70,** 2492–2496.
38. Weaver, J. C. and Astumian D (1990) The response of living cells to very weak electric fields: The thermal noise limit. *Science* **247,** 459–462.

39. Pulvertaft, R. J. V. (1964) Cytology of Burkitt's tumour (African lymphoma). *Lancet* **1,** 238–240.
40. Mercanti, D., De Stasio, G., Ciotti, M. T., et al. (1991) Photoelectron microscopy in the life science: Imaging neuron network. *J. Vac. Sci. Technol. A* **9,** 1320–1322
41. Lo Russo, G. F., De Stasio, G., Casalbore, P., et al. (1997) Photoemission analysis of chemical differences between the membrane and cytoplasm of neuronal cells. *J. Phys. D* **30,** 1794–1798
42. Cricenti, A. and Generosi R (1995) Air operating atomic force-scanning tunneling microscope suitable to study semiconductors, metals and biological samples. *Rev. Sci. Instrum.* **66,** 2843–2847.
43. Cricenti, A., De Stasio, G., Generosi, R., et al. (1996) Native and modified uncoated neurons observed by atomic force microscopy. *J. Vac. Sci. Technol. A.* **14,** 1741–1746.
44. De Stasio, G., Cricenti, A., Generosi, R., et al. (1995) Neurone decapping characterization by atomic force microscopy: A topological systematic analysis. *NeuroReport.* **7,** 65–68.
45. Bretscher, M. S. (1996) Getting membrane flow and the cytoskeleton to cooperate in moving cells. *Cell* **87,** 601–606.
46. Allen, L. A. and Aderem A (1995) A role for MARCKS, the {a} isozyme of protein kinase C and myosin I in zymosan phagocytosis by macrophages. *J. Exp. Med.* **182,** 829–840.
47. Knutton, S., Summer, M. C. B., and Pasternak, C. A. (1975) Role of microvilli in surface changes of synchronized P815Y mastocytoma cells. *J. Cell Biol.* **66,** 568–576.

25

Sample Preparation Method for Observing RNA Polymerase Activity by Atomic Force Microscopy

Sandor Kasas

1. Introduction

Transcription is a fundamental biochemical process in which an RNA molecule is synthesized according to its corresponding DNA template.

Transcription begins when an RNA polymerase (RNAP) molecule binds to a specific region of the DNA referred as the promoter. In the next step, the two strands of the DNA are separated locally to form an open promoter complex, which permits the beginning of the synthesis of the complementary RNA chain. The kinetics of this reaction have been studied in different biochemical experiments ***(1)***, which can only give population-averaged properties. Single RNAP transcription can be observed by optical microscopy through the motion of a bead tethered to the end of the DNA template, but this approach has a limited resolution ***(2)***.

Recent developments in atomic force microscopy (AFM; **refs. *3*** and ***4***) now give one the opportunity to study transcription in nearly physiological conditions with nanometer scale resolution **(Fig. 1; *5*,*6*)**.

The first step of this type of experiment consists in the formation of a stalled ternary complex ***(7)***. In a test tube, RNAP and three of the four nucleoside triphosphates (NTPs) are mixed with a specially designed DNA molecule. The protein attaches to the DNA at the promoter region to form an open promoter complex. After this, transcription starts and goes on until it stalls at a specific base along the DNA (the stall site). The DNA is specially designed to be transcribed from the promoter to the stall site by using only three different NTPs (*see* **Fig. 2**). To go further a fourth NTP is required that is not present in the test tube. These reactions allow a "sample" to be made in the test tube, the stalled ternary complex, which consists of an RNAP molecule, with a short RNA molecule already synthesized, attached to the DNA.

From: *Methods in Molecular Biology, vol. 242: Atomic Force Microscopy: Biomedical Methods and Applications*
Edited by: P. C. Braga and D. Ricci © Humana Press Inc., Totowa, NJ

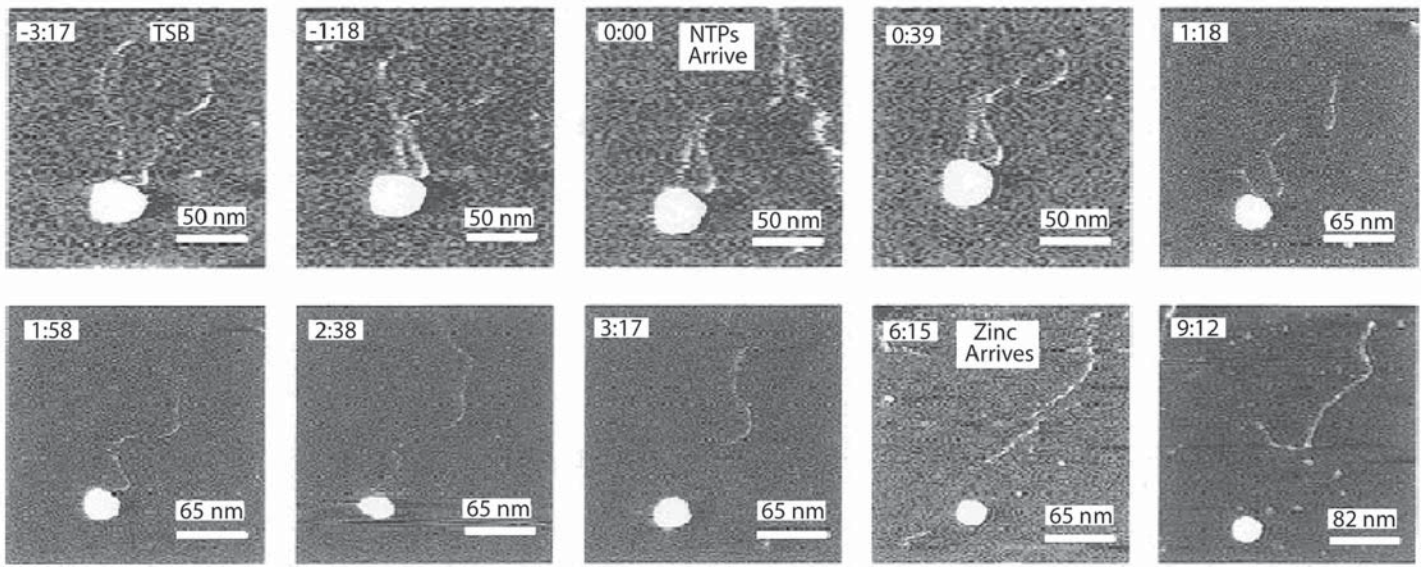

Fig. 1. Time-lapse series of images showing transcription of a 1047-bp DNA template by an RNAP molecule. On the first two images the sample is immersed in the transcription buffer (TSB). It permits a certain mobility to the DNA on the mica surface. After NTP addition (third image at time 0:00) one arm of the DNA template becomes progressively shorter until the DNA is released (2:38). The addition of zinc in the AFM chamber blocks the DNA to the mica surface and permits a better imaging. Reprinted with permission from **Ref. *5***.

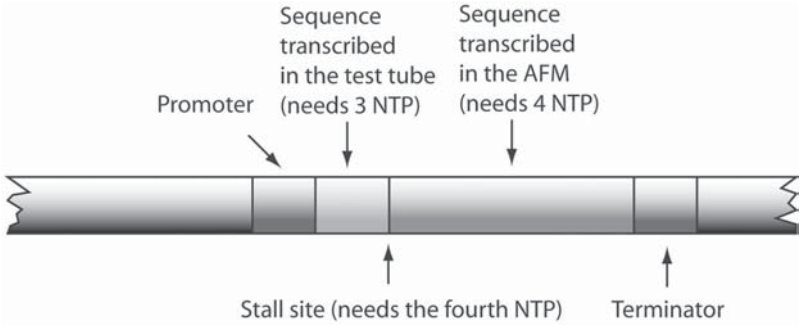

Fig 2. Schematic representation of the DNA template showing the positions of the promoter, stall site, and the terminator.

The stalled ternary complex is then deposited onto a mica surface and introduced into the AFM observation chamber. Unfortunately, the AFM tip interacts relatively strongly with the sample it is imaging. This interaction requires a relatively strong anchoring of the specimen to the support (mica in our case). Because transcription is a dynamical process, we are facing a paradox; the sample has to be fixed strongly enough to the support to permit AFM imaging and at the same time, it has to be free enough to permit its movements to occur. In the case of the transcription, this problem particularly concerns the binding of DNA to surfaces. A DNA molecule has to be attached strongly enough to the mica to permit its imaging and it has to be free enough to allow RNAP to translocate it.

This problem can partially be solved by modulating DNA adhesion to mica by the use of two different buffers: an "imaging" and a "transcription" buffer. The imaging buffer promotes DNA adhesion whereas the transcription buffer releases DNA from the surface and permits to the RNAP to pull on the DNA and to transcribe it. These buffers differ in their zinc concentrations: this ion has been demonstrated to promote DNA adhesion to the mica ***(8,9)***.

The RNAP molecule is not concerned by the adhesion/activity problem; it sticks to the mica in both transcription and imaging buffers and adhesion to mica does not inactive all the RNAPs bound to it.

An additional problem in imaging dynamical processes by AFM is the maximal scanning frequency of the microscope. The majority of biochemical reactions occur at speeds that are for the moment inaccessible to AFMs (RNAP translocates along DNA at a maximal speed between 12 and 19 bases per second; **ref. *10***). This problem can be solved by slowing the natural transcription speed. The easiest way to achieve this is by reducing the quantity of NTPs available to the RNAP.

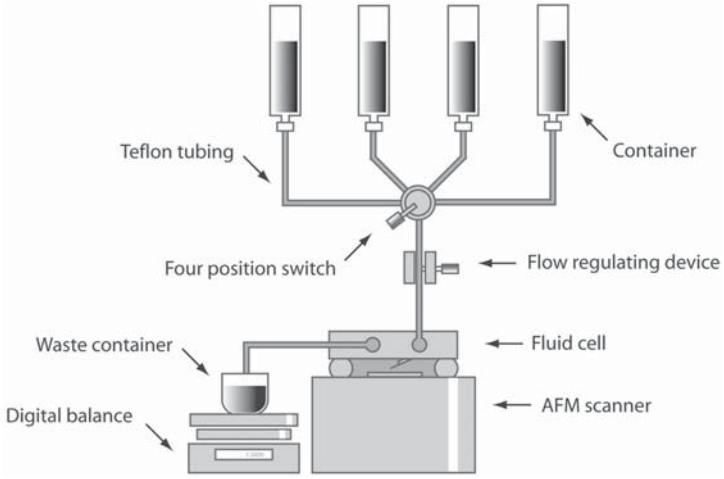

Fig. 3. Schematic diagram depicting the flow-through system. The four position switch permits to select one of the four different solutions to flow through the AFM fluid cell. The digital balance permits to determine when a new solution comes in contact with the sample.

To switch from the imaging to the transcription buffer or vice versa , one needs an exchange device that does not perturb AFM imaging. The best results are obtained by a gravity-driven flow-through system consisting of four containers suspended above the AFM and that are connected to the fluid cell through a four-position switch. A buffer is continuously flowing through the fluid cell during the experiment and the switch allows the buffer to be changed without changing the flow-rate (i.e., with a minimum perturbation). The flow rate can be controlled by a micrometer screw on the tube leading from the switch to the fluid cell. (*See* **Fig. 3**.)

A balance is used to measure the effluent to determine the flow rate. By calibrating the weight of the liquid between the switch and the fluid cell and by knowing the flow rate, one can determine when a new solution reaches the sample.

Before starting the experiment, it is advisable to check if the RNAP has conserved its activity and if it stalls at the right site when fueled by three NTPs. This test is accomplished by running the reaction in a test tube once with three and once with four NTPs. Both samples are eventually deposited onto a mica surface and imaged in air with the AFM. In the first case, one should see isolated RNAP and DNA molecules. In the second case, the RNAP molecule should be bound to the DNA at the stall site.

2. Materials

2.1. AFM (Nanoscope III)

1. Tapping mode in liquids option.
2. Tapping mode in air option.
3. Scanner with a maximal lateral scan size of about 13 μm.
4. 100-μm Long silicon nitride triangular cantilevers with a spring. constant of about 0.1 N/m. Sharpen tip with a radius of curvature of about 5–15 nm for tapping in liquids.
5. Silicon cantilevers with a nominal spring constant of 30 N/m for tapping in air.
6. Fluid cell.
7. O ring.

2.2. The Flow-Through System

1. Four containers of about 20 mL.
2. Four-arm container holder.
3. About 10 m of Teflon tubing.
4. A four-position switch.
5. A flow-regulating device (micrometer screw squeezing the tube leading from the switch to the fluid cell).
6. Digital balance.
7. A 200-mL waste container.

2.3. Buffers and Solutions

1. Transcription buffer: 20 m*M* Tris, pH 7.9, 5 m*M* $MgCl_2$, 50 m*M* KCl, 1 m*M* β-mercaptoethanol.
2. Transcription buffer with NTPs: 20 m*M* Tris, pH 7.9, 5 m*M* $MgCl_2$, 50 m*M* KCl, 1 m*M* β-mercaptoethanol, NTP mixture (ATP, CTP, GTP, UTP); 2.5 μ*M* for each NTPs.
3. Imaging buffer 20 m*M* Tris, 5 m*M* KCl, 5 m*M* $MgCl_2$, 1 m*M* β-mercaptoethanol, 1.5 m*M* $ZnCl_2$, pH 7.5.
4. Stalled ternary complex NTP solution: 100 μ*M* NTP mixture containing 3 NTP in the transcription buffer.
5. Stalled ternary complex DNA–RNAP solution: 100 μ*M* specially designed DNA (*see* **Notes 1–3; Fig. 2**); and 100 μ*M* RNAP.

3. Method

3.1. Observation of the Stalled Ternary Complexes in Air

1. Mix DNA and RNAP in a 1:1 molecular ratio in transcription buffer and incubate it for 10 min at 37°C to allow the RNAP to associate with the promoter.
2. Add the three appropriate NTPs to the solution and incubate for 5 min at room temperature to make the stalled ternary complex.
3. Deposit 5–10 μL of the solution onto freshly cleaved mica.
4. Wait a couple of minutes.

5. Rinse in excess deionized water and dry in a stream of compressed air.
6. Observe the sample using tapping-mode AFM in air.

3.2. Preparation of the Sample for AFM Imaging in Liquids

1. Prepare the flow-through system with the following buffers: transcription buffer with no NTPs, transcription buffer with the four NTPs, and imaging buffer.
2. Prepare the AFM for tapping mode imaging in liquids (*see* **Note 4**).
3. Mix DNA and RNAP in a 1:1 molecular ratio in transcription buffer and incubate it for 10 min at 37°C to allow to the RNAP to associate with the promoter.
4. Add the three appropriate NTPs to the solution and incubate for 5 min at room temperature to make the stalled ternary complex.
5. Dilute the solution 1:10 in the imaging buffer.
6. Deposit 5–10 µL of the solution onto freshly cleaved mica and introduce the sample into the AFM before any drying occurs.
7. Connect the fluid cell to the flow-through tubing and rinse the sample with the imaging buffer to wash away any loosely bound complexes and to ensure that the DNA is easily visualized.
8. Image the sample and search a field containing several RNAP molecules attached to their DNA.
9. Switch the transcription buffer with no NTPs on and let it flow through the fluid cell until the DNA shows diffusive motion on the mica.
10. Switch the transcription buffer with NTP on to reinitiate transcription and capture every frame for 5–10 min (*see* **Notes 5** and **6**).
11. Switch to the imaging buffer to re-attach DNA to the mica and capture several frames.
12. Stop the experiment and analyze the images by searching the RNAPs, which translocated their DNA. The individual images recorded by the AFM can be assembled in a movie using NIH image or Adobe Premiere (*see* **Note 7**).

4. Notes

1. The DNA should have no more than 2000–3000 base pairs. Longer molecules makes it difficult to follow the progression of the transcription.
2. The stall site should be located towards the middle of the DNA, but asymmetrically to give two different DNA arm lengths to observe directionality of movement of the RNAP in the AFM movie.
3. Among other companies Microsynth, MWG Biotech, and Eurogentech can manufacture the DNA required for this experiment.
4. The cantilever oscillation frequency for tapping mode imaging in liquids should be about 10 kHz for the cantilevers suggested above.
5. By selecting the movie option in the AFM capture menu, the microscope automatically records every frame, allowing the experimenter to concentrate to other tasks.
6. A compromise has to be found between the temporal and the spatial resolution of the AFM images. Scanning at low speed, large areas allow several RNAP–DNA complexes to be followed but with a limited temporal resolution. Inversely scan-

ning at high speed a small area diminishes the chances to capture one of the 20% active RNAP molecules. A scanning speed of 5 to 10 Hz with a resolution of 256 × 256 over a 500-nm large scan size is a good value with which to begin.

7. Because of the thermal drift, individual images taken by the AFM will be shifted. Before making an animation, the frames have to be aligned first. This can be achieved with the freeware image processing software NIH image.

Acknowledgments

The author thank Dr N. Thomson, Pr. G. Dietler, and Dr. H. Hirling for their highly constructive suggestions. This work has been supported by the Swiss National Science Foundation, grants NB 31-52587, 31-53725.98, and 21-54003.98

References

1. Sen, R. and Dasgupta, D. (1994) Intrinsic fluorescence of *E. coli* RNA polymerase as a probe for its conformational changes during transcription initiation. *Biochem. Biophys. Res. Commun.* **201,** 820–828.
2. Schafer, D. A., Gelles, J., Sheetz, M. P., and Landick, R. (1991) Transcription by single molecules of RNA polymerase observed by light microscopy. *Nature* **352,** 444–448.
3. Binnig, G., Quate, C. F., and Gerber, C. (1986) Atomic force microscope. *Phys. Rev. Lett.* **56,** 930–933.
4. Hansma, P. K., Cleveland, J. P., Radmacher, M., et al. (1994) Tapping mode atomic force microscopy in liquids. *Appl. Phys. Lett.* **64,** 1738–1740.
5. Kasas, S., Thomson, N. H., Smith, B. L., et al. (1997) *Escherichia coli* RNA polymerase activity observed using atomic force microscopy. *Biochemistry* **36,** 461–468.
6. Guthold, M., Zhu, X., Rivetti, C., et al. (1999) Direct observation of one-dimensional diffusion and transcription by Escherichia coli RNA polymerase. *Biophys. J.* **77,** 2284–2294.
7. Levin, J. R., Krummel, B., and Chamberlin, M. J. (1987) Isolation and properties of transcribing ternary complexes of *Escherichia coli* RNA polymerase positioned at a single template base. *J. Mol. Biol.* **196,** 85–100.
8. Hansma, H. G. and Laney, D. E. (1996) DNA binding to mica correlates with cationic radius: assay by atomic force microscopy. *Biophys. J.* **70,** 1933–1939.
9. Thomson, N. H., Kasas, S., Smith, B., Hansma, H. G., and Hansma, P. K. (1996) Reversible binding of DNA to mica for AFM imaging *Langmuir.* **12,** 5905–5908.
10. Kornberg, A. and Baker, T, A. (1991) *DNA Replication*, Freeman, New York, p. 246.

26

Atomic Force Microscopy of β-Amyloid

Static and Dynamic Studies of Nanostructure and Its Formation

Justin Legleiter and Tomasz Kowalewski

1. Introduction

Ordered aggregation of the β-amyloid (Aβ) peptide in the brain as plaques consisting of fibrils is an important characteristic of Alzheimer's disease (AD), a late onset neurodegenerative disease ***(1)***. Aβ derives from the endoproteolysis of the amyloid precursor protein (APP), which is a transmembrane protein containing 677–770 amino acids ***(2–9)***. The two most common forms of Aβ are the 40 and 42 residues long fragments respectively referred to as Aβ(40) and Aβ(42) (sequence shown in **Fig. 1**; **ref. *10***). The insoluble aggregated form of Aβ, which deposits in the extra cellular space in the brain and on the walls of cerebral blood vessels ***(6)***, exhibits an enhanced β-sheet conformation as opposed to the partially α-helical soluble form found in body fluids ***(11,12)***. Despite the lack of the definitive establishment of the causative role of Aβ in AD, evidence points to its aggregation and deposition in the pathogenesis of AD.

The formation of the ordered, β-sheet rich fibrils is believed to proceed via a slow nucleation-dependent mechanism that is followed by rapid "chain-growth" into protofibrils that eventually elongate and possibly coalesce to form mature amyloid fibrils (**Fig. 2; refs. *7,13–17***). The elongation of the protofibrils and fibrils appears to be of the first order ***(7,13,16,17)***. The slow step is the formation of Aβ oligomers that nucleate the process, but it is unclear what causes the formation of these small oligomers. It appears that a critical local concentration needs to be achieved. Such conditions can occur as the result of inefficient clearance of Aβ from the brain. Intra- and extracellular surfaces located inside the brain could also play a pivotal role by increasing local concentrations of Aβ to facilitate the formation of a stable nucleus. Understanding how the process of fibrillogenesis is nucleated and how it is facilitated could

From: *Methods in Molecular Biology, vol. 242: Atomic Force Microscopy: Biomedical Methods and Applications*
Edited by: P. C. Braga and D. Ricci © Humana Press Inc., Totowa, NJ

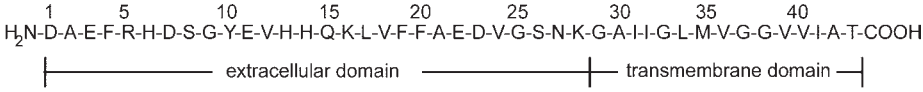

Fig. 1. The sequence of Aβ peptide ***(10)***.

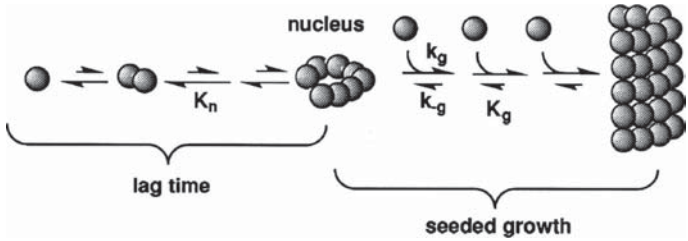

Fig. 2. A simple nucleation dependent mechanism for the growth of Aβ fibrils. A series of unfavorable protein-protein association equilibria with rate constant K_n lead to the formation of a stable nucleus. Once the nucleus is formed, growth into a fibril is achieved by a series of favorable equilibria with rate constant K_g. This shift from the unfavorable to favorable equilibria results in a critical concentration phenomenon. Once a stable nucleus is formed, fibril growth is first order ***(17)***. With permission, from the *Annual Review of Biochemistry*, Volume 66 © 1997 by Annual Reviews www.annualreviews.org.

offer valuable insights into possible targets along the disease pathway for novel treatments for AD.

Atomic force microscopy (AFM) can be used to image and study Aβ with resolution comparable to that achievable with transmission election microscopy (TEM). However, it does not require the extensive sample preparations, such as staining, that precludes the use of TEM in kinetic studies and could possibly alter the morphology of the Aβ fibrils. AFM can also obtain more complete 3D information than can be derived from the 2D cross sectional profiles obtained in TEM studies. *In situ* tapping-mode AFM ***(18,19)*** under liquids offers the ability to study Aβ fibrilization under physiological conditions in a time-dependent manner, which allows the monitoring of changes in conformation and aggregation of Aβ ***(20)***. AFM can also be used to gain insights into the interaction of Aβ with other materials that are of potential importance in AD that could either inhibit or promote Aβ self-assembly into fibrils. This type of information would be useful in evaluating specific drugs designed to inhibit the process and in the determination of where along the pathway they interact with Aβ. These types of studies could also lead to understanding of how other relevant factors (such as lipoproteins, lipid bilayers) affect fibril formation.

2. Materials

1. AFM capable of performing *in situ* operations. There are several systems commercially available from different vendors (Digital Instruments-Veeco, JEOL, Molecular Imaging, Omicron, Pacific Scanning, Quesant Instrument Corporation, Accurion Scientific Instruments, Asylum Research).
2. Standard contact mode fluid cell or fluid cell with piezoelectric accuator.
3. Low-spring-constant cantilever probes, for example, 100-μm wide-legged silicon nitride cantilevers with nominal spring constant of 0.58 N/m for *in situ* tapping mode atomic force microscopy (TMAFM) (commercially available from several vendors: Digital Instruments, Olympus, Bioforce).
4. Tapping mode. Tapping mode-etched silicon probes for *ex situ* studies. (Commercially available from several vendors: Digital Instruments, Olympus, Bioforce.)
5. Dimethylsulfoxide (DMSO).
6. Trifluoroacetic acid (TFA).
7. Phosphate-buffered saline (PBS) buffer of approx pH 7.4.
8. Mica.
9. Highly ordered pyrolitic graphite.
10. Aβ(40, 42), or other fragments that are commonly available from several vendors.
11. Nitrogen.
12. Ultra pure water.

3. Methods

The methods section discusses experimental topics (*see* **Note1**) such as preparation, handling, and incubation of Aβ samples (*see* **Note 2**), *ex situ* AFM studies of Aβ (*see* **Note 3**), *in situ* AFM studies of Aβ (*see* **Note 4**), common methods of analyzing data obtained form AFM studies of Aβ (*see* **Note 5**), and incorporating other factors into AFM studies of Aβ (*see* **Note 6**).

3.1. Preparation and Handling of Aβ Samples

3.1.1. Storage

1. Several different solvents can be used to prepare stock solutions of Aβ. Eventually, these stock solutions should be dissolved in a physiological buffer, such as phosphate-buffered saline (PBS) or Tris-HCl. Solvents that have been used to dissolve Aβ include dimethylsulfoxide (DMSO) ***(21,22)***, TFA ***(14)***, acetic acid ***(23)***, chloroform ***(24)***, physiological buffer ***(25,26)***, and deionized water ***(3,27)***. DMSO appears to be the most commonly used solvent, and the following procedure will involve the use of DMSO.
2. Aβ is easily dissolved in DMSO, and it can be used to make stock solutions that can be stored at –20°C for extended periods of time. Care should be taken to obtain accurate knowledge of the concentration of these stock solutions (usually 2–10 m*M* but this can vary). The stock solutions can also be filtered to remove any fibril seeds that may be present ***(21)***, but a larger initial concentration is

needed for this so that the final concentration remains in the approximate range indicated above.
3. Also, an independent method needs to be used to analyze the concentration of the stock solution after filtration since the removal of seeds will reduce the amount of Aβ in solution. This can be accomplished by quantitative amino acid analysis ***(21)***.
4. It is also useful to store the Aβ stock solution in smaller aliquots that will be used for individual experiments. The size of these aliquots depends on the concentration of the stock solution and the desired concentration for experiment once the stock solution is dissolved in physiological buffer as will be discussed in **Subheading 3.1.2., step 1**. This prevents waste and possible complications that may arise because of several cycles of thawing and refreezing stock solutions. Since these stock solutions are going to be dissolved into physiological buffer, it is important to keep the stock solutions concentrated enough so that upon dilution in the buffer the DMSO is diluted to less than 0.1% of the total volume. This limits the effect that the DMSO may have on the observed behavior of the Aβ in the study.

3.1.2. Incubation

1. In order to initiate the fibril formation, aliquots of the stock Aβ solution in DMSO need to be dissolved in physiological buffer. The new solution should be gently vortexed for approx 60 s to ensure thorough mixing. In order to ensure the solubility of the Aβ into physiological buffer, the buffer can initially be heated to approx 37°C prior to the addition of the DMSO Aβ stock solution.
2. Once the Aβ stock solution is dissolved in the buffer, the temperature should be held at 37°C for approximately another 30 min. These prepared incubation samples can range in concentration from 5–500 μ*M*. Lower concentrations may inhibit the formation of fibrils or may inhibit the ability to observe fibrils due to concentration depletion associated with aggregation of Aβ along the surfaces of the container.
3. Incubation of these samples can last from a few minutes to days and can be carried out at room temperature. These incubating samples should not be perturbed except to obtain aliquots for imaging to prevent the possibility of disrupting the process of self-assembly into fibrils.
4. Variation of the incubation process can easily be achieved by adding different elements to the Aβ solution, such as fibril seeds ***(28)*** or known amyloid inhibitors or promoters ***(25)***. Also, different pH, temperature ***(21)***, concentration, and other conditions can easily be varied.

3.2. Ex Situ *Studies of Aβ*

1. *Ex situ* AFM experiments have provided many insights into the fibrillization of Aβ ***(21,23,28,29)*** (*see* **Notes** and **Fig. 3**) and are especially useful as a complement to other techniques used to study the aggregation and self-assembly of Aβ. The major limitation of this technique is sample preparation, which ultimately

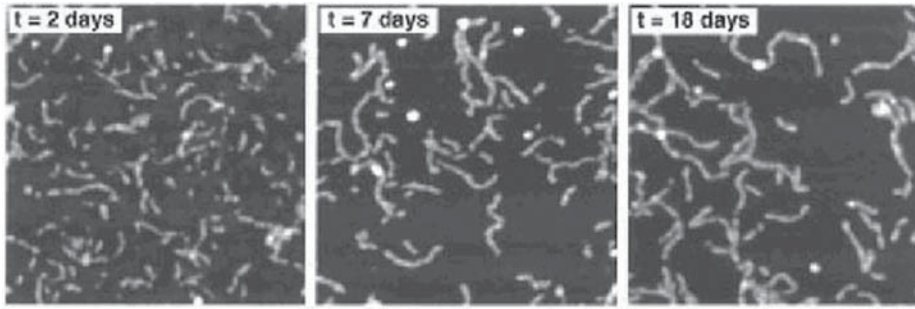

Fig. 3. *Ex situ* AFM images of an Aβ sample deposited on mica at different time intervals (2, 7, and 18 d). Each image is 500 nm by 500 nm. The development of longer protofibrils can be seen as the sample was allowed to incubate for longer times ***(28)***. Reprinted with permission from **ref. *21***. Copyright 1999 American Chemical Society.

carries the sample through a range of nonphysiological conditions, potentially leading to the perturbation of the original structure.

2. Moreover, *ex situ* AFM studies do not allow for the study of the development of the same Aβ structure over time that is possible, as will be discussed in **Subheading 3.3.**, with *in situ* AFM studies. However, by preparing several different aliquots from the same incubation at different time intervals, the development of protofibrils to mature fibrils can still be observed and studied.
3. *Ex situ* AFM is especially useful for observing changes in Aβ fibrillogenesis over extended periods of time (days).

3.2.1. Deposition

1. Deposition of Aβ onto a substrate for imaging is an important aspect of *ex situ* studies. Care must be taken to make the deposition process as noninvasive as possible as well as to reproducibly deposit the sample onto the surface. To ensure this, strict protocol should be used to deposit the sample onto the substrate.
2. To optimize the deposition process, concentrations can be adjusted to increase and decrease the amount of deposited peptide found on the surface.
3. The following is a brief procedure for depositing Aβ samples onto mica.
   a. Aliquots of 2–5 μL of incubated Aβ solution should be placed on freshly cleaved mica. Marking the backside of the mica with a small dot for sample placement is useful for locating the deposited Aβ later during imaging.
   b. The droplet is then left on the substrate for approx 30 s to 2 min, depending on the concentration of solution and the desired coverage. Once optimal conditions are found, the time the sample is allowed to incubate on the substrate should be held constant between depositions.
   c. After incubating the aliquot on the mica, the sample should be washed with 50–200 μL of ultra pure water to remove excess salts and unbound peptide. It is useful to tilt the substrate and deposit the wash above the sample on the

mica. Then, the wash can gently flow past the deposited peptide. This reduces the risk of damaging the deposited Aβ structures when applying the wash.

d. Allow the samples to dry under a gentle stream of nitrogen to prevent contamination and speed the drying process.
e. Once the mica is dry, the sample can be mounted onto a puck and imaged. Samples should be imaged as soon as possible to prevent any contamination or degradation over time.

3.2.2. Chemically Immobilized Aβ Deposition

1. *Ex situ* studies have also been carried out on thiol-based immobilization of Aβ on flat gold surfaces ***(23)***. Vapor deposition on mica can be used to prepare the gold substrates. After rinsing the substrates with ethanol, the gold substrate can be immersed in a 1 m*M* solution of 11-mercaptoundecanoic acid or a mixed solution of 11-mercaptoundecanoic acid and 3-mercaptopropionic acid (1 : 10).
2. The gold substrate should be soaked overnight and then placed in an aqueous solution of 1-ethyl-3-(3dimethlylaminopropyl)-carbodiimide (75 m*M*) and N-hydroxysuccinimide (15 m*M*) for 5 min.
3. After this, the substrates can be soaked in the diluted amyloid solutions for up to an hour. The substrates should be rinsed with deionized water after removal from the amyloid solution and allowed to dry. The substrates should be stored under argon.

3.3. In Situ *Studies of Aβ*

1. *In situ* TMAFM has been successfully applied to the study of Aβ aggregation and fibrillization ***(22,26)***. This technique offers the unique opportunity to image the fibrillization process in a dynamic way, and it can be used to study the interactions of Aβ with other important factors implicated in AD ***(14,24,25)***.
2. It can also be used in conjunction with other techniques used to study Aβ. These techniques include circular dichroism ***(14,25,30)***, fluorescence ***(30)***, and absorbance ***(30)***. It should be noted that the concentration of incubating Aβ solutions may need to be decreased. If the concentration is too large, the surface will be crowded, and the measurement of dimensions for individual particles will become difficult. However, the larger concentration of the incubating samples is also important to prevent the depletion of the sample from aggregation on the walls of the container and also to facilitate the fibrilization process. The concentration used for imaging needs to be systematically optimized.

3.3.1. Choice of Substrate

1. The choice of substrate to be used in the experiment is extremely important. Because of differing hydrophobicity and hydrophilicity of different surfaces, different effects on Aβ can be observed. The surface interactions play a significant role in aggregation and deposition, and thus in the self-assembly of Aβ into fibrillar species.

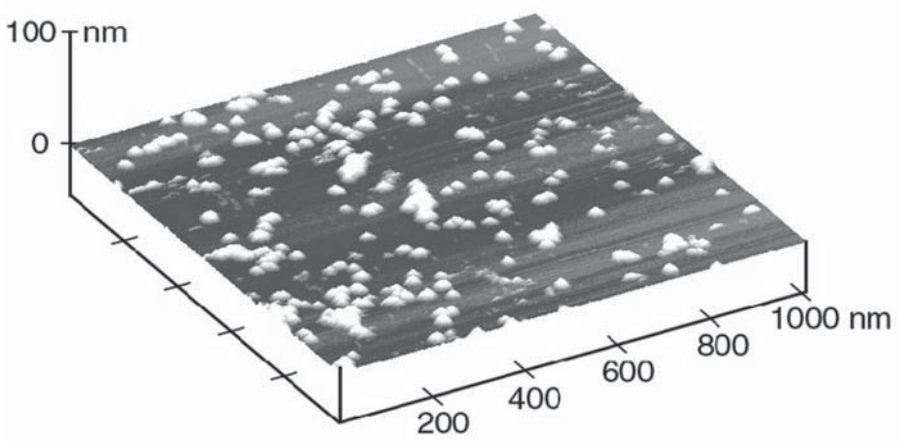

Fig. 4. 3D rendering of *in situ* AFM image of Aβ(42) on the hydrophilic surface of mica. This image was taken in PBS buffer with a peptide concentration of 500 μ*M*. The surface is covered with globular and protofibrillar aggregates of Aβ. The hydrophilic mica can be viewed as a model of the exterior of phospholipid bilayers that constitute cell membranes ***(22).***

2. Two commonly used substrates are mica and highly ordered pyrolitic graphite (HOPG) which can easily be cleaved to provide atomically flat surfaces.
3. Contrast between interaction of hydrophilic mica **(Fig. 4)** and hydrophobic graphite **(Fig. 5)** can also offer insights into the specific interactions that lead to Aβ self-assembly. The surface of mica is negatively charged in solution. Due to this negative charge, mica can be thought of as a surface that models the exterior of anionic phospholipid membranes. The interiors of phospholipid bilayers and lipoprotein particles can be modeled by the hydrophobic surface of graphite.

3.3.2. Imaging of Aliquots

Similar to the procedure briefly described in *ex situ* AFM experiments in **Subheading 3.2.**, aliquots of the same incubating sample can be imaged after different times to monitor the self assembly of Aβ into fibrils.

3.3.3. Time Lapse Imaging

1. *In situ* AFM can be used to study dynamic biological processes, including fibrilization, by time lapse imaging ***(20)***, which allows observation of the initial aggregation of Aβ into protofibrils and the elongation of these protofibrils into mature fibrils **(Fig. 6)**. In this technique, a freshly prepared sample is imaged in the same area of the surface at different time intervals, which can be hours in duration.

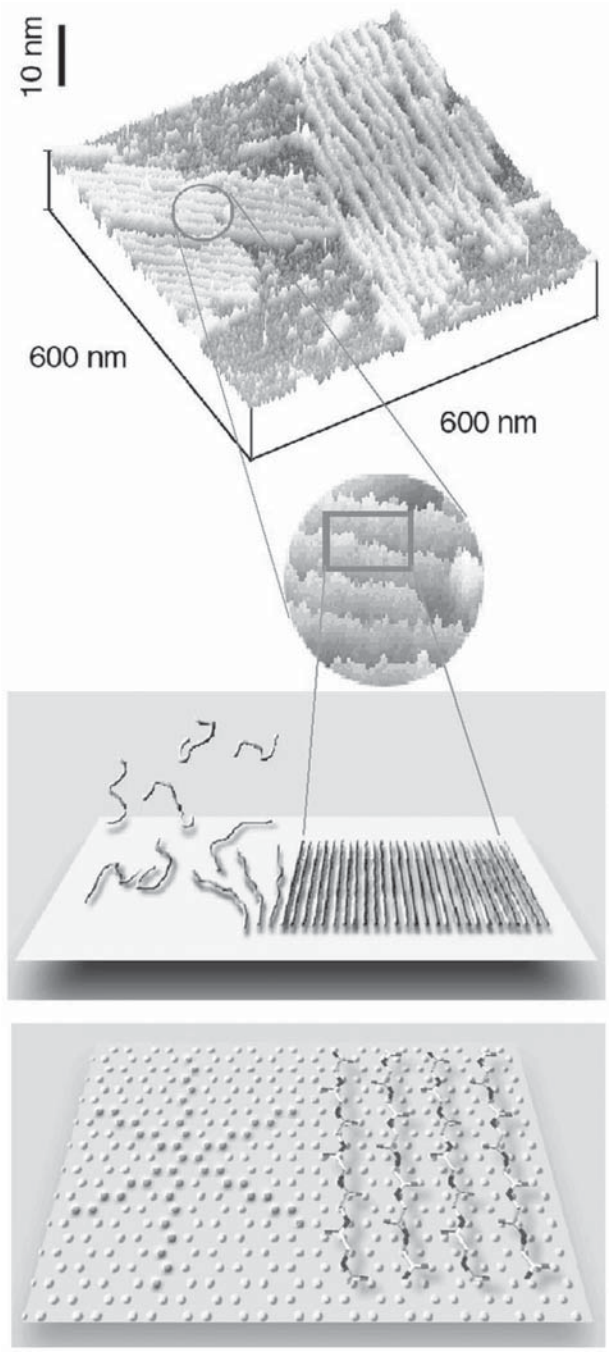

Fig. 5. 3D rendering of *in situ* AFM image of Aβ(42) on graphite. The sample was imaged in PBS buffer. The ribbon-like assemblies of Aβ preferentially orient along

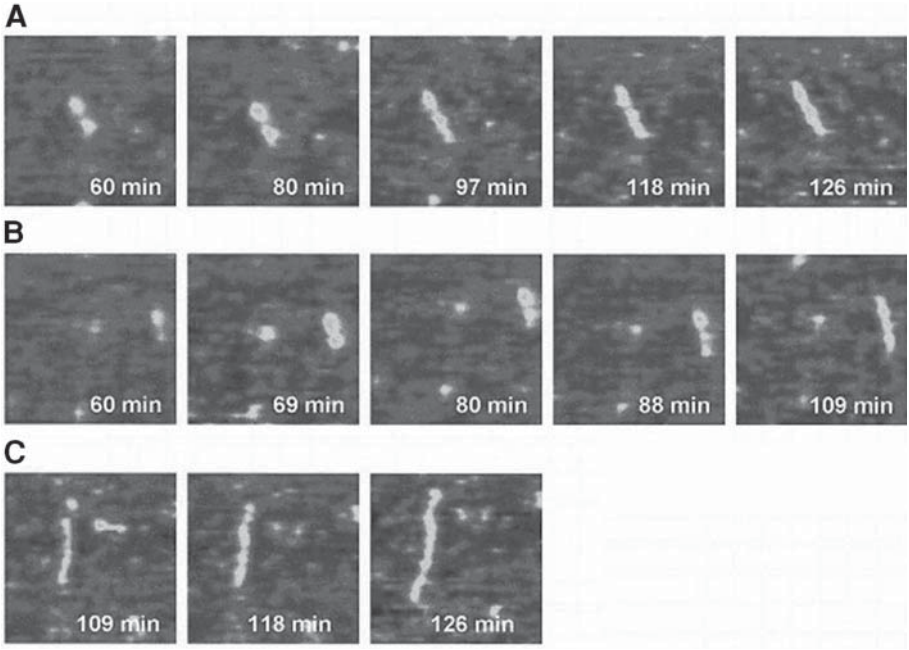

Fig. 6. *In situ* tapping mode AFM makes it possible to track the early steps of Aβ fibrillization. The above 1-μm by 1-μm images track the Aβ aggregates as they form protofibrils and elongate. **(A** and **B)** Images tracking the formation of a protofibril from two Aβ aggregates and the elongation of the protofibril by further addition of Aβ aggregates. **(C)** An Aβ protofibril is shown to elongate in two directions by the further addition of Aβ aggregates. From **ref. *26***. Copyright 2000, with permission from Elsevier.

2. It is important to maintain a good seal between the fluid cell and surface to prevent the evaporation of the solution. By monitoring the same area at different time intervals, it becomes possible to identify and track the development of individual fibrils, and to measure the rate of their elongation and detect morphological changes. Such direct observations provide insights into the mechanisms by which Aβ fibrils nucleate and grow. These insights may be then used in the determination of where along the pathway a specific compound may interfere with the fibril growth.

Fig. 5. *(continued)* crystallographic directions of graphite, presumably maximizing hydrophobic interaction with the surface. Hydrophobic graphite can be viewed as a model of the interior of phospholipid bilayers and the core of lipoprotein particles. The average lateral spacing of the aggregates is 18.8 ± 1.8 nm. The schematic illustrates the orientation of peptide chains in the aggregates based on their dimensions (bottom). The height of the aggregates above the graphite surface ranged from 1.0–1.2 nm. The dimensions of Aβ aggregates on graphite strongly suggest that Aβ adopts a β-sheet form with peptide chains perpendicular to the long axis of the ribbon ***(22)***.

3.4. Quantitative Analysis of AFM Images

1. Quantitative analysis of AFM images can easily be carried out with the aid of computer programs designed to measure heights, diameters, volumes and numbers of particles.
2. In such analysis, it is important to take into account the finite size and shape of the tip used in the experiment, since it may significantly contribute to the observed dimensions of imaged objects.
3. In time lapse *in situ* AFM, the tip contribution may remain relatively constant, provided that the tip is not damaged and that peptide molecules are not aggregating on the tip changing its size and shape. Hence when comparing results from different experiments, variability between the tips should be considered.
4. Common methods for tip characterization include the use of tip characterizers ***(31)*** and blind tip reconstruction ***(32)***.
5. A simple quantitative measurement involves monitoring the number of objects per unit area as a function of time **(Fig. 7; *21*,*22*,*26*)**. Different types of objects (i.e., oligomers, protofibrils, or mature fibrils) can be differentiated by a characteristic physical parameter like height or diameter **(Figs. 7–8; *22*,*26*)**.
6. Analysis of the population of these different forms of Aβ has shown that smaller aggregates tend to disappear as large protofibrils and mature fibrils are formed, indicating that smaller aggregates of Aβ are coalescing to form the larger structures ***(21*,*22*,*26)***.
7. Comparisons of these populations with the change in an average physical parameter (like diameter) also show if these particles are aggregating and coalescing into larger assemblies. A change in the average height or effective diameter of adsorbed material can also indicate different regimes of growth if plotted as a function of time **(Fig. 8; *22*)**.
8. Elongation rates can also be measured by an average measurement of fibril lengths as a function of time from aliquots of the same incubation or by the change in length of individual protofibrils as observed in time lapse AFM **(Fig 9; *21*,*26*)**.

3.5. Incorporating Other Factors into AFM Studies of Aβ

1. Once optimal conditions for imaging Aβ are determined, other variables can be added to gain insight into more specific interactions controlling fibrillization. For instance, the effects of glycerol and trimethylamine N-oxide, which act as chemical chaperones in the amyloid pathway, on the fibrillization of Aβ have been studied using *in situ* AFM ***(25)***.
2. AFM has also been used to study soluble Aβ oligomers by altering solution conditions ***(30)***. These oligomers may be important as intermediates between the monomeric form and the fibrillar form of Aβ and may be themselves physiologically active ***(30)***. The interaction of Aβ with planar bilayers of total brain lipid extract and DMPC deposited on a mica surface has also been reported ***(14)***.
3. The effects of Aβ on endothelial cells have been studied by imaging cells incubated with Aβ present ***(24)***. The Aβ was not directly observed in these images of endothelial cells. Rather, the vitality of the cell was monitored using AFM for cells that had been incubated with and without Aβ.

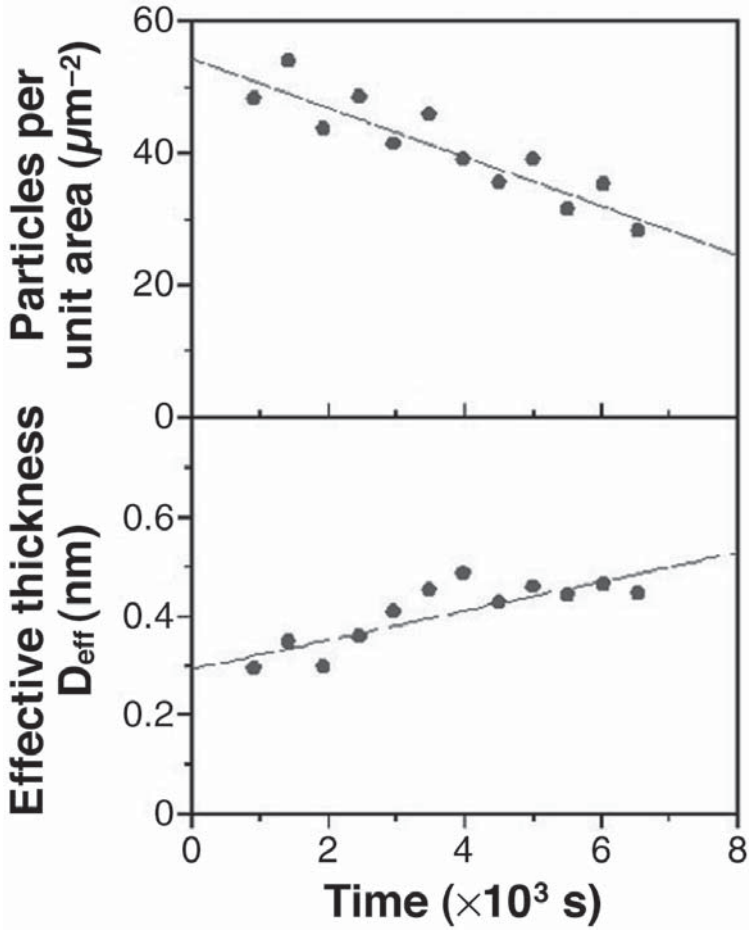

Fig. 7. Quantitative analysis of the aggregation of Aβ(42) on mica can be accomplished by studying the number of particles present in an area as a function of time. Comparison to some physical parameter (effective thickness in this instance) as a function of time can aid in determining quantitatively the aggregation of Aβ. In the above plots, it is shown that the number of individual aggregates of Aβ decreases as the effective thickness of the aggregates (corresponding to total volume) increases. This indicates that aggregates on the mica surface merge to form larger aggregates as a function of time *(22)*.

4. Notes

1. The choice of surface for AFM studies of Aβ is important in gaining insight into the role of surface interaction in the pathway of amyloid formation. Intra- and extracellular surfaces in the brain may play a role in the fibrilization of Aβ. Different surfaces can model different aspects of surfaces found in vivo. Mica is a

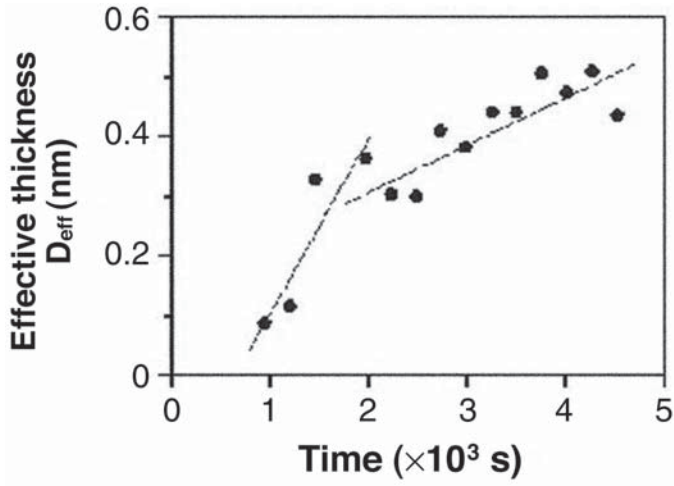

Fig. 8. Quantitative analysis of Aβ aggregation on graphite is accomplished by plotting effective diameter as a function of time for an *in situ* AFM experiment. The plot shows the appearance of an incubation time as well as two separate regimes of growth ***(22)***.

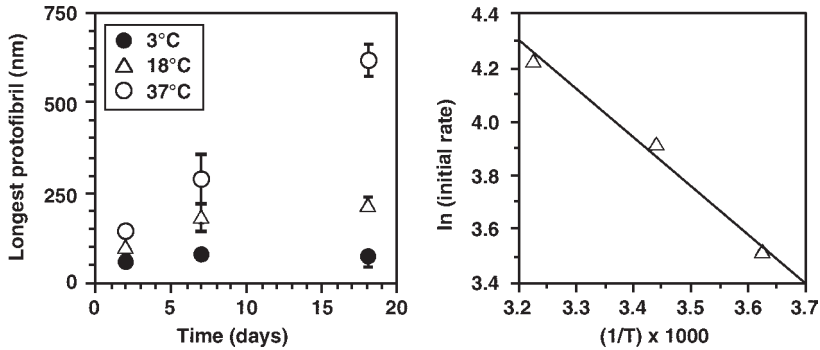

Fig. 9. The temperature dependence of protofibril growth is studied by tracking the longest protofibril as a function of time at various temperatures (left) using *ex situ* AFM. An arrhenius plot can be constructed from data of the longest protofibril. The plot on the right shows an Arrhenius plot constructed form data taken at two days for Aβ samples incubated at different temperatures. Reprinted with permission from **ref. *21***. Copyright 1999 American Chemical Society.

hydrophilic surface and can be used to model the outside of cell surfaces that are primarily composed of the hydrophilic head groups of phospholipids. Graphite, which is hydrophobic, can be used to model the interior of the lipid bilayers that

make up cell membranes. Different characteristics of aggregation have already been observed *in situ* using AFM for these surfaces **(Figs. 4–5)**. An important step towards more physiologically relevant surfaces has been recently made through the use of supported lipid bilayers ***(14)***. Substrates can provide insights into the potentially disruptive interactions of Aβ with cell membranes ***(14)***.

2. Aβ(42) has been shown to form fibrils at a higher rate than Aβ(40) ***(7,33)***. The difference between fibril formation by these two fragments could provide insights into an overall mechanism of the process. The different rates exhibited by the two different Aβ fragments can be taken advantage of in experimental design. For instance, the faster initial rate of Aβ(42) to form fibrils decreases the amount of time needed to observe the transformation of Aβ populations containing mostly protofibrils to a population containing mature fibrils. Conversely, Aβ(40), with its slower initial elongation rate, may be valuable in studying the initial formation of protofibrils and other Aβ oligomers that may be important in the amyloid pathway.
3. *Ex situ* AFM studies support the formation of protofibrils as an intermediate to the formation of mature amyloid fibrils, as protofibrils (3 nm by 20–70 nm) were observed and eventually disappeared as mature fibrils were formed ***(29)***. Subsequent *ex situ* AFM experiments showed that the formation of amyloid fibrils could be seeded by preformed fibrils, indicating the importance of nucleation ***(28)***. Another *ex situ* AFM study has shown that the elongation process of fibrilization is first order ***(21)***, and a different *ex situ* AFM experiment revealed protofibrils that were composed of individual aggregates of Aβ ***(23)***.
4. In situ AFM studies provide the unique opportunity to study Aβ fibrilization under physiological conditions at different stages of fibrillogenesis. This technique is useful for imaging initial aggregates of Aβ, the formation of protofibrils, and the maturation of fibrils. It has been shown that under physiological conditions, in contact with hydrophilic surfaces, Aβ will form 5–6 nm tall particulate aggregates that eventually form protofibrils **(Fig. 4; *22*)**. On hydrophobic surfaces, Aβ forms elongated approx 1 nm tall and approx 19 nm wide ribbons **(Fig. 5; *22*)**. *In situ* AFM studies have also been used to show the growth of protofibrils into mature fibrils over time **(Fig. 6; *22*,*26*)**.
5. Due to viscous damping when imaging in fluids, the mechanical quality factor, Q, of the cantilever is significantly reduced, resulting in larger imaging forces (tapping forces). The forces associated with imaging could disturb fragile aggregates or even inhibit their formation. Furthermore, tapping forces could be especially important in the studies of the interaction of Aβ with other molecules, such as potential drugs, since they could perturb or disrupt the interaction. In order to limit the invasiveness of the probe used to image Aβ and its interactions with other molecules *in situ*, the force used needs to be minimized. It has been demonstrated recently that tapping forces can be significantly reduced through the use of active resonance Q control ***(34–37)***. The lower force makes it possible to study weak interactions that are otherwise disrupted by the large forces normally associated with *in situ* imaging. Active Q control instrumentation is now commer-

cially available from different vendors ***(38,39)***. Lowering the tapping force could also open the way to the use of sharper tips (such as carbon nanotubes), by reducing the pressure exerted by the sharper tips on the samples, and the possibility of damage to the tips themselves.

6. Another important consideration when using *in situ* tapping mode AFM is the mode of excitation of the cantilever. There are currently two commonly used methods, acoustic excitation ***(18,19)*** and magnetic excitation ***(40,41)***. Acoustic excitation uses the sound waves produced by vertical oscillation of the piezoelectric scanner ***(18,19)***. In magnetic excitation, a magnetically coated cantilever is oscillated by passing an alternating current through the solenoid located in the vicinity of the cantilever ***(40,41)***. The advantage of this mode is that it does not rely on oscillation of the liquid, which could be potentially disturbing to the sample. Acoustic excitation is more economical since it does not require expensive magnetically coated tips.

Acknowledgments

Financial support from NIH (P50-AG05681) and from Carnegie Mellon University (start-up grant to T.K.) is gratefully acknowledged.

References

1. Dickson, D. (1997) The pathogenesis of senile plaques. *J. Neuropathol. Exp. Neurol.* **56,** 321–339.
2. Selkoe, D., Abraham, C., Podlisny, M., and Duffy, L. (1986) Isolation of low-molecular-weight proteins from amyloid plaque fibers in Alzheimer's disease. *J. Neurochem.* **146,** 1820–1834.
3. Zhu, Y. J., Lin, H., and Lal, R. (2000) Fresh and nonfibrillar amyloid β protein (1– 40) induces rapid cellular degeneration in aged human fibroblasts: evidence for AβP-channel-mediated cellular toxicity. *FASEB J.* **14,** 1244–1254.
4. Goedert, M., Trojanowski, J., and Lee, V.-Y. (1996) The neurofibrillary pathology of Alzheimer's disease, in *The Molecular and Genetic Basis of Neurological Disease, 2nd ed.* (Rosenberg, R., Prusiner, S., DiMauro, S., and Barchi, R., eds.) Butterworth-Heinemann, Boston, MA, pp. 613–627.
5. Masters, C., Simms, G., Weinman, N., Multhaup, G., McDonald, B., and Beyreuther, K. (1985) Amyloid plaque core protein in Alzheimer disease and Down syndrome. *Proc. Natl. Acad. Sci. USA* **82,** 4245–4249.
6. Lansbury, P. T., Jr. (1996) A reductionist view of Alzheimer's disease. *Acc. Chem. Res.* **29,** 317–321.
7. Jarrett, J. T., Berger, E. P., and Lansbury, P. T. (1993) The carboxy terminus of β amyloid protein is critical for the seeding of amyloid formation: implications for the pathogenesis of Alzheimer's disease. *Biochemistry* **32,** 4693–4697.
8. Roher, A., Wolfe, D., Palutke, M., and KuKuruga, D. (1986) Purification, ultrastructure, and chemical analysis of Alzheimer disease amyloid plaque core protein. *Proc. Natl. Acad. Sci. U.S.A.* **83,** 2662–2666.

9. Esch, F., Keim, P. S., Beattie, E. C., Blacher, R. W., and Culwell, A. R. (1990) Cleavage of amyloid β peptide during constitutive processing of its precursor. *Science* **248,** 1122–1128.
10. Selkoe, D. J. (1993) Physiological production of the β-amyloid protein and the mechanism of Alzheimer's disease. *Trends Neurosci.* **16,** 403–409.
11. Kelly, J. W. (1998) The alternative conformations of amyloidogenic proteins and their multi-step assembly pathways. *Curr. Opin. Struct. Biol.* **8,** 101–106.
12. Smith, M. A. (1998) Alzheimer disease. *Int. Rev. Neurobiol.* **42,** 1–54.
13. Naiki, H. and Nakakuki, K. (1996) First-order kinetic model of Alzheimer's β-amyloid fibril extension in vitro. *Lab. Invest.* **74,** 374–383.
14. Yip, C. M. and McLaurin, J. (2001) Amyloid-β peptide assembly: a critical step in fibrillogenesis and membrane disruption. *Biophys. J.* **80,** 1359–1371.
15. Lomakin, A., Chung, D. S., Benedek, G. B., Kirschner, D. A., and Teplow, D. B. (1996) On the nucleation and growth of amyloid β-protein fibrils: detection of nuclei and quantitation of rate constants. *Natl. Acad. Sci. USA* **93,** 1125–1129.
16. Esler, W. P., Stimson, E. R., Ghilardi, J. R., et al. (1996) In vitro growth of Alzheimer's disease β-amyloid plaques displays first-order kinetics. *Biochemistry* **35,** 749–757.
17. Harper, J. D. and Lansbury, J., P.T. (1997) Models of amyloid seeding in Alzheimer's disease and scrapie: mechanistic truths and physiological consequences of the time-dependent solubility of amyloid proteins. *Annu. Rev. Biochem.* **66,** 385–407.
18. Putman, C. A. J., Van Der Werf, K. O., De Grooth, B. G., Van Hulst, N. F., and Greve, J. (1994) Tapping mode atomic force microscopy in liquid. *Appl. Phys. Lett.* **64,** 2454–2456.
19. Hansma, P. K., Cleveland, J. P., Radmacher, M., et al. (1994) Tapping mode atomic force microscopy in liquids. *Appl. Phys. Lett.* **64,** 1738–1740.
20. Goldsbury, C., Kistler, J., Aebi, U., Arvinte, T., and Cooper, G. J. S. (1999) Watching amyloid fibrils grow by time-lapse atomic force microscopy. *J. Mol. Biol.* **285,** 33–39.
21. Harper, J. D., Wong, S. S., Lieber, C. M., and Lansbury, P. T. (1999) Assembly of aβ amyloid protofibrils: an in vitro model for a possible early event in Alzheimer's disease. *Biochemistry* **38,** 8972–8980.
22. Kowalewski, T. and Holtzman, D. M. (1999) *In situ* atomic force microscopy study of Alzheimer's β-amyloid peptide on different substrates: new insights into mechanism of β-sheet formation. *Proc. Natl. Acad. Sci. USA* **96,** 3688–3693.
23. Blackley, H. K. L., Patel, N., Davies, M. C., et al. (1999) Morphological development of β(1-40) amyloid fibrils. *Exp. Neurology* **158,** 437–443.
24. Lin, H., Bhatia, R., and Lal, R. (2001) Amyloid β protein forms ion channels: implications for Alzheimer's disease pathophysiology. *FASEB J.* **15,** 2433–2444.
25. Yang, D. S., Yip, C. M., Jackson Huangi, T. H., Chakrabarttyi, A., and Fraser, P. E. (1999) Manipulating the amyloid-β aggregation pathway with chemical chaperones. *J. Bio. Chem.* **274,** 32,970–32,974.
26. Blackley, H. K. L., Sanders, G. H. W., Davies, M. C., Roberts, C. J., Tendler, S. J. B., and Wilkinson, M. J. (2000) *In-situ* atomic force microscopy study of β-amyloid fibrillization. *J. Mol. Biol.* **298,** 833–840.

27. Bhatia, R., Lin, H., and Lal, R. (2000) Fresh and globular amyloid β protein (1–42) induces rapid cellular degeneration: evidence for AβP channel-mediated cellular toxicity. *FASEB J.* **14,** 1233–1243.
28. Harper, J. D., Wong, S. S., Lieber, C. M., and Lansbury, P. T. (1997) Atomic force microscopy imaging of seeded fibril formation and fibril branching by the Alzheimer's disease amyloid-β protein. *Chem. Biol.* **4,** 951–959.
29. Harper, J. D., Wong, S. S., Lieber, C. M., and Lansbury, P. T. (1997) Observation of metastable Aβ amyloid protofibrils by atomic force microscopy. *Chem. Biol.* **4,** 119–125.
30. Jackson Huang, T. H., Yang, D. S., Plaskos, N. P., et al. (2000) Structural studies of soluble oligomers of the Alzheimer β-amyloid Peptide. *J. Mol. Biol.* **297,** 73–87.
31. Xu, S. and Ansdorf, M. F. (1994) Calibration of scanning (atomic) force microscope with gold particles. *J. Microscopy* **173(Pt. 3),** 199–210.
32. Villarrubia, J. S. (1997) Algorithms for scanned probe microscope image simulation, surface reconstruction, and tip estimation. *Natl. Inst. Stand. Technol.* **102,** 425.
33. Cai, X. D., Golde, T. E., and Younkin, S. G. (1993) Release of excess amyloid β protein from a mutant amyloid β protein precursor. *Science* **259,** 514–516.
34. Tamayo, J., Humphris, A., and Miles, M. (2001) High-Q dynamic force microscopy in liquid and its application to living cells. *Biophys. J.* **81,** 526–537.
35. Humphris, A., Tamayo, J., and Miles, M. (2000) Active quality factor control in liquids for force spectroscopy. *Langmuir* **16,** 7891–7894.
36. Tamayo, J., Humphris, A., and Miles, M. (2000) Piconewton regime dynamic force microscopy in liquid. *Appl. Phys. Lett.* **77,** 582–584.
37. Humphris, A., Round, A., and Miles, M. (2001) Enhanced imaging of DNA via active quality factor control. *Surface Science* **491,** 468–472.
38. Infinitesima Limited. Bristol, UK. http://www.infinitesima.com/.
39. Asylum Research. Santa Barbara, CA. http://www.asylumresearch.com/.
40. Lantz, M. A., O'Shea, S. J., and Welland, M. E. (1994) Force microscopy imaging in liquids using ac techniques. *Appl. Phys. Lett.* **65,** 409–411.
41. Han, W., Lindsay, S. M., and Jing, T. (1996) A magnetically driven oscillating probe microscope for operation in liquids. *Appl. Phys. Lett.* **69,** 4111–4113.

27

How to Build Up Biosensors With the Cantilever of the Atomic Force Microscope

Ricardo de Souza Pereira

1. Introduction

With the advent of the atomic force microscopy (AFM), the study of biological samples has become more realistic because, in most cases, samples are not covered or fixed and this makes it possible to observe them while alive ***(1,2)***. This advantage of the AFM prompted a new invention: nanobiosensors using the cantilever (probe) of the AFM, which made possible the observation of specific molecules (including medications) as they enter or exit living cells ***(3,4)***.

The nanobiosensor is the smallest biosensor in the world and measures about 100-µm long (about the width of a hair). Beyond sensing the area of interest, this biosensor also makes possible a real-time image of exactly what is occuring on the cell ***(3,4)***.

1.1. Use of the AFM as a Heat Detector

An apparatus for measuring variation of temperature is the thermooptical detector. A reaction cell, whose bottom is a thin gold film (with immobilized enzyme), is immersed into a CCl_4 phase where a probe beam is passed. The heat (from reaction between the enzyme and its substrate) of the water phase is transferred to the gold film and the CCl_4 phase, and thus a temperature gradient is generated in the CCl_4 phase. This temperature gradient induces deflection of the probe beam and the result is registered as a graph ***(3–9)***.

Because AFM has almost the same parts as the thermooptical detector (laser beam, lens, and photodiode; **refs. *3*** and ***4***), if an enzyme was immobilized on the cantilever, one can hope that the temperature gradient generated by reaction heat (between the enzyme and its substrate) could induce a deflection of the cantilever, transforming the AFM into an apparatus that could reveal the presence of specific molecules.

From: *Methods in Molecular Biology, vol. 242: Atomic Force Microscopy: Biomedical Methods and Applications*
Edited by: P. C. Braga and D. Ricci © Humana Press Inc., Totowa, NJ

As mentioned before, an AFM equipped with an enzyme-coated cantilever (nanobiosensor) can visualize living cells, so it should be possible to detect specific molecules being absorbed by living cells and to see this happening. These assumptions were shown to be valid by experiments made with the first nanobiosensor, which had been made to detect the absorption of glucose molecules by *Saccharomyces cerevisiae* cells ***(3)***.

The deflection of the cantilever is explained by the physical phenomenon occurring when two different metal blades (each with a different coefficient of dilation) are bonded together. This is called a bimetallic system, and the presence of heat makes the blades bend. Another illustration of the phenomenon is the working of the taillights of an automobile: a bimetallic blade is heated until it bends and produces a braking light ***(4)***. The cantilever of AFM is not a bimetallic blade but can work as one because it consists of two different materials (a metal and semimetal) with different dilation coefficients: gold and silicon. If a biochemical (or chemical) reaction takes place near this so-called bimetallic blade, it is possible to produce a deflection in the cantilever. This latter produces an enormous deviation in the direction of the laser beam, which is recorded in real time by the computer (via a photodiode; **ref. *4***).

Beyond observing the absorption of glucose molecules by living cells, it was possible to visualize the inverted phenomenon: the release of specific molecules from living cells immobilized on the cantilever surface, in the first instance of this technique, the enzyme alcohol dehydrogenase type II, which transforms ethyl alcohol into glutaraldehyde and releases heat in the process ***(4)***.

Other biosensors were made using the enzymes superoxide dismutase and catalase ***(4)***, proving that this methodology is valid for all enzymes or molecules that release heat from their reactions.

1.2. Identifying Defective Genes

Tiny variations in the genetic code are what make us unique. Changes in one chemical unit in a gene's sequence, called single nucleotide polymorphisms, can influence an individual's risk for disease. Comparing variations will help identify defective genes and may lead to better diagnosis and treatments ***(4)***.

If a cantilever is coated with DNA strands, it is possible to detect genetic variations or single nucleotide polymorphisms when an individual's DNA is tested against them ***(4)***.

In a recent report, scientists from IBM demonstrated that when DNA strands are immobilized on a cantilever surface, it is possible to identify the complementary strand of the DNA in solution ***(10)***. When the immobilized and complementary strands find a match, the heat evolved from the process makes the cantilever bend. This nanomechanical property transforms the cantilever into a DNA chip, making it very useful in identifying mutations ***(10)***.

1.3. Clinical Analysis

The immobilization of para-nitrophenylphosphate on the cantilever can be used to identify cancer in the bones, prostate gland, and ovary. Para-nitrophenylphosphate is the substrate of the acid phosphatase enzyme and it is currently used in clinical analysis ***(11–14)***. The enzyme is released by tumor cells into the extracellular medium.

2. Materials

Enzymes (such as glucose oxidase, catalase, superoxide dismutase, or alcohol dehydrogenase type II) are obtained from Sigma Chemical Co. All reagents are of analytical grade. Water is double distilled and deionized.

The industrial strain of *S. cerevisiae* is commercial. The stock suspensions of living cells are prepared by adding 1.0 g of dry baker's yeast to 10 mL of water (double distilled and deionized) while stirring at room temperature. A drop of the suspension is placed on the surface of glass coverslips and allowed to dry for 15–20 min at room temperature to remove the excess of water. Therefore, the experiments are performed under a thin layer of water.

For AFM, a BioScope (Thermomicroscopes) or a BioProbe (NanoScope IIIa AFM, Digital Instruments) operating in contact mode is used in the experiments along with Si_3N_4 Nanotips (Digital Instruments) with 0.06-N/m spring constants. In some cases, the images are low-pass filtered to remove stray scan lines. All images are collected on the AFM using a scan speed of 2.5 Hz, and all imaging is performed in air at room temperature as described before ***(4)***.

3. Method

1. Stock solution of enzyme: 100 mg of enzyme is mixed in 1 mL doubly distilled and deionized water. Five microliters of this enzyme solution is spread on a 2-cm^2 area on a cover slips.
2. Building the nanobiosensor: a brand new cantilever is put in the cantilever holder of the AFM. An engage is given on the cover slips that contains the spread solution of the enzyme. After 30 s, the cantilever is taken off the cover slip surface and dried for 3 h at room temperature (*see* **Note 1**). The cantilever (with enzyme) is kept in the AFM during drying period, after which, this nanobiosensor is put in a vacuum desiccator for conservation under 5°C. To test the effectiveness of this methodology, an enzyme substrate solution is directly dropped on the nanobiosensor while it is scanning a glass surface; the reaction catalyzed by the immobilized enzyme is monitored by the deflections of the cantilever on the AFM monitor.
3. The nanobiosensors should be kept in a vacuum and under refrigeration. Under these conditions they can be used up to 2 or 3 mo after their preparation, and experiments with them are very reliable and reproducible ***(3,4)***.

4. Notes

1. If the enzyme solution invades the gold mirror area, the biosensor does not work.

References

1. Pereira, R. S., Parizotto, N. A., and Baranauskas, V. (1996) Observation of baker's yeast used in biotransformations by atomic force microscopy. *Appl. Biochem. Biotechnol.* **59,** 135–144.
2. Pereira, R. S., Durán, N., and Teschke, O. (1998) Observation of structures on *Saccharomyces cerevisiae* cell wall by atomic force microscope. *Probe Microsc.* **1,** 277–282.
3. Pereira, R. S. (2000) Detection of the absorption of glucose molecules by living cells using atomic force microscopy. *FEBS Lett.* **475,** 43–46.
4. Pereira, R. S. (2001) Atomic force microscopy: a novel pharmacological tool. *Biochem. Pharmacol.* **62,** 975–983.
5. Wu, X., Shindoh, H., and Hobo, T. (1994) A novel thermooptical detection method for enzyme reaction based on the optical beam deflection induced by reaction heat. *Microchem. J.* **49,** 213–219.
6. Wu, X., Tatsuya, M., Uchiyama, K., and Hobo, T. (1997) Noncontact and noninvasive monitoring of gas diffusion from aqueous solution to aprotic solvent using the optical beam deflection method. *J. Phys. Chem.* **101,** 1520–1523.
7. Wu, X., Uchiyama, K., and Hobo, T. (1996) Real time one dimensional imaging for reaction heat-induced optical beam deflection. *Anal. Lett.* **29,** 1993–1999.
8. Wu, X., Shindoh, H., and Hobo, T. (1995) Thermooptical flow-injection determination for hydrogen peroxide based on an enzymic reaction heat-induced optical beam deflection. *Anal. Chim. Acta* **299,** 333–336.
9. Wu, X. and Hobo, T. (1995) Monitoring and analyzing of a chemical reaction process using reaction heat-induced optical beam deflection. *Anal. Chim. Acta* **316,** 111–115.
10. Fritz, J., Baller, M. K., Lang, H. P., et al. (2000) Translating biomolecular recognition into nanomechanics. *Science* **288,** 316–318.
11. Ben-Arie, A., Hagay, Z., Ben-Hurt, H., Open, M., and Dgani, R. (1999) Elevated serum alkaline phosphatase may enable early diagnosis of ovarian cancer. *Eur. J. Obstet. Gyn. Reprod. Biol.* **86,** 69–71.
12. Magnusson, P., Larsson, L., Englund, G., Larsson, B., Strang, P., and Selin-Sjogren, L. (1998) Differences of bone alkaline phosphatase isoforms in metastatic bone disease and discrepant effects of clodronate on different skeletal sites indicated by the location of pain. *Clin. Chem.* **44,** 1621–1628.
13. Magnusson, P., Larsson, L., Magnusson, M., Davie, M. W. J., and Sharp, C. A. (1999) Isoforms of bone alkaline phosphatase: Characterization and origin in human trabecular and cortical bone. *J. Bone Miner. Res.* **14,** 1926–1933.
14. Shiele, F., Artur, Y., Floch, A. Y., and Siest, G. (1998) Total, tartrate-resistant, and tartrate-inhibited acid phosphatases in serum: Biological variations and reference limits. *Clin. Chem.* **34,** 685–690.

28

Measurement of Single Molecular Interactions by Dynamic Force Microscopy

Martin Hegner, Wilfried Grange, and Patricia Bertoncini

1. Introduction

Unbinding forces of weak, noncovalent bonds have been measured by scanning force microscopy *(1)* or biomembrane force probes *(2)*. Initially, these scanning force microscopy measurements focused on feasibility studies to measure single biomolecular interactions *(3–5)*. Recently, however, a few groups showed that these single molecule experiments give a direct link to bulk experiments where thermodynamic data are experimentally acquired *(6–9)*. In contrast with bulk experiments where averaged properties are measured, a single molecular approach gives access to properties that are hidden in the ensemble. These experiments can give insight into the geometry of the energy landscape of a biomolecular bond *(7,9–11)*. Some experiments even showed that intermediate states during unbinding (unfolding) exist which only can be detected by single molecule experiments *(12–14)*.

To understand the relation between force and energy landscape, one can consider an atomic force microscope (AFM) experiment in which the spring used to measure the forces acting on the molecular complex is weak compared with the molecular bond stiffness. The ligand is immobilized on a sharp tip attached to a microfabricated cantilever and the receptor is immobilized on a surface. When approaching the surface to the tip, a specific bond may form between ligand and receptor, e.g., complementary DNA strands or antibody–antigen. The bond is then loaded with an increasing force when retracting the surface from the tip (dynamic force spectroscopy; **Fig. 1A**). At a certain force, ligand and receptor unbind, giving rise to an abrupt jump of the tip away from the surface (**Fig. 1B**). It has been demonstrated *(6)* that the unbinding is caused by thermal fluctuations rather than by a mechanical instability. If the thermal lifetime of the bond is short compared with the time it takes to build up an

From: *Methods in Molecular Biology, vol. 242: Atomic Force Microscopy: Biomedical Methods and Applications*
Edited by: P. C. Braga and D. Ricci © Humana Press Inc., Totowa, NJ

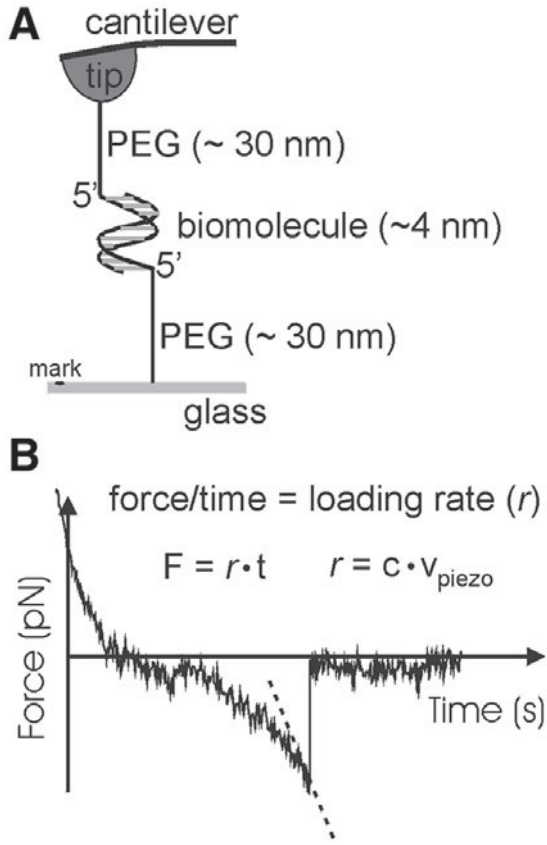

Fig. 1. **(A)** Single molecular interactions scheme measured by dynamic force microscopy. **(B)** Single biomolecule pulling experiment. The signal recorded is the force [pN] vs the time [*s*] (*c* = cantilever spring constant, v_{piezo} = pulling speed of the z piezo element). Keep in mind that the pulling of a biomolecule complex has to be performed at various pulling speeds in order to gather thermodynamic data. In the left part of the curve the cantilever is in its repulsive regime (above the time axis). As soon as the cantilever passes the equilibrium position and the biomolecular interaction has occurred, the cantilever is being deflected downwards. If a flexible cross-linker is fixing the biomolecule to the surface the linker is stretched as visible in the figure. At the point of rupture of the complex there is a sudden drop in force and the cantilever is ready for an additional pulling cycle. To extract the loading rate on the complex the derivative of the very last part of the force curve is fitted (dotted line).

observable force during a slow loading process, no unbinding event is observed. With faster loading, finite unbinding forces are observed. Therefore, unbinding forces depend on the rate of loading and on the details of the functional

relationship between bond lifetime and an applied force. The theory for these experiments has been described in great detail in the articles from Strunz et al. ***(15)***, Evans ***(10)***, and Merkel ***(11)***.

The technique has been applied to model systems such as biotin/(strept-)avidin ***(12,13)***, antibody–antigen ***(8)***, or ssDNA–ssDNA ***(9)*** where thermodynamic data existed. But now because the link from single molecule experiments to thermodynamic ensemble experiments is clearly made the technique is applicable to other systems. The applicability of single molecule experiments for gathering thermodynamic properties now permits measurement in biomolecules in which the quantity of expressed molecules is barely suitable to allow a thermodynamic approach. In these systems (for example, the binding of a drug to specific receptors) the off rate (measurable by the single molecule techniques) of the ligand–receptor plays a key role for further studies or development.

In these days when more and more precious genetically engineered drugs are being developed and used, the storage of theses compounds is crucial. If the compound is interacting with the surface of the storage container and no carrier substances like human serum albumin are allowed to be added, then the concentration of the substance in the containment is difficult to maintain during the shelf life of a drug. In a first study it was shown that force microscopy gives a suitable way to gather data from drug/storage container interactions and therefore to allow optimization of the storage container surface and buffer conditions in cases where storage problems occur ***(16)***.

2. Materials

2.1. Conversion of the Reactive Groups on the Surfaces

1. Ultrasonic bath.
2. Strong ultraviolet (UV) light source (UV-Clean, Boekel Scientific, Feasterville, PA).
3. Argon.
4. Glass slides, thickness approx 0.4 mm, cut into 0.5×0.5 mm pieces.
5. Microcantilever, spring constant < 0.03 N/m.
6. Dry toluene, crown cap, molecular sieve.
7. Amino-propyl-triethoxy-silane (APTES).
8. Mercapto-propyl-triethoxy-silane (MPTES).

2.2. Activation of the Reactive Groups by Heterobifunctional Cross-Linkers

1. Sulfosuccinimidyl 4-[*N*-maleimidomethyl]-cyclohexane-1-carboxylate (SMCC) (Pierce, Rockford, IL).
2. Poly (ethylene glycol)-α-maleimide-ω-*N*-hydroxy-succinimide-ester (MAL-PEG-NHS), molecular weight 3400, length approx 30 nm (Shearwater Co., Huntsville; AL).

3. Dimethyl sulfoxide (DMSO).
4. Buffer, e.g., *N*-hydroxyethylpiperazine-*N*'-2-ethanesulfonate (HEPES), 2-(*N*-morpholino)ethanesulfonic acid (MES; free of primary amines) adjusted to pH 7.0–7.5, phosphate-buffered saline (PBS; pH 7.3; Life Technologies, Rockville, MD).

2.3. Coupling of the Biomolecules to the Activated Surface

1. Biomolecules (i.e., thiol-modified ssDNA, water-soluble proteins exposing free cysteins).
2. Ethyl-acetate.
3. Peltier element (Melcor, Trenton, NJ).
4. Thermocouple (Thermocoax, Suresnes, France).
5. Glove box (can be used but not mandatory).

3. Methods

The methods described below outline (1) the conversion of the surface active groups to allow activation by heterobifunctional cross-linkers, (2) the activation of the newly generated groups by heterobifunctional cross-linkers, (3) the coupling of the selected biomolecules to the surface, (4) the set-up of the instrument to allow dynamic force spectroscopy, and (5) the extraction of the specific interaction parameters from the acquired data.

3.1. Conversion of the Reactive Groups on the Surfaces

The first steps of this procedure involve the cleaning of the individual surfaces (i.e., the flat glass surface and the microcantilever).

1. Mark two glass slides and clean the slides in ethanol for 10–20 min in an ultrasonic bath.
2. Dry under a stream of argon.
3. Replace ethanol in the beaker in the ultrasonic bath
4. Repeat this treatment twice.

From now on, the glass slide surfaces, and the AFM-tips (e.g., Si_3Ni_4-Microcantilever, Park Scientific, Sunnyvale, CA), are treated in parallel (*see* **Note 1**).

5. Treat the surfaces with a strong UV light source for 60 min. Place the mark on the flat surfaces towards the UV light source.
6. Mixing of silanization solution: Insert one short syringe needle with an attached balloon containing argon through the crown cap (never remove the crown cap!). Take a syringe with a syringe needle long enough to reach the silanization solution (APTES). Withdraw enough solution from stock to enable a 2% dilution in *dry* toluene. Remove dry toluene comparable with two syringes through the crown cap.
7. Put the glass slides with the mark on the top and the AFM tips in a glass container that can be sealed. Immediately silanize the surfaces in a 2% solution of APTES in dry toluene for 2 h or overnight.
8. Rinse extensively with toluene and dry under a stream of argon (*see* **Note 2**).

3.2. Activation of the Newly Generated Groups by Heterobifunctional Cross-Linkers

Immerse the surface in a 1-m*M* solution of MAL-PEG-NHS in DMSO for 2–3 h. The surfaces are again rinsed with DMSO and then with PBS buffer, pH 7.3. (*See* **Notes 3** and **4**.)

3.3. Coupling of the Selected Biomolecules to the Surface

1. The oligonucleotides with a 5π-SH modification were synthesized by Microsynth (Balgach, Switzerland) and were stored in a PBS buffer at pH 7.3 containing 10 m*M* dithiothreitol (DTT) at 4°C until use. Immediately before use, the oligonucleotides are diluted to a final concentration of 25 m*M* with PBS buffer.
2. Extract DTT from an aliquot of typically 200 µL by washing three times with 1 mL of ethyl-acetate!
3. A 50-µL drop of the oligonucleotide solution is then incubated on the poly (ethylene glycol)-ω-maleimide-modified surfaces. Put the solution of one ssDNA oligonucleotide on top of flat glass slide (mark visible on the topside) and the complementary ssDNA oligonucleotide on the AFM-tips, which are on top of a piece of Teflon.
4. To avoid drying create a humidity box. Put some water bubbles on the wall of the box and close the box with a parafilm. Incubate overnight at room temperature in a humid chamber.
5. Rinse with PBS buffer, and then the tips and surfaces are ready for use in the force experiments (*see* **Notes 5–9**).

3.4. Set-Up of the Instrument to Allow Dynamic Force Spectroscopy

Dynamic force spectroscopy measurements were performed using a commercial AFM instrument (Nanoscope IIIa, Digital Instruments, Santa Barbara, CA). The instrument has been expanded using the breakout box available from Digital Instruments. This allows an alternative control of the AFM by an external digital input–output board. We use the multifunctional DAQ board (PCI-MIO-16XE-10) from National Instruments (Austin, TX) to have additional functionality to control the approach-retract function of the force microscope. The only functions of the Nanoscope used are the initial approach using the integrated stepper motor and the feedback for the first approach towards the sample. Additional features, which are controlled through the LabVIEW software package (National Instruments, Austin, TX), are:

Changing of the retract speed after each individual interaction. The speed is increased or decreased in exponential steps starting with speeds <10 pN/s and then increased up to approx 10000 pN/s. Normally we choose six different speeds within the speed-range of four orders of magnitude.

The number of individual pulling cycles at a certain site can be defined before the location to another site on the sample is changed with nm precision.

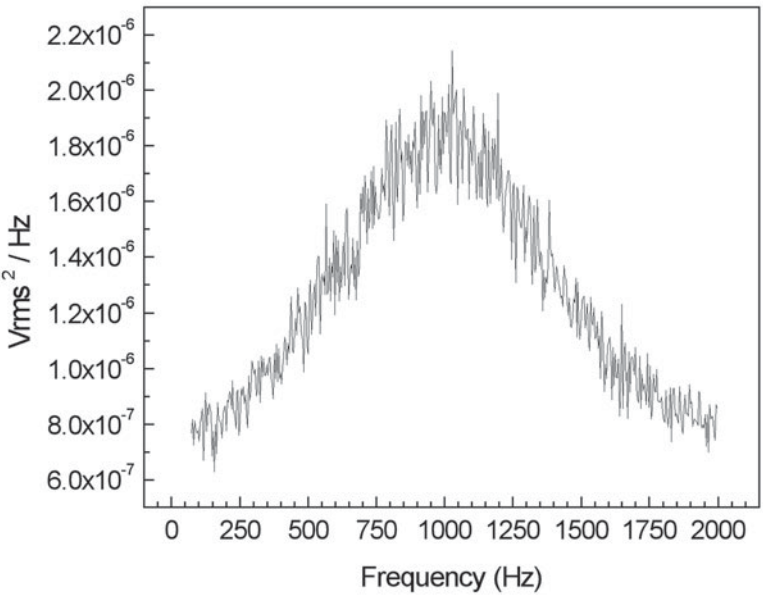

Fig. 2. The sampling rate is 4000 Hz, the frame size 1024 (step-size 3.90625 Hz), the number of points 512, spectrum shown is an average of 200 spectrums. The area under the curve is 0.00244 V_{rms}^2. With a sensitivity value of 0.0563V/nm, the spring constant is 5 pN/nm ± 10 % (compared with 10 pN/nm nominal value given by the company). The fitting and the integration of the volume can be done with commercial software (e.g., LABVIEW or Origin, OriginLab Corporation, Northampton, MA).

AFM cantilevers used for this experiment had spring constants <30 pN/nm. Each cantilever was *in situ* calibrated according to the method of Hutter ***(17)***. In short a power spectrum of the thermal vibrations of the cantilever is recorded using the LabVIEW software package (*see* **Fig. 2**). The spectrum shows a resonance peak at the natural resonance frequency. The integrated volume under the peak is directly correlated to the spring constant of the cantilever. It is important to retract the cantilever far enough from the surface (>1 μm) to avoid hydrodynamic damping. The temperature was controlled using a home-built fluid cell in which the buffer solution that immersed both the probe surface and the AFM cantilever was in contact with a Peltier element (Melcor, Trenton, NJ), driven with a constant current source (*see* **Fig. 3**). The temperature of the buffer was monitored with a thermocouple (Thermocoax, Suresnes, France). The thermocouple is calibrated with a digital thermometer and temperature measurements at different points of the cell showed deviations <2°C.

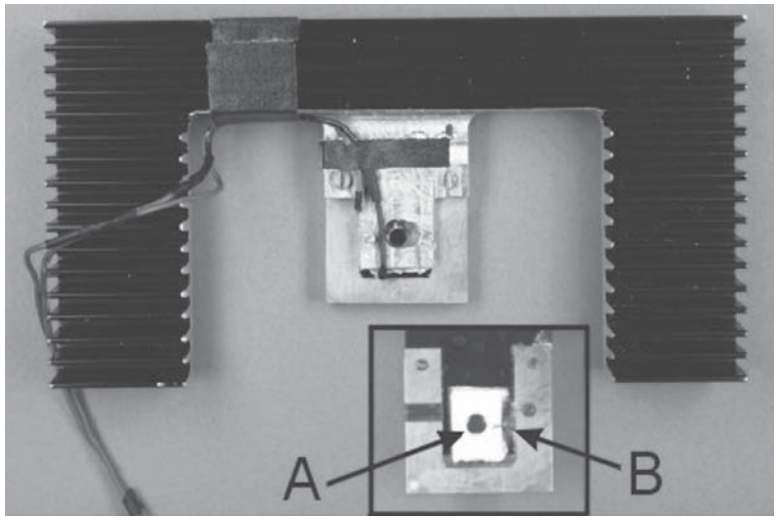

Fig. 3. Home-built fluid-cell platform allowing a precise temperature control. Big-picture complete device showing the top view of the cell including the big black heat sink block with lamellas for temperature stabilization. (*Inset*) Bottom view of the center of the fluid cell, which fits into the multimode head of the Nanoscope IIIa head. *Arrow A,* hole in the Peltier element for laser transmission. The hole is covered by a cover glass no. 1 to avoid fluid leaking and maintain angles of incidence of the laser. *Arrow B,* spring-to-clamp cantilever to the bottom of the Peltier element.

3.5. Extraction of the Specific Interaction Parameters from the Acquired Data

Write a small program to toggle through all the automatically collected force curves. The LABVIEW platform provides easy solutions, which can be expanded according to the operator's needs (*see* **Note 10**).

1. Select the force curves that show clear rupture force. Discard force curves that show no interaction or show unexpectedly long rupture distances.
2. Gather enough sample curves to obtain a reasonable number of data points to analyze your experiment. A way to analyze the data statistically is described by Izenman ***(18)***.
3. Expand your force-curve analysis software to allow automatic recognition of the last jump back of the cantilever to the equilibrium position, determination of the slope at this point, the force of unbinding, and the speed of the pulling cycle (*see* **Fig. 1B**).
4. It is important to determine the specificity of the interaction measured. Use the second sample coated with the unspecific biomolecules. Measure the interaction

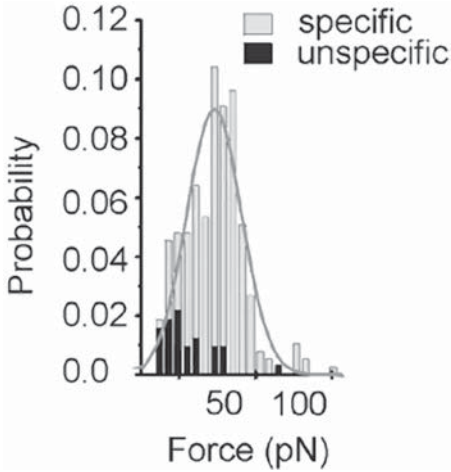

Fig. 4. Specificity check of the unbinding measurements. The force histogram can be fit with a gaussian distribution function to reveal the most-probable unbinding force (F*). Adjust the bin width according to Izenman ***(18)***. Gray bars, specific interaction; black bars, nonspecific interaction.

forces in the same way as with the 'specific' sample. You end up with a histogram comparable to **Fig. 4**.

5. Transfer your data into a diagram having the axes of F* (most probable unbinding force) and the rate of pulling. You should end up with a figure comparable to **Fig. 5**. Once you have collected and analyzed your data following our procedure you should be able to extrapolate the off rate of your system and all the other relevant parameters.

4. Notes

1. Plan to prepare the specific sample and the background sample in the same experiment. For instance we use two glass slides as substrates, one coated with the specifically interacting biomolecule (for example, ssDNA oligonucleotide) and the other with the unspecific molecule (for example, the nonhybridizing ssDNA oligonucleotide).
2. Silanization procedures provide an easy possibility to convert the surface reactive groups of silicon or glass or even silicon nitride tips of the cantilever. Remember that most groups have their own ideal preparation procedure. The activation of surfaces with trifunctional (for example, tri-ethoxy) silans easily

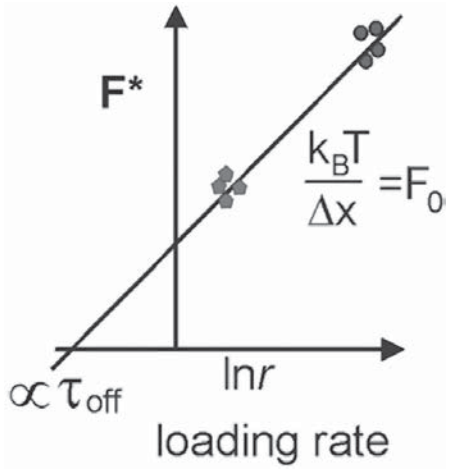

Fig. 5. Loading rate dependence of the unbinding measurements. The slope fit through the data sets provides insight into the energy landscape of the unbinding of the biomolecular interaction. If the precision of the data and the number of various pulling speeds is high enough to fit two slopes within this diagram then a probable intermediate state during unbinding can be detected.

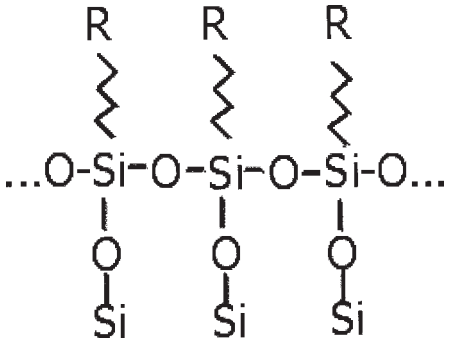

Fig. 6. Ideal surface activation (silanization).

can lead to monolayers on the surface of the sample (*see* **Fig. 6**), but there is a great chance that multilayer and aggregates of polymerized silans are formed (*see* **Fig. 7**). To reduce this possibility monofunctional silans can be used. The

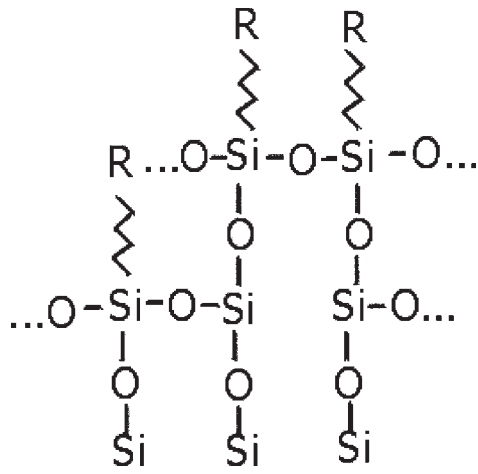

Fig. 7. Reality: partial hydrolysis during deposition, multiplayer formation, and formation of aggregates.

reactivity of these substances is comparable but one should work in an argon environment during the whole silanization procedure (glove box). Curing the surface by heating the sample (150°C) after silanization is possible but not necessary in the case of trifunctional silans.

3. Long flexible linkers are needed when single biomolecule interactions are being probed. When manipulating single globular proteins, tertiary folded RNAs or ssDNA–ssDNA pairs, additional problems must be overcome ***(19,20)***. As a result of their small dimensions (typically 1.5–6 nm) direct tethering to the surfaces is undesired. Furthermore, the nonspecific interactions of the surrounding surfaces would mask the signal of the small individual molecule. These interactions, and possible solvent exclusion within the gap, could lead to denaturation of the molecule or perturbation in the force profiles. A covalent attachment of these biomolecules to surfaces via long linkers minimizes the nonspecific interaction of the surfaces with the biomolecule, and allows probing the single protein molecules. Long linkers of some tens of nanometers from the surface allow space for free exchange of additional ligands or solution in the environment of the molecular interaction being probed. Additionally the use of long linkers allows easy discrimination of single events from multi-events. In cases were two molecular interactions happen a saw-tooth-like pattern in the retract curve is visible. The probability that two bonds break simultaneously is minimized because the length of the flexible cross-linker is comparable to the curving of the cantilever tip. Because the anchoring points are located on a highly curved surface, simultaneous ruptures are very unlikely.
4. In experiments were short linkers are applied the surfaces are immersed in a 1 m*M* solution of sulfo-SMCC in 50 m*M* HEPES buffer (pH 7.0) for 1 h at room temperature. After incubation rinse the surfaces with HEPES buffer only to remove

excess of cross-linkers. Short linkage of the ligand/receptor system on the surface is resulting in considerably more unspecific adhesion events. It is still possible to extract the "real" value of the unbinding force if the very last jump back to equilibrium is being considered ***(3–5)***. Important is the change in pulling speed during the experiment to obtain off rates and not just one interaction force. Owing to the fact that multiple binding events can rupture at the point of rupture a bimodal or higher modal distribution in the force histogram is to be expected

5. It is important to note that the activated cantilever surface has a limited lifetime ***(19,20)*** and therefore the speed of the following steps is crucial. The cantilever is thoroughly rinsed with the buffer used to store the biomolecule. Because the specificity of the cross-linker is changing with the pH and is sensitive towards free amino groups. Buffers like Tris-HCl should be avoided. Buffers of choice are PBS, HEPES, and MES, adjusted to the right pH. The thiol groups of the biomolecules are coupled at a pH ranging from 7.0–7.5 at room temperature.
6. Biomolecules have to be cleaned if stored under protective conditions like those mentioned for thiol-modified oligonucleotide (DTT has been added to prevent oxidation of the thiol to the disulfide). Extraction with organic solvent is an easy way to remove these compounds. By repeating the extraction the amount of DTT is reduced to levels that do not interfere with the covalent coupling to the maleimide group. Oligonucleotides remain in the water phase and DTT is transferred in the organic phase (top phase of the two).
7. In addition, be careful with the buffers in which the biomolecules are being delivered. Unsuitable buffers or protective agents quench the coupling reaction completely. These contaminants are removed using centrifugation membranes available from various companies (e.g., Amicon, Eppendorf, Sartorius). Calculate the dilution factor to be applied during this cleaning to bring the 'contaminant' to a level of approx 1/100 relative to the molecule to be coupled.
8. If instead of thiol groups of the biomolecule (thiol-modification on ssDNA end or free cysteine of protein) amino groups (amino-modification on ssDNA end or free lysine or terminal amino group on protein) have to be coupled to the surface, then instead of APTES, the silanization reagent MPTES can be applied and the protocol follows exactly the same description.
9. The cross-linking group maleimide has its optimal pH range from 6.5–7.5 and succinimide from 7.0–8.5. Some adjustments of pH during the individual coupling steps of the individual groups can improve the overall performance of the coupling reaction ***(19,20)***.
10. To calculate the spring constant of the cantilever and to express the cantilever deflection as a force, the cantilever deflection signal vs the voltage applied to the piezo tube (sensitivity) has to be measured. It is equal to the slope of the force curve while the cantilever is in contact with the sample surface (a cantilever deflection signal of 1–2 V on the photodiode is sufficient for obtaining a good value). Typically, with a spring constant of approximately 10 pN/nm, the sensitivity values are around 0.07–0.09 V/nm. So 1 V deflection signal on the photodiode corresponds to 110–150 pN.

Acknowledgments

The Swiss National Science Foundation and the ELTEM Regio Project Nanotechnology supported the work. Many thanks to the colleagues who were involved in developing the presented methods.

References

1. Dammer, U., Popescu, O., Wagner, P., Anselmetti, D., Güntherodt, H. J., and Misevic G. N. (1995) Binding strength between cell-adhesion proteoglycans measured by atomic-force microscopy. *Science* **267,** 1173–1175.
2. Evans, E., and Ritchie, K. (1997) Dynamic strength of molecular adhesion bonds. *Biophys. J.* **72,** 1541–1555.
3. Moy, V. T., Florin, E. L., and Gaub, H. E. (1994) Intermolecular forces and energies between ligands and receptors. *Science* **266,** 257–259.
4. Dammer, U., Hegner, M., Anselmetti, D., et al. (1996) Specific antigen/antibody interactions measured by force microscopy. *Biophys. J.* **70,** 2437–2441.
5. Hinterdorfer, P., Baumgartner, W., Gruber, H. J., Schilcher, K., and Schindler, H. (1996) Detection and localization of individual antibody-antigen recognition events by atomic force microscopy. *Proc. Natl. Acad. Sci. USA* **93,** 3477–3481.
6. Evans, E. (1998) Energy landscapes of biomolecular adhesion and receptor anchoring at interfaces explored with dynamic force spectroscopy. *Faraday Dis.* **111,** 1–16.
7. Strunz, T., Oroszlan, K., Schäfer, R., and Güntherodt, H. J. (1999) Dynamic force spectroscopy of single DNA molecules. *Proc. Natl. Acad. Sci. USA* **96,** 11277–11282.
8. Schwesinger, F., Ros, R., Strunz, T., et al. (2000) Unbinding forces of single antibody-antigen complexes correlate with their thermal dissociation rates. *Proc. Natl. Acad. Sci. USA* **97,** 9972–9977.
9. Schumakovitch, I., Grange, W., Strunz, T., Bertoncini, P., Güntherodt, H.-J., and Hegner, M. (2002) Temperature dependence of unbinding forces between complementary DNA strands. *Biophys. J.* **82,** 517–521.
10. Evans, E. (2001) Probing the relation between force-lifetime-and chemistry in single molecular bonds. *Annu. Rev. Biophys. Biomol. Struct.* **30,** 105–128.
11. Merkel, R. (2001) Force spectroscopy on single passive biomolecules and single biomolecular bonds. *Phys. Rep.* **346,** 343–385.
12. Merkel, R., Nassoy, P., Leung, A., Ritchie, K., and Evans, E. (1999) Energy landscape of receptor-ligand bonds explored with dynamic force spectroscopy. *Nature* **397,** 50–53.
13. Di Paris, R., Strunz, T., Oroszlan, K., Güntherodt, H.-J., and Hegner, M. (2000) Dynamics of molecular complexes under an applied force. *Single Mol.* **1,** 285–290.
14. Marszalek, P. E., Lu. H., Li, H. B., al. (1999) Mechanical unfolding intermediates in titin modules. *Nature* **402,** 100–103.
15. Strunz, T., Oroszlan, K., Schumakovitch, I., Güntherodt, H.-J., and Hegner, M. (2000) Model energy landscapes and the force-induced dissociation of ligand-receptor bonds. *Biophys. J.* **79,** 1206–1212.

16. Schwarzenbach, M. S., Reimann, P., Thommen, V., et al. (2002) Interferon α-2a interactions on glass vial surfaces measured by atomic force microscopy. *PDA J. Pharm. Sci. Technol.* **56,** 78-89.
17. Hutter J. L. and Bechhoefer, J. (1993) Calibration of atomic-force microscopetips. *Rev. Sci. Instrum.* **64,** 3342–3342.
18. Izenman, A. J. (1991) Recent developments in nonparametric density estimation. *J. Am. Stat. Assoc.* **86,** 205–224.
19. Hermanson, G. T. (1996) *Bioconjugate Techniques*, Academic Press, San Diego.
20. Hegner M. (2000) DNA handles for single molecule experiments. *Single Mol.* **1,** 139–144.